KnE Engineering

Conference on Science and Engineering for Instrumentation, Environment and Renewable Energy

28-29 September 2015

Knowledge E
Engaging minds

KnE Engineering

ICoSE Conference Proceedings
ICoSE Conference on Instrumentation, Environment and Renewable Energy (2015)

ICoSE Committee Members

International Advisory Board:

1. Prof. Dr.-Ing. Hans-Rolf Traenkler (UniBw Muenchen, GERMANY)
2. Prof. Dr. Ozamu Kozan (Kyoto University, JAPAN)
3. Prof. Dr. Mohamad Deraman (UKM, MALAYSIA)
4. Prof. Dr.-Ing. Mitra Djamal (ITB Bandung, INDONESIA)
5. Prof. Dr.-Ing. Dieter Pawelczak (UniBw Muenchen, GERMANY)
6. Prof. Dr. Erwin Amirudin (Universitas Riau, INDONESIA)
7. Prof. Dr. Muhamad Mat Salleh (UKM, MALAYSIA)
8. Prof. Dr. Andrivo Rusdy (NUS, SINGAPORE)
9. Prof. Dr. Warsito (Universitas Lampung, INDONESIA)
10. Prof. Dr. Charles I. Sukenik (ODU, USA)
11. Dr.-Ing. Alexander Scholz (TU Muenchen, GERMANY)
12. Dr. Yanuar Hamzah (Universitas Riau, INDONESIA)
13. Dr. Frank Alexander (USF Florida, USA)
14. Dr.-Ing. Heinrich Ruser (UniBw Muenchen, GERMANY)
15. Dr.-Ing. Martin Koch (DTU, DENMARK)

Chairman

Dr.-Ing. Lazuardi Umar

Co-Chairman

Dr.-Ing. Joachim Wiest

Committee Members

1. Dr. Iwantono Barnawi
2. Dr. Saktioto
3. Dr. Minarni
4. Dr. Juandi M
5. Dr. Awitdrus
6. Dr. Zulharman
7. Dr. Kuwat Triyana
8. Dr. Wahyu Widanarto
9. Dr. Sakti Setyawan
10. Dr. Cuk Imawan
11. Dr. Ayi Bahtiar
12. Dr. Zulharman

Secrétariat

1. Valendry Harvenda
2. Noni Febriani
3. Usman Malik
4. Wildan Adli
5. Dian Putri Oktavia
6. Elsa Maulina
7. Saidatun Khofiffah

Organizers

Universitas Riau	cellasys GmbH	TU Muenchen	Indonesian Physical Society	IMEN UKM Malaysia

Sponsors

Jurusan Fisika FMIPA Universitas Riau	Kemenristek Dikti Indonesia	Mitra Intimarga

Table of Contents

The role of SiC on the Desorption Temperature of Mg-based Hydrogen Storage Materials Prepared by Intensive Milling Method
Zulkarnain Jalil, Adi Rahwanto, Erfan Handoko, and Bambang Soegijono
6 pages, DOI 10.18502/keg.v1i1.498

Preparations and Characterizations of Hierarchical Macropore Activated Carbon Monolith Electrode from Rubber Wood for Supercapacitor Application
Erman Taer, Yusriwandi, Rika Taslim, I.D.M. Syam, and Mohamad Deraman
6 pages, DOI 10.18502/keg.v1i1.499

Effect of Aging Time on the Synthesis of Fe-doped TiO2 Thin Films by Spin Coating Method
Dahyunir Dahlan and Muhammad Anshori
6 pages, DOI 10.18502/keg.v1i1.500

Numerical Study of Plasmon Resonance Silver Nanoparticles Coated Polyvinyl Alcohol (PVA) using Bohren-Huffman-Mie Approximation
Dede Djuhana, Cuk Imawan, Vivi Fauzia, Adhi Harmoko, Windri Handayani, and Miftahussurur H. Putra
7 pages, DOI 10.18502/keg.v1i1.501

Effect of Methylammonium Iodide (CH3NH3PbI3) Perovskite Concentration on the Performance of Perovskite Solar Cell
AltafYahya AL-she'irey, Akrajas Ali Umar, Muhamad Mat Salleh, and MohdYusriAbd Rahman
6 pages, DOI 10.18502/keg.v1i1.502

Transmission Electron Microscopy Study of Magnetic Domain of Cobalt-Samarium Thin Films Fabricated Using DC Magnetron Sputtering Technique
Erwin Amiruddin and Adhy Prayitno
8 pages, DOI 10.18502/keg.v1i1.503

First Principle Calculation of Electronic, Optical Properties and Photocatalytic Potential of CuO Surfaces
Faozan Ahmad, M Kemal Agusta, and Hermawan K Dipojono
7 pages, DOI 10.18502/keg.v1i1.504

Development of a FAHP Algorithm Based Performance Measurement System for Lean Manufacturing Company
Anita Susilawati and John Tan

Preface

The 1st Conference on Science and Engineering for Instrumentation, Environment and Renewable Energy (ICoSE) 2015 was held at the Hotel Pangeran Pekanbaru, Indonesia, September 28-29, 2015.

This is a forum for more than 200 researchers, scientists and students from around 9 countries to share the latest research findings and exchange ideas regarding the innovations in measurement systems, and improvements to instrumentation for environmental analysis as well as selected topics in renewable energy. It also provides a medium for direct contacts among researchers and scientists for new international relationships and spark future collaborative research projects. The conference is jointly organized by the University of Riau (UNRI) Indonesia, cellasys GmbH R&D, Institute of Microengineering and Nanoelectronics (IMEN) Universiti Kebangsaan Malaysia and the Technische Universitaet Muenchen (TUM) Germany.

We have received approximately 160 abstracts to be presented in the seminar and around 108 papers are going to a peer-review process by at least two expert referees for a publication in this periodical and 70 papers have been accepted under rigorous and through revisions by editors and reviewers in respected fields. The accepted papers are organized into 7 chapters:

Chapter 1: Measurements, Sensors and Control Systems

Chapter 2: Materials for Electronics, Energy Conversion and Photocatalysts

Chapter 3: Renewable Energy Utilization

Chapter 4: Optoelectronics and Photonics

Chapter 5: Composites

Chapter 6: Environmental Monitoring

Chapter 7: Computational and Modelling

We are grateful to Kementerian Riset, Teknologi, dan Pendidikan Tinggi, Direktorat Jenderal Pembelajaran dan Kemahasiswaan Indonesia, Universitas Riau, Cellasys GmbH, FMIPA UR, Jurusan Fisika FMIPA UR, IMEN Universiti Kebangsaan Malaysia, Indonesian Physical Society (HFI) for providing financing and technical supports to this seminar.

Finally, we would like to take this opportunity to thank also all the members of the organizing committee, all the authors, all the reviewers, and all the local volunteers for their effort and valuable support to make ICoSE 2015 a reality. Special thanks go to the ICoSE staff for their outstanding service.

KnE Engineering

Knowledge E
Engaging minds

Conference Paper

Development of Digital Scale Based on Fluxgate Sensor

Zannuraini, Mitra Djamal, and Widyaningrum Indrasari

[1]Institut Teknologi Bandung, Jl. Ganesa No. 10, Bandung 40132, Indonesia
[2]Institut Teknologi Sumatera, Jl. Terusan Ryacudu, Desa Way Hui, Kec. Jati Agung, Lampung Selatan 35365, Indonesia
[3]Universitas Negeri Jakarta, Jl. Pemuda No. 10, Jakarta Timur 13220

Abstract

Fluxgate is a magnetic sensor which works by comparing the measurement magnetic field with the magnetic field reference. This research aims to develop digital scales using fluxgate sensor. The steps involved were sensor development, characterization, distance and mass calibration of the fabricated sensor. Here, a digital scale based on fluxgate sensor with oval vitrovac 6025Z type core, 360 windings of excitation coil and 240 windings of pick up coil was successfully fabricated. Characterization result shows that the sensor has 1669.2 mV/μT sensitivity and working area of about $\pm$ 1.9 μT, with maximum absolute error found out to be around 0.0573 μT with maximum relative error is 1.464%. Calibrated sensor value obtained reveals that the sensor works from 15.86 until 27.00 mm in distance, utilizing equation of relationship between mass and output voltage $m(V_o) = 418,79V_o^2 - 346V_o - 134.32$ with the maximum relative error obtained as low as 1.49%.

Keywords: Digital scale, Fluxgate sensor, mass calibration, ferromagnetic core

OPEN ACCESS

1. Introduction

Fluxgate is a magnetic sensor which works by comparing the measurement magnetic field with the magnetic field reference. The advantages of this sensor are small dimension, high temperature stability, low power consumption [1] compared to other available magnetic sensor, makes the measurement of very low magnet field $10^{-1} - 10^6$nT become possible, with high linearity and great sensitivity, reliability, relative simple, and more economical [2]. In order to improve the quality and output sensor, various studies has been reported by other researchers by modifying the ferromagnetic core structure [3], dimension and structure sensor, along with signal processing circuit. Various method has been reported in the development of sensor making such as conventional method (winding wire conventionally), Printed Circuit Board (PCB), micro technology, and hybrid [4]. Other variables that give effect to sensor output are geometry sensor, coil configuration, layer quantity and material of ferromagnetic core [1]. Other possible applications utilizing fluxgate sensor are vibration sensor [5], detector of magnetic material in soil subsurface [6], non-contact current and displacement measurements [7], etc. In this work, we aim to develop a digital scale utilizing fluxgate sensor.

How to cite this article: Zannuraini, Mitra Djamal, and Widyaningrum Indrasari, "Development of Digital Scale Based on Fluxgate Sensor," *KnE Engineering*, vol. 2016, 8 pages. DOI 10.18502/keg.v1i1.476

Page 1
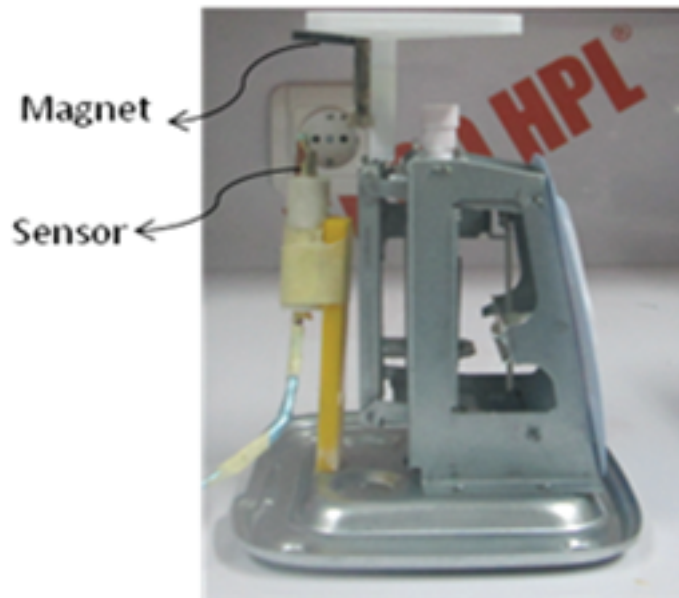
Figure 1: Frame of spring scale.
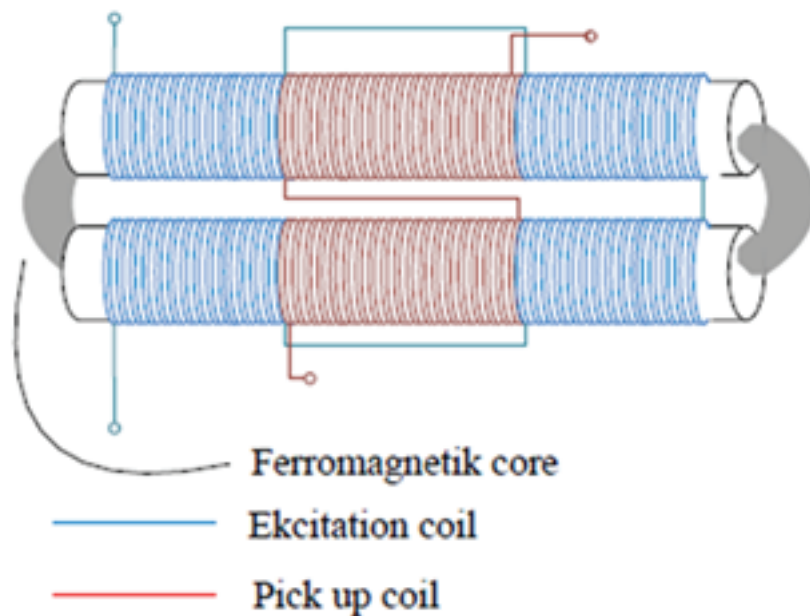
Figure 2: Design of fluxgate sensor element.

2. Method

The development of digital scale based on fluxgate sensor study used a frame of spring scale that has modified with addition fluxgate sensor, and magnet which generates a magnetic field 33.7 mT on its surface, as shown in Figure 3.

When load was put on the scale, the distance between sensor and magnet will decrease and the voltage output of sensor will increase, this change of voltage output is converted to mass quantity.
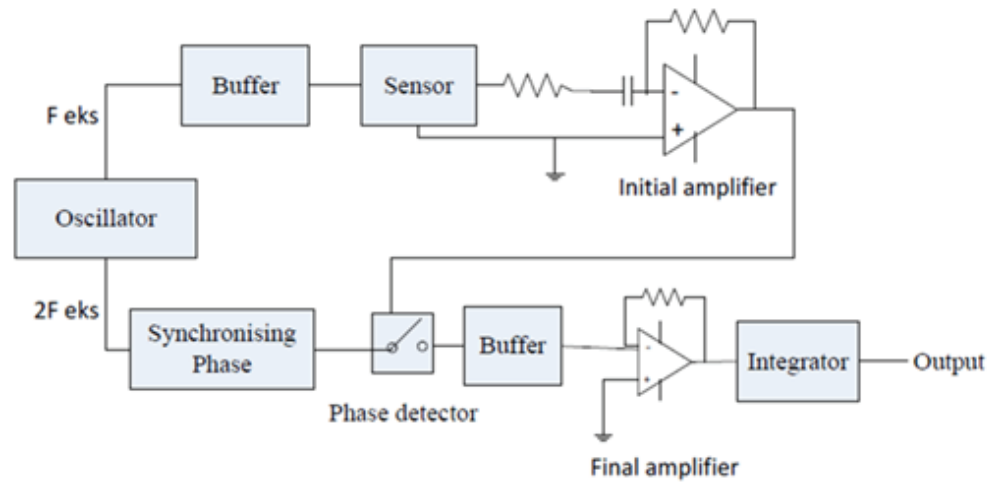
Figure 3: Scheme analog signal processing circuit.

Conventional fluxgate sensor fabricated in this study comprises of two pick up coils and four excitation coils. Each excitation coil consists of 90 windings while the pick-up coil consists of 120 windings. This coil is rolled on the sleeve insulator, and ferromagnetic core is inserted into the sleeve, as shown in the fig 3. The shape of ferromagnetic core is oval, chosen due to the core relatively symmetry results in low demagnetization effect and high sensitivity. The ferromagnetic core is Vitrovac 6025Z, as it has good magnetic properties. Based on Widyaningrum's summary (2014), superiority of vitrovac is having high permeability, (μr $\sim 10^5$), saturated by magnetic induction about 0.58 T, having low coercivity and power dissipation, high temperature stability and more resistant to external mechanical influences [6].

There are two types of circuit work in the analog signal processing circuit namely excitation circuit which generates reference magnetic field and pick up circuit that converts magnetic field to electric signal which was represent by external magnetic field.

Fluxgate needs to be characterized in order to get information about fluxgate characteristic using calibrator coil. Calibrator coil used in this study is a solenoid with diameter about 4 cm, consist of 600 windings of wire that had diameter about 0.7 mm. Characterization performed in Faraday cage, with sensor was placed in the calibrator that was positioned parallel to the direction of the east - west of the earth to reduce the influence of Earth's magnetic field on the measurement results. Then, the calibrator was energized by DC current in the range of 0.01 - 20 mA to get a magnetic field value according to eq. 1 [4].

$$B\left(I\right) = 1.9568 \cdot I - 0.0347 \tag{1}$$

The next step was distance calibration of sensor, the distance between magnet source and sensor were changed in micrometer order, this change makes output voltage of sensor changes too. So this process was obtained connection the distance to magnetic field that is represented by the output voltage. Next action is mass calibration, it is aim to get connection between the change of mass to sensor output with

Figure 4: Standard loads that used in mass calibration.
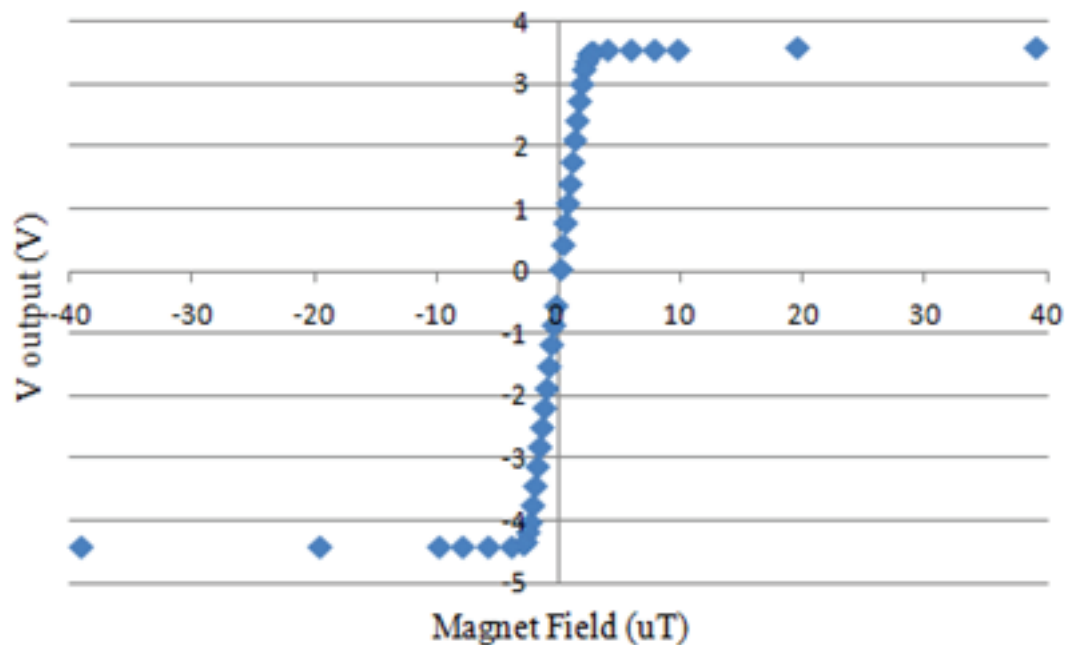
Figure 5: Hysteresis curve.

mass changes each 10 gram. Mass that was used is standard loads as shown in Figure 4.

The output of the signal processing circuit was analog voltage, and then it was converted to digital using microcontroller Arduino uno Atmega328. The result of mass measurement will be displayed on LCD 1602A which consist of 16 columns and 2 rows.

3. Result and Discussion

Fluxgate sensor was fabricated using conventional techniques with configuration 360 winding of excitations and 240 winding of pickup, having vitrovac 6025Z type core. Hysteresis curve as shown in Figure 5 obtained by characterization using calibrator coil, where magnet field value was obtained by Eq. 1.

Figure 6 explain that the core is saturated by magnetic field at ± 2.7 μT, shown that the output will be constant although the current was increased.
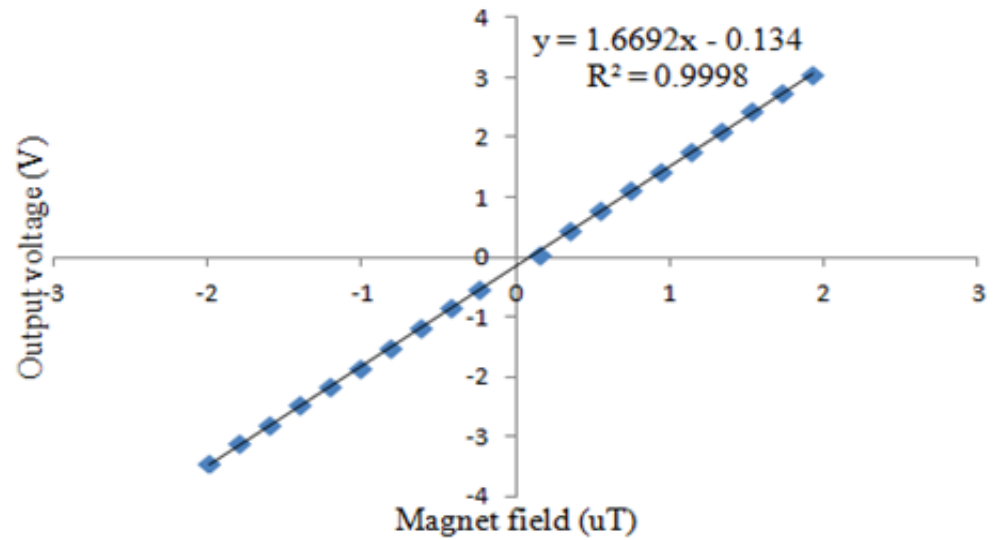
Figure 6: Graph of linear sensor in range ± 1.9 μT.
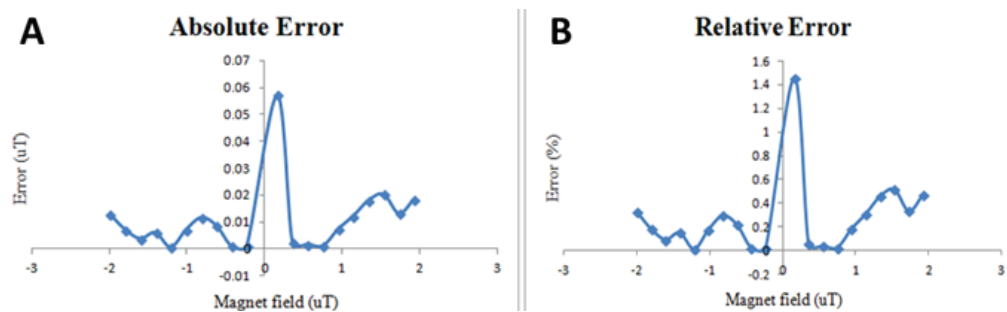
Figure 7: Error of sensor at range 1.9 μT.

The linear area from hysteresis curve is shown fig 8, explains that the sensor works in a range of ± 1.9 μT with linear equation (Eq. 2) that connecting output voltage (volts) to magnetic field (μT) on the work area.

$$V_o = 1.6692B - 0.134 \qquad (2)$$

Eq. 2 reveals sensitivity sensor obtained was about 1.6692 V/μT or 1669.2 mV/μT and resolution sensor was found to be depending on the output voltage (Eq. 3) with R^2 value of 0.9991.

$$B(V_o) = 0.599V_o + 0.0803 \qquad (3)$$

Absolute error of sensor is difference which is obtained by comparing result of magnetic field calculation in eq. 1 and result of measurement in eq. 3, as shown in fig. 7. The maximum absolute error obtained is 0.0573 μT (a) and maximum relative error sensor is 1.464% (b) at magnetic field of 0.161 μT, due to the magnetic field measured was very weak.

The result of calibration sensor to distance was shown in fig. 8, explains the working area of sensor at a range of 15.85 to 27.00 mm. In this range, the smaller distance
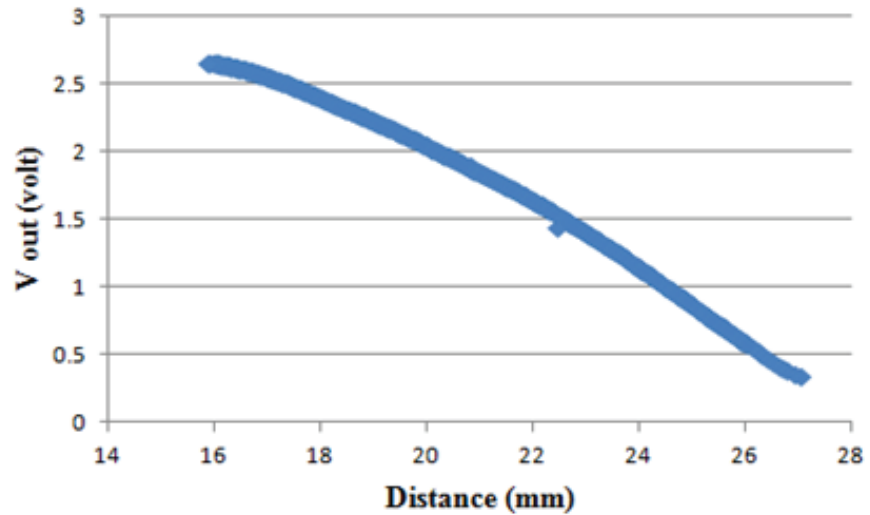
Figure 8: Graph of sensor calibration to distance.
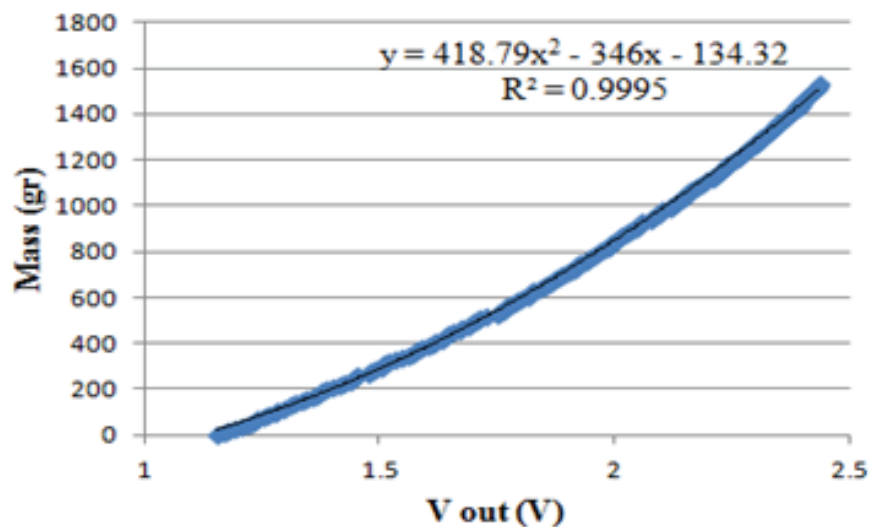
Figure 9: Mass value depends on output voltage.

between sensor and magnet, the bigger voltage output sensor that represents the measured magnet field. This result was then used to determine the distance between sensor and magnet on the scale.

To determine the mass of the measurement results, we need to use the function of the mass to the output voltage curve approach as shown in Figure 9 that is obtained by mass calibration.

From this curve with polynomial approach, we got the mass function that depends on output voltage (Eq. 4). This equation will be inserted into microcontroller as the mass of measurement results of scale.

$$m(V_o) = 418.79\, V_o^2 - 346V_o - 134.32 \tag{4}$$
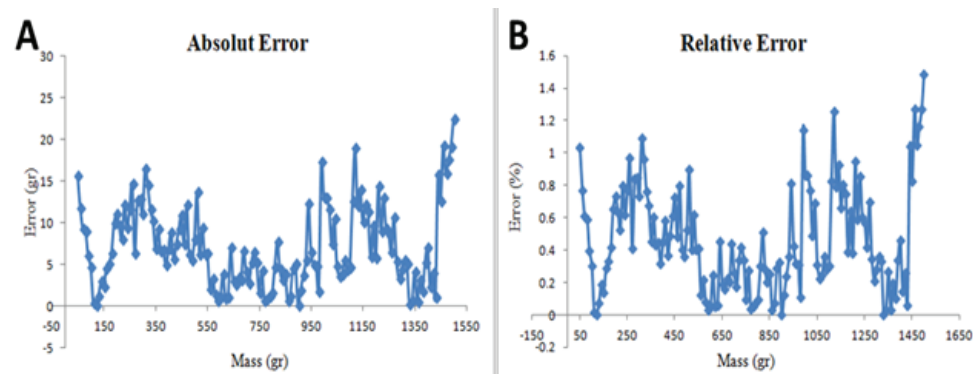
Figure 10: Absolute and relative error of digital scale.

By comparing the mass of the equation 4 with the actual mass, there is difference that is called absolute error. The maximum absolute error is 22.4 gram at measurement of mass about 1500 gram (fig. 10), and the maximum relative error is 1.49%. It also shows that the range that can be measured by the scale obtained are from 50 - 1500 gram.

4. Conclusion

Fluxgate sensor as magnetometer measures the magnetic field by comparing the measured magnetic field with the magnetic field reference. This type of sensor was successfully developed and applied in digital scales. Fluxgate sensor developed by conventional techniques, consisting of 360 excitation coils and 240 pick-ups coils with the ferromagnetic core use is Vitrovac 6025Z type. This sensor with a sensitivity of 1669.2 mV/uT, resolution 0.5991 uT/V, working in the range $\pm$ 1.9 μT, having the maximum absolute error of 0.0573 μT and the maximum relative error of 1.464%. The sensor works very well at a range 15.86 to 27 mm, thus the distance between the source magnet and sensors was regulated in this range. The maximum error absolute of scale is 22.4 gram and relative error is 1.49%. Range of mass measurement of digital scale are 50 – 1500 gram.

References

[1] P. Ripka, in *Magnetic Sensor and Magnetometers*, Artec House, 2001.

[2] Bornhoft dan Trenkler, in *Sensors a comprehensive survey*, **vol 5**, VCH Publishers Inc, New York, 1989.

[3] J. Lei, C. Lei, and Y. Zhou, Analysis and comparison of the performance of MEMS fluxgate sensors with permalloy magnetic cores of different structures, *Measurement*, **46**, 710–715, (2012).

[4] Yulkifli, Pengembangan Elemen Fluxgate dan Penggunaannya untuk Sensor-sensor Berbasis Magnetik dan Proksimiti, Disertasi ITB, 2010.

[5] S. Putra, Pengembangan Sensor Getaran Dua Dimensi Menggunakan Sistem Sensor Fluxgate, Proyek akhir ITB, 2011.

[6] W. Indrasari, in *Pengembangan Sistem Deteksi Material Magnetik Di Bawah Permukaan Tanah dengan Metode Induksi Elektromagnetik Berbasis Sensor Fluxgate*, Disertasi ITB, 2014.

[7] W. Indrasari, et al., in *Sensor Magnetik Fluxgate: Karakteristik dan Aplikasinya*, 207–214, Indonesian J of Materials Science, October Edition, 2007.

KnE Engineering

Knowledge E
Engaging minds

Conference Paper

Microseismic Wave Measurements to Detect Landslides in Bengkulu Shore with Attenuation Coefficient and Shear Strain Indicator

Muhammad Farid and Wiwit Suryanto

[1]Department of Physics, Mathematical and Natural Science Faculty, Bengkulu University, Indonesia
[2]Laboratory of Geophysics, Mathematical and Natural Science Faculty, Gadjah Mada University, Indonesia

Abstract

It has been detected that the condition of landslides that occurred in Bengkulu Shore can change the position of the shoreline. This research aimed to (1) calculate of shear strain (γ) and attenuation coefficient ($\acute{a}$) value based on microseismic data in coastal areas that experienced landslides; (2) determine the correlation between levels of landslides with shear strain and attenuation coefficient value (3) determine the correlation between the shear strain and attenuation coefficient value. Microseismic data were processed and analyzed quantitatively using the Horizontal to Vertical Spectral Ratio method (HVSR) to obtain the ground vibrations resonance frequency (f_o) and amplification factor (A). Shear strain value was calculated from the of f_o, A and Peak Ground Acceleration (α_{max}) value. Peak Ground Acceleration value was calculated based on 100-year period of recorded earthquake data. Attenuation coefficient was calculated based on the equation (2). The results of study showed that the value of shear strain in the coastal areas varied from $1.0 \times 10{-4}$ to $3.6 \times 10{-3}$, in accordance with the conditions of landslides. The attenuation coefficient value varied from 0.005 to 0.020. Level of landslides that occurred varied from moderate, to very severe. There was a tendency that the more severe the landslide level, the greater the shear strain and attenuation coefficient value were.

Keywords: Shear strain, attenuation coefficient, shore landslide

🔓 **OPEN ACCESS**

1. Introduction

Landslides on the shore in large numbers will cause the shoreline to shift landward (retrogradation). Landslides can be triggered by the occurrence of earthquakes. Schulz, et al (2012) state that large earthquakes that occur every 300-500 years trigger landslides in the coast of Oregon-United States [1]. There is an empiric correlation between the magnitude of the earthquake and landslides [2]. The earthquakes in Chi-Chi Taiwan [3], in Costa Rica, El Salvador, Guatemala and Panama often trigger landslides. The magnitude of the landslide volume is proportional to the strength of the earthquake [4]. The factors of depth, quality of the rock mass, groundwater conditions and the

How to cite this article: Muhammad Farid and Wiwit Suryanto, "Microseismic Wave Measurements to Detect Landslides in Bengkulu Shore with Attenuation Coefficient and Shear Strain Indicator," *KnE Engineering*, vol. 2016, 7 pages. DOI 10.18502/keg.v1i1.477

Page 1

Figure 1: (a) Moderate-level Landslide; (b) Severe-level Land-slide; (c) Extremely severe-level Landslide.

strength of earthquakes affect the magnitude of the landslide volume [5]. There is a significant correlation between the magnitude moment and the volume of landslides.

The stronger the earthquake, the greater the landslide volume is [6]. This research was aimed at determining the correlation between shear strain at the sediment layers and landslide level and the correlation between attenuation coefficient and landslide level in the coastal areas. Landslide conditions in Bengkulu coast are shown in Fig.1.

2. Theoretical Framework

2.1. Shear Strain

Shear strain (γ) in the sediment layer indicates the ability of the soil layer to be stretched when an earthquake [7].

The value of γ is formulated as [8]:

$$\gamma = K_g(1000 \times 10^{-6})\alpha_{max} \tag{1}$$

Where γ is the shear-strain, K_g is the seismic vulnerability index, and α_{max} is the peak ground acceleration. Value of a_{max} is calculated using the Fukushima-Tanaka Eq. [9]

$$Log\ \alpha_{max} = 1.3 + 0.41M_w - Log(R \times 0.32.10^{0.41Mw}) - 0.0034R \tag{2}$$

2.2. Attenuation Coefficient

Formulated as [10]

$$\acute{\alpha} = \frac{\pi(f2 - f1)}{v} \tag{3}$$

Where $(f_2 - f_1)$ is bandwidth, v is S-wave velocity.
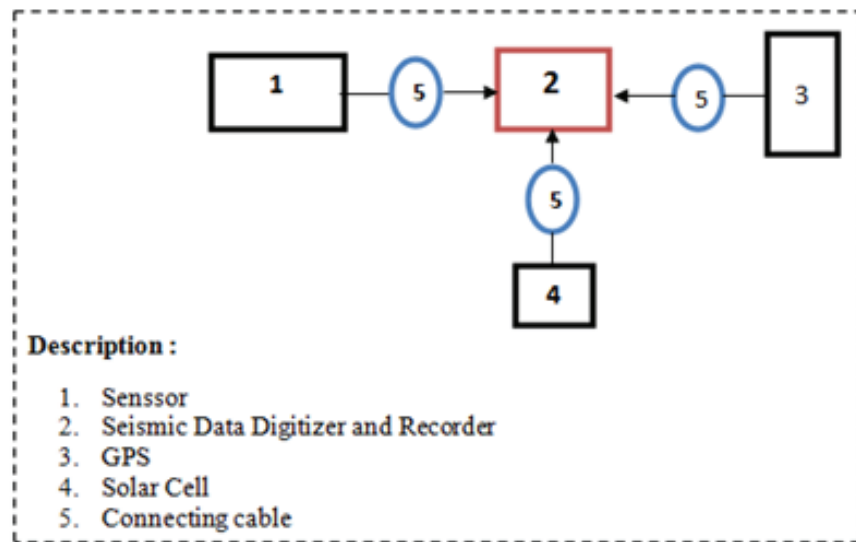
Figure 2: Parts of short period Seismometer.
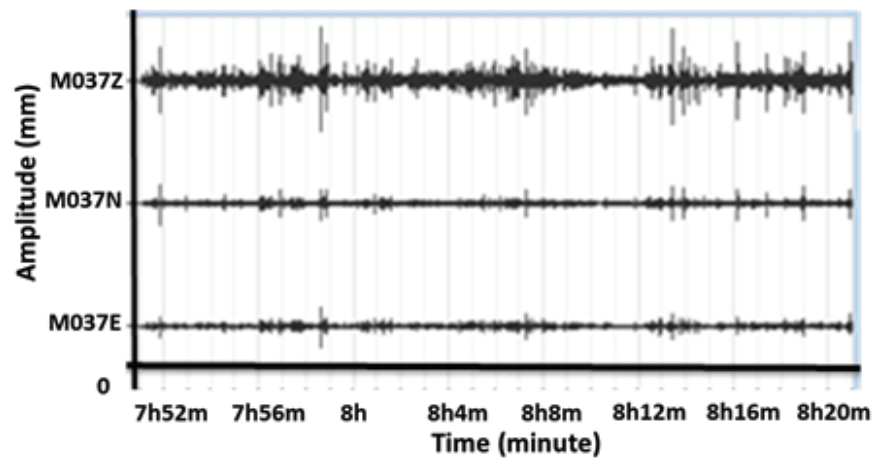
Figure 3: Data record of soil vibration in seismometer.

3. Data Acquisition

3.1. Microseismic Data

Microseismic data were acquired directly using the 3 components of short period seismometer, as shown in Fig. 2.

Data were recorded for 30 minutes at each measurement location. The sampling frequency was 100 Hz, the frequency ranged between 0.5 to 20 Hz, and filter used was a low pass filter. Microseismic survey technique conducted referred to the standard *SESAME* European Research Project 2004. Measurement data were recorded directly by seismometer as shown in Fig. 3.

Fig. 3 is a soil vibration recorded in the monitor and were analyzed with Geopsy using *HVSR* (Horizontal to Vertical Spectral Ratio) method. One of the results data processed can be seen in Fig. 4, a sepectral peak which represents f_o value at the horizontal
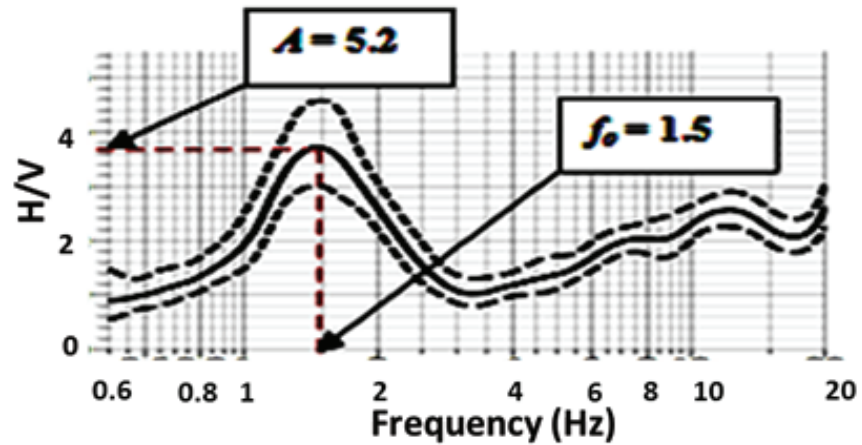
Figure 4: The results of the data processing Station-2.

axis and *A* value in the vertical axis. The value of *f* at the spectral peak is dominant frequency (f_o) and the value of *H/V* at the spectral peak is amplification factor (*A*).

3.2. Earthquake Data

Earthquake data from 1900 to 2010 were taken from the office of the Meteorology, Climatology and Geophysics Agency as secondary data. The data included the magnitude, location and distance from the earthquake center to the station. From these data the value of the Peak Ground Acceleration (α_{max}) was calculated using Fukushima-Tanaka atenuation in the Eq. (2).

4. Results And Discussion

The results of data processing from one of station can be seen in Fig. 4, namely a spectral peak from data processing Sstation-2 which produce value f_o is 1.5 and *A* is 5.2.

The value of f_o and *A* used to calculate K_g, namely K_g is A^2/f_o. The value of α_{max} calculated using Eq. (2), so that γ in Eq. (1) can be calculated. The next step is to calculate the attenuation coefficient ($\acute{\alpha}$) by using Eq. (3), where f_2–f_1 is bandwidth and v is s-wave velocity (v_s) is calculated by using,

$$v_s = \frac{(v_p - 1.36)}{1.16} \tag{4}$$

The value of v_p determined from USGS-table according to the coordinates of each station. The value of $f_2 - f_1$ manually calculated from the position of bandwidth, such as shown the Station-1 data in Fig. 5.

The value of $f_2 - f_1$ at the Fig. 5 is 1.7, v_p value at Station-1 according to the USGS table is 311 m/s. By using Eq. (3) obtained $\acute{\alpha}$ is 0.02. Results of research on f_o, *A*, α_{max}, shear strain, and attenuation coefficient in the coastal areas can be seen in Table 1.
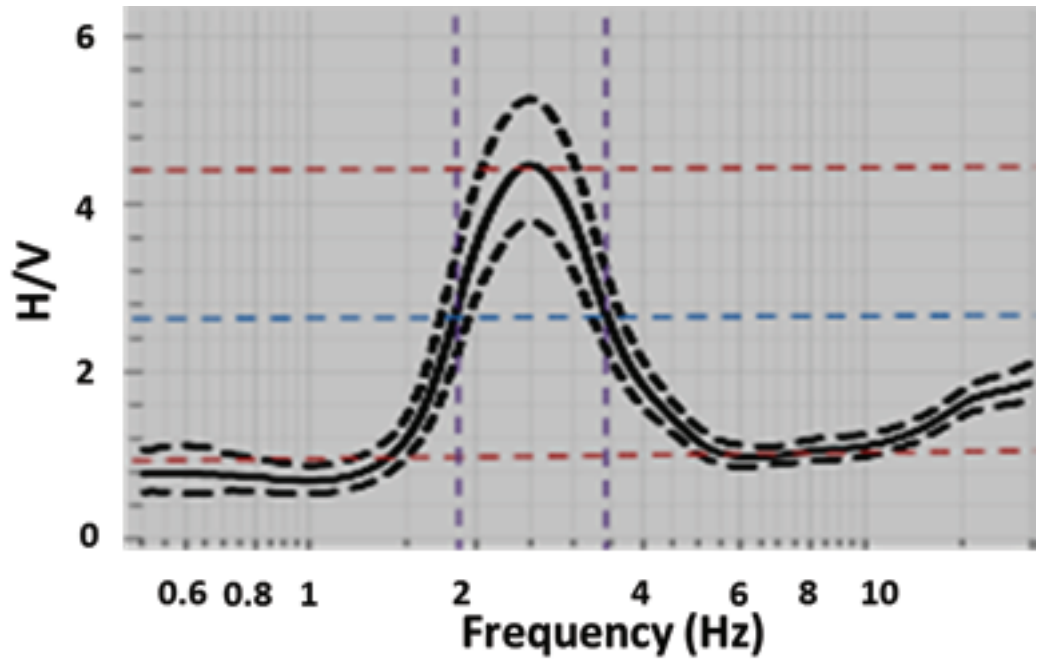
Figure 5: Method of measuring bandwidth ($f_2 - f_1$).

Station	Location		f_o	A	α_{max}	Shear Strain (γ)	Atenuation Coeff. (?)
	Latitude	Longitude					
1	-2.70	101.27	2.5	4.4	250	0.0019	0.02
2	-2.65	101.31	1.5	5.2	302	0.0032	0.015
3	-3.22	101.60	5.0	4.0	433	0.0013	0.022
4	-3.27	101.66	13.9	7.8	592	0.0027	0.022
5	-3.55	102.09	1.5	3.6	161	0.0014	0.01
6	-3.80	102.26	6.5	8.1	451	0.004	0.04
7	-3.53	102.05	4.3	4.4	279	0.0013	0.01
8	-4.02	102.35	0.7	1.1	193	0.0003	0.006

TABLE 1: The results of measurement of f_o, A, α_{max} and the calculation of γ, $\acute{\alpha}$.

The correlation between the shear strain and the attenuation coefficient is shown in Fig. 6.

The values of shear strain and attenuation coefficients changed according to landslide level which occurred in Bengkulu Shore. This difference was indicated by the geological and geomorphological conditions at the shore. The correlation between shear strain and attenuation coefficient tended to be linear. The linear conditions tended to have impacts on the landslide volume. Fig. 1 shows the greater the shear strain and attenuation coefficient values, the greater of landslide volume was. Isihara [11] states that the value of the shear strain will indicates the condition of deformation that occurs on the surface of the soil layer. At the order of shear strain value of 10-6, the sediment only experiences the thrill, but at the order of 10-3, sediment will experience landslides and liquefaction.
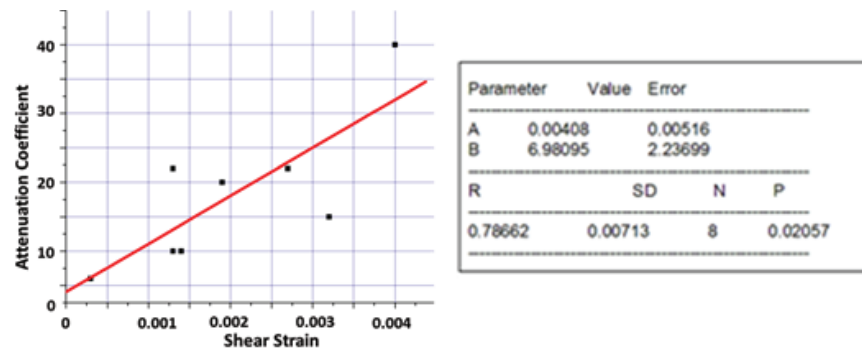
Figure 6: The correlation between shear strain and attenuation coefficient.

There is a tendency that the greater the shear strain, the more severe the landslide level will be. Similarly, there is a tendency that the greater attenuation coefficient value, the worse the condition of the landslide will be. Marzorati [12] stated that the earthquake which occurred in 1997 in Umbrië-Marche, Central Italy triggered landslides and rock falls when soils were strained. Malamud et al. [6] reported a significant correlation between the magnitude moment and landslides volume. Kudo [13] showed the geographical changes for coastal landslides due to shear strain. Our present research has managed to link the value of shear strain with landslides that occurred in Bengkulu coast, similar to research conducted by Isihara [11]. Fig. 2 shows a linear correlation between the value of shear strain and attenuation coefficient. These correlation proved that both can be linked to landslide levels.

5. Conclusion

There is a tendency, that the greater the value of shear strain or attenuation coefficient will the greater the chances of landslides in the region. Correlation between shear strain and attenuation coefficient tend to be linear.

References

[1] W. H. Schulz, S. L. Galloway, and J. D. Higgins, Evidence for earthquake triggering of large landslides in coastal Oregon, USA, *Geomorphology*, **141-142**, 88–98, (2012).

[2] B. D. Malamud, et al., Earth Surface Processes and Landforms Earth Surf. Process (2004)., Landforms 29, 687–711 (2004), Published online in Wiley InterScience www.interscience.wiley.com).

[3] B. D. Malamud, Earthquake Induced Landslides in Taiwan, Earthquake Engineering and Engineering Seismology (2004)., volume 2, nomor 2, September 2000, pp.25-33.

[4] J. J. Bommer and C. E. Rodríguez, Earthquake-induced landslides in Central America, *Eng Geol*, **63**, 189–220, (2002).

[5] C. I. Lei, Earthquake-Triggered Landslides, *1st Civil and Environmental Engineering Student Conference*, (2012).

[6] B. D. Malamud, D. L. Turcotte, F. Guzzetti, and P. Reichenbach, Landslides, earthquakes, and erosion, *Earth Planet Sci Lett*, **229**, 45–59, (2004).

[7] Y. Nakamura, Clear Identification of Fundamental Idea of Nakamura's Technique and Its Application., *World Conference of Earthquake Engineering*, (2000).

[8] M. Farid and K. Sri Brotopuspito, Wahyudi, Sunarto, W. Suryanto, The relationships among ground shear strain, shore characteristics and abrasion on the west coast of Bengkulu Province, Indonesia, *CJASR*, **2**, 143–153, (2013).

[9] M. Farid, Microseismic Study To Detect Shoreline Changes With Seismic Vulnerability Index, 2014, Peak Ground Acceleration And Ground Shear Strain Indicator In The Bengkulu Province, Dissertation, Gadjah Mada University, Yogyakarta, 2014, pp. 63-64.

[10] M. Farid and K. Sri Brotopuspito, in *Wahyudi, Sunarto, W. Suryanto, Ground Shear Strain and Rate of Erosion in The Coastal Area of North Bengkulu, Indonesia, Advanced Materials Research*, **vol 896**, 521–524, Trans Tech Publications, Switzerland, 2014.

[11] K. Ishihara, in *An Introduction to Soil Dynamic Mechanism*, Japan, 1982.

[12] S. Marzorati, L. Luzi, and M. De Amicis, Rock falls induced by earthquakes: a statistical approach, *Soil Dyn Earthquake Eng*, **22**, 565–577, (2002).

[13] K. Kudo, Practical estimates of site response, State-of-the-Art report (1995)., In: Proceedings of the Fifth International Conference on Seismic Zonation, October 17-19, Nice, France, Ouest Editions Nantes, 3, 1878-1907.

KnE Engineering

Knowledge E
Engaging minds

Conference Paper

Sinogram Restoration for Sparse Projections Applied to Noisy Data in Ultrasound Tomography

Kusminarto[1], Catur Edi Widodo[2], Gede Bayu Suparta[1], and Suryono[2]

[1]Department of Physics, Universitas Gadjah Mada, Yogyakarta, Indonesia
[2]Department of Physics, Universitas Diponegoro, Yogyakarta, Indonesia

*Corresponding Author:
Kusminarto;
kusmin@ugm.ac.id

🔓 **OPEN ACCESS**

Abstract

In some cases the number of projections in a set of tomography data is limited. This can be seen from their sinogram. If this kind of data is reconstructed, the image produced will be deteroited. In order to overcome this problem an algorithm for restoring the incomplete sinogram has been developed in previous work. In that work the developed algorithm was tested using ideal data from Shepp-Logan panthom. In this paper the same algorithm is applied to restore incomplete and noisy data in ultrasound tomography. The phantom used in this study is a concrete cylinder with a diameter of 10.62 cm. Inside cylinder there are 6 holes with a diameter of 2 cm each. These holes were filled with various materials. The phantom were scanned in ultrasound tomography scheme and the resulted sinogram then reconstructed with and without sinogram restoration. Using contrast to noise ratio (CNR) indicator the reconstructed image with sinogram restoration is better than that without sinogram restoration.

Keywords: Car; transporters; metabolism; pregnancy; nuclear receptor

1. Introduction

Tomography is an imaging technique to see the internal structure of an object by using any kind of penetrating wave or particle. The tomography image in this technique represents the cross-sectional part of the object. This is obtained by reconstructing the projection data taken from various angle of projection. These projections are presented in a Radon space as a sinogram. The optimum number of projection to obtain good image is $K = (1/2) \, \pi \, N$, where N is the number of raysum per projection [1]. In some cases the number of projection is far less than the optimum value, in other words the sinogram consists of incomplete projections. For examples due to unstable power supply during the scanning process this can cause many projections are broken or missing. In medical application of tomography the radiation dose received by patient has become a consideration. The more projections collected the more radiation dose received.

To overcome this problem researchers have developed methods to recover the missing projections or to restore the sinogram in order to get the optimum number of projections and resulting a good image. Kolehmainen et al proposed an iterative

How to cite this article: Kusminarto, Catur Edi Widodo, Gede Bayu Suparta, Suryono, "Sinogram Restoration for Sparse Projections Applied to Noisy Data in Ultrasound Tomography," *KnE Engineering*, vol. 2016, 5 pages. DOI 10.18502/keg.v1i1.478

Page 1
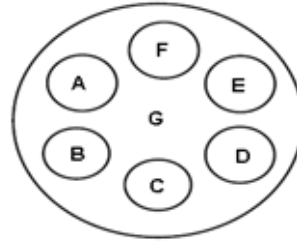
Figure 1: Holes configuration inside a cylindrical sample [9].

reconstruction, with an estimated value based on the theory of evolution [2]. In this method the Shepp-Logan phantom can be reconstructed by using 9 projections. Recur et al proposed an image reconstruction using mojette transformation of the sinogram data [3]. Reconstruction with mojette transformation does not require a fixed interval of angle of projections. This means that if the angle of projection varies due to some projections are missing, the image reconstruction still can be performed. Herman and Davidi proposed a reconstruction based on total variation minimization [4]. An image reconstruction using the metric labeling has been proposed by Singh et al [5]. Shepp-Logan phantom can be properly reconstructed using 10 projections. Rahim et al proposed a linear backprojection-based reconstruction followed by a correction value of each pixel by dividing the pixels into 8 small triangles. This method is able to reconstruct a small rectangle and a large circle using 4 projections [6]. A tomography image reconstruction using combination of wavelet transform and algebraic reconstruction technique has been proposed by Yu and Wang. In this technique the Shepp-Logan phantom can be properly reconstructed using 25 projections [7]. Widodo et al proposed a reconstruction using a sinogram interpolation of the sparse sinogram to obtain a sinogram wich fullfil the Nyquist criterion. With this method, the digital Shepp-Logan phantom with size of 250x250 can be reconstructed using 9 projection only [8]. In this paper, the sinogram interpolation proposed by Widodo et al [8] was applied to a sparse noisy sinogram of ultrasound tomography.

2. Materials and Method

The phantom is made of concrete cylinder with a diameter of 10.62 cm as shown in Figure 1. In the cylinder, there are 6 holes with a diameter of 2 cm to put some kind of mixture samples with compositions shown in Table 1.

The concrete phantom was then scanned as many as 127 raysums per projection. To simulate a sparse projection the number of projection and interval angle of projection were arranged as follows: Six sinograms with sparse regular projection data were created using $3.6°$ (50 projections), $4.5°$ (40 projections), $7.2°$ (25 projections), $9°$ (20 projections), $18°$ (10 projections), and $36°$ (5 projection) of the angular step, respectively.

The above sinograms are then interpolated to obtain 200 projections in each sinogram using the algorithm that has been developed in the previous work [8], the image
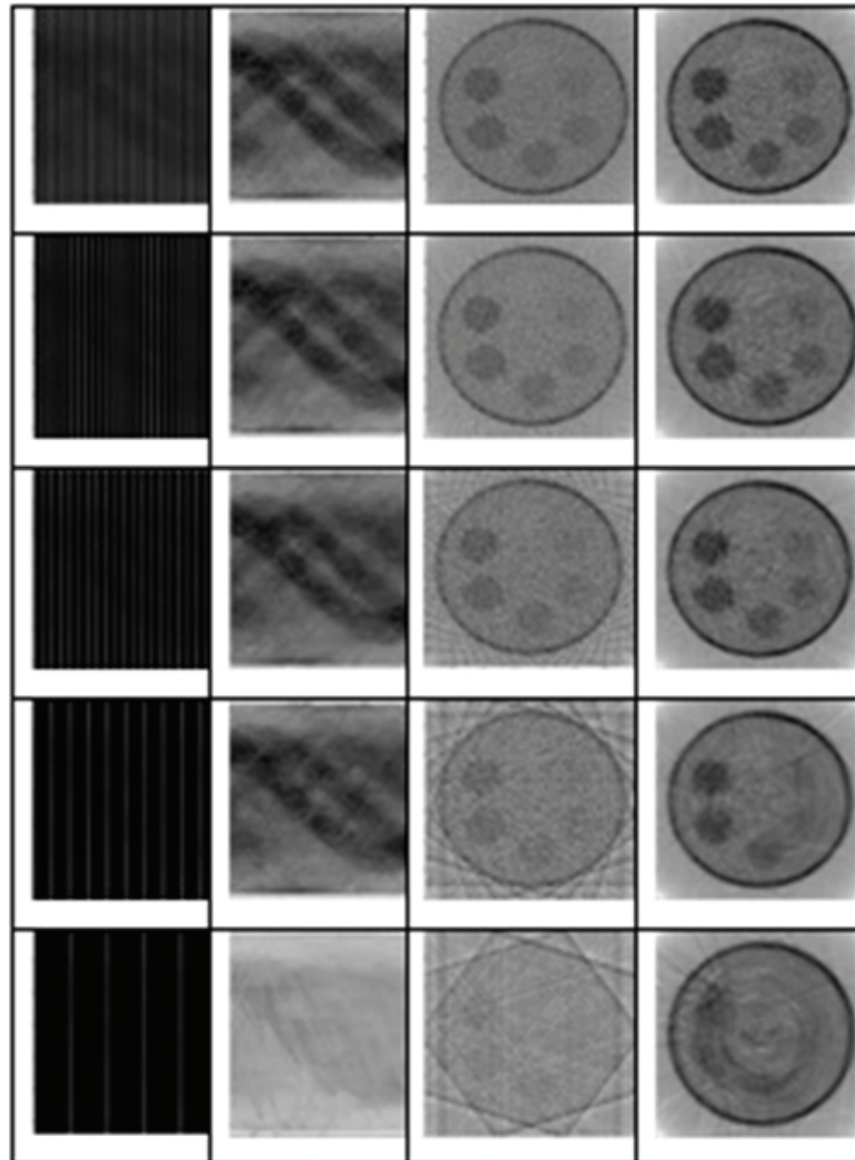
Figure 2: Reconstructed image of sparse regular projection data. First column from the left, top to bottom: data sparse regular projection in sinogram form with 3.6° (50 projections), 4.5° (40 projections), 7.2° (25 projections), 9° (20 projections), 18° (10 projections), and 36° (5 projection) angular step, respectively. Second column: interpolated sinogram, Third column: reconstructed image without sinogram interpolation. Forth column: reconstructed image with sinogram interpolation.

reconstruction then carried out using the filtered back projection method. Finally, quantitative measurements were performed such as measuring the gray level represents the ultrasonic wave velocity associated with mass density parameter.

3. Results and Discussion

The result of concrete phantom reconstruction of sparse regular projection data can be seen in Figure 2.
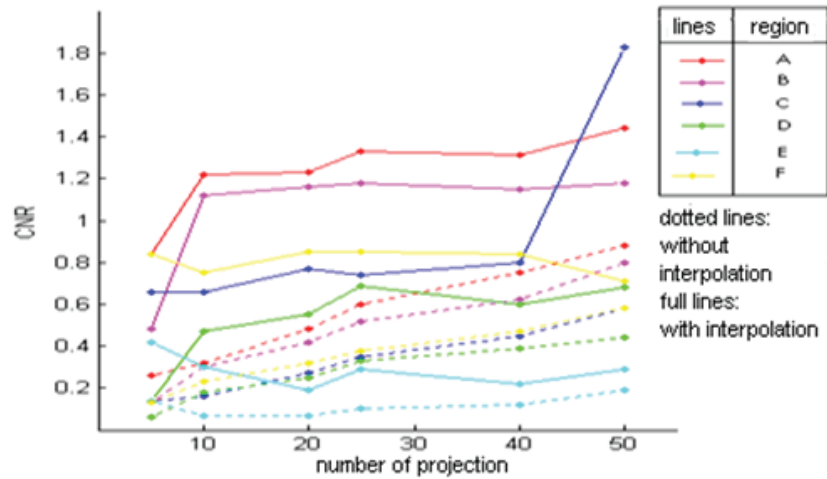
Figure 3: The relationship between the number of projection with CNR.

Sample	composition	
	material	ratio
A	clay + sand	1 : 1
B	clay + limestone + cement	1 : 1 : 1
C	cement + brick + sand	2 : 1 : 2
D	cement + limestone + sand	2 : 1 : 2
E	cement + gypsum	1 : 2
F	cement + volcanic sand	1 : 2
G	cement + volcanic sand	1 : 1

TABLE 1: Composition of concrete samples.

It can be seen in Figure 2. that the sinogram interpolation can eliminate the streak artifact in the reconstructed image (in the reconstructed image of 20 projections, 10 projections and 5 projections). The reconstructed image are smoother and the objects of phantom appear more clearly, but they are not separated in the reconstruction of 5 projections. It can be concluded that the reconstruction of the sinogram interpolation can still be accepted using at least 10 projections.

Quantitatively, we observe the results of reconstruction using the contrast to noise ratio criterion (*CNR*) by formula [10]:

$$CNR = \frac{\mu_{ROI} - \mu_{BG}}{\left[(\sigma^2_{ROI} - \sigma^2_{BG})/2\right]^{1/2}}$$

with μ_{ROI} is the average density of the object, σ_{ROI} is the standard deviation of density of the object, μ_{BG} is the average density of the background, and σ_{BG} is the standard deviation of density of the background.

Measurements of *CNR* were performed for the object on A, B, C, D, E, F, and on G as a background. The results show that the proposed method increases *CNR* significantly as seen in Figure 3.

4. Conclusions

The proposed method which is based on the interpolation of the sparse sinogram works properly even for a noisy data with 10 projections. The reconstructed image are smoother and the objects of phantom appear more clearly. This is also confirmed by the result of the calculated CNR where the interpolation of the sinogram increased the CNR of the various objects.

References

[1] A. C. Kak and M. Slaney, in *Computerized Tomographic Imaging*, The Institute of Electrical and Electronics Engineers, Inc., New York, 1999.

[2] V. Kolehmainen, M. Lassas, and S. Siltanen, Limited Data X Ray Tomography Using Nonlinear Evolution Equations, *SIAM J Sci Comput*, **30**, 1413–1429, (2008).

[3] B. Recur, P. Desbrates, and J. P. Domenger, Radon and Mojette Projections' Equivalence for Tomographic Reconstruction using Linear Systems

[4] G. T. Herman and R. Davidi, Image Reconstruction from a Small Number of Projection, *Inverse Problem*, **24**, no. 4, (2008).

[5] V. Singh, L. Mukherjee, P. M. Dinu, J. Xu, and K. R. Hoffmann, Limited view CT reconstruction and segmentation via constrained metric labeling, *Comput Vis Image Underst*, **112**, 67–80, (2008).

[6] R. A. Rahim, C. K. Thiam, and M. H. F. Rahiman, An Optical Tomography System Using a Digital Signal Processor, *Sensors (Basel)*, **8**, 2082–2103, (2008).

[7] H. Yu and G. Wang, A soft-threshold filtering approach for reconstruction from a limited number of projections, *Phys Med Biol*, **55**, 3905–3916, (2010).

[8] C. E. Widodo, K. Kusminarto, and G. B. Suparta, Tomographic Image Reconstruction from a Sparse Projection Data Using Sinogram Interpolation, *Int J Eng Technol IJET-IJENS*, **11**, 86–89, (2011).

[9] K. Suryono, G. B. Suparta, and A. Sugiharto, Ultrasonic Computed Tomography System for Concrete Inspection, *Int J Civ Environ Eng IJCEE-IJENS*, **11**, 16–21, (2011).

[10] X. Song, B. W. Pogue, S. Jiang, M. M. Doyley, H. Dehghani, T. D. Tosteson, and K. D. Paulsen, Automated region detection based on the contrast-to-noise ratio in near-infrared tomography, *Appl Opt*, **43**, 1053–1062, (2004).

KnE Engineering

Knowledge E
Engaging minds

Conference Paper

Preliminary Study of Double Beta Decay: Simulation of CaMoO$_4$ Scintillation Detector Response Function to the Gamma Ray Radiation

Mitra Djamal[1, 2], Rahadi Wirawan[3], Syeilendra Pramuditya[1], and HongJoo Kim[4]

[1]Department of Physics, Institut Teknologi Bandung, Bandung 40132, Indonesia
[2]Department of Physics, Institut Teknologi Sumatera, South Lampung 35365, Indonesia
[3]Department of Physics, Universitas Mataram, Mataram 83125, Indonesia
[4]Radiation Science Research Institute, Department of Physics, Kyungpook National University,Daegu 702-701, Korea

Abstract

CaMoO$_4$ crystal is a material candidate for the scintillation detector and double beta decay experiment to determine a neutrino mass. The objective of this work is to analyze the response function of CaMoO$_4$ using Monte Carlo GEANT4 simulation. Penelope-low energy method was used as an interaction type for the electromagnetic process. The simulation results show that the presence of the photopeak energies of gamma ray from Cs-137, Co-60 and K-40 sources can be identified and observed in the energy 0.662 MeV, 1.17 MeV, 1.33 MeV and 1.5 MeV. The photoelectric cross section interaction of CaMoO$_4$ is lower than NaI(Tl), but in other hand the incoherent cross section is vice versa.

Keywords: Scintillation, CaMoO$_4$, GEANT4, Gamma ray

OPEN ACCESS

1. Introduction

Double beta decay (DBD) is important source information about the fundamental neutrinos character such as neutrino mass. ^{100}Mo is a material element for the neutrinoless double beta decay (0νDBD) searching except for the ^{82}Se, ^{116}Cd and ^{76}Ge elements [1,2]. As a detector material, CaMoO$_4$ is a promising material candidate for the scintillation detector and double beta decay experiment to determine a neutrino mass.

In order to analyze the presence of 0νDBD peak, the information about the detector response function (DRF) is an important in the identification of the peak energy, especially in the presence of the internal and the external background radiation. Computer simulation could be done as a preliminary step for analyzing the DRF characteristic of a detector material and Monte Carlo simulation is one approach that can be applied.

Monte Carlo simulation has been established as an appropriate method for modeling and useful for predicting the experiment results, especially for validation of the detector model [3]. In the previous study, we have successfully simulated the DRF of NaI(Tl) scintillation crystal using Penelope Monte Carlo GEANT4 [4]. Furthermore, in this work we focus to study the response function characteristic of CaMoO$_4$ crystal

How to cite this article: Mitra Djamal, Rahadi Wirawan, Syeilendra Pramuditya, and HongJoo Kim, "Preliminary Study of Double Beta Decay: Simulation of CaMoO$_4$ Scintillation Detector Response Function to the Gamma Ray Radiation," *KnE Engineering*, vol. 2016, 5 pages. DOI 10.18502/keg.v1i1.479

Page 1

detector to the gamma ray radiation. The work was conducted based on the Monte Carlo simulation method using the GEANT4 simulation toolkit.

2. Methodology

2.1. Scintillation Detector

The unstable nuclide emits a type of radiation, such as α, β, or γ rays to become a stable nuclide and the amount of energy will be released in these processes. Identification of the energy based on the detected radiation, which is presented as an energy spectrum distribution.

In the energy spectrum distribution, spectral peaks can be treated as simple Gaussian. The energy resolution (R) is a parameter that describing the characteristic of the detector response function (DRF) of the energy radiation from a source.

$$R \cong \frac{FWHM}{H_0} \tag{1}$$

where FWHM is the full width at one-half of the maximum height peak and H_0 is a photopeak energy.

GEANT4 (*GEometry ANd Tracking*) is a type of Monte Carlo simulation that used to simulate the photon through the matter. This simulation, give a chance for user to reconstruct a detector model, detection system and physical interaction process involved [5]. In the GEANT4, the electromagnetic interaction process like a photo-electric effect, Compton scattering, Rayleigh scattering and pair production are implemented in the standard and low energy packages (Livermore and Penelope). They are differentiated based on the energy range for each process [6].

2.2. Simulation

Schematic design of the simulation was reconstructed as shown in Fig. 1(a). In this work, the detector model construction for the 3 in. x 3 in. was adopted from detector information [7, 8]. The precise dimension of the detector and its position must be entered in the detector construction code of GEANT4 simulation except the detail of photomultipliers. The interaction type for the GEANT4 electromagnetic process is a Penelope-low energy package with the beamon setup is about 5.0×10^7 beamon. Cs-137, Co-60 and K-40 of energy radiation are used for gamma ray point source setup.

In order to perform the counting events result in the Gaussian curve energy distribution (smearing curve) using ROOT analysis, we convert the energy resolution (R) or the full width at one-half of the maximum height (FWHM) to the Gaussian deviation (σ) based on the following formula [9].

$$\sigma = \frac{FWHM}{2.35} \tag{2}$$
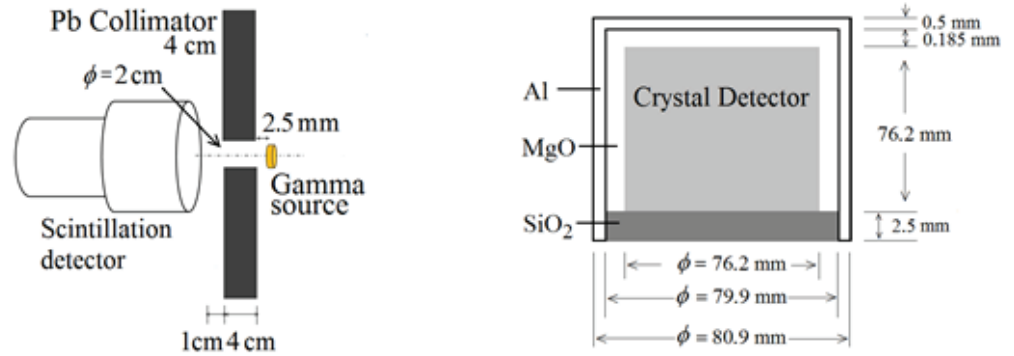
Figure 1: Schematic design of detector and simulation geometry construction.
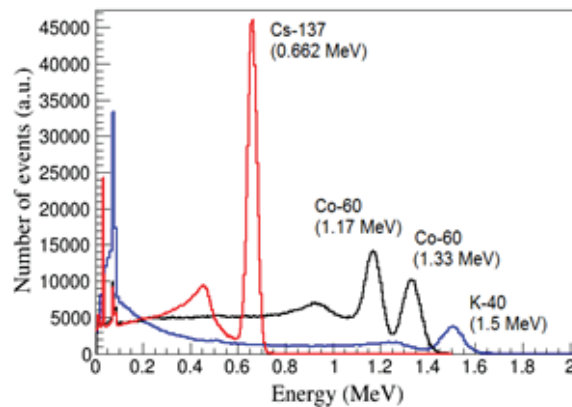
Figure 2: Energy spectrum distribution of Cs-137, Co-60 and K-40 detected using $CaMoO_4$.

3. Results and Discussion

The response function of $CaMoO_4$ detector (DRF) for the several energy radiation source was described as an energy distribution curve as shown in Fig. 2. The comparison of detector response to the Cs-137 energy in the Fig. 3 shows that the photopeak (photoelectric effect) energy of Cs-137 which detected in the CaMoO4 is lower than NaI(Tl). Although, the entries of detector that making interaction of the NaI(Tl) is less than $CaMoO_4$ i.e. 1065970 and 117412. On the other hand, the Compton edge peak of $CaMoO_4$ is higher than NaI(Tl). Fig. 4 shows the Gaussian peak of the photopeak for the several gamma energy sources like Cs-137, Co-60 and K-40.

The result shown that the photoelectric cross section interaction of the NaI(Tl) is higher than $CaMoO_4$ and for the incoherent cross section is vice versa. According to the XCOM program analysis of the value of total attenuation coefficient, these results have the same trend. The attenuation of photoelectric absorption of 0.66 MeV for NaI(Tl) is about 1.736×10^{-2} (cm^2/g) and $CaMoO_4$ is 8.466×10^{-4} (cm^2/g). The attenuation of incoherent scattering of 0.66 MeV for NaI(Tl) is about 6.604×10^{-2} (cm^2/g) and 7.549×10^{-2} (cm^2/g) for $CaMoO_4$.

In addition, we are also simulating the detector response to beta ray radiation from the Cs-137 source as an initial process for beta ray detection. The energy distribution of beta rays was described by the blue line curve as shown in the Fig. 5.
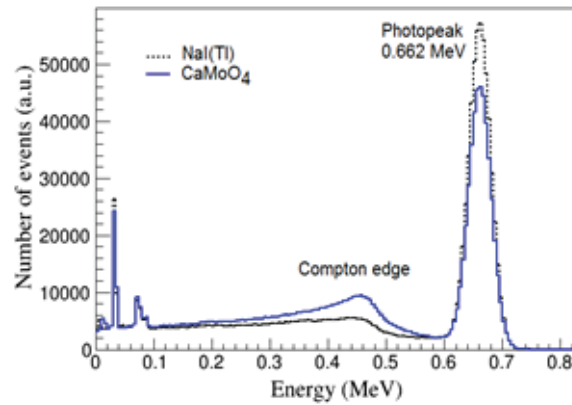
Figure 3: Energy spectrum distribution of Cs-137 detected by NaI(Tl) and CaMoO$_4$.
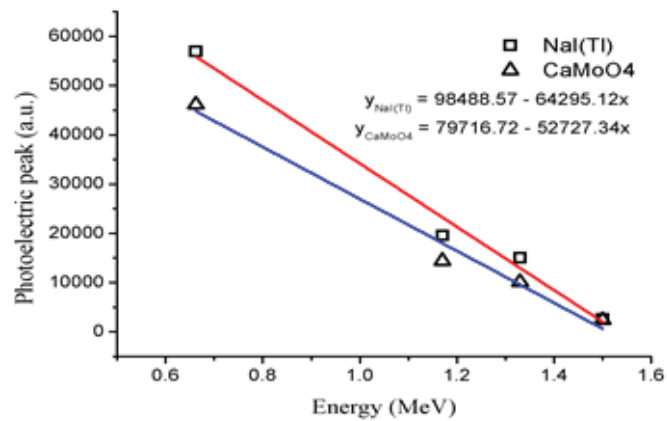
Figure 4: Gaussian peak of photopeak energy for the NaI(Tl) detector and CaMoO$_4$.
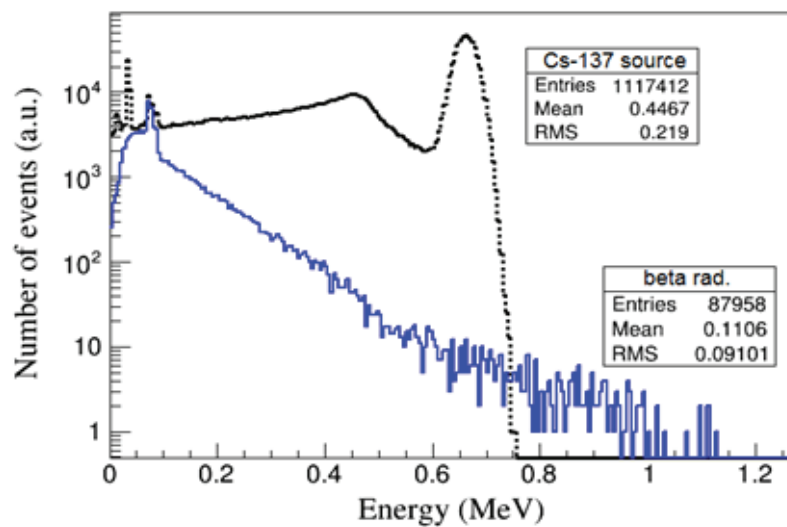
Figure 5: Energy spectrum distribution of beta radiation from Cs-137 source for CaMoO$_4$ detector.

As we know that the beta radiation is a continuous energy spectrum as depicted in the Fig. 5. The beta energies spectrum is lower than the gamma energy spectrum. In particular, double beta decay is second weak and rare process when single beta decay

energetically not allowed. Therefore, to observe the present of double beta decay energy spectrum, we need to set up the condition for the low background radiation.

4. Conclusions

The response function of $CaMoO_4$ detector (DRF) for the Cs-137, Co-60 and K-40 radiation sources was simulated using Monte Carlo GEANT4. The photoelectric cross section interaction of $CaMoO_4$ is lower than NaI(Tl), but in other hand the incoherent cross section of $CaMoO_4$ is higher than NaI(Tl). Set up condition of low background radiation is needed in order to observe the beta radiation.

5. Acknowledgment

References

[1] M. Tenconi, LUMINEU: a pilot scintillating bolometer experiment for neutrinoless double beta decay search, *Phys Procedia*, **61**, 782–786, (2015).

[2] N. Abgrall, et al., The Majorana Demonstrator Neutrinoless Double-Beta Decay Experiment, *Advances in High Energy Physics*, (2014).

[3] A. F. Bielajew, in *Fundamentals of the Monte Carlo method for neutral and charged particle transport*, Department of Nuclear Engineering and Radiological Sciences, The University of Michigan, 2001.

[4] R. Wirawan, M. Djamal, A. Waris, G. Handayani, and H. J. Kim, Investigation of Incoherent Gamma-Ray Scattering Potential for the Fluid Density Measurement,Applied, *Mech Mater*, **575**, 549–553, (2014).

[5] S. Agostinelli, et al., GEANT4-a Simulation Toolkit, *Nucl Instrum Methods Phys Res A*, **506**, 250–303, (2003).

[6] V. N. Ivanchenko, S. Incerti, Z. Francis, H. N. Tran, M. Karamitros, M. A. Bernal, C. Champion, and P. Guèye, Combination of Electromagnetic Physics Processes for Microdosimetry in Liquid Water with the Geant4 Monte Carlo Simulation Toolkit, *Nucl Instrum Methods Phys Res B*, **273**, 95–97, (2012).

[7] H. -X. Shi, B. -X. Chen, T. -Z. Li, and D. Yun, Precise Monte Carlo simulation of gamma-ray response functions for an NaI(Tl) detector, *Appl Radiat Isot*, **57**, 517–524, (2002).

[8] M. Abd-Elzaher, M. S. Badawi, A. El-Khatib, and A. A. Thabet, Determination of Full Energy Peak Efficiency of NaI(Tl) Detector Depending on Efficiency Transfer Principle for Conversion From Experimental Values, World, *J Nucl Sci Technol*, **02**, 65–72, (2012).

[9] G. F. Knoll, in *Radiation Detection and Measurement*, John Wiley & Sons Inc, New York, 2nd ed edition, 1989.

KnE Engineering

Knowledge E
Engaging minds

Conference Paper

Experiment on Laser Speckle Imaging of Apples Using A CMOS Camera

Minarni Shiddiq, Zulkarnain, and Rasmiana Poja

Laboratorium Fotonik, Jurusan Fisika, FMIPA Universitas Riau Jl. HR Soebrantas Km 12.5 Pekanbaru 28293, Indonesia

Corresponding Author:
Minarni Shiddiq; email:
minarni@unri.ac.id

 OPEN ACCESS

Abstract

Laser Speckle Imaging recently has become a promising tool to assess fruit quality and can be applied in fruit sorting. It is a non-destructive, optical method which uses light scattered of fruit surface after illuminated by laser light. Laser speckle imaging methods use He-Ne laser or diode laser as the light source yet both lasers have differences in performance and price. Diode lasers are more preferable due to their efficiency, low cost, small and compact, and varied wavelength. In this research, an optical system which consisted of a laser source and a CMOS camera was used for Laser Speckle Imaging. A 632,8 nm He-Ne laser and a 650 nm diode laser were used, their performances were compared. The samples were two kinds of apples, *Red Delicious* and *Fuji,* five samples for each cultivar. The laser light was expanded using a beam expander hence illuminated on the apple surface at 30° angle. A monochrome Thorlabs CMOS camera with camera lens was used to record the speckle patterns of the apple surface. Both lasers were kept at the same laser power by Neutral Density Filters. ImageJ software was used to calculate the gray value of the speckle pattern for each sample, the speckle gray values were compared for different laser light sources and apple types. The results showed that there is a significant difference in gray value level between both apples. Higher maximum gray values were found on the *Fuji* apples compared to the Red Delicious apples which were about 21.7 % when using He-Ne laser and 18.3 % when using diode laser. Higher maximum gray value for Fuji apples could be due to their rounder shape, firmer skin and flesh, they scatter more light. The curvature and the firmness of the fruits affected the gray value level. For each apple type, there was a slight difference in maximum gray values for both laser sources. Higher gray values were obtained when using diode laser compared to the He-Ne laser, 22.0 % difference for Fuji apples and 25.2 % difference for Red Delicious apples. These could be because of the less coherence, wider bandwidth, and irregular beam shape of the diode laser that it scatters more light and suppresses speckles.

Keywords: Laser Speckle Imaging, laser types, ImageJ, CMOS camera, apples

1. Introduction

Fruits dan vegetables are valuable agricultural commodities, however some problems still exist such as plant diseases and post harvest sorting problems of fruits and vegetables. Plant diseases of fruit and vegetables caused by pathogens can create major

How to cite this article: Minarni Shiddiq, Zulkarnain, and Rasmiana Poja, "Experiment on Laser Speckle Imaging of Apples Using A CMOS Camera," *KnE Engineering*, vol. 2016, 7 pages. DOI 10.18502/keg.v1i1.480

Page 1

economic loss in agriculture industries. Sorting fruits and vegetables before and after harvest is a very important task, the fastest and reliable sorting system which can asses maturity level is needed to maintain the quality of fruits and vegetables. Some fruits are mature after harvest but need to ripe, knowledge on the ripeness level is also needed for packaging and storage time purposes. Sankaran *et al.*(2010) has reviewed varied techniques that have been developed to detect plant diseases and the urgencies to develop a real time, fast, economical, and reliable system that is able to detect the health of plants [1]. Abbott has also reviewed some possible techniques to evaluate the quality of fruits and vegetables. Optical methods which use light with different wavelengths are the potential tool to measure and evaluate the fruits and vegetable defects. Fruit and vegetables tissues have optical properties hence can be used to assess their quality. Visible and NIR lights are being developed and able to detect fruits and vegetables contents such as proteins, carbohydrates, and fats [2]. More advanced researches on preharvest and postharvest sorting problems of fruits and vegetables are needed in order to sustain agriculture industries.

Laser is a light source that has been known to have many applications. The properties of laser light that differentiate it from other light sources makes applications of laser increase rapidly. The applications of laser have been found widely in agricultures. One of the reasons is the nondestructive effect of laser light to the biological tissues or samples compared to the molecular methods which are often destructive, more expensive, and time consuming. There are some optical methods that have been developed and got much attentions recently in agricultural research such as LICF (*Laser Induced Chlorophyll Fluorescence*) spectroscopy on plant diseases, Hyperspectral spectroscopy imaging and LSI (*Laser Speckle Imaging*) for fruits and vegetables. Some of the methods apply lasers as the light sources. Laser types used mostly He-Ne laser and diode laser. Some experiments such as Hyperspectral imaging use Halogen lamps or Leds as the light sources. There some advantages using laser than lamps such as monochromacities, coherences, higher power, more eficient in energy comsumption, and low cost. He-Ne lasers and diode lasers are often used in LCIF and LSI experiments because they are low cost, compact, eficient compared to other types of lasers. However, compared to He-Ne lasers, diode lasers have some drawbacks such as less beam quality, less coherence, and sensitive to environmental conditions [3].

Optical Instruments that can be used in fruits and vegetables sorting which are accurate, low cost, portable, needs to be developed. Many researches have been done in developing the instruments especially the sensor used. The sensors used are photodetectors which can be a photo diode, CCD arrays or CMOS camera, the latter is known as the imaging detector. CCD cameras and CMOS camera have been used in computer vision techniques for sorting and grading fruits [4,5]. The CMOS cameras are preferable because they are eficient in cost and energy. CCD and CMOS camera are used for imaging technique which images of the object being investigated can be recorded and processed.

Laser Speckle Imaging (LSI) is a system which uses the speckle patterns to investigate the properties of the surface of an object. LSI has been developed for many purposes in assessing fruits quality and ripeness, the quality of orange fruits [6], the

attribute quality of apples [7], and the ripeness of tomato [8]. Laser speckles are obtained when a diffuse surface illuminated by laser light. The speckle pattern consists of granular black and white spot. This is an interference pattern due to interference of lights reflected or scattered from different part of the surface being illuminated. The destructive interference creates dark speckle while constructive interference results in bright speckle. The laser speckle is a random phenomenon hence needs to be described statistically. Gray value and contrast are parameters which are usually used to describe a property of a speckle pattern. They are can be calculated using an image processing software such ImageJ. Contrast is simply represented by the ratio of the standard deviations and the average intensity [9].

2. Material and Methods

An optical system consisted of laser sources, a sample plate, a beam expander, a USB CMOS camera has been used for an experiment in Laser Speckle Imaging. The system was applied to asses the differences in speckle profile between two kinds of apples and two kinds of lasers. The samples were Red Delicious and Fuji apples. Each cultivar consisted of 5 samples for each laser with approximately the same equitorial diameter, color, shape, and weight. The laser sources used were a 633 nm He-Ne laser and a 650 nm diode laser. Both lasers were kept at the same power using neutral density filters. The dynamics of the speckle patterns will not be addressed in this paper . The camera was also equipped wih software for recording and saving the speckle pattern images. The images were latter processed using ImageJ software. The speckle profiles were represented by the gray value levels obtained by ImageJ software.

Figure 1 showed the optical setup for laser speckle imaging experiment. Measurements were performed first using the He-Ne laser, for both cultivars, and then using the diode laser. M1, M2, and M3 mirror were used to send the laser light to the sample surface at 30° angle. Some neutral density filters were applied to obtain the same laser power at the apple surface. A 50 mm convex lens was used to expand the light beam. The distance of the lens from the apple surface were adjusted to obtain the same size of beams on the apple surface which were less than the apple diameter. The speckle pattern formed on the surface of the apples were recorded by the CMOS camera. The recorded image then were processed using ImageJ software to obtain histograms of gray value for each speckle pattern.

3. Results and Discussion

Results of this experiment were images of speckle patterns recorded by the CMOS camera. The data were analyzed using ImageJ software and presented by gray value histogram and also using graphs of average maximum gray values. The maximum gray value is related to the contrast of the speckle pattern. Variations of data were based of apple types, laser types, and incident angle variation. There were 5 apples for each type so 10 apples for each laser, and three angle variations i.e. 30°, 45°, 60°. The three mirrors were used for easy alignment of beam size and angle. The neutral density
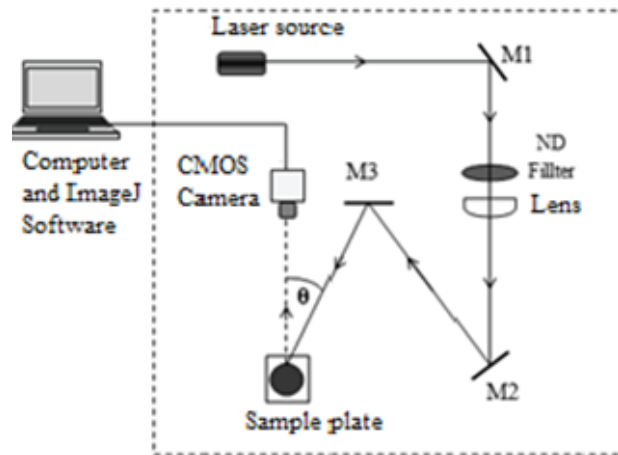
Figure 1: The optical System for Laser Speckle Imaging.

filters were used to reduce the laser intensity reaching the apple surface, the laser power of He-Ne laser was 1,10 mW and of diode laser was 1,11 mW. The sizes of laser beam for both lasers at the surface were made closely equal. The gray value were taken for the whole image without background substraction.

Figure 2 showed the comparison of the average gray value level of speckle patterns for Fuji apples at 30° angle when different laser source was used. The distributions of the speckle pattern were closely identical because of careful laser beam setup on the apple surface. However, the maximum gray value of speckle pattern when using the diode laser was higher by 22.0 %. Figure 3 showed the average gray value level of speckle pattern for Red Delicious apples taken also at 30° incident angle. The maximum gray values for both laser were different by 25.2 % and the distribution peak was shifted further to the right compared to the those of Fuji apples. Different results for different laser could be caused by different characteristics for both lasers. He Ne lasers have better beam quality, longer coherence length, more stable power and pointing. The He Ne laser has a slighltly smaller wavelength and unpolarized. Two factors that can suppress speckles are illumination of an object by sufficiently incoherent source and by wider spectral bandwidth [10], these could be the reasons why some imaging systems use a diffuse white light for illuminating objects, to reduce speckles. The diode laser resulted in higher gray value could be dominantly due to its irregularity in beam shape which scatter more light, its less coherence, and its wider bandwidth.

The maximum gray value of both apple types was different when using the same laser type. The He-Ne laser gave higher gray value for Fuji apples by 21.7 % difference compared to the Red Delicious apples while the diode laser had 18.3 % difference. The differences in gray value level for both apples could be due to the apple characteristics. The color of Fuji apples are between striped yellow to red while the color of Red delicious apples are from striped red to dark red. The shape of Fuji apples are more round while the Red Delicious apples are conic shape. The Fuji apples have dense flesh while the Red Delicious tissue is less dense or firm [11]. Those could be the reasons why the Fuji apples have higher gray values, more light is scattered.
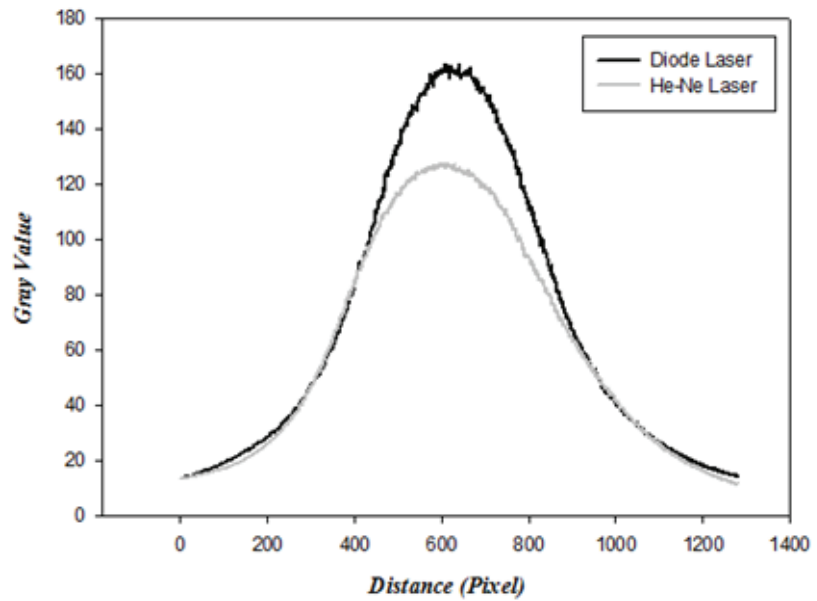
Figure 2: Gray value level comparison between two laser sources at 30⁰ angle for Fuji Apples.
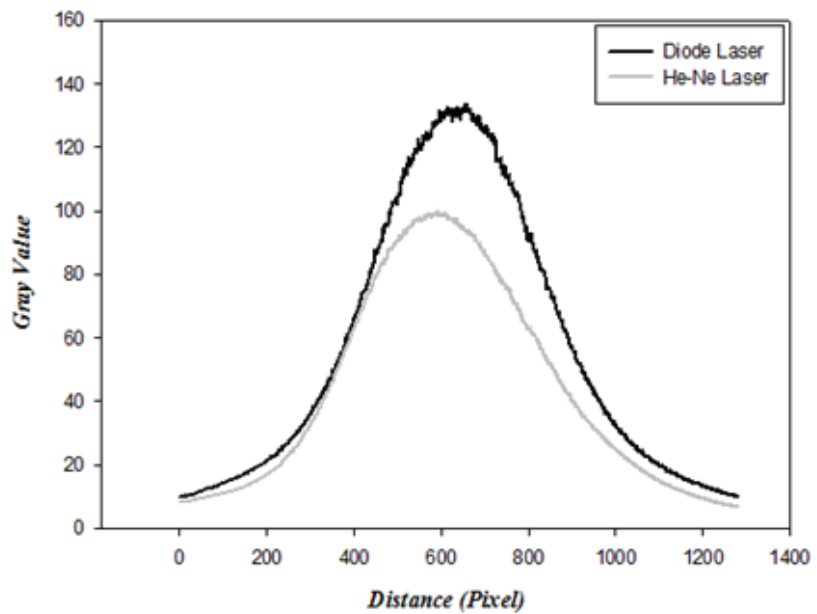
Figure 3: Gray value level comparison between two laser sources at 30⁰ angle for Red Delicious Apples.

The experiment also explored the effect of incident angle variations on the speckle patterns for both apples and for both laser types. Figure 4 showed the maximum gray value versus angle of incidence for both lasers and apple types. LHF stands for He-Ne Laser and Fuji apples, LHW for He-Ne Laser and Washington apples, LDF for diode laser and Fuji apples, and LDW for diode Laser and Washington apples.

The incident angle affected the speckle pattern for both laser and apple type. The 30⁰ angle resulted in higher maximum gray value, followed by the 45⁰ angle, then 60⁰ angle. The higher was the angle, the smaller was the maximum gray values. The reason could be less scattered light reached the fixed detector when the angle of incidence
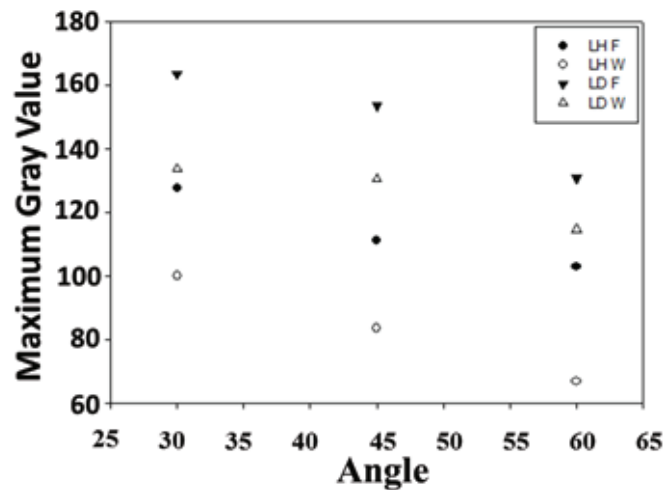
Figure 4: Gray values dependence of incident angles.

was bigger. Figure 4 also showed the differences between the maximum gray value for both laser and apple type for each angle.

4. Summary

This experiment was a simply experiment to answer whether the performance of a diode laser is comparable to the He-Ne laser's in a laser speckle imaging for fruits. The experiment results showed that there is a significant difference in gray value level between both apples. Maximum gray values were higher for *Fuji* apples compared to Red Delicious apples. These could be due to the Fuji apple shape or curvature and firmness. For each apple type, there was a slight difference in gray values for both lasers. The diode laser gave higher gray value than the He-Ne laser. These could be due to less coherence, wider bandwidth, and irregular beam shape of the diode laser.

References

[1] S. Sankaran, A. Mishraa, R. Ehsania, and C. Davis, A Review of Advanced Techniques for Detecting Plant Diseases, *Comput Electron Agric*, **72**, 1–13, (2010).

[2] J. A. Abbott, Quality measurement of fruits and vegetables, *Postharvest Biol Technol*, **15**, 207–225, (1999).

[3] H. Sun, in *A Practical Guide to Handling Laser Diode Beams, Chapter 2*, Springer, 2015.

[4] J. A. Kodagali and S. Balaji, Computer Vision and Image Analysis based Techniques for Automatic Characterization of Fruits, *a Review International Journal of Computer Applications*, **50**, 0975–8887, (2012).

[5] R. Mahendran, G. C. Jayashree, and K. Alagusundaram, Application of Computer Vision Technique on Sorting and Grading of Fruits and Vegetables, *J Food Process Technol*, no. S5, (2011).

[6] G. F. Rabelo, A. Roberto, B. Junior, and I. M. D. Fabbro, Laser Speckle Techniques In Quality Evaluation Of Orange Fruits, *Rev Bras Eng Agric Ambient*, **9**, no. 4, 570–575,

(2005).

[7] A. Zdunek and J. Cybulska, Relation of biospeckle activity with quality attributes of apples, *Sensors (Basel)*, **11**, 6317–6327, (2011).

[8] G. G. Romero, C. C. Martinez, E. E. Alanis, G. A. Salazar, V. G. Broglia, and V. GL. Alvarez, Bio-speckle activity applied to the assessment of tomato fruit ripening, *Biosyst Eng*, **103**, 116–119, (2009).

[9] D. Briers, D. D. Duncan, E. Hirst, S. J. Kirkpatrick, M. Larsson, W. Steenbergen, T. Stromberg, and O. B. Thompson, Laser speckle contrast imaging: theoretical and practical limitations, *J Biomed Opt*, **18**, p. 066018, (2013).

[10] J. W. Goodman, Some fundamental properties of speckle, *J Opt Soc Am*, **66**, 1145–1150, (1976).

[11] B. Dobrzañski, J. Rabcewicz, and R. Rybczyñski, Handling of Apple: transport techniques and efficiency vibration, damage and bruising texture, firmness and quality, B. Dobrzañski Institute of Agrophysics Polish Academy of Sciences, LUBLIN, ISBN 83-89969-55-6

Knowledge E

Engaging minds

Conference Paper

Evaluation of TLCD Damping Factor from FRF Measurement Due to Variation of The Fluid Viscosity

Lovely Son, Mulyadi Bur, and Meifal Rusli

Kampus Limau Manis, Andalas Universiy, Indonesia

Abstract

Tuned Liquid Column Damper (TLCD) has become an alternative solution for reducing low frequency vibration response of machines and structures. This is not surprisingly that the damper has simply structure and low maintenance cost. The main disadvantage of using TLCD is the complexity in controlling TLCD damping factor experimentally. Theoretically, damping factor can be controlled by adjusting the orifice dimension. However, this method is time consuming and not appropriate conducted in the real application. A more simply method for adjusting TLCD damping factor is by varying the fluid viscosity. This research is aimed to evaluate the effect of fluid viscosity to the damper performance. Two DOF shear structure with TLCD is used as the experimental model. Several TLCD fluids with different viscosity are evaluated. Evaluation of TLCD damping factor due to variation of the fluid viscosity is conducted by comparing the Frequency Response Function (FRF) obtained from the experimental data.

Keywords: TLCD, vibration, structure, damper, viscosity

1. Introduction

Nowadays, several methods have been developed to reduce vibration response of mechanical and structural system in accordance with either serviceability or safety criteria. For a large structure such as building and bridge, strengthening the structural system or installing of the base-isolation could be very costly or too difficult to perform. For this case, incorporating a passive damper into the structure is relatively less expensive and much simpler to be realized. Therefore, many research works on the passive damper such as Dynamic Vibration Absorber(DVA) have been conducted in recent years[1,2,3]. Among passive DVA, Tuned Liquid Column Damper(TLCD) is of great interest for some of its characteristics such as easy implementation, low cost of construction and maintenance and no need to add mass to the structure if the liquid is used as water supply[4]. The passive DVA performance is greatly depend on the selection of the damper natural frequency and damping factor. In TLCD, the natural frequency can be varied by adjusting the column dimensions or the liquid level inside the damper[5]. Meanwhile, TLCD damping is affected by the degree of turbulence flow of the fluid due to TLCD column junction and the built in orifice. However, variation of TLCD damping by modifying of the orifice hole is difficult to be conducted experimentally[6].

How to cite this article: Lovely Son, Mulyadi Bur,and Meifal Rusli, "Evaluation of TLCD Damping Factor from FRF Measurement Due to Variation of The Fluid Viscosity," *KnE Engineering*, vol. 2016, 6 pages. DOI 10.18502/keg.v1i1.481

Page 1
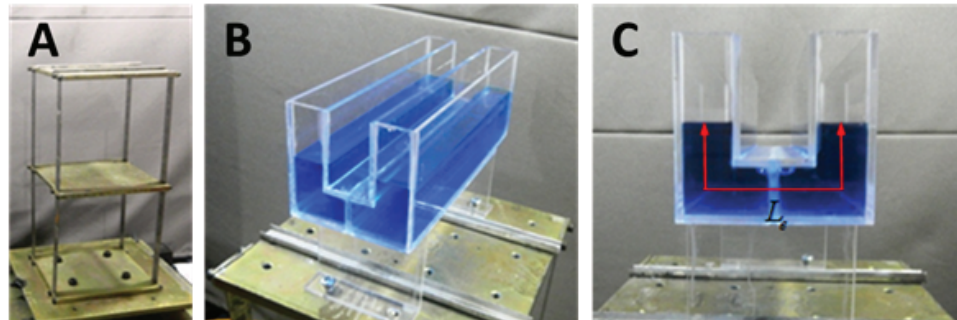
Figure 1: Structural testing model and TLCD.

Components		Value
Beam	Dimension	210 mm × 20 mm × 1 mm
	Material	Stainless Steel: E = 190 GPa, ρ = 7700 kg/m^3, v = 0.26
Rectangular block	Dimension	200 mm × 200 mm × 10 mm
	Material	AISI 1020: E = 200 GPa, ρ = 7900 kg/m^3, v = 0.29
TLCD	Dimension	Height = 73 mm, Width = 79 mm, Column width = 20 mm
	Material	Acrylic

TABLE 1: Specifications of structural testing model and TLCD

A simply method for adjusting the fluid damping inside TLCD is by varying the fluid viscosity. In this research, three TLCD fluids with different viscosity are evaluated experimentaly. The TLCD performance is analysed by comparing the measured FRF response of the structure with TLCD.

2. Experimental Setup

Two-DOF shear structure as shown in Fig. 1 is used as the testing model. The structure model consists of two rectangular blocks made of the steel plate that connected using four steel beams. The base of structure is fixed to the ground that made of a rectangular steel plate. The ground has two pairs of slider bearing at its bottom. Therefore, it can move freely in the horizontal direction. The TLCD damper is positioned at the top of the second floor of the structure. The damper housing is made of the acrylic plate as shown in Fig. 1. The column cross-section of TLCD damper is the uniform rectangular shape.

The structural testing model and TLCD spesification are shown in Table 1. The experimental model consist of three components i.e Steel beam, Rectangular block and TLCD as shown in Table 1. It should be noted that the TLCD dimensions are selected so that the natural frequency of the fluid inside TLCD column match with the first natural frequency of the structure. To increase the fluid damping, an orifice plate is positioned in the middle of horisontal column. The plate has 115 holes and each holes diameter are 3 mm. The experimental setup is shown in Fig. 2.
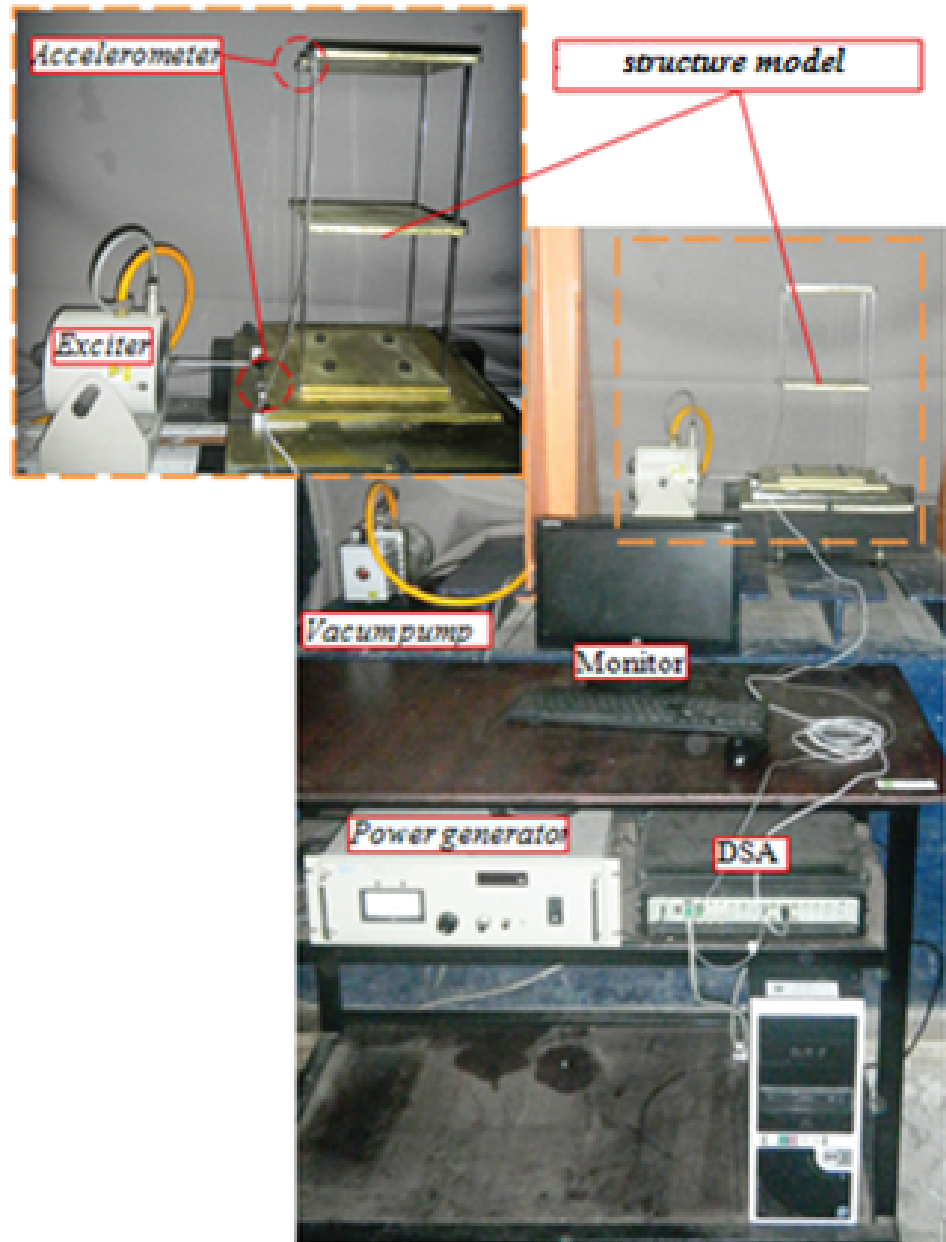
Figure 2: Experimental setup.

As shown in Fig. 2, the ground of the structure is excited horizontally by a vibration exciter. The excitation signal from the exciter is a random signal with frequency range from 0 until 10 Hz. Two accelerometers located at the ground and the second floor of the structure are used to measure the acceleration data. These data are acquired by B&K Pulse Digital Signal Analyser(DSA).

3. Experimental Results

To analyse the liquid viscosity effect, three lubricants PERTAMINA SAE 10, SAE 40 and SAE 20W-50 are utilized as the TLCD fluid. Because of the TLCD performance also
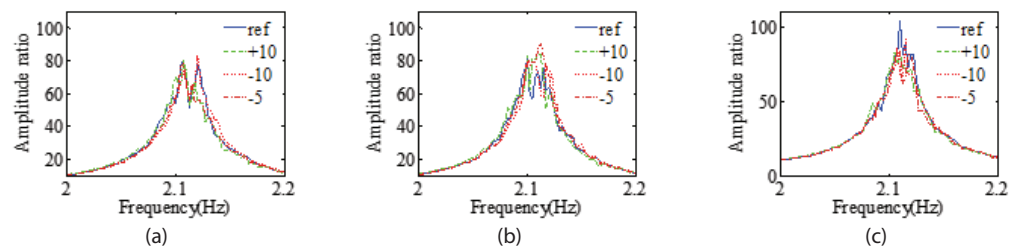
Figure 3: Frequency response of structure with TLCD, (a) using SAE 10 oil (b) using SAE 40 oil (c) using SAE 20W-50 oil.

depends on the fluid natural frequency, the experiments are conducted for several fluid levels. According to theoretical analysis[5], the fluid level is one of the dynamic parameters which affects the TLCD natural frequency. The reference level is denoted as the optimum fluid level which theoretically calculated [7]. This reference level is related to the fluid length L_e = 100 mm as shown in Fig. 1. Another level +10,-10 and -5 are obtained by added or reduced the fluid volume by 10 ml or 5 ml, respectively. The amplitude ratio which describes the Frequency Response Function (FRF) of the structure is calculated by dividing the frequency response of the 2nd floor with the frequency response of the excitation signal. Figure 3 shows the amplitude ratio of the structure with TLCD. Because of the TLCD damper is designed according to the 1st natural frequency of the structure then the enlargement of frequency response is focused to the area located near to this frequency zone.

The TLCD liquids are varied from SAE 10, SAE 40 and SAE 20W-50, respectively. It should be note that the viscosity of SAE 20W-50 is larger than that of SAE 40 in the room temperature. Figure 3 shows that for low viscosity liquid, the dynamic vibration absorber phenomenon can be simply detected. The absorber effect is seen clearly from the separation of two peak frequencies close to 2.1 Hz as shown in Fig. 3(a) for SAE 10 fluid. This results indicate that the optimum TLCD damping factor can be obtained when using low viscosity of TLCD liquids. The dynamic absorber effect reduces when the fluid viscosity is large as shown in Fig. 3(c) for SAE 20W-50 fluid. In this condition, the separation of two peak frequeny cannot be seen clearly.

Comparison of the maximum amplitudo ratio of the structure is shown in Fig. 4. Here, the maximum amplitude ratio is calculated as the mean of maximum peaks of the frequency response curve in Fig. 3. The x- axis of bar chart in Fig.4 is arranged from the low viscosity to the high viscosity fluid. The y-axis in Fig.4 describes the percentage of maximum amplitude in comparison to the case without TLCD. As shown in Fig. 4, the maximum amplitude ratio increases when the fluid viscosity increase. The reason for this condition is the fluid motion become small so that the dynamic absorber effect decreases when the fluid viscosity is large. In this condition, two frequency peaks which detected in the case of low viscosity condition becomes a single peak which indicates the system change to a one degree of freedom(1 DOF) system.
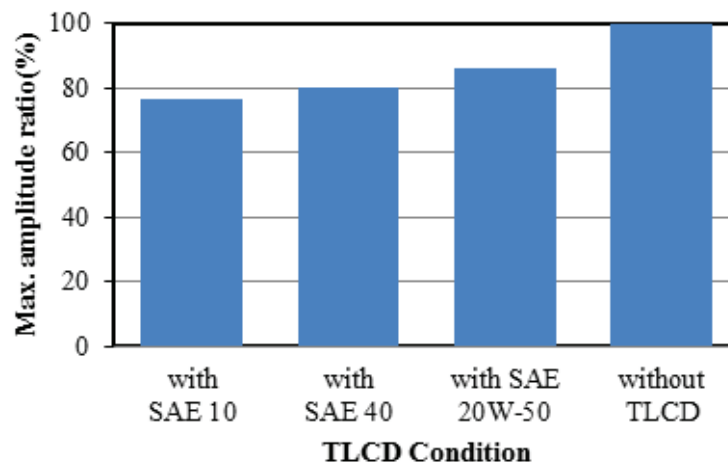
Figure 4: Comparison of maximum amplitude ratio.

4. Summary

Experimental evaluation of TLCD performance due to variation of TLCD liquid viscosity has been conducted. The experimental results show that the frequency response of the structure reduces by adding the TLCD to the structure. However, the optimum condition for TLCD damper largely depends on the damping value of the fluid system inside the TLCD column. The experimental results show that increasing the TLCD liquid viscosity will reduce the absorber performance. This condition is due to the optimum condition of TLCD damping factor closes to the case with low viscosity fluid (SAE 10). For larger viscosity fluids, the fluid motion is small and the DVA effect reduces.

5. Acknowledgment

References

[1] L. Son and M. Bur, Effectivity study of Double Dynamic Vibration Absorber on Building Structure due to Seismic Load, Unpublished Hibah Bersaing Research Report, Andalas University, 2013.

[2] P. Chaiviriyawong, S. Limkatanyu, and T. Pinkaew, Simulations of Characteristics of Tuned Liquid Column Damper Using An Elliptical Flow Path Estimation Method, The 14th World Conference on Earthquake Engineering, China, 2008.

[3] M. Rusli, M. Bur, and L. Son, Dynamic Vibration Absorber for Squeal Noise Suppression in Simple Model Structures, *Int J Struct Stab Dyn*, **15**, p. 1450078, (2015)., IJSSD.

[4] A. Di Matteo, F. L. Iacono, G. Navarra, and A. Pirrota, A Novel Mathematical Model For TLCD: Theoretical and Experimental Investigations, Vulnerability, Uncertainty, and Risk@ASCE 2014.

[5] L. Son, M. Bur, and M. Rusli, (2015)., Response Reduction of Two DOF Shear Structure Using TMD and TLCD by Considering Absorber Space Limit and Fluid Motion, The 2nd International Conference on Mechanical Engineering (ICOME), Indonesia, 2015.

[6] M. Reiterer and F. Ziegler, Combined Seismic Activation of a SDOF-Building with a Passive TLCD Attached, *13th World Conference on Earthquake Engineering*, (2004).

[7] J. P. Den Hartog, in *Mechanical Vibrations*, McGraw-Hill Book Company, New York, 4th ed edition, 1956.

KnE Engineering

Knowledge E
Engaging minds

Conference Paper

Design and Development of Gas Sensor Based On Acoustic Resonance

Melany Febrina[1], Mitra Djamal[1,2], and Martin Liess[3]

[1]Physics Department of Institut Teknologi Bandung, Bandung
[2]Physics Department of Institut Teknologi Sumatera, Lampung
[3]Engineering Sciences Department of Hochschule RheinMain, Germany

Abstract

Determination of the specific toxic, harmful, or flammable gases concentration i.e. butane, cannot be done directly. It requires devices that can do this measurement without any direct contact between the gas and human (observer) i.e. gas sensors. These sensors are typically used in security systems or early warning system. This research is about design and development of a gas sensor based on acoustic resonance. The sensor that has been developed is acoustic resonator based sensor, with two speakers as the sources of acoustic vibrations. This sensor is made to work at its resonance frequency. Since the resonance frequency of acoustic resonator is influenced by the speed of sound in the acoustic resonator, and the speed of sound is influenced by the density and concentration of the gas in the acoustic resonator, the changing of gas concentrations will cause resonance frequency shifting of the acoustic resonator. So, by taking measurement of resonance frequency shifting of resonator, gas concentration can be determined. This research was conducted in four stages, the first stage is designing of acoustic resonator, the second stage is manufacturing and initial testing of the acoustic resonator, the third stage is conditioning stage to make acoustic resonator works at its resonance frequency automatically, and the final stage is the testing stage of acoustic resonator using butane. Based on the research conducted, it can be concluded that the acoustic resonator system can work accurately and precision to detect the changing of butane gas concentration. Absolute error and relative error are relatively small, the largest of absolute error is 7.69% and the largest relative error is 0.47%.

Keywords: Acoustic resonator, gas sensor, gas concentration, resonance frequency, butane

🔓 **OPEN ACCESS**

1. Introduction

The application of gas sensing mostly used in industry and academia, such as: in industrial production [3, 4]; in the automotive industry [5]; in medical applications [6]; in monitoring indoor air quality [7]; and in environmental studies [8]. Some studies have established as a subject of the gas sensing technology since past fifty years. There are three main investigation of gas sensing are various types of sensors, research on the principles of sensing, and fabrication techniques [9].

How to cite this article: Melany Febrina, Mitra Djamal, Martin Liess, "Design and Development of Gas Sensor Based On Acoustic Resonance," *KnE Engineering*, vol. 2016, 6 pages. DOI 10.18502/keg.v1i1.482

Page 1

Gas sensor is a tool for gas sensing, these sensors typically used in a safety system. Gas sensor measures the concentration of gas in its vicinity. Gas sensor can be classified based on variations on electrical properties and other properties. For electrical properties, gas sensor consists of metal oxide semiconductor, polymer, carbon nanotubes, and moisture absorbing material. While other properties, gas sensor consists of optic methods, acoustic methods, gas chromatograph, and calorimetric methods. Many types of gas sensors have been developed. Each of them has advantages and disadvantages [1]. Based on the principles of gas detection, gas sensor can be categorized into two i.e. non-optical sensors and optical sensors [2]. Non-optical sensor is a gas sensor that detects gas by interacting directly with the gas to be tested. Advantages from non-optical sensor are low cost of fabrication and short response time, while the disadvantages are relatively low sensitivity and selectivity [15]. The optical sensor is a gas sensor that detects gas without interacting directly with the gas to be tested by utilizing the optical properties of the gas. Among these two types, the optical sensor has several advantages such as: long lifetime, reliable, stable at ambient temperature and easy to be designed and manufactured [15]. Here, the author will make a gas sensor by using two methods, namely optical methods and acoustic methods. By using the optical methods it is briefly easy to reach higher sensitivity, selectivity and stability than non-optical methods with longer lifetime. These methods have short response time. Its performance will not deteriorate with environmental changes or catalyst poisoning caused by certain gases, etc. the basic principle of optical methods for gas sensing is based on spectroscopy. However, the constraints of these applications for gas sensors are in miniaturization and cost is relatively high. Only a few commercial gas sensors are based on the principles of optics [15].

For acoustic or ultrasonic methods, it can improve the weaknesses of the gas sensor by chemical methods, such as short lifetime [15]. Measurements parameters involved in the acoustic method basically are divided into 3 categories namely speed of sounds, attenuation and the acoustic impedance. First parameter involved that is speed of sound determine many properties of gas and can be used for measuring speed of sound, such as to identify a specific type of gas through the speed of sound is different from others in the group [9], to detect gas concentration target, based on mathematical reasoning that is proportional to the time difference of sound propagation [4], and to calculate the molar weight of the composition or different gases in a mixture based on some equations of thermodynamics [11]. Attenuation is when an acoustic wave travels through a medium, there is the energy lost as thermal or scattered energy called attenuation [12]. Each of gas has different attenuation properties, hence providing a way to detect specific gases. Attenuation could also combine with sound speed to determine gas properties [13]. For acoustic impedance density of the gas can be determined by the acoustic impedance, because the acoustic impedance is given by a simple equation: $Z = \rho C$, where ρ is the density of gas and C is the speed of sound. Thus, the acoustic impedance is measured and the speed of sound, the gas density can be calculated [14].

For the initial stage, the author will use the acoustic methods to make the initial prototype of gas sensor using acoustic resonator. Acoustic resonator made to work
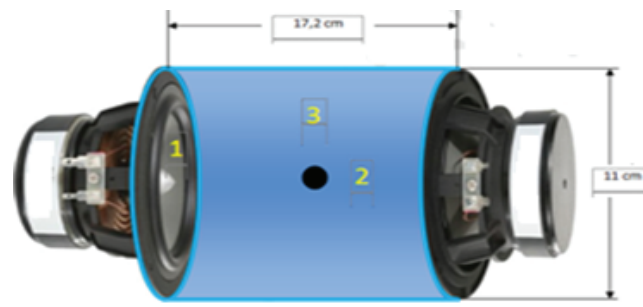
Notes :

1: Speaker
2: Microphone
3: Alumunium tube

Figure 1: Resonator design.

automatically at its resonance frequency, and it is expected to detect changing in gas concentration contained in the acoustic resonator.

2. Methodology

This research was conducted in four phases. The first phase is designing the resonator, the second phase are manufacture of resonator and initial testing in order to obtain a resonance frequency of the resonator. The third phase is the conditioning resonator to work automatically at the resonance frequency. The final phase of this research is testing directly to butane. Resonator is designed by using alumunium tube, 2 speakers, and a microphone. Resonator is made using alumunium tube with diameter 11 cm, 17.2 cm in length, and 0.5 cm in thick. Design of resonator can be seen in Fig. 1.

3. Results and Discussions

Resonator will work in accordance with the principle of organ pipes, where the resonant frequency will be influenced by the speed of sound in a resonator which is influenced by the concentration of gas in the resonator. The resonator is designed to be able to work at the resonant frequency. This is done because the resonance of the resonator will be affected by the speed of sound in the resonator, while the speed of sound in the resonator will be strongly influenced by the type of gas contained in the resonator and gas concentration contained in the resonator. So it should work on the resonator resonance frequency. If the type of gas in the resonator is different and different concentration, then the resonance frequency of the resonator working will also vary. Based on this principle, resonators are constructed can be used as a simple gas sensor. The resonance frequency of the resonator can be seen in Fig. 2.

From Fig. 2 it can be seen, there are two of high peak amplitude of the output signal from the microphone on 400Hz and 3.8 kHz.

The system is used as a gas sensor based on the principle of resonance. As noted in the previous section that weight or concentration of gas in resonator will affect the speed of sound in the resonator, while the speed of sound in resonator changes will affect the resonance frequency of the resonator. So, to be able to detect changes in gas consentration, then the system needs to be conditioned in order to work at
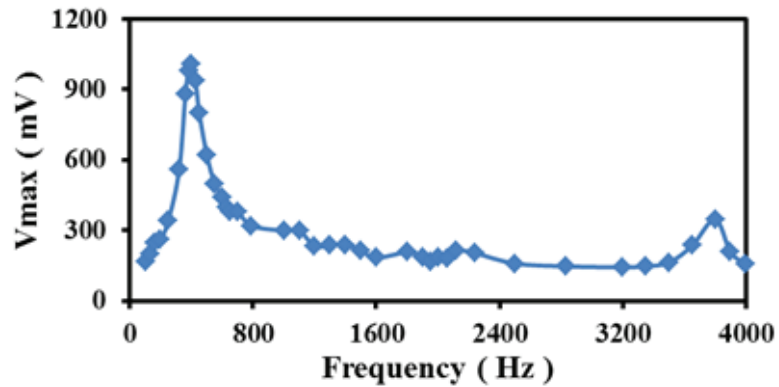
Figure 2: Resonance frequency of the resonator.
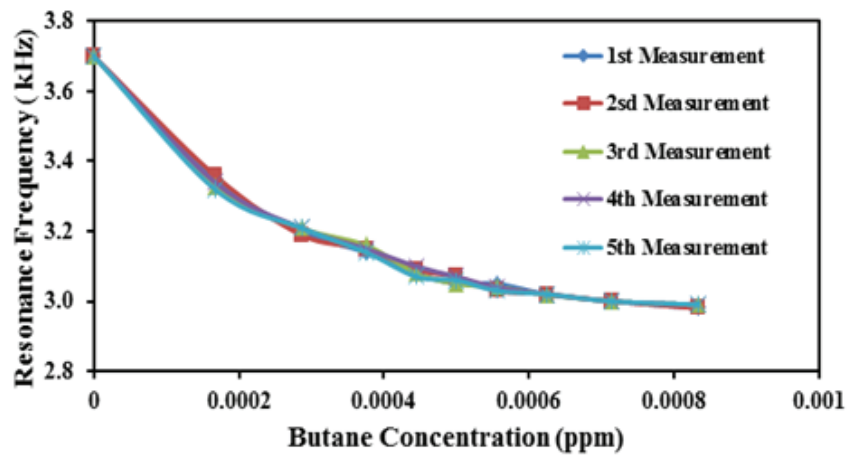
Figure 3: Effects of butane concentration changing against resonance frequency of resonator.

the resonant frequency automatically without a signal from frequency generator. In this test, the resonance frequency of resonator is approximately 3.7 kHz. Resonant frequency automatically obtained do not differ much from the initial measurements i.e. 3.8 kHz.

For direct gas testing, butane (C_4H_{10}) and nitrogen (N_2) gases were used. The purpose is to determine the effect of butane concentration changing in the resonator against the resonance frequency of the resonator system. The system is conditioned to work automatically. From the measurements that have been done, the effect of butane concentration changing against the resonance frequency of resonator can be seen in Fig. 3.

The purpose of this resonator is to determine the concentration of the gas contained in the resonator, so Fig.4 can be used to get the fuction of concenration to the resonance frequency of resonator. The fuction of concentration against the resonance frequency of resonator is:

$$Concentration = 99133.89 - 92357.75f + 28710.76f^2 - 2977.168f^3 \quad (1)$$

where f is the resonant frequency.
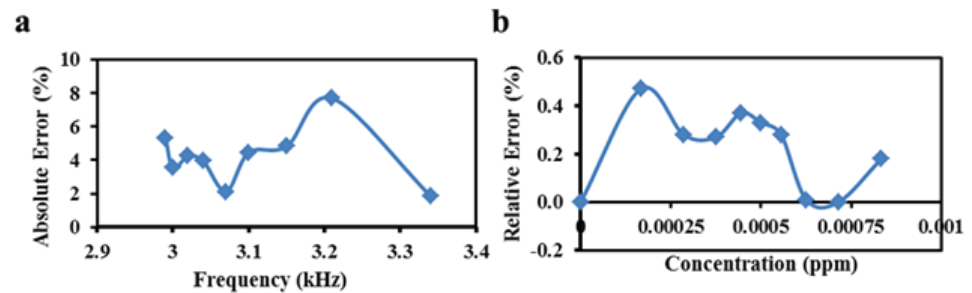
Figure 4: (a) Absolute error of the system and (b) relative error of the system.

The absolute error and the relative error of the system can be seen in Fig.5 (a) and Fig.10(b).

On Fig. 4(a) can be seen that the largest absolute error of the system is 7.69%, and on Fig. 4(b) can be seen the largest relative error of the system is 0.47%. It is mean the system resonator accurate and precision to detect the butane concentration changing.

4. Conclusions

According to the result, can be concluded that the resonator system accurate to detect the butane concentration changing, with the largest absolute error is 7.69%, and the resonator system has high precision with the largest relative error is 0.47%.

References

[1] Optical Gas Sensing: a review, IOP Publishing, Measurement Science and Technology, (2012).

[2] Liess M., in *Gas Sensing*, Hochschule RheinMain University of Applied Sciences, Germany, 2014.

[3] E. D. McNaghten, A. M. Parkes, B. C. Griffiths, A. I. Whitehouse, and S. Palanco, Detection of trace concentrations of helium and argon in gas mixtures by laser-induced breakdown spectroscopy, *Spectrochim Acta B At Spectrosc*, **2009**, 1111–1118, (2009).

[4] M. Shan, X. Li, C. Zhu, and J. Zhang, Gas concentration detection using ultrasonic based on wireless sensor networks., *Proceedings of the 2nd International Conference on Information Science and Engineering (ICISE)*, 2101–2106, (2010).

[5] H. Zheng, Experiment study of continuous emission monitoring system based on differential optical absorption spectroscopy. (2008).

[6] A. Elia, C. di Franco, P. M. Lugara, and G. Scamarcio, Photoacoustic spectroscopy with quantum cascade lasers for trace gas detection, *Sensors (Basel)*, **2006**, 1411–1419, (2006).

[7] Y. Wang, K. Wang, Q. Wang, and F. Tang, Measurement of CH4 by differential infrared optical absorption spectroscopy., *Proceedings of the 9th International Conference on Electronic Measurement & Instruments*, 1761–1766, (2009).

[8] G. F. Fine, L. M. Cavanagh, A. Afonja, and R. Binions, Metal oxide semi-conductor gas sensors in environmental monitoring, *Sensors (Basel)*, **10**, 5469–5502, (2010).

[9] H. Bai and G. Shi, Gas sensors based on conducting polymers, *Sensors (Basel)*, **2007**, 267–307, (2007).

[10] M. Sonoyama, Y. Kato, and H. Fujita, in *Application of ultrasonic to a hydrogen sensor*, 2010.

[11] S. Jacobson, New developments in ultrasonic gas analysis and flowmetering, *Proceedings of IEEE International Ultrasonics Symposium*, 508–516, (2008).

[12] L. W. Schmerr and S. J. Song, in *Ultrasonic Nondestructive Evaluation Systems: Models and Measurements*, Springer, New York, NY, 2007.

[13] A. Petculescu, B. Hall, R. Fraenzle, S. Phillips, and R. M. Lueptow, A prototype acoustic gas sensor based on attenuation, *J Acoust Soc Am*, **2006**, 1779–1782, (2006).

[14] S. Mylvaganam, M. Halstensen, H. Engen, and K. Esbensen, Gas density metering in ultrasonic gas flowmeters using impedance measurement and chemometrics., *Proceedings of 1999 IEEE Ultrasonics Symposium*, 435–439, (1999).

[15] L. Xiao, C. Sitian, L. Hong, H. Sha, Z. Daqiang, and N. Huansheng, Review: A Survey on Gas Sensing Technology, *Sensors (Basel)*, **2012**, 9635–9665, (2012).

KnE Engineering

Knowledge E
Engaging minds

Conference Paper

Efficient Mixer in Baking "Galamai" Process by Using Camera Sensor

Rahmadi Kurnia and Faris AlFaruqi

Department of Electrical Engineering Andalas University, Padang, Indonesia

Abstract

One of Indonesian traditional food, expecially in Minangkabau called galamai was baked with inefficient and complicated manner. At least 4 or 5 person were needed to mix 30 kg galamai batter for 6 hours during baking process. This research solved those problems. The aim of this work was to displace a human labor with an automatic machine to make it more efficient. The basic idea of this reseach is to desain an automatic mixer by using camera sensor for controling the speed of DC machine. This mixer was worked base on the fact galamai batter characteristics that its color and viscosity will change during cooking process. Discoloration in galamai batter will be captured by camera sensor as a data input. Images data of the color of galamai batter will be converted in grayscale images. The intensity of gray scale image became an input for FIS (Fuzzy Inference System) which controled the speed of machine. The speed of motor will increase when the grayscale color of galamai batter is low. The system could controled turning speed of motor automatically with acuration of speed value is more than 96.4% and synchronized in variation of galamai batter volume.

OPEN ACCESS

1. Introduction

Galamai, one Indonesian traditional food from Minangkabau especially in Payakumbuh is made of glutinous rice flour, sugar and coconut milk. In this current time, people still use a manual process to cook galamai. For instance, to produce 30 kg galamai, all the ingredients were mixed by 4 or 5 person during 6 hours baking process. In case of the batter of galamai was roasted on the fire, it should be continuously mixed without stopping to avoid conglomeration product. However, this manner was inefficient as too much wasted effort and time undertaken during baking process. In case of the plate of batter galamai was not covered during mixing process, it was possible that a lot of dust and sweat affected in the galamai batter. Therefore, the galamai also unhygienic for people.This work tackled such kind of problems. We make a mixer system by using a DC machine as replacing human labor to mix galamai batter. The speed of DC machine was controlled automatically. The plate of mixer was covered and the material was made of aluminum.

There are various methods to control the DC machine such as: cascade control system [1], PID controller [2] and neural network based controlling operation with fuzzy modeling [3]. In this work, the DC machine was controlled based on fuzzy logic rules.

How to cite this article: Rahmadi Kurnia and Faris AlFaruqi, "Efficient Mixer in Baking "Galamai" Process by Using Camera Sensor," *KnE Engineering*, vol. 2016, 7 pages. DOI 10.18502/keg.v1i1.483

Page 1
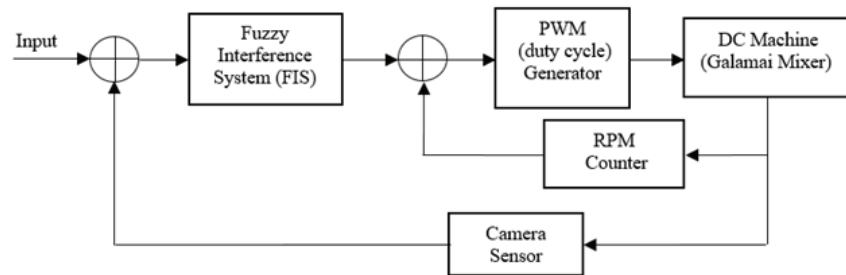
Figure 1: Efficient mixer control block diagram.

The fuzzy membership function determined in accordance with discoloration of galamai In fact, the color of galamai batter was degraded from white to black during this process. This color degradation was observed by camera sensor which put in front of galamai batter during baking process. When the color of galamai batter discolorized to the dark color, its velocity was also becomes more viscous. Therefore, the speed of DC machine was reduced due to the increasingly thickened batter will make the rotation of motor restrained. The system detected this condition by a RPM counter. Then, it generated the microcontroller to magnify the DC motor voltage for stability motor speed.

Previous research has suggested that camera sensor and DC machine can be applied for human daily live. The camera and DC machine are compact and affordable, which makes them attractive for versatile applications including surveillance and computer vision. Some of successful application of these technologies are in automatic door that controlled by smart camera [4], belt conveyor for security checkpoint surveillance by using camera network[5], and smart coffee mixer which can stopped automatically when a suitable of coffee color is reached [6]. In this paper, we designed an efficient mixer in baking galamai which adapted with volume of galamai batter.

2. Methods

At first, the DC machine was set with 55 Pulse Width Modulation (PWM) for minimum starter. PWM Signal is a method for generating an analog signal using a digital source. A PWM signal consists of two main components that define its behavior: a duty cycle and a frequency. In this work, the freqwency was fix because the speed of DC machine should keep consttant. Figure 1 shows the overall view of the mixer system with camera sensor:

When the DC machine switched on and start to mix the galamai batter, there are two feedback loops to control the system. First feedback loop is camera sensor that capture the the color of galamai batter periodically. The second is RPM (rotation per minute) counter for DC machine's speed control.To make the best product of galamai, the batter was mixed without stopping during roasting at temperatures of 100-120 degrees Celsius. Therefore, DC machine *is required to keep rolling at constant speed*.

Camera sensor captured the galamai batter frequently. When the camera sensor captured the batter image, it still in true color format or also known as an RGB frame.
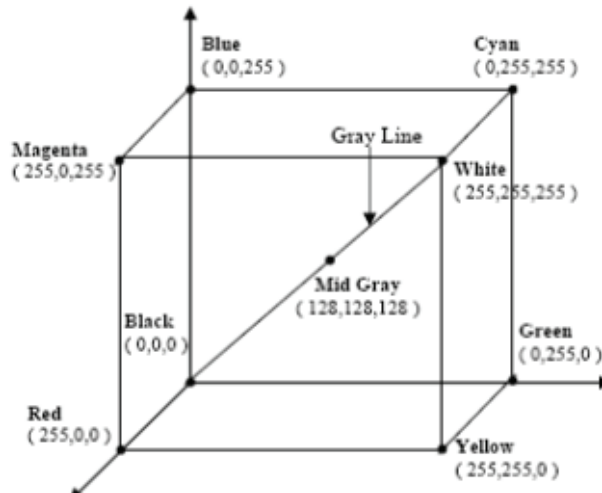
Figure 2: RGB color space [7].

A true color image is an image in which each pixel is specified by three values (0 - 255) one each for the red (R), green (G), and blue (B) components of the pixel scalar. Most often image data are collected from an RGB device. RGB spaces are native to displays, and digital cameras. Each imaging system has its own RGB color space that depends upon the spectral sensitivities of its color sensors and its settings. It is possible to calibrate an imaging device by determining the relationship between its RGB space and a device independent. Figure 2 shows the RGB color space.

In this work, we convert the color of galamai batter ffrom RGB to gray level image. Gray levels represent the interval number of quantization in gray scale image processing. There are 256 gray levels in an 8 bit gray scale image, and the intensity of each pixel can have from 0 to 255, with 0 being black and 255 being white. The gray scale of RGB was obtained by determining the average of each pixel as follows [8]:

$$I = \frac{R + G + B}{3} \tag{1}$$

where I is intensity or gray level of each pixel.

The gray level of each pixel in batter image determined to obtain tthe average of gray level image. This avaerage value was as an input to Mamdani Fuzzy Inference System (FIS). In this step, FIS determined the relationship between average of gray level image and pulse width modulation (PWM) of DC machine as an input. In this paper, the maximum average of gray level image was 200 due the color of batter was not absolutely white. From some experiment results, an appropriate interval of average gray level image and the duct cycle of PWM DC machine as shown in table 1.

Based on tabel 1, the input membership fuction of fuzzy interference system for duty cycle PWM and average gray scale image was described in Fig. 3. While, output variable of fuzzy interference system is RPM. We set the RPM from 0 to 100 rotations per minute. We devided four speed condition of RPM Speed as shown in Figure 4.

As the set speed is varied due to the galamai batter dicoloration, the PWM duty cycle also varies. In Figure 1, there are two ways to get RPM of DC machine in the

Color	Average Gray level	Duty Cycle of PWM
Whitish	97 -255	Very Low
Light Grey	42- 118	Low
Dark Grey	Dec-88	Midle
Black	0 - 32	High

TABLE 1: Gray Level and PWM Classification.
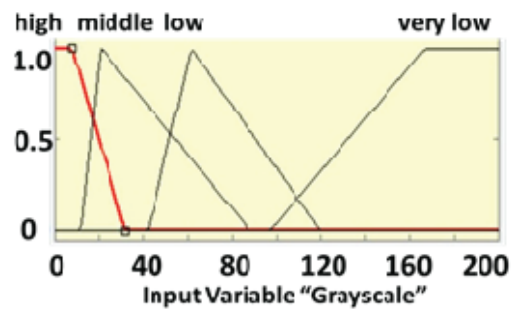
Figure 3: FIS input membership function.
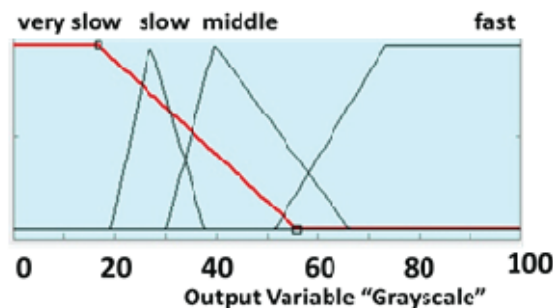
Figure 4: FIS output membership fuction.

system. First, the RPM number of DC machine was counted directly by Adruino when the DC machine was switch on. The second, the RPM number of DC machine was obtained from defuzzification of FIS output which is related with gray level image of batter galamai. These two PWM numbers were compared each other to get the constant speed. Two numbers of these RPM must be equal. If RPM number of Adruino is less than RPM number of FIS output, the PWM generator will increase the duty cycle. Therefore the DC machine rotates faster. If RPM number of Adruino is more than RPM number of FIS output, the PWM generator will decrease duty cycle so that the DC machine become slowly. These step work continuously during baking process

3. Results

In this research, we used two samples batter galamai : the 250 ml and 500 ml. Both were analized separately during baking process. Camera sensor capture the batter 4
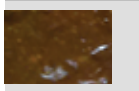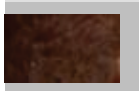
No.	Batter color	Gray Scale Pixel Intensity	No.	Batter color	Gray Scale Pixel Intensity
1		194,2451	3		63,3895
2		96,7731	4		43,8092

Table 2: Batter galamai pixel intensity

Case	Grayscale	Duty cycle PWM [%]	Rpm counter	Rpm fuzzy	RPM Error [%]
1	151.425	21.067	22	21.026	4.427
2	153.449	20.565	25	20.828	16.688
3	98.840	26.996	26	27.511	5.812
4	98.639	28.502	32	28.055	12.328
5	65.727	37.302	40	38.148	4.630
6	65.310	37.804	38	38.237	0.624
7	41.481	28.176	46	45.714	0.622
8	41.319	28.678	45	45.727	1.616

Table 3: RPM and Duty Cycle PWM in 250 ml batter galamai

times as shown in table 2. From the table we observe that the pixel intensity of batter galamai was decrease from light to dark.

We analyze the RPM and duty cycle PWM of each two samples for 8 cases. Table 3 and 4 shows the results:

From table 3, RPM number was increase as the discoloration of gray scale. This condition is caused by the velocity of batter galamai becomes more viscous during baking process. Therefore the duty cycle PMW also increase to reach a constant speed of mixer. From the table 3, we obtained that the average error percentage between RPM counters and RPM Fuzzy is 3.6%. It means that the speed of mixer is commonly

Case	Grayscale	Duty cycle PWM [%]	Rpm counter	Rpm fuzzy	RPM Error [%]
1	146.705	23.075	22	21.580	1.909
2	147.634	22.573	22	21.509	2.232
3	97.772	28.957	28	28.123	0.439
4	96.572	28.455	28	28.187	0.668
5	71.031	39.216	38	37.254	1.963
6	69.584	39.718	38	37.278	1.900
7	41.481	30.180	46	45.714	0.622
8	38.907	29.678	45	45.635	1.411

Table 4: RPM and Duty Cycle PWM in 500 ml batter galamai.
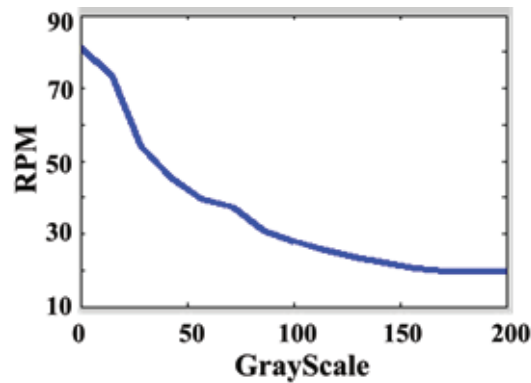
Figure 5: FIS output membership function.
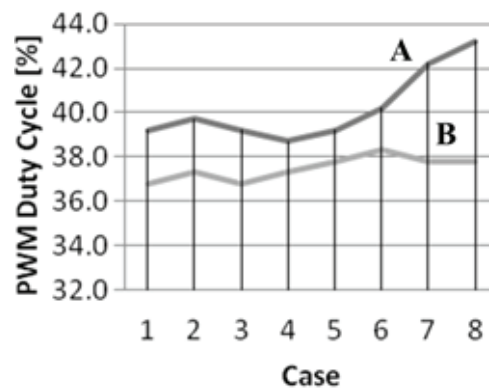
Figure 6: PWM values of various volume.

constant while the gray level and velocity of baked galamai were changed with accuracy of speed value is 96.4 % The complete PWM output of FIS membership function for 500 ml galamai batter was described in Figure 5.

Figure 6 shows the comparison of PWM duty cycle ratio between 250 ml and 500 ml galamai batter for 8 cases observation. From the figure, a big volume of batter galamai requires PWM duty cycle ratio more than the small one.

4. Summary

The proposed a mixer which is designed and implemented using camera sensor to make galamai efficiently is completely succeeded. The system controlled turning speed of motor automatically with accuracy of speed value is 96.4 % and also can be adaptive in variation of galamai batter volume. Simulation results indicate that the proposed efficient mixer can keep its speed constant in various velocities. The system has a good performance in various volume of galamai batter.

5. Acknowledgement

References

[1] A. S. Abd Elhamid, Cascade Control System od Direct Curent Motor, *World Appl Sci J*, **18**, 1680–1688, (2012).

[2] P. Kumar and R. Mishra, Implementation of FPGA based PID Controller for DC Motor Speed Control System, *International Journal of Engineering Trends and Technology*, **4**, no. 3, (2013).

[3] G. Madhusudhana Rao and B.V.S. Ram, Speed Control of Multi Level Inverter Designed DC Series Motor with Neuro-Fuzzy Controllers, *Journal of Computing*, **1**, no. 1, (2009).

[4] J. -C. Yang, C. -L. Lai, H. -T. Sheu, and J. -J. Chen, An intelligent automated door control system based on a smart camera, *Sensors (Basel)*, **13**, 5923–5936, (2013).

[5] Z. Wu and R. J. Radke, (2011)., Real Time Airport Security Checkpoint Surveillance Using a Camera Network, Workshop CNWASA, IEEE Conf.Computer Vision and Pattern Recognition, 25-32.

[6] I. Intyas, 2012, Implementasi Fuzzy Logic dan Sensor Warna pada Mesin Pengaduk Kopi Otomatis, Padang, Thesis.

[7] A. Noor, et al., Understanding Color Models:A Review ARPN, *Journal of Science and Technolog*, **2**, no. 3, (2012).

[8] M. Rahmadi Kurnia, et al., Object Recognition through Human-Robot Interaction by Speech, Proceedings of the 13th IEEE International Workshop on Robot and Human Interactive Communication (RO-MAN 2004).

Conference Paper

Application of Gold Nanoseeds in Surface-Enhanced Raman Spectroscopy for Detection of Urea

Nur Adliha Abdullah, Norhayati Abu Bakar, Muhamad Mat Salleh, and Akrajas Ali Umar

Institute of Microengineering and Nanoelectronics (IMEN), Universiti Kebangsaan Malaysia, 43600 UKM Bangi, Selangor, Malaysia

Abstract

This paper reports a study to detect urea by a homemade surface-enhanced Raman Spectroscopy (SERS) sensor using gold- nanoseeds (AuNS). The nanoseeds were prepared by the first of two steps of the seed-mediated technique where the sizes of the nanoseeds were controlled through the heat treatment periods. It was demonstrated that gold- nanoseeds (AuNS) with the averages sizes of 15-20 nm can be utilized to enhance the Raman peaks intensities of urea. The enhancement intensities of the Raman peaks are linear with the urea concentrations where the lowest urea concentration that was detected using AuNS from this study is 0.0901 g/L.

Keywords: surface-enhanced Raman spectroscopy (SERS), gold-nanoseeds (AuNS), urea, chemical sensors

🔓 OPEN ACCESS

1. Introduction

High level of urea in blood or in urine may indicate renal failure. Most methods used to determine urea are based on indirect chemical process such as enzymatic and chemical assays [1]. Enzymatic methods use the urea-metabolizing enzyme urease, which degrades urea into ammonia. The produced ammonia is measured by a pH indicator [2]. Meanwhile, chemical assays used particular chemicals to form colored product [3]. All of these methods are time consuming and may have byproducts from the chemical reactions that interfere in the measurement result. It is a great interest to use a direct spectrometric determination of urea. Raman Spectroscopy (RS) technique is one of the possible techniques where urea is able to produce a specific Raman shift spectrum. However, due to the limitations of RS such as weak Raman signal and small cross section of Raman scattering, surface-enhanced Raman spectroscopy (SERS) has been developed [4]. SERS is an optical sensor system that highly sensitive as compared to normal RS which allows the detection of single molecule even at low concentration of sample [5]. The enhancement in SERS is provided by the localized-surface plasmon resonance (LSPR) of nanostructured metals such as gold, silver, copper and platinum.

This paper reports the application of gold nanoparticles to enhance Raman shift spectrum of urea using a homemade SERS sensor system. The nanoparticles were prepared using a simple of seed-mediated technique.

How to cite this article: Nur Adliha Abdullah, Norhayati Abu Bakar, Muhamad Mat Salleh, and Akrajas Ali Umar, "Application of Gold Nanoseeds in Surface- Enhanced Raman Spectroscopy for Detection of Urea," *KnE Engineering*, vol. 2016, 6 pages. DOI 10.18502/keg.v1i1.484

Page 1

2. Experimental

Gold(III) chloride trihydrate ($HAuCl_4 . 3H_2O$) (99.9%), trisodiumcitrate ($C_6H_5Na_3O_7$), sodium borohydride ($NaBH_4$) and urea powder were purchased from Sigma Aldrich and used without further purification. Gold nanoseeds (AuNS) were prepared by the first of two steps of the seed-mediated technique where 0.5 mL of 0.01 M $HAuCl_4 . 3H_2O$, 0.01 M $C_6H_5Na_3O_7$ and 0.1 M cooled $NaBH_4$ were mixed in deionized water. The colloidal of gold-nanoseeds were heated using microwave for 10s, 30s and 60s respectively and characterized using Uv-Vis Spectrometer (Hitachi U- 3900H), particle size analyzer (PSA) and field- emission scanning electron microscopy (LEO SUPRA 55VP FESEM). Urea solutions in pure water of four different concentrations ranging from 0.1M to 2.0 M were prepared and then mixed with the colloidal of AuNS. The SERS substrates were prepared by dropping the pure urea or the mixed urea-AuNS solutions onto cleaned quartz substrates and left to dry at the room temperature. The detection of urea was studied by recording Raman spectra of the prepared SERS substrates using a homemade SERS sensor system that consists of a laser as light source (523nm), a fiber probe, a spectrometer QPro-60 (Ocean Optics) and a sensor chamber.

3. Results and Discussion

Figure 1 shows the FESEM images of gold- nanoseeds (AuNS) thin films on ITO substrates that were prepared with variation of heat treatment periods. The AuNS have quasi-spherical shaped with average diameter as measured by the particle size analyzer were 8, 11, 15 and 20 nm corresponding to 0, 10s, 30s and 60s heat treatment periods respectively. Hence, we may have variation of the nanoseeds sizes through heat treatment periods of the colloidal. In the next discussion, we refer the localized-surface plasmon resonance (LSPR) based on the nanoseeds sizes.

Figure 2 shows the LSPR absorption spectra of colloidal gold- nanoseeds samples with variation of the particles sizes. Each sample has one LSPR peak ranging from 503 nm to 512 nm according to the increasing sizes of nanoseeds respectively. The intensities of peaks are increasing with the nanoseeds sizes. This results is agreed with the previous research [6].

Figure 3 shows the Raman spectra of urea samples excited with 532 nm laser light. The concentration of urea used is 0.5 M. The samples are pure urea and urea mixed with AuNS of different sizes. The Raman spectrum of the pure urea has two sharp peaks at 548 cm^{-1} and 1012 cm^{-1}, and a small broad peak at 1181 cm^{-1}. It is observed that two samples, urea mixed with 15 nm and 20 nm AuNS are able to enhance the Raman peaks intensities. Meanwhile for the other two samples, 8 nm and 11 nm AuNS, the samples are not able to enhance the Raman scattering signal. This means that the samples with small size of AuNS and low LSPR peaks are not able to assist urea molecules to produce the Raman scattering signal because smaller nanoparticles will have less surface area and low conductivity of electron for oscillation. Thus, less light is absorbed by the surface which weakens its electromagnetic field and reduces the
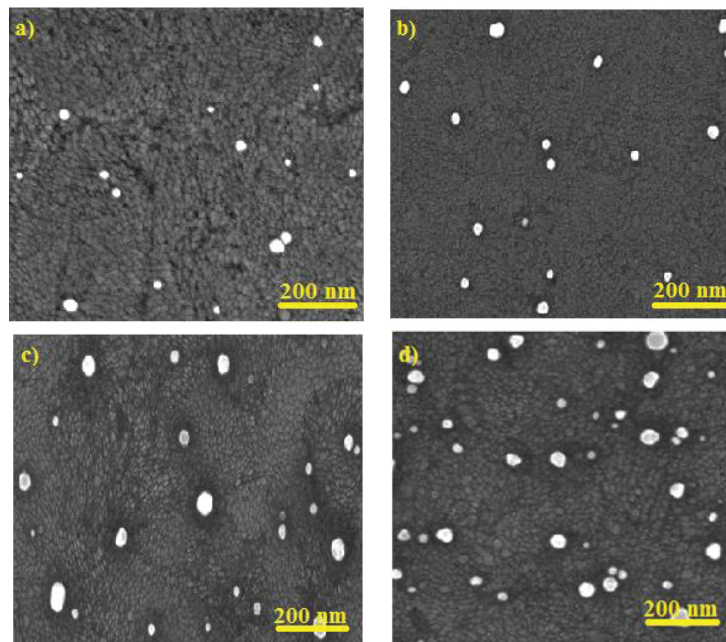
Figure 1: FESEM images of gold-nanoseeds prepared at different heat treatment periods: (a) 0, (b) 10, (c) 30 and (d) 60s.
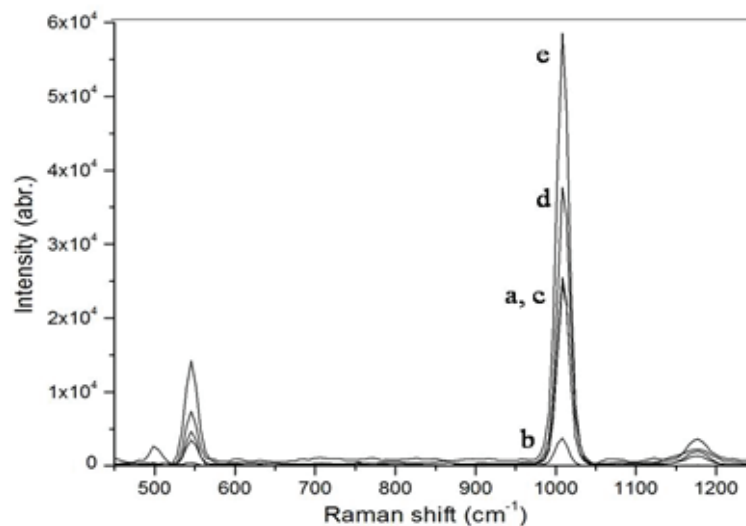
Figure 2: Absorption spectra of thelocalized- surface plasmon resonance (LSPR) of colloidal gold-nanoseeds with variation of the nanoseeds sizes: (a) 8 nm, (b) 11 nm, (c) 15 nm, and (d) 20 nm.

signal of Raman scattering [7]. From these results, we may concluded that the effective sizes of the AuNS to enhance the Raman scattering are about 15-20 nm.

Figure 4 shows the SERS spectra of urea samples with variation of urea concentrations; 0.1M, 0.5M, 1.0M and 2.0M. The size of AuNS used in this measurement is 15 nm. It was observed that the enhancement intensities of the Raman peaks are linear with urea concentrations. The linearity correlation coefficients (r) are 0.968 and 0.996 for peaks at 548 cm^{-1} and 1012 cm^{-1} respectively (Figure 5). The lowest urea concentration that was detected using AuNS from this study is 0.1 M which is 0.0901 g/L. The AuNS used in this study were prepared using a simple technique that involves
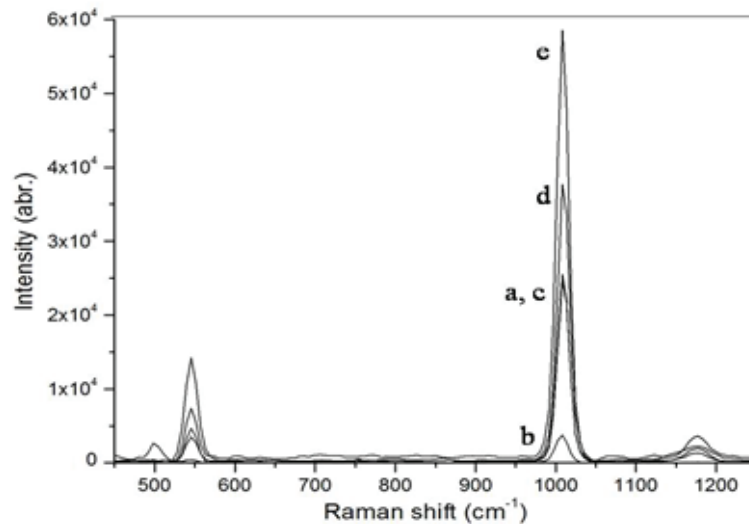
Figure 3: SERS spectra of urea samples taken with 532 nm excitation. (a) 0.5M urea, and 0.5M urea mixed with (b) 8 nm (c) 11 nm (d) 20 nm (e) 15 nm AuNS.
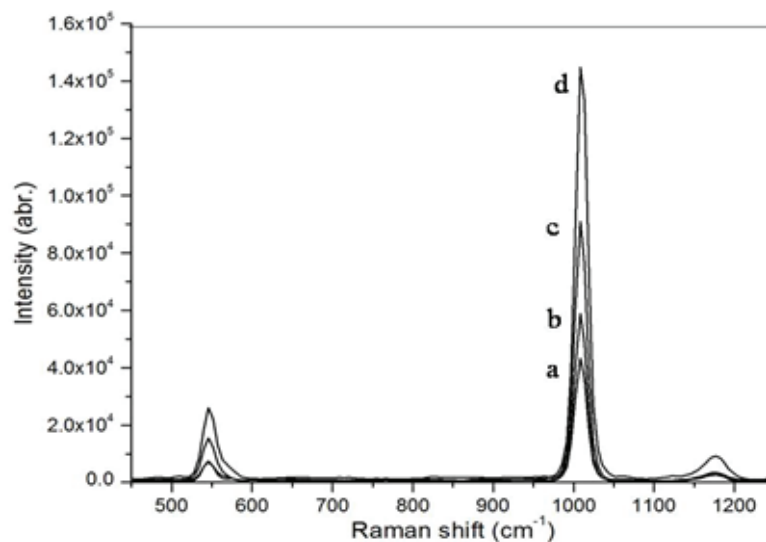
Figure 4: SERS spectra of 15nm gold-nanoseeds for variation concentrations of urea: (a) 0.1 M, (b) 0.5 M, (c) 1.0 M and (d) 2.0 M.

only the seeding process. Hence, to improve the sensing sensitivity of the SERS system, we have to prepare gold nanoparticles using a complete process of the seed- mediated growth technique.

4. Conclusion

We have demonstrated that gold-nanoseeds (AuNS) with the averages sizes of 15-20 nm can be utilized to enhance the Raman intensity of urea. The nanoseeds were
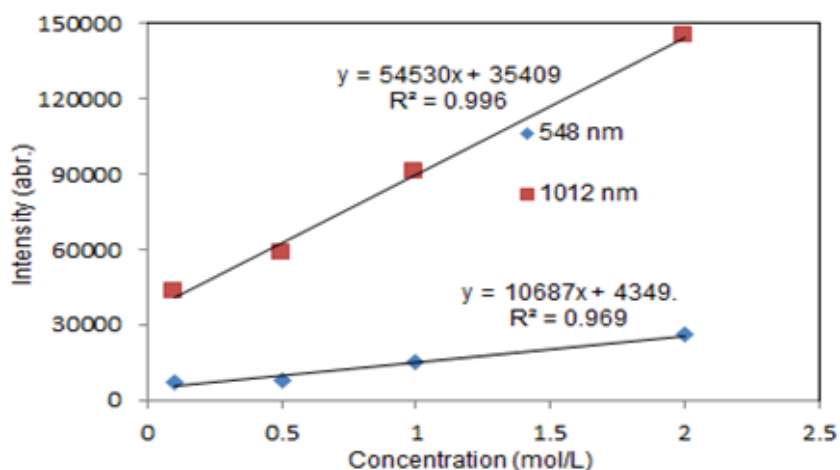
Figure 5: Linearity correlation of 15 nm gold- nanoseeds for variation concentrations (M) of urea: (a) 0.1, (b) 0.5, (c) 1.0 and (d) 2.0.

prepared by the first step of the seed-mediated technique where their sizes were controlled by the heat treatment. Using our homemade surface-enhanced Raman spectroscopy (SERS) sensor we are able to detect the urea concentration as low as 0.0901 g/L in seeding state of gold.

5. Acknowledgement

References

[1] M. Tak, V. Gupta, and M. Tomar, A highly efficient urea detection using flower-like zinc oxide nanostructures, *Mater Sci Eng C*, **57**, 38–48, (2015).

[2] B. Krajewska, Ureases I. Functional, catalytic and kinetic properties: A review, *J Mol Catal, B Enzym*, **59**, 9–21, (2009).

[3] P. Kumar, P. R. Lambadi, and N. K. Navani, Non-enzymatic detection of urea using unmodified gold nanoparticles based aptasensor, *Biosens Bioelectron*, **72**, 340–347, (2015).

[4] S. McAughtrie, K. Faulds, and D. Graham, Surface enhanced Raman spectroscopy (SERS): potential applications for disease detection and treatment, *J Photochem Photobiol Photochem Rev*, **21**, 40–53, (2014).

[5] M. V. Chursonova, L. Germash, V. O. Yukhymchuk, V. M. Dzhagan, I. A. Khodasevich, and D. Cojoc, Optimization of porous silicon preparation technology for SERS applications, *Appl Surf Sci*, **256**, 3369–3373, (2010).

[6] W. Haiss, N. TK. Thanh, J. Aveyard, and D. G. Fernig, Determination of size and concentration of gold nanoparticles from UV-vis spectra, *Anal Chem*, **79**, 4215–4221, (2007).

[7] S. Hong and X. Li, Optimal size of gold nanoparticles for surface- enhanced Raman spectroscopy under different conditions, *J Nanomater*, **49**, 1–9, (2013).

Knowledge E
Engaging minds

Conference Paper

Colour Classification Using Entropy Algorithm in Real Time Colour Recognition System for Blindness People

Gurum Ahmad Pauzi and Warsito

Physics Department, Faculty of Mathematics and Natural Sciences, University of Lampung, Jalan Sumantri Brojonegoro No. 01, Lampung 35141, Indonesia

Abstract

This article describes the real time instrumentation system to help blindness people for recognize a colour. Colour image captured by the digital camera, and it classified into ten basic colours names (black, brown, cyan, red, orange, yellow, green, blue, magenta, gray and white) by using entropy algorithm. The conclusion of colour classification will be informed to the user in sound or vocal information. This study has used two colour models HSV (hue, saturation and value) and RGB (red, green and blue). The accuracy of Classification using HSV has 90%, and RGB model has 71.5%.

Keywords: Colour Classification, visual impairment, blindness, entropy algorithm

🔓 **OPEN ACCESS**

1. Introduction

Colour has a crucial role in the activities of human life as a guide for completing various activities. Colour is an important factor to perceive and analyze characteristics of an object such as determining the dimensions of an object, and spacing [1]. This variable is the basic for distinguishing one object to another. It can provide a psychological effect on a person such as mood, feeling and perception [2]. The Inability to see the colour becomes a major problem for people with visual impairments or blindness.

A digital colour obtained from combination of RGB (red, green and blue) values are built based on the represents the x-axis, y and z coordinates of Cartesian space. There are also colour HSV models (Hue, Saturation and Value) and other model. The format of these colours can be converted using a specific equation [3]. In reality, although there are many colours from RGB combinations, not all colour name needs to be recognized. The colour of an object generally identified by grouping to the basic colour names such as black, brown, cyan, red, orange, yellow, green, blue, magenta, gray and white. An object called with a certain colour if the colour is most dominant in viewing area. The Viewing area is the middle area in a landscape image that has been observed in real time.

According to the WHO notes that in 2010, the number of people with visual impairment is estimated to be 285 million, with 39 million are blind [4]. These data showed an increasing number of patients with eye disorders in worldwide ranging from 161

How to cite this article: Gurum Ahmad Pauzi and Warsito, "Colour Classification Using Entropy Algorithm in Real Time Colour Recognition System for Blindness People," *KnE Engineering*, vol. 2016, 5 pages. DOI 10.18502/keg.v1i1.485

Page 1
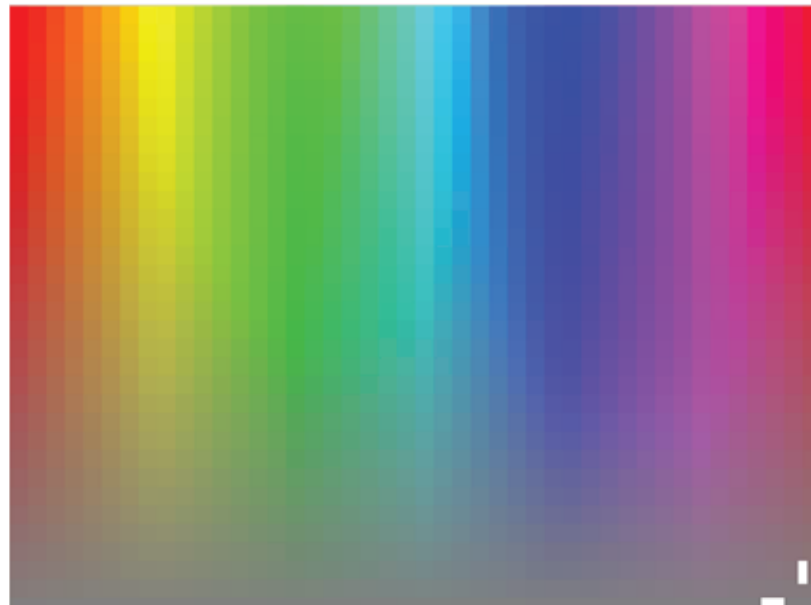
Figure 1: Variation combination of RGB value in 8-bit formats.

million people (about 2.6% of the total world population) consist of 124 million people with low vision capability and 37 million blind in total [5]. WHO on 30 September 1999 launched the Global Commitment Vision 2020 as The Right of Sight is an idea to cope with visual impairment and blindness. This can be prevented or rehabilitated in an integrate manner to reduce the amount of blindness in 2020 [6]. The inventions of the devices for detection and classification colours are expected to be part of the solution to help blindness people in carrying out his activities.

2. Methodology

2.1. Training Colour Test with Entropy Algorithm

The data, the digital colours are obtained from variation combination RGB value in 8-bit formats, is represented by Fig 1.

The data modified and entered in table columns form consist with value of R, G, B and colour names. Here is the problem; every person has a different perception in the classification many colour to basic colours names. It can be caused by many factors such as environmental influences, keen of the eyes and even the colour blind. The RGB data is converted into the HSV format by using the HSV equation [3]. In 3-dimension form, HSV model is described as an inverted hex cone. The determination limit of each groups of colour is based on a specific coordinate. Black is height from the base, white is the middle peak area of inverted cone, and the other colour is determined by the angle degree of circle of hex cone. Thus the HSV value and Colour Name put in the table too. Not all combination RGB data is used for training to the entropy algorithm, only at 450 RGB and HSV values are taken by random. The result of entropy algorithm is the decision tree form to simplify the rules.
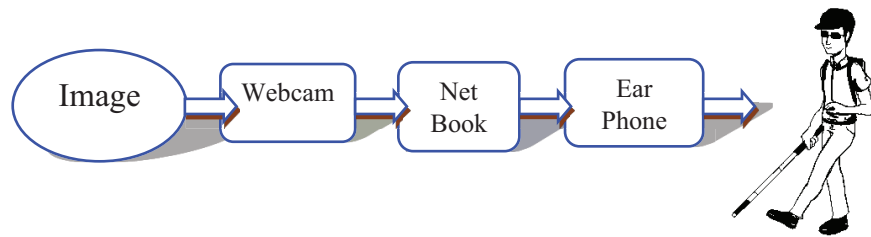
Figure 2: Block diagram instrumentation system.

3. Hardware

The block diagram system is used in Fig 2.

Image captured by webcam which external webcam connected to the net book. The colour names Information done by sound from ear phone. The hardware and software in this system are controlled by program. The block diagram of the program is represented by Fig 2.

4. Calculating the RGB Value in Viewing Area

If P is length of half of the width of the image to be processed (- P for the starting point pixel and + P for the end point pixel) and k is index of start or end pixel coordinate. Coordinates of the pixel can be determined by using the Equation:

$$i_k = \left(\frac{image\ width - 1}{2} \right) + P \tag{1}$$

$$j_k = \left(\frac{image\ high - 1}{2} \right) + P \tag{2}$$

The dominant colour of an object is considered as the main colour of the object. The dominant colour is detected by calculating the average colour of each R, G, and B value of all the pixels certain areas.

4.1. Software

Software that has been built consists of three parts: The Interfacing part; Software designed by using Delphi 7 that have a function to capture an image from webcam with * .bmp format. The image captured every 100 ms (frames per second). This method is carried out to observe objects that have changed colour every time. Image processing part; This part is consists of the calculating the time length of the image that has unchanged, only image that has not changed for certain time would be processed, and it calculated of average RGB value of the central area and determinate of the colour name with entropy algorithm. The sound output part; the sound output is obtained by storing the sound in * .wav format when a colour name was found. Each colour is represented by a single sound. Fig. 4 shows the screen shoot the program that has been created.
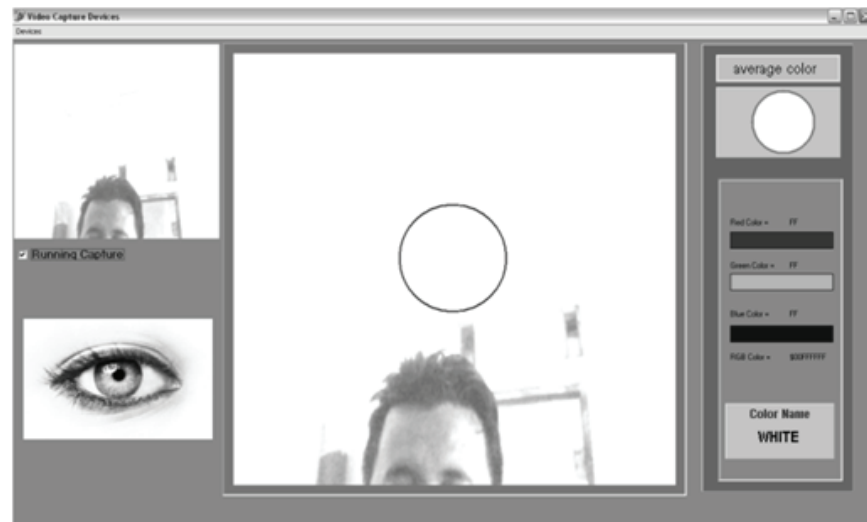
Figure 3: The screen shoots of the program.

5. Result and Discussion

The results of this research are average each RGB value at viewing area. The HSV value is taken by converting equation [3]. Decision tree for RGB and HSV colour model produced by Weka 3.6.0 free software, and it must be converted to a rule in list instruction in a program.

6. Colour Classification Algorithm Entropy

This research used the grouping method based on the general perception of the name of a colour. Colour not grouping based on the coordinates in the HSV colour models [7]. The training results using entropy algorithms of cross validation test on the RGB colour format is 71% where Correctly Classified Instances obtained from 450 data. The results of cross validation test on the HSV colour format is 90% where Correctly Classified Instances obtained from 450 data. Model RGB had smaller success because absence of standard patterns in the grouping of colours. HSV format is higher because in the conversion equation from RGB to HSV had a rounding condition to the certain value. Based on an experiment shows that the HSV colour models Easier to Observe and classify than RGB colour models [1,8]. Object decision tree models of HSV colour seen in the Fig 5.

At the real-time camera system the image captured continuously. When the camera or position of the object is moving or shifting the picture will be changed every time. If all images must be processes in the program, they will be consuming the time. The program is designed not processing all the captured images only when the image is unchanged at certain intervals time.

Some of the difficulties in this system are that is dependent on the quality of camera. Sometimes at the testing showed that the RGB values of same image from difference camera are not always same. There is a camera noise that quite disturb but that is
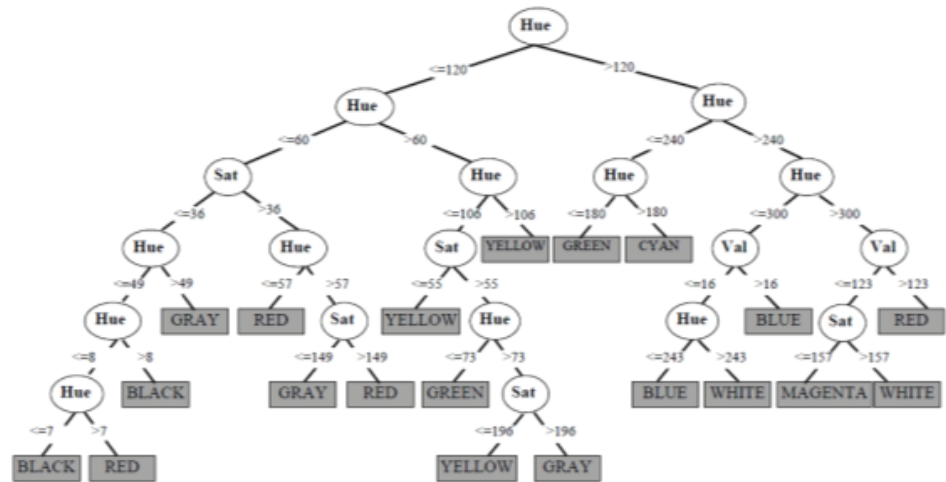
Figure 4: Decision tree Classification in HSV colour model.

not become big obstacle. It required retraining with entropy algorithm for every new camera that will be used.

7. Summary

The conclusion of this research is that the entropy algorithm can be used to classify colours into basic name. Classification using the HSV model is better and efficient than RGB model.

References

[1] P. M. Ong and E. R. Punzalan, Comparative Analysis of RGB and HSV Colour Models in Extracting Colour Features of Green Dye Solutions, (2014), DLSU Research Congress 2014, De La Salle University, Manila, Philippines March 6-8, 2014.

[2] J. Andrew, Elliot and Markus A. Maier. Colour Psychology, *Eff Perceiving Colour Psychol Functioning Hum Annu Rev Psychol*, **65**, 95–120, (2014).

[3] P. Nishad and R. M. Chezian, Various Colour Spaces and Colour Space Conversion Algorithms, *Journal of Global Research in Computer Science*, **4**, no. 1, (2013).

[4] `www.who.int/features/factfiles/blindness/blindness_facts/en/index.html`, WHO, 10 facts about blindness and visual impairment, (2013), Update October 2013.

[5] P. Ibrahim and J. Jagdish, Colour Recognition for Blind and Colour Blind People, *International Journal of Engineering and Innovative Technology (IJEIT)*, **2**, no. 6, (2012).

[6] R. D. Thulasiraj and R. Muralikrishan, Vision 2020, The global initiative for right to sight, *Community Ophthalmol*, **2001**, 20–22, (2001).

[7] Y. Tian and S. Yuan, Clothes Matching for Blind and Colour Blind People., ICCHP 2010, Springer-Verlag. Berlin Heidelberg 2010, Part II, *LNCS*, **6180**, 324–331, (2010).

[8] N. M. Ali, et al., Performance Comparison between RGB and HSV Colour Segmentations for Road Signs Detection, *Appl Mech Mater J*, **393**, 550–555, (2013).

KnE Engineering

Knowledge E
Engaging minds

Conference Paper

Room Searching Performance Evaluation for the JagaBot^{TM} Indoor Surveillance Robot

Mohamad Hanif Md Saad, Rabiah Adawiyah Shahad, and Aini Hussain

[1]Dept. of Mechanical & Material Engineering, Faculty of Engineering & Built Environment, Universiti Kebangsaan Malaysia, 43600 Bangi, Selangor DE, Malaysia
[2]Dept. of Electric, Electronic & Systems Engineering, Faculty of Engineering & Built Environment, Universiti Kebangsaan Malaysia, 43600 Bangi, Selangor DE, Malaysia

Abstract

This paper reports the evaluation of the performance of room searching capability for the JagaBot^{TM} Indoor Surveillance Robot. The ultimate objective of the JagaBot^{TM} is to be applied as an event actor, inspecting the secured environment automatically and feeding the dynamic view of the surrounding to remote user. It can also be used to communicate with persons inside the monitored area. A web service based instruction panel was used to command the JagaBot^{TM} to designated rooms. The JagaBot^{TM} then navigates itself to the room automatically, scanning for the QR code marker attached to room door, tracking a designated trail of lines through its QR code and line tracking camera. The result of this room's searching procedure shows that the JagaBot^{TM} achieved its objective of correct room finding in favorable time. A 100% correct search result was obtained with an average velocity of 0.1748 m/s under the current setting.

Keywords: Indoor Surveillance Robot, QR code, and web service

⚿ OPEN ACCESS

1. Introduction

Automated Ground Vehicle (AGV) type robot has been used in many applications including surveillance. The Smart Engineering System Research Group (SESRG) has successfully designed an AGV type robot, called the JagaBot^{TM}, for surveillance application. The robot is tasked with monitoring the environment dynamically, going from room to room and also to act as an actor, one which is commanded remotely to inspect a particular room upon detection of an anomalous event from that room (for example, from Closed Circuit Television (CCTV) observation manually or automatically).

There are several AGV robot developed for surveillance system, for example [1] presented a prototypical multi-robot surveillance system that is able to monitor an outdoor environment autonomously and visual surveillance system mounted on the mobile robot as developed by [2]. A navigation architecture for autonomous mobile robot was developed by [3] to run in environment based on stereo vision camera utilizing the Binocular Stereo Vision Based Obstacle Avoidance technique. A robot for intruder detection and surveillance task was developed by [4] and [5] demonstrated a surveillance robot capable of capturing and transmitting video on rough terrains. [6] has incorporated unique feature of surveillance robot, which is travelling capability on both land and water.

How to cite this article: Mohamad Hanif Md Saad, Rabiah Adawiyah Shahad, and Aini Hussain, "Room Searching Performance Evaluation for the JagaBot^{TM} Indoor Surveillance Robot," *KnE Engineering*, vol. 2016, 6 pages. DOI 10.18502/keg.v1i1.486

Page 1

2. JagaBo TM Infrastructure

The JagaBot^{TM} infrastructure is shown in Fig. 1 (b). The web service based command mechanism of JagaBot^{TM} is shown in Fig.1 (a). The instruction panel can be replaced by desktop instruction panel or android device based instruction panel. However, the web service act as the main communication hub for JagaBot^{TM}. Several versions of the JagaBot was developed. The version shown in Fig. 1 (b), which is the JagaBot-J03, is the latest version of the JagaBot^{TM} **[7]**.

It uses an Intel NUC mini PC as the main controller, connected with a web cam for Quick Response (QR) code reading, a downward pointing line tracking camera, and two forward pointing wireless Internet Protocol (IP) camera for monitoring purposes. It also has two main screen, the larger one is used to display the Graphical User Interface (GUI) and the remote telecommunication module while the smaller one is used as a control panel. A Teensy microcontroller act as a field controller, connecting the NUC Mini PC to the sensor and actuator and all the instrumentation circuit below. The JagaBot^{TM} is move by two Direct Current (DC) motor and powered by 2 12V sealed lead acid battery.

3. Objective of Study

The objective of the study is to establish the performance of the JagaBot^{TM} in achieving targeted room for inspection and to derive a mathematical model depicting the target to arrival time with JagaBot^{TM} current location.

Figure 2 shows JagaBot^{TM} path in detecting the desired room. JagaBot^{TM} will go through the red line track for straight movement. When the green line marker is detected, JagaBot will make a turn based on the side detected and scan the QR code provided. If the QR code gives correct room reading, JagaBot^{TM} will enter the room.

4. Experiment Design

From the X_S starting point, the robot were assigned to move to any of the rooms (room 1 (D1), 2 (D2), 3 (D5), 4 (D3), 5 (D4), 7 (D7)) using the web service based command panel. The experiment were repeated for several times. The floor plan of the experiment location is shown in Fig. 3 below.

Figure 4 shows the sequence of JagaBot^{TM} movement. It started from identifying the command for the room to be searched. Then, JagaBot^{TM} will move forward and find the room markers. Once JagaBot^{TM} detect the marker, it will turned to identify the room using QR code displayed in front of the door. If the QR code shows the wrong room, JagaBot^{TM} will turn back and continuously move forward to find the correct room. If the identified QR code shows the correct room, JagaBot^{TM} will enter the room for inspection. We have also develop a model to estimate the arrival time ($T_{Target)}$ to destination.

(a)

(b)
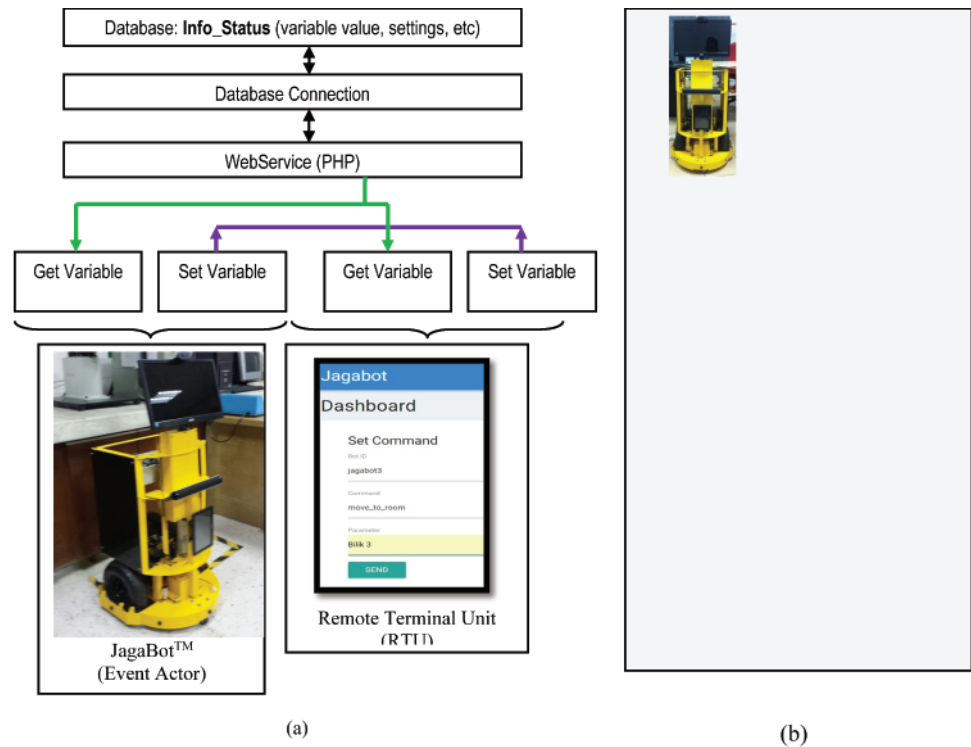
Figure 1: Jagabot TM, (a) Jagabot TM Web service Based Command, (b) Closeup of the Jagabot TM [7].

5. Results

Table 1 shows the JagaBot^{TM} performance evaluation. The time taken for each target is measured using Eq. 1.

$$T_{Target} = T_{straight} + T_{QRC} + T_{QRI} * N + T_{Initial}$$ (1)

Where,

T_{Target}: Estimated time for JagaBotT^M to reach target room.

T_{QRC}: Time spent when scanning correct QR code (Measured experimetally).

T_{QRI}: Time spent when scanning incorrect QR code (Measured experimetally).

$T_{straight}$: Time taken to move in a straight line from X$_s$ (shifted by T$_{Initial}$) to targeted door

Marker (Measured experimentally).

N : Number of turn.

$T_{Initial}$: Pick up time required for the JagaBot^{TM} motor to ramp up to nominal speed.

5.1. Accuracy

Both T$_{Target}$ and T$_{Measured}$ depends on N and the distance from starting point. The T$_{Target}$ is estimated using Eq. 1 and measured experimentally (T$_{Measured}$). The results of the experiment shows that all room were identified and reached succesfully. The average
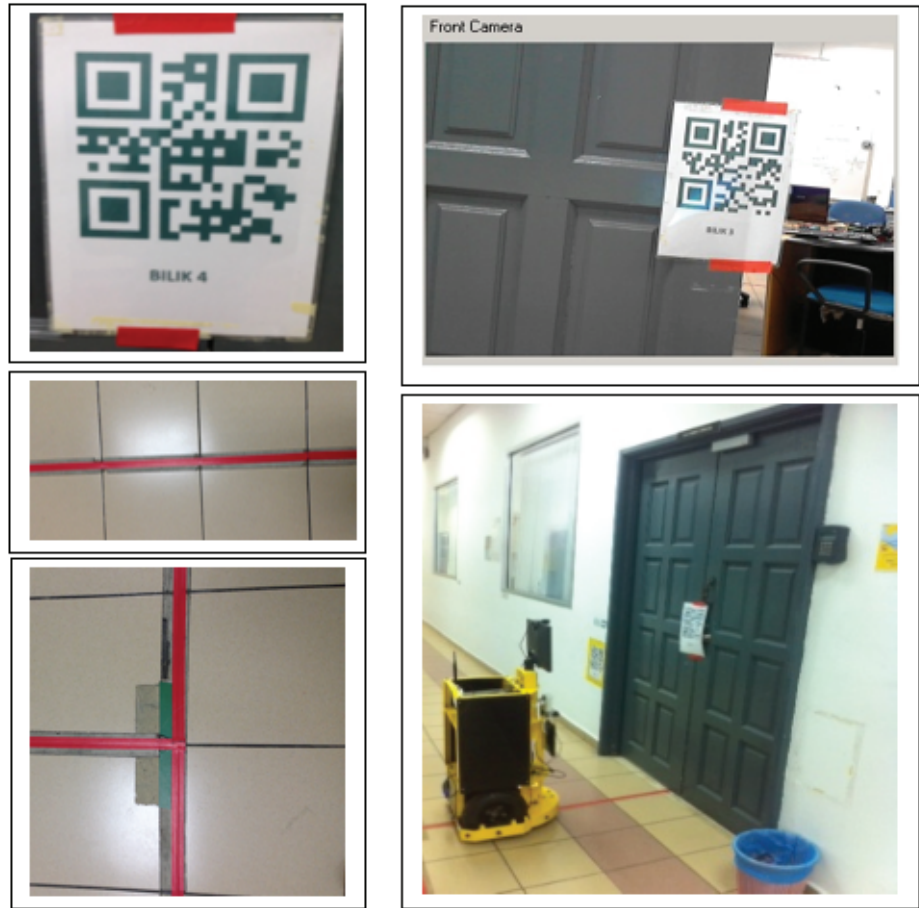
Figure 2: QR-Code Depicting The Door (Left,Top), The lines Tracked (left, Middle), Door Marker (Left , Bottom), JagaBot TM Inspecting the Door (Right Bottom), Doors are opened automatically and JagaBot TM Enters (Right Top).
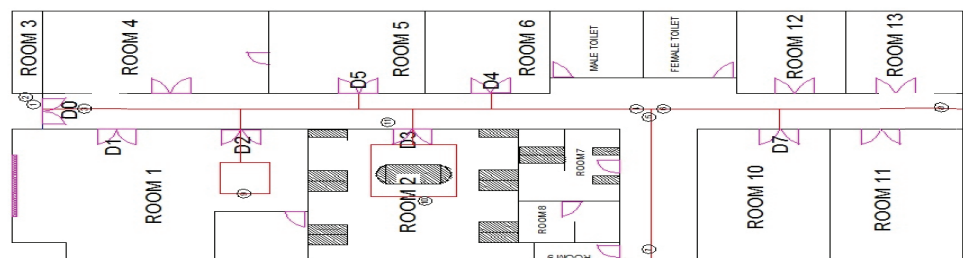
Figure 3: Design Floor Plan.
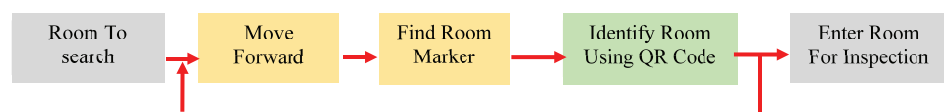
Figure 4: Sequence of Jagabot Movement.

percentage of error between T_{Target} and $T_{measured}$ is 3.14% only, which indicates that the model is in good agreement with the real system behaviour.

Room	Distance (m)	Turn	Test Run 1	Test Run 2	Test Run 3	Estimated Time (T_{Target})	Actual Time ($T_{Measured}$)	Error	Error (%)	Speed (m/s)
room 1	1.07	0	8	9	8	13.26	13.62	0.0275	2.75	0.128
room 2	6.18	1	44	46	44	47.56	44.53	0.0680	6.80	0.138
room 5	10.08	2	73	73	74	74.94	77.43	0.0332	3.32	0.140
room 3	12.78	3	98	95	94	95.45	93.97	0.0157	1.58	0.134
room 4	15.38	4	120	121	124	115.39	119.3	0.0338	3.38	0.126
room 7	27.18	5	196	194	193	187.98	192.82	0.0257	2.57	0.140

Average percentage of error = 3.14%

TABLE 1: JagaBo TM performance evaluation.
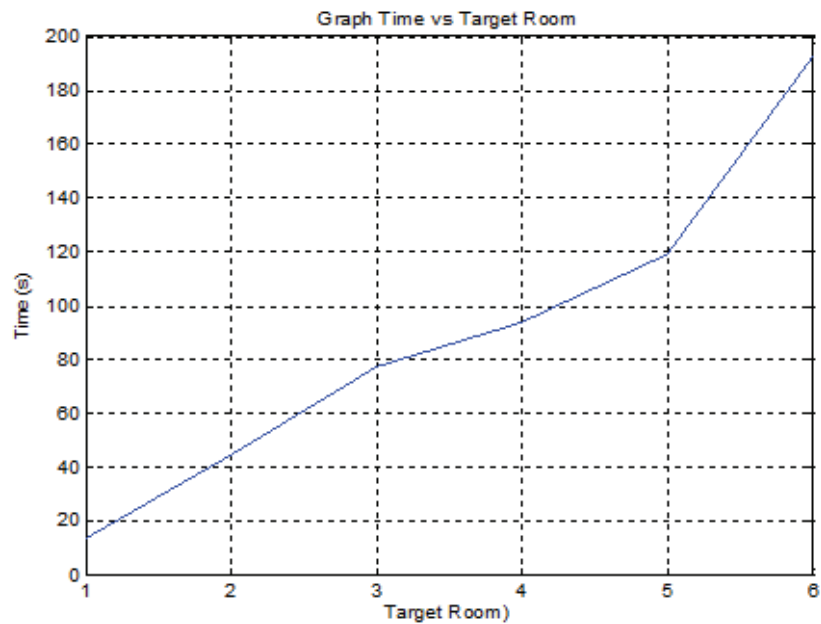
Figure 5: Time taken by JagaBot to reach target room.

5.2. Speed of Detection and Reach

The average measured value of $V_{Straight}$ ($V_{Straight}$ = Distance / $T_{straight}$) is 0.1748 m/s. However, $T_{Measured}$ and T_{Target} depends on the room distance and number of verification it has to do before reaching the correct target. Figure 5 shows speed and time performance of JagaBot^{TM}

6. Conclusion

The JagaBot^{TM} was proven to be able to detect all room using QR code accurately. Good agreement was obtained between predicted arrival time to target room (T_{Target}) and the measured arrival time($T_{Measured}$), with an average percentage of error of 3.14%. Using this model, it would be possible to accurately estimate the arrival time based on JagaBot^{TM} current location. In future, the JagaBot^{TM} will be integrated into our

smart environment system, Sekitar. We will also work on various improvement to the JagaBot^{TM} system to improve the speed and the detection accuracy.

7. Acknowledgement

References

[1] H. Schulz, T. Rohling, and D. Schulz, Autonomous camp surveillance with a coordinated multi robot system, 1–6, (2009), 2009 IEEE International Workshop on Safety, Security Rescue Robotics (SSRR).

[2] M.-S. Yu, H. Wu, and H.-Y. Lin, A visual surveillance system for mobile robot using omnidirectional and PTZ cameras, 1–6, (2010), Proceedings of SICE Annual Conference 2010.

[3] S. Kumar and P. Awasthi, Navigation architecture for autonomous surveillance rover, *Int. J. Comput. Theory Eng.*, **1**, 231–235, (2009).

[4] N. Gonc, M. Shanmugavel, and B. White, in *Indoor active surveillance*, 1129–1136, 1995.

[5] S. Keshri, A Real-time Scheme of Video Stabilization for Mobile Surveillance Robot (2013).

[6] V. Divya, S. Dharanya, S. Shaheen, and A. Umamakeswari, Amphibious Surveillance Robot with Smart Sensor Nodes, 2–5

[7] M. A. Hannan, et al., in *JagaBotTM: Intelligent Patrol Robot For Comprehensive Surveillance System Using Complex Event Processing Approach, Bangi, Selangor*, 2015.

KnE Engineering

Knowledge E
Engaging minds

Conference Paper

Performance of OFDM-Based WiMAX System Using Cyclic Prefix

Benriwati Maharmi

Electrical Engineering Department, Sekolah Tinggi Teknologi Pekanbaru, Jl. Dirgantara 4, Pekanbaru (28289), Indonesia

Abstract

The WiMax (Worldwide Interoperability for Microwave Access) is a technology in broadband wireless access, which employs OFDM (Orthogonal Frequency Division Multiplexing) as an alternative transmission to enable high speed data in communication system. This research aim is to analyze the performance system of the OFDM-Based WiMAX, which used the cyclic prefix. The model was designed in four schemes of simulation method, the BPSK (Binary Phase Shift Keying, QPSK (Quadrature Phase Shift Keying), 16 QAM (Quadrature Amplitude Modulation) and 64 QAM. Each scheme was investigated BER (Bit Error Rate) on AWGN (Additive White Gaussian Noise) channel and multipath Rayleigh fading channel, which had applied the cyclic prefix. By simulation of the cyclic prefix was produced the modulation measurement of the BPSK, QPSK, 16 and 64 QAM. The performance result of Eb/No 15 dB was obtained the BER of BPSK and QPSK of 1.11E-11, the BER of 16 QAM and 64 QAM of 8.69E-06 and 0.00333 respectively. Those results indicated much smaller BER value than EbNo 0 dB which BPSK and QPSK of 1 BER, 1.5 and 1.75 BER for 16 QAM and 64 QAM respectively. In conclusion, a higher value of EbNo, hence the BER value would be lower.

Keywords: BER measurement, Cyclic prefix, OFDM, WiMAX

OPEN ACCESS

1. Introduction

Advances in broadband mobile communication provide information access that easy, cheap and reliable, both in the presentation of high-speed data and multimedia accesses. Those features can be provided by WiMAX technology. The WiMAX standard of 802.16 is one of the BWA (Broadband Wireless Access) issued by the IEEE (Institute of Electrical and Electronics Engineering), which has developed with variants that have advantages in certain circumstances [1]. Particularly 802.16e standard supports portable and mobile applications, which adopts OFDM technique [2]. The OFDM as multicarrier modulation can overcome the problems of various kinds of propagation (multipath), including NLOS (Non Line Of Sight) conditions between the bases station to the user. The OFDM can also overcome the problem of delay spread and the ISI (Inter Symbol Interference).

The physical layer, a Media Access Control layer (MAC) and the application layer in the network system based on mobile WiMAX IEEE 802.16e was a very important rule to be consideration for simulation models design [3]. Sharef *et al* [4] studied the
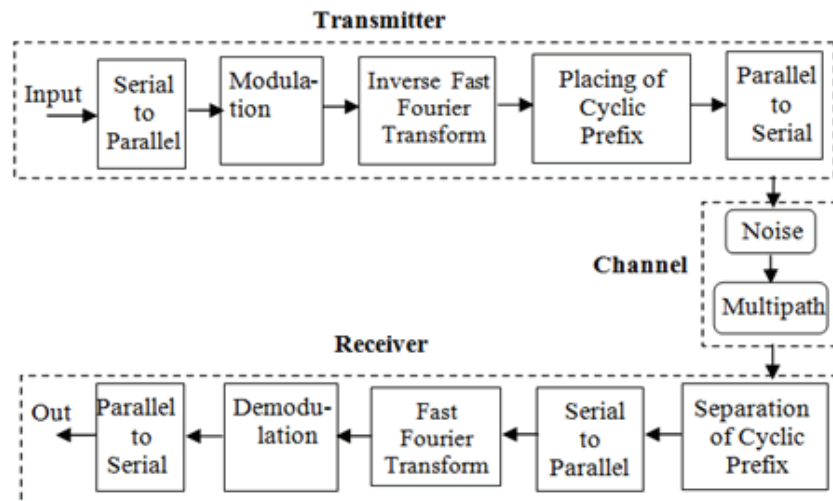
Figure 1: Block diagram of OFDM scheme.

physical layer performance of WiMAX IEEE 802.16e that refer to channel model of ITU (International Telecommunication Union). They investigated the effect of multipath fading and Doppler shift using the cyclic prefix. The cyclic prefix is a data duplicate in the OFDM symbol before transmitting to minimize inter symbol interference and inter channel interference [5]. The length of cyclic prefix might influence in the OFDMA system performance [4].

A cyclic prefix reduces the effects of ISI and delay spread, which is caused by increasing of the symbol duration in the parallel sub-channels in the OFDM system. In other hand, the OFDM symbol is cyclically extended by the guard time to avoid inter carrier interference and let the receiver to take multipath energy in efficient manner. The modulation schemes such as BPSK, QPSK and QAM are used to modulate the signal of an OFDM. A transmission of a data link is involved the potentially errors. Then, a BER and probability error can be used to evaluate performance of the OFDM-based WiMAX system. Meanwhile, the improving of performance of the OFDM-based WiMAX system has still challenged [6]. Therefore, this paper aim is to simulate the OFDM-based WiMAX system performance, which analyzed the BER in AWGN channel and Rayleigh fading channel. That was investigated the performance of the OFDM system using cyclic prefix with modulation of BPSK, QPSK, 16 QAM and 64 QAM.

2. Methodology

The proposed model in this paper used the modulation and demodulation techniques to investigate the performance of OFDM-based WiMAX system. According those modulation techniques, the parameters of performance system that would be investigated as: Bit Error Rate (BER); Signal against Eb/No and Probability error (*Pe*). The simulation design in this proposed model was used the cyclic prefix guard interval. A block diagram of the OFDM scheme of simulation model is shown in Fig. 1. The performance of OFDM Scheme was simulated using Matlab software.

It can be seen in Fig. 1, the simulation design of OFDM-Based WiMAX scheme consist of three main sub-systems: transmitter, channel and receiver. In this model, the transmitter and receiver stations were assumed perfect synchronization, to investigate the performance of the WiMAX OFDM modulation. The cyclic prefix length was assumed longer than the maximum spread delay to avoid the influence of ISI. The simulation was done by looking at the results of the BER versus EbNo in AWGN and Rayleigh fading channels. All experiments were performed to the level of modulation BPSK, QPSK, 16 QAM and 64 QAM.

The *Pe* is the assumption that the error rate occurs in the system due to noise and fading effect in the channel and also for cable losses at the transmitter and receiver. The *Pe* for M-ary PSK was calculated using the following Equation [7]:

$$Pe \simeq erfc\left(\sqrt{\frac{E_b}{N_0}} \, sin\frac{\pi}{M}\right) \tag{1}$$

The *Pe* for M-ary QAM was calculated using the following Equation [6]:

$$Pe \simeq 2\left(1 - \frac{1}{M}\right) erfc\left(\sqrt{\frac{3E_s}{2(M-1)N_0}}\right) \tag{2}$$

3. Result and Discussion

The simulation of model added the cyclic prefix and 2000 samples of simulation running, which 256 subcarrier. Constellation signal was BPSK, QPSK, 16 QAM and 64 QAM that used the model channel of AWGN and Rayleigh Fading. Regarding simulation result, the performance of WiMAX OFDM with BPSK and QPSK modulation were a lot better than the 16 QAM and 64 QAM in term of the comparison between values of EbNo (dB) and BER. It can be seen in Table 1, the influences of EbNo in the AWGN channel and Rayleigh fading channel to values of BER. The EbNo value of 0 dB was obtained the BER of BPSK and QPSK of 0.07865, the BER of 0.141 to 16 QAM and the BER of 0.1998 for 64 QAM. The EbNo 10 dB was obtained the values of 3.363e-005 BER for BPSK and QPSK, BER of 0.00439 to 16 QAM and BER of 0.03848 to 64 QAM. Therefore, the higher provision of the EbNo values affected the smaller noise generated. As the result, the performance of the system would be better.

The simulation results to investigate the effects of CP using adaptive modulation techniques and compared the performance of OFDM in terms of BER and Eb/No (dB) that can be seen on Figure 2(A). Besides, the BER theoretical value with respect to the adaptive modulation technique to estimate the theoretical value of Eb/No(dB) with 256 subcarriers that can be seen on Figure 2 (B).

The simulation result of *Pe* is depicted in Table 2. It can be seen in Table 2, the *Pe* of WiMAX OFDM using BPSK modulation was much better than QPSK modulation. That was seen from the rapid decline in the value of *Pe* upon increasing of EbNo. The *Pe* values for 16 QAM was smaller than the *Pe* values for 64 QAM. The effect of EBNo 0 (dB) on the *Pe* value for BPSK and QPSK was 1, 16 QAM of 1.5 *Pe* value and 64 QAM of

Value of Eb/No (dB)	MODULATION			
	BER	BER	BER	BER
	BPSK	QPSK	16 QAM	64 QAM
0	0.07865	0.07865	0.141	0.1998
1	0.05837	0.05837	0.1212	0.1801
2	0.04094	0.04094	0.1019	0.1611
3	0.02682	0.02682	0.08341	0.143
4	0.01616	0.01616	0.06594	0.1259
5	0.008794	0.008794	0.04995	0.1096
6	0.004227	0.004227	0.03593	0.09392
7	0.001745	0.001745	0.02426	0.07886
8	0.0005981	0.000598	0.01517	0.06445
9	0.0001631	0.000163	0.00864	0.05088
10	3.36E-05	3.36E-02	0.00439	0.03848
11	4.91E-06	4.91E-06	0.00194	0.02763
12	4.71E-07	4.71E-07	0.0007225	0.01862
13	2.68E-08	2.68E-08	0.0002182	0.01161
14	8.06E-10	8.06E-10	5.10E-05	0.006591
15	1.11E-11	1.11E-11	8.69E-06	0.003335

TABLE 1: The measurement of BER results for model of the OFDM-WiMAX system.
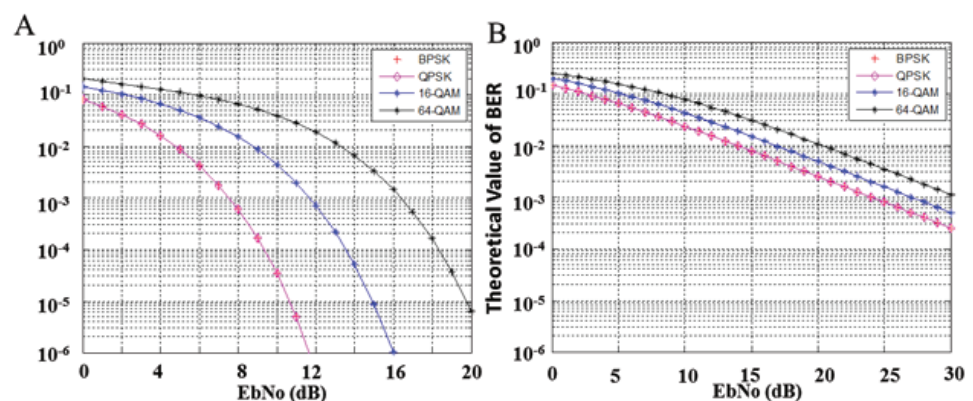
Figure 2: The performance of OFDM in terms of BER and Eb/No(dB) and (B) theoretical value of BER in OFDM Systems.

1.75 of *Pe* value. The EbNo 5 dB was obtained *Pe* value of 0.0027 and 0.03389 for QPSK and BPSK respectively. Whilst, the *Pe* value of 16 QAM and 64 QAM were 0.476 and 1.095 respectively.

The simulation result of the probability of error versus Eb/No (dB) was obtained using Matlab software that depicted on Figure 3.

Value of Eb/No (dB)	MODULATION			
	Pe	Pe	Pe	Pe
	BPSK	QPSK	16 QAM	64 QAM
0	1	1	1.5	1.75
1	0.1797	0.3428	0.9821	1.446
2	0.05778	0.1797	0.7906	1.326
3	0.02014	0.1003	0.6579	1.235
4	0.00729	0.05778	0.5566	1.159
5	0.0027	0.03389	0.476	1.095
6	0.0003857	0.02014	0.41	1.038
7	0.0003857	0.01207	0.3551	0.9865
8	0.0001478	0.00729	0.3089	0.9399
9	5.70E-05	0.004427	0.2696	0.8972
10	2.21E-05	2.70E-03	0.2359	0.8578
11	8.598E=06	1.65E-03	0.207	0.8211
12	3.36E-06	1.02E-03	0.182	0.787
13	1.32E-06	6.25E-04	0.1603	0.755
14	5.17E-07	3.86E-04	0.1414	0.7249
15	2.04E-07	2.39E-04	0.1249	0.6965
16	8.83E-08	1.48E-04	0.1105	0.6698
17	3.17E-08	9.17E-05	0.09779	0.6445
18	1.26E-08	5.70E-05	0.08667	0.6204
19	4.97E-09	3.55E-05	0.07688	0.5976
20	1.97E-09	2.21E-05	0.06825	0.5759

TABLE 2: The result of Probability of error (Pe) for OFDM modulation scheme.

Constellation of four digital modulation signals was shown the probability of error for EbNo of BPSK modulation rapidly decreasing by increasing of EbNo values. This modulation technique is suitable for long distance transmission. While, QPSK modulation was reliable comparing to 16 QAM and 64 QAM. The QPSK modulation was reliable with the ability to carry twice of the data rate than the BPSK. Modulation of 16 QAM and 64 QAM was less reliable than the BPSK and QPSK modulations. However, the modulation of 16 and 64 QAM were efficient to applying in the frequency spectrum, and were suitable for transmission that closes to the BTS. The 64 QAM was also requiring higher bandwidth and better data rate than others.
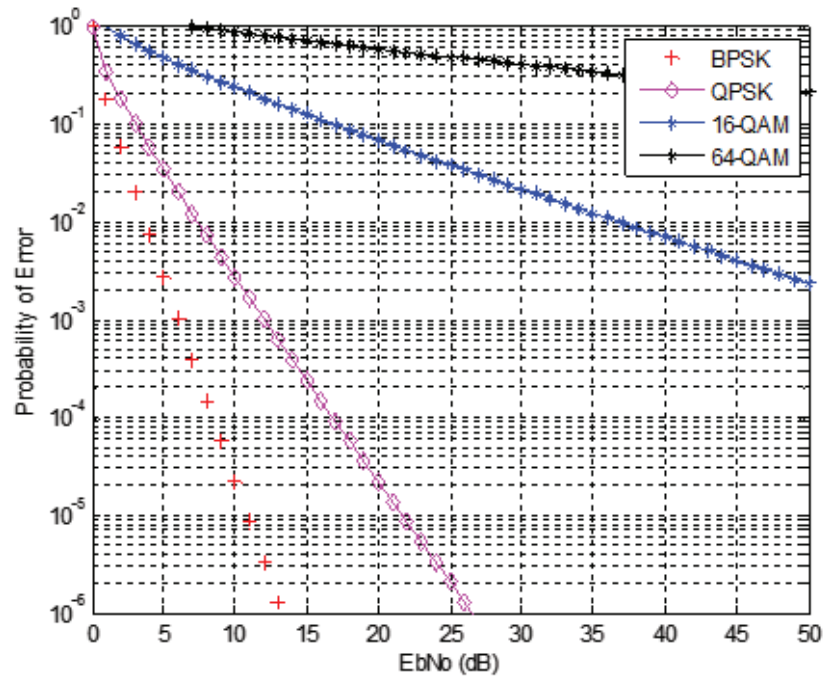
Figure 3: The Probability of Error (Pe) For OFDM Modulation.

4. Summary

This paper was proposed to investigate the performance of OFDM-Based WiMAX system using cyclic prefix implemented in the BPSK, QPSK, 16 QAM and 64 QAM modulations schemes. The schemes of simulation model were performed by Matlab software. The simulation model showed that the performance of BPSK and QPSK modulations were better than the 16 QAM and 64 QAM modulations. The probability of error (*Pe*) at EbNo 0 dB was obtained *Pe* value of 1 for BPSK and QPSK. The *Pe* value of 16 QAM and 64 QAM were 1.5 and 1.75 respectively. The greater of EbNo value, hence *Pe* value would be smaller. The BPSK is better for long distance transmission due to small the error probability (*Pe*). While, the 64 QAM has a high data rate, that is suitable for close transmission to the BTS (Base Transceiver Station). In conclusion, the cyclic prefix has advantage to minimize Inter Symbol Interference (ISI) that generated the smaller BER, which it can improve the performance of the OFDM-based WiMAX system.

References

[1] A. Ghosh, D. R. Wolter, J. G. Andrews, and R. Chen, Broadband wireless access with WiMax/802.16: current performance benchmarks and future potential, *Commun Mag IEEE*, **43**, 129–136, (2005).

[2] J. Rakesh, W. Vishal, and U. Dalal, A survey of mobile WiMAX IEEE 802.16m standard, *Int. J. Comp. Sci. Inf. Secur*, **8**, 125–131, (2010).

[3] R. Jain, C. So-in, and A. K. Tamimi, System-level modeling of IEEE 802.16E mobile WiMAX networks: key issues, *Wirel Commun IEEE*, **15**, 73–79, (2008).

[4] Z. T. Sharef, A. E. Alaradi, and B. T. Sharef, in *Performance evaluation for WiMAX 802.16e OFDMA physical layer, Comp. Society*, 351–355, IEEE, 2012.

[5] W. Henkel, G. Taubock, P. Odling, P. O. Borjesson, and N. Petersson, in *The cyclic prefix of OFDM/DMT - an analysis, Int. Sem. on Broadband Com*, IEEE, Zurich, 2002.

[6] V. Grewal and A. K. Sharma, Performance evaluation of WiMAX network with AMC and MCCDMA for mobile environments, *Int. J. Multimed Ubiquitous Eng.*, **7**, 107–118, (2012).

[7] F. Xiong, in *Digital Modulation Techniques*, Artech House, 2nd ed edition, 2006.

Conference Paper

Application of Short Time Fourier Transform and Wavelet Transform for Sound Source Localization Using Single Moving Microphone in Machine Condition Monitoring

Meifal Rusli, Lovely Son, Mulyadi Bur, and Agus Arisman

Department of Mechanical Engineering, Faculty of Engineering, Andalas University, Kampus Limau Manis, Padang 25163- Indonesia

Abstract

The paper discusses means to predict sound source position emitted by fault machine components based on a single microphone moving in a linear track with constant speed. The position of sound source that consists of some frequency spectrum is detected by time-frequency distribution of the sound signal through Short Time Fourier Transform (STFT) and Continues Wavelet Transform (CWT). As the amplitude of sound pressure increases when the microphone moves closer, the source position and frequency are predicted from the peaks of time-frequency contour map. Firstly, numerical simulation is conducted using two sound sources that generate four different frequencies of sound. The second case is experimental analysis using rotating machine being monitored with unbalanced, misalignment and bearing defect. The result shows that application of both STFT and CWT are able to detect multiple sound sources position with multiple frequency peaks caused by machine fault. The STFT can indicate the frequency very clearly, but not for the peak position. On the other hand, the CWT is able to predict the position of sound at low frequency very clearly. However, it is failed to detect the exact frequency because of overlapping.

Keywords: Short time Fourier transform, Continuous wavelet transform, Sound source localization, Condition monitoring

 OPEN ACCESS

1. Introduction

Sound source localization is a complex work that acoustic engineers face today. Some standards based on microphone arrays are used to analyze the noise source. In general, the methods are categorized into three: near-field acoustic holography, beamforming, and inverse method. Most of these methods were developed using 20 channels or more of microphones and data acquisition [1]. Meanwhile, other researchers have been trying to develop sound source localization method with minimal number of microphone, like binaural and inter-aural sound localization [2].

Likewise, the vibration and acoustic signal analysis are very important methods in condition monitoring and fault diagnostics of machine components. With the rapid development of the signal processing techniques, the analysis of stationary and transitory signals has largely been based on well-known spectral techniques such as: Fourier

Transform and wavelet transform [3,4,5]. Then, to localize sound sources using acoustic signals, some methods also have been developed. For instance, sound source localization using time frequency histogram by two microphones [6], through the fusion between visual reconstruction with a stereoscopic camera pair with several microphones [7], and the application of envelope and wavelet transform to enhance the resolution of the received signals through the combination of different time-frequency contents [8].

This paper discusses about the implementation of a single microphone that is moving in a linear track and constant speed to detect sound source position. The sound position and frequency peaks are be detected by the peak of the time-frequency distribution of the sound signal using short time Fourier transform (STFT) and continues wavelet transform (CWT). Firstly, numerical simulation is conducted by two loudspeakers as the sound sources that generate four different frequencies of sound signals. The second case is the sound generated by a rotating machine with unbalanced, misalignment and bearing defect. Each defect generates specific frequency of vibration and sound. This single moving microphone method has benefit that could be developed for autonomous or robotic condition monitoring system with simpler and cheaper devices and analysis rather than multi-channel microphones array.

1.1. Short Time Fourier Transform and Continuous Wavelet Transform in Moving Microphone

The acoustic signals from faulty components are basically non-stationary. There are two basic approaches to analyze a non-stationary vibration and acoustic signal in time and frequency domain simultaneously. One approach is short time Fourier transform (STFT) by splitting an acoustic signal into segments in time domain by proper selection of a window function and then to carry out a Fourier transform on each of these segments separately and to deliver an instantaneous spectrum. Another approach is the continuous wavelet transform (CWT), where the non-stationary acoustic signal to be analyzed is filtered into different frequency bands, which are split into segments in time domain and their frequency contents and energy are analyzed. Wavelet analysis overcomes the disadvantage of STFT since CWT uses a windowing technique with variable sized regions. Wavelet analysis allows the use of long time intervals where we want more precise low-frequency information, and shorter regions where we want high-frequency information. In this analysis Morlet function is applied for basic wavelet function.

Furthermore, when a fixed source is measured by a moving microphone over a period of time, the distance between source and microphone is no longer constant, but as a function of time. When the moving microphone is approaching closer the sound source, the emitting sound needs less time to reach the microphone, the waveform is compressed resulting in an increase of frequency, especially when the microphone moves at very high speed. This phenomenon is known as the Doppler Effect [9]. Likewise, because the distance decreases, the amplitude increases and becomes maximum when the microphone in the closest position to the sound source. The highest peak in
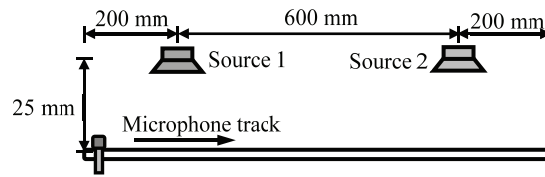
Figure 1: The numerical simulation model.
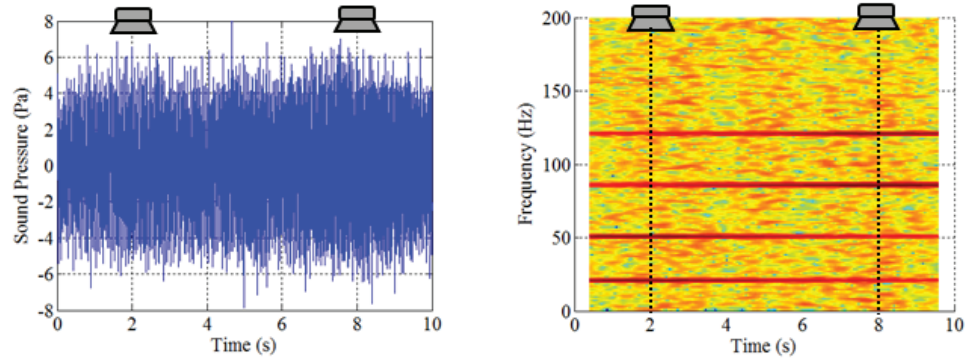
Figure 2: The time waveform (left) and the time-frequency spectrogram using STFT (left) of the sound signal in numerical model.

time-frequency distribution of the sound signal is then detected as the sound source position in each frequency.

2. Numerical Simulation

Firstly, a numerical simulation is conducted using two loudspeakers generating four different frequencies of sound like illustrated in Fig. 1. The first loudspeaker generates sinusoidal sound at frequencies of 25 and 50 Hz, and the second one generates 85 and 125 Hz of signal. The microphone moves on the track one meter length with low speed of 0.1 m/s. Both sound sources generate random noise with the signal to the noise ratio of 5. The sound signal from the microphone in time domain and time-frequency distribution by STFT is depicted in Fig. 2, while time-frequency wavelet energy distribution is shown in Fig. 3.

The result of wavelet transform is not easy to be understood compared with the FFT result. In a broad sense, and it is better to speak about the approximated frequency corresponding to a scale by the relationship of $F_a = F_c/(a.T_d)$. Where F_c is the center frequency of wavelet, a and T_d are the scale and the sampling period, respectively. Fig. 3 shows that by STFT, the sound at frequency of 20 Hz and 50 Hz are detected at the first loudspeaker position. Meanwhile the sound at frequency of 85 and 125 Hz are detected at the second loudspeaker position. However, it is not easy to distinguish the peak from the frequency line.

On the other hand, in time-frequency wavelet energy distribution like shown in Fig. 3, the sound position at low frequency can be detected more clearly at the first sound source. However, two higher frequencies at the second sound source are not detected well. Although zooming in order to increase frequency resolution is done at 100 Hz
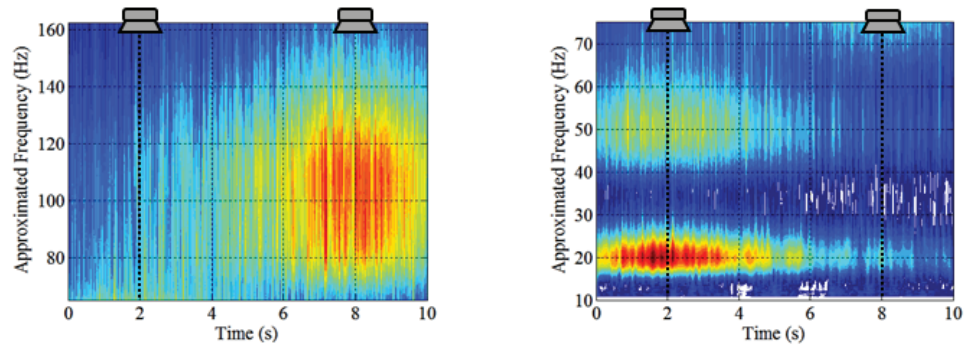
Figure 3: Time-frequency wavelet energy spectrum at different frequency range.
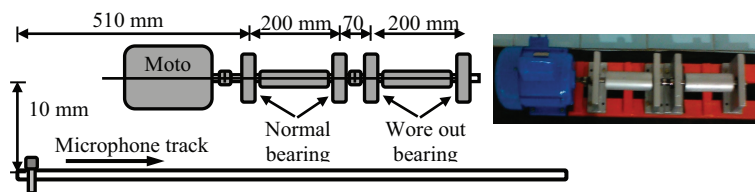
Figure 4: The rotor dynamics model.

to 160 Hz of frequency range, the sound at frequency of 85 Hz and 125 Hz are found merging into a single peak distributed from 85 Hz to 120 Hz. One of the drawbacks of CWT is the overlapping occurred at higher frequency [4]. The spectrum peaks at frequencies of 85 Hz and 125 Hz are too close each other in both position and frequency distance, so the overlapping makes both frequency peaks merge in a single distributed peak. The resolution of the CWT is very good at high scale, which means it is very satisfied at low frequency. Therefore, the CWT will contribute well to detect the sound source at relatively low frequency or longer distance of frequency peaks of spectrum.

3. The Rotor Dynamics Model

The second case is the application of both methods in a simple rotating machine consists of an electric motor, two pairs of ball bearing with two thick rotor and shaft like illustrated in Fig. 4. The right pair has fault wore out bearings, so they have more clereance or loosness between inner ring, outer ring and the ball. The shaft between the electrical motor and both pairs of bearing-shaft-rotor are connected by flexible coupling. Morever, aligning and balancing process are unavailable in this case, so the unbalance and the misaligment signal may appear in the sound analysis. The micro-phone moves at very low speed of 0.024 m/s. The timewave of sound signal and time-frequency spectogram using STFT is shown in Fig. 5, while the time-frequency wavelet energy spectrum are shown in Fig. 6.

The sound signal in time domain presented in Fig. 5 shows that higher pressure level of sound generated by wore out pair of bearing part. Most energy is emitted at the first harmonics rotation frequency about 48 Hz like confirmed by the time-frequency spectrogram using STFT. It is shown that pairs of bearing-shaft-rotor part generate the sound at the first harmonic. However the wore out part generates the highest energy
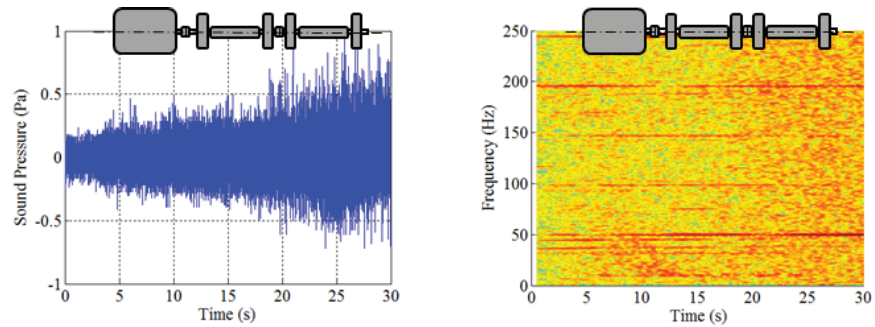
Figure 5: Time wave of sound signal (left), and time-frequency spectrogram by STFT (right).
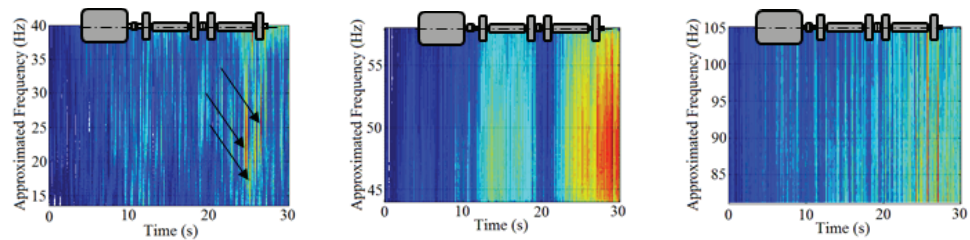
Figure 6: The time-frequency spectrogram using CWT in various frequency ranges.

of sound. It is possibly caused by unbalanced and misalignment occurred in both part. Moreover, the second, the third, fourth, and fifth harmonic are also generated along the system that is possibly caused by the bearings looseness or clearance. In addition, some signal at sub-harmonics frequency also observed to be omitted by the electrical motor.

Fig. 6 shows the time-frequency spectrogram using CWT in various frequency ranges. At sub harmonics frequency range, it is found that some transient sound emitted by last wore out bearing around the FTF of bearing frequency. Furthermore, CWT also shows that the highest energy emitted from wore out part at rotation frequency at 48 Hz, higher than generated by the normal one. In addition, higher energy also emitted by the last bearing at the second and the third frequency harmonics. The same problem is found when using CWT at higher frequency. The application of CWT is difficult to observe the frequency of signal clearly because of the overlapping phenomenon. The overlapping increases significantly by longer time period of sampling.

4. Conclusion

This paper has presented the application of single moving microphone to predict the sound source position for machine condition monitoring. It is observed qualitatively that the time-frequency distribution of sound signal by STFT and CWT are possible to be used to predict the sound source position. The STFT time-frequency distribution shows the frequency clearly, although not so clearly for the position of the peak. On the other hand, the CWT could predict the position of sound at low frequency very clearly, but in contrast, it failed to shows the exact frequency because of overlapping. Combination of STFT and CWT could be applied to overcome the both drawbacks in

machine condition monitoring. Furthermore, the implementation of band pass filter could be proposed to improve the CWT in higher frequency.

5. Acknowledgement

References

[1] J. Lanslots, F. Deblawe, and K. Janssens, Selecting Sound Source Localization Techniques for Industrial Applications, *Sound Vibrat*, 6–9, (2010).

[2] C. Faller and J. Merimaa, Source localization in complex listening situations: selection of binaural cues based on interaural coherence, *J Acoust Soc Am*, **116**, 3075–3089, (2004).

[3] K. Shibata, A. Takahashi, and T. Shirai, Fault diagnosis of rotating machinery through visualization of sound signal, *J Mech Syst Signal Process*, **14**, 229–241, (2000).

[4] P. W. Tse, W. Yang, and H. Y. Tam, Machine fault diagnosis through an effective exact wavelet analysis, *J Sound Vibrat*, **277**, 1005–1024, (2004).

[5] H. Bendjama, S. Bouhouche, and M. Boucherit, Application of Wavelet Transform for Fault Diagnosis in Rotating Machinery, *International Journal of Machine Learning and Computing*, **2**, no. 1, 82–87, (2012).

[6] P. Aarabi and S. Mavandadi, Robust sound localization using conditional time–frequency histograms, *Inf Fusion*, **4**, 111–122, (2003).

[7] J. Cech, R. Mittal, A. Deleforge, and J. Sanchez-Riera, Active-Speaker Detection and Localization with Microphones and Cameras Embedded into a Robotic Head (2013), IEEE-RAS International Conference on Humanoid Robots, Atlanta, United States, Oct 2013.

[8] O. M. Bouzid, G. Tian, J. Neasham, and B. Sharif, Envelope and Wavelet Transform for Sound Localization at Low Sampling Rates in Wireless Sensor Networks, *Journal of Sensors*, **2012**, (2012).

[9] B. Ginn, J. Gomes, and J. Hald, Recent advances in Rail Vehicle Moving Source Beamforming, Internoise, 15-18 September 2013, Innsbrug-Austria.

KnE Engineering

Knowledge E
Engaging minds

Conference Paper

Design and Implementation of SMS Based Anomalous Event Mitigation Process for Complex Event Processing Application

Mohamad Hanif Md Saad[1], Rabiah Adawiyah Shahad[2], and Aini Hussain[2]

[1]Dept. of Mechanical & Material Engineering, Faculty of Engineering & Built Environment, Universiti Kebangsaan Malaysia, 43600 Bangi, Selangor DE, Malaysia
[2]Dept. of Electric, Electronic & Systems Engineering, Faculty of Engineering & Built Environment, Universiti Kebangsaan Malaysia, 43600 Bangi, Selangor DE, Malaysia

Abstract

This paper describes the design and implementation of SMS based event mitigation for Complex Event Processing (CEP) application. The CAISER^{TM}'s CEP platform were used to develop event processing systems which detects and identifies complex events based on patterns of previous and current lower order events. CAISER^{TM} then generates mitigation action for anomalous events and executes them via 3 types of SMS based notification. An implementation of the SMS based event mitigation in a CEP based Server Farm Monitoring system is also described in this paper. The performance of the event mitigation process using SMS is evaluated and described in this paper.

Keywords: Complex Event Processing, CAISER^{TM}, Event Mitigation, and SMS

Corresponding Author:
Mohamad Hanif Md Saad;
email:
hanifsaad@ukm.edu.my

OPEN ACCESS

1. Introduction

Nowadays, the integration of smart sensors and actuators in surveillance system is increasing tremendously. The massive information from those sensors and devices can be simple and complex, where it is hard to keep track off [1]. Thus, the Complex Event Processing (CEP) approach is used in detecting meaningful events effectively. CEP is a tool for analyzing and processing the sequence of complex events of information [2] from various of sources and producing fast mitigation action based on specific scenario to improve the operation, performance, and security [3], [4]. It is a technology that can identify and solve problems in real time, thus improving the performance of business process, schedule and control processes, network monitoring, performance prediction, active monitoring, and intrusion detection [2].

CAISER^{TM} (Computer Assisted Intelligent Event Processor) [5], a CEP development tool developed by the Smart Engineering System Research Group (SESRG), can be used to develop CEP applications to manage and process hundreds of event, alarms, and notifications in business (purchase, payment, fraudulent transaction), scientific (Supervisory Control and Data Acquisition, Remote Monitoring), engineering (Building Management System, Factory Monitoring, Operation Monitoring), and domestic (home alarm system, community monitoring, elderly monitoring) sector. It can also
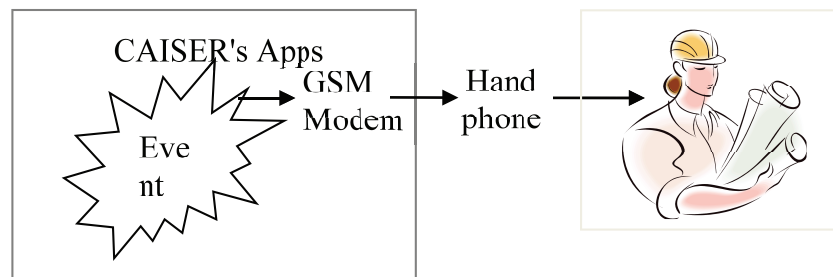
Figure 1: Event Mitigation Via Notification (A^0).

automatically generate and execute mitigation action for the anomalous event based on user settings and rules. CAISER^{TM} is innovative because it is a component based on CEP system development tool, which enables the improvement to CEP apps developed using CAISER^{TM} via the upgraded adapters itself, without the need to recompile the application again. CAISER^{TM} uses probabilistic rule-based system to sift through incoming raw event from event producers to identify and predict derived events and based on the user-defined knowledge base, it will generate and execute mitigation action for the detected events.

One of CAISER^{TM}'s main applications is the Early Warning & Notification System (Sistem Notifikasi & Amaran Awal, SNAA^{TM}), a CEP based network facility monitoring system developed using CAISER^{TM} for Perbadanan Putrajaya (PPJ). SNAA^{TM} has been successfully used to monitor the network facility (server farm, telecommunication rooms, network stability) for PPJ that manages Putrajaya (the Malaysian Government's administrative capital city) and directly benefitting more than 80,000 inhabitants of Putrajaya and all Malaysian government agencies and ministries in Putrajaya. The SNAA^{TM} has been in operation since 2013 without fail and runs 24 hours per day & 365 days per year. It processes in average 34 million sensor reading and thousands of events per day.

2. Event Mitigation Process via SMS

One of CAISER^{TM}'s event mitigation adapter is the Short Messaging Service (SMS) notification adapter. There are three types of notification supported by CAISER^{TM}:

(i) Type 0 (A^0): This type of notification is for the purpose of informing the user only.

e.g.:
Server Room. Temperature High

(ii) Type 1 (A^1): This type of notification is to instruct the user or the receiver to execute mitigation action based on the instruction in the message. The receiver can be a human operator or a machine.

e.g.:
Server Room. Aircond Off. Turn ON the auxiliary aircond unit.
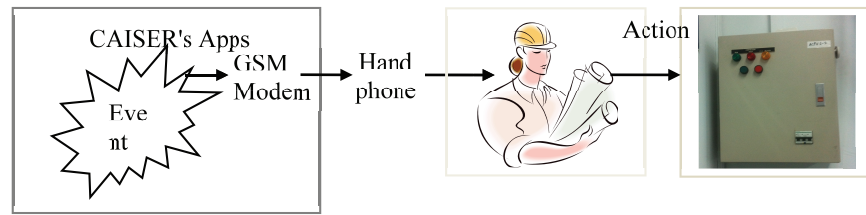
Figure 2: Event Mitigation Via Notification (A^1).
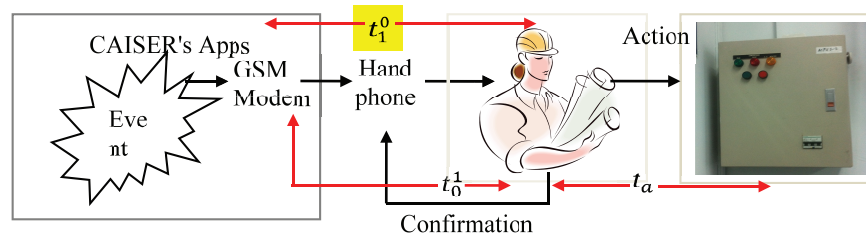
Figure 3: Event Mitigation Via Notification (A^2).

(iii) Type 2 (A^2): This type of notification instruct the server and receiver to execute mitigation action and to confirm back to CAISER^{TM} that the mitigation action was executed. Verification must be done within the stipulated time given.

e.g.:

ServerRoom.ArcondOff.Turn ON the auxiliary aircond unit within 10 minutes and Reply AX23 OK

The receiver of A^2 must reply AX23 OK to the application server within 10 minutes, failure of doing so will force the server to initiate second layer event mitigation action.

3. Results and Discussion

A) Performance A^0 and A^1 (t_1^0)

Figure 4 shows time latency of event notification via SMS. It is found that an average time for SMS notification received from detected event time is 3.95 minutes. This including internal processing time for event processing and internal processing time for transmitting SMS by Telco Provider. The event detection database used to perform this evaluation consist of more than 370 event detection rule and more than 400 action generation rules. We suspect that the high number Cinterion MC35I of rules might have

Measured Data	100
Min (minutes)	3
Max (minutes)	8
Average (minutes)	3.95
Std.Dev.	0.988571

TABLE 1: SMS Measured Performance.
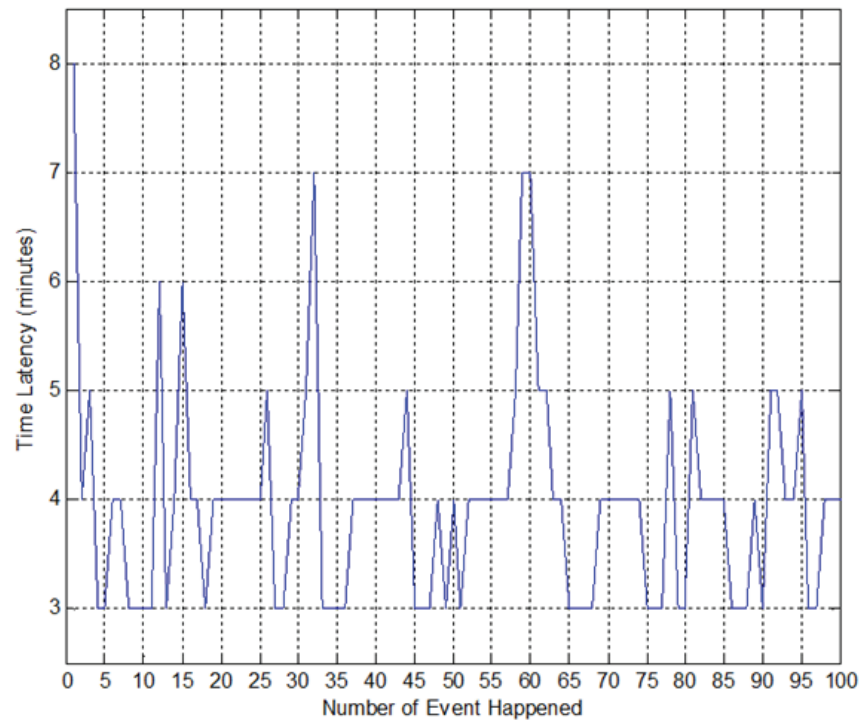
Figure 4: Time Latency (t_0^1) for A^0 and A^1 via SMS.

caused the performance of the system to degrade. We used the as the Global System for Mobile (GSM) modem to send the SMS from the system.

We observed that the performance of t_1^0 for A^2 is statistically closed to A^0 and A^1's(t_1^0). The total time can be defined as $\mathrm{T}_{action}= t_1^0 + t_a + t_0^1$, where t_a is the time taken from the operator to execute the instruction and t_0^1 the time taken for the operator's confirmation message to reach the system. t_a is highly dependant on the user / receiver's time of action execution whereas t_0^1 was observed to be statistically simillar to t_1^0.

4. Conclusion

The observed average latency of 3.95 minutes is acceptable for non-critcal applications such as for environment monitoring and building energy management. The design of the event mitigation action using the multilevel notification (A^0, A^1, A^2) structure is unique to CAISER^{TM} and helps a lot in developing smart systems. In future, the notification system will be improved further to reduce the latency and we will also be developing a similar notification topology using telegram the open sourced social messaging application.

5. Acknowledgement

References

[1] P. Dekkers, Complex Event Processing, *Enterprise Inf Syst*, **1**, p. 101, (2007).

[2] J. Garcia and I. Montemayor, "A Complex Event Processing System For Monitoring of Manufacturing Master of Science Thesis," 2012.

[3] M. Mendes, P. Bizarro, and P. Marques, A framework for performance evaluation of complex event processing systems, *Proceedings of the second international conference on Distributed event-based systems*, 313–316, (2008).

[4] V. Govindasamy, R. Ganesh, G. Nivash, and S. Shivaraman, Prediction of events based on Complex Event Processing and Probabilistic Fuzzy Logic, 494–499, (2014).

[5] M. H. M. Saad, Complex Event Processing For Smart Engineering System, 2015, PhD Dissertation, Bangi.

KnE Engineering

Knowledge E
Engaging minds

Conference Paper

First Principles Calculations Study of Lithium-Montmorillonite for Humidity Sensor Application

Triati Dewi Kencana Wungu and Suprijadi

Dept. of Physics, Faculty of Mathematics and Natural Sciences, Institut Teknologi Bandung, Jl. Ganesa 10 Bandung 40132, Indonesia

Abstract

In this study, we performed calculations on the water molecule adsorbed on lithium montmorillonite using first principles-calculation by means of electronic-structure calculation, with emphasis on approaches based on Density Functional Theory (DFT). The mechanism of water molecule adsorption on the surface of lithium-montmorillonite was investigated from the electronic structure point of view to seek the possibility of using montmorillonite as humidity sensor. The effects of the Van der Waals force to the electronic properties of water molecule on the surface of montmorillonite was also considered and obtained that the structure is more stable energetically. The interaction of water molecule with surface of montmorillonite yields the rotation of the hydrogen atoms of water molecule due to the occurrence of repulsive interaction between two positive ions of hydrogen of water molecule and lithium. From the calculations, lithium-montmorillonite can be considered as a good material for humidity sensor application since there is an electrical change observed even though it is a relatively small that is 0.657 eV.

Keywords: DFT, lithium-montmorillonite, water molecule

OPEN ACCESS

1. Introduction

Interest in research associated with humidity sensor has been growing rapidly in recent years for human comfort. Different kinds of materials including polymer [1], composite [2] and ceramic [3,4] have been applied as humidity sensor. Recently, clay-based mineral such as Montmorillonite (MMT) has been nominated as a good material for humidity sensor since it has a high specific surface area and/or excellent adsorptive capacity [5].

Adsorption of water molecules in the MMT is a great importance for ensuring reliability of MMT as humidity sensor. Fortunately, the water molecules enable easy penetration and separates weakly-bonded layers of MMT. The weakly-bonded layers of MMT are driven by the isomorphic substitution in layers of MMT, which causes the negative charges and subsequently weakens the attraction among the MMT layers [6]. Hence, metal exchangeable cation coordination within the negatively charged MMT is required to neutralize MMT.

How to cite this article: Triati Dewi Kencana Wungu and Suprijadi, "First Principles Calculations Study of Lithium-Montmorillonite for Humidity Sensor Application," *KnE Engineering*, vol. 2016, 6 pages. DOI 10.18502/keg.v1i1.490

Page 1

The humidity sensitivity of the sensor is also depending on the cationic mobility of the exchangeable cation of MMT. It has been reported that Lithium-MMT in an organic solution has shown good electrical conductivity as compared with other alkali metal exchangeable cations (Li- > Na- > K- > Mg- > Ca- > Sr- > Ba-MMT) [7]. Therefore, in the present study, we focused on the Lithium-MMT and its interaction with water molecule. The mechanism of water molecule adsorption in Lithium-MMT will be described as well as investigation on the structure and electronic properties of water on Lithium-MMT from the atomic scale point of view to get a better understanding on how MMT can be useful for the application of humidity sensor.

2. Computational Method

All electronic properties calculations have been performed using the Density Functional Theory (DFT) within Kohn-Sham formula implemented in Vienna Ab initio Simulation Packages (VASP) [8,9] at an absolute zero temperature. The generalized gradient approximation (GGA) within the Perdew–Burke–Ernzerhof (PBE) functional was employed for the exchange-correlation energy [10]. The Brillouin zone was sampled using 5×5×1 Monkhorst-Pack k-point grid and the cut-off energy was 520 eV. The cut-off energy was chosen based on the high accuracy precision mode applied in the calculation which is giving the following formulation of cut-off energy:

$$E_{cut-off} = 1.3 * ENMAX \qquad (1)$$

where ENMAX is the largest pseudopotential file supported in VASP code. Among the O, Si, H, Al, and Mg, the largest ENMAX belongs to the Oxygen atom with the value of 400 eV.

The total energy difference value was set to 0.01 meV giving considerable savings in computational cost and considered to provide high accuracy. Hence, the total energies in this calculation were converged to 0.01meV.

The MMT structure was modelled as one unit cell which consists of 40 atoms and repeated periodically. The isomorphic substitution was taken into account in the alumina octahedral layers by replacing one of Al atom by Mg atom. The Li atom was placed on top of the surface of optimized MMT. A water molecule was then added on top of the optimized Li-MMT. The oxygen atom of a water molecule was initially designed towards the surface of MMT and then the relaxation optimization was started to be calculated. Hence, the total numbers of atom within a unit cell of the H_2O/Li-MMT were 44 atoms. The Van der Waals force correction was included in this calculation using D2 method of Grimme [11].

3. Results and Discussion

In this calculation we compared both structures of MMT and H_2O/Li-MMT. The results of geometry optimization using the DFT calculation for both MMT and H_2O/Li-MMT structures are depicted in Figure 1. In this present study, we only consider to only one
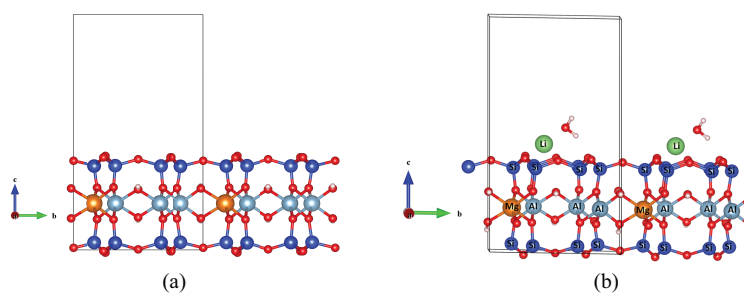
Figure 1: (a) The optimized structure of MMT viewed as a periodic system (1x2x1). A unit cell of MMT is defined as the number of 40 atoms within a frame. (b) The optimized structure of a water molecule adsorbed on Li-MMT viewed as a periodic system (1x2x1). A unit cell of H_2O/Li-MMT is defined as the number of 44 atoms within a frame.

water molecule due to efficient, cost computational reasons, and because we believe it can covered and provides all our investigations needed.

Figure 1a corresponds to the optimized structure of MMT viewed as a periodic system (1x2x1). Despite the fact that Li atom might be trapped in the cavity of alumina octahedral layer, however, due to hydration environment, the Li atom may locate in the cavity of silicate tetrahedral layer of MMT. Therefore in this calculation, we initially located Li atom on top of the MMT surface as shown in Figure 1b. Figure 1b corresponds to the optimized of H_2O/Li-MMT structure viewed as a periodic system (1x2x1). Due to the fact that the water molecules are able to penetrate and then separate weakly-bonded layers of MMT, hence in this calculation, a water molecule is also located on top of the MMT surface. Each slab of MMT is separated by a vacuum at around 10 Å from the MMT surface.

As shown in Fig. 1b, Li atom is facing towards the oxygen atom of a water molecule. This is positively due to the highest electronegativity possessed by oxygen atom of a water molecule. The attraction interaction between the Li atom and a water molecule creates a transfer of charge and a weakly Li-H_2O bonding. The response of the Li-MMT based-sensor to a water molecule is therefore indicated by the change in its electronic properties of Li-MMT. As it is well known that Li-MMT is an insulator like behavior, adsorption of a water molecule will eventually change the electronic properties of Li-MMT either to semiconductor or to metallic behavior or even not to change at all. Although most commonly known that the Li atom can burn the oxygen atom of a water molecule causing a fire in the case of Li battery application, the need of material supported for preventing fire for sensor application should be invented as well.

In our previous calculation, through the density of states analysis, we found that the H_2O/Li-MMT structure is still having an insulator behavior but with the smaller band gap (change from 4.13 eV to 3.88 eV) [12]. The density of states gives the number of allowed electron (or hole) to occupy states per volume at a given energy. The band gap was determined from the conduction and valence bands edge near the Fermi level.

In the case where the Li atom is located at the alumina octahedral layer, the orientation of the OH groups of MMT is changed due to the strong interaction between Li and H atom of the OH groups [13]. However, in the case where the Li atom is located at the MMT surface or in the cavity ditrigonal of silica tetrahedral layers, the OH groups

do not change significantly but still perpendicular with the *b*-axis of this figure instead. This is because the Li atom is preferred approaching a water molecule than moving to the alumina octahedral layer. The water molecule is responsible for the lifted Li atom from the MMT surface. This is also due to the electronegativity of an Oxygen atom of a water molecule which is higher than the Li atom, making the Li-O bond is stronger. Furthermore, the interaction of water molecule with surface of MMT yields the rotation of the H atoms of water molecule due to the occurrence of repulsive interaction between two positive ions of H of water molecule and Li.

In this study, we considered the Van der Walls force correction in the calculation to obtain better results and we found that the band gap of the total density of states is 3.473 eV which is 0.407 eV smaller than calculation without considering the Van der Waals force correction. The total density of states of H_2O/Li-MMT as depicted in Figure 2 is clearly showing that the structure has an insulator behavior. Although humidity sensor requires the high sensitivity of Li-MMT, meaning that Li-MMT is expected to be changed from insulator to semiconductor after a water molecule adsorption, we still consider it as a good material for humidity sensor application since the electrical change was still observed even though it is a relatively small that is 0.657 eV.

Aside of an electrical property analysis, it is important as well to investigate the total energy of H_2O/Li-MMT to determine reactivity of the water adsorption on Li-MMT. In this calculation, we found that the total energy is more stable (-313.93 eV) than calculation without the Van der Waals correction based on reference no. 12 that is -294.60 eV. The negative value of the total energy corresponds to the spontaneous reaction between Li and a water molecule. If we compare previous calculation [12], the Van der Waals correction gives results to the higher reactivity than without applying such correction. Therefore, for the purpose of humidity sensor application then the Van der Waals correction is a great deal importance.

4. Summary

In this study, we performed DFT calculations on the water molecule adsorbed on Li-MMT. The purpose of this study is to determine the possibility whether the Li-MMT can have a chance as a good material for humidity sensor application. The water molecule involved in a unit cell of MMT is only one due to efficient, cost computational reasons, and because we believe it can covered and provides all our investigations needed.

The interaction of a water molecule with surface of MMT yields the rotation of the Hydrogen atoms of water molecule due to the occurrence of repulsive interaction between two positive ions of Hydrogen of water molecule and Lithium. In this study, the change electrical property of Li-MMT was observed through the density of state analysis. The band gap of 3.473 eV was obtained through the density of states which is indicating that H_2O/Li-MMT is an insulator. A relatively small band gap change was confirmed that Li-MMT is able to detect a water molecule in a relatively low concentration. Therefore, Li-MMT is expected to be a good material for the humidity sensor application.
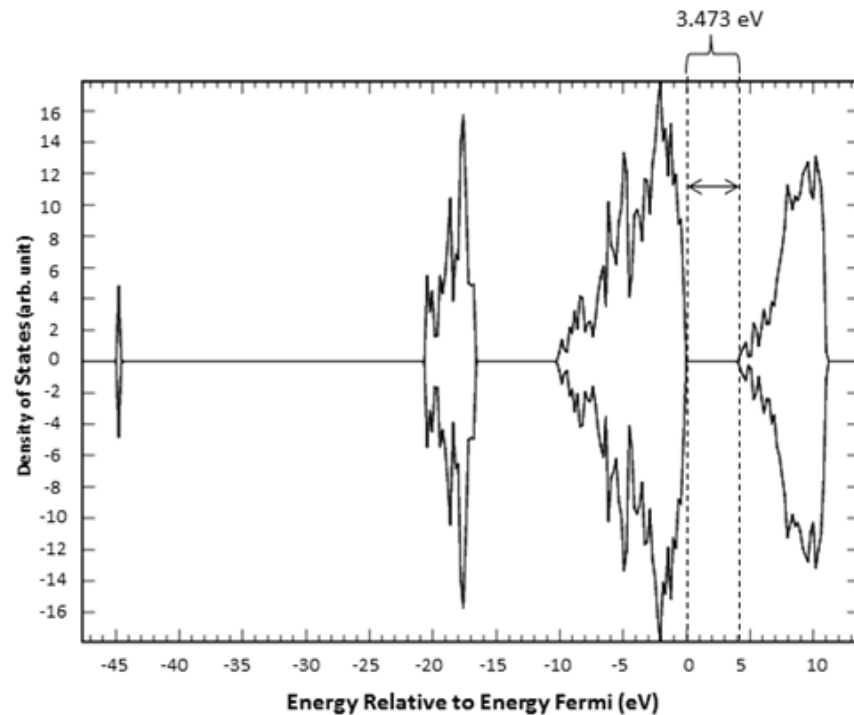
Figure 2: The total density of states of the H$_2$O/Li-MMT structure. The Fermi energy is set equal to zero. The wide band gap of 3.473 eV value is observed.

5. Acknowledgements

References

[1] Y. Sakai, Y. Sadaoka, and M. Matsuguchi, Humidity Sensors Based on Polymer Thin Films, *Sens Actuators B Chem*, **35-36**, 85–90, (1996).

[2] X. Li, X. Chen, Y. Yao, N. Li, X. Chen, and X. Bi, Multi-Walled Carbon Nanotubes/Graphene Oxide Composite for Humidity Sensing, *IEEE Sens J*, **13**, 4749–4756, (2013).

[3] K.-S. Chou, Tzy-Kuang Lee, Feng-Jiin Liu, Sensing Mechanism of A Porous Ceramic As Humidity Sensor, *Sens Actuators B Chem*, **56**, 106–111, (1999).

[4] K. P. Biju and M. K. Jain, Sol-Gel Derived TiO2:ZrO2 Multilayer Thin Films for Humidity Sensing Application, *Sens Actuators B Chem*, **128**, 407–413, (2008).

[5] Pi-Guey Su, Ching-Yin Chen, Humidity Sensing and Electrical Properties of Na- and K-montmorillonite, *Sens Actuators B Chem*, **129**, 380–385, (2008).

[6] J. Mering, On The Hydration of Montmorillonite, *Transactions of the Faraday Society*, **42**, B205–B219, (1946).

[7] C. Kato, K. Kuroda, and K. Hasegawa, Electrical Conductivity of A Montmorillonite-Organic Complex, *Clay Miner*, **14**, 13–20, (1979).

[8] G. Kresse and J. Furthmuller, Efficiency of Ab Initio Total Energy Calculations for Metals and Semiconductors using A Plane-wave Basis Set, *Comput Mater Sci*, **6**, 15–50, (1996).

[9] G. Kresse and J. Furthmüller, Efficient iterative schemes for ab initio total-energy calculations using a plane-wave basis set, *Phys Rev B Condens Matter*, **54**, 11169–11186, (1996).

[10] J. P. Perdew, K. Burke, and M. Ernzerhof, Generalized Gradient Approximation Made Simple, *Phys Rev Lett*, **77**, 3865–3868, (1996).

[11] S. Grimme, Semiempirical GGA-type density functional constructed with a long-range dispersion correction, *J Comput Chem*, **27**, 1787–1799, (2006).

[12] T. DK. Wungu, F. Rusydi, H. K. Dipojono, and H. Kasai, A Density Functional Theory Study on the Origin of Lithium-Montmorillonite's Conductivity at Low Water Content: A first investigation, *Solid State Commun*, **152**, 1862–1866, (2012).

[13] T. D. K. Wungu, S. M. Aspera, M. Y. David, H. K. Dipojono, H. Nakanishi, and H. Kasai, Absorption of lithium in montmorillonite: a density functional theory (DFT) study, *J Nanosci Nanotechnol*, **11**, 2793–2801, (2011).

KnE Engineering

Knowledge E
Engaging minds

Conference Paper

Integrated Remote Sensing and GIS for Calculating Shoreline Change in Rokan Estuary

Sigit Sutikno, Ferry Fatnanta, Ari Kusnadi, and Keisuke Murakami

[1]Civil Engineering Dept., University of Riau, Indonesia
[2]Ministry of Public Works and Public Housing, The Republic of Indonesia
[3]Civil Engineering Dept., University of Miyazaki, Japan

Corresponding Author: Sigit
Sutikno; email:
ssutikno@unri.ac.id

🔓 **OPEN ACCESS**

Abstract

This paper presents an application of satellite remote sensing techniques to detect and to analyze the spatial changes as well as quantify the shoreline change in Rokan estuary, Riau Province, Indonesia. Coastal zone of Rokan estuary, a place through which Rokan River flows into Malacca Strait is dynamically changed because of the hydrodynamic nature and high sediment transport in downstream of Rokan River. By integrating modern techniques of remote sensing and GIS (Geographic Information System), the rates of shoreline change would be easily and quickly determined for a regional area. Landsat satellite images were used with a combination of histogram thresholding and band ratio method for shoreline change detection for last 14 years from 2000 to 2014. The shoreline data then were adjusted for serving as an input for GIS tool to estimate the erosion and deposition rates. The statistical method called as LRR (Linear Regression Rate) in DSAS (Digital Shoreline Analysis System) was used in this study. The results of this study present shoreline changes map of Rokan estuary for last 14 years. Quantitatively, the shoreline of Rokan estuary is dynamically changed over a time because accretion rate is very high. The accretion rates in Halang, Barkey, and Serusai Island within 14 years are 67 m/yr, 53 m/yr, and 114 m/yr respectively. This occurs because of the hydrodynamic nature and high sediment transport in downstream of Rokan River.

Keywords: remote sensing, GIS, shoreline change, DSAS

1. Introduction

Coastal zone and its environmental management require the information about shorelines and their changes. There are several approaches to calculate the rates of shoreline change such as numerical models and remote sensing technique. The rapid development of remote sensing and GIS technology lead to develop some applications more powerfull for shoreline change analysis. Besides some traditional computation from modeling, the integrated remote sensing and GIS also support effective results to coastal engineers and managers. By integrating modern techniques of remote sensing and GIS (Geographic Information System), the rates of shoreline change would be easily and quickly determined for a regional area. By the input data from extracted shoreline information from satellite image, GIS tool can be used to calculate long-term

How to cite this article: Sigit Sutikno, Ferry Fatnanta, Ari Kusnadi, and Keisuke Murakami, "Integrated Remote
Sensing and GIS for Calculating Shoreline Change in Rokan Estuary," *KnE Engineering*, vol. 2016, 9 pages.
DOI 10.18502/keg.v1i1.491

Page 1

shoreline change rate. This approach is very effective because it would save time, costs and manpower [1].

This paper presents an application of satellite remote sensing techniques to detect and to analyze the spatial changes as well as quantify the shoreline change in Rokan estuary, Riau Province, Indonesia. Coastal zone of Rokan estuary, a place through which Rokan River flows into Malacca Strait is dynamically changed because of the hydrodynamic nature and high sediment transport in downstream of Rokan River. Currently, the use of satellite imagery dataset is very important role in providing data for analysis and monitoring of coastal areas due to the available data in long time period. Landsat TM (thematic mapper) and ETM+ (Enhanced Thematic Mapper) with 15 and 30 m spatial resolution are satellite imagery dataset that can be used for analysis and monitoring of shoreline change [2], [3], [4]. Landsat satellite images, such as Landsat 5 TM, Landsat 7 ETM+ and Landsat 8 OLI (Operational Land Imager) were used with a combination of histogram thresholding and band ratio method for shoreline change detection for last 14 years from 2000 to 2014. Image processing applied in this study included geometric rectification; atmospheric correction; on-screen shoreline digitizing for tracking the shoreline position of Rokan estuary.

With historical shoreline data input, the erosion and deposition rates can be estimated by ovelaying using GIS tool. The rate of shoreline change can be calculated by DSAS (Digital Shoreline Analysis System), an extension for ArcGIS. DSAS is a digital shoreline analysis tool that can be used to compute rate-of-change statistics for a time series of historical shoreline data which is developed by United States Geological Survey (USGS) [5]. The statistical methods called as LRR (Linear Regression Rate) in DSAS was used in this study. The LRR method can be determined by fitting a least squares regression line to all shoreline points for a particular transects. However, the LRR method is easy to employ and based on accepted statistical concepts with acceptable accuracy [6-8].

2. The Nature Condition of Rokan Estuary

The study area is located in Rokan Hilir Regency which is stretched from 1°14′0″ N, 100°17′0″ E to 2°45′0″ N, 101°21′0″ E as shown in Figure 1. Rokan River is one of four major rivers in Riau Province, Indonesia, which its length is about 400 kilometers. The river sourced from the Barisan Mountains in the west, and drained northeast-ward along Rokan Hulu Regency and Rokan Hilir Regency with estuarine located near the port town of Bagansiapiapi draining the water to Malacca Strait. The shoreline of Rokan estuary is dynamically changed over a time because of the hydrodynamic nature and high sediment transport in downstream of Rokan River. There are several islands that formed as a result of this process, and from time to time growing. Rahmansyah [9] investigated the rate of sediment transport in around Rokan estuary, and reported that the supply of suspended solids entering through either sequentially streamflow into the ebb tide and at low tide to high tide for Rokan estuary are 329,079.770 gr/sec and 297,900.580 gr/sec respectively.
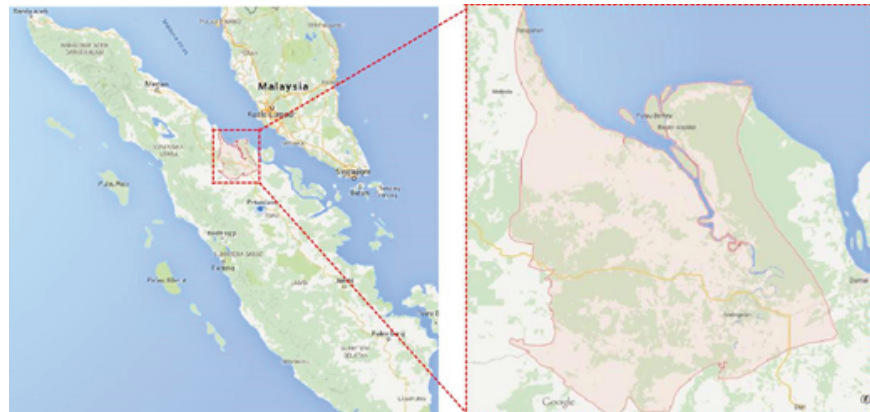
Figure 1: The Study Area.

Aquisition date	Satelit	Sensor	Resolution
10/04/2000	Landsat 5	TM	30 m
29/08/2002	Landsat 7	TM	30 m
03/08/2004	Landsat 7	ETM+	15 m, 30 m
11/11/2007	Landsat 7	ETM+	15 m, 30 m
17/06/2009	Landsat 7	ETM+	15 m, 30 m
22/05/2011	Landsat 7	ETM+	15 m, 30 m
23/03/2014	Landsat 8	OLI	15 m, 30 m

TABLE 1: List of Landsat scenes used for Rokan estuary study

3. Methodology

3.1. Data

Satellite data used in this study consisted of 7 years of data records, such as Landsat TM 2000, Landsat TM 2002, Landsat ETM+ 2004, Landsat ETM + 2007, Landsat ETM + 2009, Landsat ETM + 2011, and Landsat-8 OLI / TIRS 2014. Landsat TM has a resolution of 30 m, while the Landsat ETM+ and Landsat-8 OLI band 8 have a resolution of 15 m. Path and Row position is on the Path 127 and Row 29 or UTM 40N. Specifications of those satellite data are presented in Table 1. Selection of the data was based on availability and quality of the satellite data

3.2. Remote Sensing

Analysis and interpretation of Landsat data consists of cropping the image, image enhancement, geometric correction, digitization, and overlapping. Cropping the image was made to take the focus area of research to save storage in a computer memory. Image enhancement was the combination of bands needed to make clearer the boundary between land and water that will ease the process of digitization coastline. For Landsat TM and ETM+, the combination of histogram threshold and band ratio
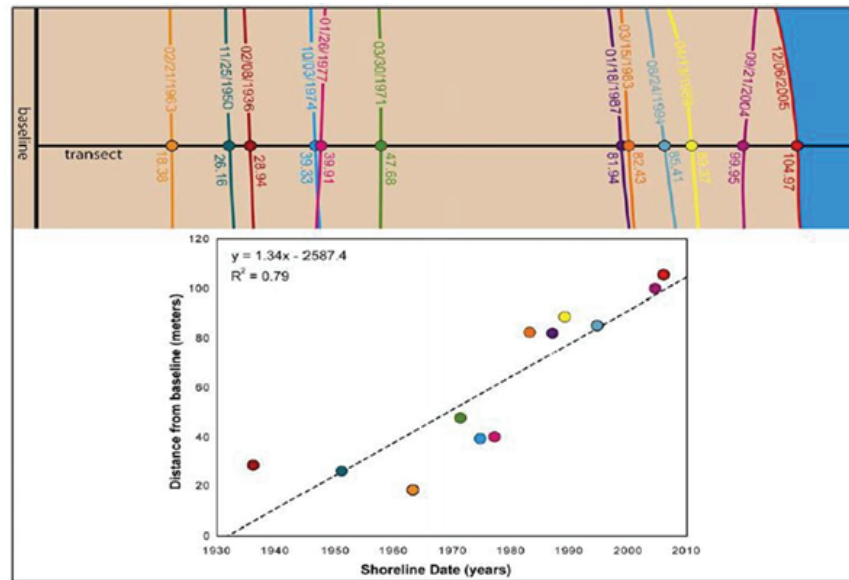
Figure 2: The method of LRR calculation (Source: Thieler, 2009).

techniques is proposed by using band 2, 4, and 5 to separate water and land directly [3]. Other approach is to use single band thresholds such as band 5 or band 7 of Landsat TM and ETM+ to extract water-land interface because they are useful in clear water conditions [10]. The Landsat image data were obtained in GeoTiff format which have been corrected so that the geometric correction was omitted. After classification, raster images would be converted to vector images. The final step is to export into shapefile format for processing in GIS tool.

3.3. GIS

Statistical analysis based on GIS was performed to determine the level of shoreline change or the rate of coastal erosion. This was done by using the software DSAS (Digital Shoreline Analysis System), an extension for ArcGIS. Shoreline analysis using DSAS consists of three main stages, such as : to set up baseline parallel to the shoreline as the reference line, to choose parameter for transects perpendicular to the baseline that divides coastline in sections, and to calcule the rate of change each section. Linear Regression Rates (LRR) method, a statistical method is chosen to present the computational results. The LRR can be determined by fitting a least squares regression line to all shoreline points for a particular transect as shown in Figure 2 [5]. The regression line is placed so that the sum of the squared residuals (determined by squaring the offset distance of each data point from the regression line and adding the squared residuals together) is minimized.
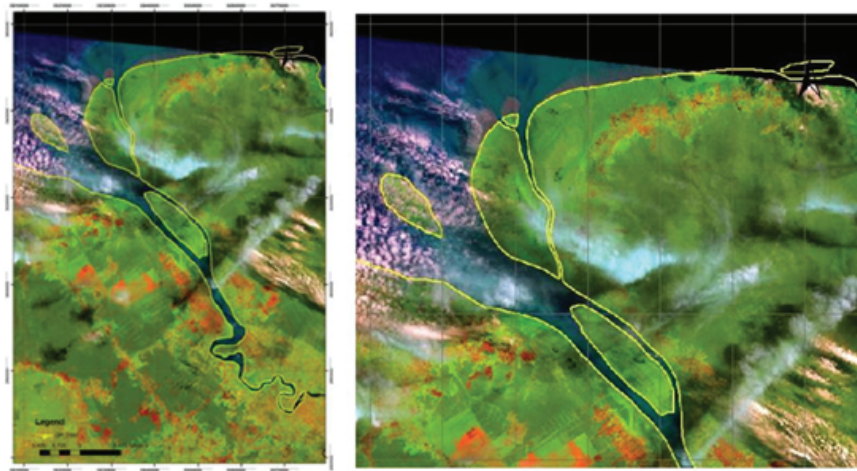
Figure 3: Shoreline extracted from Landsat-7 2002 with composite band 542.
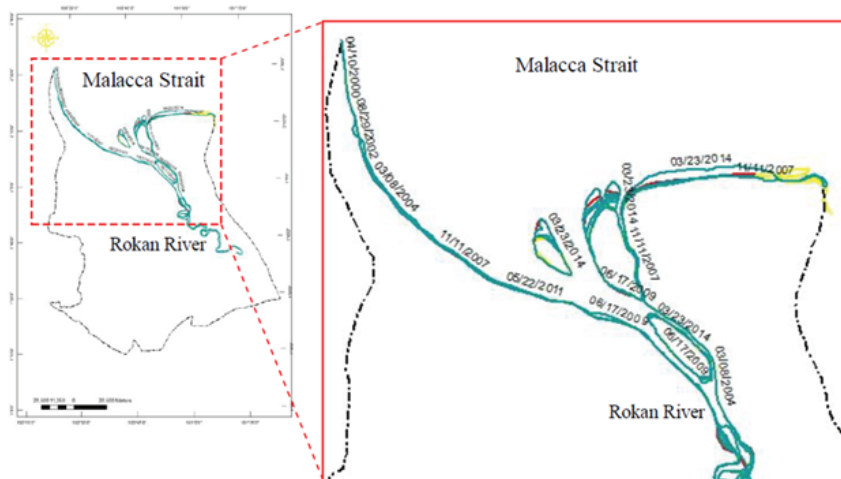
Figure 4: Shoreline extracted from Landsat 2000 ~ 2014.

4. Result and Discussion

4.1. Extracting Shoreline

The image processing, such as cropping, enhancement, and correction were applied for 7 years of Landsat data records. Fig. 3 shows an example result of the image processing for Landsat-7 2002. By using combination of bands 542, the boundary between land and water become clearer that make easier to digitize the shoreline. By image processing and digitizing, the historical shorelines data of Rokan estuary for the last 14 years can be extracted from Landsat. The extracted shoreline data are shown in Fig. 4. From the extracted shoreline data, the historical of shoreline change can be analyzed by overlaying process. Identification of coastal abrasion and coastal accretion during 14 years, from 2000 to 2014 can be carried out by overlaying the oldest and the newest shorelines, and the result is shown in Fig. 5.
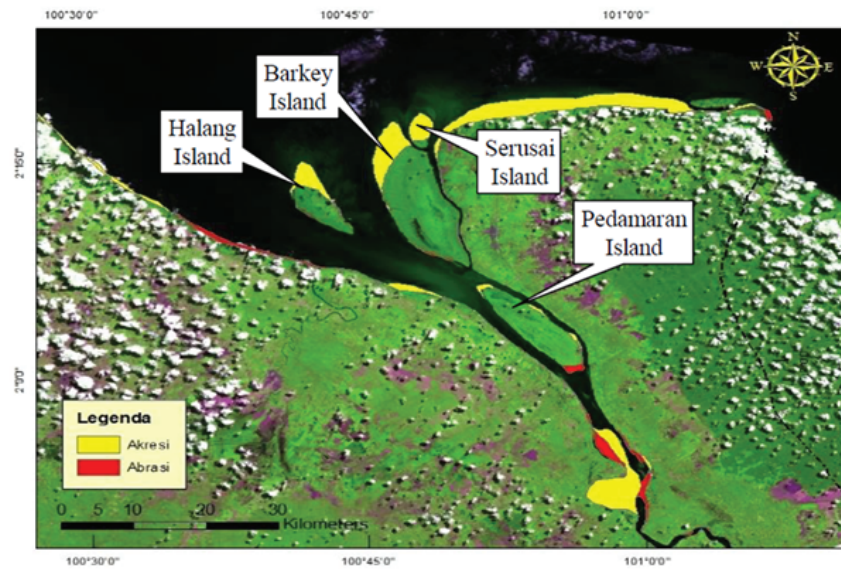
Figure 5: Abrasion and accretion area of Rokan estuary during 2000 ~ 2014.

As shown in Fig.5, accretion phenomena are very high in Rokan estuary which are dominanly occur in North area. On the other hand, abrasion phenomena are very low. This occurs because the sediment transport in Rokan river is very high which is about 297,900 gr/sec to 329,079 gr/sec [9]. There are three islands in downstream area namely Halang, Barkey, and Serusai Island which the accretion rate is very high, and an island in upstream area, Pedamaran Island which the accretion rate is relatively low. Over all, the abrasion rate in Rokan estuary is relatively low, and the accretion rate is very high as shown in Fig. 6. Historically, accretion occurrence from 2000 to 2007 was not too high, but starting from 2007, the accretion rate was gradually increased. The maximum accretion rate occurred during last 3 years from 2011 to 2014. Those phenomena occur probably caused by the activity or land use change in Rokan watershed that is need to be studied further. However, the abrasion rate in Rokan estuary was very small from 2000 to 2011. It was little bit increased from 2011 to 2014.

4.2. Shoreline Change Analysis

Multiple shoreline positions along with fictitious baseline are the basic requirement for analyzing the shoreline. Long-term rates of change were calculated for entire study areas at each transect for 14 years i.e. 2000 to 2014 using LRR method considering 7 datasets. The study area was divided into five zones for handling the data and visualization of the results at appropriate level. Fig. 7 shows an example result of the shoreline change analysis for Zone-2 which is located in Pedamaran Island. There are 157 transects established in this zone with 250 meter interval. The figure shows the rate of shoreline change in each transect number. It can be seen that the positive and negative rates of change show the beach accretion and beach abrasion correspondingly. As a result, abrasion occurs in Area-1 and accretion in Area-2, Area-3, and Area-4. The average rate of shoreline change within 14 years from 2000 to 2014 in Area-1, Area-2,
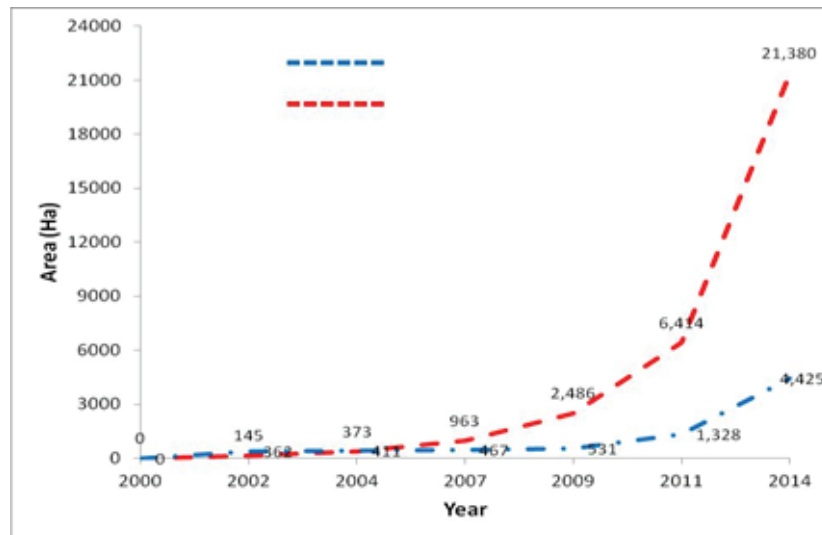
Figure 6: Rate of abrasion and acresion of Rokan estuary during 2000 ~ 2014.
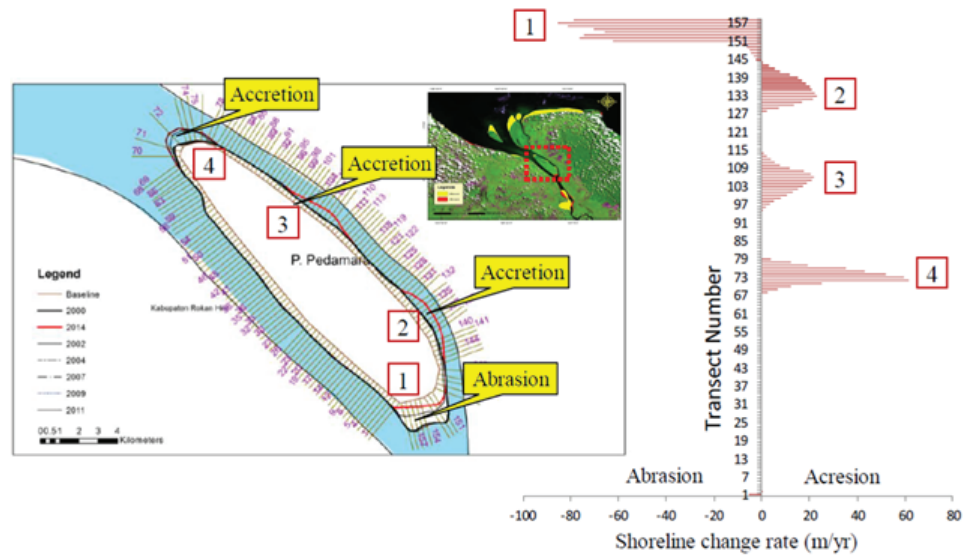
Figure 7: Shoreline change rate of Pedamaran Island (Zone-2), Rokan estuary during 2000 ~ 2014.

Area-3, and Area-4 are -44 m/yr, 13 m/yr, 10 m/yr, and 28 m/yr respectively. These phenomena indicate that Pedamaran Island is dynamically changed within this period. The upstream area of river flow tends to occur abrasion, while the downstream area occur accretion.

The shoreline change phenomena in Pendamaran Island also occur in the three other islands, namely Halang, Barkey, and Serusai Island. The shoreline change phenomena in Halang, Barkey, and Serusai Island, which are located in downstream area little bit different with that of in Pedamaran Island. As shown in Fig. 8, the rate of shoreline change in downstream islands is higher than that of in upstream island. The rate of accretion in downstream islands is very high, such as 67 m/yr, 53 m/yr, and 114 m/yr for Halang, Barkey, and Serusai Island respectively. However, the rate of abrasion is
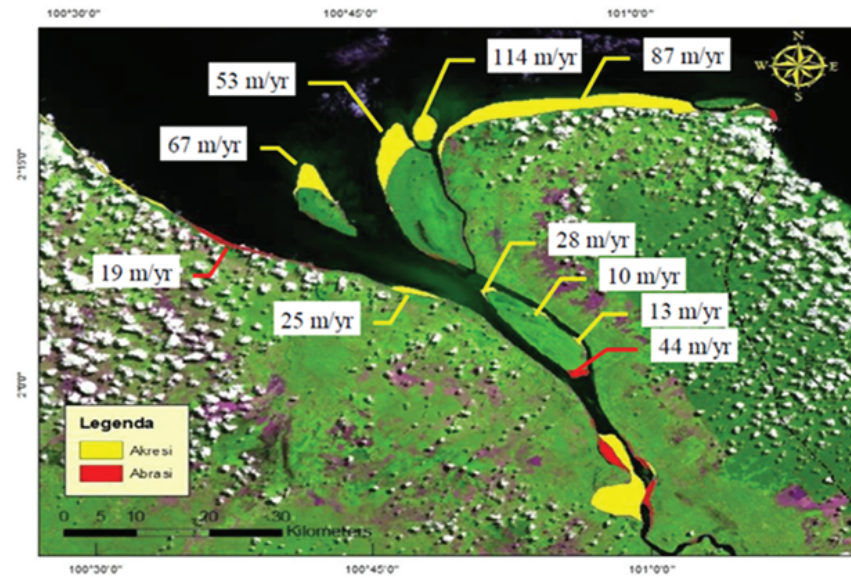
Figure 8: Shoreline change rate each lcation in Rokan estuary during 2000 ~ 2014.

very small. These phenomena make those three downstream islands become wider over a time.

5. Conclusion

The integration between remote sensing and GIS technology is very useful because it can be used to overview the long-term shoreline changes in the concerned area quickly. The paper showed that Rokan estuary shoreline could be determined rapidly by the improved band ratio. The shoreline change rates could be calculated by statistical method which was built in the extension of GIS tool. Quantitatively, the shoreline of Rokan estuary is dynamically changed over a time because accretion rate is very high. The accretion rate in Halang, Barkey, and Serusai Island within 14 years from 2000 to 2014 is 67 m/yr, 53 m/yr, and 114 m/yr respectively.This occurs because of the hydrodynamic nature and high sediment transport in downstream of Rokan River.

References

[1] T. P. T. Pham, H. D. Duan, and D. Van To, Integrated remote sensing and GIS for calculating shoreline change in Phan-Thiet coastal area, *Int. Symp. Geoinformatics Spat. Infrastruct. Dev. Earth Allied Sci.*, 1–6, (2008).

[2] T. Van and T. Binhz, Application of remote sensing for shoreline change detection in Cuu Long estuary, *VNU Journal of Science, Earth Sciences*, no. 25, 217–222, (2009).

[3] , A. Ghorbanali, N. Nouri, et al., Coastline change detection using remote sensing, *Int J Environ Sci Technol*, **4**, 61–66, (2007).

[4] H. M. El-Asmar and M. E. Hereher, Change detection of the coastal zone east of the Nile Delta using remote sensing, *Environ Earth Sci*, **62**, 769–777, (2011).

[5] E. Thieler, et al., (2009), Digital Shoreline Analysis System (DSAS) version 4.0 – An ArcGIS extension for calculating shoreline change.

[6] S. Sutikno, Rate of Shoreline Change Analysis of Bengkalis Coast Using Satellite Imagery Data, *The 31st Annual Conference of Indonesian Association of Hydraulic Engineer*, 616–625, (2014).

[7] W. P. Beach, A. S. Genz, C. H. Fletcher, R. A. Dunn, L. N. Frazer, and J. J. Rooney, The Predictive Accuracy of Shoreline Change Rate Methods and Alongshore Beach Variation on Maui, Hawaii, *J Coast Res*, **23**, 87–105, (2007).

[8] R. S. Kankara, S. C. Selvan, B. Rajan, and S. Arockiaraj, An adaptive approach to monitor the Shoreline changes in ICZM framework: A case study of Chennai coast, *Indian J Mar Sci*, **43**, (2014).

[9] in *W. Rahmansyah and Rifardi, "Suspended Solids in Rokan River Estuary, Riau Province, Indonesia*, 1–14, Repos. Univ, Riau, 2014.

[10] S. Bagli and P. Soile, Morphological Automatic Extraction of Pan-European Coastline from Landsat ETM Images 5th Int. Symposium on GIS and Computer Cartography for Coastal Zone Management, Integrating Information in Coastal Zone Management, Genova, August 2003.

Conference Paper

New Approach for Airflow Measurement Using Thermal Resistance Simulation

Lazuardi Umar, Yanuar Hamzah, and Rahmondia N. Setiadi

Department of Physics, Fisika FMIPA University of Riau Indonesia, Kampus Bina Widya Sp. Baru Pekanbaru 28293, Indonesia

Abstract

This paper presents a new model-based approach to detect and compensate errors of positive temperature coefficient (PTC) sensors used for airflow measurement. From modeling and simulation, it can be shown that the thermal resistance of the sensor at self-heating mode was influenced by air flow magnitude. The sensor of type EPCOS-AG B59010 in a steel case, length 20 mm, diameter 2 mm was characterised over the flow rate range between 0 and 6 m/s and modeled to determine coupling thermal resistance interaction R_{th} between the medium surrounding and sensor's structure. Soiling caused by dust transported with the air on the sensor surface changing in the thermal resistance has observed and simulated in an experiment using a cylindrical sheath of PTFE – *Polytetrafluorethylen* with known heat conductivity λ_S = 0.24 W/Km and diameter D. Parameters of model were then calibrated by evaluating current-voltage I(U)-characteristic at air velocity of v = 0m/s, and recalibration is then also used to correct the model parameters for v ≠ 0m/s. Result shows the soiling has exceeded critical thickness at D/d = 9 wherein the thermal resistance tends to be constant meaning cleaning sensor surface or replacing are needed.

Keywords: airflow measurement, PTC sensor, thermal resistance, soiling, simulation

🔓 **OPEN ACCESS**

1. Introduction

There is a variety of airflow sensors on the market which meet specific application especially for commercial and private purpose [1]. The ceramic PTC thermistor is considered as an ideal sensor for monitoring the airflow and has several advantages such as simple structure and rugged. For long-time application, the sensor has disadvantages due to their longterm stability and soiling on its surface, so that it has to be recalibrated.

Positive temperature coefficient (PTC) thermistor sensors are constructed from sintered metal oxide ceramic and its electrical resistance change with temperature. They are sensitive but highly non linear. Their sensitivity, reliability, ruggedness and ease in use, have made them popular for research applications but less commonly used for industrial applications. Furthermore, the raw signal from the thermistor is extremely non-linier [2].

This paper presents a new approach model-based method of automatic self-control of PTC airflow sensors using thermal resistance measurement. The parameters of the

How to cite this article: Lazuardi Umar, Yanuar Hamzah, and Rahmondia N. Setiadi, "New Approach for Airflow Measurement Using Thermal Resistance Simulation," *KnE Engineering*, vol. 2016, 7 pages. DOI 10.18502/keg.v1i1.492

Page 1
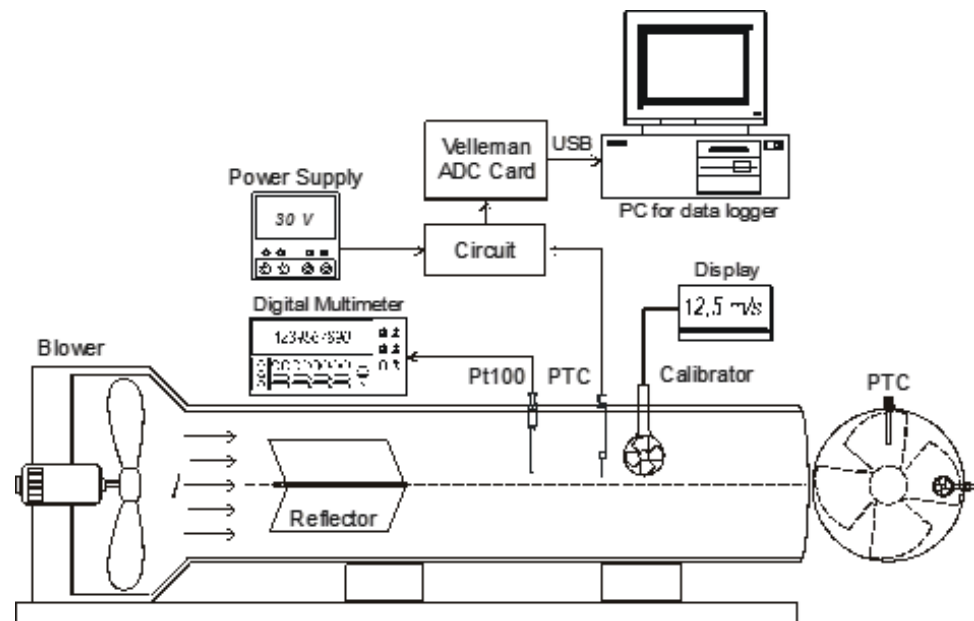
Figure 1: Schematic diagram of the airflow measurement system.

model were also determined from the sensor's current-voltage curve (I-U-characteristics) at certain defined states, and are used to correct the measured data. With this self-calibration procedure, failure due to soiling on sensor's surface can be detected and effectively compensated to enhance the reliability and accuracy measurement especially in hostile environments.

2. Materials and Methods

2.1. Design and Construction of The Experiments

Airflow measurement experiments were carried out in an experimental setup for calibration consisting of a wind tunnel with an air reflector and a blower, a calibration circuit, an anemometer calibrator and a personal computer for data acquisition as shown schematically in Fig. 1. The tunnel was constructed using a PVC pipe ($\varnothing$ 10 cm; length 150 cm). For appropriate measurement of airflow, a blower with a $12V_{DC}$ operating voltage was used for generating a homogeneous and constant air current in wind tunnel. The velocity of the air entering the wind tunnel was varied by changing the operating voltage, from 0 m/s to a maximum speed. A stand of a scale and a holder were provided on the table with an additional anemometer to allow observation of the airflow profile in two dimensions over the entire tube cross section. An anemometer of the Electronic Wind Speed Indicator was used to measure the airflow independently of the incident flow direction.

The PTC sensor was attached at the front of the wind tunnel for characterization. Due to the heat dissipation of the blower motor, the ambient temperature T_M of the measured airflow in the tunnel increased and resulted in the shift of the sensor's I(U) curve. This ambient temperature was measured with a metal-housed temperature

sensor PT100 and subsequently used for modeling of the I(U)-curve in order to obtain the parameters of the sensor and the parameters related to air velocity. A computer equipped with an Analog to Digital Card (ADC) type Velleman drived by a program PC Lab-2000 has been used for data acquisition of the air velocity, whereas curve modeling and graphic processing has been done using the program MathCad, Sigma Plot and Table Curve.

2.2. Heat Transfer and Airflow Measurement

The airflow was measured using the PTC Top of Form

Sensor type EPCOS-AG (Cat. Nr. B59010), enclosed in the stainless steel housing and suitable particularly well for airflow monitoring. In self heating mode, the sensor is heated and responds to a change in external cooling conditions due to airflow by changing its power consumption [3, 4]. The electrical power input is equal to the power lost to convective heat transfer,

$$I^2 \left(R_{T0} \cdot e^{B\left(\frac{T_S - T_C}{T_S}\right)} + R_0 \right) = \frac{1}{R_{th}} \left(T_S - T_M \right) \cdot \quad (1)$$

where I is the input current, T_S and T_M the temperatures of the sensor and fluid respectively and R_{th} the thermal resistance that indicates the heat coupling between sensor and its surrounding medium. Parameters R_{T0} denote sensor resistance at the specified temperature T_0, R_0 initial resistance, B proportional to the activation energy and T_C the Curie temperature. Such parameters show the behaviour of the sensor during operation. According to [5], thermal resistance R_{th} as a function of fluid velocity vwas determined by means of the following equation,

$$R_{th} = (a + b.v^c)^{-1} \quad (2)$$

where a, b, and c are coefficients R_{th} obtained from calibration (c ~ 0.5). Combining Eq. 1 and Eq. 2 allows us to eliminate the thermal resistance and solving for the fluid velocity,

$$v = \left\{ \left[\left(I^2 \cdot R_{T0} \cdot e^{B\frac{T-T_C}{T}} + R_0 \right) \left(T_S - T_M \right)^{-1} - a \right] /b \right\}^{1/c} \quad (3)$$

Using the formal Steinhart-Hart equation [6] for the temperature dependence of the electrical resistance with three parameters, the air velocity then can be measured with a relative error < 3 %.

2.3. Sensor Calibration

In Fig. 2, a simple electrical circuit for calibration the I(U) characteristic of PTC sensor in the self-heating mode is shown. The sensor was calibrated in still air (v = 0 m/s) and in at a different air flow (v ≠ 0 m/s). To obtain the thermal resistance and sensor parameters, the I(U) characteristic was modeled after Eq. 1.

(a)

(b)
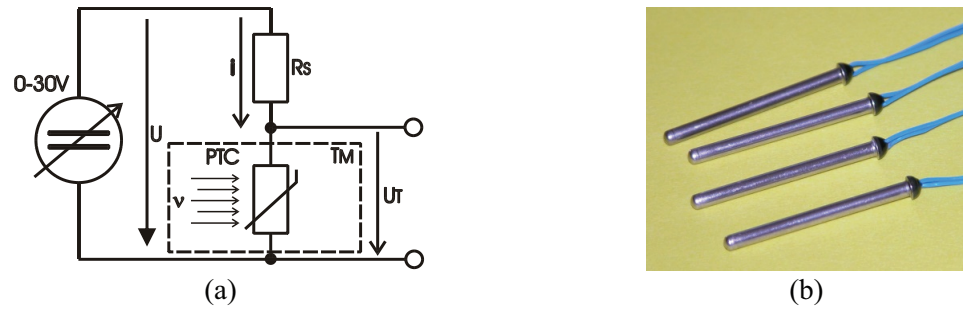
Figure 2: Simple circuit for characterisastion of PTC sensor (a) and sensor B59010 in (b).

Heat conductivity (λ_S)	0,24 W/Km
Density (ρ)	2,15 g cm^{-3}
Specific heat (c)	1,01 kJ kg^{-1} K^{-1}
Temperature max. (ϑ)	260 °C
Diameters of PTC (d)	2 mm
Diameters of sheath (D)	3 ... 8 mm

TABLE 1: Characteristic of the cylindrical sheath with L = 22 mm.

The sensor output data can then be kept within the specification through continuous re-calibration, a necessary maintenance will be signaled only if the deviation from the reference exceeds a threshold.

2.4. Simulation of Soiled Sensor

For long-time applications the airflow sensor is successively soiled by dust transported with the air, thus changing the heat transfer to medium. Soiling increases the diameter of the sensor from the initial value d to D. The changing of the thermal resistance is observed using a cylindrical sheath with known heat conductivity λ_S and diameter D, as shown in Fig. 3 and Table 1. For the measurements, a Teflon (PTFE – *Polytetrafluo-rethylen*) sheath was used with following physical characteristics:

An increasing in the diameter of cylindrical sheath changes the overall thermal resistance R$_{th,overall}$. As a result, the function of fluid velocity v according to King's law has been extended in order to fit more data set for obtaining better results as follows [7]:

$$R_{th,overall} = R_{W,S} + \frac{1}{2\pi L \lambda} \cdot \ln\left(\frac{D}{d}\right) + \frac{1}{\left(a_0 \left[1 + a_1 \cdot \left(\frac{D}{d}\right)^{0.5} \right]^2 - b_0 \sqrt{\left(\frac{D}{d}\right) \cdot v} + b_1 \cdot \left(\frac{D}{d}\right)^{1.6} v^{1.6} \right)}$$

(4)

In Eq. 4, the thermal resistance R$_{th,S}$ describes the heat transfer of the thermal source (sensor material) to the surface of the sensor, and it is exemplar specific and temporally constant. The second term in Eq. 4 describes the thermal resistance through heat conduction of the sensor soiling and the third term depicts extended King's law.
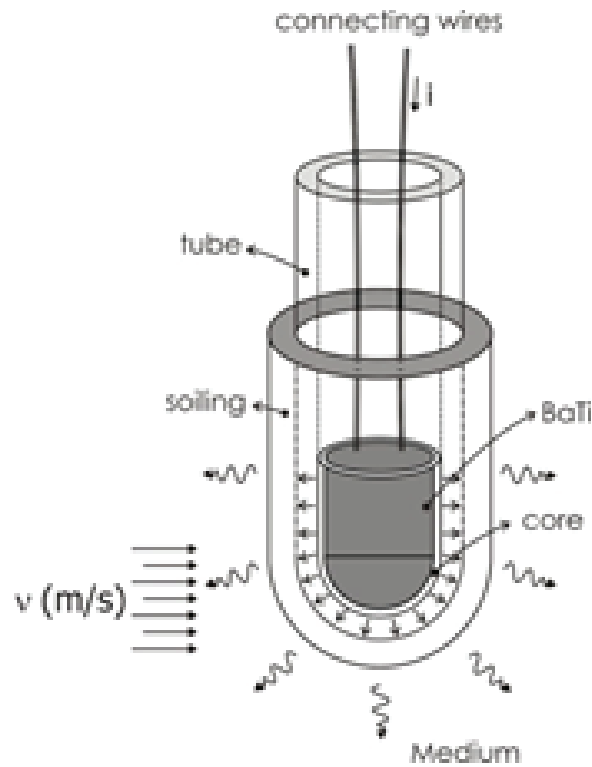
Figure 3: Simulation of soiled sensor of EPCOS-AG B59010 with a cylindrical teflon sheath.
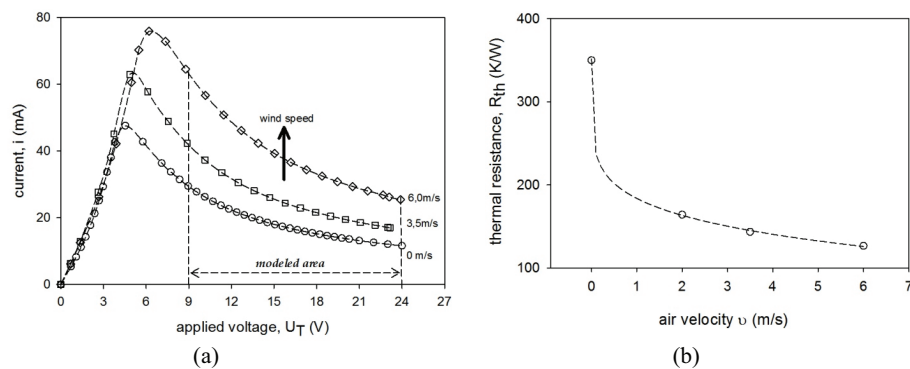
Figure 4: The I(U)-characteristic of the sensor at various air velocities and modeled area (a) and the thermal resistances decrease against the increasing of velocities in (b).

3. Results and Discussion

3.1. Modeling of the I(U)-Curve

The current-voltage curve (I-U) of the observed sensor at various velocities obtained in the present work ranged from 0 to 6.0 m/s, see Fig. 4. There was a current shift toward higher levels with the increase of the velocities due to more heat transfer to the environment. It led the sensor to compensate in order to retain the equilibrium state. This is caused by a better thermal conductivity flowing - than in still air. The changing in the current shifts the voltage-current characteristic of the sensor (I-U curve) and results in the changing of the heat transfer, thus its thermal resistance.
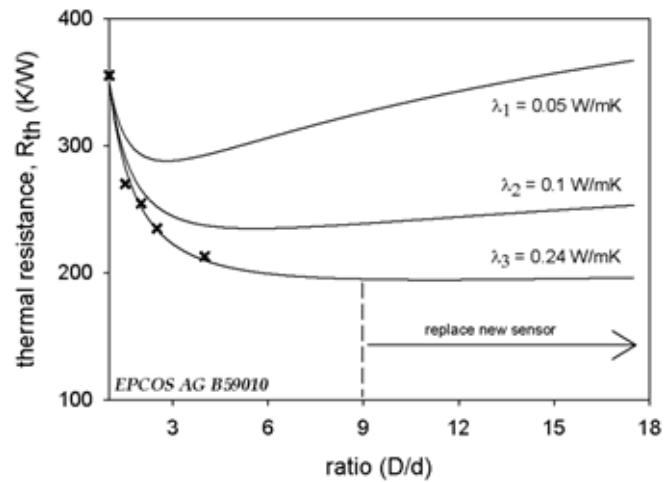
Figure 5: Variation of thermal resistance at different diameter ratio (D/d), measured at constant temperature of 30∘C.

The thermal resistance and the sensor parameters were obtained from the modeling of the I(U)-curve at a given range according and the results showed that the thermal resistances in still air (R_{th} = 350K/W at v = 0 m/s) and at various air velocities (R_{th} = 126.7K/W at v ≠ 0 m/s) are differed clearly from one another, or decreased around 63% at v = 6 m/s, while the sensor parameters R_{T0} = 32.67Ω, R_0 = 4.99 10^{-7}Ω, B = 73,88 and T_C = 378.53K are remain constant since there were no recrystallization of the sensor material.

3.1.1.

3.2. Self-Calibration of the Sensor Parameter

The "effective" diameter D of the soiled sensor is time-dependent. According to Eq. 5, a larger D has influence on the thermal resistance and also on the sensitivity of R_{th}. Fig. 5 represents the simulation of thermal resistance for v = 0 m/s as a function of the diameter ratio, D/d after Eq. 4.

In Fig. 5, the thermal resistance of was simulated at various diameter coating. At the beginning of the soiling, the thermal resistance in air was very large, since air has a low thermal conductivity. Thereby the total resistance is determined by the boundary of layer-resistance. With increasing sheath diameter, the thermal resistance decreases as teflon sheat has a better thermal conductivity than air. In Fig. 5, it appears that for λ = 0.24 W/mK the thermal resistance after (D/d) ≈ 9 is no longer decrease and tends to remain constant. In this case, the soiling has exceeded critical thickness and the PTC thermistor sensor must be cleaned or changed.

From the known type-specific thermal parameters such as a_i and b_j in Eq. 4, the exemplary-specific electrical parameters R_{T0}, R_0, B, T_C and R_{th} are estimated from the sensor with known D prior to the first use. The "effective" diameter D is calculated with an assumed value of λ (the influence of λ is small and all relevant soiling matters have very similar thermal conductivity values.)

4. Conclusion

In this work, a model-based method of self-control of PTC air-velocity sensors has been presented to determine sensor parameter and thermal resistance used for airflow detection. The sensor's I(U)-characteristics is corrected at certain defined states, i.e. when v = 0 m/s, and used to correct the measured data, also when $v \neq$ 0 m/s. With this self-calibration procedure, errors like contamination of the sensor surface by dust, ohmic bridges, shortcuts and ageing of the electrical parameters, are detected and effectively compensated, without the need to take several additional measurements.

References

[1] C. Jiang, G. Liu, and J. Jiang, A Self-Validating Algorithm for Hot Thermistor Constant Differential Temperature Air Flow Sensor, *Proceedings of the 2005 IEEE Conference on Control Applications Toronto*, (2005).

[2] P. M. Aleksi, et al., A Thick Film NTC Thermistor Air Flow Sensor, *Proceedings of 24th International Conference on Microelectronics (MIEL 2004)*, (2004).

[3] C. Xu, X. Guo, H. Jiang, Z. Zhang, and S. Liu, Modeling and Simulation of Self-heating Effect with Temperature Difference Air Flow Sensor, *2014 15th International Conference on Electronic Packaging Technology*, 655–659, (2014).

[4] M. Horn and L. Umar, Sensorsystem zur Messung der Luftgeschwindigkeit mit automatischer Selbstüberwachung und Selbstkalibrierung, *Proceeding of ITG/GMA Fachtagung Sensoren und Meßsysteme 2002*, (2002).

[5] L. V. King, On the convective heat transfer from small cylinders in a stream of fluid. Determination of convective constants of small platinium wires with application to hot-wire anemometry, *Phil. Trans R. Soc*, **214A**, 373–432, (1924).

[6] Fenwal, NTC/PTC Thermistor Standard Products Catalog, Fenwal Electronics Inc., Mass., USA (1985).

[7] V. D. I. Wärmeatlas, in *VDI-Verlag GmbH*, German, Düsseldorf, 1997.

Knowledge E
Engaging minds

Conference Paper

Methods and Applications of Label-Free Cell-Based Systems

Joachim Wiest

Cellasys GmbH – R&D, Ohmstrasse 8, 80802 Munich, Germany

Abstract

Label-free monitoring of living cells is used in various applications such as drug development, toxicology, regenerative medicine or environmental monitoring. The most prominent methods for monitoring the extracellular acidification, oxygen consumption, electrophysiological activity and morphological changes of living cells are described. Furthermore, the intelligent mobile lab (IMOLA) – a computer controlled system integrating cell monitoring and automated cell cultivation – is described as an example of a cell-based system for microphysiometry. Results from experiments in the field of environmental monitoring using algae are presented. An outlook toward the development of an organ-on-chip technology is given.

Keywords: microphysiology, cell-based assay, microsensors, environmental monitoring, toxicology, drug development

🔓 **OPEN ACCESS**

1. Introduction

To allow the continuous and therefore dynamic monitoring of the vitality of living cells, the method of investigation must not interact with the living probe. Therefore, labels or markers which bind to receptors (e.g. the G-protein coupled receptor (GPCR)) are prohibited. Beside methods based on optical analysis [1] a variety of mainly electro-chemical methods are available. Those methods address e.g. the extrusion of H_3O^+, cellular consumption of dissolved oxygen, electrophysiological activity and changes in the dielectricity of whole cells or the transmembrane flux of ions. Extrusion of H_3O^+ (extracellular acidification) are addressed by light addressable potentiometric sensors (LAPS) [2], ion sensitive field effect transistors (ISFETs) [2,3] or with metal-oxide based sensors [4]. The main principle to measure dissolved oxygen consumption (cellular respiration) is amperometry [5,6]. Electrophysiological activity or action potentials can be measured with micro-electrode arrays (MEAs) [2] while changes in dielectricity (e.g. beating of cardiomyocytes) or the transmembrane flux of ions (e.g. lysis of the cellular membrane) are addressed with impedance measurement [7,8] .

The Cytosensor Microphysiometer is a monitoring system based on the LAPS [9]. It gained acceptance for eye irritation assessment in 2009 [10]. The Bionas DiscoveryTM 2500 system [11] incorporates ISFETs, amperometric microsensors and impedance structures – manufactured in silicon technology - for live cell monitoring. Different commercial systems for electrophysiological monitoring with MEAs are available

How to cite this article: Joachim Wiest, "Methods and Applications of Label-Free Cell-Based Systems," *KnE Engineering*, vol. 2016, 5 pages. DOI 10.18502/keg.v1i1.493

Page 1
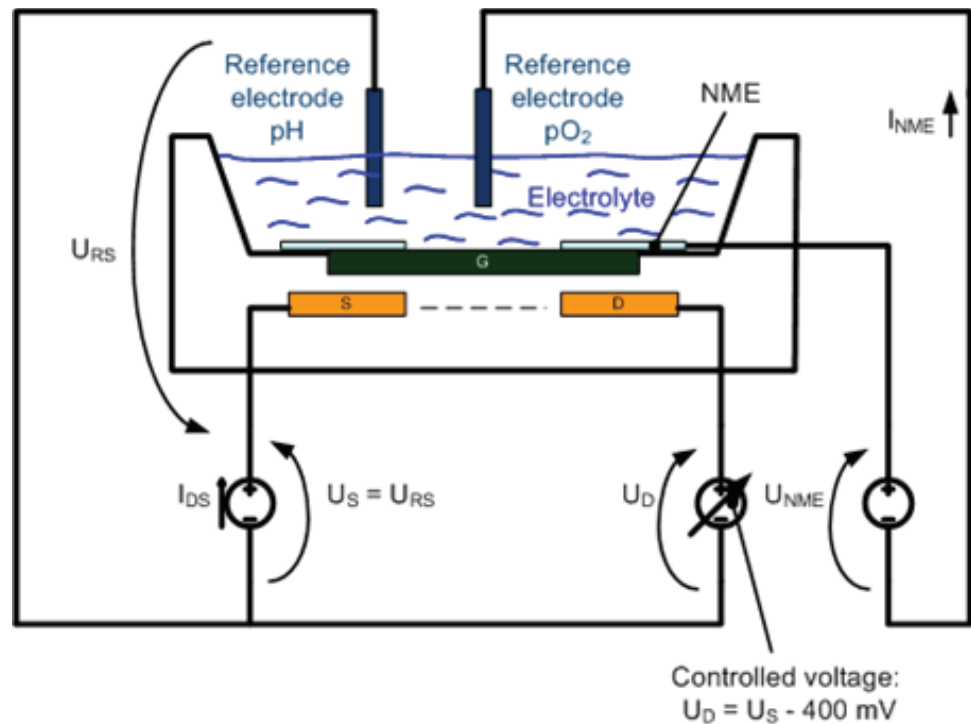
Figure 1: Principle of the CVFET. The gate electrode of a conventional ISFET is surrounded with a noble metal electrode where a cyclic potential is applied.

from Multichannel Systems MCS GmbH (Reutlingen, Germany) or Neuroproof GmbH (Rostock, Germany). Various systems for impedance monitoring were described by Schwarzenberger et al. [8]. A system which combines impedance measurement with opto-analytical methods is the intelligent microplate reader (IMR) from HP Medizintechnik GmbH (Oberschleißheim, Germany) [12].

2. Materials and Methods

The principle of the ISFET was extended toward the monitoring of dissolved oxygen [13] and further developed toward a cyclic voltammetry field effect transistor (CVFET) [14]. Figure 1 shows the principle of the CVFET. The pH-sensitive gate electrode of the ISFET is surrounded by a noble metal electrode (NME) where cyclic voltammetry vs. an external silver/silver-chloride reference electrode is performed. Whenever an electrochemical reaction at the NME provokes production of H_3O^+ or OH- the so-caused change in pH is also detected at the ISFET. That allows a more detailed interpretation of the electrochemical process [14].

The 6xIMOLA-IVD (Figure 2) is a turn-key ready system for automated label-free analysis of living cells [15]. The system is mounted in an incubator to allow monitoring at 37°C. It incorporates BioChips for simultaneous monitoring of extracellular acidification, cellular respiration and changes in cellular morphology. To enable automated analysis with defined standard operating procedures (SOPs) a fluidic system including switch valves, a computer controlled peristaltic pump and a software application for control and data acquisition is integrated. To be able to perform replicates, positive,
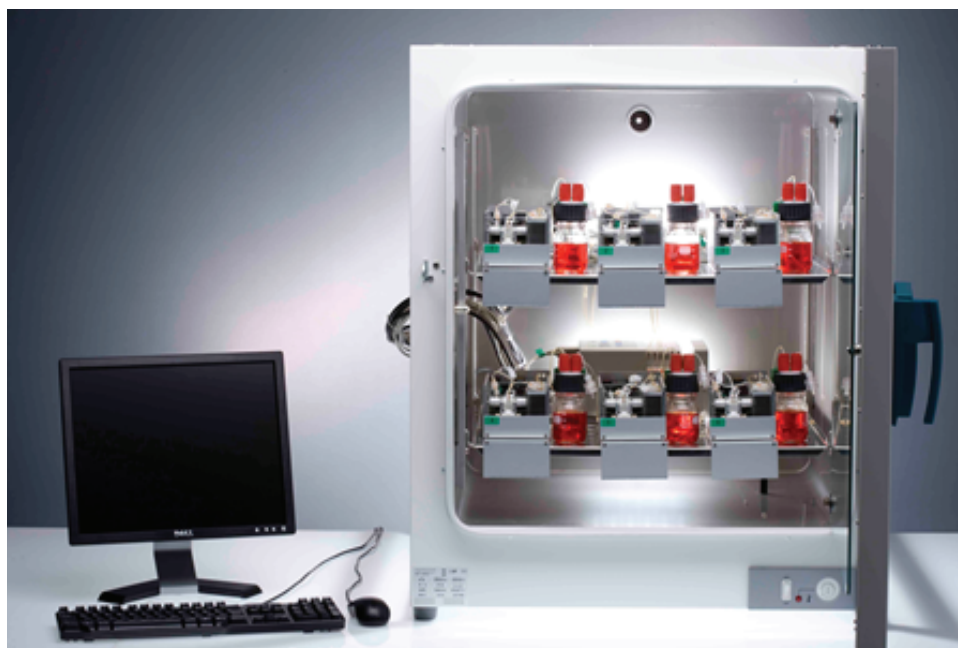
Figure 2: 6xIMOLA-IVD system. Six stations with BioChips are each extended with fluidic modules to switch between 4 different media flasks (24 channels). The measurement is arranged in an incubator to keep the living cells at 37°C. A computer takes care of the control and data acquisition.

negative and a blank control six parallel modules are set up. Since each module can be programmed to switch between four media flasks, 24 channels are possible.

3. Results

The capability of the 6xIMOLA-IVD for applications in fields as toxicology, cancer research or environmental monitoring was shown [15]. Figure 3 shows an example where the photosysnthetic activity of algae is inhibited during the presence of the xenobiotic Metamitron [16]. Recent experiments were performed on the algae chlorella kessleri with samples from Indonesian palm oil [17]. First results where the photosynthetic activity of the algae under the influence of samples from palm oil was monitored indicate that the algae increase their metabolism due to the availability of palm oil.

4. Discussion

Various types of microsensors are available for label-free monitoring of parameters of living cells. Integration of those sensors into a computer controlled monitoring system including a fluidic system allows long-term investigation of living cells and their interaction with changes in their microenvironment. Applications in the field of toxicology with cells in monolayer were performed by different groups. Results from the field of environmental monitoring using cells in suspension were presented. New developments are heading toward the investigation of 3D cell structures to allow the modeling of organ functions with label-free cell based assays [18].
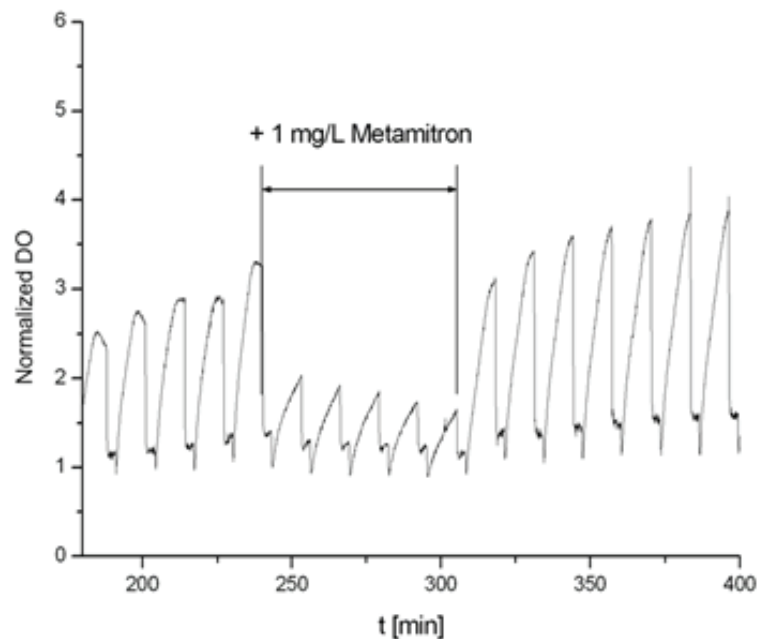
Figure 3: Photosynthethic activity of the algae chlorella kesleri. The photosynthetic activity is inhibited during the presence of Metamitron.

References

[1] Y. Fang, Non-Invasive Optical Biosensor for Probing Cell Signaling, *Sensors (Basel)*, **7**, 2316–2329, (2007).

[2] Q. Liu, C. Wu, H. Cai, N. Hu, J. Zhou, and P. Wang, Cell-based biosensors and their application in biomedicine, *Chem Rev*, **114**, 6423–6461, (2014).

[3] P. Bergveld, Thirty years of ISFETOLOGY – What happened in the past 30 years and what may happen in the next 30 years, *Sens Actuators B Chem*, **88**, 1–20, (2003).

[4] M. Brischwein, H. Grothe, J. Wiest, et al., Planar Ruthenium Oxide Sensors for Cell-on-a-chip Metabolic Studies, *Chem Anal Warsz*, **54**, 1193–1200, (2009).

[5] J. Wiest, M. Brischwein, J. Ressler, A. M. Otto, H. Grothe, and B. Wolf, Cellular Assays with Multiparametric Bioelectronic Sensor Chips, *Chimia (Aarau)*, **59**, 243–246, (2005).

[6] Y. Eminaga, M. Brischwein, J. Wiest, J. Clauss, et al., Self calibration of a planar dissolved oxygen sensor, *Sens Actuators B Chem*, **177**, 785–791, (2013).

[7] L. Doerr, U. Thomas, D. R. Guinot, C. T. Bot, S. Stoelzle-Feix, M. Beckler, M. George, and N. Fertig, New Easy-to-Use Hybrid System for Extracellular Potential and Impedance Recordings, *J Lab Autom*, 1–14, (2014).

[8] T. Schwarzenberger, P. Wolf, M. Brischwein, R. Kleinhans, F. Demmel, A. Lechner, B. Becker, and B. Wolf, Impedance sensor technology for cell-based assays in the framework of a high-content screening system, *Physiol Meas*, **32**, 977–993, (2011).

[9] H. M. McConnell, J. C. Owicki, J. W. Parce, D. L. Miller, G. T. Baxter, H. G. Wada, and S. Pitchford, The cytosensor microphysiometer: biological applications of silicon technology, *Science*, **257**, 1906–1912, (1993).

[10] T. Hartung, L. Bruner, R. Curren, C. Eskes, A. Goldberg, P. McNamee, L. Scott, and V. Zuang, First alternative method validated by a retrospective weight-of-evidence approach to replace the Draize eye test for the identification of non-irritant substances for a defined applicability domain, *ALTEX*, **27**, 43–51, (2010).

[11] P. Mestres and A. Morguet, The Bionas technology for anticancer drug screening, *Expert Opin Drug Discov*, **4**, 785–797, (2009).

[12] F. Demmel, M. Brischwein, P. Wolf, F. Huber, C. Pfister, and B. Wolf, Nutrient depletion and metabolic profiles in breast carcinoma cell lines measured with a label-free platform, *Physiol Meas*, **36**, 1367–1381, (2015).

[13] `www.cvfet.orgwww.cvfet.org`, (2015).

[14] Y. Eminaga, J. Wiest, M. Brischwein, H. Grothe, and B. Wolf, in *Multiparametric Microsensors on Lab-on-chip Systems for the Detection of Dissolved Substances, IMCS-14 Booklet, 83*, AMA Services GmbH, Nuremberg, 2012.

[15] D. Weiss, M. Brischwein, H. Grothe, B. Wolf, and J. Wiest, Label-free monitoring of whole cell vitality, Engineering in Medicine and Biology Society (EMBC), 2013 35th Annual International Conference of the IEEE, 1607-1610, 3-7 July 2013.

[16] J. Wiest, T. Stadthagen, M. Schmidhuber, M. Brischwein, J. Ressler, U. Raeder, H. Grothe, A. Melzer, and B. Wolf, Intelligent Mobile Lab for Metabolics in Environmental Monitoring, *Anal Lett*, **39**, 1759–1771, (2006).

[17] L. Umar, F. A. Alexander, and J. Wiest, Application of Algae-Biosensor for Environmental Monitoring, 37th Annual International Conference of the IEEE EMBS, Milano, Italy, 25– 9 August, 2015, 7099-7102.

[18] F. A. Alexander and J. Wiest, Online, Label-free Monitoring of Organ-on-a-Chip Models: The case for Microphysiometry, 37th Annual International Conference of the IEEE EMBS, Milano, Italy, 25–29 August, 2015, 7091-7094.

KnE Engineering

Knowledge E
Engaging minds

Conference Paper

Preparation and Characterization of Calcium Oxide Heterogeneous Catalyst Derived from AnadaraGranosaShell for Biodiesel Synthesis

Nurhayati, Muhdarina, Amilia Linggawati, Sofia Anita, and Tengku Ariful Amri

Chemistry Department, Faculty of Mathematics and Natural Science, University of Riau Pekanbaru, Indonesia

Abstract The aims of this study were to prepare and characterize environment-friendly calcium oxide (CaO)heterogeneous catalysts from blood cockle (*Anadaragranosa*) shells and utilizefor the synthesis of biodiesel. In this study, biodiesel was produced by transesterification reaction of waste frying oil with methanol using the CaO catalyst. The catalysts were prepared by crushing and calcining of *Anadara granosa* shellsat 800°C and 900°C for 10 hours.The resulting CaO catalyst were characterized using X-ray diffraction (XRD), thermogravimetric analysis (TGA), X-ray flourescense spectrometry (XRF), and Fourier transform infrared spectroscopy (FTIR). XRD patterns of calcined catalyst showed intense peaks of calcium oxide (2θ = 32.24^o,37.38^o and64.16^o), and it was consistent with XRF results (>99% of CaO found) that revealed calcium was the major element present in the *Anadara granosa* shells. The maximum yield of biodiesel produced was 82.25% under reaction conditions of catalyst loading of 3 wt.%, methanol to oil ratio of 15:1, reaction time of 3 h, temperature of 60°C and using a catalyst calcined at 900°C.

Keywords: Biodiesel, CaO, Heterogeneous catalyst, *Anadaragranosa*shell, Waste frying oil

OPEN ACCESS

1. Introduction

Population growth and industrial development has resulted in increased demand for energy. Fossil fuels tend to be environmentally not friendly, and therefore required the development of alternative renewable energy sources that are environmentally friendly and provide a solution to the increasing demand for these fuels. One of the alternatives that can be developed at this time to address these problems is the production of biodiesel from natural sources. Biodiesel,alsoknown as fatty acid methyl ester,is regarded as the best substitute for conventional petro-based diesel fuel since it is nontoxic, biodegradable and renewable [1].

Biodiesel is usually obtained from the transesterification reaction between the oil with methanol in an alkaline or acid catalyst [2]. But the production value is higher than the value derived from the production of petroleum-based fuels. To lower the price and make biodiesel competitive with petroleum, then the selection of basic materials and catalysts which are cheaper to manufacture biodiesel needs into account. The

commonly catalyst used for the transesterifcation reaction is alkaline catalysts such as KOH and NaOH. Heterogeneous catalyst which has the form of a solid has some advantages: easily separated from the mixture by filtration, do not require a lot of water in the filtration process and can be recycled and reusable [3,4].

Among the heterogeneous catalysts that have been used for the manufacture of biodiesel, calcium oxide (CaO) is an oxide of a strong base which has high catalytic activity.CaO as a base catalyst has many advantages, for example, the low temperature and short time of reaction conditions, as well as the low cost of the catalyst [5]. In addition, the use of CaO catalyst for biodiesel synthesis besides not toxic, the potential for the formation of soap is also very small compared to using base catalyst, i.eNaOH or KOH [6]. CaO is commercially available with high price, and that the research to obtain CaO with low cost from renewable feedstock is interesting topic until this time. The potential raw material for this purpose is shells from several mollusk and eggshell [7]. Blood cockle (*anadaragranosa*) shells have a good potential to be used as CaO heterogeneous catalysts in the manufacture of biodiesel because it contains calcium carbonate ($CaCO_3$) that will decompose to CaO at high temperature and its abundance of waste that has not been widely utilized. Moreover, utilization of *anadaragranosa* shells for biodiesel synthesis is expected to reduce the production price and that it will raise the economic value.

Synthesis and characterization of biodiesel using heterogeneous catalysts from blood cockle shells have been studied elsewhere [8]. The different temperature and time of calcination catalyst will result in different catalyst properties and activities to biodiesel conversion.The aim of this study was to synthesize and characterize catalyst derived from blood cockle shells (*anadaragranosa*). The catalyst was tested on the transesterification of waste cooking oil (WCO) to producebiodiesel with the variation parameters of time and temperature reactionin order to obtain the maximum biodiesel production.

2. Materials and Methods

2.1. Materials

Blood cockle shells and WCO samples were collected from households and cafetaria. The chemicals used in this study were methanol (99.8% purity, Sigma Aldrich), potassium hydroxide (KOH) solution prepared to 0.1 N using KOH pellets (99.99% purity, Sigma Aldrich), iso-propanol (99% purity, Merck), phenolphthalein indicator, potassium hydrogen pthalat and distilled water. All the chemicals and reagents were of analytical grade.

2.2. Preparation of CaO catalysts

CaO used in this study comes from the shells waste of blood cockle (*anadaragranosa*). Blood cockle shells were cleaned using water to remove dirt and sand that remains. Then, the shells was washed using distilled water until clean. Shells was coarsely

grounded using a mortar pestle, dried in an oven at a temperature of 110 ^{o}C overnight and calcined10 hours at temperature of 800°C and 900 °C. After calcination, the shells were finely crushed and sifted using a sieve that passes the 200 mesh and stored in a desiccator.

2.3. Catalyst characterization

The properties catalyst derived from *anadaragranosa* shell were characterized including: analysis thermal using Thermal gravimetric and Differencial thermal analysis (TG/DTA), crystalline structure using X-ray diffraction (XRD),composition using X-ray flourescence (XRF) and functional group using Fourier transform infrared spectroscopy (FTIR).

2.4. Synthesis biodiesel

The transesterification reactions of WCO using catalyst derived from *Anadaragranosa* shell was performed in a three-necked batch reactor 500 ml equipped with a thermometer and a reflux condenser. A total of 100 g of the WCO sample was heated above the boiling point of water (temperature 105°C) for 30 minutes, then the oil cooled to a temperature of 50°C. On a separate place a mixture catalyst and methanol was refluxed for 1 hour. Samples of WCO (50°C) was then added to the mixture of catalyst and methanol and stirred for 3 h at a temperature of 60°C. After the reaction completed, the flask was dipped into cold water, and then the mixture was put into a separating funnel and allow to stand at room temperature overnight so that it will form two layers. The next day, the glycerol was removed from the separating funnel. Crude biodiesel was formed, collected and washed with warm water. Yield of biodiesel was calculated according to equation below:

$$Yield\ (\%) = \frac{Weight\ of\ Biodiesel\ produced}{Weight\ of\ WCO\ used}\ x\ 100 \tag{1}$$

3. Results and Discussion

3.1. Catalyst characterization

Thermogravimetry is a technique to measure the change in weight of a compound as a function of temperature or time. Fig. 1 shows TGA of the decomposition of $CaCO_3$ derived from *anadaragranosa* shell at atmospheric pressure 1 atm. The decomposition is started at a temperature of $\sim$600°C and completed before 800°C. When $CaCO_3$ decomposed into CaO and CO_2, the weight of shell reduced to $\sim$58%. Furthermore, the decomposition reaction is endothermic that on reaction it required heat or calorie which is shown in reducing curve of DTA in line with $CaCO_3$ decomposition. Empikul, et al. [6] characterized solid oxide catalysts derived from the industrial waste shells of egg, golden apple snail, and meretrixvenus using TGA and SDTA. They also found high
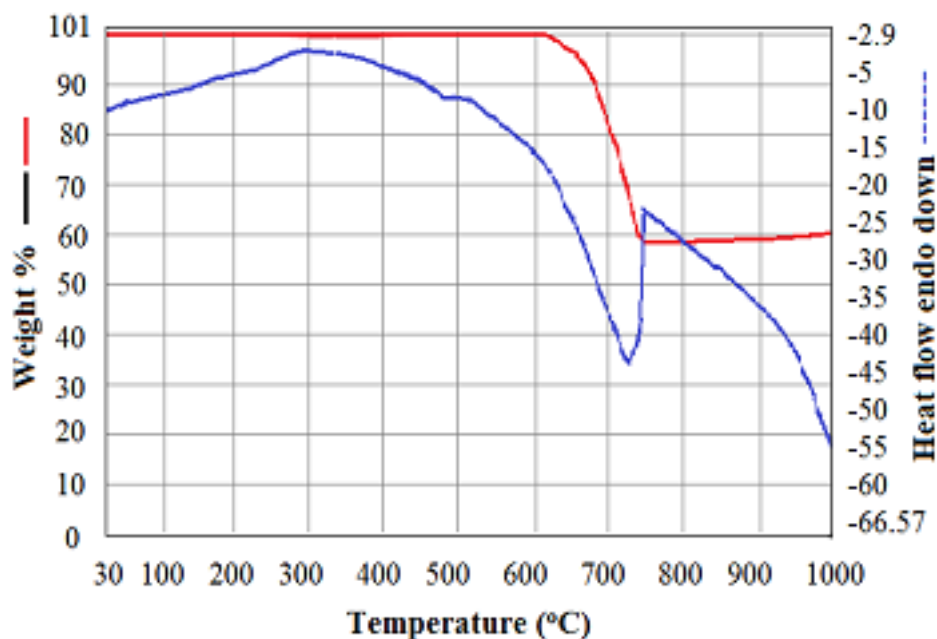
Figure 1: TG/DTA curves of *AnadaraGranosa*.

temperature range is required to transform $CaCO_3$ to CaO (above 700 ^{o}C). Nakatani et al. [9] reported that the transformation of oyster shell composed of $CaCO_3$ to CaO required the combustion temperature at 700 ^{o}C or above. From TGA curve (Fig. 1) it can be noted that the decompotion raw material (*anadaragranosa* shell) should be completed on calcination at 800°C for 10 h, however, from XRD there was still $CaCO_3$ peaks appeared (Fig. 2).

The result of XRD analysis of CaO catalyst derived from Anadaragranosa shell calcinated at 800°C and 900°C for 10 h was presented in Fig.2. It is seen from the figure that CaO was formed on calcination at 800°C and 900°C for 10 h. This is indicated by presence of diffraction peaks 2θ at 32.24^o, 37.39^o, 53.88^o, 64.18^o, 67.40^o, 79.66^o and 88.50^o. The CaO diffraction pattern is in accordance with the standards of JCPDS. Catalyst calcining at 800°C for 10 h contained mineral of *Calcite* ($CaCO_3$)at 2θ of 29.35^o and 47.12^o (Fig. 2a). This shows that the decomposition of $CaCO_3$ to CaO on calcination of *anadaragranosa* shell at 800°C for 10 h still not completed. This is because cockle shell type of *Anadaragranosa* has a very hard shell layer so it is difficult to decompose at a temperature of 800°C. On the other hand, some peaks of $Ca(OH)_2$ were also appeared at 2θ of 17.87^o, 28.55^o, 34.18^o, 47.51^o and 50.71^o. The formation of $Ca(OH)_2$ is due to the reaction between CaO with H_2O in the air. The XRD analysis of *anadaragranosa* shell calcined at 800°C and 900°C for 3 h has been reported [8]. The XRD pattern of catalyst derived from the shell calcined 800°C for 3 h still showed more $CaCO_3$ peaks compared to the XRD result of this study. Moreover, the intensity $Ca(OH)_2$ peak from the shell calcined 900°C for 3 h is much higher than that in this study.

The FTIR spectra of CaO catalyst derived from *Anadaragranosa* shell calcined 10 h at 800°C and 900°C were shown in Fig. 3. The FTIR spectra of raw and decomposed sample were obtained using KBr method at room temperature and the spectra were
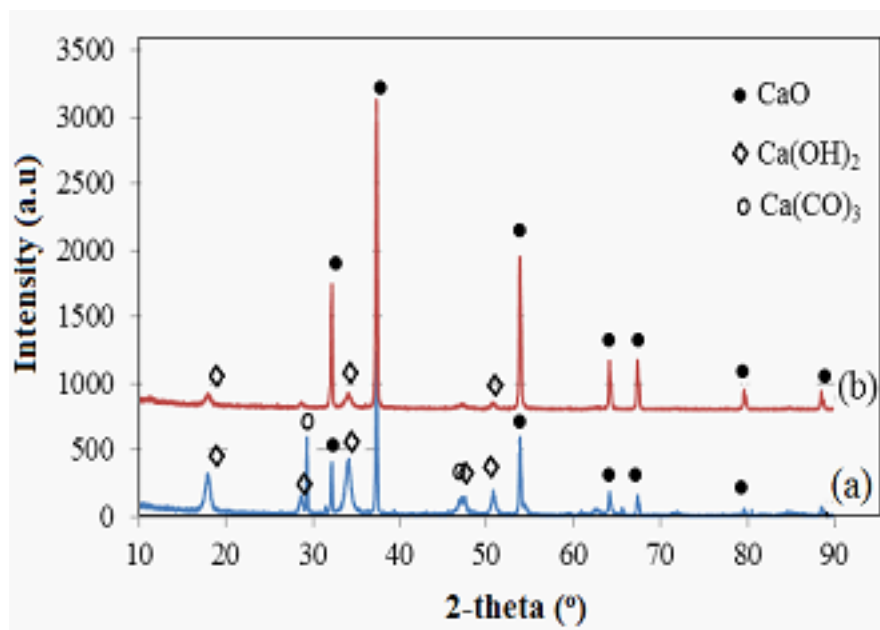
Figure 2: XRD pattern of *Anadaragranosa* shell shellcalcined 10 h (a).800°C and (b). 900°C.

Calcination temperature	Composition, weight fraction (wt.%)							
	CaO	K_2O	SrO	Cl_2O	Fe_2O_3	MnO	SO_3	SnO_2
800°C	99.14	0.29	0.25	0.13	0.02	0.02	0.12	-
900°C	99.09	0.37	0.28	0.12	0.03	0.03	-	0.02

TABLE 1: XRF analysis of *AnadaraGranosa*shell calcined 10 h at 800°C and 900°C.

recorded at 400-4000 cm^{-1}. The raw material (uncalcined) shell showed spectral FTIR bands corresponded to $CaCO_3$. The broad transmission band at approximately 3379 cm^{-1} can be attributed to OH stretching vibration from water. Sharp peaks at 2517, 1735, 1461 and 861 cm^{-1} were characteristic peaks of C-O stretching and bending modes of $CaCO_3$. Similar peaks also observed by Margaretha et al. [3] using *Pomacea* sp. shell as catalyst. Besides, the characteristic absorption of C=O between 2000 and 1500 cm^{-1} indicates the presence of calcium carbonate over the catalysts. On calcining the raw material to 800°C and 900°C for 10h all those bands disappeared. The broad band at ~1621 cm^{-1} and sharp band at 3641 cm^{-1} areassociated with OH stretching vibration mode of water physisorbed on the surface of the CaO. This is related to OH in Ca(OH)$_2$ as shown in the XRD pattern. Furthermore, broadbandsof CaO appeared at around 530 cm^{-1} (for catalyst calcined 800°C) and 500 cm^{-1} (for catalyst calcined 900°C).

The determination of chemical composition of catalyst was performed using X-ray flourescense (XRF) and the results are shown in Table 1. It can be seen from the table that the majorities composition of the catalyst was calcium oxide (CaO). The table shows the results of quantitatively characterization by XRF in which the chemical composition of calcium oxide (CaO) has the largest percentage by weight with the percentages of CaO obtained were 99.14 % and 99.09 % respectively. Besides CaO,
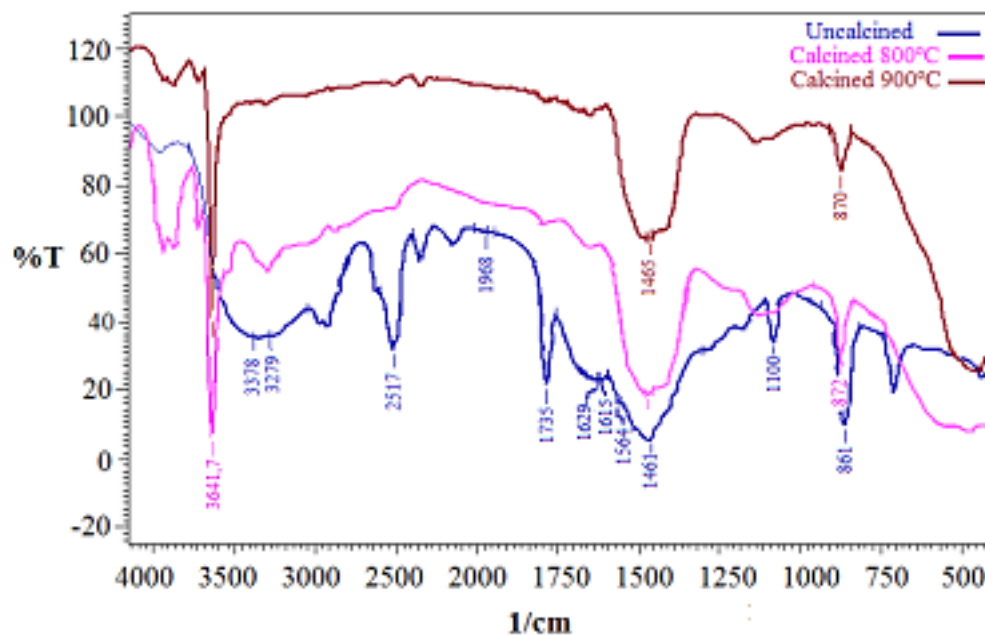
Figure 3: FTIR of *Anadaragranosa*shells:raw, calcined 10 h at 800°C and 900°C.

catalyst from this *Anadaragranosa* shells also contained small amounts of oxides such as K_2O, SrO, Cl_2O, Fe_2O_3 and MnO.

3.2. Transesterification of WCO

The catalyst used for producing biodiesel in this study was derived from blood cokle shells (*Anadaragranosa*) calcined at 800°C and 900°C for 10 hours. Transesterification was done using basic materials of waste cooking oil (WCO) and methanol. Theyield of biodiesel produced here can be seen in Figure 4. Figure 4a shows the effect of reaction time on the biodiesel yield. It can be seen from the figure that the yield of biodiesel increased with increasing reaction time. The longer the reaction time of transesterificationthen the more the opportunity of reactant molecules to collide, so the yield of biodiesel results increased. The optimum biodiesel resultwas obtained at a reaction time of 3 h, and a longer time the yield will decline. This is because in the early stages of the transesterification reaction, the biodiesel production took place rapidly and then the rate declined until it reaches equilibrium at the reaction time of 3 hours. If reaction time is too long it will result in the formation of glycerol and emulsion in the product, increasing the viscosity and affect the purity of biodiesel. Maximum yield biodiesel synthesized using the catalyst calcination at 800°C is 79.28 %. This resultis lower than the biodiesel results obtained with the use of catalyst calcination at 900°C for 10 h (82.25%). The low biodiesel obtained using catalyst calcined at 800°C is due to incomplete decomposition of $CaCO_3$ to CO_2 and CaO.

In addition to reaction time, the temperature of transesterification reaction affects the biodiesel yield. In order to get the optimum biodiesel reaction conditions it must be maintained at a temperature around the boiling point of methanol (around 64°C) [1]. In this study, transesterification process was carried out at temperature from 50°C
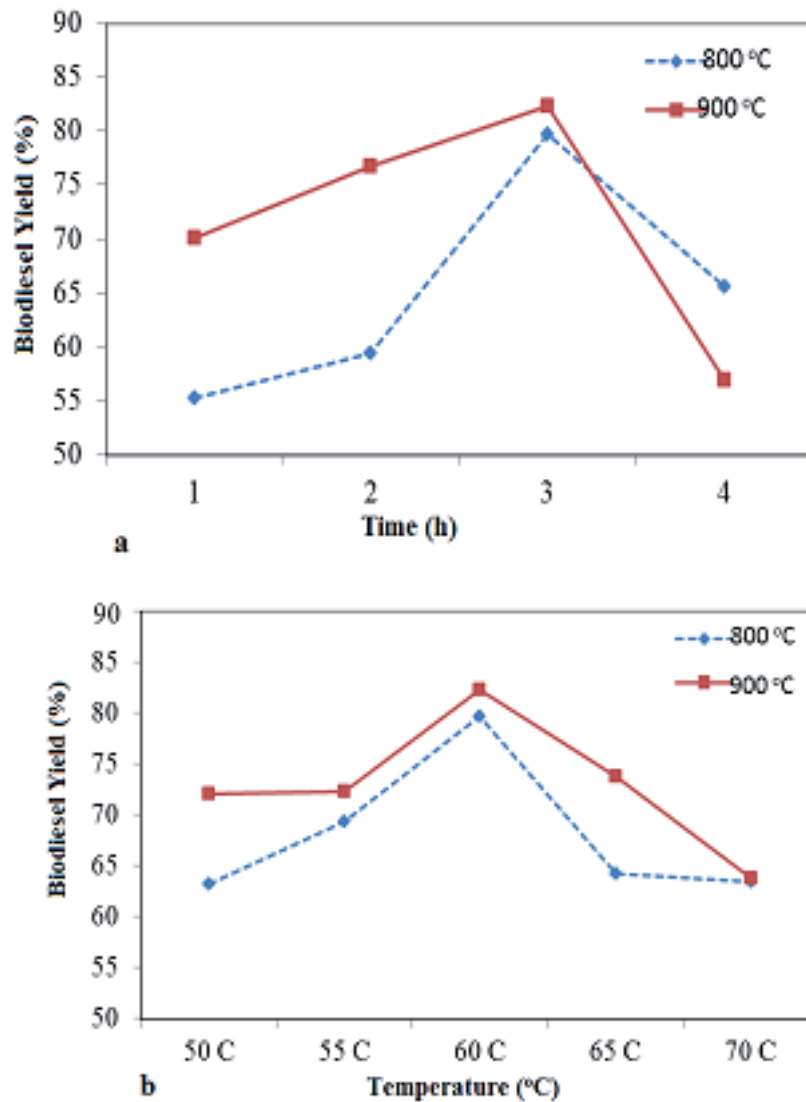
Figure 4: Biodiesel yield at different time (a) and temperature (b) reaction (weight of catalyst 3 g, molar ratio of methanol to oil 15:1).

to 70°C. The yield of biodiesel produced can be seen in Figure 4b. It can be seen that the yield of biodiesel increased as the temperature increased, and the maximum yield was at the reaction temperature of 60°C which is 82.25%. It also shows that the rise in temperature after reaching optimum condition do not lead to increase the results of biodiesel, and even became more decreased. This is because if the reaction temperature is too high it can lead to evaporate or loss of methanol and that the yield biodiesel will reduce.

4. Conclusion

Based on the results of research conducted, it can be concluded that the minimum temperature *Anadaragranosa*shell decomposited to obtain Calcium oxide was 800°C. The higher decomposition temperature used will improve the crystallinity of CaOas

shown on the XRD diffractogram. The formation of CaOwas also supported by FTIR spectra in the area around 500 cm^{-1} which indicate the presence of Ca-O vibration. It is confirmed by the XRF data showing the percentage of CaO in the samples > 99 %. The maximum biodiesel yield was 82.25% which was produced in the transesterification reaction using catalyst CaO from shell of *anadaragranosa* calcination at 900°C for 10 h, under reaction conditions of catalyst loading of 3 wt.%, methanol to oil ratio of 15:1, reaction time of 3 h and temperature of 60 ^{o}C.

5. Acknowledgements

References

[1] F. Ma and M. A. Hanna, Biodiesel production: a review, *Bioresour Technol*, **70**, 1–15, (1999).

[2] A. Macarioa, G. Giordanoa, B. Onidab, D. Cocinab, A. Tagarelli, and A. M. Giuffrèd, Biodiesel production process by homogeneous/heterogeneous catalytic system using an acid–base catalyst, *Appl Catal A Gen*, **378**, 160–168, (2010).

[3] Y. Y. Margaretha, H. S. Prastyo, A. Ayucitra, and S. Ismadji, Calcium oxide from Pomacea sp. Shell as a catalyst for biodiesel production, *Intern J. En. Environ Eng.*, **3**, 33–41, (2012).

[4] C. Samart, C. Chaiya, and P. Reubroycharoen, Biodiesel production by methanolisis of soybean oil using calcium supported on mesoporous silica catalyst, *Energy Convers Manage*, **51**, 1428–1431, (2010).

[5] M. Kouzu, S. Yamanaka, J. Hidaka, and M. Tsunomori, Heterogeneous catalysis of calcium oxide used for transesterification of soybean oil with refluxing methanol, *Appl Catal A Gen*, **355**, 94–99, (2009).

[6] N. Viriya-Empikul, P. Krasae, B. Puttasawat, B. Yoosuk, N. Chollacoop, and K. Faungnawakij, Waste shells of mollusk and egg as biodiesel production catalysts, *Bioresour Technol*, **101**, 3765–3767, (2010).

[7] A. Birla, B. Singh, S. N. Upadhyay, and Y. C. Sharma, Kinetics studies of synthesis of biodiesel from waste frying oil using a heterogeneous catalyst derived from snail shell, *Bioresour Technol*, **106**, 95–100, (2012).

[8] M. Nurhayati and W. Utami, in *Mollusk Shell Waste of Anadara Granosa as a Heterogeneous Catalyst for the Production of Biodiesel*, 36–39, Prosiding Seminar Nasional Kimia UGM Yokyakarta, W., 2013.

[9] N. Nakatani, H. Takamori, K. Takeda, and H. Sakugawa, Transesterification of soybean oil using combusted oyster shell waste as a catalyst, *Bioresour Technol*, **100**, 1510–1513, (2009).

KnE Engineering

Knowledge E
Engaging minds

Conference Paper

Charge Carriers Motion in P3HT:CappedZnO Nanoparticles Blend Films; Impact of Capping Agents

Ayi Bahtiar[1], Yayah Yuliah[1], Lusi Safriani[1], Nagisa Kawate[2], and Yukio Furukawa[2]

[1]Department of Physics, UniversitasPadjadjaran Jl. Raya Bandung-Sumedang KM. 21 Jatinangor-Sumedang Indonesia
[2]Department of Chemistry and Biochemistry, School of Advanced Science and Engineering, Waseda University, Shinjuku-ku, Tokyo 169-8555, Japan

Abstract Blend of conjugated polymer poly(3-hexylthiophene) or P3HT and Zinc Oxide nanoparticles (ZnO-NP) has been intensively used as active material for high performance hybrid solar cells. However, agglomeration of ZnO-NP hinders efficient charge carriers transfer both from P3HT to ZnO-NP and their transport within ZnO-NP which cause to low performance of solar cells. Capping of ZnO-NP is currently applied to avoid this agglomeration effect. In this study, we used three different capping agents to cap ZnO-NP, namely small semiconducting molecules squaraine, 2-naphthalene and insulating polymer polyvinylpyrrolidone. We conducted temperature dependence of photoinduced infrared absorption spectroscopy to study charge carriersmotion in the P3HT:cappedZnO nanoparticles blend films. The measurement was carried out with light irradiation of 532 nm and temperature ranging from 78 to 300 K. The spectra were analyzed by a bimolecular carrier recombination method with Arrhenius activation energy. Two parallel charge carrier recombination processes are observed, namely polarons recombination along polymer chain (intra-chain) and inter-chain polarons recombination in the P3HT-chains. At low temperatures, polarons recombine along polymer chains (intra-chain) with activation energy between 19-23 eV for all samples. However, the inter-chain polaron motion is influenced by capping agents as shown by a variation in its activation energy ranging from 28 to 58 eV.

Keywords: Hybrid solar cells, ZnO nanoparticles, Capping Agents, Charge Carriers Motion

 OPEN ACCESS

1. Introduction

Hybrid conjugated polymers inorganic nanocrystals solar cells have been intensively studied in the past decades due to their potential for low-cost and high performance renewable energy devices. The combination of flexibility and relative easy to control the optoelectronic properties of conjugated polymers and metal oxide nanocrystals, high performance of hybrid solar cells is expected to be realized. Although, many attempts have been carried out, the power conversion efficiency (PCE) of hybrid solar cells is still in the range of 3-4% [1-2], which is far below the PCE of fully organic solar

How to cite this article: Ayi Bahtiar, Yayah Yuliah, Lusi Safriani, Nagisa Kawate, and Yukio Furukawa, "Charge Carriers Motion in P3HT:CappedZnO Nanoparticles Blend Films; Impact of Capping Agents," *KnE Engineering*, vol. 2016, 8 pages. DOI 10.18502/keg.v1i1.495

Page 1

cells which has already reached 11% [3]. Three main issues are identified as the cause of low PCE of hybrid solar cells, i.e. the agglomeration of nanocrystals, the difficulty to control the morphology of the blend conjugated polymers-inorganic nanocrystals and the lack of understanding of charge carrier motion in the active layer of hybrid solar cells.

Conjugated polymer poly(3-hexylthiophene) or P3HT has been frequently used as a model material for donor material of polymer and hybrid solar cells due to its superior optoelectronic properties such as high absorption coefficient, high hole mobility and easy to be formed in thin films by use of low cost and simple methods. Meanwhile, metal oxide nanoparticles, in particular zinc oxide nanoparticles (ZnO-NP) has been widely developed as donor material for hybrid solar cells due to its superior optoelectronic properties and its relatively easy to be synthesized by using solution methods. However, the agglomeration of ZnO-NP causes ineffective charge transfer of exciton from P3HT and electron transport within ZnO-NP and to the electrode leads to the low PCE of hybrid P3HT:ZnO-NP solar cell. ZnO-NP is therefore must be capped to avoid the agglomeration. Small moleculesare commonly used as capping agents to avoid the agglomeration of metal oxides nanoparticles [4,5].

In this paper, we report our study on charge carriers motion in active layer of hybrid solar cell based on blend of P3HT:ZnO-NP uncapped and capped with three different materials. We used small semiconducting moleculessquaraine (SQ) and 2-naphthalene (2-NT) and insulating polymers polyvinylpyrrolidone (PVP) as capping agents to avoid agglomeration of ZnO nanoparticles. Photoinduced infrared absorption (PIA) spectroscopy is used to study charge carrier motion in the blend films of P3HT:capped ZnO-NP. PIA enables us to observe the positive charge carrier or positive polaron motion in the film to clarify the charge recombination process that affect the PCE of solar cells [6]. In this study, we report temperature dependence of PIA spectra of blend P3HT:capped ZnO-NP films to obtain the activation energies of the recombination process of positive and negative carriers in the films and to clarify the effect of capping agents on the charge carrier transport in the hybrid P3HT:ZnO-NP films.

2. Experimental Method

ZnO-NP was synthesized by use of sol gel method as described in our previous work [7]. The ZnO-NP and PVP are dissolved in methanol, whereas the P3HT, SQ, 2-NT were dissolved in chlorobenzene (CB). The optical absorption of each solution and their blend were measured by use of T70+UV-Vis spectrometer. The particle size of ZnO-NP ismeasured by Transmission Electron Microscopy (TEM JEOL JEM 1400). Blend thin films of P3HT:capped ZnO-NP were prepared by use of spin coating technique on BaF$_2$ substrates. For each sample, 33 mg of P3HT was dissolved in 1 ml CB and 15 mg of ZnO-NP were dissolved in 1 ml mixed solvents containing 95% CB and 5% methanol. Both solutions were ultrasonicated for 15 minutes. Small amount of capping agent solution was added to the ZnO solution prior to ultrasonication process. After both solutions were well mixed forming homogeneous solution, the P3HT solution was poured into ZnO solution and the ultrasonicated again for 15 minutes to form well
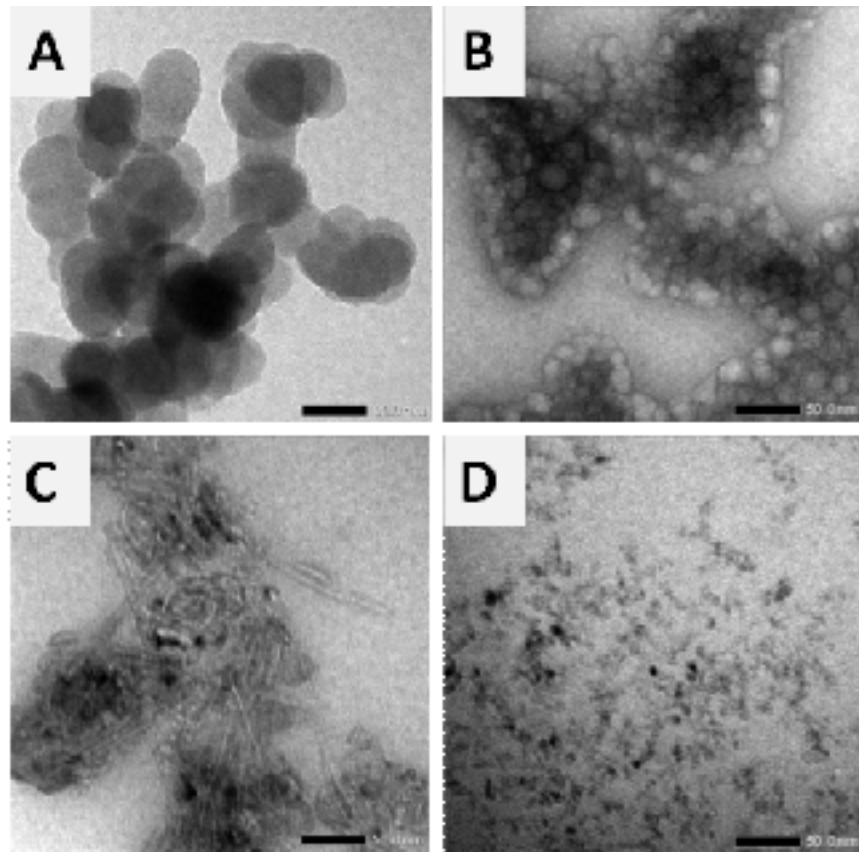
Figure 1: TEM images of (a).ZnO-NP, (b).SQ-capped ZnO-NP, (c). 2-NT-capped ZnO-NP and (d).PVP-capped ZnO-NP. The scale bar is 50 nm.

mixed P3HT:cappedZnO-NP solution. All films were thermally annealed at 150∘C for 60 minuted.

PIA spectra were measured on an FTIR spectrometer (FTS-7000, Varian) equipped with an MCT detector by using the different spectrum method [6]. Thin film of P3HT:capped ZnO nanoparticles put in the cold head of a cryostat (Oxford Instruments DN1754) under vacuum. The film was irradiated with 532-nm continouous-wave laser. The PIA spectra were measured the temperature range from 78 to 300 K by using acontroller (Oxford Instruments ITC502S).

3. Results and Discussion

Fig. 1 shows TEM images of highly diluted ZnO-NP in methanol and ZnO-NP capped by SQ, 2-NT molecules and PVP polymer. The concentration of pristine and capped ZnO-NPs can not precisely determined. We diluted them until UV-Vis optical absorbance less than of the solutions is reached. The average diameter of ZnO-NP is 40 nm. Capping by SQ and 2-NT can clearly cover the surface of ZnO-NP as shown with bright images in Fig. 1(b) and (c). However, the effect of capping ZnO-NP by PVP polymer was unclear which might be caused by too large size of PVP. These results show that capping process by small molecules was successfully carried out.
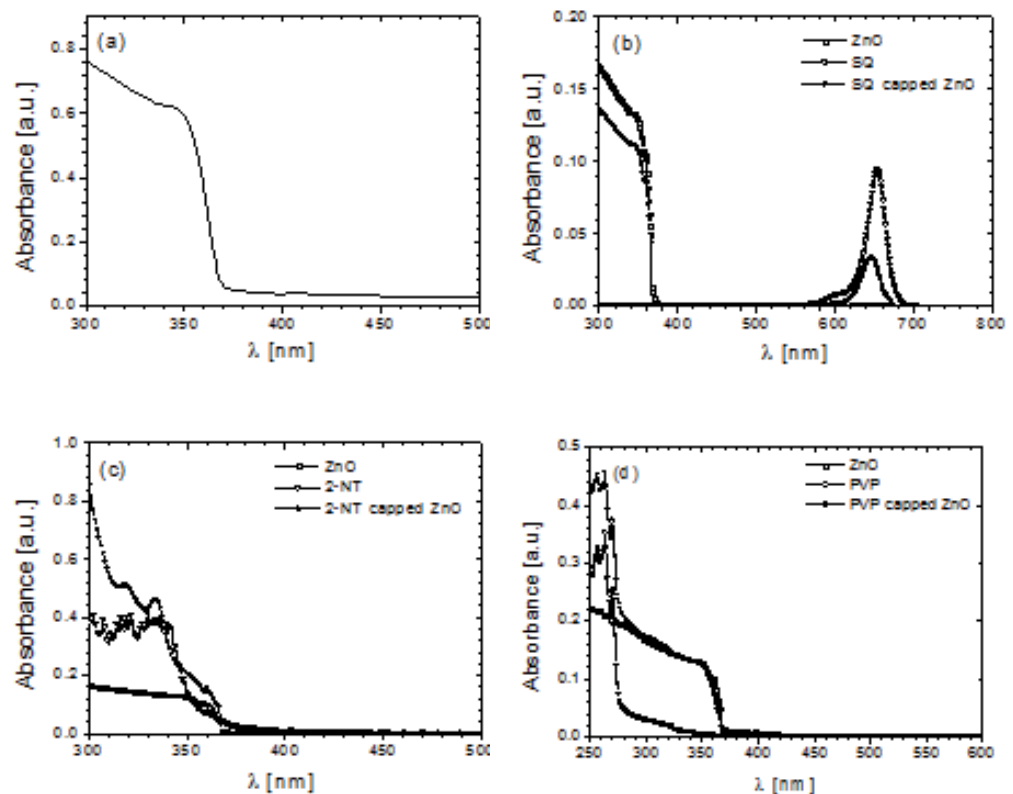
Figure 2: Absorbance spectra of (a).ZnO-NP in methanol, (b).ZnO-NP, SQ and SQcapped ZnO-NP, (c). ZnO-NP, 2-NT and 2-NTcapped ZnO-NP, (d). ZnO-NPs, PVP and PVPcapped ZnO-NP.

The optical absorbance of highly diluted solution of ZnO-NP, capping agents and ZnO capped by SQ, 2-NT and PVP are displayed in Figure 2(a)-(d). The ZnO-NP has absorption at wavelength below than 370 nm. The calculated optical bandgap of ZnO nanoparticle is 3.38 eV which is higher than that of its bulk (3.37 eV). It indicates that the synthesized ZnO forms nanoparticles as confirmed by TEM image of ZnO-NP with average diameter of 40 nm. Absorption spectra of capped ZnO nanoparticles clearly consist of the optical absorption of capping agent and ZnO-NP. This shows that capping agents can cover the ZnO nanoparticles as also confirm by TEM image displayed in Fig. 1(b) and (c). However, the effect of PVP capping on ZnO-NP can not be observed in TEM image as displayed in Fig. 1(d).

PIA spectra of blend films P3HT:ZnO-NP and P3HT:capped ZnO-NP measured at 77 K are displayed in Fig. 3. The observed spectra exhibit complicated features which are attributed to the interaction between an electronic transition and vibrational transitions of photogenerated carriers.The band at 1256 cm^{-1} is well-known assigned due to positive polaron contribution [8]. The difference absorbance ($\square$A) at 1240 cm^{-1} and 1450 cm^{-1} was used as the intensity of the polaron absorption was applied to determine the activation energy of charge carriers recombination process.
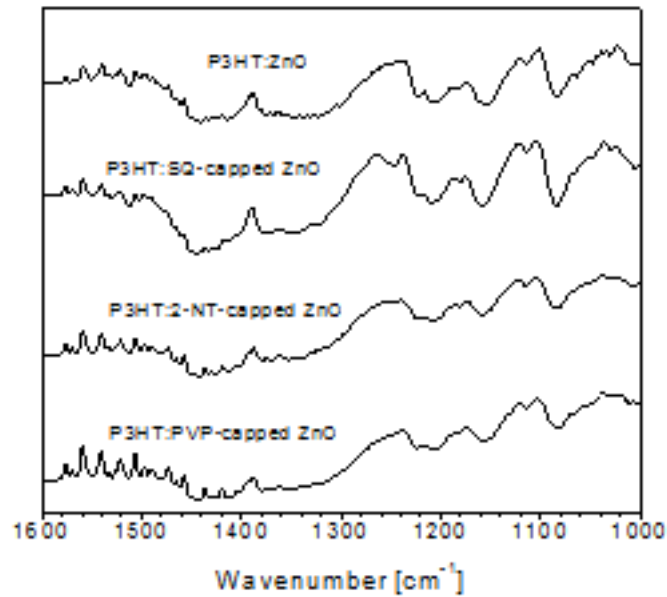
Figure 3: PIA spectra of P3HT:ZnO-NP and P3HT:capped ZnO-NP at 77 K.

The recombination dynamics of photogeneratedcarriers can be simply expressed by [6]:

$$\frac{d[P]}{dt} = \phi F - k_r[P][N] \tag{1}$$

where F is the rate of the formation of the excited states in P3HT:ZnO-NP film; ϕ is the effective efficiency of charge separation; [P] and [N] are the concentrations of positive carriers (positive polaron) and negative carriers (the anion), respectively and k_r is the carrier recombination rate. By assuming that the number of positive and negative carriers is equal, the absorbance due to positive polaron can be defined by$\Delta A = \sigma[P]$, where □ is the absorption cross-section of the band. By assuming that recombination rate can be expressed by the Arrhenius-type activation energy:

$$k_r = C \exp\left(-\frac{\Delta E}{k_B T}\right) \tag{2}$$

where k_B is Boltzmann's constant and T is temperature. The relation between difference absorption and activation energy (□E) caused by carriers recombination is:

$$\ln\frac{1}{(\Delta A)^2} = -\left(\frac{\Delta E}{k_B T}\right) + \ln\frac{C}{\phi F \sigma^2 l^2} \tag{3}$$

where l is the thickness of the film.

The plots of ln (1/□A^2) versus 1/T plots (Arrhenius plot) of films are displayed in Fig. 4. The data can be considered as two straight lines ranging from low temperature of 78 to 120 K and high temperature of 140 to 300 K. A deflection point is observed at around 130 K. These data shows the existence of two parallel recombination processes of positive and negative carriers.
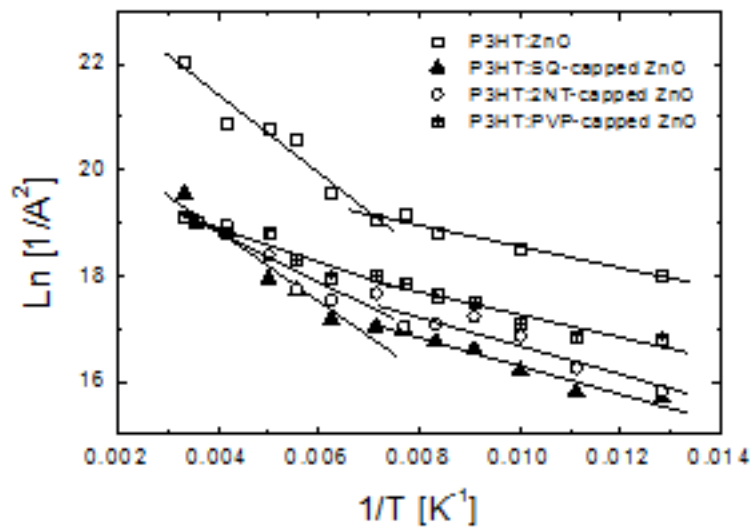
Figure 4: Plot of ln (1/$\square$A^2) versus 1/T of all films. The lines were determined by least squares method.

The activation energies at low and high temperatures for all films are listed in Table 1. For P3HT:ZnO-NP uncapped film, the activation energy $\square$E at low temperatures (78-120 K) is 17 meV, while at high temperature (140-300 K) is 64 meV. The different value of activation energy can be explained by the existence of two types of positive polaronmotion in the film. The low activation energy is attributed to polaron motion along polymer chain, whereas the higher activation energy to polaron motion from one chain to another polymer chains or inter-chain motion [9]. The polaron motion from one P3HT-chain to another P3HT chains is natural properties of charge carriers mobility in the polymer that strongly depend on temperature. Thus the intra- and inter-chainpolaron motion correlates strongly with performance of a solar cell.

The activation energies at low temperature of all samples are almost equal around 20 meV. This indicates that the energy required for positive polaron moves along P3HT chain is not influenced by capping agents. Similar value is also obtained from films of P3HT:PCBM and P3HT:10%ZnO-NP:PCBM as reported in our previous work [7]. A significant change of $\square$E is observed at high temperature. The inter-chain polaron motion is strongly affected by capping agents. The activation energy is decreased from 57 to 40 and 28 meV when the ZnO nanoparticles are capped by small molecules squaraine (SQ), 2-napthalene (2-NT) and polymer PVP, respectively, which might be related to the molecular size of the capping agents. The molecular size is increased from SQ to 2-NT and PVP, thus larger molecular size of capping agents facilitate positive polaroneasier to move from one P3HT-chain to another P3HT-chain (interchain). Based on the value of activation energy at high temperatures, the PVP-capped ZnO-NP can expected to improve the perfomance of hybrid P3HT:ZnO-NP solar cells due to the easy of polaron to move to another P3HT-chain and can reach the anode and finally produce electricity.

Sample	ΔE at low T (meV)	ΔE at high T (meV)
P3HT:ZnO-NP	17±2	64±2
P3HT:SQcapped ZnO-NP	23±5	57±6
P3HT:2NTcapped ZnO-NP	23±6	40±13
P3HT:PVPcapped ZnO-NP	19±3	28±17

TABLE 1: Activation energy ΔE determined from PIA measurement.

4. Conclusions

The photogenerated charge carriers motion in the blend films of P3HT:ZnO-NP and P3HT:capped ZnO-NP were investigated by use of PIA spectroscopy at various temperature from 78 to 300K. The activation energy that obtained from PIA measurement at low temperatures and high temperatures are related to the positive carrier motion along P3HT chain or intra-chain and inter-chain, respectively. The intra-chain polaron motion is not influenced by the capping agents, while the inter-chain motion strongly depends on capping agents due to the difference of their molecular size.

5. Acknowledgement

References

[1] S. S. Li and C. W. Chen, Polymer-metal-oxide hybrid solar cells, *J Mater Chem A Mater Energy Sustain*, **1**, 10574–10591, (2013).

[2] Y. S. Jung, J. S. Yeo, B. K. Yu, and D. Y. Kim, Spontaneous phase separation of a zinc oxide interfacial layer in bulk heterojunction organic photovoltaics, *Sol Energy Mater Sol Cells*, **134**, 291–297, (2015).

[3] J. You, L. Dou, K. Yoshimura, T. Kato, K. Ohya, T. Moriarty, K. Emery, C. C. Chen, J. Gao, G. Li, and Y. Yang, A polymer tandem solar cell with 10.6efficiency, *Nat Commun*, **4**, 1446–1455, (2013).

[4] P. Ruankham, L. Macaraig, T. Sagawa, H. Nakazumi, and S. Yoshikawa, Surface modification of ZnO nanorods with small organic molecular dyes for polymer-inorganic hybrid solar cells, *J Phys Chem C*, **115**, 23809–23816, (2011).

[5] E. Rezasoltani, M. Wang, I. G. Hill, and C. Silva, The influence of molecular interface modification on the charge dynamics of polymeric semiconductor:ZnO heterostructure, *J Appl Phys*, **116**, 074502-1–, 074502–074507, (2014).

[6] Y. Furukawa, K. Seto, K. Nakajima, Y. Itoh, J. Eguchi, T. Sugiyama, and H. Fujimura, Infrared and Raman spectroscopy of organic thin films used for electronic devices, *Vib Spectrosc*, **60**, 5–9, (2013).

[7] L. Safriani, A. Aprilia, A. Bahtiar, M. Risdiana, M. Kartawidjaja, T. Apriani, K. Kanazawa, and Y. Furukawa, Preparation of ZnO nanoparticles for blend of P3HT:ZnO nanoparticles: PCBM thin film and its charge carrier dynamics, *AIP Conf Proc*, **1554**, 101–104, (2013).

[8] Y. Furukawa, Vibrational spectroscopy of conducting polymers: Fundamentals and Applications, in *Vibrational Spectroscopy of Polymers: Principles and Practice*, N. J. Everall, J. M. Chalmers, and P. R. Griffiths, Eds., 537–556, John Wiley and Sons, New York, 2007.

[9] A. Bahtiar, Hybrid solar cells of conjugated polymers metal-oxide nanocrystals blends; state of the art and future research challenges in Indonesia, *AIP Conf Proc*, **1554**, 12–19, (2013).

Conference Paper

Substitution of Local TiO_2 on the Synthesis of $Li_4Ti_5O_{12}$(LTO) for Anodes Lithium Ion batteries

Slamet Priyono[1], Arin Gudesma[2], Ramlan[2], and Bambang Prihandoko[1]

[1]Research Center for Physics-Indonesia Institute of Sciences, KomplekPuspiptekGd 442 Serpong, Tangerang Selatan, Banten, 15314, Indonesia
[2]FMIPA, Sriwijaya University, Jl. Palembang-Prabumulih Km. 32 KabupatenOgahIlir, Sumatera Selatan, Indonesia

Abstract Substitution of local TiO_2 on the synthesis of $Li_4Ti_5O_{12}$ for anodes lithium ion battery with solid state reaction method had been done. This study aimed to substitute raw materials TiO_2 and determine the length of sintering time. Synthesis was done by mixing the raw materials like local TiO_2 and $LiOH.H_2O$ in a stoichiometric then milled for 15 hours followed by calcination at a temperature of 600°C with sintering time of 2 hours for each samples. Sintering was done by varying the length of sintering time i.e. 4, 6 and 8 hours at a temperature of 850 °C. In this study the effect of sintering time on the material characteristics and performance of battery cells studied in detail. The characterization was conducted by the XRD to determine the structure and the LTO phases, SEM/EDX test to determine the morphology, surface topography and composition of all samples. PSA testwas performed to determine the particle size while battery cell performance was tests with automatic charge-discharge battery cycler. From characterization found that the maximum length of time that is resistant to sintering samples 6 hours. The resulting active material has an LTO phase with spinel crystal structure simple cubic, but not produced a single phase, there are some impurity phases. The results of SEM/EDX provides irregular morphology, have pores, many impurities and varying sizes. Charge-discharge measurement showed that optimum sintering was got at 6 h which gave specific capacity about 50 mAh/g.

Keywords: Local TiO_2, Sintering, $Li_4Ti_5O_{12}$, Anode, Lithium Ion Battery

🔓 **OPEN ACCESS**

1. Introduction

Lithium ion battery has advantage in high energy and power density, this advantage make battery technology is suitable for portable electronics, power tools, and hybrid/full electric vehicle [1]. If electric vehicles (EVs) replace the majority of gasoline powered transportation, Li-ion batteries will significantly reduce greenhouse gas emission [2]. Beside these, Lithium ion battery has certain fundamental advantages rather than other chemistries such as lead acid and Ni-cd batteries. Firstly, Li has the lowest reduction potential of any element; its allowing Li based batteries to have the highest possible cell potential. Also, Li is the third lightest element and has one of the smallest ionic radii of any single charged ion. These factors allow Li-based batteries to have high gravimetric and volumetric capacity and high power density [3].

How to cite this article: Slamet Priyono, Arin Gudesma, Ramlan, and Bambang Prihandoko, "Substitution of Local TiO_2 on the Synthesis of $Li_4Ti_5O_{12}$(LTO) for Anodes Lithium Ion batteries," *KnE Engineering*, vol. 2016, 6 pages. DOI 10.18502/keg.v1i1.496

Page 1

For some practical applications like hybrid electric vehicles (HEV) or electric vehicles (EV), lithium ion batteries have to be re-charged very fast, and therefore the relevant electrode materials have to work at high rates, while maintaining the excellent capacity and cycling stability [4,5]. $Li_4Ti_5O_{12}$ (LTO) is found to be a promising material for negative electrodes in lithium-ion batteries because it have good structural stability, considered to be extremely safe, low cost, and zero strain material (negligible volume change during charge/discharge) and the theoretical capacity is 175 mAh/g. LTO can be synthesized by various techniques such as solid state reaction, sol-gel, microwave, combustion, hydrothermal methods, etc. The main disadvantages of LTO are that it have a poor rate capability and low electronic conductivity [6].

Generally, LTO synthesized with TiO_2(technical) as Ti sources and $LiOH.H_2O$ (technical, Germany) as Li sources whichall raw materials are imported from overseas. In this research, LTO was made from local TiO_2 and $LiOH.H_2O$ using solid state reaction with varying sintering time. Local TiO2 was extracted from ilmenite by certain process. The use of local TiO_2 to subtitute TiO_2 (technical) will affect the synthesis process of LTO especially at sintering time. Therefore this research will be focused on determining long time sintering and to know the influence on the characteristics both materials and electrochemical properties of LTO.

2. Experiment

LTO was prepared by using the solid-state reaction method from stoichiometric mixture of raw materials. The starting materials were lithium hydroxyl hydrate ($LiOH.H_2O$, Germany) and titanium dioxide (TiO_2, local product, 97%). All materials were ball milled by planetary ball mill for 15 h. The precursor was calcined at 600°C for 2 h and then sintered at 850°C for 4, 6, and 8 h to get optimum sintering time. All heat treatment was done under atmosphere with heating rate of 3°C/min. The synthesized materials were characterized by using the conventional x-ray diffractometer (XRD, Rigaku) and scanning electron microscope (SEM, Hitachi) and particle size analyzer (PSA, Cilas 1190).

The electrochemical characteristics were evaluated by means half test. The sample slurry was prepared by mixing active material powders (LTO) with binder (PVDF) and conductive carbon (acetylene black) at a weight ratio of 85:10:5 in N-N dimethylacetamide (DMAC). Subsequently, the slurry was coated on a copper foil using the doctor blade technique and dried at 80°C for 1 h to evaporate DMAC solvent. The electrode foil was cut to 14 mm diameter discs, which were used to assemble the coin cell in glove box. Li metal foil was used as the counter electrode and reference electrode in the cell. LiPF6 was used as electrolyte.Charge discharge test was done by automatic battery cycler WBCS3000 to get capacity materials.
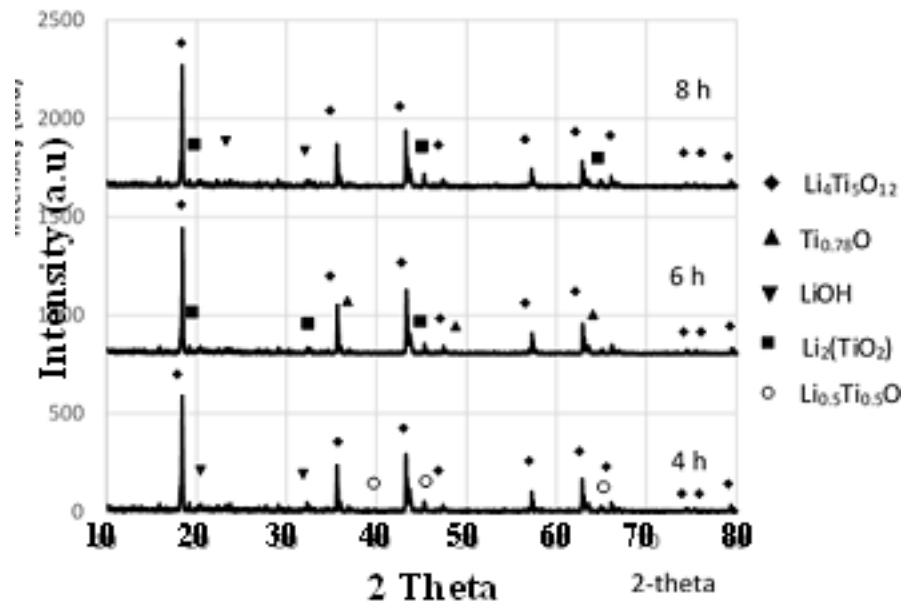
Figure 1: XRD spectra of $Li_4Ti_5O_{12}$ which synthesized with different sintering time (a) 4 h, (b) 6 h, and (c) 8 h.

Sintering time	Lattice constant (A^3)	Unit cell Volume (A^3)	Calculated density $(g.cm^{-3})$
4 h	8.3564	583.51	3.484
6 h	8.3542	583.06	3.568
8 h	8.3586	583.98	3.553

TABLE 1: Lattice information of LTO ($Li_4Ti_5O_{12}$).

3. Result and Discussion

Fig 1 shows the spectra of XRD diffraction pattern with different sintering times. The main phase, LTO ($Li_4Ti_5O_{12}$), denoted by diamond sign. Fig 1.a where the sample sintered for 4 h showed that LTO phase is formed by chemical formula ($Li_4Ti_5O_{12}$), and the small other phases like $Li_{0.5}Ti_{0.5}O$ and LiOH phases which denoted by circle and inverted triangle respectively. The presence of LiOH phase indicated that sintering time is not enough for chemical reaction betwen $LiOH.H_2O$ and localTiO_2. Fig 1.b where the sample sintered for 6 h shows LTO ($Li_4Ti_5O_{12}$) phase and still appear impurity phases like $Li_2(TiO_3)$ and $Ti_{0.78}O$. Altought it still contains impurity phase but this sample has no LiOH phase. It indicated that 6 h sintering time is enough for this proces. While in the sintering time for 8 h, LTO is formed but it containedLiOH again. So,the optimum sintering time for synthesis of LTO using local raw material TiO_2 is 6 hours at a temperature of 850 ° C. The number of phase obtained in XRD analyze due to so many elements impurities contained in TiO_2 local as raw materials.

Basically sintering process is densification or solidification process of compound that formed in calcination process. Longer time for sinteringmakesmaterial denserandmore solid. In atomic scale, density of material is not only affected by mass but also lattice
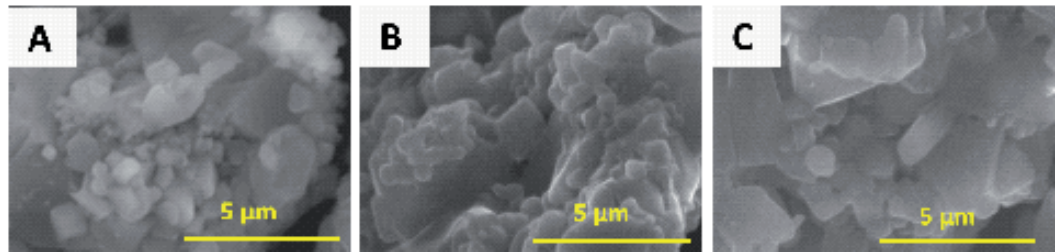
Figure 2: SEM images of $Li_4Ti_5O_{12}$ powders which synthesized with different sintering time (a) 4 h, (b) 6 h, and (c) 8 h.

constant, becausedensity also determined by unit cell volume. Table 1 shows sintering time make material denser especially in 6 h sintering time than others sample.Samples which sintering time for 4 and 8 h have lower density than 6 h because they contain LiOH phase which have ligher mass.

Fig. 2 shows SEM images with a magnification of 10 K SE of $Li_4Ti_5O_{12}$ powders which synthesized with different sintering time (a) 4 h, (b) 6 h, and (c) 8 h. SEM analyze was done to know the effect of varying sintering time on morphology of material surface. It is apparent that all powders have similar morphologies. All samples have polyhedral shape, smooth texture, no porous and agglomeration. The particles that were synthesized at 6 h looked bigger than 4 h and the particles that were synthesized at 8 h bigger than 6 h due to grain growth at long sintering time. Normaly, sintering process will increases the rate of grain growth and indirectly reduce porosity and make material denser. But, this result is not shown like that because impurity phases contained in materials.

Particle size is one importance factor which affect electrochemical properties of electrode material because the small and uniform particle was good for contact between active materials and electrolyte[7].The resulting powder particle size of the old sinter 4, 6, and 8 hours are 46.66μm, 52.05μm and 52.67 μm, respectively. Increased long sintering causes the particle size increased due to the grain growth duringhigh temperature diffusion and a longer length of time. In the process of grain growth occur crystal growth aggregate grain size increases. Long sintering influence both the level crystalline a material and diameter of the particle size.

Fig. 3 shows the charging-discharging profile of synthesized $Li_4Ti_5O_{12}$ (a) 4 h, (b) 6 h and (c) 8 h with 0.1 C-rate for coin cell against Li metal. The cell was charged to 3.0 V and discharged to 0 V vs. Li/Li+. According the charge-discharge graphs, the sample which has lowest capacity is sample 4 h. Its sample has capacity about 45 mAh/g. While the 6 h and 8 h samples have capacity about 52 mAh/g. All capacities are very low compared by theoretical values about 175 mAh/g because synthesized $Li_4Ti_5O_{12}$ have many impurities and big particle size (50 um). The data indicated that charge/dischrge characteristics for all battery samples are about same. Thus, the sintering time does not significantly affect the performance of battery. In charge-discharge curve, all graphs seem as staircase curves. These graph have two working potential at 1.5 V and 1.6 V. It means that all samples have two dominant phases. Potential at 1.55 V correspond with $Li_4Ti_5O_{12}$ phase while potential at 1.65 V correspond with Li_2TiO_3 phase. Others phases

(a)

(b)

(c)
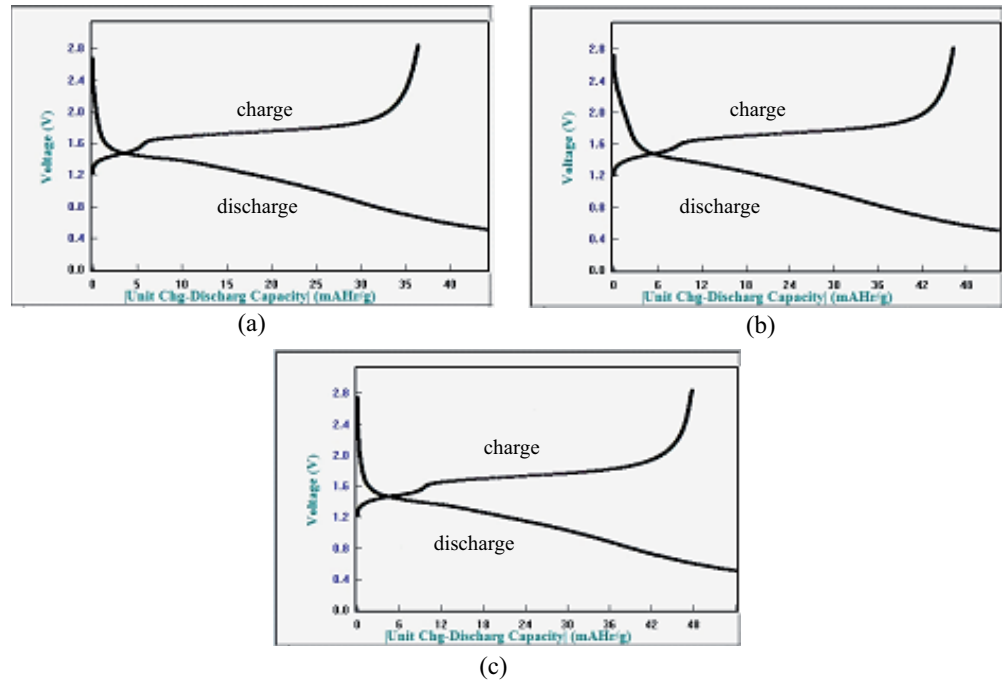
Figure 3: Charge/discharge characteristics of synthesized $Li_4Ti_5O_{12}$ (a) 4 h, (b) 6 h and (c) 8 h.

like LiOH, $Ti_{0.78}O$ and $Li_{0.5}Ti_{0.5}O$ are not appearing in CD curves because of very little. Charging potential of $Li_4Ti_5O_{12}$ is longer than charging potential of Li_2TiO_3, it means that $Li_4Ti_5O_{12}$ more dominant than Li_2TiO_3 phase.

4. Conclusion

Substitution of local TiO_2 on the synthesis of LTO has been successfully done by solid state process at 6 h sintering process. Synthesized LTO still have other phases like Li_2TiO_3, LiOH, and $Ti_{0.78}O$ that caused from element impurities from local TiO_2. All samples have polyhedral shape, smooth texture, no porous and agglomeration. Increasing sintering time cause the particle size increase due to the grain growth during high temperature diffusion. The biggest material was 52.67 μm that sintered at 850°C for 8 h. In charge-discharge curve, all graphs seem as staircase curves because of presence two dominant phase such as $Li_4Ti_5O_{12}$ and Li_2TiO_3. The best capacity is 52mAh/g obtained by sintering for 6 h. The specific capacity is very determined by impurity contain, phases and particle size.

References

[1] H. Li, Z. Wang, L. Chen, and X. Huang, Research on Advanced Materials for Li-ion Batteries, *Adv Mater*, **21**, 4593–4607, (2009).

[2] H. Zhang, Y. Chen, J. Li, C. He, and Y. Chen, Li4Ti5O12/CNTs composite anode material for large capacity and high-rate lithium ion batteries, *Int J Hydrogen Energy*, **39**, 16096–16102, (2014).

[3] N. Nitta, F. Wu, J. T. Lee, and G. Yushin, Li-ion battery materials: present and future, *Mater Today*, **18**, 252–264, (2015).

[4] X. Chen, X. Guan, L. Li, and G. Li, Defective mesoporous $Li_4Ti_5O_{12}$-y: an advanced anode material with anomalous capacity and cycling stability at a high rate of 20 C, *J Power Sources*, **210**, 297–302, (2012).

[5] C. C. Yang, H.-J. Hwu, S. J. Lin, W.-C. Chien, and J.-Y. Shih, Preparation of High-rate performance $Li_4Ti_5O_{12}$/C Anode Material in $Li_4Ti_5O_{12}$/$LiFe_{0.5}Mn_{0.5}PO_4$ Batteries, *Electrochim Acta*, **125**, 637–645, (2014).

[6] V. D. Nitya, R. K. Selvan, K. Vediappan, S. Sharmila, and C. W. Lee, Molten salt synthesis and characterization of $Li_4Ti_{5-x}Mn_xO_{12}$ (x=0.0, 0.05 and 0.1) as anodes for Li-ion batteries, *Appl Surf Sci*, **261**, 515–519, (2012).

[7] F. Gu and G. Chen, Carbon coating with Oleic Acid on $Li_4Ti_5O_{12}$, *Int J Electrochem Sci*, **7**, 6168–6179, (2012).

KnE Engineering

Knowledge E
Engaging minds

Conference Paper

Meso Carbon Micro Bead (MCMB) Based Graphitized Carbon for Negative Electrode in Lithium Ion Battery

Fadli Rohman[1], Kartika Sari[2], Achmad Subhan[1], and Bambang Prihandoko[1]

[1]Research center for Physics - LIPI, Kawasan PUSPIPTEK SerpongTangerang Selatan
[2]North Sumatera University, Jl. Bioteknologi No.1, Medan

Abstract Lithium ion battery performance of graphitized Meso Carbon Micro Beads (MCMB) as an anode material was investigated in full cell battery system containing $LiCoO_2$ cathode, PE separator and $LiPF_6$ electrolyte. The commercial MCMB, which was fabricated by $Linyi^{TM}$, was sintered at 500°C for five hour to make graphitized MCMB. The microstructure of graphitized MCMB was characterized using XRD and SEM to show the crystalinity, crystal phase and morphology of the MCMB particle. The result indicated that the crystal phase of the sample was changed into graphitized carbon .The electrode was made using coating method. We used copper foil as the substrate for anode. The anode materials consist of graphitized MCMB (active material), Polyvinylidene fluoride/PVDF (binder) and acetylene black (additive material). Full cell battery was tested using charge-discharge and cyclic voltammetry (CV) methods. From the CV characterization, cyclic voltammograms of the cell show characteristic lithium intercalation through reduction-oxidation peak. Charge-discharge test showed the discharge and charge capacity of the cells. According charge discharge test, commercial MCMB was better that graphitized MCMB.

Keywords: Graphitized carbon, MCMB, anode material, lithium ion battery

🔓 **OPEN ACCESS**

1. Introduction

Lithium ion battery has been widely used as energy storage system for applications such as in the field of portable electronic, e.g. in mobile phone, notebook computer, gadget, camera [1] and also for electric vehicles and hybrid electric vehicles [2]. There are many parameters that should be optimized, including the energy density, safety, rate capability, cost, sustainability [2] and cycle life [3] to get better performance of the Li-ion batteries.

Carbon-based anode has been widely used as anode for commercial batteries such as mesocarbonmicrobead, artificial and natural graphite, carbon fiber or C-C composites material [4], carbon nanotube, and also graphene [5]. Natural graphite was the most promising material for lithium-ion battery because of its low cost and flat potential profile, high columbic efficiency in proper electrolytes and relatively high reversible capacity. Synthetic graphite has many properties that are the same as those of natural graphite. Besides that, it has many unique merits such as high purity, variety of

How to cite this article: Fadli Rohman, Kartika Sari, Achmad Subhan, and Bambang Prihandoko, "Meso Carbon Micro Bead (MCMB) Based Graphitized Carbon for Negative Electrode in Lithium Ion Battery," *KnE Engineering*, vol. 2016, 6 pages. DOI 10.18502/keg.v1i1.497

Page 1

structures suitable for smooth Li intercalation and diffusion. Graphitized MCMB is one of the benchmark synthetic graphite materials for lithium-ion battery [6].

Graphitized MCMB was better than MCMB before graphitization.Graphitized MCMB has many advantages e.g., high packing density that guarantees high-energy density, small surface area that decreases the irreversible capacity corresponding to electrolyte decomposition. Most of the surfaces of MCMB spheres are composed of edge-plane surfaces, thus Li$^+$ intercalation becomes easier and the rate capacity increases and MCMB can be easily spread onto copper foil [6]. So, it was very interesting to analyze the synthetic graphite like graphitized MCMB to improve the performance of anode in the lithium ion battery.

2. Experimental

2.1. Preparation and characterizations of MCMB

The commercial MCMB was fabricated by LinyiGelon^{TM} with specific surface area $\approx$ 1.5 m^2/g. This material was then sintered at 500°C for five hours to make graphitized carbon. Commercial and graphitized MCMB were characterized by X-Ray Diffraction (XRD, Rigaku) using Cu $\kappa\alpha$ (λ = 1.541862 Å) to identify crystal phase of these material in the range 5° - 90° of two theta. The XRD technique could identify the graphitization of the material with crystal phase identification of these materials (commercial and graphitized MCMB). Scanning Electron Microscopy (SEM, SU3500, Hitachi) with tungsten as electron source was used to observe the morphology and to determine the particle size of these particles.

2.2. Preparation of the electrode and full cell battery

The full cell battery of commercial and graphitized MCMB were investigated in pouch cells. The positive electrode was prepared by commersial electrode LiCoO$_2$ (MTI Corp., USA) with the thickness of active material was 100 μm. The negative electrode were prepared using commercial and graphitized MCMB as the material active with the composition of slurry i.e. 85 wt% active material, 5 wt% acetylene black, and 10 wt% PVdF dispersed in DMAC as a solvent. Full cell battery was prepared by assembling positive electrode, negative electrode, and Celgard microporous polyethylene (PA grade, 25μm thickness) as separator with LiPF$_6$ 1 M as electrolyte.

2.3. Battery testing

Cyclic voltammetry (CV, WonaTech WBCS3000) experiment was performed on the batteries with scanning rate 0.1 μA/s and potential range 2.5 – 4.5 volt. Charge discharge (CD, WonaTech WBCS3000) characteristic was recorded to determine the charge-discharge capacity at work voltage.
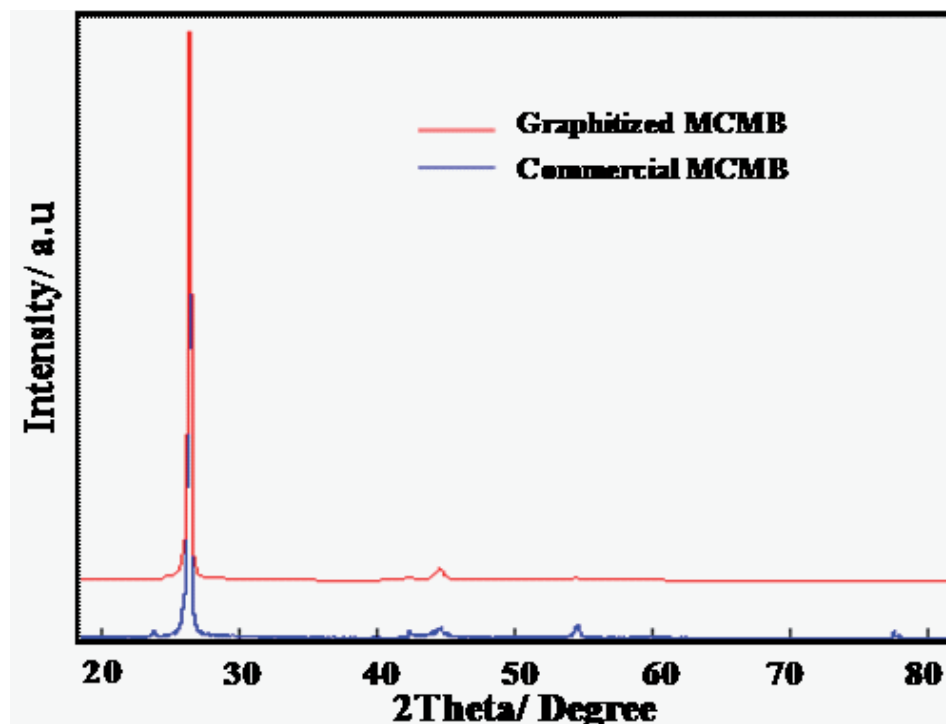
Figure 1: X-Ray diffractogram of commercial MCMB and and graphitized MCMB sintered at 500°C for five hours.

3. Result and Discussion

3.1. MCMB characterizations

XRD pattern (Fig. 1) showed the shifting of diffraction peak of commercial MCMB and graphitized MCMB. It indicated that there was a phase change in the crystal structure. ByRietvieldmethod ofinterpretation, there are three phase in the commercial MCMB i.e. graphite-2H (48.8%), graphite-3R (39%), and carbon (12.6%), while for the graphitized MCMB has single phase, graphite-2H (100%).SEM image (in Fig. 2) show the morphologyand size of the MCMB particles. Both of samples had a spherical structure with diameter range 5 – 20 μm.

3.2. Electrochemical and battery performance analysis

According to the cyclic voltammogram of the samples, it was typically the same. But, it was little bit different in the reduction peak (discharge voltage). The oxidation peak was 4.2 volt, while the reduction peak was 3.6 volt and 4 volt (for graphitized MCMB), while 3.5 volt and 4 volt for commercial MCMB. There are two reduction peaks in the cyclic voltammogram of the samples. It indicated that other material was performed as anode material in the cell, such as acetylene black.

Charge-discharge was performed at rate 0.1 C to measure the charge and discharge capacity of the samples. From the charge-discharge measurement, it shows that the commercial was better than the sample. In the first cycle, charging capacity of the
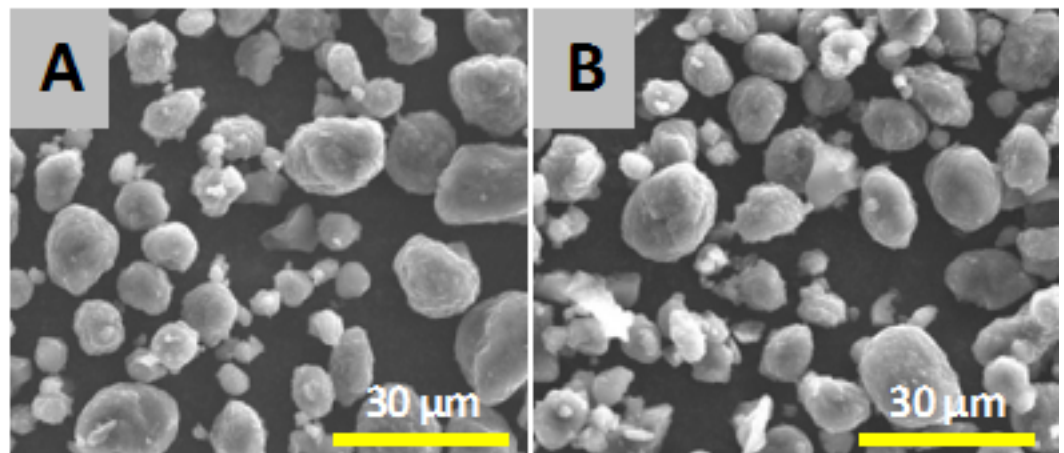
Figure 2: SEM images of (a) commercial MCMB and (b) graphitized MCMB sintered at 500 °C for five hours.
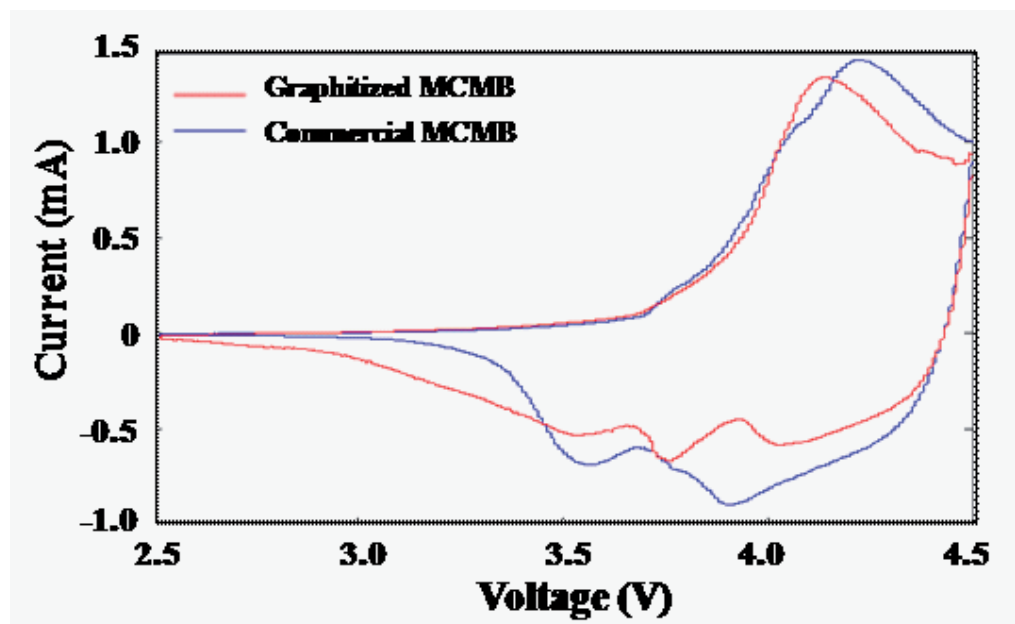
Figure 3: Cyclic voltammogram with scan rate 0.1mV/s of commercial MCMB and graphitized MCMB sintered at 500 °C for five hours.

commercial MCMB was 3.4 mAh, while the graphitized MCMB was 3.0 mAh. For discharge capacity, the commercial MCMB has 1.5 mAh, while the graphitized MCMB has 1.3 mAh. This effect was probably happened because of stability of MCMB structure, lithium intercalation process, and coating process.

4. Summary

Graphitized MCMB were prepared by sintering process at 500°C for five hours. Structure and morphology were evaluated by XRD and SEM, respectively. According to the XRD diffractogram, the diffraction peak showed the graphitized MCMB was produced. In the SEM image, the morphology of the particles was typically the same, spherical structure with diameter 5 – 20 μm. Reduction and oxidation peak in cyclic voltammogram
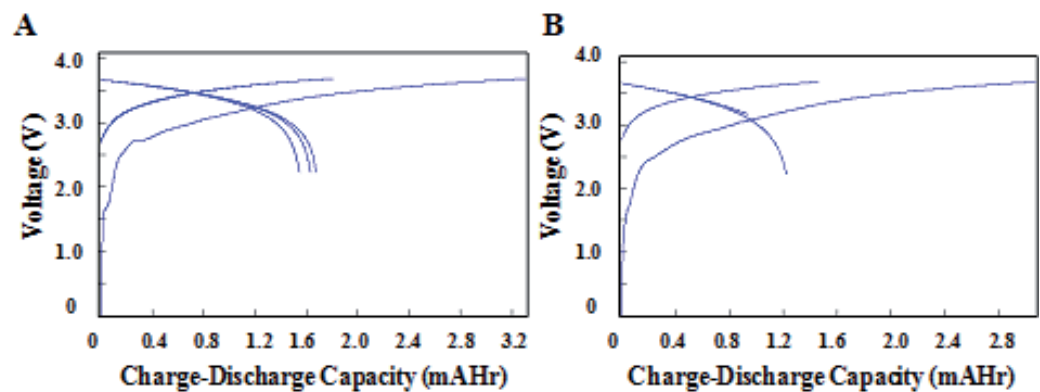
Figure 4: Comparison charge-discharge profile at C-rate 0.1 Cof (A) commercial MCMB and (B) graphitized MCMB sintered at 500 °C for five hours.

indicated the electrochemical reaction of the sample. The oxidation peak was 4.2 volt, while the reduction peak was 3.6 volt and 4 volt (for graphitized MCMB), while 3.5 volt and 4 volt for commercial MCMB. Charge-discharge profileshowedcharge-discharge capacity of the commercial MCMB was 3.4 mAh and 1.5 mAh, while the graphitized MCMB was 3.0 mAh and 1.3 mAh, respectively. It indicated that the commercial MCMB was better than graphitized MCMB.

5. Acknowledgement

References

[1] C. Ding, T. Nohira, R. Hagiwara, A. Fukunaga, S. Sakai, and K. Nitta, Electrochemical performance of hard carbon negative electrodes for ionic liquid-based sodium ion batteries over wide temperature range, *Electrochim Acta*, **176**, 344–349, (2015).

[2] R. Wu, G. Xia, S. Shen, F. Zhu, F. Jiang, and J. Zhang, In-situ growth of LiFePO$_4$ nanocrystals on interconnected carbon nanotubes/mesoporous carbon nanosheets for high-performance lithium ion batteries, *Electrochim Acta*, **153**, 334–342, (2015).

[3] D. Miranda, C. M. Costa, and S. Lanceros-Mendez, Lithium ion rechargeable batteries: state of the art and future needs on microscopic and theoretical models and simulations, *J Electroanal Chem*, **739**, 97–110, (2015).

[4] S. Hossain, Y.-K. Kim, Y. Saleh, and R. Loutfy, Comparative studies of MCMB and C-C composite as anodes for lithium-ion battery systems, *J Power Sources*, **114**, 264–276, (2003).

[5] Y. Abu-Lebdeh and I. Davidson, in *Nanotechnology for Lithium-Ion Batteries*, 117–162, Springer, Canada.

[6] M. Yoshio, R. J. Brodd, and A. Kozawa, in *Lithium-Ion Batteries*, Springer-Verlag, New York, 2009.

KnE Engineering

Knowledge E
Engaging minds

Conference Paper

The role of SiC on the Desorption Temperature of Mg-based Hydrogen Storage Materials Prepared by Intensive Milling Method

Zulkarnain Jalil[1], Adi Rahwanto[1], Erfan Handoko[2], and Bambang Soegijono[3]

[1]Department of Physics, Syiah Kuala University (Unsyiah), Banda Aceh, Indonesia
[2]Department of Physics, Jakarta State University (UNJ), Jakarta, Indonesia
[3]Research Centre for Materials Science (RCMS), University of Indonesia (UI), Jakarta, Indonesia

Abstract Magnesium, theoretically, have the ability to absorb hydrogen in large quantities ($\sim$ 7.6wt%). However,the kinetic reaction is very slow, therebyhindering the application of magnesium for hydrogen storage material. In this paper, we reported a series of preliminary studieson magnesiuminserting with silicon carbide (2 wt%) obtain by mechanical millingmethod. The vibratory mill type apparatus was used for 180 hours. As the results, structuralcharacterization by XRD showed that the crystallite size after milling for 180 hours decreased around tensnanometer. It was also found that the desorption temperature for the sample after 180 milling inform us that the material decomposed at 330∘C. It can concluded that Mg catalyzed with 2 wt% of silicon carbide (SiC) can be prepared by vibratory ball milling.

Keywords: MgH_2, catalyst, nanoparticle, hydrogen storage, reactive milling

🔓 **OPEN ACCESS**

1. Introduction

Among the metal hydrides, magnesium has the theoretically highest weight capacity for hydrogen storage (7.6 wt.%), lightweight and a reasonably low cost [1]. However, high working temperature, slow reaction kinetics and difficult activation limit the practical application of Mg-based hydrides. Many efforts have been done to improve the adsorption properties and reaction kinetics such as element substitution (metal or metal oxides) as catalyst in nanometer scale and modification of ball milling technique as well [2-5]. Recently, the reactive ball milling under hydrogen atmosphere was also successfully introduced to prepare hydrogen storage materials [6,7].

In order to find a more suitable co-catalyst material to be used with magnesium, Ranjbar et al [8], introduced a new catalyst based on silicon carbide (SiC) to be inserted in magnesium as host material. It was found that by using SiC as an additive, the grain size of MgH_2 was decreased, and at the same time increased the defect concentration, which subsequently prevent the agglomeration of MgH_2 crystallitesas well. The sorption properties were improved and the kinetics was also very fast. By using this finding as a motive of our study, here we report our work on Mg catalyzed with 2wt% of SiC prepared by vibration ball milling (VBM). The aim of this study was to

Page 1

synthesize nanocrystalline Mg-SiC by mechanical alloying using intensive mechanical milling method.

2. Materials and Method

In this experiments, Mg (Merck, 0.03 mm, 95%), SiC (99.9%, −400 mesh, Sigma Aldrich) powders wereused. The powders were filled into a home-made hardened steel vial and sealed together with 10 balls (5.6 mm in diameter). The powders were milled in avibratory ball mill (VBM, Kawasaki) at a rotational speed of 900 rpm (ball to powder ratio 10:1) for 180 hours. Every several hours of milling time (30, 40, 60, 80, 100, 160 and 180 hour) small amount of powder were separated into a small container for further characterization. This method was then called as Intensive Mechanical Alloying (IMA). Structural changes occurred on the samples during milling were then characterised by XRD (Philips, PW 3710, Co-Kα radiation). A high resolution scanning electron microscopy (SEM JEOL,JSM-5310LV) was used to observe the morphological changes during the milling process. The onset temperature (T$_{onset}$) was investigated using DTA (Shimadzu, D-50) with a flow rate of 20 ml/min and heating rate from 20-450◦C.

3. Results and Discussions

Figure 1 shows the evolution of the XRD diffraction pattern for Mg-2wt% SiC as a function of milling time and intensity. At early stage of milling, the starting mixture shows the presence of microcrystalline materials. Then, it can be seen for the next milling time that the diffraction peaks broaden but no changes in the 2θ position. The as-received sample composed mainly Mg. The Mg peaks locate at 2θ = 37,86°; 40, 56; 43, 66; 56, 8; 68, 06; 75, 28; 82, 5; 84, 24, and 87, 14. SiC peak was not detected due to the amount of SiC was too small (2 wt %). Thus, it is difficult to detect by XRD. The same result was found after 30 h milling.

When the milling time increase up to 40 hour, the XRD patterns still not change significantly. But, at 60 hour the peak broadening was start to appear. At 80 to 100 hour, the Mg peaks were broadening significantly. At 160 hour and 180 hour the peak unity in one peak and composed one phase. It can be seen that the powders already reduced into nanocrystalline. We can conclude that the Mg particles completely decrease after milling in 180 hours. This is due to the high energy vibration ball mill. This result showed that mechanical alloying using VBM is very attractive and promising method to synthesize nanostructure materials for solid hydrogen storageconsidering the applied mechanical deformation between ball and powders. Thus, making use of higher energy during milling promotes the formation of nanostructure of magnesium.

The SEM micrographs of Fig. 2 show secondary electron image of powders intensively milled in the VBM before milling (Fig. 2a), milling 60h (Fig. 2b) and milling 180 hours (Fig. 2c). The surface of the powder for 0 h and 60 h are irregular, as a result of the fracturing during the milling process. The SEM image after 180 hours of milling
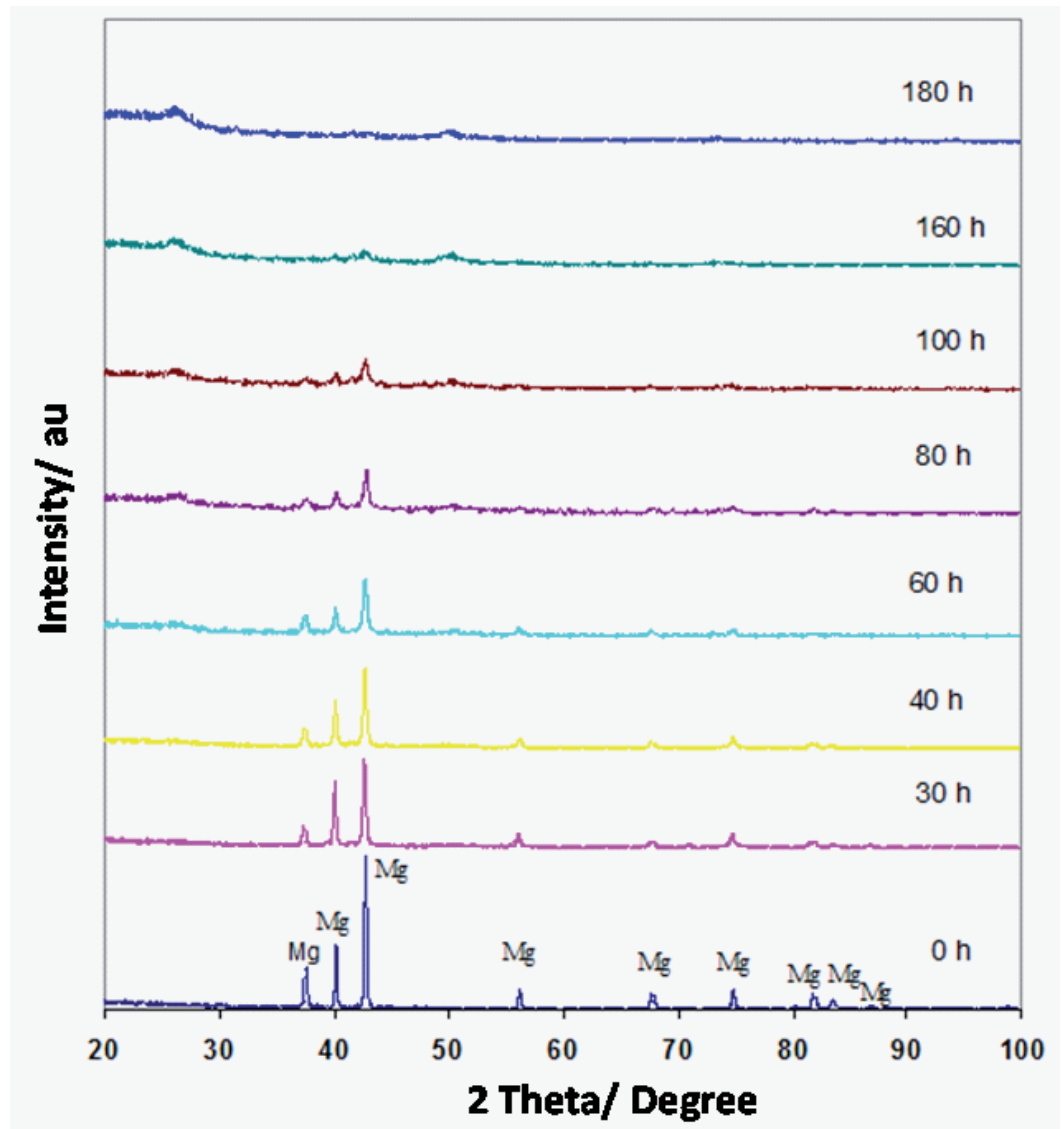
Figure 1: X-ray diffraction patterns of Mg-2wt% SiC produced via VBM.

shown the finer powder. It seem the powder was already in nanocrystal scale. If we compare with XRD, this is consistent with the structural analysis by XRD.

This indicates that the powders is un-uniformly distributed on the metal surface and the grain size, calculated by Scherrer method [9], reaches around tens nanometer after 180h of milling. However, the formation of nanocrystalline material is obtained after long milling (in 180 hours). These results suggest that deformation during milling take longer time due to the ductility of magnesium. Important to note, the silicon carbide in the composites helps to break the magnesium particles into smaller sizes due to itshardness. Ranjbar et al. [8], has clearly demonstrate that the addition of SiC can help to generate smaller MgH_2 nanocrystals and it was found that the MgH_2 peaksin the XRD pattern became very broadened. They indicated that long ballmilling was beneficial for the conversion of Mg powder to MgH_2 andalso helpful for reducing the grain sizes of powders.
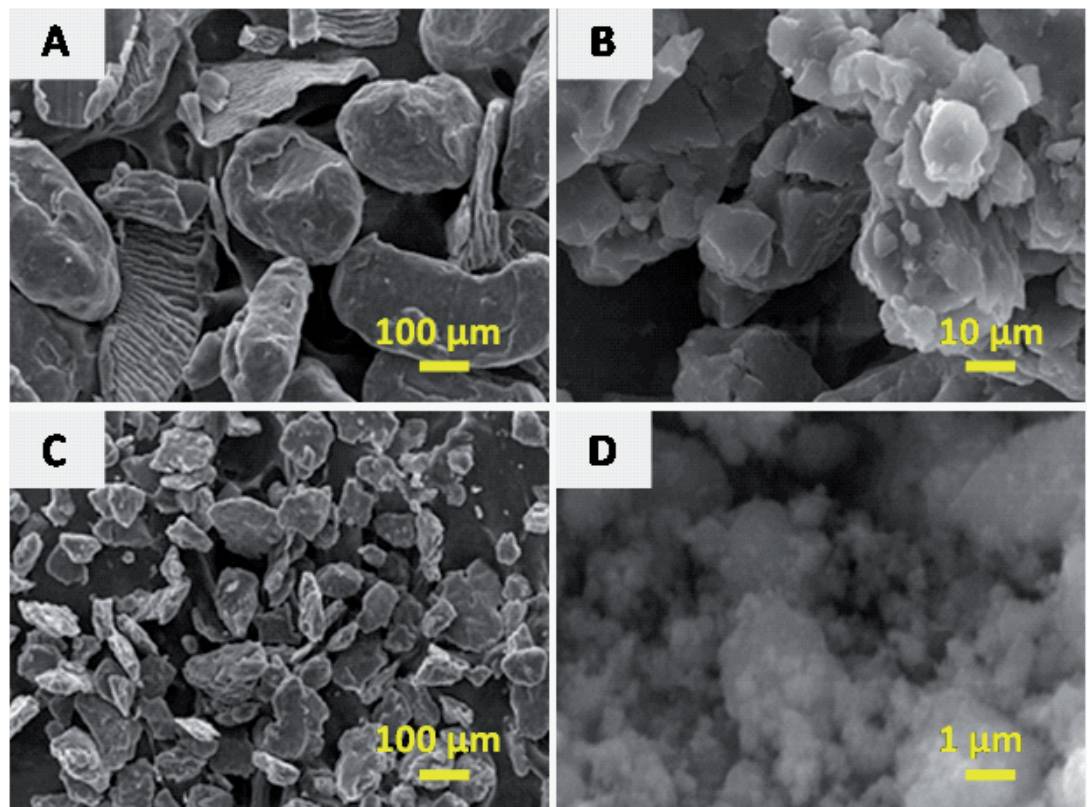
Figure 2: SEM image of Mg-2wt% SiC, (A)before milling, (B) 60, (C)30 and (D) 180 h.
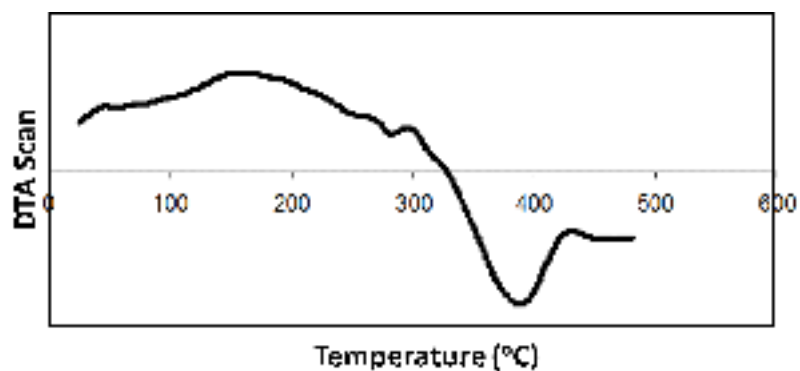
Figure 3: DTA scan of Mg-2wt% SiC after milling 180 h.

Thermal investigation for the sample after 180 milling give information on the state of the material decomposition. Here, it can be clearly seen that the material decomposed at temperature 330∘C (Figure 3). However, this temperature is still high for Mg-based hydrogen storage materials application. It seem that the crystallite size have not a strong influence on the desorption temperature changes.

Kurko et al. [10], explained that this situation occurred due to agglomeration of the material during the milling process. Therefore the reduction of agglomeration is believed will improve the thermal properties of Mg-based hydrogen storage materials.It is already known that the hydrogen storage properties of light metal hydrides is improved with reduced particle agglomeration [11]. Due to the decrease agglomeration

will shorten the diffusion path of hydrogen atoms. Therefore, it is suggested that a significant amount of strain, disorder and defects should be created during milling process, which shorten hydrogen diffusion paths [12].

4. Conclusions

Mg catalyzed with 2 wt% of silicon carbide (SiC) prepared via vibratory ball milling has been successfully done. This process results in high surface area powders with finely dispersed SiC- particles on the surface of Mg. The Mg-SiC material exhibits a microstructure in nanometer scale. Thermal investigation for the powders after 180 millingshown that the material decomposed at temperature 330∘C. Due to these results, nanocrystalline Mg-SiC is suggested a further work for improvement the sorption properties and the kinetics of Mg-based hydrides as hydrogen storage material.

References

[1] L. Schlapbach and A. Züttel, Hydrogen-storage materials for mobile applications, *Nature*, **414**, 353–358, (2001).

[2] L. Wang, Y. Wang, and H. Yuan, Development of Mg-based hydrogen storage alloy, *J Mater Sci Technol*, **17**, no. 6, (2001).

[3] H. Yuan, Y. An, G. Xu, and C. Chen, Hydriding behavior of magnesium-based hydrogen storage alloy modified by mechanical ball-milling, *Mater Chem Phys*, **83**, 340–344, (2004).

[4] N. Cui, P. He, and J. L. Luo, Magnesium-based hydrogen storage materials modified by mechanical alloying, *Acta Mater*, **47**, 3737–3743, (1999).

[5] T. Ichikawa, N. Hanada, S. Isobe, H. Leng, and H. Fujii, Composite materials based on light elements for hydrogen storage, *Mater Trans*, **46**, 1–14, (2005).

[6] W. Oelerich, T. Klassen, and R. Bormann, Metal oxides as catalysts for improved hydrogen sorption in nanocrystalline Mg-based materials, *J Alloys Compd*, **315**, 237–242, (2001).

[7] R. A. Varin, T. Czujko, E. B. Wasmund, and Z. S. Wronski, Hydrogen desorption properties of MgH2 nanocomposites with nano-oxides and Inco micrometric- and nanometric-Ni, *J Alloys Compd*, **446-447**, 63–66, (2007).

[8] A. Ranjbar, Z. P. Guo, X. B. Yu, D. Wexler, A. Calka, C. J. Kim, and H. K. Liu, Hydrogen storage properties of MgH2–SiC composites, *Mater Chem Phys*, **114**, 168–172, (2009).

[9] M. Abdullah, Derivation of Scherrer Relation Using an Approach in Basic Physics Course, *Jurnal Nanosains & Nanoteknologi*, **1**, no. 1, (2008).

[10] S. Kurko, Z. Raskovic, N. Novakovic, B. P. Mamula, Z. Jovanovic, Z. Bascarevic, J. G. Novakovic, and Ljiljana Matovic, Hydrogen storage properties of MgH2 mechanically milled with α and β-SiC, *Int J Hydrogen Energy*, **36**, 1184–1189, (2011).

[11] M. Ismail, N. Juahir, and N. S. Mustafa, Improved Hydrogen Storage Properties of MgH2 Co-Doped with FeCl3 and Carbon Nanotubes, *J Phys Chem C*, **118**, 18878–18883, (2014).

[12] J.-J. Jiang and M. Gasik, Michael Gasik, An electrochemical investigation of mechanical alloying of MgNi-based hydrogen storage alloys, *J Power Sources*, **89**, 117–124, (2000).

Conference Paper

Preparations and Characterizations of Hierarchical Macropore Activated Carbon Monolith Electrode from Rubber Wood for Supercapacitor Application

Erman Taer[1], Yusriwandi[1], Rika Taslim[2], I.D.M. Syam[1], and Mohamad Deraman[3]

[1]Department of Physics, University of Riau, 28293 SimpangBaru, Riau, Indonesia
[2]Departement of Industrial Engineering, Islamic State University of Sultan SyarifKasim, 28293 SimpangBaru, Riau, Indonesia
[3]School of Applied Physics, Faculty of Science and Technology, UniversitiKebangsaan Malaysia, 43600 Bangi, Selangor, Malaysia

Abstract Preparation of hierarchical macropore activated carbon monolith (HMACM) from rubber wood was investigated. The samples were prepared with small cutting of rubber wood in cross sectional method. The electrode preparation was started by pre-carbonization process followed by carbonizationat 600^oC and physical activation process at 900^oC in N_2 and CO_2 gas atmosphere, respectively. The samples then were followed by chemical activation process with combination of chemical activation agent of KOH and HNO3 solutions. The HMACMs were neutralized by immersing the samples in copious amount of water and dried the samples for 24 hours. Porosity properties were performed by N_2 adsorption-desorption data and morphology characterization was analyzed by scanning electron microscope (SEM) instrument. The electrochemical properties was studied by electrochemical impedance spectroscopy, cyclic voltammetry and charge-discharge at constan current methode. The SEM micrograph and adsorption-desorption data were also proved that the HMACM sample have a hierarchical macropore at the surface and crossectional section. The porosity data shown the HMACM sample have BET surface area of 331 m^2/g with average pore diameter of 1.7 nm. Equivalent series resistance and optimum capacitance specific of the HMACM electrode of 0.77 Ohm and 154 F/g, respectively. In conclusion, this study showed that the preparation method would propose as a simple method of HMACM electrode preparation technique for supercapacitor applications.

Keywords: Hierarchical Macropore, Rubber wood, Supercapacitor.

1. Introduction

Supercapacitor was one of the energy storage devices beside the capacitor, batteries and fuel cell [1]. Supercapacitor has a higher energy than capacitors but showed lower power. If was compared to batteries, supercapacitors has a higher power but a lower energy. Supercapacitor comprises two current collectors, two electrodes that were restricted by separator and dipped into the electrolyte [2]. An electrode was an important component in determining the capacity of energy and power that can be

How to cite this article: Erman Taer, Yusriwandi, Rika Taslim, I.D.M. Syam, and Mohamad Deraman, "Preparations and Characterizations of Hierarchical Macropore Activated Carbon Monolith Electrode from Rubber Wood for Supercapacitor Application," *KnE Engineering*, vol. 2016, 6 pages. DOI 10.18502/keg.v1i1.499

Page 1

storage in supercapacitor cells. In the past decade has been done a lot of research to get the best supercapacitor with modifications to the electrode.The supercapacitor electrode can be made from a porous carbon material [3]. One source of carbon that is cheap and easily obtained materials derived from biomass. Several reports have been revealed the energy and power generated by a carbon electrode from biomass materials [4]. Biomass materials that has been used as a precursor for carbon electrode for supercapacitor application such as rubber wood sawdust [5], peanut shells [6], and emptyfruit bunches [7], poplar wood [8] and paulownia flower [9].

The ability to store the energy and power at an electrode were determined by the nature of the porosity of the material. The main properties of pore which includes an average pores size and pores distribution. An electrode materials with an average pore were micro-porous will tend to produce supercapacitor cells with higher energy density but lower power density [10]. On the other side, carbon material with an average pore was meso-pore will tend to produce supercapacitor cells with higher power density [10]. Materials with pores which were dominated by micro pores will produce a high surface area. The surface area is often believed to be a key factor for determining the energy value of a cell supercapacitor. Some reports also stating some materials with low surface area was capable to produce a supercapacitor cell with relatively high energy.

This study was shown the carbon electrode with relatively low surface area can produce a supercapacitor cell with good electrodes properties. Carbon electrodes have been made from rubber wood branch. Rubber wood branch was cut by cross section side to preserve the nature of the existing of natural macro-pores. Fabricating of carbon electrodes such as this way has an advantage that without need for adhesive materials and pore composed with uniformly. The absence of adhesive on the electrode may decrease the electrode intrinsic resistance and the existing a hierarchical macro-pores would increase the charge transfer in the electrode. Both of these factors are believed a carbon electrodes from rubber wood as a potential candidate as a supercapacitor electrode material.

2. Experimental

HMCM were made from rubber wood that was cutted by transversely to maintain the hierarchical macro-pore structure on the electrode. The sample was then carbonized in N_2 gas atmosphere at a temperature of 600 °C and then the followed by physical activation by using CO_2 gas at a temperature of 900°C. Chemical activations were performed by usingthe activating agent of 3 M KOH and25% HNO_3. Supercapacitor cells were assembled in the form of coins cell type using two electrodes, two current collector, and a separator. Physical properties and electrochemical characterization were performed on the HMCM samples. The physical properties such as surface morphology and surface area of carbon electrodes were characterized. The electrochemical properties were measured includes the specific capacitance, cells resistance, energy density and power density. The electrode surface morphology was performed with a scanning electron microscopy (SEM) measurement and the surface area studied by N_2

gas isothermal absorption-desorption method. The electrochemical properties testing carried out using the electrochemical impedance spectroscopy (EIS), cyclic voltamme- try (CV) and charge and discharge (CDC) method by solatron 1286 measurement.

3. Results and Discussions

Figure 1 was shown the EIS data for supercapacitor cell with HMAC electrode from rubber wood. Figure 1A displays a Nyquist plot where the shape of the curve obtained were a semicircle, a line with 45 degree and a line with 90 degree to the Z' axis. Semicircular shape can be used to determine the equivalent series resistance (ESR), contact resistance an electrode with current collector and combined with an electrolyte resistance (Rp) which is the intersection of the curve to the Z' axis with a lower resis- tance value [2]. Carbon electrode intrinsic resistance (Rs) which was the intersection of the curve on the Z' axis at a larger value. The magnitude of ESR, Rp, Rs were 0.77 Ω, 0.73 Ω and 1.5 Ω, respectively. The resistive properties of the supercapacitor cell was comparable to the supercapacitor cell electrode from poplar wood [8]. Figure 1B and 1C showed the relationship between frequency with the real and imaginary capacitance. The data in Figure 1C can be used to determine the relaxation time (τ) which to be related to the frequency peaks, where τ =1/f, where relaxation time was 25,12 seconds. The relaxation time is related to the time required for the ions can difuse in completely into the pores of electrodes. Figure 1D showed the relationship specific capacitance (Csp) against frequency. The highest Csp value was shown at the lowest frequency of 0.01 Hz was 154.03 F/g. The specific capacitance value of the supercapacitor cell in current study was comparable to the specific capacitance value for supercapacitor was fabricated from the electrodes from other biomass materials as listed in Table 1.

Figure 2A showed the measurement data of the electrochemical properties of super- capacitor cells using cyclic voltammetry method. Cyclic voltammograms showing a rectangle shape, this shape was a good capacitive characteristic of electrodes for car- bon supercapacitor [3]. Figure 2B displays measurement data for galvanostatic charge- discharge of supercapacitor cell. The CDC measurement data showed the standard form for supercapacitors using carbon materials electrodes. Based on the data in Figure 2B by using the formula P=vi/m dan E=vit/m [4] can be determined the relationship between power density (P) versus energy density (E) and was shown in Figure 2C. Figure 2C showed that maximum power density and maximum energy density, respec- tively 420 Watt / kg and 2.8 Watt h/kg. The magnitude of power density and energy density, which is related to a supercapacitor with HMCM electrode was a commonly reported by other researcher, the comparison of power density and energy density of supercapacitor cells with HMACM electrodes was shown in Table 1. Figure 2D was showed the N2 gas isotherm adsorbtion-desorption data for HMACM sample. The isotherm data was showed the type 1 based on UPAC classification [11]. The type 1 absorption-desorption data indicated the HMACM eletroda have a pores in the range of microporous [11]. Based on DR equation can be obtained the SBET, Smicro, SEXTERNAL, pore diameter and pore volume were 331.54 m2 / g, of 224.704 m2/g,106.830 m2/g, 15.491 Å, 0.051 cm3/g. respectively.
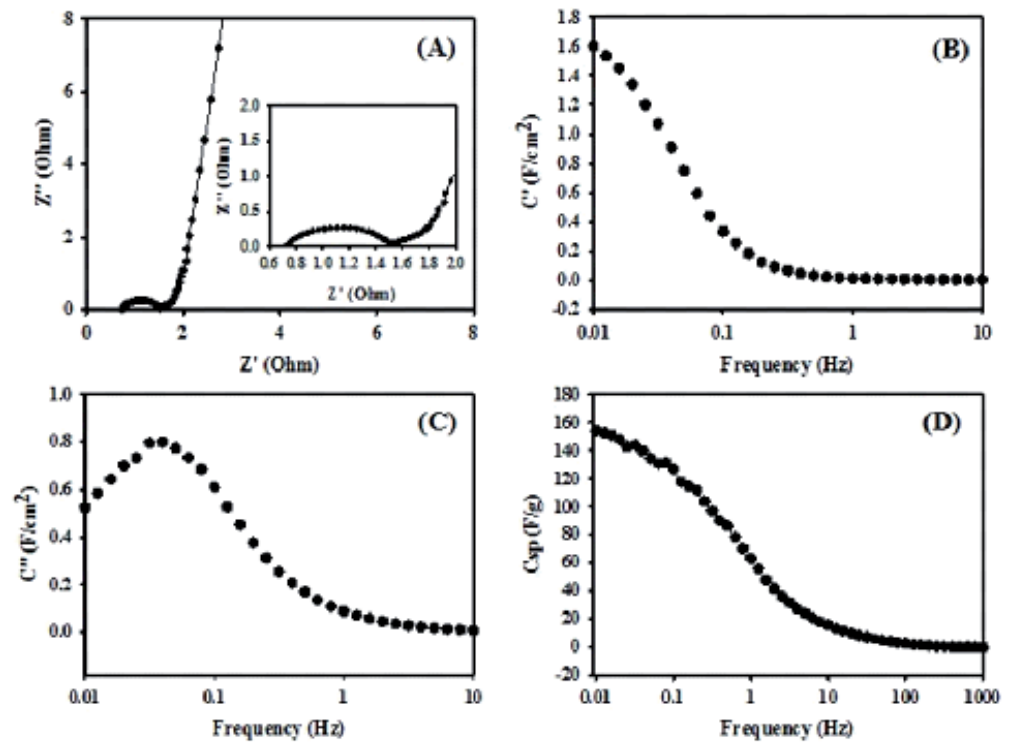
Figure 1: The electrochemical properties of supercapacitor cells were elucidatedby using EIS method.

Type of biomass	Energy (Wh.Kg^{-1})	Power (W Kg^{-1})	Capacitance (F g^{-1})	Reference
Peanut Shell	19.30	1007	99	[6]
Rubber wood sawdust	2.63	291	138	[4]
Oil palm fruit bunches	4.297	173	150	[7]
Paulownia flower	44.5~22.2	247~3781	297	[9]
Poplar wood			234	[8]
Rubber wood	2.90	420	154	Present study

TABLE 1: Comparison of energy, power, and capacitance varioustypes ofbiomass material.

Figure 3 were shown the SEM micrograph of the surface (A) and cross sectional (B) part of HMCM electrode. Figure 3A shows that HMCM electrode has pores with uniform in size macro of pores. Figure 3B was showed that the macro pores has a shape like an elongated pipe, this shape will provide convenience for the ion can penetrate further into the meso and micro pore of carbon electrode.

4. Conclusions

Preparation of HMCM electrode for supercapacitor application has successfully carried out. HMCM electrode showed good resistive properties and capacitive characteristic, from the all of analysis the HMCM route was an interesting strategy for the used at rubber wood as a potential candidate for supercapacitor electrodes.
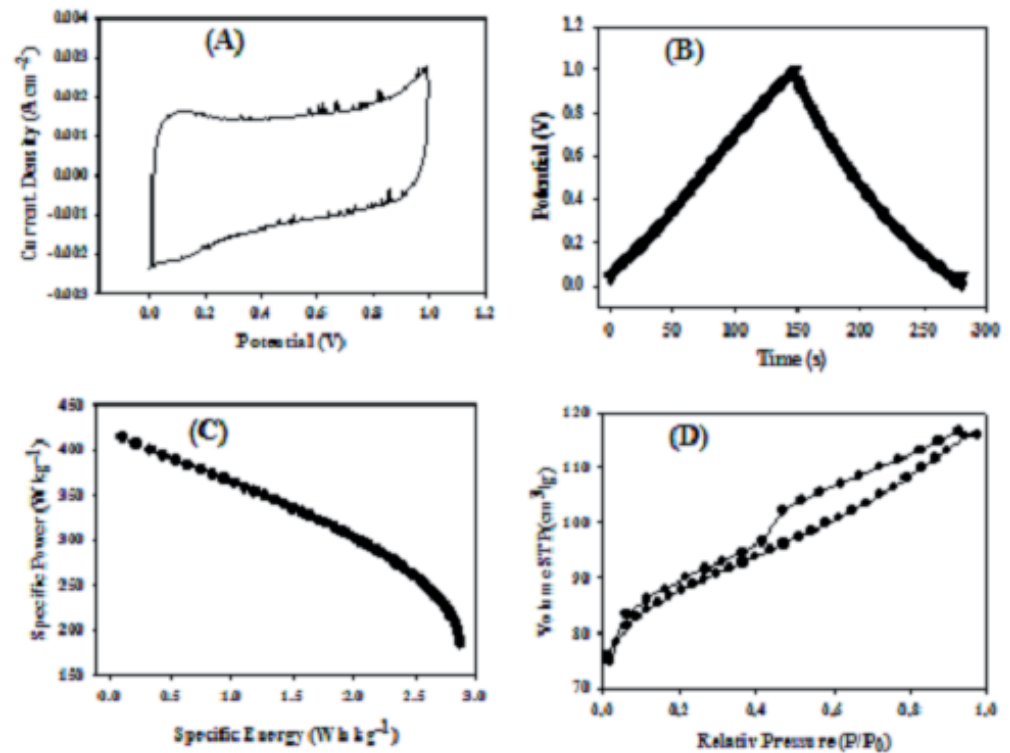
Figure 2: CVdata (A),CDCdata (B), energy density versus power density (C) and the N_2 gas absorption-desorption data for the HMCM electrodes.
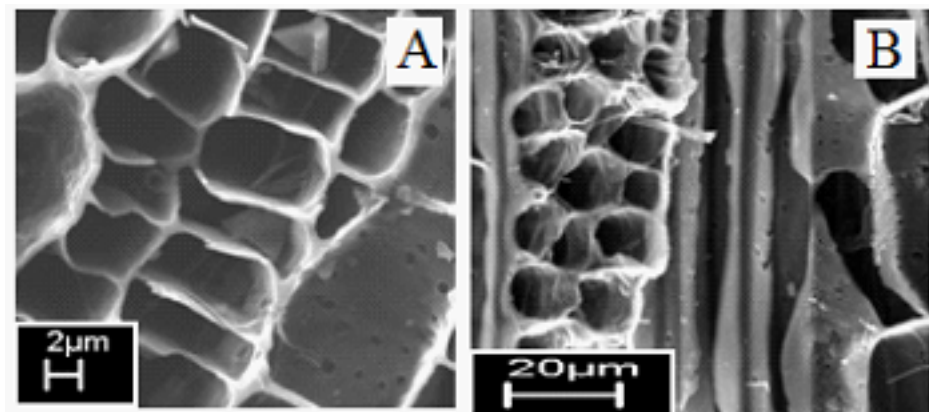
Figure 3: SEM micrograph of HMACM electrod from rubber wood, (A) surface and (B) crossectional section.

5. Acknowledgements

References

 [1] A. Burke, R. Kotz, and M. Carlen, *J Power Sources*, (2000).

 [2] A. Burke, R&D considerations for the performance and application of electrochemical capacitors, *Electrochim Acta*, **53**, 1083–1091, (2007).

 [3] E. Frackowiak and F. Béguin, Carbon materials for the electrochemical storage of energy in capacitors, *Carbon*, **39**, 937–950, (2001).

 [4] E. Taer, M. Dareman, I. A. Talib, A. Awitdrus, S. A. Hashmi, and A. A. Umar, *Int J Electrochem Sci*, **6**, no. 8, 3301–3315, (2011).

 [5] E. Taer, M. Deraman, I. A. Talib, A. A. Umar, M. Oyama, and R. M. Yunus, Physical, electrochemical and supercapacitive properties of activated carbon pellets from pre-carbonized rubber wood sawdust by CO_2 activation, *Curr Appl Phys*, **10**, 1071–1075, (2010).

 [6] X. ia. He, P. Ling, J. Qiu, et al., *Journal of power sources*, 109–113, (2013).

 [7] R. Farma, M. Dareman, A. Awitdrus, et al., in *Bioresuorce Technology*, 254–261, 2013.

 [8] M. C. Liu, B. Kong, P. Zhang, Y. C. Luo, and L. Kong, Porous wood carbon monolith for high-performance supercapacitors, *Electrochim Acta*, **60**, 443–448, (2011).

 [9] J. Chang, G. Zhiyong, W. Xiaorui, and D. Wu, *Electrochimica Acta*, 290–298, (2015).

[10] J. Chimiola, G. Yushin, R. Dash, and Y. Gogotsi, *J Power Sources*, **158**, 765–772, (2006).

[11] K. S. W. Sing, D. H. Everret, R. A. W. Haul, L. Moscou, R. A. Pierotti, J. Rouquerol, and T. Siemieniewska, Reporting physisorption data for gas/solid systems with special reference to the determination of surface area and porosity (Recommendations 1984), *Pure Appl Chem*, **57**, 603–619, (1985).

Knowledge E
Engaging minds

Conference Paper

Effect of Aging Time on the Synthesis of Fe-doped TiO$_2$ Thin Films by Spin Coating Method

Dahyunir Dahlan and Muhammad Anshori

Department of Physics, Andalas University, LimauManis Padang 25163, West Sumatera, Indonesia

Abstract The synthesis of Fe-doped TiO$_2$ thin film using spin coating method was studied. Effects of aging time on the deposited thin film were investigated. Titanium butoxide (C$_{16}$H$_{36}$O$_4$Ti) as a precursor solution was mixed with the FeCl$_3$. Spin coating process was carried out on three types of precursor solution: (1) spin-coating process performed immediately after the precursor solution was made, (2) spin-coating process performed after solution was aged for 24 hours, (3) aged for 24 and (4) spin-coating after aging the precursor for 72 hours. Heating was carried out on the resulting thin film at temperature of 400°C. The morphology of TiO$_2$ layers was characterized using Scanning Electron Microscope (SEM) and Atomic Force Microscope (AFM). Elemental and phase composition of the films was determinedusing EDX and X-ray diffraction (XRD). We found that the best TiO$_2$ layer is obtained when spin-coating process is done after aging the precursor for 72 hours. The layer shows a more uniform particle distribution on the substrate and a more monodisperse particle size dominated by the anatase phase.

Keywords: TiO$_2$thin film, Fe doped TiO$_2$, spin coating, aging time.

🔓 **OPEN ACCESS**

1. Introduction

TiO$_2$ coating has been investigated by many researchers because TiO$_2$is stable, non-toxic with band gap of 3.21 eV making it possible for photovoltaic [1] and photocatalytic [2] application. It is well known TiO2 nanoparticles with good physico-chemical properties are mainly dominated by three phasesnamely anatase, rutile and brookite. On a nanometer scale or in a thin layer form,TiO$_2$ nanoparticles are transparent and have a wide surface area [3]. To improve the performance of thin film TiO$_2$for photovoltaics application purpose such as dye sensitized solar cell, TiO$_2$ layer has been modified by the addingmetal dopant such as Fe [4] and Zn [5]. It is also reported that to improve the crystal size of TiO$_2$, treatment such as by varying aging time of the precursor can be performed [6].

Various methods has been reported to produce a thin layer of TiO$_2$such as electrophoretic deposition [7], electrodeposition [8], doctor blades [9], RF sputtering [10], sol gel [11], dip-coating [12], spin coating, etc. In this study, we use a spin coating method to deposit TiO$_2$ layer. The purpose of this research is to investigate the effect of aging time on the morphology and phase of Fe-doped TiO$_2$synhesized by spin coating

How to cite this article: Dahyunir Dahlan and Muhammad Anshori, "Effect of Aging Time on the Synthesis of Fe-doped TiO$_2$ Thin Films by Spin Coating Method," *KnE Engineering*, vol. 2016, 6 pages. DOI 10.18502/keg.v1i1.500

Page 1

method. From this study, it was found that the Fe-doped TiO_2 with aging time for precursor of 72 hours with annealing temperature of 400ºC produced better TiO_2 thin film. This finding may find useful in potential application in TiO_2 utilizing thin film such as photocatalytic and photovoltaic applications.

2. Experiment

Synthesis solution comprises a mixture of 13% vol. titanium (IV) butoxide ($C_{16}H_{36}O_4Ti$) (Aldrich 99.9%), 65% vol. ethanol, 4% vol. HCl, 5% vol. aquabidest (H_2O), and 13% vol. $FeCl_3$. All the ingredients were stirred for 1 hour with a magnetic stirrer C-Mag HS7. The solution was then divided into four portions. One portion was used in direct spin coating while the others were aged for 24, 48 and 72 hours prior to spin coating. Changes in aged solution were observed at a predetermined time. Spin coating parameters (rate of 2,500 rpm for 30 seconds) were the same for all samples. Deposition of TiO_2 layer was doneon microscope glass substrate. Prior to spin coating process, the glass substrateswere washed in the ultrasonic cleaner (Bransonic) for 30 minutes by using distilled water, then washed with acetone. The deposited layer was heated at a temperature of 400°C in the furnace. Characterization was performed using Scanning Electron Microscope (SEM + EDX) Hitachi S-3400N + Horiba-EMAX, Atomic Force Microscope (AFM) and X-ray Difraction (XRD) Shimadzu-7000.

3. Results and Discussion

Fig. 1 shows the typical morphology of the TiO_2 layer synthesized using spin coating technique from a solution of $C_{16}H_{36}O_4Ti$ that was aged for 72 hours, heated at a temperature of 400 °C. By using SEM technique, micrograph obtained at magnification of 40,000x shows that TiO_2 layer looks flat and solid. The thickness of the layers is estimated to be below 200 nm. All of the samples prepared regardless of its treatment and modification ((1) spin-coating process performed immediately after the precursor solution was made, (2) spin-coating process performed after solution was aged for 24 hours, (3) aged for 24 and (4) spin-coating after aging the precursor for 72 hours) have the same morphology when viewed with SEM prior to the aging time. In order to obtain clear information on the surface morphology of the TiO_2 layer, then AFM imaging (Fig 2) was later performed.

Atomic force microscopy (AFM) micrograph of Fe doped TiO_2 sample was later carried out to study the thickness and uniformity of the particles grown. Fig 2(a) shows amicrograph of TiO_2 layer synthesized from a solution ofsol-gelspin coating process, done directly without aging using spin-coating process. The image was taken immediately after the solution was made, without heating treatment. It is clearly visible that the film obtained forms two different layers that have uneven thickness. No grain of TiO_2particles is visible because the paste contains a lot of water. The absence of TiO2 aggregates viewed is also due to the incomplete formation of TiO_2 aggregates via Ostwald ripening process. After heating treatment at 400°C (Figure 2b.), the surface of the layer began to be filled by TiO_2 particles. Despite having uneven distribution,
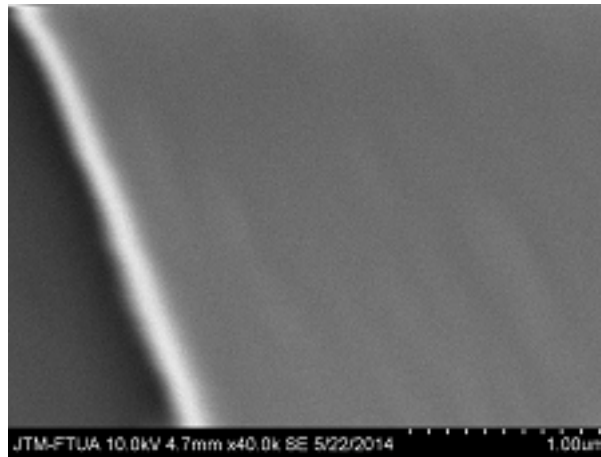
Figure 1: Scanningelectronmicroscope image of TiO$_2$ layer synthesized from solution of C$_{16}$H$_{36}$O$_4$Ti with aging time for 72 hours and heated at a temperature 400∘C.

Sampel	Element	Mass %	Atom %
Before heating 400°C	Cl	531	5.05
	C	6.83	9.93
	Ti	5633	48.42
	Fe	29.38	29.25
	O	2.15	7.35
After heating 400°C	Cl	3.26	4.96
	C	5.97	3.08
	Ti	58.68	55.70
	Fe	28.04	23.91
	O	4.14	12.35

TABLE 1: The elemental composition of TiO$_2$ layer for the precursor solution aged for 72 hours.

particlebuildupoccursin someparts of the surface.We found that the best TiO$_2$ layer is obtained when spin-coating process is done after aging the precursor for 72 hours. The layer shows a more uniform particle distribution on the substrate and a more monodisperse particle size dominated by the anatase phase.

Fig. 2c displays TiO$_2$ layer produced after the spin coating sol gel solution after aging for 46 hours. Similar to Fig. 4a, here the layer thickness is still uneven and the formed two layers were still in dry pasta shape. When the sample is heated at a temperature of 400 °C (Fig 2d), the surface of the TiO$_2$ layer began to form evenly. The particles produced ware almost uniform in size on the order of ten nanometers. When the synthesis is done after aging the precursor for 72 hours (fig 2e), the layer of TiO$_2$ produced a more even distribution. The surface looks more delicate because particles are smaller than before. This shows that aging of the precursor for 72 hours produces a good TiO$_2$ layer. Aging treatment affects the size and agglomeration of particles [4]. If TiO$_2$ layer is heated at 400 °C, it will form a homogeneously-distributed layer with a more uniform thickness across the surface of the substrate (fig 2f).
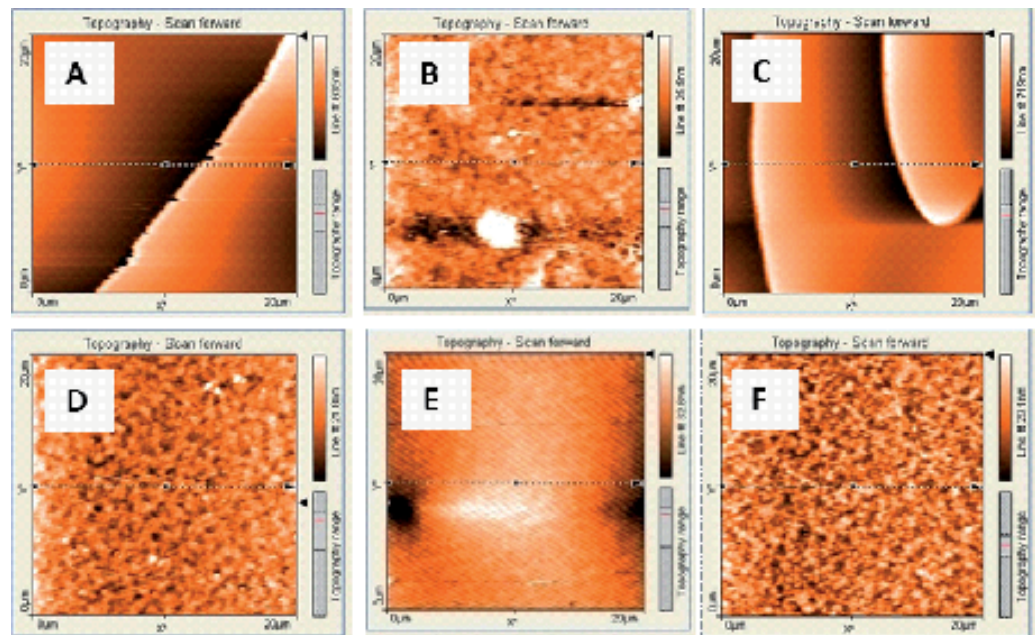
Figure 2: Atomic force microscopy micrograph of TiO$_2$ layer synthesized by spin coating method: a. without aging and without heating, b. without aging but heating at 400∘C, c. with aging for 48 hours without heating, d. with aging for 48 hours and with heating at 400∘C, e. after aging 72 hours but without heatingand f. After aging 72 hours and heating 400°C.

The EDX results (Table 1) show that a thin layer that was heated to 400 °C produced more atomic percentage of Ti and O atoms. This finding indicates that the annealing process enhanced the formation of TiO$_2$ nanoparticles. From EDX elemental mapping performed, the presence of Fe elements indicates that Fe was successfully doped into TiO$_2$ nanoparticles.

Fig. 3 shows the X-ray diffraction pattern of thin film layer of TiO$_2$ synthesized using precursor solution of C$_{16}$H$_{36}$O$_4$Ti that was aged for 48 and 72 hours and annealed at a temperature 400 °C (the same samples with Fig.2d and Fig.2f). From here, it can be clearly seen that the main peak for anatase of (101) and (004) was obtained at a diffraction peak of 25.28 and 37.81° [2]. The diffraction peak obtained is in agreement with the standard for JCPDS of TiO$_2$ anatase (File no 21-1272). From here we can see that finer and smoother obtained for sample prepared at longer aging time of C$_{16}$H$_{36}$O$_4$Ti that is 72 hours. This might due to the fact that the longer aging times provide much more reaction time to produce more TiO$_2$ nanoparticles according to Ostwald ripening process. From the spectra obtained, it can be clearly seen that there is no other TiO$_2$ phase observe in the XRD pattern. The presence of neither Fe element nor Fe alloy was seen in both of the spectra also indicating that the Fe might exist is such small amount. It is expected as the Fe elements trace in the EDX elemental mapping composition is also quite small. This phenomena obtained reflects that the Fe doping in both TiO$_2$nanoparticles prepared at both aging time is successfully performed. The peaks obtained at both 21° and 30.58° are from ITO coated glass substrate (JCPDS file no 88-2160).
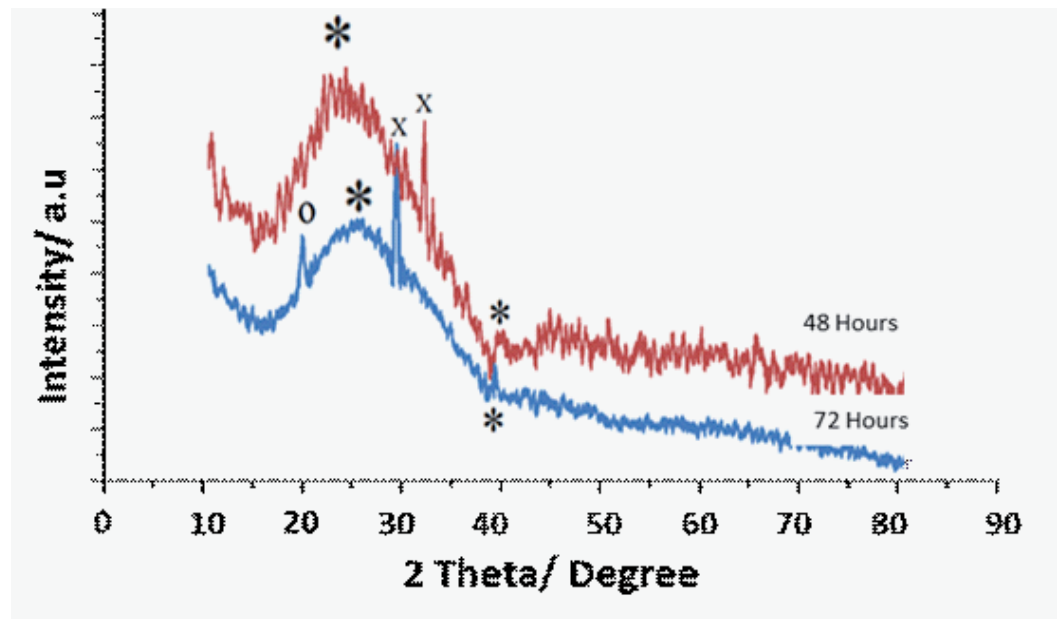
Figure 3: XRD pattern of TiO_2 films synthesized with aging time solution for 48 and 72 hours, both of samples were annealed at 400°C.

4. Conclusion

Fe doped TiO_2 thin film has successfully synthesized using spin coating method by preparing an aged precursor solution of $C_{16}H_{36}O_4Ti$. From this work, it was found that the precursor solution of $C_{16}H_{36}O_4Ti$ aged at 72 hours produced better thin film anatase TiO_2 compared to $C_{16}H_{36}O_4Ti$ aged at 48 hours judging from its AFM image and XRD spectrum. It is expected that the film produced may find use in potential application such as dye sensitized solar cell.

References

[1] G. Liu, J. C. Yu, G. Q. M. Lu, and H.-M. Cheng, Crystal facet engineering of semiconductor photocatalysts: motivations, advances and unique properties, *Chem Commun (Camb)*, **47**, 6763–6783, (2011).

[2] A. A. Umar, M. YA. Rahman, S. K. M. Saad, and M. M. Salleh, Effect of NH3 Concentration on the Performance of Nitrogen doped TiO2 Photoelectrochemical Cell, *Int J Electrochem Sci*, **7**, 7855–7865, (2012).

[3] M. Ouzzine, J. A. Macia-Agullo, M. A. Lillo-Rodenas, C. Quijada, and A. Linares-Solano, Synthesis of high surface area TiO2 nanoparticles by mild acid treatment with HCl or HI for photocataytic propene oxidation, *Applied Catalysis B Environmental*, (2014).

[4] B. Kilic, N. Gedic, S. P. Mucur, and A. S. Hergul, Band gap engineering and modifying surface of TiO2 nanostructures by Fe2O3 for enhanced-performance of dye sensitized solar cell, *J. Mater Sci. Smiconductor Process*, **31**, 363–371, (2015).

[5] S. K. M. Saad, A. A. Umar, M. Y. A. Rahman, and M. M. Salleh, Porous Zn-doped TiO2 nanowall photoanode: effect of Zn2 concentration on the dye-sensitized solar cell performance, *Appl Surf Sci*, **353**, 835–842, (2015).

[6] H. I. Hsiang and S. C. Lin, Effect of aging on nanocrystalline anatase-to-rutile phase transformation kinetics, *Ceram Int*, **34**, 557–561, (2008).

[7] J. Kumar, A. Srivastava, and A. Bansal, Production of self cleaning cement using modified titanium dioxide, Int. J. Innovative Research in Sci, *Eng. And Tech.*, **2**, 2688–2693, (2013).

[8] N. Ghrairi and M. Bouaicha, Structural, morphological, and optical properties of TiO2 thin films synthesized by the electro phoretic deposition technique, *Nanoscale Res Lett*, **7**, p. 357, (2012).

[9] S. Patra, S. Bruyere, P. T. Taberna, and F. Sauvage, Electrodeposition of TiO2 using ionic liquids, *Elecrochemistry Lett*, **3**, D-15–D-18, (2014).

[10] T. H. Meen, J. K. Tsai, Y. S. Tu, T. C. Wu, W. D. Hsu, and S. J. Chang, Optimization of the dye-sensitized solar cell performane by mechanical copression„ **9**, p. 523, (2014).

[11] S. Vyas, R. Tiwary, K. Shubham, and P. Chakrabarti, Study of target effect on the structural, surface and otical properties of TiO2 thin film faabricated by RF sputring method, *Superlattices Microstruct*, **80**, 215–221, (2015).

[12] M. Kavitha, C. Gopinathan, and P. Pandi, Synthesis and characterization of TiO2 nanopowder in hydrothermal and sol-gel method, Int, *J. Adv. Res Tech.*, **2**, 102–108, (2013).

[13] F. Bensouici, T. Souier, A. Iratni, A. A. Dakhel, R. Tala-Ighil, and M. Bououdina, Effect of acid nature in the starting solution on surface and photocatalytic properties of TiO2 thin films, *Surf Coat Tech*, **251**, 170–176, (2014).

KnE Engineering

Knowledge E
Engaging minds

Conference Paper

Numerical Study of Plasmon Resonance Silver Nanoparticles Coated Polyvinyl Alcohol (PVA) using Bohren-Huffman-Mie Approximation

Dede Djuhana[1], Cuk Imawan[1], Vivi Fauzia[1], Adhi Harmoko[1], Windri Handayani[2], and Miftahussurur H. Putra[1]

[1]Departemen Fisika, FMIPA Universitas Indonesia, Depok 16424, Indonesia
[2]Departemen Biologi, FMIPA Universitas Indonesia, Depok 16424, Indonesia

Corresponding Author: Dede
Djuhana; email:
adede.djuhana@sci.ui.ac.id

🔓 **OPEN ACCESS**

Abstract In this study, we have investigated the LSPR spectra of the silver nanoparticles (Ag-NPs) coatedby polyvinyl alcohol (PVA) by means of a numerical study using Bohren-Huffman-Mie (BHMie) approximation. The LSPR of Ag-NPs shifted to red-shift as the diameter size of Ag-NPs and the thickness of PVA increased. The peak of the LSPR spectra exponentially increased as the thickness increased. Interestingly, there have three characteristic of the LSPR spectra, small, intermediate, and large diameter. In small diameter, the dipole resonant mode contributed to the LSPR spectra while in large diameter, the LSPR spectra originated from the quadrupole resonant mode. In contrast to intermediate diameter, the LSPR spectra originated from the competition between the dipole and the quadrupole mode. For this reason, at small and large diameter the LSPR peak has one peak and increased then until a certain thickness showed constant. Different at intermediate diameter, the LSPR peak appeared more one peak with major peak increased then until a certain thickness trend to decrease and minor peak followed at small diameter behavior.

Keywords: Silver nanoparticle, BHMie approximation, PVA coating, dipole and quadrupole expansion

1. Introduction

In decades, the noble nanoparticlesresearch has been a great attention because of its potential application such as electronics, environments, computers, biotechnology, sensors, pharmacy, etc based on the localized surface plasmon resonance (LSPR) effect [1].The silver nanoparticles (Ag-NPs) is a part of the noble nanoparticles has also attracted many researchers since their application in biosensor, biomedical, and, antimicrobial [2]. To maintain the stability of the Ag-NPs for practical purpose, usually Ag-NPs combined with some polymeric composites such as polyvinyl alcohol (PVA), polypyrrole (PPy), carbonxymethyl cellulose (CMC) [3,4], biocompatible molecu-lessuch as bovine serum albumin (BSA) [5,6] and semiconductor such assilica [7]. Numerous studies have been also reported in numerical approximation to investigate the LSPR spectra, such as determining the interaction between Ag-NPs and PVA using density functional theory (DFT) to calculate the binding energy [8], finite different time domain (FDTD)method to produce the LSPR spectra Ag-NPs nanocubes [9], and

the calculation the scattering intensity in the nanoshell model [10,11]. However, there have been little studies in the LSPR spectra to Ag-NPs coated PVA with respect to the thickness of PVA variation.

In this study, we have systematicallyinvestigatedthe LSPR spectra corresponds to the diameter of Ag-NPs and the thickness of PVA variation based on Bohren-Huffman-Mie approximation (BHMie). From this approximation, we can produce the LSPR spectra that consists of the absorption, scattering, and extinction cross section as a function of the wavelength. According to this study, we can analyze the effect of the diameter size of Ag-NPs and the thickness of PVA to the LSPR spectra Ag-NPs.

2. Numerical Method

We have performed the LSPR spectra of Ag-NPs coated PVA by means of BHMie approximation [12,13] which was written in Matlablanguage. According to BHMie, we calculated theabsorptionC_{abs}, scatteringC_{sca}, and extinction C_{ext}cross section as a function of the wavelength function, were written as:

$$C_{sca} = \frac{2\pi}{k^2} \sum_{n=1}^{\infty}(2n+1)(|a_n|^2 + |b_n|^2),$$

$$C_{ext} = \frac{2\pi}{k^2} \sum_{n=1}^{\infty}(2n+1)\Re(a_n + b_n),$$

$$C_{abs} = C_{ext} - C_{sca}$$

(1)

with

$$a_n = \frac{\psi_n(y)[\psi'(m_2 y) - A_n\chi'_n(m_2 y)] - m_2\psi'_n(y)[\psi_n(m_2 y) - A_n\chi_n(m_2 y)]}{\xi_n(y)[\psi'_n(m_2 y) - A_n\chi'_n(m_2 y)] - m_2\xi'_n(y)[\psi_n(m_2 y) - A_n\chi_n(m_2 y)]}$$

$$b_n = \frac{m_2\psi_n(y)[\psi'_n(m_2 y) - B_n\chi'_n(m_2 y)] - \psi'_n(y)[\psi_n(m_2 y) - B_n\chi_n(m_2 y)]}{m_2\xi_n(y)[\psi'_n(m_2 y) - B_n\chi'_n(m_2 y)] - \xi'_n(y)[\psi_n(m_2 y) - B_n\chi_n(m_2 y)]}$$

$$A_n = \frac{m_2\psi_n(m_2 x)\psi'_n(m_1 x) - m_1\psi'_n(m_2 x)\psi_n(m_1 x)}{m_2\chi_n(m_2 x)\psi'_n(m_1 x) - m_1\chi'_n(m_2 x)\psi_n(m_1 x)}$$

$$B_n = \frac{m_2\psi_n(m_1 x)\psi'_n(m_2 x) - m_1\psi_n(m_2 x)\psi'_n(m_1 x)}{m_2\psi_n(m_1 x)\chi'_n(m_2 x) - m_1\chi_n(m_2 x)\psi'_n(m_1 x)}$$

(2)

where $k^2 = \omega^2\mu$, $x = kD$, $y = k(t+D)$, m_1 and $m_2$denoted the refractive index Ag-NPs and coating PVA respectively, and the functions ψ_n, $-\xi_n$, and $\chi_n$were Ricatti-Bessel function. In this study, we used a single sphere model of Ag-NPs and coated by PVA. The diameter D of Ag-NPs was varied from 20 nm to 100 nm and the thickness t of PVA was from 10 nm to 200 nm. The property of dielectric constant Ag-NPs used from Palik's experiment [14], the refractive index of PVA was n_{PVA} = 1.531 [15], and the refractive index of the medium was n_a = 1.3334 [16]. The illustration model of Ag-NPs coated by PVA is shown as Fig. 1.

3. Results and Discussion

Fig. 2 showed the LSPR spectra of Ag-NPs, the absorption, scattering, and extinction as a function of the wavelength from D = 20 nm to 100 nm with respect to the thickness of
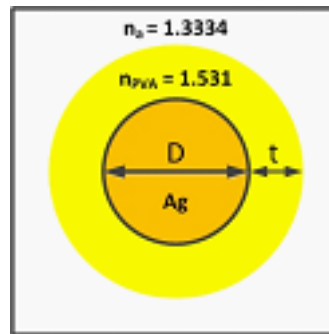
Figure 1: The illustration model of the Ag-NPs coated by PVA, *D* is diameter of Ag-NPs, *t* is the thickness of PVA, n_{PVA} is the refractive index of PVA and n_a is the refractive index of medium.

PVA. The LSPR spectra exhibited shifting to larger wavelength or red-shift as the size of Ag-NPs and the thickness of PVA increased. Similar observations were also reported by Ananth [6] and Mbhele [17]. The red-shift phenomenon of the LSPR Ag-NPs was simply can examined by scattering [18]. Increasing the particle size will increase the scattering process and the external driving field becomes non uniform across each particle. For this reason, the peak LSPR spectra will shift to larger of wavelength or red-shift.

Next, we have also determined the peak of LSPR spectra based on Fig. 2 and were plotted as the thickness of PVA which was given in Fig. 3. The peak of LSPR was obtained from the absorption cross section with reason it was simply determined than scattering or extinction cross section. As look details, we have observed that the LSPR spectra can be divided by three regions. First region located in small diameter (D = 20-50 nm) with the LSPR spectra showed one peak. Second region in intermediate diameter (D = 60-80 nm) with the peak of LSPR showed one more peak, first peak appeared at low wavelength and second peak at high wavelength. Third region in large diameter (D > 80 nm) and the peak of LSPR became one peak again. Furthermore, it was found that the peak of LSPR spectra exponentially increased as the thickness of PVA increased. Similar pattern was also reported by Chumanov [19]. In the case of small and larger diameter, the peak of LSPR spectra increased then until a certain thickness exhibited constant. In contrast to intermediate diameter, the peak of LSPR spectra increased then until a certain thickness of PVA trend to decrease. The peak of LSPR showed higher than small and large diameter for the second peak and relatively same for the first peak. Further analyzed, we have found the dipole and quadrupole resonant mode contributed to the LSPR spectra of Ag-NPs coated PVA. For small diameter, the plasmonic resonant mode was dominantly first-order quasi-static dipole. The electromagnetic energy caused the electron cloud displacement forming the dipole field in the particle. At this condition, the external driving field relatively showed uniform and the absorption process was more dominant. So, it was clear the peak of LSPR appeared only one peak. Then, increasing the particle size, the interaction between the incident energy with the particles produced the external driving field was not uniform. Therefore, the dynamic depolarization happened in the particle and the second-order LSPR such as quadrupole resonant mode will contribute to the LSPR spectra. Thus, the dipole and the quadrupole resonant mode attributed the LSPR spectra at intermediate
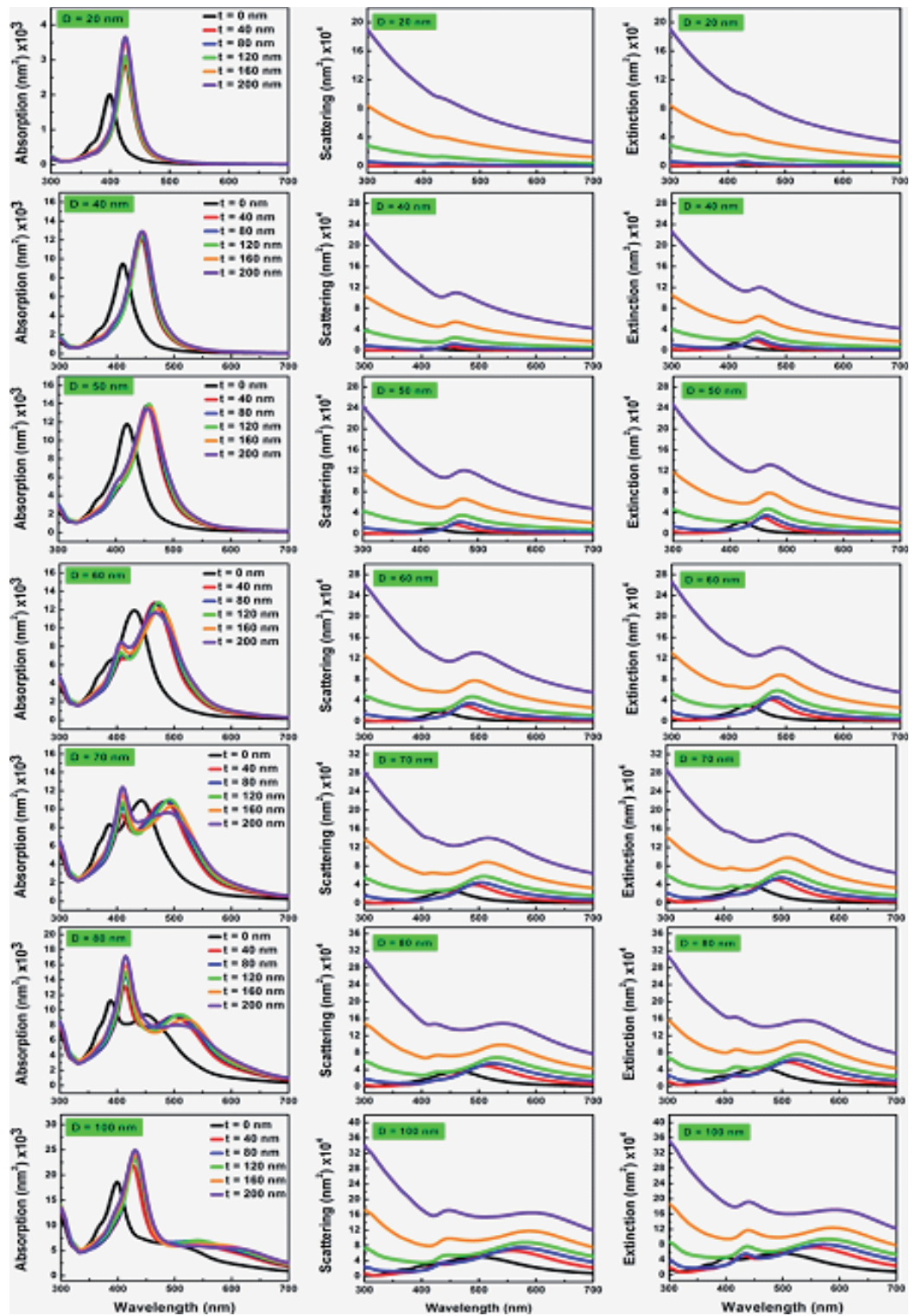
Figure 2: The LSPR spetra of Ag-NPs coated PVA from diameter D = 20 nm to D = 100 nm with respect to PVA thickness variation from t = 10 nm to t = 200 nm.

diameter. Consequently, one more peaks was found in the LSPR spectra. Then, the quadrupole resonant mode became dominant in the LSPR spectra in large diameter [20].
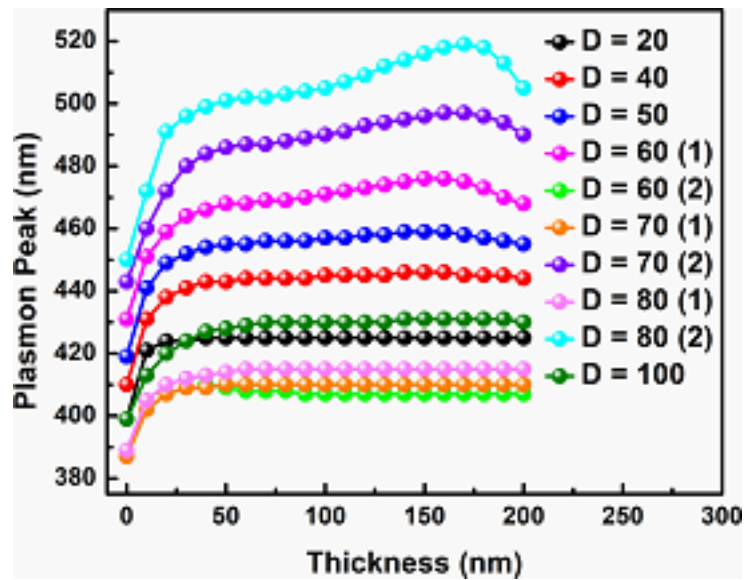
Figure 3: The peak of the LSPR spectra of Ag-NPs coated PVA with respect to diameter of Ag-NPs (D = 20-100 nm) and thickness of PVA variation (t = 0-200 nm).

4. Conclusions

In conclusions, we have systematically investigated the LSPR spectra of Ag-NPs coated PVA by means of numerical study based on BHMie approximation. The LSPR spectra shifted to red-shift as the diameter and the thickness increased. It was found the LSPR spectra showed three characteristic for small, intermediate, and large diameter. At small diameter, the dipole resonant mode contributed to the LSPR. At intermediate diameter, the dipole and the quadrupole resonant mode competed to the LSPR spectra. At large diameter, the quadrupole resonant mode was dominant to the LSPR spectra. Consequently, the LSPR spectra showed one peak at small and large diameter and more one peak at intermediate diameter.

5. Acknowledgements

References

[1] E. Hutter and J. H. Fender, Explotation of localized surface plasmon resonance, *Adv Mater*, **16**, 1685–1706, (2004).

[2] Q. H. Tran, V. Q. Nguyen, and A. T. Le, Silver nanoparticles: synthesis, properties, toxicology, application and perspective, *Adv. Nat. Sci. Nanosci. Nanotechnol.*, **4**, p. 033001, (2013).

[3] H. K. Citte, N. V. Bhart, N. S. Karmakar, D. C. Kothari, and G. N. Shinde, Synthesis and characterization of polymeric composites embedded with silver nanoparticles, *World J Nano Sci Eng*, **2**, 19–24, (2012).

[4] M. Ghanipour and D. Dorranian, Effect of Ag-nanoparticles doped in polyvinyl alcohol on the structural and optical properties of PVA films, *J Nanomater*, **1155**, 1–10, (2013).

[5] A. J. Singh, B. M. Bandgar, M. Kasture, B. LV. Prasad, and M. Sastry, Synthesis of gold, silver and their alloy nanoparticles using bovine serum albumin as foaming and stabilizing agent, *J Mater Chem*, **15**, 5115–5121, (2005).

[6] A. N. Ananth, S. C. Daniel, T. A. Sironmani, and S. Umapathi, PVA and BSA stabilized silver nanoparticles based surface-enhanced plasmon resonance probes for protein detection, *Colloids Surf B Biointerfaces*, **85**, 138–144, (2011).

[7] Y. Kobayashi, H. Katakami, E. Mine, D. Nagao, M. Konno, and L. M. Liz-Marzán, Silica coating of silver nanoparticles using a modified Stober method, *J Colloid Interface Sci*, **283**, 392–396, (2005).

[8] H. L. Chou, C. M. Wu, F. D. Lin, and J. Rick, Interaction between silver nanoparticles and polyvinyl alcohol nanofibes, *AIP Adv*, **4**, p. 087111, (2014).

[9] L. J. Sherry, R. Jin, C. A. Mirkin, G. C. Schatz, and R. P. Van Duyne, Localized surface plasmon resonance spectroscopy of single silver triangular nanoprisms, *Nano Lett*, **6**, 2060–2065, (2006).

[10] H. Suzuki and I. S. Lee, Calculation of the Mie scattering field inside and outside a coated spherical particles, *Int J Phys Sci*, **3**, 38–41, (2008).

[11] A. L. Aden and M. Kerker, Scattering of electromagnetic waves from two concentric spheres, *J Appl Phys*, **22**, 1242–1246, (1951).

[12] G. Mie, Beiträge zur optic trüber medien, speziell kolloidaler metallösungen, *Ann Phys*, **25**, 377–445, (1908).

[13] C. F. Bohren and D. R. Huffman, in *Absorption and scattering of light by small particles*, 181–219, Wiley-Interscience Publication, John Wiley & Sons, 1983.

[14] E. D. Palik, in *Handbook of optical constant of solids I*, 350–357, Academic Press, 1997.

[15] R. Kumar, A. P. Singh, A. Kappor, and K. N. Tripathi, Fabrication and characterization of polyvinyl-alcohol-based thin-film optical waveguides, *Opt Eng*, **43**, p. 2134, (2004).

[16] H. Chen, X. Kou, Z. Yang, W. Ni, and J. Wang, Shape- and size-dependent refractive index sensitivity of gold nanoparticles, *Langmuir*, **24**, 5233–5237, (2008).

[17] Z. H. Mbhele, M. G. Salemane, C. C. E. van Sittert, J. M. Nedeljković, V. Djoković, and A. S. Luyt, Fabrication and characterization of silver-polyvinyl alcohol nanocomposites, *Chem Mater*, **15**, 5019–5024, (2003).

[18] C. Tabor, R. Murali, M. Mahmoud, and M. A. El-Sayed, On the use of plasmonic nanoparticle pairs as a plasmon ruler: the dependence of the near-field dipole plasmon coupling on nanoparticle size and shape, *J Phys Chem A*, **113**, 1946–1953, (2009).

[19] D. D. Evanoff Jr and G. Chumanov, Synthesis and optical properties of silver nanoparticles and arrays, *Chem Phys Chem*, **6**, 1221–1231, (2005).

[20] J. P. Clarkson, J. Winans, and P. M. Fauchet, On the scaling behavior of dipole and quadrupole modes in coupled plasmonic nanoparticles pairs, *Opt Mater Express*, **1**, 970–979, (2011).

KnE Engineering

Knowledge E
Engaging minds

Conference Paper

Effect of Methylammonium Iodide (CH$_3$NH$_3$PbI$_3$) Perovskite Concentration on the Performance of Perovskite Solar Cell

AltafYahya AL-she'irey, Akrajas Ali Umar, Muhamad Mat Salleh, and MohdYusriAbd Rahman

institute Micro Engineering and Nanoelectronics, UniversitiKebangsaan Malaysia, 43600, BangiSelangor, Malaysia

Abstract The effect of Methylammonium Iodide (CH$_3$NH$_3$PbI$_3$) perovskites(MIP) concentration on the performance of perovskites sensitized solar cell (PSC) was studied. Three MIP concentrations, namely 0.2, 0.4, and 1.0 M were prepared. In this study PSC with a sandwich structure of ITO/TiO$_2$/ MIP /electrolyte/ Pt film was fabricated for this purpose. It was found that power conversion efficiency (PCE) increased with the increasing the concentration of MIP, from 0.01 to 0.21% as the concentration increase from 0.2 to 1.0 M. Photoluminescence (PL) study showed that the increase of the MIP concentration decrease therecombination of carrier in the device. Electrochemical impedance spectroscopy (EIS) analysis also shows that with the increased of MIP concentration results in the decreased of the R$_{ct}$ due to the improvement of the carrier transport in the devices.

Keywords: Perovskite Solar Cell, CH$_3$NH$_3$PbI$_3$, TiO$_2$microtablet

Corresponding Author:
AltafYahya AL-she'irey;
email:
aaltaf_yahya2006@yahoo.
com

1. Introduction

Perovskite material such as (CH$_3$NH$_3$PbI$_3$) is one of the most important candidates for high absorber materials in thin film photovoltaic (PV) applications. This material demonstrates many interesting properties including high absorption coefficient, direct bandgap, high stability, and high carrier mobility. Perovskite can be fabricated by mixing(CH$_3$NH$_3$I) with PbI$_2$indimethylformamide. It absorbs light very strongly from visible region to near infrared region. A perovskite solar cell has so far generated power conversion efficiency as high as 15% [1, 2]. Owing to its excellent optical properties, perovskite could be used as sensitizer in the dyesensitizes solar cell (DSSC) system. In this work, we study the effect of MIP concentration on the power conversion of the DSSC with structure of ITO/TiO$_2$/ MIP /electrolyte/ Pt. It was found out that the efficiency increased with increasing of the MIP concentration. The device fabrication and its performance relationship with the concentration will be discussed.

🔓 **OPEN ACCESS**

2. Experiment

2.1. Preparation of TiO_2 microtablet

TiO_2 microtablet on ITO substrate was prepared using a liquid phase deposition method at room temperature by immersing a cleaned ITO substrate into a growth solution that contains 5 mL of 0.5 M ammonium hexafluorotitanate($(NH4)_2$ TiF_6) purchased from Sigma - Aldrich), and 5 mL of 1.0 M Boric Acid, (H_3BO_3, RM Chemicals). The substrate was positioned vertically in the solution by hanging the substrate with an adhesive tape. The reaction was kept undisturbed for 4h. After that, the substrate was taken out from the solution and washed with a copious amount of pure water. Then, the sample was annealed at 400 °C for l h to obtain an anatase phase.

2.2. Preparation of $CH_3NH_3PbI_3$

The $CH_3NH_3PbI_3$ perovskite was prepared using the following step. Firstly,30 mL of hydro iodic acid and 27.8 ml methylaminewere mixed together and stirred in ice bath for 2 h. The resulting solution was then evaporated by using a rotatory evaporator operated at 50°C for 2h. The powder of CH_3NH_3I was then obtained using this approach. The powder was wash for three times in diethyl ether, and then dried under vacuum for 1 h. To prepare the MIP with different concentration,0.1 g of CH_3NH_3I was mixed with different concentration of PbI_2, namely 0.2, 0.4, and 0.1M, in 20 mL dimethylformamide where the reaction was carried out for 15 h at 60 °C.

2.3. PSC device

PSC with structure of ITO /TiO_2/ perovskite/ electrolyte /Pt was fabricated. Prior to the reaction, preferably the perovskite was deposited onto the TiO_2 microtablet by immersing the TiO_2 modified ITO substrate into the perovskite solution for 1h at room temperature. By taken the sample out and dried on a hotplate at 50°C for 15 min, thin film of perovskitewas successfully grown on TiO_2 microtablet. The PSC device was then prepared by clamping the substrate together with a Pt nanostructure electrode grown on ITO substrate(thickness approximately150nm). An electrolyte containing iodide/triiodide redox couplewas then injected into the space between the platinum counter electrode and the photoanode. The active area of the cell was 0.25cm^2.

3. Result and Discussion

We have successfully grown the TiO_2 microtablet on the ITO surface using the LPD method (see Fig.1A). From the Fig. 1A it can be seen that the TiO_2 microstructure actually composed ofuniquely quasi square shape of a tablet-like structure that grow
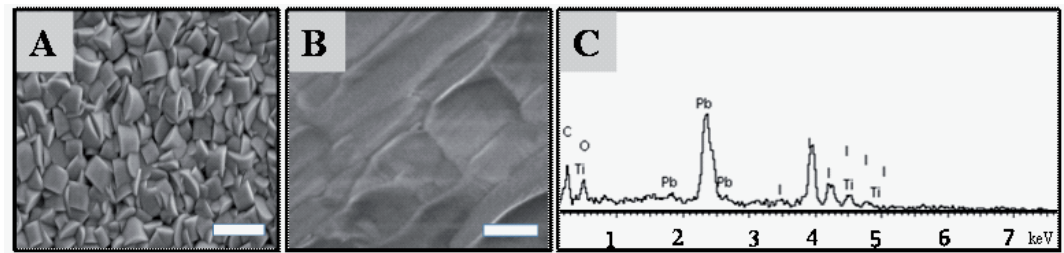
Figure 1: FESEM image of TiO_2microtablet(A) and TiO_2–covered MIP(B). (C) EDX result of TiO_2covered MIP. Scales bar is 2 μm in A and B, respectively.

$CH_3NH_3PbI_3$ concentration (M)	η(%)	J_{sc} (mA/cm^2)	V_{oc} (V)	FF	R_s (Ωcm^{-2})	R_{ct} (Ωcm^{-2})
0.2	0.01	1.59	0.38	0.01	114	1891
0.4	0.05	1.06	0.54	0.09	104	1820
1.0	0.21	0.3	0.46	1.52	109	1228

TABLE 1: Photovoltaic parameters of $CH_3NH_3PbI_3$ with three different concentrations as sensitizer for PSC device.

in high density on the substrate surface. These compactly grown microtablets are randomly arranged on the substrate surface without a particular orientation growth. As also can be seen in the Fig.1A the TiO_2microtablet has covered the ITO surface without the presence of any crack or open surface. The average diameters and thickness of TiO_2microtablet was found to be ca. 2.78 and ca. 4.35 μm, respectively. The thickness obtained for TiO_2microtablet in this study is suitable for DSSC application [1,5]. Thus, we expect promising performance can be achieved utilizing TiO_2microtablet as pho-tovoltaic material for DSSCs application. Fig.1 B shows the FESEM images of the MIP layer grown on the TiO_2microstructure thin film. As can be seen from image, the MIP layer homogeneously covers the TiO_2microtablet, leaving no exposed TiO_2structure. This condition should be useful for DSSC application [9].

The energy dispersive X-ray (EDX) spectrometry has been used to verify the forma-tion of MIP TiO_2microtablet (Fig.1C). As the Fig.1C reveals, there are three main peaks which are related to the elements exists in the perovskite structure of $CH_3CH_2PbI_2$ namely C, Pb and I. Other than these three main elements, the peaks represent Ti and O elements were also observed in the EDX spectrum. From the spectrum, we can conclude that the sample prepared is in high quality as no peaks related to the impurities were observed.

TiO_2microtablet was then used as photoanode in the study of the effect of MIP concentration on the performance of the PSC. Figure 2 shows typical PSC, utilizing three different concentration of MIP response under a simulated AM 1.5G sunlight irradiation. The photovoltaic parameters of PSC are recorded in table 1. As can be seen from Figure 2, the PCE increased with the increasing of MIP concentration .The highest performance was obtained using MIP with concentration of 1M with PCE recorded for this device is 0.21 %.The increase of the performance can be associated with the decreasing of
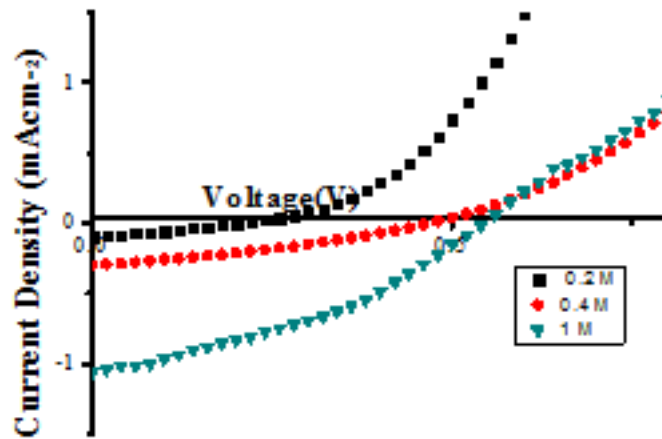
Figure 2: ($J-V$) characteristics of $CH_3NH_3PbI_3$ with different concentrations as sensitizer for PSC device.
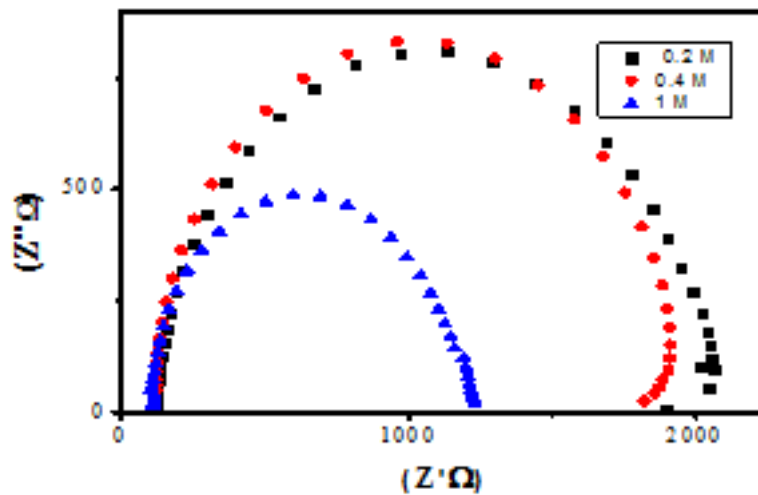
Figure 3: EIS spectra of $CH_3NH_3PbI_3$ with different concentrations as sensitizer for PSC device.

device R_{ct} resistance (discussed later in EIS section). However, the performance of the device dramatically drops when MIP with concentration higher than 1M was used. At this condition, the quality of the thin film is low, causing a high recombination rate and the series resistance [3,6] contributing the decrease in PCE of the device.

EIS measurement was carried out to confirm these phenomena. Figure 3 shows a typical Nyquist plot for impedance spectra of TiO_2 microtablet based PSC device with different concentration of MIP. The frequency use is from 0.1 to 10^6 Hz with alternating current (ac) amplitude of 400 mV. Here, we will denote that the charge transfer resistance (R_{ct}) is attributed to the charge transfer process at the interface between TiO_2 /perovskite layer/ electrolyte. From the spectra we can see that the R_{ct} decreased
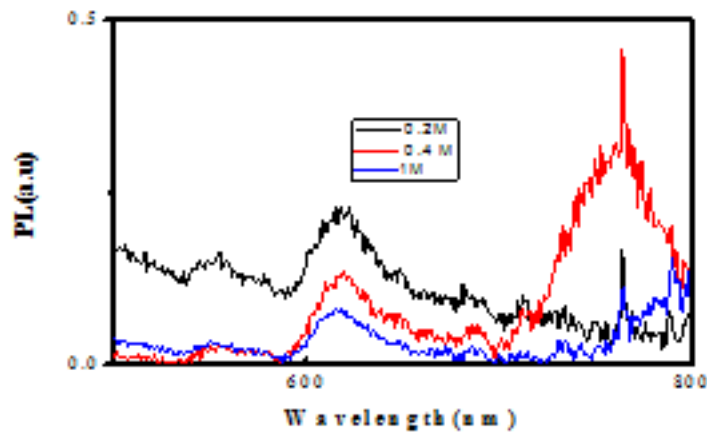
Figure 4: PL spectra of $CH_3NH_3PbI_3$ perovskite with various MIP concentrations as sensitizer in PSC device.

with the increasing of the concentration of MIP. The low R_{ct} for the device utilizing 1.0 M MIP indicates lower recombination phenomena that will contribute to a higher lifetime of exciton in the device [7].

To further verify the recombination phenomena of MIP as a sensitizer on TiO_2 microtablet PSC device, we carried out the photoluminescence (PL) characterization. The characterization was carried out using an excitation wavelength of 300 nm. The PL spectra of PSC device with different concentration of MIP are shown Fig. 4. PL analysis confirmed that the recombination is decrease with the increase of MIP concentration. This can be seen by the decreasing of the PL intensity upon the increase of MIP concentration, indicated by the decreasing of red emission as concentration of MIP layer increased .The decreasing of the red emission also indicates the MIP layer of higher concentration has a good crystal quality [8]. Besides, PL curves quenching behavior when MIP layer with higher concentration used shows a good charge transport process, leading to a higher performance of PSC device [4, 5].

4. Conclusion

We found that the performance of PSC increases with the increasing of the MIP concentration. EIS and PL analysis shows that by effectively incorporating MIP into PSCresulthigh excitonlife time and lowers the recombination. Thus, improved performance of the PSC device is achieved.

References

[1] Q. Chen, H. Zhou, Z. Hong, S. Luo, H. S. Duan, H. H. Wang, Y. Liu, G. Li, and Y. Yang, Planar heterojunction perovskite solar cells via vapor-assisted solution process, *J Am Chem Soc*, **136**, 622–625, (2014).

[2] W. Abu Laban and L. Etgar, *Energy Environ Sci*, **6**, 3249–3253, (2013).

[3] A. A. Umar, S. Nafisah, S. K. M. Saad, S. T. Tan, A. Balouch, M. M. Salleh, and M. Oyama, *Sol Energy Mater Sol Cells*, **122**, 174–182, (2014).

[4] C. R. Li, H. T. Deng, J. Wan, Y. Y. Zheng, and W. J. Dong, Photoconductive properties of organic–inorganic hybrid perovskite (C6H13NH3)2(CH3NH3)m−1PbmI3m+1:TiO2 nanocomposites device structure, *Mater Lett*, **64**, 2735–2737, (2010).

[5] J. You, Z. Hong, Y. Yang, Q. Chen, M. Cai, T. Bin Song, C. Chao Chen, S. Lu, Y. Liu, H. Zhou, and Y. Yang, *Nano Lett*, (2014).

[6] H. S. Kim, C. R. Lee, J. H. Lm, K. B. Lee, T. Moehl, A. Marchioro, S. J. Moon, R. H. Baker, J. H. Yum, J. E. Moser, and M. Gratzel, *Sci Rep*, **2**, p. 3, (2012).

[7] V. Dhas, S. Muduli, S. Agarkar, A. Rana, B. Hannoyer, R. Banerjee, and S. Ogale, *Sol Energy Mater Sol Cells*, **85**, 1213–1219, (2011).

[8] G. Maculan, A. D. Sheikh, A. L. Abdelhady, M. I. Saidaminov, M. A. Haque, B. Murali, E. Alarousu, O. F. Mohammed, T. Wu, and O. M. Bakr, CH3NH3PbCl3 Single Crystals: Inverse Temperature Crystallization and Visible-Blind UV-Photodetector, *J Phys Chem Lett*, **6**, 3781–3786, (2015).

[9] L. Etgar, P. Gao, Z. Xue, Q. Peng, A. K. Chandiran, B. Liu, M. K. Nazeeruddin, and M. Grätzel, Mesoscopic CH3NH3PbI3/TiO2 heterojunction solar cells, *J Am Chem Soc*, **134**, 17396–17399, (2012).

KnE Engineering

Knowledge E
Engaging minds

Conference Paper

Transmission Electron Microscopy Study of Magnetic Domain of Cobalt-Samarium Thin Films Fabricated Using DC Magnetron Sputtering Technique

Erwin Amiruddin[1] and Adhy Prayitno[2]

[1]Department of Physics Faculty of Mathematics and Natural Sciences Riau University, KampusBinaWidyaSimpangBaru, Tampan, Pekanbaru, Riau - Indonesia 28293
[2]Department of Mechanical Engineering Faculty of Engineering Riau University, KampusBinaW-idyaSimpangBaru, Tampan, Pekanbaru, Riau - Indonesia 28293

🔓 **OPEN ACCESS**

Abstract Alloys of cobalt samarium (Co-Sm) in the form of thin films were fabricated using dc magnetron sputtering technique. The films were fabricated as a function of samarium concentration ranging from 0 to 28 at.% in order to investigate the relationship between microstructure, coercivity and magnetic domain structure. Magnetic domain structures in the films have been studied by Lorentz microscopy using transmission electron microscopy (TEM). In this technique, the TEM was operated in the defocused mode. The results show that the magnetic image of $Co_{90}Sm_{10}$ film has fairly coarse structure with magnetization ripple and the domains ranging over 200-300 nm. The domain size is much larger than the grain size of $Co_{90}Sm_{10}$ film. The "multiparticle" or interaction domains suggested that there is strong exchange coupling between the magnetization of the neighbouring grains inside each of them. The hysteresis loop for this film shows a small coercivity with high magnetization value and high loop squareness, indicating a greater proportion of magnetic material.

Keywords: CoSm thin films, coercivity, magnetization, domain, and loop squareness

1. Introduction

The relationship between microstructure and magnetic anisotropy or coercivity in magnetic materials with magnetic domain configuration especially when the materials in the form of thin films has long been a subject of interest for their potential applications such as high density magnetic recording media. According to previous researcher [1] magnetic recording media for high-density magnetic data storage with low noise require a material consisting of small and magnetically isolated grains. In small grain sizes of about 10 nm or below, high magnetocrystalline anisotropy is needed in order to avoid thermal fluctuation that tends to destabilize the magnetization of the recorded bits [2]. Early attempts to grow CoSm alloys in the form of thin films exhibiting large coercivity values and could be used as a high-density magnetic recording medium were carried out by some researchers [3]. Some recording experiments have been investigated, for example, by Velu and Lambeth [4] and Velu *et al.* [5]. However,

How to cite this article: Erwin Amiruddin and Adhy Prayitno, "Transmission Electron Microscopy Study of Magnetic Domain of Cobalt-Samarium Thin Films Fabricated Using DC Magnetron Sputtering Technique," *KnE Engineering*, vol. 2016, 8 pages. DOI 10.18502/keg.v1i1.503

Page 1

the growth characteristics of CoSm alloys including the concentration range [6], the epitaxial relation between CoSm alloy films and underlayer materials [7], interaction effects [8], and the magnetic switching volume [9] suggest that improved magnetic properties of CoSm films could be obtained by utilization and optimisation of appropriate deposition conditions.

It is well known that magnetic properties of thin magnetic layers have predominantly affected by several parameters such as preparation conditions, films fabrication methods and utilization of underlayer materials. In order to obtain high density magnetic recording with low noise media it is necessary to have thin films with high coercivityandloop squareness and reduced magnetic domain size. Therefore, understanding domain size relationship with coercivity is one of the important steps in further development of high density magnetic recording media. The morphology of rich non magnetic phase and magnetic domain configuration are important since these phase can act as the nucleation sites of reverse domains. This phenomenon should be understood in order to obtainthe best method in developing higher coercivity values of magnetic thin films. Observed magnetic domain structure is one of the methods to studythe mechanisms of magnetic reversal in magnetic thin films. Previous researcher [10] have studied and observed magnetic domains of some ferromagnetic alloys in the form of thin films. Observations and analyses of magnetic domain structure for thin films have been studied by variety of method [11,12].

2. Experimental Procedures

Alloys of cobalt samarium in the form of thin films were fabricated by depositing Sm and Co onto Si (100) substrates using dc magnetron sputtering technique at JOULE laboratory Salford University UK. The magnetron sputtering system that has been used in this work was an Ion Tech 2000 UHV Deposition System available at Salford University. A pneumatically actuated gate valve isolates these two chambers. The sputtering system has a rotating carousel and shutters controlled by computer and able to fabricate the films with varying input power for Co and Sm targets. The pressure inside the sputtering chamber prior to deposition was 5×10^{-8} mbar. The films were fabricated as a function of samarium concentration ranging from 0 to 40 at. % under the sputtering condition of $12 \times 10^{--3}$ mbar argon gas pressure. The base pressure inside the sputtering chamber prior to deposition was 5×10^{-8} mbar.Magnetic domain structures in the films have been studied by Lorentz microscopy using transmission electron microscopy (TEM, JEOL 3010, with in situ ion beam bombardment for radiation damage studies). In this technique, the TEM was operated in the defocused mode. The compositions of CoSm films were analysed by energy dispersive spectroscopy (EDS). Magnetic properties such as coercivity (Hc), loop squareness (S) of the films were measured using alternating gradient force magnetometer (AGFM).

3. Result and Discussion
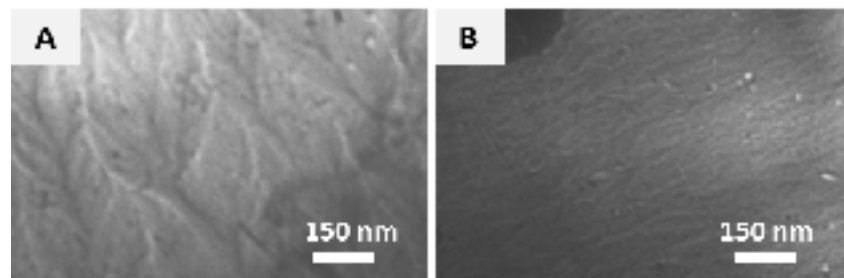
Figure 1: Magnetic domain structure of (a) $Co_{90}Sm_{10}$ and (b) $Co_{80}Sm_{20}$ films observed using Lorentz microscopy.

3.1. Magnetic Domain Structure

The effects of the CoSm film composition on magnetic domain structure are analysed through the Lorentz microscopy technique using electron transmission microscopy (TEM). In this technique, the TEM was operated in the defocused mode. Figure 1A and (B) show Lorentz microscopy images for $Co_{90}Sm_{10}$ and $Co_{80}Sm_{20}$ thin films respectively. The magnetic image of $Co_{90}Sm_{10}$ film shows a fairly coarse structure with magnetization ripple and the domains ranging over 200-300 nm. Here the domain size is much larger than the grain size of $Co_{90}Sm_{10}$ film (Fig. 2). The "multiparticle" or interaction domains shown in Fig.1a suggest there is strong exchange coupling between the magnetization of the neighbouring grains inside each of them. The hysteresis loop for this film (Fig. 4A) shows a small coercivity with high magnetization value and high loop squareness, indicating a greater proportion of magnetic material. The film with increased Sm concentration exhibits a very fine micromagnetic structure with less well defined magnetic domains and domain walls. This can be seen in Fig. 1B.

3.2. Microstructural Properties of Samples

The TEM image shown in Fig 2A reveals the detailed microstructure of a $Co_{90}Sm_{10}$ film. The grains are non-uniform with irregular shapes and are identified by similar lattice fringes observed in the HRTEM image. Each grain is separated from the adjacent grain by grain boundaries labelled by letters GB. These grain boundaries are several nmin width, have darker contrast and are supposed to contain amorphous material without an obvious crystal structure. This film contains small crystals (nanocrystals) with lattice fringes as indicated by arrows.$Co_{80}Sm_{20}$ films show remarkably different grain morphology as shown in Fig. 2B. The film contains smaller (3-5 nm) size nanocrystals with distorted lattice fringes surrounded by disordered material as indicated by arrows. The electron diffraction pattern from this film shown diffuse rings characteristic of amorphous material.Moreover, it is clear that lattice fringes become less visible as Sm concentration is increased, indicating a highly defective increasingly amorphous state. Further increase of Sm concentration leads the distorted lattice fringes to completely disappear as shown in Fig.2C. This indicates that at higher Sm concentration the film becomes almost completely amorphous. This result is supported by the selected area diffraction patterns inserted in Fig. 2C showing extremely diffuse rings. The decrease
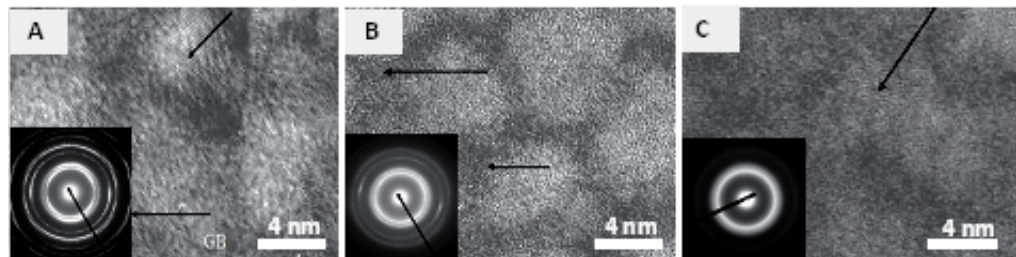
Figure 2: TEM image of (A) $Co_{90}Sm_{10}$ film showing the crystallites in the amorphous matrixwith grain boundaries labelled by letters GB, (B) $Co_{80}Sm_{20}$ film showing more uniform grains which are well separated from their neighbours and (C) $Co_{72}Sm_{28}$ thin film. Arrow indicates nanocrystals.

in the coercivity of CoSm films for Sm concentration beyond 20 at. % is attributed to the inception and completion of the amorphous state.

3.3. Magnetic Properties

The magnetic properties such as coerciviy of the CoSm thin films were obtained from alternating gradient force magnetometry (AGFM) measurement. Fig. 3 shows the important effect of Sm concentration on the coercivity of CoSm thin films. As seen with an initial increase of samarium concentration, the coercivity increases and reaches a maximum value at around 19 - 22 at. % Sm, followed by a decrease with further increase in Sm concentration. Thecoercivity maximum at 19 - 22 at. % Sm was found to lie between the crystalline Co_5Sm and Co_7Sm_2 compound compositions.

The convex dependence of coercivity on the samarium concentration is governed by several mechanisms depending on samarium concentration of the films. In the range between 0 and 20 at. % Sm, the average grain size increases slightly as shown in the TEM micrographs in Fig. 2, while the grain separation also increases with the addition of Sm concentration from 0 to 20 at.%. The grain distribution for the film with Sm concentration of 20 at. % is more uniform than that of film with lower Sm concentrations i.e., 10 at. %. Moreover, the degree of crystallinity decreases as Sm concentration is increased. Thus the increase of coercivity in this range can be qualitatively understood in terms of the combined effect of initial increase in size of relatively tightly coupled grains followed by the increase in grain separation, which ultimately reduces exchange coupling between weakly coupled grains or clusters and uniformly sized grains. However, in the rangebetween 20 and 40 at. % Sm, the size continues to decrease. This result is supported by the selected area diffraction (SAD) pattern where the diffraction rings become broader inserted in Fig.2, suggesting that the degree of crystallinity decreases as Sm concentration is increased. This effect could certainly lead to the decrease in the coercivity for the films with Sm concentration of more than 20 at. %. Moreover, the convex dependence of coercivity on Sm concentration could be related to retained regions of the $Co_{17}Sm_2$, Co_5Sm and Co_7Sm_2phases. These are marked on Fig. 3. The highest value of the coercivity of CoSm thin films which is obtained in the region around $Co_{80}Sm_{20}$ is close to the putative Co_5Sm and Co_7Sm_2 phase boundary.
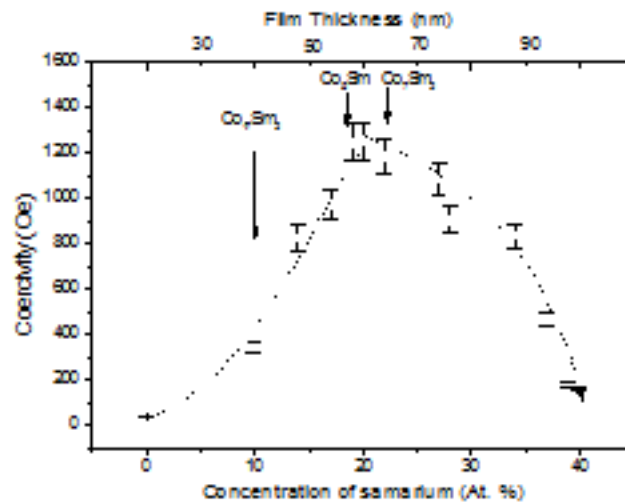
Figure 3: The coercivity of $Co_{100-x}Sm_x$ thin film as a function of Sm concentration (at. %).

Figure 4 shows typical hysteresis loops measured by AGFM for three representative compositions of $Co_{100-x}Sm_x$ alloy thin films; for x =10 the film exhibits low coercivity, x = 20 gives high coercivity and x = 40 much lower coercivity. For the film with low samarium concentration (10 at. % Sm) shown in Fig. 4 (a), the coercivity is small (340 Oe). The hysteresis loop is almost square with squareness or remanenceratio (M_r/M_s) of nearly unity. As already stated, when the concentration of samarium is increased to 20 at.%, the coercivity is at its highest (1254 Oe) with a remanence ratio less than unity as shown in Fig 4(b). Fig. 4(c) shows the hysteresis loop for a film with samarium concentration of about 40 at.% which corresponds to a coercivity of 160 Oe. It is worth noting that in this hysteresis loop the squareness is much less then unity and contrasts strongly with that in Fig 4(a).

The variation in hysteresis loop squareness (S) as a function of the Sm concentration of the films is shown in Fig. 5. The loop squareness is found to decrease as the Sm concentration is added. One possible mechanism for the higher S values in low Sm concentrations is a greater exchange coupling interaction resulting from a small grain separation as evident in TEM images (Fig. 2). This is supported by the large domain size as shown in Fig. 1(a). The generally lower loop squareness (S) observed in the films with higher Sm concentration can be attributed to less interaction between grains. This was supported by the small domain size as shown in TEM micrograph (Fig.1b) obtained for these films, which is typical of more isolated micromagnetic units. This result is in agreement with the observation by previous researcher [13].

4. Conclusion

The domain size of cobalt samarium alloy ($Co_{90}Sm_{10}$) is much larger than the grain size of that alloy in film. The "multiparticle" or interaction domains suggest there is
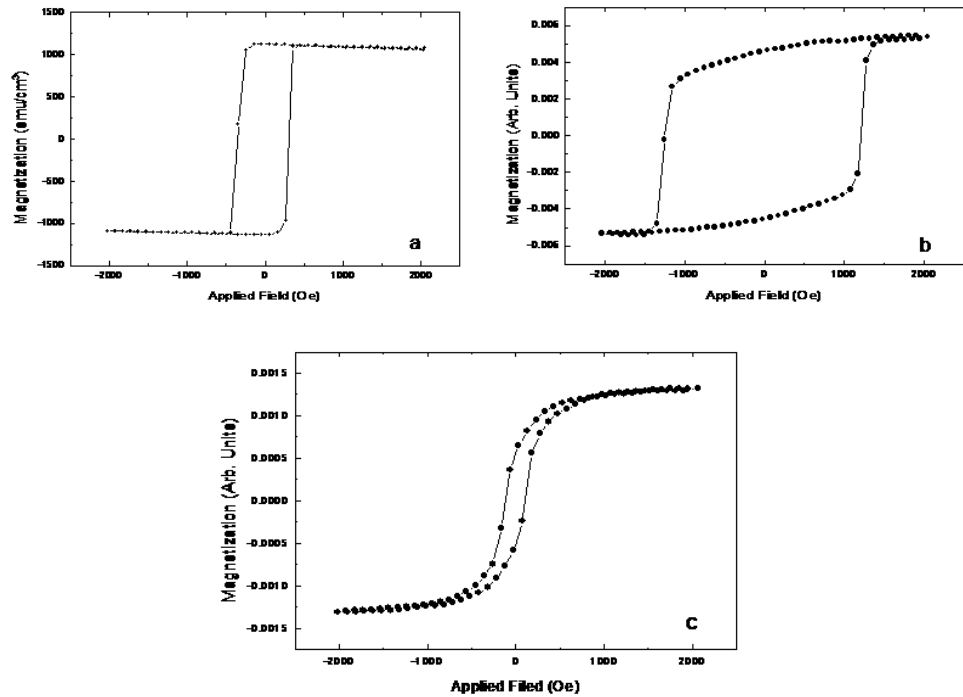
Figure 4: Hysteresis loops for $Co_{100-x}Sm_x$ thin film with varying samarium concentration (a) x=10, (b) x=20 and (c) x=40.
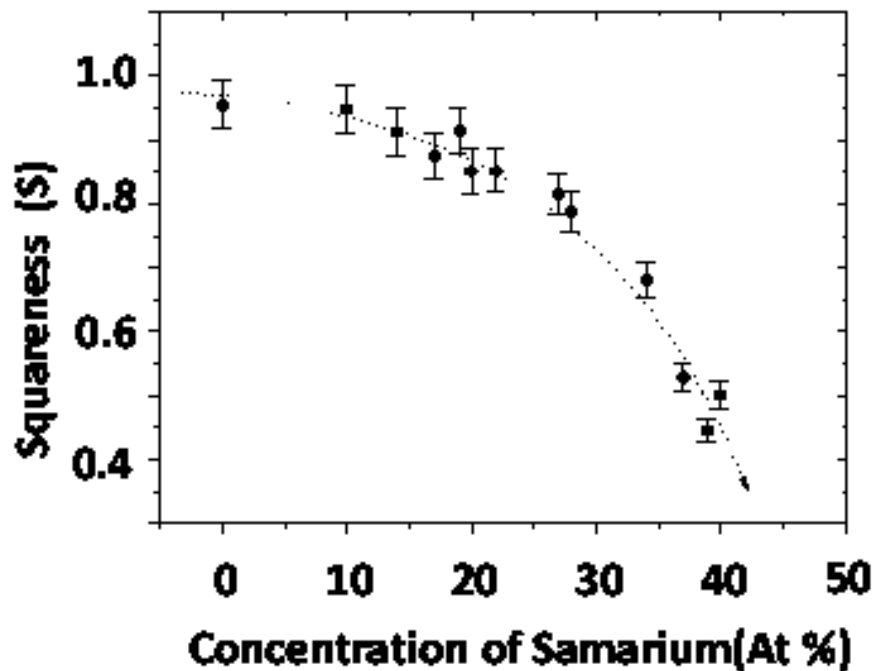
Figure 5: Variation of squareness (*S*) as a function of samarium concentration.

a strong exchange coupling between the magnetization of the neighbouring grains inside each of them. The hysteresis loop for this film shows a small coercivity with high magnetization value and high loop squareness, indicating a greater proportion of magnetic material. It is probable that the domain boundaries occur at grain boundaries

where the intergranular exchange coupling is not strong.The film with increased Sm concentration exhibits a very fine micromagnetic structure with less well defined magnetic domains and domain walls. For films with Sm concentration of 28 at. % and more, no Lorentz image could be observed, implying that the film has very small domains and/or for very low magnetization both of which make it difficult to resolve by any contrast Lorentz microscopy. The maximum value of the film's coercivity lies between the Co_5Sm and Co_7Sm_2 equilibrium compound compositions. This behaviour could be due to a contribution of high magnetic anisotropy from small regions of Co_5Sm; no evidence of this compound was found in the electron diffraction patterns.

5. Acknowledgments

References

[1] M. F. Doerner, K. Tang, T. Arnoldussen, H. Zeng, M. F. Toneyand, and D. Weller, Microstructural and thermal stability of advanced longitudinal media, *IEEE Trans Magn*, **36**, 43–47, (2000).

[2] S. H. Charap, P. Lu, and Y. He, Thermal stability of recorded information at high densities, *IEEE Trans. Magn.*, **33**, p. 978, (1997).

[3] H. C. Theuerer, E. A. Nesbitt, and D. D. Bacon, High Coercive Force Rare Earth Alloy Films by Getter Sputtering J, *Appl Phys (Berl)*, **10**, p. 2994, (1969).

[4] E. MT. Velu and D. N. Lambeth, High density recording on SmCo/Cr thin film media, *IEEE Trans Magn*, **28**, 3249–3254, (1992).

[5] E. M. T. Velu, D. N. Lambeth, J. T. Thornton, and P. E. Russel, AFM structure and media noiseofCoSm/Cr thin films and hard diskJ, *Appl Phys (Berl)*, **75**, p. 6132, (1994).

[6] V. Geiss, E. Kneller, and A. Nest, Magnetic behavior of amorphous Sm-Co Alloy films,J, *Appl Phys, A Mater Sci Process*, **27**, 79–88, (1982).

[7] M. Benaissa, K. M. Krishnan, E. E. Fullerton, and J. S. Jiang, Magnetic anisotropy and its microstructural origin in epitaxially grown SmCo thin films, *IEEE Trans Magn*, **34**, 1204–1206, (1998).

[8] S. A. Majetich, K. M. Chowdary, and E. M. Kirkpatrick, Size and interaction effects in the magnetization reversal in SmCo5 nanoparticles, *IEEE Trans Magn*, **34**, 985–987, (1998).

[9] E. W. Sigleton, Z. S. Shan, Y. S. Jeong, and D. J. Sellmyer, Magnetic switching volumes ofCoSm thin films for high density longitudinal recording, *IEEE Trans Magn*, **31**, 2743–2745, (1995).

[10] B. Ghebouli, S.-M. Cherif, A. Layadi, B. Helifa, and M. Boudissa, Structural and magneticproperties of evaporated Fe thin films on Si(1 1 1), Si(1 0 0) and glass substrates, *J Magn. Magn. Mater.*, **312**, 194–199, (2007).

[11] A. Hubert and R. Schafer, in *Magnetic Domains, The Analysis of Magnetic Microstructures*, Springer, Berlin, 1998.

[12] Y. G. Park and D. Shindo, Electron holography on remanent magnetization distribution of melt-spun Nd-Fe-B magnets, *J Electron Microsc (Tokyo)*, **53**, 43–47, (2004).

[13] S. A. Bendson and J. H. Judy, Magneticproperties of cobalt rare-earth thin filmsIEEE Trans, *Magn*, **9**, 627–631, (1973).

Conference Paper

First Principle Calculation of Electronic, Optical Properties and Photocatalytic Potential of CuO Surfaces

Faozan Ahmad[1,2], M Kemal Agusta[1], and Hermawan K Dipojono[1]

[1]Department of Engineering Physics, Bandung Institute of Technology, Bandung, Indonesia
[2]Department of Physics, Bogor Agricultural University, Bogor, Indonesia

Abstract We have performed DFT calculations of electronic structure, optical properties and photocatalytic potential of the low-index surfaces of CuO. Photocatalytic reaction on the surface of semiconductor requires the appropriate band edge of the semiconductor surface to drive redox reactions. The calculation begins with the electronic structure of bulk system; it aims to determine realistic input parameters and band gap prediction. CuO is an antiferromagnetic material with strong electronic correlations, so that we have applied DFT + U calculation with spin polarized approach, beside it, we also have used GW approximation to get band gap correction. Based on the input parameters obtained, then we calculate surface energy, work function and band edge of the surfaces based on a framework developed by Bendavid et al (J. Phys. Chem. B, 117, 15750-15760) and then they are aligned with redox potential needed for water splitting and CO_2 reduction. Based on the calculations result can be concluded that not all of low-index CuO have appropriate band edge to push reaction of water splitting and CO2 reduction, only the surface CuO(111) and CuO(011) which meets the required band edge. Fortunately, based on the formation energy, CuO(111) and CuO(011) is the most stable surface. The last we calculate electronic structure and optical properties (dielectric function) of low-index surface of CuO, in order to determine the surface state of the most stable surface of CuO.

Keywords: Cupric oxide, DFT, dielectric function, GW approximation, photocatalytic potential.

🔓 **OPEN ACCESS**

1. Introduction

Photocatalytic reaction on the surface of semiconductor requires the appropriate photocatalytic potential or band edge of the semiconductor surface to drive redox reactions. The necessities that the conduction band minimum (CBM) have to lie above the reduction reaction potential and the valence band maximum (VBM) have to lie below the oxidation reaction potential. DFT calculation provides a theoretical mean to calculate the band edge potential of material. But we cannot perform the calculation through bulk system, because, within a periodic DFT calculation of bulk, the eigenvalues are not properly referenced to any absolute scale. However, when the DFT calculations performed onslabsystem which consists of an infinite surface and vacuum, the eigenvalues will be referring to the vacuum potential [1]. The next problem is

How to cite this article: Faozan Ahmad, M Kemal Agusta, and Hermawan K Dipojono, "First Principle Calculation of Electronic, Optical Properties and Photocatalytic Potential of CuO Surfaces," *KnE Engineering*, vol. 2016, 7 pages. DOI 10.18502/keg.v1i1.504

Page 1
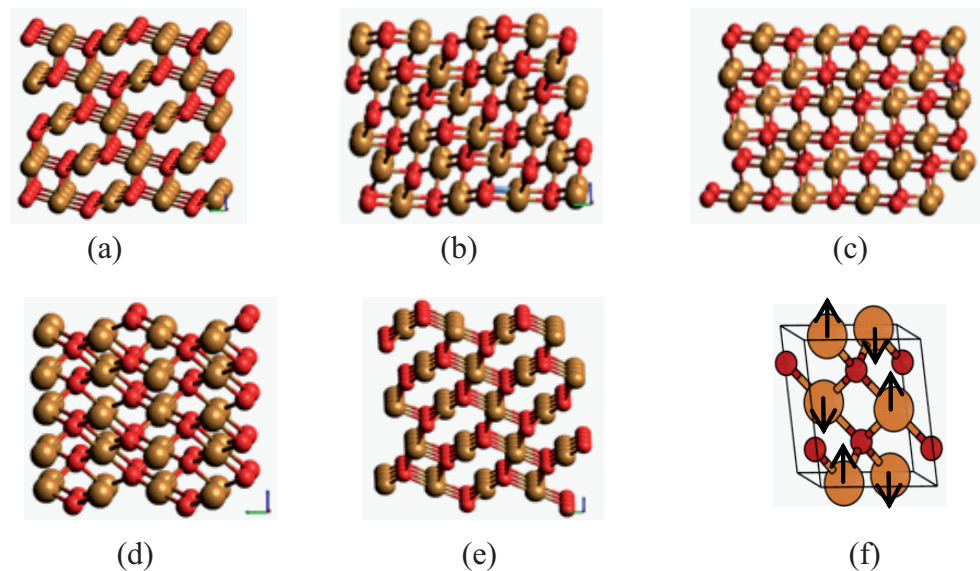
Figure 1: The extended structure of CuO surface (2x2); CuO(111) (a), CuO(011) (b), CuO(101) (c), CuO(010) (d), CuO($\bar{1}$11) (e), and the unit cell of bulk and antiferromagnetic spin ordering (f).

the DFT calculation of VBM and CBM often doesn't show the actual value, because the weakness of the DFT in predicting bandgap of strong electron correlation system. Fortunately, Perdew and Levy showed that the band gap center (BGC) can be predicted exactly using DFT [2].

Cupric oxide or tenorite (CuO) has been attractive attention because of its interesting properties as a p-type semiconductor with a narrow band gap (1.2-1.7 eV). CuO has been used as an effective modifier of photocatalyst TiO_2 and ZnO in water splitting and CO_2 reduction system. In this paper we will calculate surface energy, work function, photocatalytic potential, electronic and optical properties theoretically from first principle.

2. Computational Method

Spin-polarized calculations based on density functional theory are performed using the Quantum Espresso package [3]. Generalized gradient approximation (GGA) based on the Perdew–Burke–Ernzerhof (PBE) functional is used for the exchange-correlation energy. The projector augmented wave (PAW) and norm conserving (NC) method is used to describe the ionic core pseudopotential. CuO has a monoclinic structure with space group C2/c1 (a = 4.690 Å, b = 3.420 Å, c = 5.131 Åand β = 99.540°). The CuO surface is modeled by at least five layers a 1×1 unit cell (see Fig.1). The Brillouin zone is sampled using $4 \times 4 \times 1$ Monkhorst–Pack k-points. Surface relaxation is considered by optimizing the two topmost layers of the surface and keeping the other layers in their bulk parameters. One shot GW method or G_0W_0 approximation and optical properties calculation are conducted using Yambo package [4]. Here we have calculated the properties of CuO surface, namely work function, surface formation energy, photocatalytic potential, electronic properties and optical properties

The calculation of electronic structure of bulk is performed using DFT+U and GW method to predict theoretical band gap. Based on the realistic value of computed bandgap, the band edge of CuO is calculated using Eq.1. Band gap center (E_{BGC}) obtained from DFT calculation of CuO surface have to be referenced to vacuum potential that can be calculated by measuring electrostatic potential of the surface [1].

$$E_{VBM} = E_{BGC} - \tfrac{1}{2}E_g,$$
$$E_{CBM} = E_{BGC} + \tfrac{1}{2}E_g. \qquad (1)$$

The next calculations are work function (ϕ) and surface energy (γ). Work function is defined as the difference in energy between an electron at rest in the vacuum and an electron at the Fermi level. Whereas, surface energy is defines as the excess energy at the surface of a material compared to the bulk. Fermi level in semiconductor often define as VBM (the highest occupied eigenvalue). Work function and surface energy for stoichiometric surface are calculated using Eq.2 and Eq.3, respectively [1,5].

$$\phi = E_{vac} - E_F, \qquad (2)$$

$$\gamma = \frac{1}{2A}\left[E_{surf} - \frac{N_s}{N_b}E_{bulk}\right], \qquad (3)$$

where E_{surf} is the total energy of stoichiometric slab, E_{bulk} is the total energy of bulk, A is the unit surface area, N_s is the number of atoms in slab, and N_b is the number of atoms in bulk.

3. Photocatalytic Potential

The calculation begins with the electronic structure of bulk to predict theoretical band gap using DFT+U and G_0W_0 method. Hubbard potential (U) in this calculation is applied simultaneously to the Cu 3d and O 2p state. The G_0W_0 correction is carried out on the top of DFT+U calculation. The acceptable value of U is constrained by the valid value of calculated local magnetic moment of atom. The experimental data for band gap of CuO is about 1.67 eV at zero Kelvin temperature [6] and local magnetic moment of atom Cu (μ) is about 0.62 up to 0.74 μ_B [7,8]. Table 1 show that the value of theoretical bandgap calculated in DFT+U method is still underestimate, but the G_0W_0 over DFT+U can open the band gap approaching the experimental result.

To calculate band edge, firstly we have to calculate the reference vacuum potential that can be obtained by calculating electrostatic potential of CuO surfaces in DFT+U framework. The electrostatic potential was averaged in the x and y directions to get the potential along the z direction. Fig. 2 shows a method of how to calculate E_{BGC} and E_{VBM} that are referenced to E_{VAC} of CuO(111) surface from electrostatic potential.

Once we get E_{BGC} and band gap we can calculate the band edge position by applying Eq.1 and based on calculated E_{VBM} (with assumption that $E_F \cong E_{VBM}$), we also can

Method	μ-Cu [μ_B]	Direct band gap [eV]	Indirect band gap [eV]
DFT+U, U=1	0.67	0.63	0.38
DFT+U, U=3	0.74	1.66	1.41
DFT+U+G_0W_0,U=0.3	-	1.50	2.37
DFT+U+G_0W_0,U=0.35	-	1.69	2.47
DFT+U+G_0W_0,U=0.4	-	1.77	2.51

TABLE 1: Band gap and local magnetic moment of CuO calculated in DFT+U and G_0W_0 method calculations.
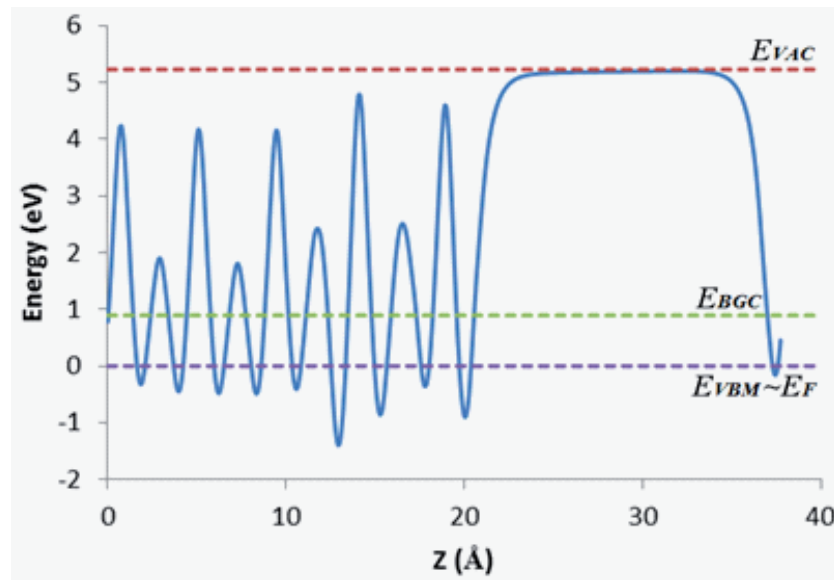
Figure 2: Calculated electropotential along z-axis of CuO(111) surface using DFT+U.

compute work function (ϕ) by following Eq. 2. Finally, to know the most probable or most energetically favorable surface we calculate surface energy through Eq.3. Table 2 shows the calculated work function, E_{BGC}, E_{VBM}, E_{CBM} and surface energy of CuO surfaces. From the result we can see that CuO(111) have the lowest surface energy, this is indicate the CuO(111) is the most stable surface, CuO(101) have the lowest energy needed to extract an electron from the bulk crystal indicated by the lowest work function, CuO($\bar{1}$11) have the lowest E_{VBM}, and CuO(101) have the highest E_{CBM}.

In Fig. 3, we compare the photocatalytic potential of CuO surfaces with redox potential of water and reduction potential of CO2/CH3OH in pH=7.0 (by assumption the

Surface	Work Function (ϕ) [eV]	Band gap Center (E_{BGC}) [eV]	E_{VBM} [eV]	E_{CBM} [eV]	Surface Energy (γ) [J/m^2]
CuO(111)	5.22	-4.82	-5.66	-3.99	0.38
CuO($\bar{1}$11)	5.71	-5.75	-6.58	-4.91	0.82
CuO(010)	5.67	-5.29	-6.13	-4.46	1.02
CuO(101)	4.68	-4.23	-5.07	-3.40	0.89
CuO(011)	5.31	-4.81	-5.64	-3.97	0.60

TABLE 2: Work Function and Surface Energy of CuO calculated within in DFT+U.
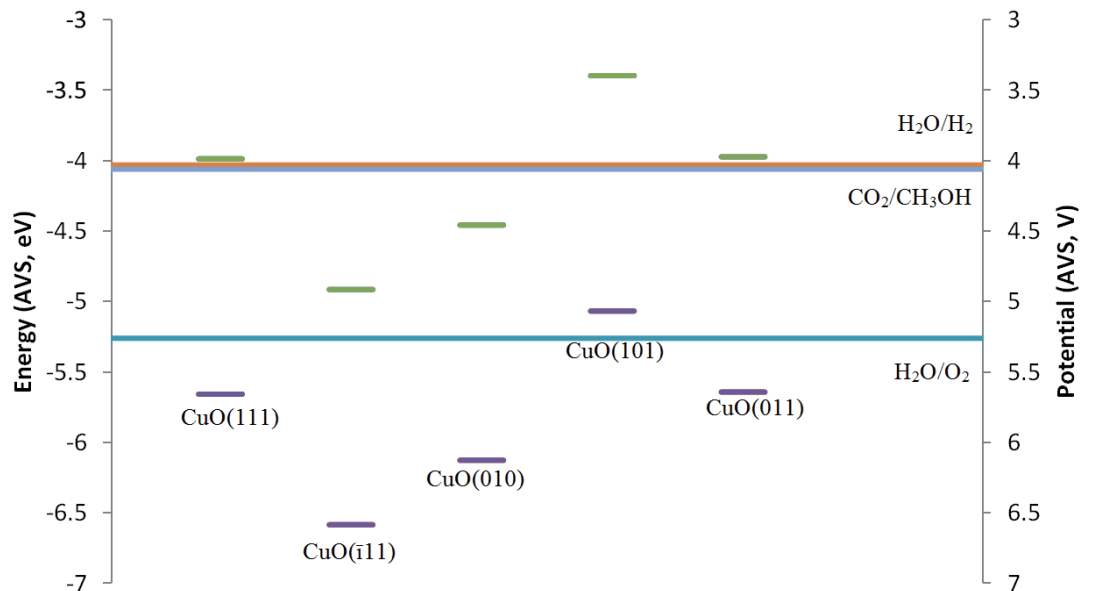
Figure 3: Calculated band-edge position of CuO surfaces in comparison to redox potential of H_2O/O_2, H_2O/H_2, and CO_2/CH_3OH at pH = 7 (refers to AVS: absolute vacuum energy scale).
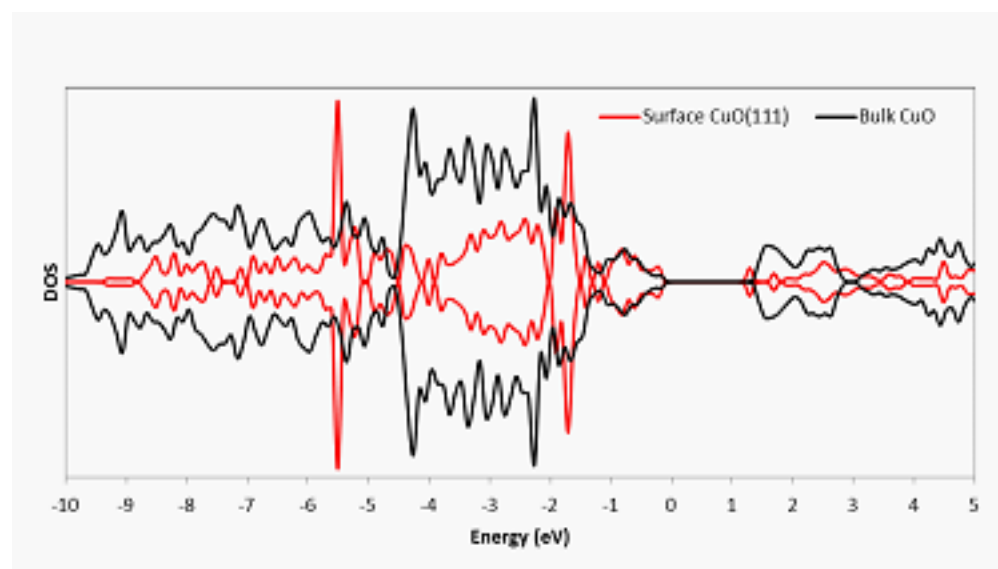
Figure 4: Calculated DOS of surface CuO(111) and bulk.

pH of neutral CuO surfaces are 7.0). It is appears that not all of low-index CuO have appropriate band edge to push reaction of water splitting and CO2 reduction, only the surface CuO(111) and CuO(011) which meets the required band edge. Fortunately, based on the surface energy, CuO(111) and CuO(011) is the most stable surface.

4. Electronic and Optical Properties of Surface

Here we consider electronic and optical properties of the most stable surface CuO(111). The electronic properties are computed using DFT+U, while the optical properties are calculated by solving BSE (Bethe Salpeter Equation).
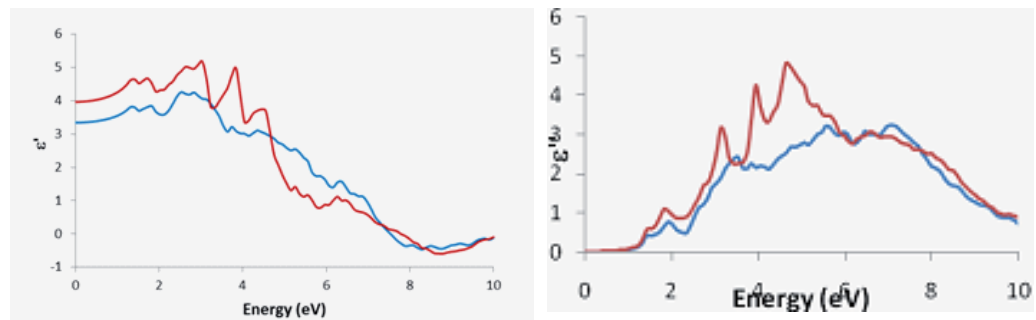
Figure 5: Calculated dieletric function ϵ' (a) and ϵ'' (b) for different light polarization, x-polarization are represented by blue lines and y-polarization are represented by red lines.

In Fig. 4, DOS (density of state) of bulk CuO and surface CuO(111) are presented. It appears a new state or surface state in the band gap. The surface state have important role in photocatalyst, it act as intermediate or trapping state which will reduce recombination rate, so that the electron and hole have more possibility to interact with reactant.

Fig. 5 shows the calculated dielectric function $\epsilon(\omega)$ that consist of ϵ' (dispersive or real part of ϵ) and ϵ'' (absorptive or imaginary part of ϵ). Here we compare between the dielectric function with different light polarization, namely x-polarization (ϵ_{xx}) and y-polarization (ϵ_{yy}). Both of dielectric functions for different polarizations are not identic, this indicates an anisotropy feature of the surface that related (suggested) to the present of surface state [9]. For further analysis of this feature we need RAS (reflected anisotropy spectroscopy).

5. Summary

We have performed DFT calculations of photocatalytic potential, electronic structure, and optical properties of low-index surfaces of CuO. Our calculation show that the calculated photocatalytic potential of CuO (the most stable surface CuO(111)) is sufficient to push reaction of water splitting and CO_2 reduction. New state on band gap and anisotropy feature of dielectric function for different light polarization is suggested related to surface state of CuO(111).

References

[1] L. I. Bendavid and E. A. Carter, First-principles predictions of the structure, stability, and photocatalytic potential of Cu_2O surfaces, *J Phys Chem B*, **117**, 15750–15760, (2013).

[2] J. P. Perdew and M. Levy, M. Physical content of the exact kohn-sham orbital energies: band gaps and derivative discontinuities, *Phys Rev Lett*, **51**, 1884–1887, (1983).

[3] P. Giannozzi, S. Baroni, N. Bonini, M. Calandra, R. Car, C. Cavazzoni, D. Ceresoli, G. L. Chiarotti, M. Cococcioni, I. Dabo, A. Dal Corso, S. de Gironcoli, S. Fabris, G.

Fratesi, R. Gebauer, U. Gerstmann, C. Gougoussis, A. Kokalj, M. Lazzeri, L. Martin-Samos, N. Marzari, F. Mauri, R. Mazzarello, S. Paolini, A. Pasquarello, L. Paulatto, C. Sbraccia, S. Scandolo, G. Sclauzero, A. P. Seitsonen, A. Smogunov, P. Umari, and R. M. Wentzcovitch, QUANTUM ESPRESSO: a modular and open-source software project for quantum simulations of materials, *J Phys Condens Matter*, **21**, p. 395502, (2009).

[4] A. Marini, C. Hogan, M. Grüning, and D. Varsano, yambo: an ab initio tool for excited state calculations, *Comput Phys Commun*, **180**, 1392–1403, (2009).

[5] J. Hu, D. Li, J. G. Lu, and R. Wu, Effects on electronic properties of molecule adsorption on CuO surfaces and nanowires, *J Phys Chem C*, **114**, 17120–17126, (2010).

[6] F. Marabelli, G. B. Parravicini, and F. Salghetti-Drioli, Optical gap of CuO, *Phys Rev B Condens Matter*, **52**, 1433–1436, (1995).

[7] J. B. Forsyth, P. J. Brown, and B. M. Wanklyn, Magnetism in cupric oxide, *J Phys C Solid State Phys*, **21**, 2917–2929, (2000).

[8] B. X. Yang, T. R. Thurston, J. M. Tranquada, and G. Shirane, Magnetic neutron scattering study of single-crystal cupric oxide, *Phys Rev B Condens Matter*, **39**, 4343–4349, (1989).

[9] C. Hogan and R. Del Sole, Optical properties of the GaAs(001)-c(4 × 4) surface: direct analysis of the surface dielectric function, *Phys Status Solidi*, **242**, 3040–3046, (2005).

KnE Engineering

Knowledge E
Engaging minds

Conference Paper

Preparation and Characterisation of PVdF-LiBOB-Based Solid Polymer Electrolyte

Christin Rina Ratri, R. Ibrahim Purawiardi, Titik Lestariningsih, Achmad Subhan, and Etty Marti Wigayati

Research Centre for Physics, Indonesian Institute of Sciences, KawasanPuspiptekSerpongGd. 442Banten 15314, Indonesia

Abstract Electrolyte plays a key role in lithium-ion battery system.Safety and reliability factor was the main background of the development of solid polymer electrolyte as a substitute the conventional electrolyte in liquid form. Preparation and characterisation of a polymer electrolyte system based on lithium bis(oxalato) borate or LiBOB salt and PVdF as the host matrix has been performed. LiBOBsalt and PVdFpolymer were dissolved in DMAC solvent followed bysolid polymer electrolyte forming by means of doctor blade method. The membranes obtained were characterised by FT-IR, XRD, and EIS. It was shown that the electrolyte exhibited higher room ionic conductivity with the increase of salt concentration, with highest conductivity value of 1.22×10^{-6} Scm^{-1} for 70% LiBOB concentration.

Keywords: doctor blade, polymer electrolyte, LiBOB, PVdF

OPEN ACCESS

1. Introduction

The necessity of the sources of renewable energy is increasing with the development of portable electronic gadgets as well as electrical vehicles. Rechargeable lithium-ion battery or secondary battery has taken many attention because its high energy density and long life cycle [1]. Electrolyte contributes greatly in a lithium-ion battery system in terms of ion transport. Liquid electrolyte commonly used by lithium-ion batteries consists of electrolyte salts such as lithium hexafluorophosphate (LiPF$_6$) and carbonate solvents such as ethylene carbonate (EC), propylene carbonate (PC), dimethyl carbonate (DMC), ethyl methyl carbonate (EMC), or diethyl carbonate (DEC). LiPF$_6$ has conductivity as high as $> 10^{-2}$ Scm^{-1} in room temperature, but low thermal stability at high temperature; [2] its decomposition yields HF that has destructive properties towards battery cathode cells [3].

Since its invention by Lischka et.al, [4] new electrolyte saltLiBOB has been developed as LiPF$_6$ substitute [5]. Conductivity of LiBOB is relatively lower than LiPF$_6$ (approximately 6×10^{-3} Scm^{-1}) but it has better thermal stability as well as capacity retention compared to LiPF$_6$ [6,7]. Lithium-ion battery requires reliability at high temperature such as for electric vehicle and oil and gas application, therefore safety issue is considered an important factor. Safety and reliability factor was the main background of the development of solid polymer electrolyte as a substitute the conventional electrolyte in liquid form. Batteries with liquid electrolyte in carbonate

How to cite this article: Christin Rina Ratri, R. Ibrahim Purawiardi, Titik Lestariningsih, Achmad Subhan, and Etty Marti Wigayati, "Preparation and Characterisation of PVdF-LiBOB-Based Solid Polymer Electrolyte," *KnE Engineering*, vol. 2016, 7 pages. DOI 10.18502/keg.v1i1.505

Page 1

solvent is potentially explosive because the materials are volatile and easily flammable at temperature higher than 60^oC, therefore polymer electrolyte has been widely developed as a safer alternative [8].

Polymer electrolyte was widely developed to obtain more compact and lightweight lithium-ion battery, but complied with safety requirements [9]. PVdF has some benefits compared to other polymers, e. g higher dipole moment and dielectric constant, which are important factors for lithium salt ionization [10]. Besides, PVdF is also advantageous in terms of mechanical strength, electrode-electrolyte interaction, good porosity control in multiple polymer/solvent system, and high anodic stability due to -C-F- bonds which has strong electron-withdrawing properties [11]. In its development, there are three kinds of polymer electrolyte: dry solid polymer electrolyte, gel polymer electrolyte, and porous polymer electrolyte [12]. Dry solid polymer electrolyte system was chosen for this experiment due to its simplicity in structure and higher mechanical strength compared to gel polymer electrolyte [13]. From the characteristics of electrolyte salts and polymers in lithium-ion battery system, PVdF and LiBOB were chosen as polymer host and carrier, respectively. The purpose of this experiment is to obtain PVdF and LiBOB-based solid polymer electrolyte and to study the effect of LiBOB salt addition in solid polymer electrolyte system.

2. Experimental Method

LiBOB salt was synthesized using solid state reactionaccording Wigayati, et.al. [14]. Precursor All materials were obtained from Merck Millipore and Sigma Aldrich, with purity of > 98%.PVdF was dissolved in DMAC and mixed at 70^oC temperature. LiBOB salt with varied ratio was then added into the solution. PVdF-LiBOB solution was casted on a glass substrate using doctor blade technique with 400 μm thickness and dried in room temperature with low humidity.

The formed membrane was dried in the oven to evaporate excess solvent.The phase and crystal structure of polymer electrolyte was observed using X-Ray Diffraction (XRD)Rigaku type Smartlab under Cu Kα radiation within 2θ range of 0-80°.Functional groups and intermolecular binding were observed using Fourier Transform Infra-Red (FT-IR) Thermoscientific type Nicolet iS-10 with attenuated total reflectance (ATR) method, operated at wave number range of $4000 – 600$ cm^{-1}.

Impedance test of polymer electrolyte was performed using Hioki LCR HiTester type 3522-50. The measurement of bulk resistance (Rb) can be determined from Cole-Cole plot obtained from impedance test. Hence, the conductivity (σ) was calculated using simple formula σ = L/(Rb x A), with L and A are sample thickness and surface area of the stainless stel plate, respectively.
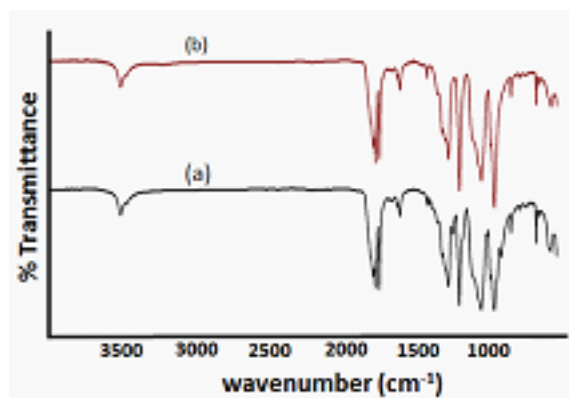
Figure 1: FT-IR characterisation of (a) commercial, and (b) synthesized LiBOB.

(a)   (b)
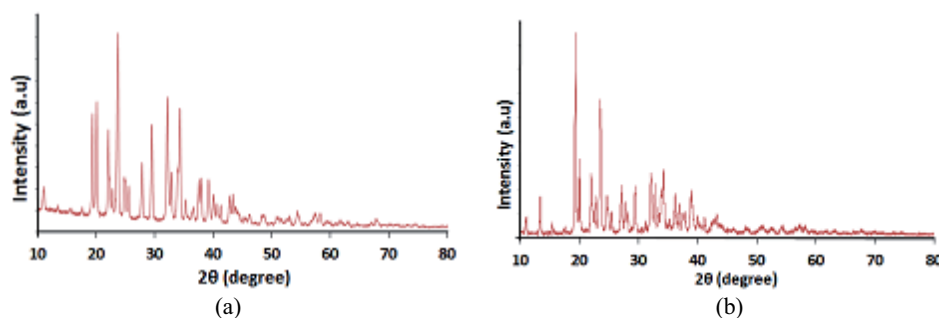
Figure 2: XRD characterisation of (a) commercial and (b) synthesized LiBOB.

3. Results and Discussion

3.1. Characterisation of synthesized LiBOB

Crystal structure, composition, and functional groups of synthesized LiBOB were presented in FT-IR and XRD analysis results at Fig. 1 and 2. It was shown in Fig. 1 that functional groups formed in synthesized LiBOB were close in reference to commercial LiBOB salt. [15]. Vibration peak at wave number 1750, 1640, and 1442 cm^{-1} indicate C=O stretch, COO asymmetric stretch, and COO symmetric stretch, respectively. Fingerprint region of LiBOB compound was characterised by vibration peak at wave number 1372, 1297, 1070, and 982 cm^{-1}.

These peaks represented B-O stretch, C-O-B-O-C stretch, O-B-O symmetric stretch and O-B-O asymmetric stretch, respectively. Vibration peak at wave number 3513 cm^{-1} represented O-H stretch, indicating that hydrate crystal was formed in LiBOB hydrate phase. The appearance of this phase was also observed in XRD analysis result as shown in Fig. 2.

XRD diffraction pattern was illustrated in Fig. 2(a) for commercial LiBOB and Fig. 2(b) for synthesized LiBOB. Both figure of peak diffraction analysis exhibited LiBOB and LiBOB hydrate phase. For commercial LiBOB in Fig. 2(a), LiBOB phase (ICDD/PDF4 #00-056-0139) [16] was indicated by three strongest lines at d-spacing 2.78, 4.42, and 4.58 Å. LiBOB hydrate phase (ICDD/PDF4 # 01-073-9447)[16] was indicated by three strongest lines at d-spacing 2.62, 4.03, and 3.20 Å.
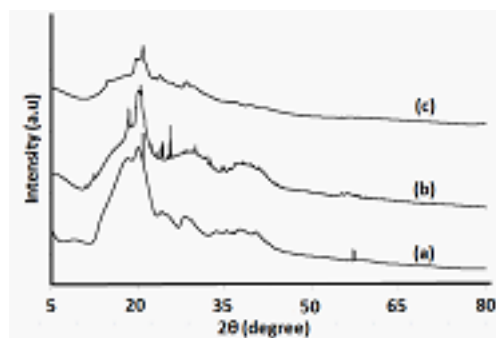
Figure 3: X-Ray diffraction spectra for (a) 30%, (b) 50%, and (c) 70% LiBOB concentration.

For synthesized LiBOB in Fig. 2(b), LiBOB phase (ICDD/PDF4 #00-056-0139) [16] was indicated by three strongest lines at d-spacing 4.57, 2.31, and 3.28 Å. LiBOB hydrate phase(ICDD/PDF4 # 01-073-9447) [16] was indicated by three strongest lines at d-spacing 3.75, 2.79, and 4.04 Å.

3.2. XRD analysis

X-Ray diffractograms of solid polymer electrolyte sample with 30%, 50%, and 70% addition of LiBOB were illustrated at Fig. 5.

Diffraction peak analysis showed that β-PVdF phase which supposedly appeared at 2θ = 20,9^o did not appear because LiBOB crystal phase was more dominant at 2θ range of 5° to 45°. This showed that LiBOB particle was distributed evenly within PVdF matrix as polymer host [17].

3.3. FT-IR analysis

PVdF and LiBOB functional groups within solid polymer electrolyte system was presented at Fig. 6. It was seen that solid polymer electrolyte spectrum for 50% LiBOB concentration was a combination of functional groups as well as fingerprints of pure PVdF and LiBOB. Vibration peak at wavenumber 1810, 1633, 882, and 723 cm^{-1} were typical fingerprint of LiBOB compound, which represented vibration of C=O oscillation, C-O-O assymetric stretch, O-B-O assymetric stretch, and C-O-O bending vibration, respectively. Vibration peak of PVdF fingerprints were also seen at wavenumber 1403 cm^{-1} which was CH$_2$ scissoring, and C-F stretch at 1074 cm^{-1}. There were also typical vibration peak of β-PVdF phase at 838 cm^{-1}, which were CH$_2$ rocking and assymetric stretch of CF$_2$ [18].

FT-IR spectrum comparison of PVdF-LiBOB solid polymer electrolyte system with LiBOB concentration of 30%, 50%, and 70% was pas presented at Fig. 7. Vibration peak showing C-O-O asymmetric stretch from LiBOB at wave number 1633 cm^{-1} was seen more clearly with more LiBOB concentration.

Conversely, CH$_2$ in-plane bending or rocking which was distinctive fingerprint of β-PVdF phase was even more reduced. This suggested that LiBOB particle was distributed

(a)   (b)
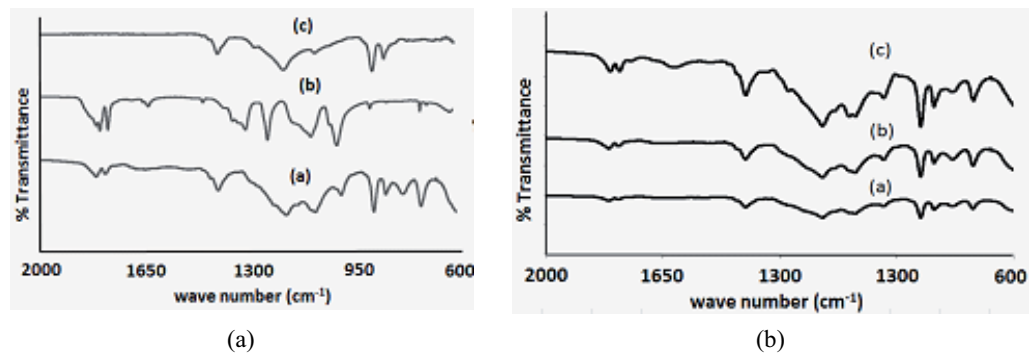
Figure 4: FT-IR spectrum of (a) pure PVdF, pure LiBOB, and PVdF-LiBOB membrane, and (b) PVdF-LiBOB membrane with LiBOB concentration of 70%, 50%, and 30%.

LiBOB content, %	Conductivity, Scm^{-1}
30	2.66×10^{-9}
50	3.96×10^{-8}
70	1.22×10^{-6}

TABLE 1: Room temperature conductivity of PVdF-LiBOB solid polymer electrolyte.

evenly within solid polymer electrolyte system, as was also shown in the SEM scan results of the membrane.

3.4. Electrochemical Impedance Spectroscopy analysis

The ionic conductivity of PVdF-LiBOB solid polymer electrolyte system was observed using electrochemical impedance spectroscopy (EIS). Bulk resistivity value obtained from the Cole-Cole plot was used to calculate the room temperature conductivity of PVdF-LiBOBsolid polymer electrolyte, which result was presented on Table 1.

Impedance test exhibited increasing conductivity on addition of LiBOB salt. At 30% salt concentration, LiBOB particle functioning as conductor was agglomerated within polymer matrix as shown at Fig. 4. The highest conductivity at 70% salt concentration was affected by higher amount of LiBOB particle distributed within PVdF polymer matrix. Studies performed by Xi et.al [19] on characterisation of PVdF-LiClO$_4$-based solid polymer electrolyte in propylene carbonate (PC) solvent showed ionic conductivity as high as $1 \times 10^{-5} Scm^{-1}$ at room temperature. Stephan and Nahm [20] also reported similar result for PVdF-LiPF$_6$-based solid polymer electrolyte system. PEO-LiClO$_4$-based solid polymer electrolyte system showed lower conductivity, i.e 1×10^{-8} Scm^{-1}.

4. Conclusion

PVdF-LiBOB-based solid polymer electrolyte system has been synthesized and characterised. Solid polymer electrolyte synthesized from PVdF polymer host and LiBOB salt filler using doctor blade method was evenly distributed throughout the surface as well as membrane layer. Even though the distribution of LiBOB particle was relatively homogenous within PVdF matrix as polymer host, but at low salt concentration there

was a possibility of agglomeration. The ionic conductivity of the solid polymer electrolyte system increased with addition of LiBOB salt. The ionic conductivity of solid polymer electrolyte system with 30%, 50%, and 70% salt concentration was 2.66×10^{-9}, 3.96×10^{-8}, dan 1.22×10^{-6} Scm^{-1}respectively, at room temperature (25°C). The ionic conductivity of this solid polymer electrolyte system can be enhanced with addition of filler and plasticiser.

5. Acknowledgement

References

[1] L.-Z. Fan, T. Xing, R. Awan, and W. Qiu, Studies on lithium bis(oxalato)-borate/propylene carbonate-based electrolytes for Li-ion batteries, *Ionics Kiel*, **17**, 491–494, (2011).

[2] L. Larush-Asraf, M. Biton, H. Teller, E. Zinigrad, and D. Aurbach, On the electrochemical and thermal behavior of lithium bis(oxalato)borate (LiBOB) solutions, *J Power Sources*, **174**, 400–407, (2007).

[3] X.-L. Wu, S. Xin, H.-H. Seo, J. Kim, Y.-G. Guo, and J.-S. Lee, Enhanced Li conductivity in PEO–LiBOB polymer electrolytes by using succinonitrile as a plasticizer, *Solid State Ion*, **186**, 1–6, (2011)., Elsevier B.V.

[4] U. Lischka, U. Wietelmann, and M. Wegner, Lithium bisoxalatoborate used as conducting salt in lithium ion batteries

[5] K. Xu, S. Zhang, and T. R. Jow, LiBOB as Additive in LiPF[sub 6]-Based Lithium Ion Electrolytes, *Electrochem Solid-State Lett*, **8**, p. A365, (2005).

[6] X. Cui, H. Zhang, and S. Li, Electrochemical performances of a novel lithium bis (oxalate) borate-based electrolyte for lithium-ion batteries with LiFePO4 cathodes, *Ionics*, **20**, no. 6, 789–794, (2014).

[7] B.-T. Yu, W.-H. Qiu, F.-S. Li, and L. Cheng, Comparison of the electrochemical properties of LiBOB and LiPF6 in electrolytes for LiMn2O4/Li cells, *J Power Sources*, **166**, 499–502, (2007).

[8] Y.-H. Li, X.-L. Wu, J.-H. Kim, S. Xin, J. Su, Y. Yan, J.-S. Lee, and Y.-G. Guo, A novel polymer electrolyte with improved high-temperature-tolerance up to 170°C for high-temperature lithium-ion batteries, *J Power Sources*, **244**, 234–239, (2013)., Elsevier B.V.

[9] X. Wang, C. Gong, D. He, Z. Xue, C. Chen, Y. Liao, and X. Xie, Gelled microporous polymer electrolyte with low liquid leakage for lithium-ion batteries, *J Membr Sci*, **454**, 298–304, (2014)., Elsevier.

[10] W. Li, Y. Xing, X. Xing, Y. Li, G. Yang, and L. Xu, PVDF-based composite microporous gel polymer electrolytes containing a novelsingle ionic conductor SiO2(Li), *Electrochim Acta*, **112**, 183–190, (2013)., Elsevier Ltd.

[11] J. Nunes-Pereira, C. M. Costa, and S. Lanceros-Méndez, Polymer composites and blends for battery separators: state of the art, challenges and future trends, *J Power Sources*, **281**, 378–398, (2015).

[12] K. Murata, S. Izuchi, and Y. Yoshihisa, An overview of the research and development of solid polymer electrolyte batteries, *Electrochimica Acta*, **45**, no. 8, 1501–1508, (2000).

[13] J. Y. Song, Y. Y. Wang, and C. C. Wan, Review of gel-type polymer electrolytes for lithium-ion batteries, *J Power Sources*, **77**, 183–197, (1999).

[14] E. Wigayati, et al., Synthesis and Characterization of LiBOB as Electrolyte for Lithium-ion Battery (2014).

[15] V. Aravindan and P. Vickraman, A study on LiBOB-based nanocomposite gel polymer electrolytes (NCGPE) for Lithium-ion batteries, *Ionics Kiel*, **13**, 277–280, (2007).

[16] ICDD Products - WebPDF-4+, `http://www.icdd.com/products/webpdf4.htm` .

[17] M. Jacob, Effect of PEO addition on the electrolytic and thermal properties of PVDF-$LiClO_4$ polymer electrolytes, *Solid State Ion*, **104**, 267–276, (1997).

[18] J. F. Mano, Ftir and Dsc Studies of Mechanically Deformed B-Pvdf Films, *J. Macromol. Sci. Phys.*, **40**, 517–527, (2001).

[19] J. Xi, X. Qiu, J. Li, X. Tang, W. Zhu, and L. Chen, PVDF-PEO blends based microporous polymer electrolyte: effect of PEO on pore configurations and ionic conductivity, *J Power Sources*, **157**, 501–506, (2006).

[20] Manuel Stephan, Review on composite polymer electrolytes for lithium batteries, *Polymer (Guildf)*, **47**, 5952–5964, (2006)., Elsevier Ltd.

KnE Engineering

Knowledge E
Engaging minds

Conference Paper

Effect of Co-Ti Substitution on Magnetic Properties of Nanocrystalline BaFe$_{12}$O$_{19}$

Erfan Handoko[1], Mangasi AM[1], Zulkarnain[2], and Bambang Soegijono[3]

[1]Dept. of Physics, Faculty of Mathematics and Natural Sciences. State University of Jakarta, Jakarta 13220, Indonesia
[2]Dept. of Physics, Faculty of Mathematics and Natural Sciences. University of Syiah Kuala, Banda Aceh
[3]Dept. of Physics, Faculty of Mathematics and Natural Sciences. University of Indonesia, Depok 16424, Indonesia

Abstract The synthesis of nanocrystalline BaFe$_{12-2x}$Co$_x$Ti$_x$O$_{19}$ with variations of x (x = 0, 1, 2, and 3) have been investigated. The formation of polycrystalline samples that the cationic of Co^{2+} and Ti^{4+} in Co-Ti substituted Fe in BaFe$_{12}$O$_{19}$ ferrites structure were prepared by solid state reaction method. The crystal structure, microstructure, and magnetic properties were characterized using powder X-ray diffraction, scanning electron microscope (SEM) and permagraph meter, respectively. The results show that the nanocrystalline BaFe$_{12-2x}$Co$_x$Ti$_x$O$_{19}$ has single phase with polycrystalline structure, the grain size decrease by doping, the coercivity (Hc) and saturation magnetization (Ms) decrease with increasing Co-Ti substitutions.

Keywords: Nanocrystalline, polycrystalline, BaFe$_{12}$O$_{19}$, coercivity, Co-Ti substitution

🔓 OPEN ACCESS

1. Introduction

Recently, investigations of barium ferrite BaFe$_{12}$O$_{19}$ as hard magnetic material has been developed. The enhancement of magnetic properties such as saturated magnetization (Ms), remanence (Mr), and coercive force (Hc) become major interest to be investigated. An effect of the various processes[1] and designing crystal structure of the barium ferrite to magnetic properties were investigated systematically [2-5]. In order to improve the magnetic properties, the nanocrystalline BaFe$_{12}$O$_{19}$ ferrites has potential opportunity to be developed. As reported, the development of the barium ferrite compositions were substituted by Ba and (Sr) [6-8]. In order to understand the magnetic properties of BaFe$_{12}$O$_{19}$, the Fe was substituted by Al, Sn, NiSn, Ti, or Co[9-13]. Furthermore, the improvement of coercivity of BaFe$_{12}$O$_{19}$ is needed to realize magnetic absorption materials such as microwave [14-16].

In this report, we have synthesized nanocrystalline BaFe$_{12-2x}$Co$_x$Ti$_x$O$_{19}$ with x = 0, 1, 2, 3. The formations of polycrystalline samples that the cationic of Co^{2+} and Ti^{4+} in Co-Ti substituted Fe in BaFe$_{12}$O$_{19}$ ferrite were prepared by solid state reaction method. The crystal structure, microstrusture and magnetic properties of BaFe$_{12-2x}$Co$_x$Ti$_x$O$_{19}$ will be discussed systematically.
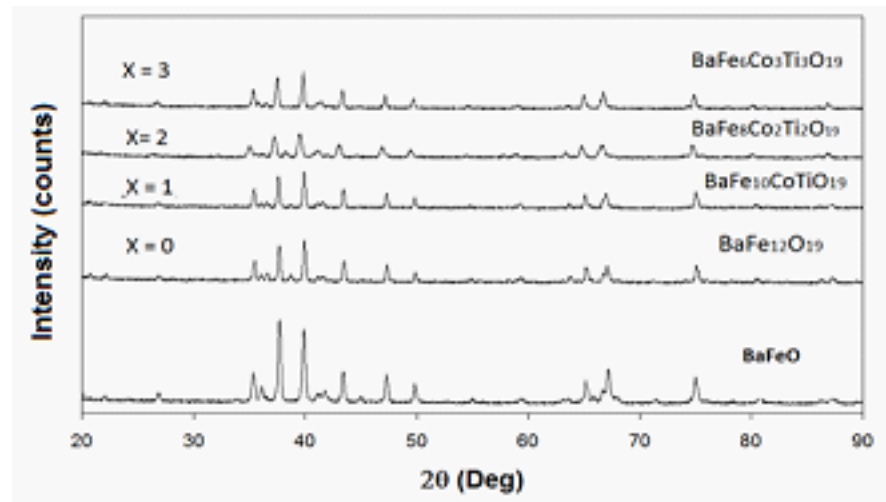
Figure 1: XRD patterns of $BaFe_{12-2x}Co_xTi_xO_{19}$ samples with x = 0, 1, 2, 3.

2. Experimental

Magnetic materials of the $BaFe_{12-2x}Co_xTi_xO_{19}$ samples with x = 0, 1, 2, 3 were synthesized by ultrasonic mixing process from $BaCO_3$, Fe_3O_4 (from iron sand), Co_3O_4, and TiO_2. The compositions and the stoichiometry of samples were diluted in demineralized water. Then, the solution was calcinated at 750^oC for 30 minutes and sintered at 1100^oC for 3 hours. The formations of polycrystalline samples that the cationic of Co^{2+} and Ti^{4+} in Co-Ti substituted Fe in $BaFe_{12}O_{19}$ ferrite by solid state reaction method have been obtained. The crystal structure of samples powders were investigated by X-ray diffraction (XRD) Phillips diffractometer. The morphology was examined by JEOL JSM 5310LV scanning electron microscope (SEM). The magnetic measurement was carried out by permagraph at room temperature.

3. Results and Discussion

The XRD pattern of the $BaFe_{12-2x}Co_xTi_xO_{19}$ (x=0, 1, 2, 3) ferrites. The peaks of hematite (BaFeO) coincide with magnetite/iron sand (x=0). It's believed that magnetite from iron sand can be used for the barium ferrite. The peaks for the substituted barium ferrite (x=1, x=2, and x=3) also coincide with non-substituted ferrite (x=0). The results prove that formation of $BaFe_{12-2x}Co_xTi_xO_{19}$(x=0, 1, 2, 3) ferrites at 1100^oC can be synthesized. It is 100^oC lower than classical barium ferrite. In the substituted barium ferrite, the dopants of Co^{2+} and Ti^{4+} occupy the structure.

The XRD pattern of doped barium ferrite (x=1) is shown in Figure 2. The refinement by *HighScore Plus Version 3.0e PANalytical software* indicates that the crystallite size is 50 nm. It's confirmed that the $BaFe_{12-2x}Co_xTi_xO_{19}$ has polycrystalline structure.

The Figure 3 indicates that the microstructure of doped barium ferrite has different grain size with undoped. The grain size decreases by increasing the doping, as result the nanocrystalline structure has formed.
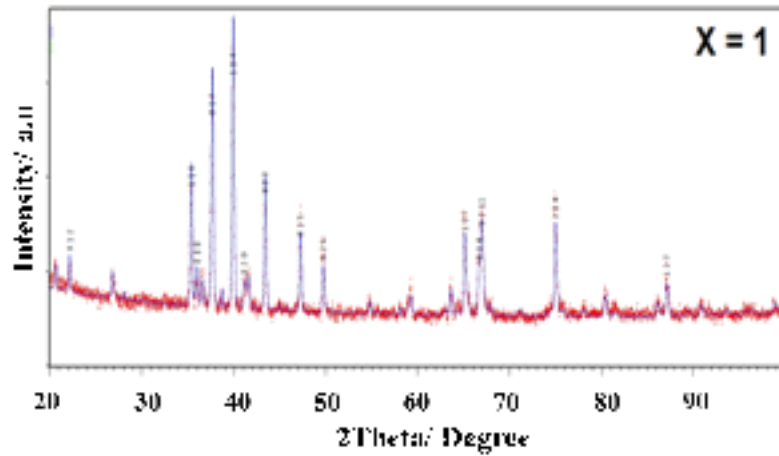
Figure 2: The refinement of XRD data of $BaFe_{12-2x}Co_xTi_xO_{19}$ (x = 1).
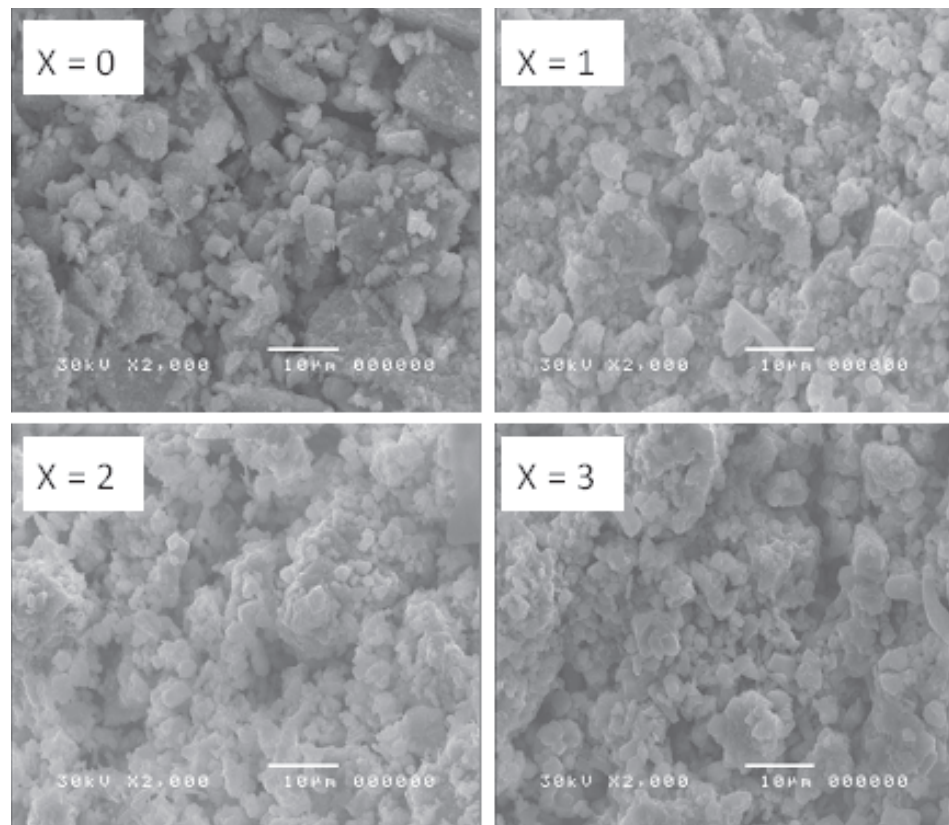
Figure 3: SEM photographs of $BaFe_{12-2x}CoxTi_xO_{19}$ samples with x = 0, 1, 2, 3.

Figure 4 shows the hysteresis loops of the magnetic behavior of the as-synthesized barium ferrite. Meanwhile, the table 1 is the datas for hysteresis loops of the barium ferrite as shown in Figure 4. As can be seen in the Figure 4, the undoped barium ferrite samples have larger coercive force (Hc), area, and the higher remanen (Mr) than doped barium ferrite. The coercive force of barium ferrite (x=0) is about 85.06 kA/m. While, the doped barium ferrites rapidly decrease up to 0.939 kA/m at x=1. The reduction of the crystal anisotropy in x=1 cause the weak uni-axial anisotropy along the c-axis of

Composition (x)	Mr (T)	Hc (kA/m)	Ms (T)	Mr/Ms (T)
0	0.045	85.060	0.124	0.365
1	0.020	0.939	0.084	0.234
2	0.004	24,028	0.024	0.159
3	0.005	23,987	0.015	0.372

TABLE 1: Data for hysteresis loops of the barium ferrite.
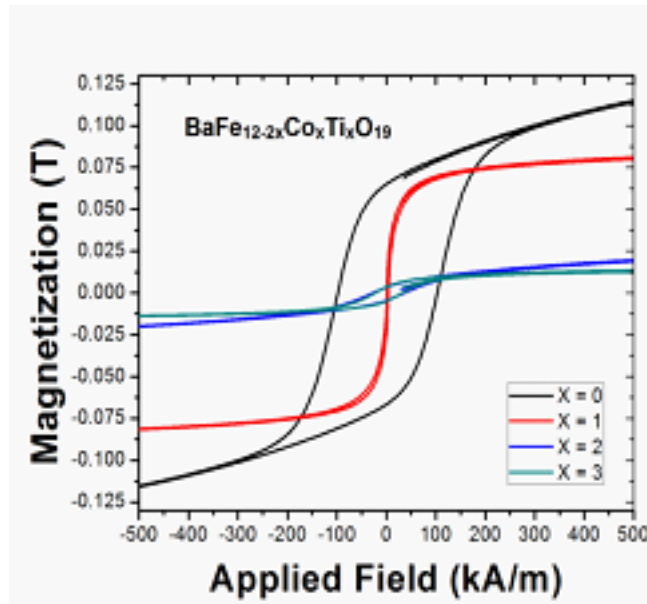
Figure 4: The room temperature hysteresis loops of $BaFe_{12-2x}Co_xTi_xO_{19}$ samples with x = 0, 1, 2, 3.

the doped barium ferrite. Substitution of Co-Ti decreases the coercive force of barium ferrite significantly. Further, Co-Ti increases the coercivity Hc= 24.028 kA/m at x=2 and Hc= 23,987 kA/m at x=3. These results were predicted due to increasing the crystal anisotropy. Furthermore, the low coercivity explains that the doped barium ferrite is the soft magnetic material.

4. Conclusions

In conclusions, the $BaFe_{12-2x}Co_xTi_xO_{19}$ with x = 0, 1, 2, 3 have been synthesized by ultrasonic mixing process. According to XRD meansurement, the samples have formed polycrystalline structure and the crystallite size about 50 nm. Meanwhile, the magnetic properties i.e. coercivity (Hc) and saturation magnetization (Ms) decrease with increasing Co-Ti substitutions.

5. Acknowledgments

References

[1] H. Sozeri, *J Alloys Compd*, **486**, 809–814, (2009).

[2] U. Topal and H. I. Bakan, *J Eur Ceram Soc*, **30**, 3167–3171, (2010).

[3] P. E. Garcia-Casillas, A. M. Beesley, D. Buenoc, J. A. Matutes-Aquino, and C. A. Martinez, Remanence properties of barium hexaferrite, *J Alloys Compd*, **369**, 185–189, (2004).

[4] J. Dho, E. K. Lee, J. Y. Park, and N. H. Hur, *J Magn Magn Mater*, **285**, 164–168, (2005).

[5] M. M. Rashad, M. Radwan, and M. M. Hessien, Effect of Fe/Ba mole ratios and surface-active agents on the formation and magnetic properties of co-precipitated barium hexaferrite, *J Alloys Compd*, **453**, 304–308, (2008).

[6] U. Topala, H. Ozkanb, and H. Sozeri, *J Magn Magn Mater*, **284**, 416–422, (2004).

[7] P. Kerschla, R. Gr. ossingerb, C. Kussbachb, R. Sato-Turtellib, K. H. M. Ullera, and L. Schultza, *J Magn Magn Mater*, **242–245**, 1468–1470, (2002).

[8] K. S. Martirosyan, E. Galstyan, S. M. Hossain, Y.-J. Wang, and D. Litvinov, Barium hexaferrite nanoparticles: synthesis and magnetic properties, *Mater Sci Eng B*, **176**, 8–13, (2011).

[9] P. Hernfindez, C. de Francisco, J. M. Mufioz, J. Ifiiguez, L. Torres, and M. Zazo, *J Magn Magn Mater*, **157/158**, 123–124, (1996).

[10] V. N. Dhage, M. L. Mane, A. P. Keche, C.T. Birajdar, and K. M. Jadhav, *Physica B*, **406**, 789–793, (2011).

[11] P. A. Marino-Castellanos, J. C. Somarriba-Jarque, and J. Anglada-Rivera, *Physica B*, **362**, 95–102, (2005).

[12] A. Gonzalez-Angeles, G. Mendoza-Suarez, A. Gruskova, I. Toth, V. J. Warik, J. I. Escalante-Garca, and M. Papanova, *J Magn Magn Mater*, **270**, 77–83, (2004).

[13] P. A. Marino-Castellanos, J. Anglada-Rivera, A. Cruz-Fuentes, and R. Lora-Serrano, *J Magn Magn Mater*, **280**, 214–220, (2004).

[14] A. Gruskova, J. Slama, R. Dosoudil, D. Kevicka, V. Jancarik, and I. Toth, Influence of Co–Ti substitution on coercivity in Ba ferrites, *J Magn Magn Mater*, **242–245**, 423–425, (2002).

[15] A. Ghasemia, A. Hossienpour, A. Morisako, A. Saatchi, and M. Salehi, *J Magn Magn Mater*, **302**, 429–435, (2006).

[16] J. Qiu, H. Shen, and M. Gu, *Powder Technol*, **154**, 116–119, (2005).

Conference Paper

Synthesis of Novel Nano-Strawberry TiO$_2$ Structures with the Aid of Microwave Inverter System: Growth Time Effect on Optical Absorption Intensity

Athar Ali Shah, Akrajas Ali Umar, and Muhamad Mat Salleh

Institute of Microengineering and Nanoelectronics, Universiti Kebangsaan Malaysia, 43600, Bangi, Selangor, Malaysia

Abstract A novel anatase TiO$_2$ with nanostrawberry-like structure with high porosityhas been synthesised on ITO, with the aid of microwave power in a very short duration of 6 minutes. The growth of these novel TiO$_2$ nanostructures on ITO is attained stoichiometrically by using ammonium hexafluorotitanate, Hexamethylenetetramine, and Boric acid as precursor, capping agent, and reducing agent, respectively. Optical absorption intensity and thickness of these nanostructure layers can be varied by the growth time. A highly porous, 2.25 μm thickest layer has been successfully synthesised on ITO, andthe average diameter of these nanostructures was foundapproximately 70$\pm$2.5nm. These highly porous nanostructures are expected to begood candidate for photocatlysis applications and efficient photovoltaic performances of dye sensitised solar cells.

Corresponding Author: Athar Ali Shah; email: athar.shah@yahoo.com

OPEN ACCESS

1. Introduction

A wide range application of TiO$_2$ as a semiconductor in photocatlysis [1], sensors [2], optical devices [3], fuel cells [4], and dye sensitized solar cell [5] has made its research worthy. It exists in three mineral forms, anatase, rutile, and brookite [6]. Among these forms, anatase is preferred, due to its crystalline structure, and high photocatalytic activity, stable, non-toxic, and cheaper as well , and surface energy of anatase facets 101, 200, and 001 are 0.44 Jm^{-2}, 0.53 Jm^{-2}, 0.90 Jm^{-2}, respectively [6]. In recent years, a variety of synthesis methods such as hydrothermal method, solvothermal method, sol-gel method, direct oxidation method, chemical vapour deposition (CVD), electrodeposition, sonochemical method, and microwave method have been used for the preparation of TiO$_2$ nanostructured [7]. Studies has shown that growth of anatase TiO$_2$ nanostructuresincreases in reduced time, when temperatures are kepthigh, during chemical reactions in liquid phase deposition method (LPD) [8]. Microwave heating has privileges of rapidness, energy saving, and uniformity over conventional heating [9]. Thermal heating process involve conduction, convection, and radiation, which involves indirect heating, whereas in microwave heating, electromagnetic waves are directly

absorbed at the molecular level [10], which leads to save the energy and can be the reason of rapid reaction. Most important features of microwaveare to polarize the materials of high dielectric constant, and power generation in these materials due to their high dielectric loss, and hence quick and efficient heating is attained [11]. Many researchers have reported synthesis of anatase TiO_2, which has limited the synthesis time up to 3 hours [12-13]. In this research paper, we report synthesis of anatase TiO_2nanostructures assisted by 180W micro wave power in 6 minutes.

2. Experimental

Precursor, Amoniumhexafluorotitanate $(NH_4)_2TiF_6$, and HMT $(C_6H_{12}N_4)$ were purchased from Sigma-Aldrich USA. Boric acid (H_3BO) from WAKO company Japan, and ITO (indium tin oxide) substrate of sheet resistance ca. 9-22 Ω,/square was purchased from VinKarola instruments USA. We have synthesized TiO_2nano structures on ITO assisted by microwave (inverter system). ITO substrates were dusted by high quality soft cotton, and then after they were passed through a process of ultrasonication, using acetone and 2-propanol respectively. These substrates were immersed in a solution, which contained 1.5 ml of each precursor (NH_4TiF_6), boric acid, and surfactant (HMT), whereas the concentration of precursor, boric acid, and surfactantwere 0.1 M, 0.06, and 0.03M. It took 6 minutes to grow TiO_2 nanostructure on ITO, when microwave power was set at 180 watt. For the same combination of these molarities, growth time of nano structures was increased by repeating growth cycles. These cycles were named as 1X, 2X, 3X,4X, 5X, and 6X representing growth times 6, 12, 18, 24, 30, and 36 minutes respectively. For each growth cycle, freshly prepared solution was used in new reaction bottle to avoid any residue contamination of previous reaction cycle. After these growth cycles, these substrates were rinsed with pure water in abundant and were dried with nitrogen gas. Finally, each substrate was annealed in air at 350°C for an hour.

X-ray diffraction method (BRUKER D8 Advance) with CuKα radiation of wavelength 0.154 nm of scan step 2°/min, Field Emission Scanning Electron Microscope (FESEM) technique (ZeiSS SUPRA 55VP), and UV/VIS spectrometer (Lambda 900 Perkin-Elmer) were used to carry out investigations regarding the Structure, surface morphology, and optical properties, respectively for these samples.

3. Results and Discussion

In order to characterise synthesised nanostructures, XRD analysis was carried out for these samples, which is shown in Figure 1. The values of '2Θ' correspondent to diffracted peaks attained from X-ray diffraction pattern of the samples are 25.20, 37.88, 48.08, 53.80, and 55.08. According to file JCPDS No.21-1272, values of '2Θ', 25.28, 37.88, 48.05, 53.89, and 55.06 are correspondent to facets 101, 004, 200, 105, and 211 respectively for TiO_2 anatase phase. The structure of the samples are obviously in anatase phase, because the diffraction peaks attained for the samples at '2Θ' strongly match with the results of JCPCDS card No.21-1272, and their high exposure
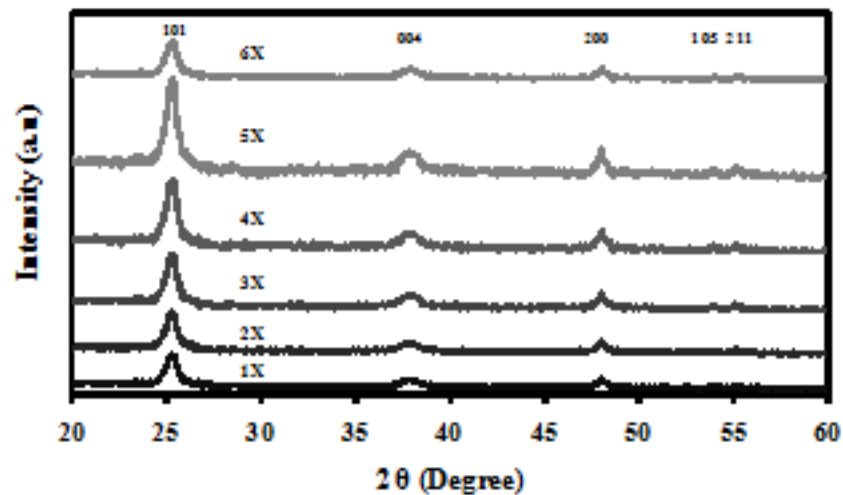
Figure 1: XRD diffracted peaks of novel TiO_2 nanostrawberry structures at 2Θ (degree), 25.28, 37.88, 48.05, 53.89, and 55.06 match with anatase facets 101, 004, 200, 105, and 211, respectively, when growth time was set for 1X-6X cycles.
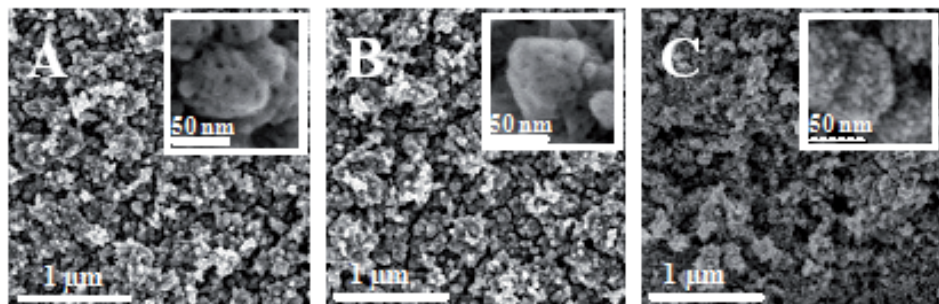
Figure 2: Low resolution FESEM images of homogeneous growth of novel TiO_2 nanostrawberry structures and (b)-Inset, high resolution FESEM images showing the effect (size and porosity) of growth cycles: (A) 2X, (B) 5X, and (C) 6X.

of facet 101 along with unusual slightly more exposure of facet 200 confirms novel TiO_2 nanostructure. On analysis, it is found that for each sample, ratio of the peaks corresponding to the facet 101 to facet 200 is (0.08, 0.083, 0.11, 0.12, 0.20, and 0.47 respectively for 1X-6X) increasing, which depicts increasing exposure of facet 200 with respect to facet 101 as the growth time is increased. It is also observed that position of the peaks does not change, whereas the intensity of the peaks increases with increase in growth time. It portrays that growth time has affected the quantity, and orientation of anatase phase TiO_2 nanostructures

A unique TiO_2 nanostructuredepicted from XRD analysis was verified by low and high resolution images of the samples attained by using FESEM facility. A very homogeneous growth of highly porous, like nanostrawberry structureson ITO can be seen in fig.2.

It is observed that after first growth cycle average diameter of TiO_2nanostrawberries is 60± 5nm, and after second growth cycle some porosity is seen on the surface of TiO_2 nanostrawberry structures, which is shown in inset fig. 2-A. For further growth cycles, porosity is increased to a great extent, whereas size of TiO_2 nanostrawberry structures
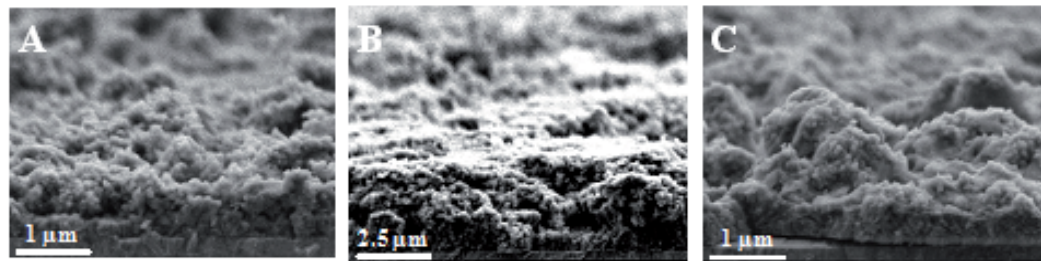
Figure 3: FESEM images; Effect of growth cycles on thickness of TiO_2 layers. Samples (A) 2X, (B) 5X, and(C) 6Xof thickness 658 nm, 2.25 μm, and 547 nm respectively.

are slightly increased, which are shown in high resolution FESEM images in inset fig. 2.B-C.

The mechanism of formation of anatase TiO_2 like nanostrawberry structure is based on use of hexamethylenetetramine as decoupling between hydrolysis and polycondensation of Ti-ions and NH_3. Hydrolysis of hexamethylenetetramine ($C_6H_{12}N_4$) produces NH_3 and OH^{--}, and further hydrolysis of ammonium (NH_3) produces NH_4 and OH^-. Hydrolysis of ammonium hexafluorotitanate produces NH_4^+ and $(TiF_6)^{2-}$. Further hydrolysis of $(TiF_6)^{2-}$ produces Ti^{4+}, $Ti(OH)_6^{2-}$, and fluorine ions. The predicted reaction, $Ti(OH)_6^{2-} \rightleftharpoons TiO_2 + 2H_2O + (OH)^{--}$ does not show stability. Here terminated fluorine ions play a role to form HF by combining with hydrogen ions released from hydrolysis of boric acid. The synergetic effect of HF and HMT leads to produce unique anatase TiO_2 like nanostrawberry structure. Microwave power has provided sufficient energy to these ions to react more efficiently. Hence the active solvation and particularbonding effect of capping agents lead to produce porous TiO_2 nano structures with exposed facets [101], and [200].

It is also observed that thickness of TiO_2 layer grown on ITO increases after each growth cycle, unless it reaches to its maximum, and then after the next growth cycles, it starts depleting. It is found that 280 nm, 658 nm, 691 nm, 1.65 μm, and 2.25μm thick layers are synthesised when growth time is set for 1X-5X cycles, respectively. However, after sixth cycle, TiO_2 layer is depleted to a great extent and just 547 nm is left on ITO. Fig. 3 shows the FESEM images of thickness of TiO_2 layers attained on ITO after 2 X, 5 X and 6X growth cycles. It is apparent that growth cycles (1X-5X) have not affected the morphology of TiO_2 nanostrawberry structures, but have increased porosity, size and layer thickness of TiO_2 nanostrawberry structures on ITO. Depletion in thickness after sixth cycle can be due to these factors, (a) inadequate support to large sized nanoparticles grown on the top of small sized nanoparticles with low adhesion, and (b) the decrease in compactness, which is caused by increasing porosity beyond a certain growth cycle.

Ultravoilet-visible (UV/Vis) absorption spectra analysis of these samples was carried out to scrutinize the usefulness of novel TiO_2 nanostrawberry structures in photochemical processes and photonics. In order to investigate the effect of growth time on optical absorption capabilities of these novel highly porous TiO_2nanostructures, a thickness-based normalised UV/V is absorption spectra is plotted, which is shown in fig.4. It is
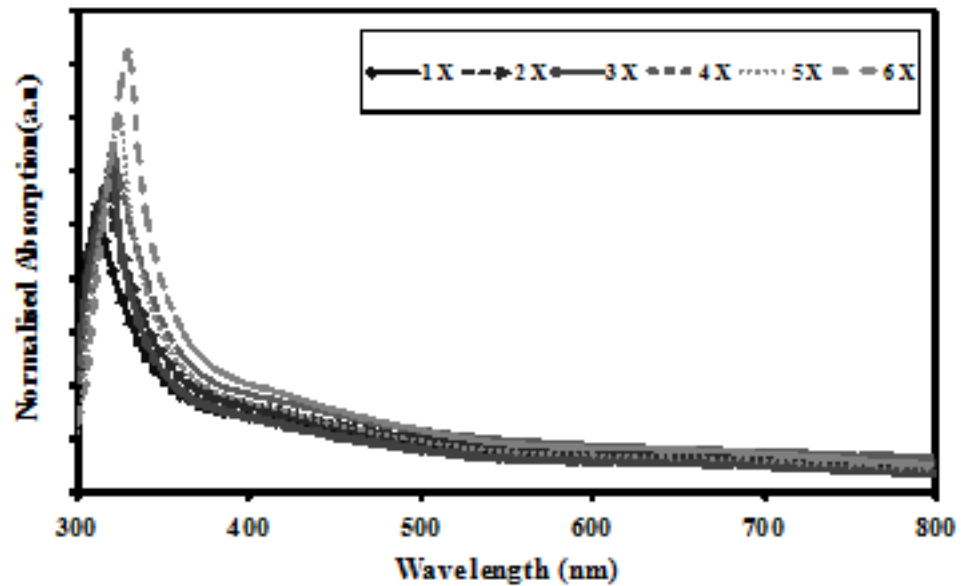
Figure 4: Thickness-based Normalised optical absorption spectra of TiO$_2$nanostrawberry structures for the growth cycles 1X-6X. Red shift is observed for higher growth cycles.

observed that absorption level increases by increasing the number of growth cycles (1X-6X), and their optimum absorption is at wavelength 320±10 nm approximately.

Matching these results with figures 2, and 3, strengthen that optical absorption level is directly proportional to porosity, which has shown its dependence on growth time. The increasing trend in absorption level is also shared by hickness, which is mounting hereover 1X-5X. If this rise in intensity has its prominentshare due to the porosity of nanostructures then absorption level should still be rising even when it is judged for standard normalised thickness. Fig. 4 reveals this fact for the samples 1X-6X, even though the thickness of sample6Xis reduced but has shown its highest normalised absorption intensity level forhighly porous structure. A slight red shift in wavelength of 20 nm corresponding to optimum absorption is observed by increasing growth cycles 1X-6X, which indicates lowering down of band gap in these nanostructures, which should be due to exposure of the surface containing high electron density, and XRD analysis also advocates that increasing exposure of high energy facet 200 is because of increase in growth time.

4. Conclusion

In conclusion, a novel porous nanostrawberry anatase TiO$_2$ structure has been successfully synthesised on ITO, with the aid of microwave power in a very short duration. Porosity of these nanostructure layers can be increased by varying the growth time. So far 2.25 μm optimised thick layer can be deposited on ITO, and the average diameter of these highly porous nanostructures is 70±2.5 nm. It is found that growth time has its encouraging effect on optical absorption intensity. Due to its high absorption at 320±10 nm wavelength, these highly porous anatase phase TiO$_2$ like nanostrawberry structures can be helpful to enhance photocatalytic processes, and can be used to

enhance photon-current efficiency of dye sensitised solar cells as well, when applied as a photo-electrode.

References

[1] S. K. M. Saad, et al., Porous (001)-faceted Zn-doped anatase TiO2 nanowalls and their heterogeneous photocatalytic characterization, *RSC Advances*, **4**, 57054–57063, (2014).

[2] J. Nisar, Z. Topalian, A. De Sarkar, L. Österlund, and R. Ahuja, TiO2-based gas sensor: a possible application to SO2, *ACS Appl Mater Interfaces*, **5**, 8516–8522, (2013).

[3] A. F. Khan, M. Mehmood, T. Ali, and H. Fayaz, Structural and optical studies of nanostructured TiO2–Ge multi-layer thin films, *Thin Solid Films*, **536**, 220–228, (2013).

[4] J. Tang, J. R. Durrant, and D. R. Klug, Mechanism of photocatalytic water splitting in TiO2. Reaction of water with photoholes, importance of charge carrier dynamics, and evidence for four-hole chemistry, *J Am Chem Soc*, **130**, 13885–13891, (2008).

[5] A. A. Umar, S. Nafisah, S. KM. Saad, S. T. Tan, A. Balouch, M. M. Salleh, and M. Oyama, Poriferous microtablet of anatase TiO2 growth on an ITO surface for high-efficiency dye-sensitized solar cells, *Sol Energy Mater Sol Cells*, **122**, 174–182, (2014).

[6] M. Lazzeri, A. Vittadini, and A. Selloni, Structure and energetics of stoichiometric TiO2 anatase surfaces., *Physical Review B*, **36**, no. 15, (2001).

[7] M. M. Byranvand, et al., A Review On Synthesis Of Nano-TiO2 Via Different Methods, *Journal of Nanostructures*, 1–9, (2013).

[8] A. A. Umar, M. Y. A. Rahman, S. K. M. Saad, M. M. Salleh, and M. Oyama, Preparation of grass-like TiO2 nanostructure thin films: effect of growth temperature, *Appl Surf Sci*, **270**, 109–114, (2013).

[9] Y. U. Bykov, K. I. Rybakov, and V. E. Semenov, High-temperature microwave processing of materials, *Journal of Physics D: Applied Physics*, **34**, no. 13, p. R55, (2001).

[10] E. T. Thostenson and T.-W. Chou, Microwave processing: fundamentals and applications, *Compos, Part A Appl Sci Manuf*, **30**, 1055–1071, (1999).

[11] A. A. Salema, Y. K. Yeow, K. Ishaque, F. N. Ani, M. T. Afzal, and A. Hassan, Dielectric properties and microwave heating of oil palm biomass and biochar, *Ind Crops Prod*, **50**, 366–374, (2013).

[12] Y. Tao, C.-Y. Wu, and D. W. Mazyck, Microwave-assisted preparation of TiO2/activated carbon composite photocatalyst for removal of methanol in humid air streams, *Ind Eng Chem Res*, **45**, 5110–5116, (2006).

[13] B. S. Shirke, P. V. Korake, P. P. Hankare, S. R. Bamane, and K. M. Garadkar, Synthesis and characterization of pure anatase TiO2 nanoparticles, *J Mater Sci Mater Electron*, **22**, 821–824, (2011).

Knowledge E
Engaging minds

Conference Paper

Synthesis and Characterization of Fibrous Bimetallic CuPt Nanoparticles

Elvy Rahmi[1,2], Setia Erlila[2], Mardiani Samsir[2], Akrajas Ali Umar[1], Muhamad Mat Salleh[1], and Mohd Yusri Abd Rahman[1]

[1]Institute of Microengineering and Nanoelectronics (IMEN), Universiti Kebangsaan Malaysia, 43600 Bangi, Selangor, Malaysia
[2]Sekolah Tinggi Agama Islam Negeri STAIN Batusangkar, West Sumatera, Indonesia

Abstract This paper reports a facile methode for the synthesis offibrous bimetallic CuPt Nanoparticles (CuPt NPs) using the liquid phase deposition methods deposited directly on an indium-tin oxide (ITO) substrate. The electron microscopy analysis result shows that CuPt NPs, constructed by networked-nanorod of diameter ca. 3.5 nm and length approximately 5.5 to 6.5 nm, exhibits aquasi sphericalmorphology and fibrous structure with diameter approximately 196 ± 98 nm. The differences of individual element miscibility and the effect of lattice-mismatch between Pt and Cu isthe key factorfor the formation of fibrous structure. XPS analysis indicated that the fibrous bimetallic CuPt NPs feature metallic properties with highly reactive surface. This may increase the charge-transfer reactions in catalytic, electrochemistry and sensors application.

Keywords: fibrous structure, lattice-mismatch effect, CuPt

🔓 **OPEN ACCESS**

1. Introduction

Bimetallic nanoparticles synthesis with large surface area, such as fibrous structure, has received considerable attention because of their ability to enhance electrical, magnetic, and catalytic properties [1, 2]. Platinum based bimetallic nanocrystal is amongs the metal nanoparticle that is used in a broad range of applications, such as catalysis [3], electrocatalysis [4], and sensing [5] due to its peculiar electrical and catalytic properties.Up to now, there are many Pt-based bimetallic nanostructures fabricated and performed an extraordinary catalytic properties in wide range of applications, particularly in acetone hydrogenation, electrocatalytic oxidation of methanol and the CO oxidation process. This paper report an effective approach to synthesize fibrous bimetallic CuPt nanoparticle that was prepared using liquid-phase deposition method. The nanoparticle is characterized by network nanorods forming highly porous structure. X-ray photoelectron spectroscopy analysis reveals that the structure exhibit active surface chemistry and potential to enhance catalytic performance.

How to cite this article: Elvy Rahmi, Setia Erlila, Mardiani Samsir, Akrajas Ali Umar, Muhamad Mat Salleh, and Mohd Yusri Abd Rahman, "Synthesis and Characterization of Fibrous Bimetallic CuPt Nanoparticles," *KnE Engineering*, vol. 2016, 6 pages. DOI 10.18502/keg.v1i1.508

Page 1
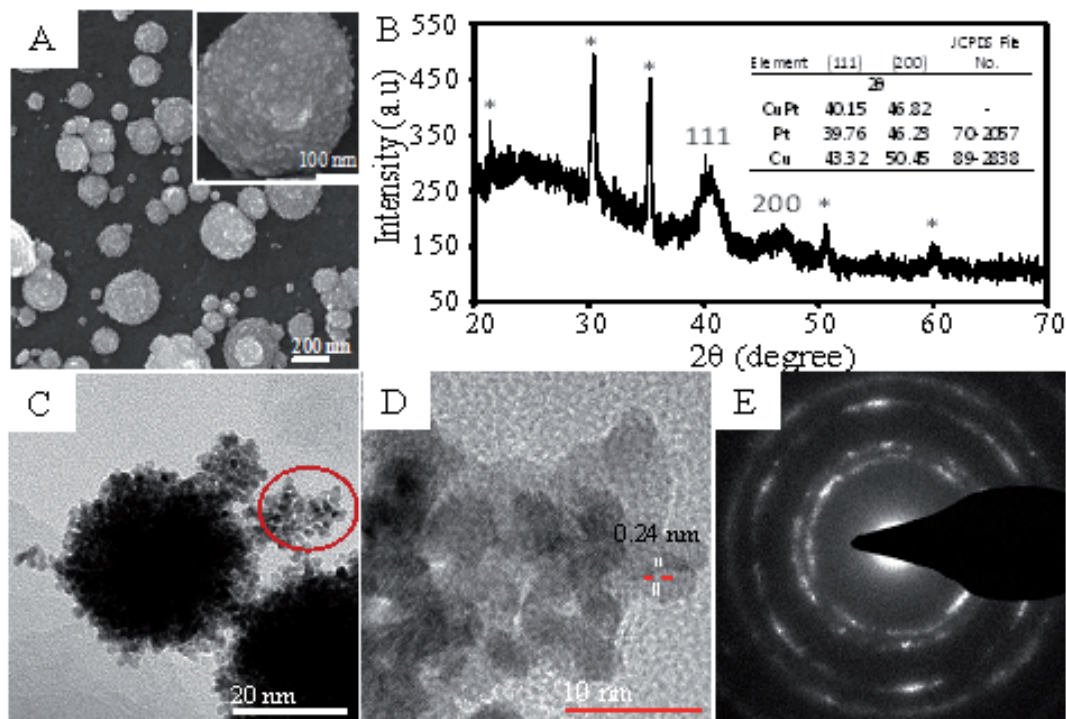
Figure 1: (A) FESEM image of fibrous bimetallic CuPt NPs. The inset in A is the high-resolution of the CuPt NPs. (B) XRD spectrum of fibrous bimetallic CuPt NPs. (C) Low resolution and (D) high-resolution TEM images of fibrous bimetallic CuPt FNPs, (E) SAED diffraction pattern from the nanostructure.

2. Experimental Section

Potassium hexachloroplatinate (K_2PtCl_6), Copper(II)Sulfate ($CuSO_4$) anhydrous, Sodium dodecyl sulfate (SDS) and Formic acid were all from Fluka. All chemicals were used as received. ITO substrate (sheet resistance of 9–22 Ω per square was purchased from a VinKarola instrument, USA) was cleaned by consecutive ultrasonication in acetone and ethanol for 30 min, respectively prior to the growth process.

The bimetallic CuPt NPs deposited on the ITO substrate were prepared following our recently reported method [6], by simply immersing the clean substrate into a 15 mL aqueous solution that contained 1 mM K_2PtCl_6, 0.2 mM $CuSO_4$ anhydrous, 10 mM SDS and 10 mM formic acid and continuously stirred at 400 rpm during the reaction. The growth temperature and time was set to 40 ^{0}C and 4 h, respectively. Then the sample was removed from the growth solution and rinsed with a copious amount of deionized water. The final product was dried with a flow of nitrogen gas.

The morphology of bimetallic CuPt NPs was characterized by field emission scanning electron microscope (FESEM) Hitachi S-4800 operated at an accelerating voltage of 2 kV and high-resolution transmission electron microscopy(HRTEM) FEI Tecnai G2 F20 operated at accelerating voltage of 200 kV and 10-6 Pa with X-twin objectives lens. The atomic composition, structural properties and chemical state of bimetallic CuPt NPs was analyzed by energy-dispersive X-ray mapping (EDX-mapping), X-ray diffraction (XRD) and X-ray photoelectron spectroscopy (XPS) analysis. EDX apparatus is equipped with X-maxN 80T detector. Moreover, XRD apparatus is equipped with XRD BRUKER D8

Advance system with CuKα irradiation (λ = 1.541Å) and XPS apparatus is equipped with operated at a scan rate of 10 °/min and Ulvac-PHI XPS *Quantera* II, with Al Kα – 1486.6 eV mono-chromated scanning X-ray source, respectively.

3. Results and Discussion

The thin layer of CuPt NPs with fuzzy gray color was observed on the ITO substrate after a growth process for 4 h in the growth solution containing K_2PtCl_6, $CuSO_4$ anhydrous, SDS and formic acid. The typicalFESEM analysis result of the sample is illustrated on Fig.1a. An uneven distribution of CuPt NPs nanoparticles was formed that covers nearly 65% of the ITO substrate.The nanoparticle exhibited quasi spherical shape with anextremely rough surfaces and diameter of approximately 196±98nm.

To obtain the information of bimetallic CuPt NPs phase, XRD analysis was carried out to CuPt NPs sample. the sample was characterized by XRD. Fig. 1b reveals two prominent peaks, i.e. at 2θ = 40.15^o and 46.82^{o}corresponds to the Pt crystal plane (111) and (200) respectively, but slightly shifted. When observed the others peaks are belongs to by the ITO substrate. To clarify the formation of bimetallic CuPt NPs, the present XRD result is compared to individual Ag and Pt (the inset table in Fig.1b). The formation of bimetallic CuPtNPs could be signed by the two prominent peaks of bimetallic CuPt NPs are fell in between those of the two pure metal elements where slightly higher angle compared to the individual Pt, i.e. 0.39 ^{o} to 0.59 ^{o} and lower angle compared to the individual Cu, i.e. 3.17^o to 3.63^o. This condition indicate that the intermetallic compound was formed upon introduction of Cu ions into the Pt host lattice [7].

To evaluate how the structure of bimetallic CuPt NPs, high-resolution TEM analysis was carried out (Fig.1D). As shown in the Fig.1D, large number of nanorod overlapping constructed CuPt NPs structure. The length and diameter nanorod are approximately 5.5 to 6.5 nm and 3.5 nm respectively. As have been mentioned previously, the current reaction is modification of our previous approach for synthesis of Pt fibrous cubes. Changing of nanoparticle morphology from the fibrous cubes (PtNCs) to quasi sphericalCuPt NPs was due to the introduction of the Cu^{2+} ion into the growth solution. The differences of individual element miscibility and the effect of lattice-mismatch, between Pt and Cu which is as high as 8.2%, is assume the key factor for the modificationof the morphology. With a fibrous morphology, the CuPt NPs may provide a high active surface area for enhanced surface reaction and may accelerate the diffusion of reactant and product onto the surface in catalytic application process.

High-resolution TEM image for single nanorod (Fig.1d) revealed that nanoparticle is single crystal as evidenced by the lattice fringes across the full extent of nanorod particle. The d-spacing value of approximately 0.24 nm. The comparison between d-spacing value of PtNCs (111) faceted and CuPt NPs reveals that the nature of crystal has grown along the [111] direction. The crystallinity of CuPt NPs has been also revealed by Selected-area electron diffraction (SAED) pattern (Fig 1E). Due to the some of nanorods structure overlapping difraction, it caused the polycrystalline detected, practically the structure is monocrystalline.
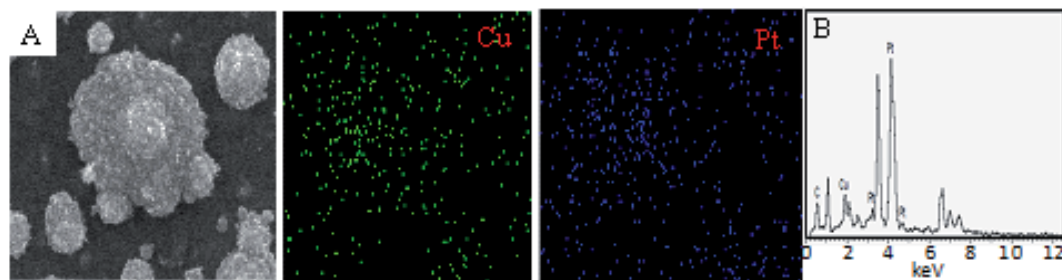
Figure 2: EDX mapping (A) and spectrum (B) of Bimetallic CuPt NPs.
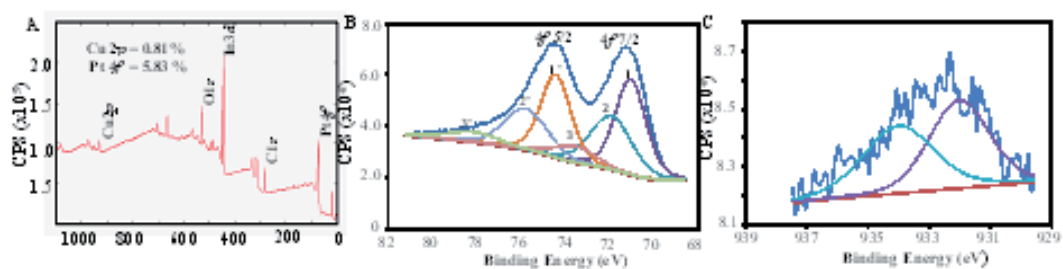
Figure 3: (A) Wide-spectrum scan of bimetallic CuPt NPs. High-resolution spectra for Cu 2*p* (B), and Pt 4*f* (C).

To further confirm the formation of bimetallic CuPt NPs and the element distribution in bimetallic CuPtNPs, Energy-Dispersive X-ray mapping analysis was carried out. The result is shown in Fig.2. Fig.2 reveals, the CuPtNPs is clearly constructed by the Cu and Pt element which are homogeneously distributed on CuPt NPs structure. The atomic composition analysis shows that Cu concentrations are much lower compared to Pt, namely 1:5.4. As also observed from the analysis result, carbon elements was detected in the fibrous bimetallic CuPt NPs structure. It is simply analyzed that it come from the surfactant source.

XPS analysis was employed to know the chemical state and the surface composition of the CuPt NPs. The result is shown in Fig. 3. Gaussian–Lorentzian (G–L) mixed function (70% Gaussian and 30% Lorentzian components) with Shirley-type background as the peak line shape was used in the curve fitting process. Based on survey scan analysis (Fig.3.a), we found that the molar ratio of Cu and Pt is approximately as high as 1:7.2 on the surface. This ratio is slightly different from the bulk elemental analysis using EDX mapping, i.e. as high as 1:5.4. Nevertheless Pt element is still predominant. Fig. 3b and c show the typical high resolution spectra for Cu (2*p*) and Pt (4*f*) core level states.On the typical high resolution spectra Pt4*f*, there are three pairs of overlapping GL Curves on Pt 4*f*7/2, it means, Pt has three oxidation states of Pt, namely Pt (0) at 71.05 eV (curve 1), Pt^{2+} at 71.97 (curve 2) and and Pt^{4+} at 73.61 (curve 3) eV (Fig. 3B). It reveals that the Pt has been reduced from Pt^{4+} to Pt $^{2+}$ and Pt 0 species in intermetallic compound. The Metallic state of Pt in CuPt NPs shows a negative shift if it is compared to the pure Pt, i.e. 71.3 eV [8]. It may be caused by the perturbed electronic interaction between Pt and Cu atomic orbit and in turn to its alloy formation. The evidentiary of bimetallic formation also can be seen with the presence of Pt (0) is the predominant species, as high as 52.45%.

Meanwhile on the typical high resolution spectra Cu *2p* show two pairs of overlapping GL Curves. Based on curve fitting on Cu*p*3/2, it infers that Cu has two oxidation state, i.e. at 932.01 eV and 934.0 eV binding energy respectively. It means, Cu is composed by two oxidation states, namely Cu (0) and Cu^{2+} species respectively. If we see the relative intensities of avery oxidation state, the intensity of Cu (0) species is higher then Cu^{2+} species, i.e. 51.10%. The comparison of Cu (0) binding energy (current result) and pure Cu was also occured. A negative shift of binding energy is appeared when metallic state of Cu is compared to the system of pure Cu (932.63 eV) [9]. It can be understood that Cu has electron donating property and it has a possibility to donate the electron to the half filled of Pt *f*-orbital in the formation of bimetal nanoparticle. Considering that metallic state of Cu and Pt have high intensity in the compound and shows negative energy shifting, it indicates the CuPt NPs is conformed completely formed.

4. Summary

In this experiment, CuPt NPs were synthesized directly on an indium tin oxide (ITO) substrate by Liquid phase deposition methods. The FESEM and HRTEM analysisshows that a fibrous bimetallic CuPt NPs nanoparticles was formed and cover nearly 65% of the ITO substrate.The nanoparticle is constructed by large number of nanorods overlapping. Through the molar ratio of Cu^{2+} to Pt^{4+} ion in growth solution preparation as high as 1:5, the geometry of nanoparticle could be efficiently adjusted, the average diameter of the nanoparticle is approximately 196 ± 98 nm.The differences of individual element miscibility and the effect of lattice-mismatch between Pt and Cu isthe key factor for the formation of fibrous morphology. XPS analysis revealed that the higher percentage of Cu (0) and Pt (0) species established, indicates that the CuPt NPs surface is chemically reactive and may be considered as a potential in nanocatalyst.

References

[1] H. You, S. Yang, B. Ding, and H. Yang, Synthesis of colloidal metal and metal alloy nanoparticles for electrochemical energy applications, *Chem Soc Rev*, **42**, 2880–2904, (2013).

[2] B. N. Wanjala, J. Luo, B. Fang, D. Mott, and C.-J. Zhong, Gold-Platinum Nanoparticles: Alloying and Phase Segregation, *J Mater Chem*, **21**, 4012–4020, (2011).

[3] A. A. Umar, E. Rahmi, A. Balouch, Y. A. R. Mohd, M. M. Salleh, and M. Oyama, Highly-Reactive Agpt Nanofern Composed of 001-Faceted Nanopyramidal Spikes for Enhanced Heterogeneous Photocatalysis Application, *J Mater Chem A Mater Energy Sustain*, **2**, 17655–17665, (2014).

[4] J. B. Xu, T. S. Zhao, and Z. X. Liang, Synthesis of Active Platinum– Silver Alloy Electrocatalyst toward the Formic Acid Oxidation Reaction, *J Phys Chem C*, **112**, 17362–17367, (2008).

[5] R. Sundar Dey and C. Retna Raj, Development of an Amperometric Cholesterol Biosensor Based on Graphene– Pt Nanoparticle Hybrid Material, *J Phys Chem C*, **114**,

21427–21433, (2010).

[6] A. Balouch, A. A. Umar, S. T. Tan, S. Nafisah, K. MS. Siti, M. M. Salleh, and M. Oyama, Fibrous, Ultra-Small Nanorod-Constructed Platinum Nanocubes Directly Grown on the Ito Substrate and Their Heterogeneous Catalysis Application, *RSC Advances*, **3**, 19789–19792, (2013).

[7] Z. Peng, H. You, and H. Yang, An Electrochemical Approach to Ptag Alloy Nanostructures Rich in Pt at the Surface, *Adv Funct Mater*, **20**, 3734–3741, (2010).

[8] P. R. Norton, Surface Analysis of Platinum by X-Ray Photoelectron Spectroscopy (Xps), *Surf Sci*, **44**, 624–628, (1974).

[9] M. C. Biesinger, L. W. M. Lau, A. R. Gerson, and Smart R. S. C., Resolving Surface Chemical States in Xps Analysis of First Row Transition Metals, Oxides and Hydroxides: Sc, Ti, V, Cu and Zn, *Appl Surf Sci*, **257**, 887–898, (2010).

KnE Engineering

Knowledge E
Engaging minds

Conference Paper

Effect of Growth Temperature on ZnO Nanorod Properties and Dye Sensitized Solar Cell Performance

Marjoni Imamora Ali Umar[1], Fitri Yenni Naumar[2], Muhamad Mat Salleh[2], Akrajas Ali Umar[2], and Mohd. Yusri Abd. Rahman[2]

[1]Department of Physics Education, Faculty of Tarbiyah dan Ilmu Keguruan, Institut Agama Islam Negeri (IAIN) Batusangkar, 27213, West Sumatera, Indonesia
[2]Institute of Microengineering and Nanoelectronics (IMEN), Universiti Kebangsaan Malaysia, 43600 Bangi, Selangor, Malaysia

Abstract Nanostructure of semiconductor materials zinc oxide (ZnO) is widely used in fabrication of solar cell devices. The performance of such devices is strongly depending on the nanostructures of the thin films used. In this paper reports the effect of growth temperature during synthesis of one-dimensional (1-D) anatase ZnO nanorod arrays through hydrothermal process facing their structure, morphology, and optical properties. The ZnO nanorod was first synthesized use the solution concentration and time fixed at 0.04M and 1 hour. The growth temperature were varied from 70, 80, 90 and 100 °C. The effect of growth temperature on the structural, morphology, and optical absorption of ZnO nanorod were studied by using X-ray diffraction (XRD), field emission scanning electron microscopy (FESEM), and UV–vis spectroscopy. The regularity, diameters, heights, and surface densities of the ZnO nanorods were increased with the growth temperature.The optimum results of FESEM characterizations showed that the grown ZnO nanorods have diameters of 64.14 ± 8.3 nm, heights of 363.72 ± 34 nm and surface densities of 182 numbers/μm^2 which was obtained at temperature of 90 °C. The optimum ZnO nanorod film was utilized as photo anode in dye sensitized solar cells. The DSSC yielded Jsc of 0.86 mA/cm^2, Voc of 0.49 V, and FF of 38 %, resulting in PCE of 0.16 %.

Keywords: growth temperature, one-dimensional, ZnO nanorod array, DSSC

🔓 **OPEN ACCESS**

1. Introduction

Research efforts on one dimensional (1-D) ZnO nanostructures such as nanorod still have high interest rates since a few decades ago because it has unique properties for many applications such as sensor, solar cell, electronics devices and etc.[1]. Numbers of scientific papers related on the ZnO nanostructure whether fundamental or practical application has become the evidence of their popularity. One of the main aspects in this research is to synthesize the ZnO nanorod with regular rod, small diameter, higher, and optimum of their surface densities but also an improved quality of their optical and electronic properties. Tian, Voigt [2] mention the extended and oriented nanostructures are desirable for many applications. Besides, the direct fabrication of

complex nanostructures with controlled crystalline morphology, orientation and surface architectures remains a significant challenge.

Previously, oriented carbon nanotubes and ZnO nanorod shave been prepared by high-temperature vacuum deposition techniques. However, this method makes the structure of ZnO becomes damaged and increase the preparation cost. A variety of methods have been reported for fabricating arrays of aligned ZnO nanostructure, including vapour phase transport, metal organic chemical vapour deposition (MOCVD), and hydrothermal processes. However, vapour-phase transport and MOCVD usually require single-crystal substrates and high operation temperature.

In this paper, ZnO nanorod was provided through a hydrothermal process and the effect of the temperature during preparation step to their properties and DSSC performance is also investigated. This research is expected to find the lowest temperature to produce a better ZnO nanorod and applied of them on DSSC device with better performance and low cost.

2. Experimental

ZnOnanorods arrays were prepared on FTO glass substrates which were pre-coated with ZnO nanoparticles using hydrothermal process. ZnOnanorods which first seed layers prepared by alcohothermal process which contain of zinc acetate (Zn $(H_3COO)_2$ H2O) (98%, Sigma Aldrich) in ethanol to form ZnO seeded-substrate. The ZnO seeding substrate was subject to annealing at 350 °C in air for an hour and followed by immersing them in closed vial containing zinc nitrate hexahydrate (99%, Sigma Aldrich) and hexamethyl-tetramine (99%), Sigma Aldrich) in DI water. Next, the final concentration of that solution was maintained at 0.04 M and then inserts them in heating drying oven with various temperature such as 70, 80, 90 and 100°C for 1 hour. The detail of the ZnOnanorods preparation processes has been described very well elsewhere [3, 4]. The resultant ZnOnanorod were characterized by X-Ray diffraction (XRD), Halo DB-20 UV-Vis spectrometer, and Carl Zeiss Supra 55VP field emission scanning electron microscopy (FESEM) to investigate their composite-structure, optical absorbance properties and morphology as well. Besides, the current (J)–voltage (V) curve of cell underactive area of 0.23 cm^{2}was recorded by a Keithley model 237 measurement, which were presented in the "Result and discussion "section.

ZnOnanorod will be used as photo anode in dye sensitized solar cells (DSSC). Installation of a DSSC solar cell device was made by clamp the photo anode with counter electrode and put insulating material between of them. Furthermore, the electrolyte is injected into the active area to make the DSSC device can work to convert sunlight coming through photo anode to become electric current. The DSSC performance of the solar cell with active area of 0.23 cm^2 was investigated by current–voltage measurement under 100 mW/cm^2 simulated AM 1.5 G sunlight using Gambry 1000 interface measurement unit.

The electrolyte used is s standard iodolyte. Dye solution prepared by dissolving 7.0 mg powder dyes N-179 in 20 ml of ethanol to a concentration of 0.3 mM. The counter electrode was used of 40 μl a liquid plastisol which in-situ coated on the FTO substrate
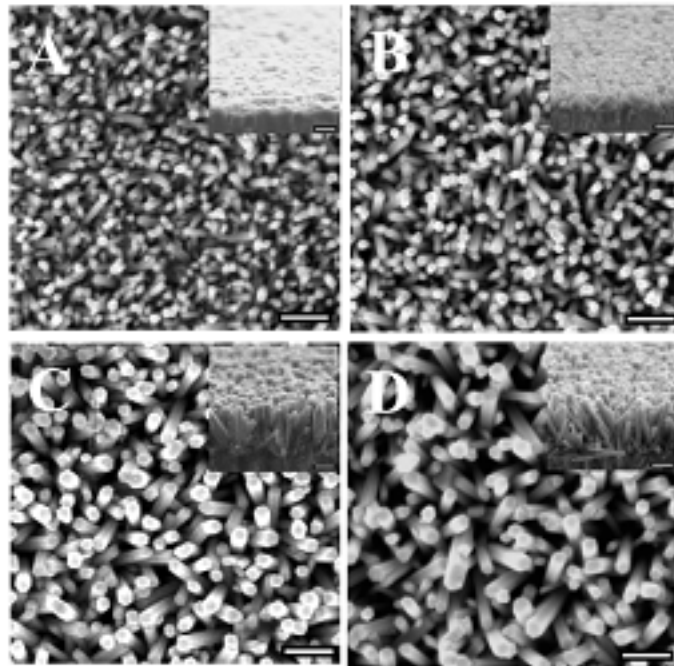
Figure 1: FESEM image variations in temperature (A) to 70, (B) 80, (C) 90 and (D) 100 ° C with scale bar 200 nm. The inset picture in each image shows a cross-sectional FESEM micrograph of the corresponding image (scale bar in 200 nm).

at 2000 rpm for 30 seconds. The same step was repeated up to 3 times on each substrate where each of them heated at 100 ° C for 10 minutes. Next, that substrate was annealed at 450° C for 1 hour. Prior to the installation of solar cell devices do, photoanode consisting of ZnOnanorod grown on FTO soaked into 20 ml of N-719 dye solution with a concentration of 0.3 mM, for 2 hours. This immersion is carried out in a dark room, as N-719 is very sensitive and unstable under light radiation, photo anode left to dry in the air and kept so in this process photo anode is not exposed to light.

3. Result and discussion

The ZnONanorods has been successfully synthesized by using hydrothermal process. Fig. 1A shows the ZnOnanorods FESEM image on FTO grown at 70^oC followed by annealing at 350^oC for 1 h. In this case, the ZnOnanorod has not been formed perfectly. Meanwhile, by increase of grown temperature to 80^oC causes the ZnONanorod has been start to grow on the FTO substrate with average diameter about 33.69 nm (see Fig. 1B). Furthermore, this average diameter increases to 64.14 nm when it was grown at 90^oC with a uniform size and regular form as shown in Figure 1C. Lastly, the increase in the growth temperature to 100^oC even made a reduced the average diameter to 55.64 nm with irregular and not uniform size.

Fig 2. shows the XRD peaks of ZnOnanorods which was prepared by using a variety of grown temperature. This it found that the S70 sample XRD peaks observed are too weak which mean the growth processes has not occurred properly at this temperature. Nanorod growth started to grown with better form in samples S80 and S90. The sample
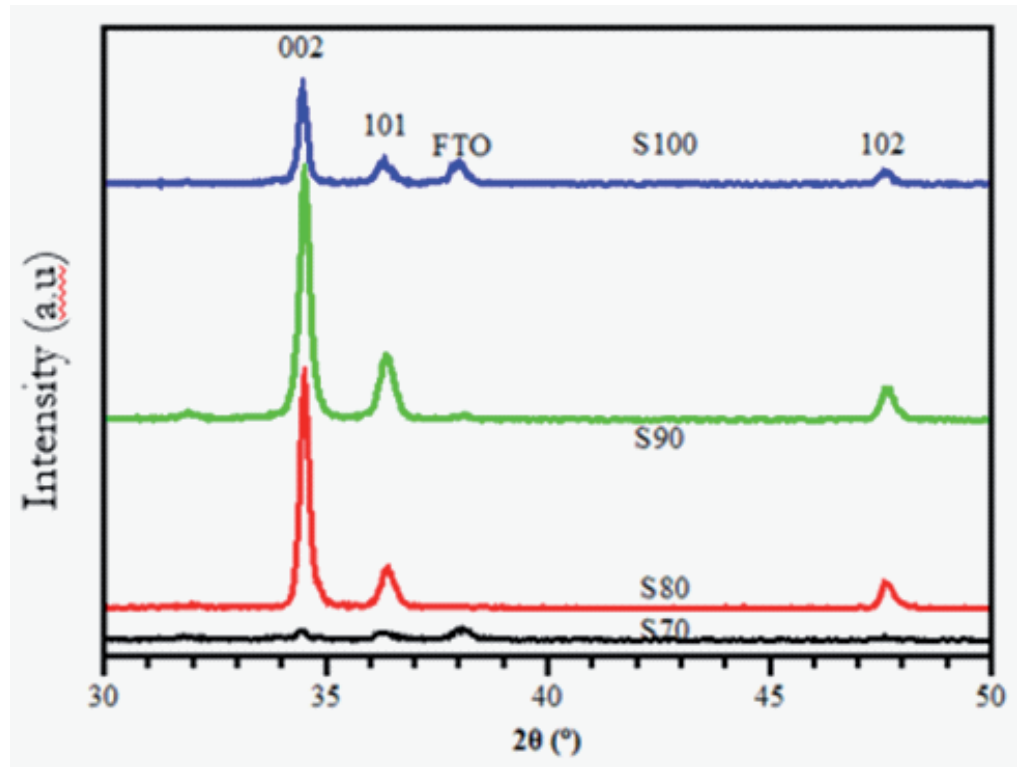
Figure 2: XRD spectra of ZnO nanorods at grown temperature of 70, 80, 90 and 100°C..

Label Samples	Voc (mV)	Jsc (mA/cm^2)	PCE (%)	FF (%)
S80	0.44	0.40	0.06	0.34
S90	0.49	0.86	0.16	0.38
S100	0.47	0.71	0.12	0.35

TABLE 1: DSSC performance parameters of ZnO nanorod grown at the growth temperature variations.

S100 shows the higher and there are additional peaks of FTO substrate. This means that, the growing process began to fail because of the water solvent boiling begins at a temperature of 100°C. As can be seen from these spectra, 3 main peaks namely at 2θ= 34.50, 36.50, and 47.80 where obtained. According to JCPDS file: No. 84-1286 for ZnO the peak was shown above associated with plane of (002), (101), and (110) phase. It was found that only the ZnO peak was detected in those spectra, showing the preparation step does not affect the impurities occurred. Besides, the border peaks show the formation of ZnO nanostructure, which good accordance with previous report [1, 5]. The intensity of the ZnO (002) increases and the peak width decreases with the growth processing time increased.

Figure 3 shows the current density–voltage (J–V) graph of DSSC constructed with plastisol as counter electrode under illumination of a simulated AM 1.5 G sunlight at 100 mW/cm^2. A typical DSSC exhibited a short circuit current density (Jsc) of 0.16 mA/cm^2, an open circuit voltage (Voc) of 0.49 V, and a fill factor (FF) of 38% which was obtain at sample S90. The detail of the DSSC parameter of the sample was described at table 1.
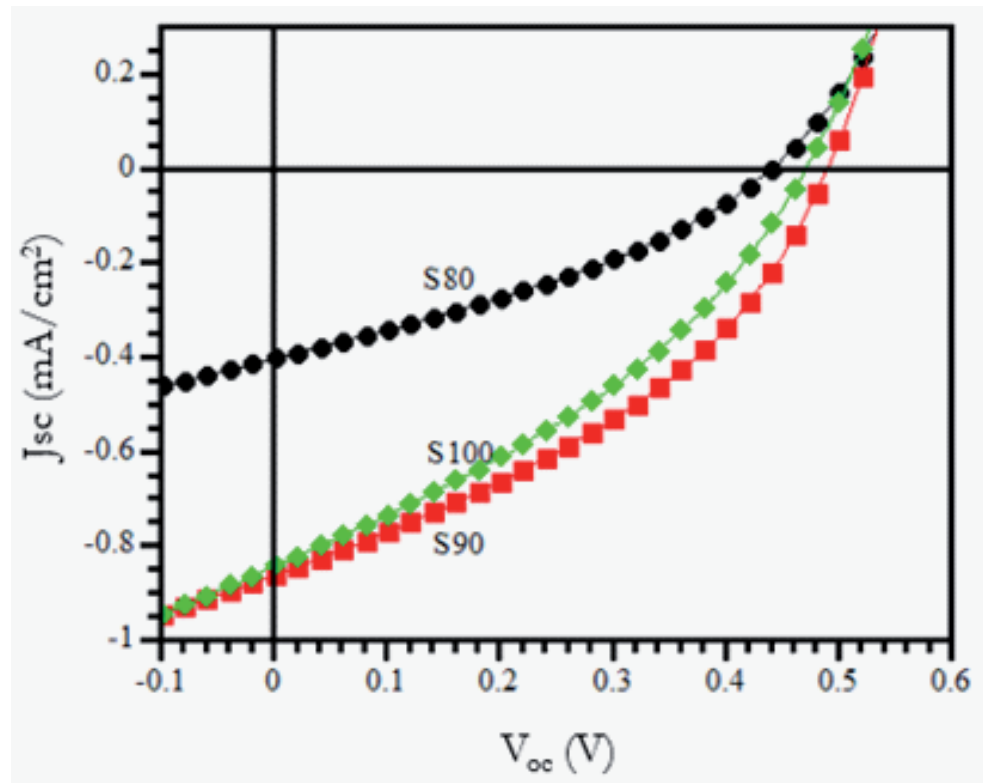
Figure 3: JV curve of a solar cell DSSC devices ZnO nanorod in bright conditions by varying the growth temperature.
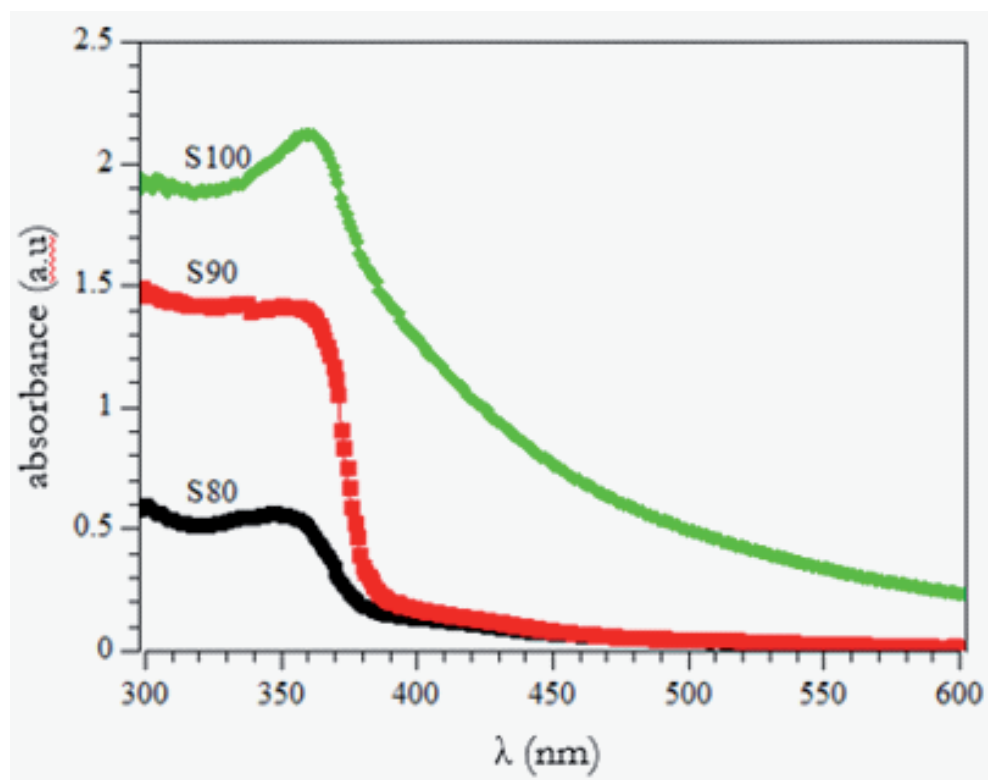
Figure 4: The optical absorption spectrum of ZnO nanorod grown by varying the growth temperature.

Fig 4 shows the optical absorption spectrum of ZnOnanorod grown with the growth temperature variations. The optical absorption of sample S80 and S90 is the same as the optical absorption variations sample first. While the S100 has the highest intensity of the sample, which corresponds to the sample has the highest elevation nanorod. Optical absorption for the S100 has a shoulder that is shaped like a top, which may be due to sample density nanorod has a small, high altitude that makes it easy to apply thermal vibrations of optical radiation

4. Conclusion

The study on the implementing of ZnONRs parameter at various growth temperatures have been performed. The broad peak, and clearly XRD spectra confirm the effect of ZnO nanorods formation. The best photovoltaic performance of DSSC with platisol as a counter electrode which exhibited the J_{sc} of 0.86 mA/cm^2, V_{oc} of 0.49 V, and FF of 38 %, resulting the PCE of 0.16 % was obtained at ZnONRs which prepared at growth period of 1h, growth temperature of at 90°C.

5. Acknowledgment

References

[1] H. Chen, X. Wu, L. Gong, C. Ye, F. Qu, and G. Shen, Hydrothermally grown ZnO micro/nanotube arrays and their properties, *Nanoscale Res Lett*, **5**, 570–575, (2009).

[2] Z. R. Tian, J. A. Voigt, J. Liu, B. McKenzie, M. J. McDermott, M. A. Rodriguez, H. Konishi, and H. Xu, Complex and oriented ZnO nanostructures, *Nat Mater*, **2**, 821–826, (2003).

[3] L. Roza, M. YA. Rahman, A. A. Umar, and M. M. Salleh, Direct growth of oriented ZnO nanotubes by self-selective etching at lower temperature for photo-electrochemical (PEC) solar cell application, *J Alloys Compd*, **618**, 153–158, (2015).

[4] I. Iwantono, et al., Effect of growth temperature and time on the ZnO film properties and the performance of dye-sensitized solar cell (DSSC), *J Solid State Electrochem*, 1–5, (2015).

[5] A. Chrissanthopoulos, et al., Synthesis and characterization of ZnO/NiO p–n heterojunctions: ZnO nanorods grown on NiO thin film by thermal evaporation, *Photonics and Nanostructures - Fundamentals and Applications*, **9**, no. 2, 132–139, (2011).

KnE Engineering

Knowledge E
Engaging minds

Conference Paper

Effect of Concentration Ratio of Precursor-SurfactantSolutionon The Performance of Boron-doped ZnO Nanotubes Dye Sensitized Solar Cells

Iwantono[1], Gusyeri Andika[1], Fera Anggelina[1], Liszulfah Roza[2,3], and Akrajas Ali Umar[2]

[1]Department of Physics, Faculty of Mathematics and Natural Sciences, Universitas Riau, Pekanbaru, 28131, Indonesia
[2]Institute of Microengineering and Nanoelectronics (IMEN), Universiti Kebangsaan Malaysia (UKM), Bangi, 43600, Selangor, Malaysia
[3]Department of Physic Education, Faculty of teacher Training and Education, Muhammadiyah University of Prof. Dr. Hamka, Jakarta, 972011, Indonesia

Abstract Boron doped zinc oxide (ZnO) nanotubes have successfully been grown using seed-mediated hydrothermal method at various concentrations of precursor-surfactant solution. The growth of ZnO nanotubes was carried out at a temperature of 90°C for 8 hours and a drop in temperature to 50°C for 16 hours. In this study, the effect of concentration ratio of precursor-surfactant was evaluated. Samples were characterized using UV-Vis Spectroscopy, X-ray diffraction (XRD), Field Emission Scanning Electron Microscopy (FESEM) and Energy Dispersive X-ray (EDX). UV-Vis spectra of the samples showed that the ZnO nanotubes were grown on the Flourine Tin Oxide (FTO) and the strong absorption occurred in the wavelength range of 300-400 nm, which is typical spectrum for hexagonal-nanostructure. XRD patterns showed five diffraction peaks at 2θ = 32.05°, 34.5°, 36.35°, 47.75° and 56,9°. The analysis of EVA Diffrac Plus confirmed the peaks were represented to the lattice of (100), (002), (101), (102), and (110) respectively. FESEM images of the samples showed the hexagonal-shaped ZnO nanotubes with an average diameter of 50-340 nm and an average thickness of 1.2 - 4.4 μm observed for all samples. Uniformity the size and shape of ZnO nanotubes become higher as concentrations of ZNH decreased. The EDX spectra of the samples showed the percentage of weight of Zn, O, and B was 69.35%, 21.60% and 4.76% respectively, while the percentage of their atoms was 33, 06%, 42.08% and 13.71% respectively. The B-doped ZnO nanotubes solar cells were fabricated by arranging a sandwich structure, consisting of the FTO, ZnO nanotubes, dye, electrolyte and platinum thin film. I-V characteristics of cell were carried out under irradiation of 100 mWcm^{-2} halogen lamp. The I-V curves produced the highest efficiency from the cells utilizing the B-doped ZnO nanotubes with their concentration ratio of precursor-surfactant of 0.1 M : 0.04 M as the active material, which was 0.352%. This value is much higher than that of pure ZnO nanotube based DSSC of 0.05%.

Keywords: Boron, Dye Sensitized Solar Cells, Zinc-Oxide (ZnO) Nanorods, Hydrothermal method

OPEN ACCESS

1. Introduction

In the last decade, one-dimensional nanostructured materials have attracted considerable attention. *Zinc Oxide* (ZnO)among oxide systems has been chosen as one of short wavelength device materials. ZnO has wide-direct band gap energy of 3.3 eV [1,2] comparable to that of TiO_2 3.2 eV [3]. The interesting optical and electronic properties, such as transparent, high transmittance, easy to deposit on many substrates and low cost materials, make nanostructured ZnO as one of most potential active materials for solar cells [4]. Furthermore, some nanostructured ZnO have successfully been produced in diverse groups of growth morphologies, such as ZnO nanowires [5], nanotubes, nanobelts and tetrapods, [6] andnanosheets [7]. Some physical parameters need to be controlled in order to apply ZnO nanostructures for many applications, such as geometrical shape, crystal morphology and orientation [8]. Some efforts have been performed in order to improve the properties of ZnO nanostructures by doping various elements, such as In [9], Al [10], Ga [11] and B [12]. Among them, B-doped ZnO nanotubes are capable of reaching high conductivity, electric mobility and low resistivity [13].

Although some techniques have produced metal-doped ZnOnanorods, such as thermal evaporation and vapor-liquid-solid, but these methods need sophisticated equipment and high temperatures. On the other hand, wet chemical methods, including seed-mediated hydrothermal growth method provides more promising route in producing well-aligned doped ZnO nanostructures, including B-doped ZnO nanotubes. The method allows the synthesis of ZnO nanostructures at lower temperature, more effective and convenient for use with simple and low cost equipments, which can improve the performance of metal-doped (including B-doped) ZnOnanostructures based Dye Sensitized Solar Cells (DSSCs).

In this present paper, we deal with the synthesis of B-doped ZnO nanotube arrays grown by a simple seed-mediated hydrothermal technique on FTO with ZnO seedlayer. The main goal of this work is to establish the effect of the boron-doped solution and concentration ratio of precursor-surfactant solution on the optical and structural properties of the grown ZnO nanotubes and on the performance of B-doped ZnO nanotubes based DSSCs.

2. Experiments

In order to grow ZnO nanotube arrays on the FTO substrate, the seed-mediated hydrothermal growth method was performed. This method principally contains of two steps, namely seeding and growing processes. The seeding process was carried out in order to ZnO seed layer by depositing zinc acetate dihydrate (ZAD) on the substrate. Meanwhile, the growing process took a place in aqueous solution containing Trymethyl borate, zinc nitrate hexahydrate (ZNH) and hexa-methylene-tetramine(HMT).

In this seeding process, ZnO nanoseeds were coated on the FTO by using a method of alcohol-thermal seeding. This technique was firstly begun by forming a thin layer of ethanolic solution of 10 mM zinc acetate dihydrate ($Zn(CH_3COO)_2 2H_2O$) on a FTO by

using spin-coating technique at 3000 rpm for 30 seconds. This process was carried out in order to make sure the solution was evenly distributed on the substrate and to get the sufficient thickness of the seed growth on the substrate. The sample was then dried at 100 ^oC on a hot-plate for 15 minutes and then cooled down to 60^oC. These procedures were repeated three times in order to get appropriate thickness of ZnO nanoseeds. The sample was finally annealed at 350^oC for 1 hour in a furnace. Growth process was started by immersing the ZnO nanoseed coated FTO in the growth solution. The growth solution was prepared by varying concentration of precursor-surfactant (ZNH-HMT) solutions: 0.04 M : 0.06 M; 0.04 M : 0.08 M; 0.04 M : 0.1 M; 0.04 M : 0.14 M; 0.06 M : 0.04 M; 0.08 M : 0.04 M; 0.1 M : 0.04 M; 0.14 M : 0.04 M. Boron doping was preparing by mixing 0.055 mL *Trymetil borate* in 5 mL *DI water* (0.4 mM solution). The sample was put in the oven for 8 hours at 90°C. The temperature was then decreased to 50°C in 16 hours. Finally, the sample was annealed in the furnace at 250°Cfor 30 minutes. XRD method performed in order to examine the structure and phase structure of the ZnO nanostructures by using diffractometer model Bruker D8 Advance. The morphology of the samples was observed using field-emission scanning electron microscopy (FESEM) analysis (Zeiss Supra 55VP FESEM) with the magnification of 10000× and 50000×. The thickness of the ZnO nanostructures was estimated from the cross-sectional image of the FESEM. The elemental analysis was carried by using energy dispersive x-ray (EDX) spectrometer. Optical spectrophotometer UV–Vis Lambda 900 Perkin Elmer was employed to study the optical absorption of the ZnO samples. The absorbance of the samples was measured in the wavelength ranging from 300 to 800 nm.

Before fabrication the DSSC, the gallium doped ZnO nanostructures were immersed into 0.3 mM N719 dye solution for 2 hours. The samples were then taken out, rinsed gently with ethanol and then dried under a flow of nitrogen gas. Platinum film as a catalyst coated on counter electrode was prepared by spin coating platinum pellets at 1000 rpm for 30 seconds on the FTO substrate. The samples were then dried at 100 ^oC on a hot-plate for 5 minutes and then cooled down to 60^oC. The platinum film coating process was repeated three timesin order to get appropriate thickness of Pt films. The sample was finally annealed at 400^oC for 30 minutes in a furnace. An standard electrolyte namely iodolyte was used. A DSSC was fabricated by arranging the sandwich structure of the parafilms between the ZnO nanostructures and the platinum counter electrode. The electrolyte was injected into the cell and filled via a capillary. The performance study of the DSSC was carried out by observing the current–voltage characteristics in the dark and under illumination using an AM 1.5 simulated halogen light with an intensity of 100 mW cm^{-2}. The illuminated area of the cell was 0.23 cm^2. The current–voltage curves in the dark and under illumination were recorded by a Gamry 1000 interfaced with a personal computer.

3. Results and Discussion

Fig. 1 (A) showed UV-Vis spectra of 4 samples with different concentrations of precursor (ZNH) of 0.06 M, 0.08 M, 0.1 M and 0.14 M, with constant concentration of
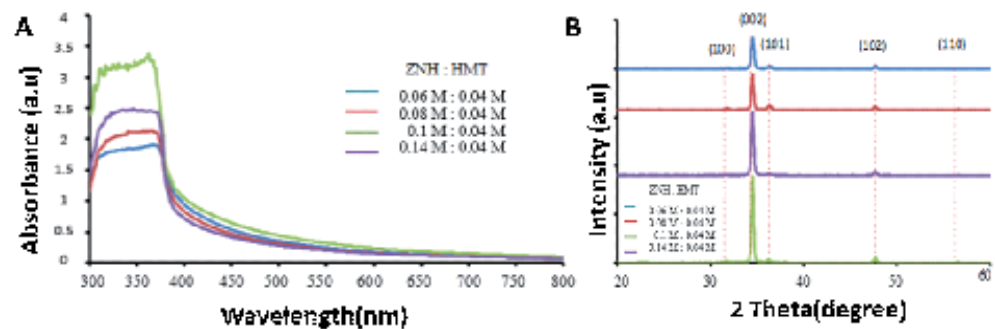
Figure 1: (A) UV-Vis spectra of samples containing Boron-doped Zno nanotubes with diferent ZNH concentration and (B) XRD patterns of boron-doped ZnO nanotubes with various ZNH concentrations.

HMT surfactant of 0.04 M. The figure showed the strong absorption observed at the wavelength range 300-400 nm. The absorption peak occurred at a wavelength of 370 nm for all samples. There was sharp cross point at about 370 nm, which represented good structural quality of ZnO nanostructures [14]. The XRD pattern of the samples of Boron-doped ZnO nanotubes with various ZNH concentrations was shown in Fig. 1(B). At the figure, it was shown 5 diffraction peaks at 2θ = 32.05°, 34.50°, 36.35°, 47.75° and 56.55°. EVA diffract plus analysis confirmed the 5 diffraction peaks represented to crystal orientation of (100), (002), (101), (102), and (110). The strongest diffraction peak at 2θ = 34.50° which represented to (002) crystal orientation was preferred orientation, that represented to hexagonal structure of ZnO [15].

FESEM images of the samples with different ZNH concentration of 0.06M, 0.08 M, 0.1M and 0.14M with concentration of HMT of 0.04 M, as shown in Fig. 2. From the images, it can be seen that ZnO nanotubes were grown onto FTO for all samples with its cross-section of hexagonal shape with various diameter size. Homogenity in size and shape of ZnO nanotubes increased with decreasing ZNH concentration. The diameter of ZnO nanotubes was in the range of 50-340 nm and the thickness of about 1.2 – 4.4 μm for all samples. The diameter of 0.06 M ZNH sample was 100-125 nm, while the diameter of 0.08 M and 0.1 M samples was 125-210 nm and the diameter of 0.14 M ZNH sample was 190-340 nm, with geometrical shape of nanosheet was observed. The cross-section images showed the thickness of ZnO nanotubes increased with increasing ZNH concentration until 0.1 M and decreased as the concentration of ZNH higher than 0.14 M. The thickness of samples was 1.2 μm, 3.5 μm, 4.2 μm and 4.1 μm, respectively. Fig. 3 illustrated EDX spectra of the samples and showed the peaks of Zn and O clearly at 1 keV and 0.58 keV, respectively. At the figure, it was also observed other peaks, which represented to C and B.

Fig. 4(A) illustrates the I-V characteristics in dark condition of the DSSCs utilizing the samples prepared at various precursor concentrations. The I-V curves are the typical characteristics of diode-like. It can clearly be seen that the cells do not show rectification property since the dark current in the reverse bias is not significantly different than that in the forward bias. Thus, the device does not allow the current to be dominant in one direction either in forward or reverse bias. For both biases, the different in the current for all cells is also small indicating that the concentration of
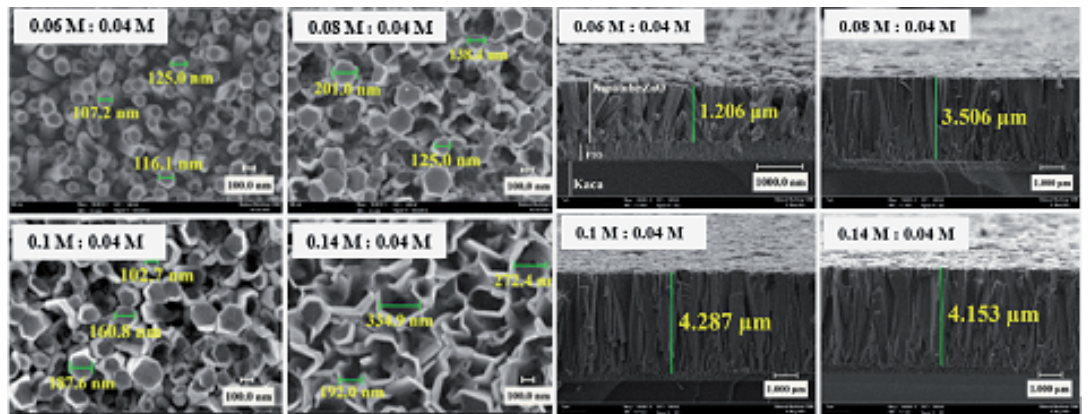
Figure 2: FESEM images of boron-doped ZnO nanotubes at magnification of 50.000X and cross-sectional images of boron-doped ZnO nanotubesat various ZNH concentration.
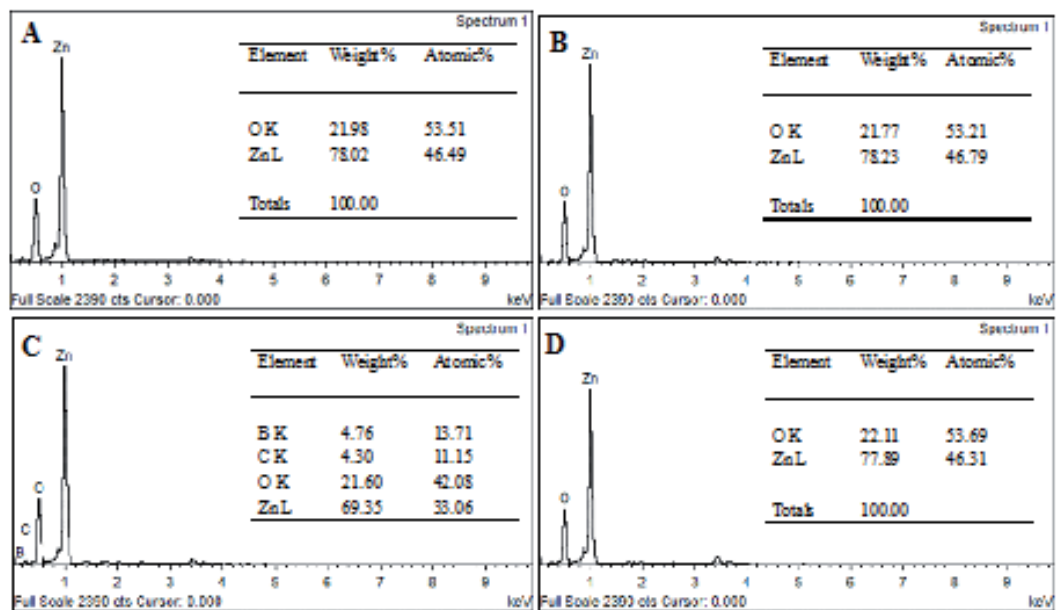
Figure 3: EDX spectra of B-doped ZnO nanostructures prepared at various precursor concentration.

precursor does not influence the dark current. However, the dark current in the device is quit high in both biases, which is in the mA range. This characteristic will result in high photocurrent and power conversion efficiency once the cells are illuminated with light. Fig. 7 shows the J-V curves of the DSSCs utilizing the ZnO nanostructures prepared at various ZNH concentrations under 100 mW cm^{-2} light illuminations. It is noticed that the cell with 0.1 M ZNH concentration generates the highest output power, whereas the device with 0.06 M ZNH concentration performs the lowest output power. The J-V curves do not follow the shape of that of silicon solar cell. The slope of J-V curves is quite high, indicating high internal resistance of the devices, leading to small fill factor (FF) illustrated in Table 1. The photovoltaic parameters are analyzed from Fig. 4(B) and described in Table 1. As can be clearly seen from the table, the cell utilizing ZnO nanostructures grown at 0.1 M concentration demonstrates the highest J_{SC} and η, while that utilizing the ZnO sample prepared at 0.06 M ZNH concentration performs the lowest J_{SC} and η. The increase in J_{SC} and η with the ZNH concentration
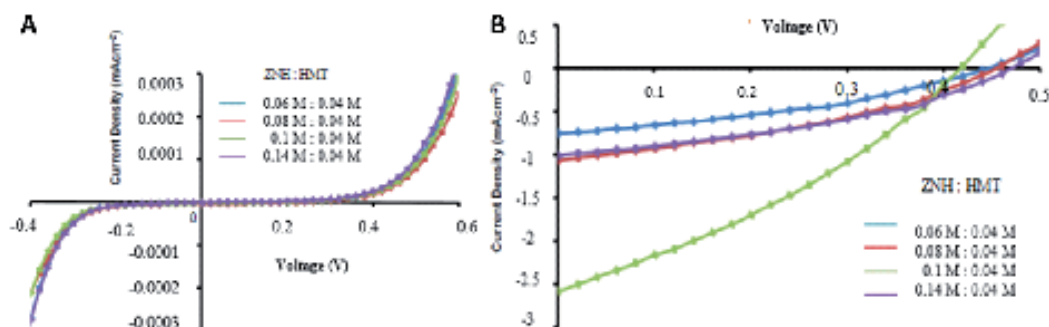
Figure 4: (A) I-V curve in dark condition of the DSSCs and (B) J-V curves of the DSSCs utilizing the ZnO nanostructures at various ZNH concentrations.

(ZNH : HMT)	V_{OC}(V)	J_{SC}(mAcm^{-2})	V_{MPP}(V)	J_{MPP}(mAcm^{-2})	FF (%)	η (%)
0.06 M : 0.04 M	0.46	0.75	0.28	0.592	0.503	0.166
0.08 M : 0.04 M	0.36	1.06	0.36	0.557	0.499	0.201
0.1 M : 0.04 M	0.42	2.57	0.24	1.47	0.342	0.352
0.14 M : 0.04 M	0.48	1.00	0.36	0.598	0.5375	0.215

TABLE 1: Physical and photovoltaic parameters of the DSSCs utilizing the ZnO nanostructures grown at various precursor concentrations.

could be explained by the UV-Vis absorption spectra as illustrated in Fig. 1(A). The B-doped ZnO nanostructures grown at 0.1 M possess the highest optical absorption. This sample absorbs the highest number of photon and consequently generates the highest number of electron-hole pairs, thus the J_{SC} and η are improved. From the table is also noticed that the J_{SC} and η decrease as the ZNH concentration increase. However, this trend is not seen for V_{OC}. Generally, the highest J_{SC} and η obtained from this work are still low. This might be due to the sensitization effect of the N719 dye loading into ZnO film in this work was still small. The small sensitization effect is due to small surface area for dye loading. The low in J_{SC} and η might also be caused by high power loss which is caused by high leakage current in this device as illustrated the I-V curves in dark condition shown in Fig. 4(A).

4. Conclusions

Boron-doped ZnO nanotubes have successfully been grown on the FTO at various concentration of ZNH. The UV-Vis spectra of the samples showed the strong absorption at the wavelength range 300-400 nm for all samples. The absorption peak was observed at 370 nm, which represented the good structural quality of ZnO nanostructures. XRD peak of ZnO nanotubes occurred at 2θ = 34.50° and other lower peaks. FESEM images showed the diameter of ZnO nanotubes in the range of 50-340 nm and the thickness of about 1.2 – 4.4 μm for all samples. The hexagonal geometrical shape was observed for all ZnO nanotubes. The homogenity in size and geometrical shape increased with decreasing ZNH concentration. EDX spectra of the samples observed the weight percentage of compound of Zn, O, and B which was 69.35%, 21.60% and 4.76%, respectively and the atomic percentage of the samples was 33.06%, 42.08% and 13.71%,

respectively. The DSSC was fabricated by arranging the sandwich structure, containing ZnO nanotube coated FTO, dye, electrolyte and platinum coated FTO. Analyzing their I-V characteristics resulted the maximum efficiency of 0.352% from the DSSC based on ZnO nanotube with its precursor-surfactant concentration ratio of 0.1 M : 0.04 M.

5. Acknowledgements

References

[1] J. Cembrero, A. Elmanouni, B. Hartiti, and M. Mollar, Nanocolumnar ZnO films for photovoltaic applications, *Thin Solid Films*, **451-452**, 198–202, (2004).

[2] A. E. Rakhshani, Thin ZnO films prepared by chemical solution deposition on glass and flexible conducting substrate, *Appl Phys, A Mater Sci Process*, **81**, 1497–1502, (2005).

[3] H. Gao, G. Fang, M. Wang, N. Liu, L. Yuan, C. Li, and L. Ai, **43**, 3345–3351, (2008).

[4] A. Witjaksono, in *Tesis Metalurgi dan Material Fakultas Teknik*, Universitas Indonesia, Depok, 2011.

[5] Q. Zhang, C. S. Dandeneau, X. Zhou, and G. Cao, ZnO Nanostructures for Dye-Sensitized Solar Cells, *Adv Mater*, **21**, 4087–4108, (2009).

[6] Y. Nakamura, *Adv. Mater*, **21**, 4087–4108, (2006).

[7] A. E. Suliman and Y. W. Tang, *Sol. Energ. Mat. Sc*, **91**, p. 1658, (2007).

[8] H. Wang, S. Baek, J. Song, J. Lee, and S. Lim, Microstructural and optical characteristics of solution-grown Ga-doped ZnO nanorod arrays, *Nanotechnology*, **19**, p. 075607, (2008).

[9] Y. Park, E. Nam, D. Jung, and S. Suh, Journal, *Bull Korean Chem Soc*, **28**, p. 12, (2007).

[10] C. Prajapati and A. Kushwana, Journal, *Mater Chem Phys*, **142**, 276–285, (2013).

[11] C. H. Hsiao, C. S. Huang, S. J. Young, I. EE. Member, S. J. Chang, J. J. Guo, C. W. Liu, and T. Y. Yang, *IEEE Trans Electron Dev*, **60**, (2013).

[12] S. Yadav, (2012).

[13] A. Adriyanto and U. Santoso, Synthesis and properties of Boron doped ZnO thin films by spray CVD technique at low substrate temperature, *Journal of Engineering Science and Technology (IJEST)*, (2002).

[14] M. Y. A. Rahman, A. A. Umar, R. Taslim, M. M. Taslim, and M. M. Salleh, Effect of organic dye, the concentration and dipping time of the organic dye N719 on the photovoltaic performance of dye-sensitized ZnO solar cell prepared by ammonia-assisted hydrolysis technique, *Electrochim Acta*, **88**, 639–643, (2012).

[15] Y. Xi, W. Z. Wu, H. Fang, and C. G. Hu, Integrated ZnO nanotube arrays as efficient dye-sensitized solar cells, *J Alloys Compd*, **529**, 163–168, (2012).

Conference Paper

Cyclic Voltammometry of Binderless Activated Carbon Monoliths based supercapacitor from Mixtures of Pre-carbonized of Fibers of Empty Fruit Bunches and Green Petroleum Coke

AwitdrusAwitdrus[1], Mohamad Deraman[2], IbrahimAbuTalib[2], Rakhmawati Farma[1], Najah Syahirah M. Nor[2], Maria MuhammadIshak[2], and Besek Nurdiana M. Dolah[2]

[1]Departement of Physics, Faculty of Mathematics and Natural Sciences, University of Riau, 28293, Pekanbaru, Riau, Indonesia
[2]School of Applied Physics, Faculty of Science and Technology, Universiti Kebangsaan Malaysia, 43600 Bangi, Selangor, Malaysia

Abstract Binderless activated carbon monoliths (BACMs) prepared from mixtured of pre-carbonized of fibers of oil palm empty fruit bunches (EFB) and green petroleum coke were used for preparing the carbon based supercapacitor cells. The symmetrical supercapacitor cells were fabricated by using two BACMs electrode prepared for each selected holding time of activation and various compression pressure. The electrochemical behavior of supercapacitor cells were measured at room temperature by using cyclic voltammetry (CV) technique. The maximum specific capacitance (C_{sp}) of the cells values were 35.9 and 82.5 F/g for holding time of activation of 1.5 and 2 h, respectively, at the compression pressure of 7.5 metric tons.

OPEN ACCESS

1. Introduction

Supercapacitor is an energy storage device that stored energy at the interface of electrochemical double-layer formed by ionic charges electrolyte with electronic charges on the surface of pores in the electrode.Its energy and power density can complement the function of batteries and dielectric capacitors. Due to the outstanding properties of supercapacitors, the supercapacitor has been successfully used for a wide number of commercial and industrial equipment, such as digital telecommunication systems, hybrid electrical vehicles, uninterruptible power supply (UPS), and pulsed laser technique [1].

Common materials were used as supercapacitor electrodes including metal oxide [2], electronically conducting polymer [3] and porous materials such as activated carbon [4]. Activated carbon has advantageous because of its high surface area, good thermal and electrical conductivity, high stability, low cost and commercial-large scale availability [5]. Activated carbon can be prepared from biomass precursors and fossil-fuel based precursors by physical or chemical or combination of physical and chemical activation. For the activated carbon in the form of fine-grained, fabrication of

How to cite this article: AwitdrusAwitdrus, Mohamad Deraman, IbrahimAbuTalib, Rakhmawati Farma, Najah Syahirah M. Nor, Maria MuhammadIshak, and Besek Nurdiana M. Dolah, "Cyclic Voltammometry of Binderless Activated Carbon Monoliths based supercapacitor from Mixtures of Pre-carbonized of Fibers of Empty Fruit Bunches and Green Petroleum Coke," *KnE Engineering*, vol. 2016, 8 pages. DOI 10.18502/keg.v1i1.511

Page 1

the electrodes for supercapacitorrequired an addition of binder in order to bind the carbon particles into pellets or monolith. However, the addition of binder can reduce the porosity and decreasing the electrical conductivity [5]. Therefore, the activated carbon monoliths (ACMs) without using binder is highly recommended in order to be potentially used as electrodes in supercapacitor.

In our previously studies, the ACMs were prepared without using binder from mixtures of various percentage of self-adhesive carbon grain (SACG) from fiber of oil palm empty fruit bunches (EFB) and green petroleum cokes (GPC) [6-7]. The mixture of 90% of SACG and 10% of GPC was found to yield the best result in term of a higher electrical conductivity, pores structure and electrochemical properties. Therefore, the present study, the BACMs from mixture with a such composition were used but with the adding of the treatment based on CO_2 activation with the different holding time of activation.

2. Materials and Methods

The raw materials used in this study were fibers of EFB supplied by Stable-Win Sdn. Bhd., Malaysia and GPC obtained from Pertamina UP II Dumai Refinery, Indonesia. Fibers of EFB were pre-carbonized at low temperature 280°C in the vacuum furnace using our method previously reported to produce self-adhesive carbon grain (SACG) [8]. The GPC was milled for 36 h and sieved to produce fine powder that can pass through a 53 μm sieve. The SACG were then mixed with 10% by weight of GPC and then milled for 1 h to obtain homogeneous mixtures of SACG and GPC. The green monoliths (GM-A, GM-B, GM-C) were prepared by applying 4.5, 6 and 7.5 metric ton of compression pressure on ~0.75 g of powder in a mould with diameter of 20 mm respectively.

The carbonization of the GMs to obtain carbon monolith (CMs) was carried out in a carbonization furnace up to 800°C under a 1.5 L/min flowing N_2 gas using our previous multi-step heating profile [7]. The CO_2 activation on the CMs to produce BACMs was carried out at 800°C for 1.5 and 2 h in a flow of 1 L/min CO_2 gas with a heating rate of 10°C/min, respectively. The BACMs were polished to a thickness of ~0.4-0.5 mm and then washed to remove the activating agent with distilled water until pH 7. The electrodes were labeled as BACM-A1.5, BACM-A2, BACM-B1.5, BACM-B2, BACM-C1.5 and BACM-C2. BACM-A1.5 corespond to the electrode prefared from 4.5 metric ton compression pressure and holding time of activation of 1.5 h, and etc.For studying of the electrochemical behavior of the BACMs electrodes, the symmetrical supercapcitor cells were fabricated using two BACMs electrode prepared for each selected holding time of the activation and compression pressure. The supercapacitor cells consist of stainless steel foil 316L as the current collector (thickness of 0.02 mm), 1 M of H_2SO_4 as the electrolyte and a teflon ring as separator (thickness 0.2 mm) were fabricated.

The electrochemical behavior of the supercapacitor cells was investigated by cyclic voltammetry (CV) technique. The CV measurement were carried out at the room temperature. From the voltammogram data, the C_{sp} of the electrode was determined using equation

$$C_{sp} = \frac{2i}{S\,m} \tag{1}$$

where i is the electric current, m is the mass of electrode and S is the scan rate.

3. Results and Discussion

Cyclic voltammogram (CV) of cells at voltage range of -1 – 1 V and a scan rate of 5 mV/s in 1 M H_2SO_4 electrolyte solution are shown in Fig. 1 and 2 for holding time of activation of 1.5 and 2 h respectively. In the middle of potential region of voltammogram there is a tiny peak (hump) for BACM-C2 cell as a result of redox reaction (based on Faradaic charge-discharge) (Fig. 2). The redox peaks occurred almost in the middle of voltage (∼0 V). This redox peaks indicate that the BACM-C2cell were formed by pseudocapacitance. While for BACM-A2 and ACM-B2 no redox peaks were observed indicating that these cells are based on the electrostatic supercapacitor. Fig. 1 shows a significant redox peaks for the cell of BACM-A1.5, while BACM-C1.5has no significant redox peaks. Compared to the holding time of activation of 1 hour [9], the holding time of activation of 1.5 and 2 hours were very effective to improve the performance of supercapacitor. Hu et al. reported that the effect of activation of CO_2 [10] and holding time of activation of carbon electrodes could eliminate the redox peaks as observed in our study.

Redox processes occurring at the electrode-electrolyte interface can improve pseudocapacitance electrodes. Since, the capacitance is the sum of the double-layer capacitance and pseudocapacitance (Faradaic) [11], these redox peaks arise as a result of the availability of surface functional groups [11,12]. Bichat et al. who researched on seaweed as starting material for electrode observed that the profile of CV in 1 Molar H_2SO_4electrolyte produced a similar curve inour study [13].

The anode and cathode peak arose due to the transformation reversible of quinones/hidroquinon (-OC = O). Wang et al. found that the redox peakwas expected to occur because of the concentration of anions on the pore surface of the electrode as a function of surface potential [14]. It is obvious that the surface anion concentration increased sharply with the potential increment. This regime corresponds to the increase of current density reaching maximum corresponds to crest of the hump. Then, the ion accumulation near the electrode surface became to be slower as the electric potential increased. In our study, these functional groups remain in all electrodes for activation timeof 1 h sufficiently removes all the functional groups from the electrodes.

The specific capacitance values for all the cells using BACMs measured at various compression pressures and activated at 800ºC with holding time of activation for 1.5 and 2 hours are shown in Fig 3. As can be seen in this legend, each compression pressure, the specific capacitanceswere increased with increasing the holding time of activation.
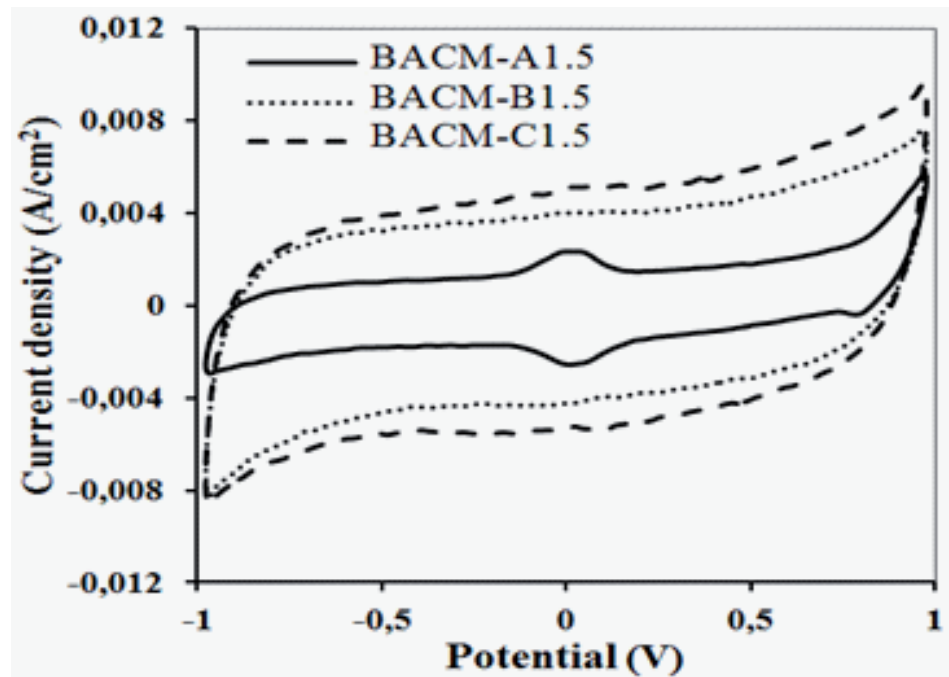
Figure 1: Profiles of CV at a scan rate of 5 mV/s.
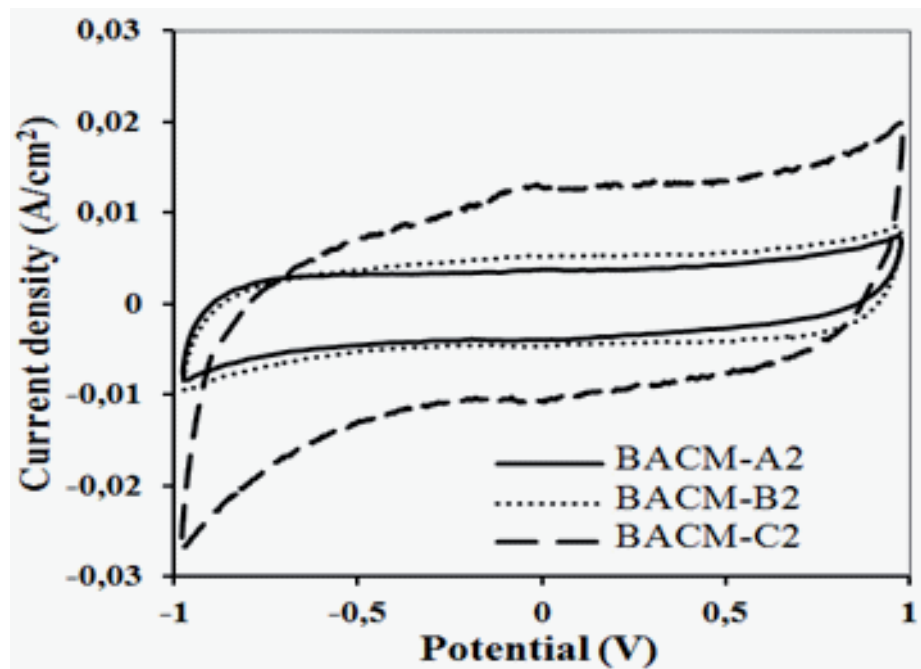
Figure 2: Profiles of CV at a scan rate of 5 mV/s.

The rofile of CV at various scan rates with the voltage range of -1 – 1 V for cells by using BACM-C1.5 and BACM-C2 electrodes are shown in Fig. 4 and5 respectively. As expected, as the scan rate increases, the potential window becomes to be larger since the current density increases. According to Xu et al., the current density increases with increasing scan rate because the cell has a faster reversibility response of charge-discharge [15]. For high voltage scan rate, the cyclic time becomes to be faster and
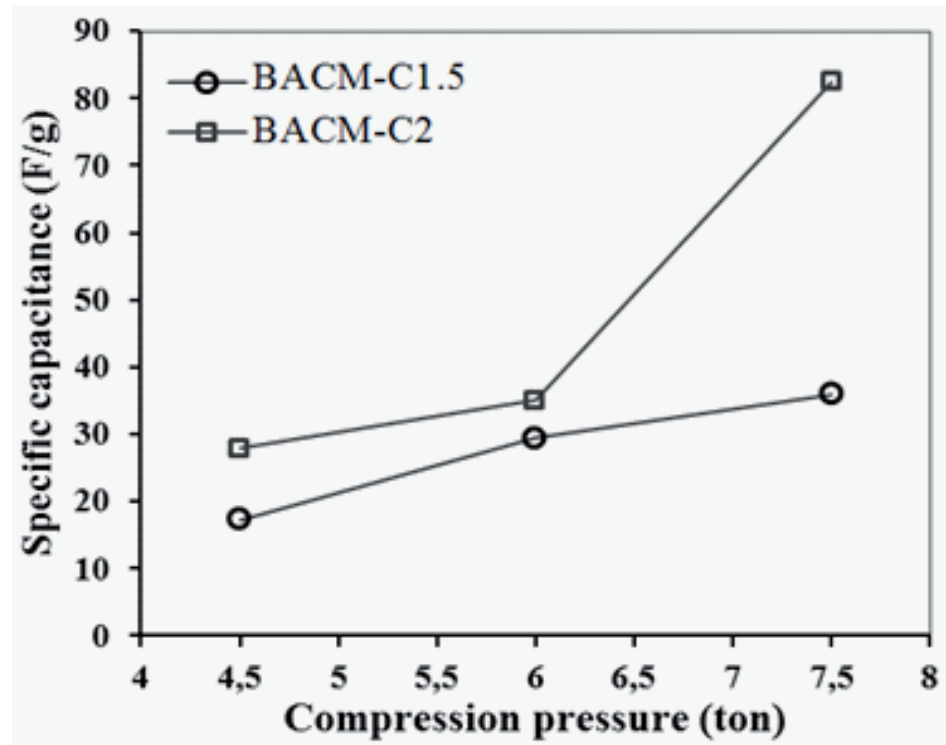
Figure 3: Specific capacitance with different holding time of activation.

No.	Sampel	Specific capacitance (F/g)				
		5 (mV/s)	15 (mV/s)	25 (mV/s)	50 (mV/s)	100 (mV/s)
1.	BACM-A1.5	17.3	14.0	11.5	8.9	6.5
2.	BACM-A2	27.1	24.9	23.0	19.8	15.8
3.	BACM-B1.5	29.5	26.9	23.9	20.7	13.4
4.	BACM-B2	35.1	32	29.0	24.3	18.5
5.	BACM-C1.5	35.9	30.9	28.3	23.0	17.3
6.	BACM-C2	82.5	76.0	68.6	53.3	38.1

TABLE 1: Specific capacitance of supercapaacitor with various scan rate.

therefore the electrolyte ions do not have time to diffuse into the pores. Consequently, the square characteristic of potential window decrease resulted from ain order pore structure, andhighly unordered pore network [16]. CV slowly becomes tilted from the horizontal line as the scan rate increase, which indicates the value of ESR significantly increase because of ionic conductivity of H_2SO_4 electrolyte becomes to be smaller [10].

The specific capacitance of the BACM-C1.5 and BACM-C2for various scan rates obtained from CV data is shown in Table 1. The increment of the scan rate caused specific capacitance decreased gradually. The specific capacitance decrease correspondent to scan rate increases due to the limited transfer of ions to the surface of the electrode pores causing some pores are not accessible at high scan rate. At low scan rate, the current is small, iR loss can be ignored, and supercapacitor cells can be considered as a pure capacitor. In contrast, at high scan rate, the current also increased and iR loss become significant and supercapacitor cells act as a pure resistive device
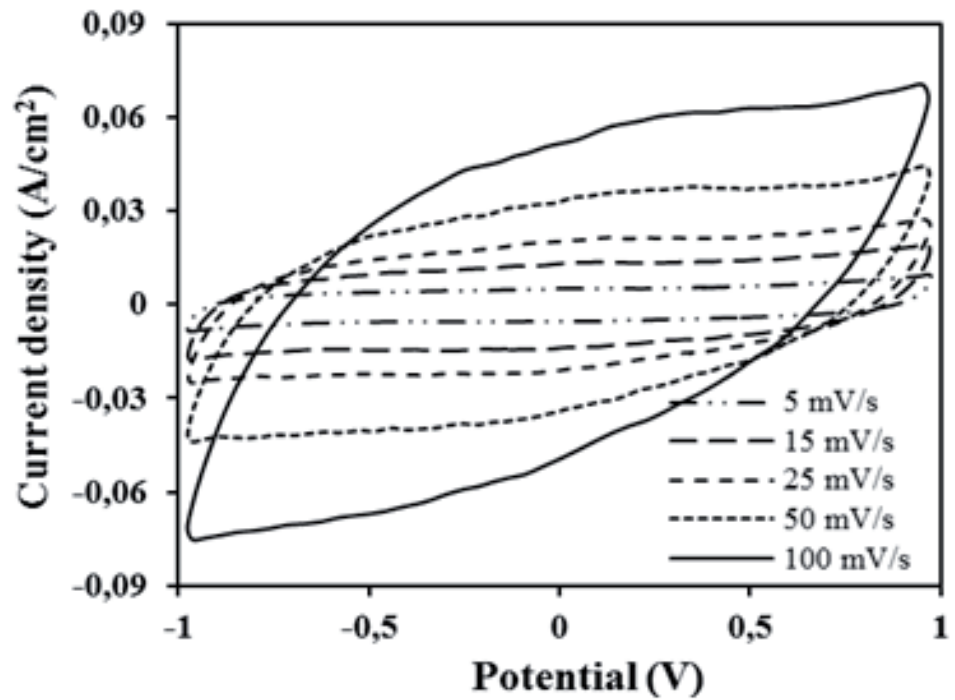
Figure 4: Profile of voltammograms with various scan rates for BACM-C1.5.
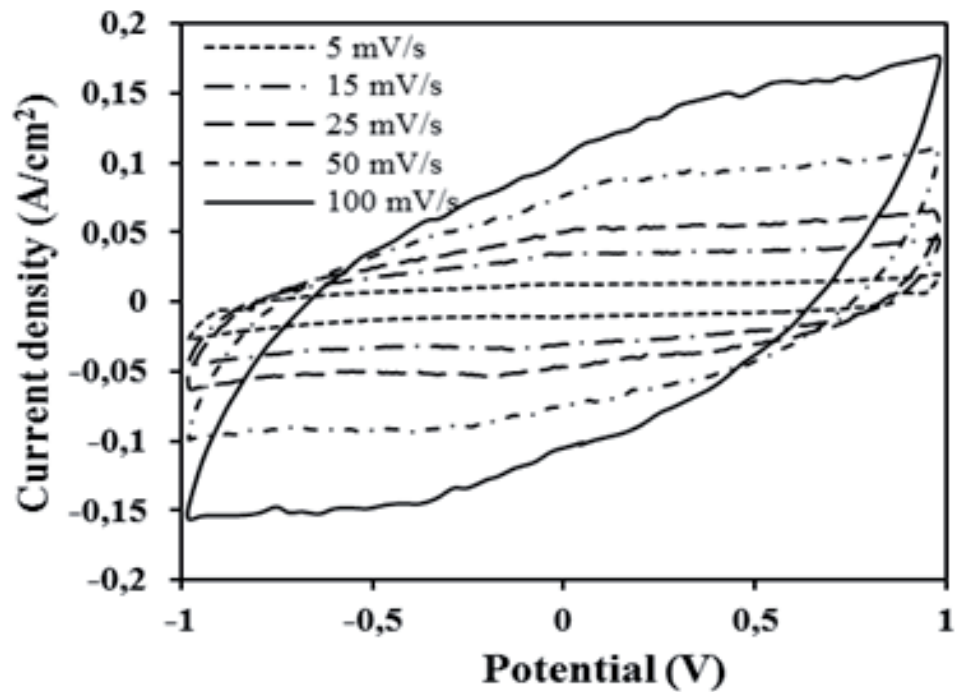
Figure 5: Profile of voltammograms with various scan rates forBACM-C2.

[17]. According to Ma et al., in a high scan rate (100 mV/s), electrons transfers and ion diffusion occurred quickly caused by the specific capacitance decreases [18].

4. Conclusion

BACM consisting of pre-carbonized of EFB (90% by weight) and GPC (10%) were pressed with various compression pressure of 4.5, 6 and 7.5 metric ton, respectively. These BACM were carbonized at 800°C, and activated for 1.5 h and 2 h by CO_2 at 800°C which were used as electrodes in symmetrical supercapacitor cells. We observe that the electrochemical behavior of supercapacitor cells were changed and strongly depending on the compression pressure and holding time of activation. The better specific capacitance were resulted from the compression pressure at 7.5 metric ton and holding time of activation of 2 h.

References

[1] C. Vix-Guterl, E. Frackowiak, K. Jurewicz, M. Friebe, J. Parmentier, and F. Beguin, Electrochemical energy storage in ordered porous carbon materials, *Carbon*, **43**, 1293–1302, (2005).

[2] D. Yang, Pulsed laser deposition of cobalt-doped manganese oxide thin films, *J Power Sources*, **198**, 416–422, (2012).

[3] G. Nystrom, M. Stromme, M. Sjodin, and L. Nyholm, Rapid potential step charging of paper-based polypyrrole energy storage devices, *Electrochim Acta*, **70**, 91–97, (2012).

[4] R. Farma, M. Deraman, A. Awitdrus, I. A. Talib, E. Taer, N. H. Basri, J. G. Manjunatha, M. M. Ishak, B. N. Dollah, and S. A. Hashmi, Preparation of highly porous binderless activated carbon electrodes from fibres of oil palm empty fruit bunches for application in supercapacitors, *Bioresour Technol*, **132**, 254–261, (2013).

[5] A. G. Pandolfo and A. F. Hollenkamp, Carbon properties and their role in supercapacitors, *J Power Sources*, **157**, 11–27, (2006).

[6] A. M. Deraman, I. A. Talib, R. Omar, M. H. Jumali, E. Taer, and M. H. Saman, Microcrystallite dimension and total active surface area of carbon electrode from mixtures of pre-carbonized oil palm empty fruit bunches and green petroleum cokes, *Sains Malays*, **39**, 83–86, (2010).

[7] M. Deraman, I. A. Awitdrus, I. A. Talib, R. Omar, M. H. Jumali, M. M. Ishak, S. K. M. Saad, E. Taer, M. M. Saman, R. Farma, R. M. Yunus, , M. Abdullah, W. Srigutomo, and S. Viridi, Electrical conductivity of carbon pellets prepared from mixtures of pyropolymers from oil palm bunches and petroleum green coke, *AIP Conf Proc*, **1325**, 50–54, (2010).

[8] M. Deraman, R. Omar, S. Zakaria, I. R. Mustapa, M. Talib, N. Alias, and R. Jaafar, Electrical and mechanical properties of carbon pellets from acid (HNO3) treated self-adhesives carbon grain from oil palm empty fruit bunch, *J Mater Sci*, **37**, 3329–3335, (2002).

[9] M. .. Awitdrus, (2015).

[10] C.-C. Hu, C.-C. Wang, F.-C. Wu, and R.-L. Tseng, Characterization of pistachio shell-derived carbon activated by a combination of KOH and CO2 for electric double-layer capacitor, *Electrochim Acta*, **52**, 2498–2505, (2007).

[11] H. Yu, J. Wu, L. Fan, Y. Lin, K. Xu, Z. Tang, C. Cheng, S. Tang, J. Lin, M. Huang, and Z. A. Lan, novel redox-mediated gel polymer electrolyte for high-performance superkapasitor, *J Power Sources*, **198**, 402–407, (2012).

[12] J. J. Moore, J. H. Kang, and J. Z. Wen, Fabrication and characterization of single wallet nanotube supercapacitor electrodes with uniform pores using electrophoretic deposition, *Mater Chem Phys*, **134**, 68–73, (2012).

[13] M. P. Bichat, E. Raymundo-Pinero, and F. Beguin, High voltage supercapacitor built with seaweed carbons in neutral aqueous electrolyte, *Carbon*, **48**, 4351–4361, (2011).

[14] H. Wang and L. Pilon, Physical interpretation of cyclic voltammetry for measuring electric double layer capacitans, *Electrochim Acta*, **64**, 130–139, (2012).

[15] J. Xu, L. Gao, J. Y. Cao, W. C. Wang, and Z. D. Chen, Preparation and electrochemical capacitance of cobalt oxide (Co_3O_4) nanotubes as supercapacitor material, *Electrochim Acta*, **56**, 732–736, (2010).

[16] D. Liu, J. Shen, N. Liu, H. Yang, and A. Du, Preparation of activated carbon aerogels with hierarchically porous structures for electrical double layer capacitors, *Electrochim Acta*, **89**, 571–576, (2013).

[17] W. G. Pell and B. E. Conway, Voltammetry at a de Levie brush electrode as a model for electrochemical superkapasitor behavior, *J Electroanal Chem*, **500**, 121–133, (2001).

[18] C. Ma, Y. Song, J. Shi, D. Zhang, X. Zhai, M. Zhong, Q. Guo, and L. Liu, Preparation and one-step activation of microporous carbon nanofibers for use as supercapacitor electrodes, *Carbon*, **51**, 290–300, (2013).

KnE Engineering

Knowledge E
Engaging minds

Conference Paper

Performance Analysis of Solar Updraft Power Generator in Indonesia

Hadyan Hafizh, Hiromichi Shirato, and Daiki Yui

Department of Civil & Earth Resources Engineering, Kyoto University, 615-8540 Kyoto, Japan

Abstract

Solar updraft power generator (SUPG) is a renewable energy facility capable of harnessing the solar energy. The first large prototype of SUPG was built in 1980's in Manzanares, Spain to evaluate the projected performance of the facility and to serve as verification tools for future power simulator development. In this paper, the performance of a solar updraft power generator is assessed using the developed mathematical model. The model is validated by comparison with experimental data of Manzanares SUPG. The validated model is then used to calculate the amount of energy produced in seven selected locations in Indonesia. The selected cities in Indonesia exhibited a higher average monthly energy production compared to those in Manzanares. In particular a site like Kupang, would generate two times the energy of the Manzanares SUPG. The power production is sufficient for the needs of this isolated area in Indonesia and has the potential to solve the energy issue.

Keywords: Indonesia, Power Production, Renewable Energy, Solar-Induced Wind Energy

🔓 **OPEN ACCESS**

1. Introduction

A solar updraft power generator consists of three main parts which are solar collector, solar tower and wind turbine. It offers compelling concepts in producing electrical power by utilizing the solar radiation to increase the airflow temperature, making it less dense than the ambient air which induces a buoyancy force in the form of an updraft flow [1]. The desired kinetic energy from the updraft flow will be extracted by one or series of wind turbine located at the center of solar collector. The energy conversion is complex, but in principle, it is not an obscure theory. The conversion process can be explained as follows. When solar radiation arrived at the surface of the solar collector, part of it is absorbed by the ground under the solar collector and most of the solar radiation is transmitted to the down layer of the ground. The ground and the solar collector will also emit radiation, making the modeling of heat transfer process more complex [2]. Furthermore, the absorbed solar radiation is then transferred in form of heat flux to the airflow via convection process and to the down layer of the ground through conduction process. These mechanisms create the differences in the properties of airflow such as pressure, density, and temperature, between the inside and the outside of SUPG system. The pressure difference conceives the inertia force while the density difference – due to temperature difference – organizes the buoyancy force. These two forces are the main driving force in the SUPG system.

(a)   (b)
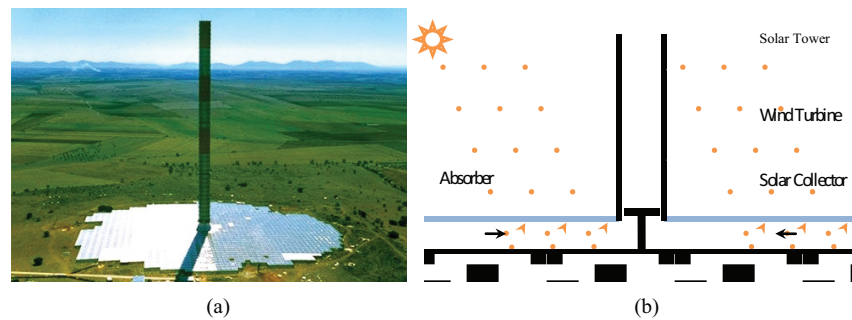
Figure 1: (a) A picture of the Manzanares SUPG in Spain, (b) Illustration of the Manzanares SUPG showing its main parts.

Although the physics behind the energy conversion process is complex, this power plant provides uncomplicated design where turbines and generators are the plant's only moving parts. Therefore, a lot of researchers have been captivated by the potential benefits that this power generator might offer for a clean power production. However, it has an inherent low efficiency compared to the other conventional power generator. Much effort have been devoted to improve its efficiency such as adding thermal storage equipment [3,4], studying the influence of geometry to the power production [5,6,7], or modifying the design of the SUPG [8,9,10]. With this reason, we investigate the performance of a solar updraft power generator expected to provide the remote regions in Indonesia with electric power. This study also presents the analysis about the influence of geometrical and physical parameters such as tower height, collector radius and temperature difference, on the power output. The physical parameters of a solar updraft power generator were determined by using the numerical simulation.

2. Mathematical Model

The performance analysis of solar updraft power generator is based on a mathematical model which has been developed in [11]. This mathematical model is derived from the mass, momentum, and energy balance equations with addition of one state equation. Several assumptions have been implemented to these equations such as inviscid, incompressible, and one dimensional axisymmetric flow. To verify the simulation assumption and procedure, the Manzanares SUPG has been considered as test case. Dimension of the Manzanares SUPG are as follows [12]: solar collector radius, 122 m; solar tower height 200 m; solar tower radius, 5.08 m; solar collector height, 2 m. A picture and illustration of the Manzanares SUPG are presented in Fig. 1.

The maximum mass flow rate inside the solar tower can be obtained by applying the momentum balance equation on a control volume in the tower. In addition, the change of airflow density can be represented by the change of airflow temperature which is known as the Boussinesq approximation [13]. The equation for mass flow rate $\dot{m}$ is then given by
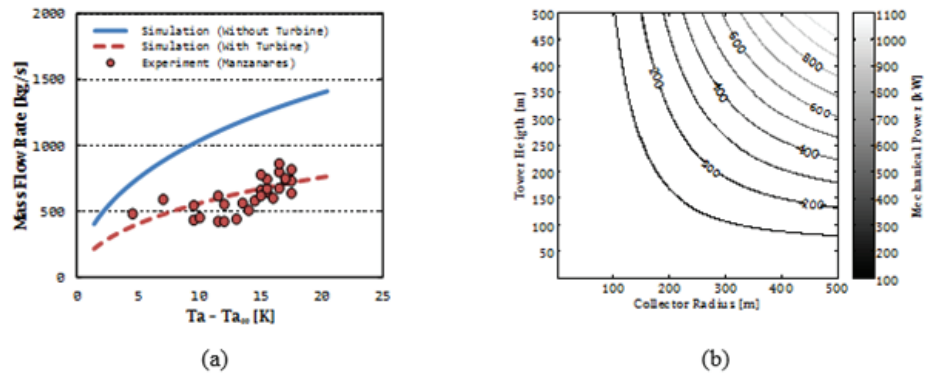
Figure 2: (a) Model validation, (b) Effects of tower height and collector radius to the power.

$$\dot{m} = \rho \pi r_{tow}^2 \sqrt{2g \frac{T_a - T_{a\infty}}{T_{a\infty}} h_{tow}} \tag{1}$$

where ρ is the airflow density, g is the gravity constant, T_a is the updraft temperature, $T_{a\infty}$ is the ambient air temperature, and r_{tow}, h_{tow} are the tower radius and tower height respectively. The mechanical power P delivered by the turbine is obtained as

$$P = \frac{\dot{m}^3 C_P}{2\rho^2 \pi^2 r_{blade}^4} \tag{2}$$

where r_{blade} is the radius of turbine blade and C_P is the coefficient of power. The suitable value of C_P should be obtained from experimental data.

In order to validate the developed model, the simulated mass flow rate is then compared with the experimental result of the Manzanares SUPG. Simulated mass flow rate are calculated for two cases. The first case is simulation without energy extraction or without turbine configuration. This case will give the maximum amount of mass flow rate. The second case is simulation with energy extraction or with turbine configuration. The mass flow rate from the latter case will be less than the former case since part of its kinetic energy has been extracted. The results are presented in Fig. 2 (a) which shows the simulated mass flow rate for two cases together with the experimental mass flow rate from the Manzanares experiment. It is observed that the simulation result is in good agreement with the experimental data, demonstrating that the developed model is reliable and can be used for the study of power production in Indonesia.

Fig. 2 (b) shows the effect of tower height and collector radius on the generated mechanical power. The mechanical power was computed for Irradiance $I = 1000$ W/m^2. The tower height and the collector radius are varied linearly up to 500 m. It is recognized that the power production increases with the increase in the size of power generator.
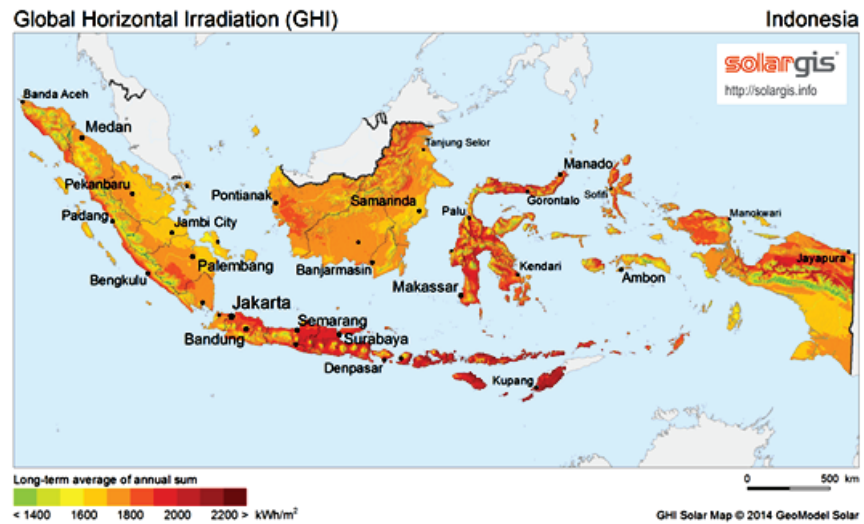
Figure 3: Solar radiation map of Indonesia [16].

3. Results and Discussion

Evaluation of solar updraft power generator performance in selected regions in Indonesia is discussed. In the current investigation, 7 regions have been selected for feasibility study of constructing a solar updraft power generator. They are: Pekanbaru in Sumatra Island, Semarang in Java Island, Pontianak in Kalimantan Island, Kupang in Nusa Tenggara Island, Makasar in Sulawesi Island, Ambon in Maluku Island, and Jayapura in Papua Island. These locations have been selected to represent regions of different major Island in Indonesia. These regions are marked with rectangle boxes in solar radiation map of Indonesia (Fig. 3). The meteorological data such as solar radiation and ambient air temperature are retrieved from [14,15]. The monthly solar radiation data were selected in the current work. These data are then used to calculate the power for each selected regions by using the developed mathematical model.

The results of simulated monthly energy production are presented in Fig.4. In this figure, the performance of a solar updraft power generator was calculated for the same geometry as the Manzanares SUPG. The energy production in Kupang is the highest among the selected regions (304.1 kWh/day in September). This is closely followed by Makassar and Semarang (270.6 kWh/day and 265.7 kWh/day, both in August). Ambon and Pekanbaru have the highest record of energy production in October and March while the other two locations are Pontianak and Jayapura, where the highest energy production is observed in August and in September respectively.

Table 1 shows a comparison between the simulated average monthly energy in Indonesia and the measured average monthly energy in Manzanares, Spain. The energy outputs are presented in kWh/month in order to estimate how many houses could be powered. With assumption that the average electricity consumption for a household is 250 kWh/month where the consumption is mainly for lighting, TV, fans, iron, rice cooker, and water pump, thus a solar updraft power generator could provide the electricity for about 20 to 30 houses in isolated area in Indonesia.
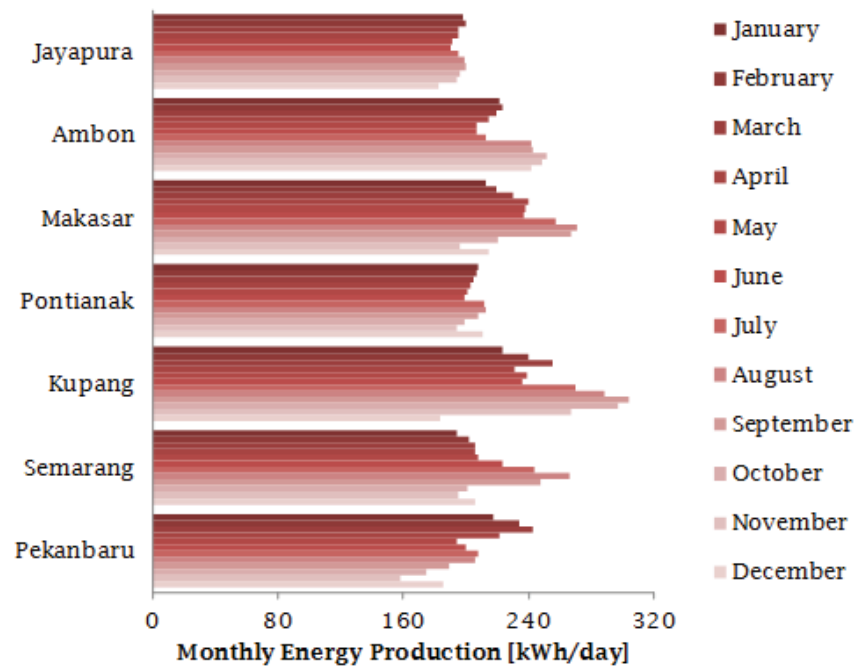
Figure 4: Calculated energy production in selected locations in Indonesia.

Selected Locations	Average Monthly Energy [kWh/month]
Pekanbaru	6081.66
Semarang	6493.24
Kupang	7583.55
Pontianak	6147.07
Makassar	7003.19
Ambon	6834.48
Jayapura	5844.31
Manzanares	3682.50

TABLE 1: Average Monthly Energy in Selected Locations.

Furthermore, the monthly energy production in all selected locations in Indonesia showed a higher value compared to those in Manzanares, Spain. A site like Kupang, where it has the highest energy production per month among the selected locations, would generate two times the energy of the Manzanares SUPG.

4. Summary

The performance of a solar updraft power generator in selected locations in Indonesia has been assessed to evaluate its feasibility. The assessment is conducted by using a developed model which has been validated by comparing the simulated results with the experimental data where a good agreement has been obtained [11]. The result shows that a solar updraft power generator in sunny areas of Indonesia, such as Kupang, would generate twice the energy than an identical one in areas such as

Manzanares, Spain. In addition, the energy outputs could potentially provide 20 to 30 household's electrical needs for a month in remote area in Indonesia.

References

[1] W. Haaf, K. Friedrich, G. Mayr, J. Schlaich, and I. Solar Chimneys Part, Principle and Construction of the Pilot Plant in Manzanares, Int, *J. Sol Energy*, **2**, 3–20, (1983).

[2] M. A. S. Bernardes, T. W. Von Backström, and D. G. Kröger, Analysis of some available heat transfer coefficients applicable to solar chimney power plant collectors, *Sol Energy*, **83**, 264–275, (2009).

[3] M. A. S. Bernardes and X. Zhou, On the heat storage in solar updraft tower collectors – Water bags, *Sol Energy*, **91**, 22–31, (2013).

[4] M. A. S. Bernardes, On the heat storage in solar updraft tower collectors – Influence of soil thermal properties, *Sol Energy*, **98**, 49–57, (2013).

[5] M. A. S. Bernardes, et al., Thermal and technical analyses of solar chimneys, *Sol Energy*, **75**, 511–524, (2003).

[6] J. Li, P. Guo, and Y. Wang, Effects of collector radius and chimney height on power output of a solar chimney power plant with turbines, *Renew Energy*, **47**, 21–28, (2012).

[7] M. Ghalamchi, A. Kasaeian, and M. Ghalamchi, Experimental study of geometrical and climate effects on the performance of a small solar chimney, *Renew Sustain Energy Rev*, **43**, 425–431, (2015).

[8] M. Zhang, X. Luo, T. Li, L. Zhang, X. Meng, K. Kase, S. Wada, C. W. Yu, and Z. Gu, From dust devil to sustainable swirling wind energy, *Sci Rep*, **5**, p. 8322, (2015).

[9] L. M. Michaud, Vortex process for capturing mechanical energy during updward heat-convection in the atmosphere, *Appl Energy*, **62**, 241–251, (1999).

[10] M. W. Simpson, A. J. Pearlstein, and A. Glezer, Electric power generation using buoyancy-induced vortices, ICREPQ 13-Spain, (2013) ISSN 2172-038 X, no. 11.

[11] H. Hafizh and H. Shirato, Aerothermal simulation and power potential of a solar updraft power plant, *J Struct Eng JSCE*, **61A**, 388–399, (2015).

[12] W. Haaf, Solar Chimneys Part II: Preliminary Test Results from the Manzanares Pilot Plant, Int, *J. Sol Energy*, **2**, 141–161, (1984).

[13] G. Nellis and S. Klein, in *Heat Transfer*, Cambridge University Press, New York, 2009.

[14] M. Rumbayan, A. Abudureyimu, and K. Nagasaka, Mapping of Solar Energy Potential in Indonesia using ANN and GIS, *Renew Sustain Energy Rev*, **16**, 1437–1449, (2012).

[15] `http://www.dataonline.bmkg.go.id`

[16] `http://www.solargis.info`

Conference Paper

Comparison of Remotely Sensed Wind Data over Sulawesi and Maluku Islands Sea Areas

Faisal Mahmuddin, Misliah Idrus, Hamzah, Juswan Sade, and Rosmani

Naval Architecture Department, Engineering Faculty, Hasanuddin University, Jalan Perintis Kemerdekaan km. 10, Tamalanrea, Makassar, Indonesia

Abstract

In order to obtain accurate prediction of ocean wind energy, long term data are needed. However, one data sources might not able to provide long duration data. Therefore, the data need to be combined with other sources of data. However, before combining the data, it is important to compare and validate them to confirm their accuracy. In the present study, wind speed data collected by QuikScat and SSM/I (SSMIS) missions are compared and analyzed. QuikScat data were collected by a satellite with the same name, while Special Sensor Microwave Imager (SSM/I) and Special Sensor Microwave Imager Sounder (SSMIS) data are processed and offered by Remote Sensing System (RSS). SSM/I (SSMIS) are passive microwave radiometers carried onboard Defense Meteorological Satellite Program (DMSP). For the comparison, 5 (five) arbitrary positions over Sulawesi and Maluku islands sea areas are chosen for the analyses. For the evaluation purposes, beside time series of daily data from several chosen positions in research location, several statistical parameters are also computed and compared such as mean, standard deviation, root mean square (RMS), correlation coefficient.

1. Introduction

It is known that wind characteristics such as speed and direction, have seasonal variation. They are varied depending on time and location. Therefore, in order to maximize the harvested power, wind turbine system needs to be relocated from time to time. For this purpose, the National Institute for Environmental Studies (NIES) of Japan has studied and proposed a sailing-type floating turbine structure [1]. The structure is pontoon shaped and has no mooring system. It is supposed to be able to navigate with its own sails and azimuth thrusters. More detail studies about the structure can also be found in references 2 and 3.

Similar concept has also been introduced by Mahmuddin et al. [4, 5] to harvest ocean wind energy around Sulawesi and Maluku islands sea areas. The structure is known to be mobile floating structure (MFS). The MFS is designed not to sail but it can be relocated to other locations with higher energy density every certain time. In order to determine the location of the MFS, in the same studies, the energy density of the sea areas around Sulawesi and Maluku islands has also been assessed and

How to cite this article: Faisal Mahmuddin, Misliah Idrus, Hamzah, Juswan Sade, and Rosmani, "Comparison of Remotely Sensed Wind Data over Sulawesi and Maluku Islands Sea Areas," *KnE Engineering*, vol. 2016, 6 pages. DOI 10.18502/keg.v1i1.513

Page 1

simulated in order to predict the power production of the MFS in the areas. In the previous analysis, data collected by satellite QuikScat had been used. The satellite QuikScat used a scatterometer to measure the wind speed 10m above sea surface. However, QuikScat satellite operated only for around 10 years which are from year 1999 to 2009. Therefore, other sources of satellite data are needed to obtain longer data period to be used in analysis. Longer data period would improve the accuracy of long term assessment results.

There are numerous other satellite data sources that can be used for analysis. The summary of satellite data and their duration can be found in reference 6. Because of the convenience way to obtain the data, the present study uses data processed and offered by Remote Sensing System (RSS). RSS processed and analyzed data from several satellites. The data can be downloaded freely from their website. The data source processed by RSS which has the longest period is the data obtained from the Special Sensor Microwave Imager (SSM/I) and the Special Sensor Microwave Imager Sounder (SSMIS) missions. SSM/I (SSMIS) are passive microwave radiometers carried onboard Defense Meteorological Satellite Program (DMSP). The measurement device is different with the one used by QuikScat because QuikScat utilized scatterometer for its observations. However, before combining the QuikScat and the SSM/I (SSMIS) data in the analysis, it is important to compare and validate the data to confirm their accuracy. In the present study, wind speed data collected from QuikScat and SSM/I (SSMIS) missions are compared and analyzed. For this purpose, 5 (five) arbitrary positions over Sulawesi and Maluku islands sea areas are chosen for the analyses.

For the evaluation purposes, beside time series of daily data from several chosen positions in research location, several statistical parameters are also computed and compared such as mean, standard deviation, root mean square (RMS) and correlation coefficient.

2. Wind Data Models

There are numerous wind data models that could be used in a long term prediction of wind speed. The present study uses 2 (two) products of RSS which are SSM/I (SSMIS) and QuikScat.

3. SSM/I and SSMIS

The Special Sensor Microwave Imager (SSM/I) and the Special Sensor Microwave Imager Sounder (SSMIS) are satellite passive microwave radiometers. This series of instruments has been carried onboard Defense Meteorological Satellite Program (DMSP) satellites since 1987. The instruments are referred to by satellite number starting from F08 to F18. Ocean measurements derived from the radiometer observations include Surface Wind Speed, Atmospheric Water Vapor, Cloud Liquid Water, and Rain Rate [7]. The spatial resolution of the data is 25 x 25 km.
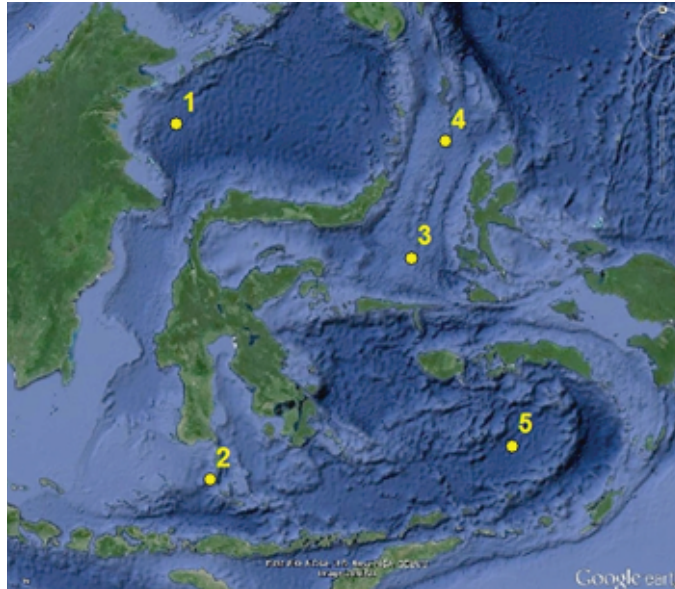
Figure 1: Location of the research and chosen positions.

3.1. QuikScat

The US launched SeaWinds scatterometer in June 1999. It continued to operate until November 2009. The SeaWinds scatterometer is active microwave radar with dual-beam, conical scan 1 m diameter reflector antenna, operating in Ku-band at 13.402 GHz [8]. The primary mission of these SeaWinds scatterometers was to measure winds near the ocean surface. They are also useful for some land and sea ice applications. The SeaWinds instruments are the third in a series of NASA scatterometers that operate at Ku-band (i.e., a frequency near 14 GHz). The first instrument was flown in 1978 on SeaSat mission, which was followed by the second Ku-Band scatterometer flown 18 (eighteen) years later on Japan's Midori-I (ADEOS-I) spacecraft in August 1996 named NSCAT.

4. Research Area

The location of the present study is the sea areas around Sulawesi and Maluku islands of Indonesia. Over the sea areas, 5 positions are chosen arbitrarily for data analysis. The map of research area and chosen positions are shown in the following Fig. 1. The basic image of the figure was produced using Google Earth version 7.1.2.2041.

The chosen positions are shown as yellow dots with their numbers in the map above. The exact coordinates of the chosen locations are shown in the following table.

In the present study, 1 (one) year data which is in year 2000 are extracted from each data sources to be compared. From all type of data available from RSS website, 3-day averaged data were chosen.

No	Longitude	Latitude
1	119	3.50
2	120	-7.00
3	126	-0.50
4	127	3.00
5	129	-6.00

TABLE 1: Coordinates of computed positions.
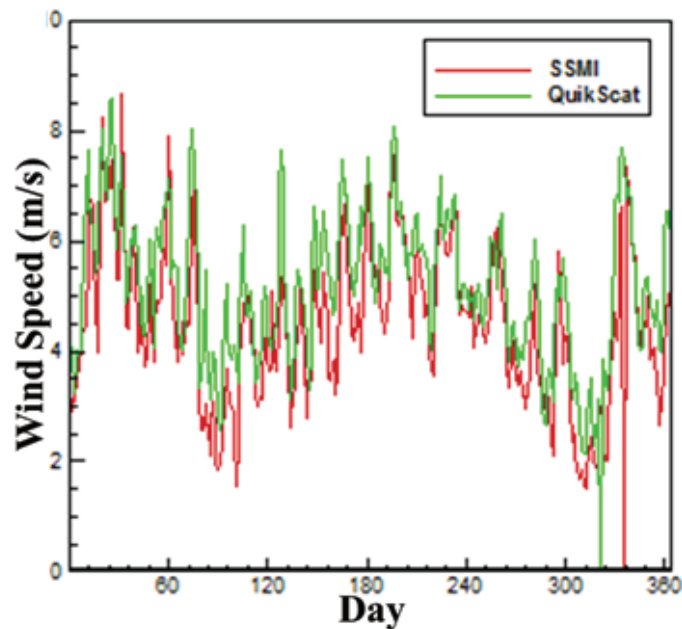
Figure 2: Daily wind speed comparison.

5. Results and Analysis

After extracting the wind speed information of the chosen positions from the data sources, the average of daily wind speed from chosen locations are computed and shown in the following figure. It can be seen from the Figure 2 that the general tendency are similar. However, magnitudes are found to be slightly different. It can also be noted that a line from each data sources reaches zero wind speed which indicates that no data available for the day. In order to observe more detail about the difference, the data above are averaged to obtain monthly averaged data. The computation results are shown in the following figure.

From Fig. 3, it can be seen that general tendencies of the wind speed are in a good agreement. However, significantly different magnitude of the wind speed can be observed. Moreover, in order to evaluate more closely the data, the statistical parameters of the data are computed and compared. The computation results are shown in the following table.

From the table above, it can be seen that difference can be found in all parameters. The two first compared parameters are mean speed and root mean square (RMS)
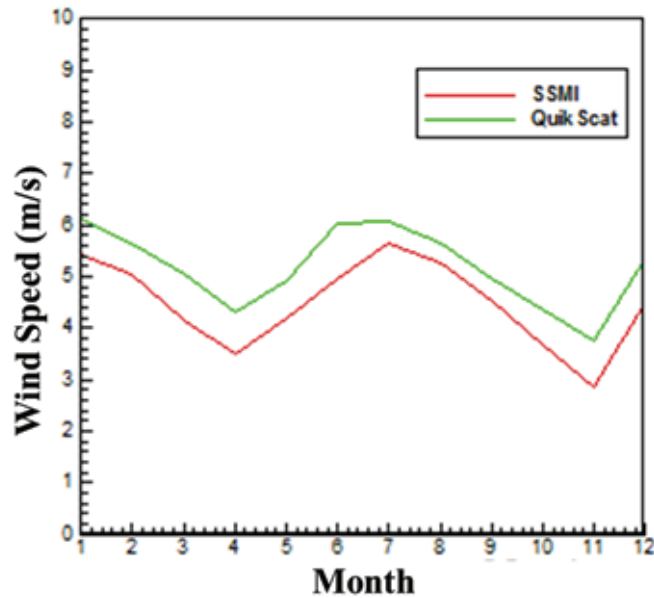
Figure 3: Monthly averaged wind speed comparison.

Parameters	SSMI	QuikScat
Mean	4.480	5.188
RMS	4.553	5.240
Standard deviation	0.810	1.020
Correlation coefficient	-0.358	-0.404

TABLE 2: Statistical parameters comparison.

which represent average of compared data. Both variables show difference of approximately 14%. Moreover, the table also shows that the standard deviation of QuikScat data is higher 0.21 point as compared to the one computed from SSMI data which means that Quikscat data has larger data range as compared to SSMI data.

The last row of the table shows that both correlation coefficients are in negative which means that both data have same tendencies. Higher negative value of Quikscat can be expected from higher standard variation as shown in third row. The differences and tendencies of the parameters could confirm the tendency found in Fig. 3. The finding found above should be considered when using satellite data to determine the wind energy density in certain areas.

6. Summary

The present study compared the QuikScat and SSM/I (SSMIS) data. It is found from the computation results that the tendencies of the computed Quikscat and SSM/I (SSMIS) data are in a good agreement but the magnitudes are significantly different. The difference between the data is approximately 14%. The finding should be considered in using the data for long term assessment analysis including for wind energy prediction.

Acknowledgment

References

[1] National Institute for Environmental Studies (NIES), Report on research results for sailing type offshore wind turbine, Makuhari Messe, Japan, October 2007.

[2] K. Takagi, K. Yamamoto, M. Kondo, T. Funaki, and Z. Kawazaki, Conceptual design of a very large mobile structure for the renewable energy plant., *Proceedings of the Asia Pacific Workshop on Marine Hydrodynamics*, 239–244, (2002).

[3] K. Takagi, Hydroelastic behavior of VLMOS in beam seas, *Proceeding of 14th International Offshore and Polar Engineering Conference*, **Vol. 4**, 616–621, (2004).

[4] F. Mahmuddin, M. Idrus, and Hamzah, Analysis of Ocean Wind Energy Density around Sulawesi and Maluku Islands with Scatterometer Data, *Energy Procedia*, **65**, 107–115, (2015).

[5] F. Mahmuddin, M. Idrus, and Hamzah, Analysis of Wind Energy Potential with a Mobile Floating Structure around Sulawesi and Maluku Islands of Indonesia, *Proceeding of the 34th Conference on Ocean, Offshore, and Arctic Engineering*, **9**, 64–73, (2015).

[6] I. R. Young, S. Zieger, and A. V. Babanin, Development and Application of a Global Satellite Database of Wind And Wave Conditions, *Proceeding of the 34th Conference on Ocean, Offshore, and Arctic Engineering*, **7**, 62–71, (2015).

[7] Remote Sensing System, SSMI/SSMIS, URL at `http://www.remss.com/missions/ssmi`.

[8] J. Winterfelt, in *Comparison of Measured and Simulated Wind Speed Data in the North Atlantic, GKSS Report 2008/2*, GKSS-Forschungszentrum, Geesthacht, 2008.

Conference Paper

Value Chain Analysis of Palm Oil Biodiesel through a Hybrid (ISO-Eco) Life Cycle Assessment Approach

Yosef Manik[1] and Anthony Halog[2]

[1]Engineering Management Study Program, Institut Teknologi Del, Sitoluama-Laguboti, Toba Samosir 22381, North Sumatra, Indonesia
[2]School of Geography, Planning and Environmental Management, the University of Queensland, Brisbane Qld 4072, Australia

Abstract

This study assesses the life-cycle impacts of palm oil biodiesel value chain in order to provide insights toward holistic sustainability awareness on the current development of bio-based energy policy. The assessment methodology was performed under a hybrid approach combining ISO-14040 Life Cycle Assessment (ISO-LCA) technique and Ecologically-based Life Cycle Assessment (Eco-LCA) methodology. The scope of this study covers all stages in palm oil biodiesel value chain or is often referred to as "cradle-to-grave" analysis. The functional unit to which all inputs and outputs were calculated is the production of 1 ton of biodiesel. For the analysis, life cycle inventory data were collected from professional databases and from scholarly articles addressing global palm oil supply chains. The inventory analysis yields a linked flow associating the land used, fresh fruit bunch (FFB), crude palm oil (CPO), per functional unit of 1 kg of palm oil biodiesel (POB). The linked flow obtained in the inventory analysis were then normalized and characterized following the characterization model formulated in stocktickerISO-LCA guidelines. The aggregation of ecological inputs was classified based on the mass and energy associated to each unit process in the value chain, which are cultivation, extraction, conversion, and utilization. It is noted that compared to other unit processes, cultivation is the most crucial unit process within the whole palm oil biodiesel value chain. This study serves as a big picture about the current state of palm oil biodiesel value chain, which will be beneficial for further improving oversight of the policy making and service toward sustainable development.

Keywords: Palm oil, biofuel, Life Cycle Assessment, value chain analysis, sustainability

OPEN ACCESS

1. Introduction

Biofuels production pathway through conversion of plant oils into fatty acid methyl ester (FAME) or biodiesel opens an opportunity for economic growth and energy security for producing countries. Among the different plant oil feedstock, palm oil is considered as a potential feedstock due to its high oil content and yield [1,2]. However, concerns over environmental and social impacts related to production of palm oil have been rising [3,4].
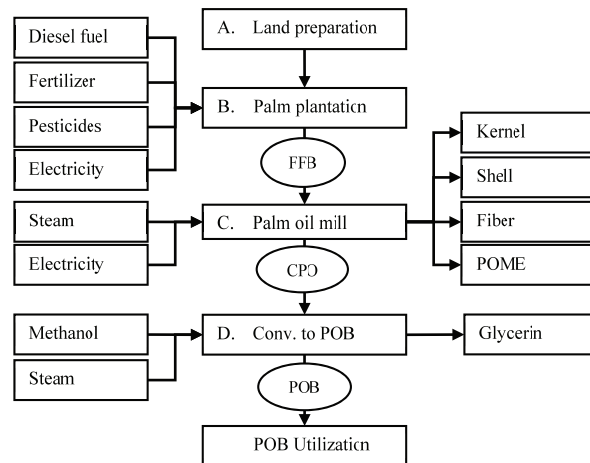
Figure 1: Process Flow Diagram of Palm Oil Biodiesel [16].

Various tools and methodologies for assessing and benchmarking environmental impacts of different product system have been developed and implemented. In order to advance the decision making process that favors sustainability at various levels (e.g., policies, regulations and practices), an integrated life cycle sustainability assessment (LCSA) framework has been developed [5,6]. This framework combines the application of the static life cycle analysis with dynamic system modeling and simulation to show the possible evolutionary trajectories of given scenarios.

This study aims to demonstrate the LCSA methodology in the static life cycle analysis part through a novel approach that couples the ISO 14040 Life Cycle Assessment (ISO-LCA) [7] and the Ecologically-based LCA (Eco-LCA) [8] methodologies on a value chain of palm oil biodiesel. By applying this hybrid LCA approach, it is expected that a more comprehensive life analysis can be performed and, thus, it can provide far-reaching information about the sustainability impacts of palm oil biodiesel, which in turns will be useful for decision makers to make well-informed policies.

2. Methodology

For the ISO-LCA, the scope of this study covers all stages in palm oil biodiesel supply chain from land clearing, cultivation, milling and conversion, up to the utilization of biodiesel in vehicles (Fig. 1). The functional unit used in this study is the production of 1 metric ton of palm oil biodiesel (POB). Detailed unit processes and input-output flows referred for the inventory analysis are shown on Fig. 1 which covers material and energy flows on each unit process. The impact assessment uses the standard procedure given in ISO 14040 as well as the guidelines and characterization factors given in the handbook of LCA [9]. Inventory data for this study were collected from secondary and surrogate databases [10,11,12,13,14,15]. Process Flow Diagram of Palm Oil Biodiesel [16]

For the Eco-LCA, the system boundary was extended to include the role of ecosystem goods and services. The biodiesel supply chain here was simplified to a "gate-to-gate" system starting from cultivation and ending at the refining step used for

Impact Category	Quantity	Unit
Land use	0.21	[ha.a]
Global warming	9,415.20	[kg CO_2-eq]
Human toxicity	7.80	[kg 1,4-DCB-eq]
Eco-toxicity (freshwater)	1,771.40	[kg 1,4-DCB-eq]
Eco-toxicity (terrestrial)	244.20	[kg 1,4-DCB-eq]
Photo-oxidant formation	0.20	[kg C_2H_4-eq]
Acidification	10.10	[kg SO_2-eq]
Eutrophication	3.20	[kg PO_4^{3-}-eq]
Abiotic res. Depletion	4.00	[kg Sb-eq]

TABLE 1: Life Cycle Impact Analysis per ton of POB.

the production of palm oil biodiesel. Similar to the ISO-LCA, the functional unit is one metric ton of POB. A key assumption in the chosen production route is that the production facilities are all located closed to each other, which is reasonable since palm oil biodiesel is typically produced in the same location as the palm oil milling plant and is located in-situ with plantation.

The information flow for material and energy for each process at the economy level was approximated using the most relevant available economic sectors in Economic Input-Output analysis table provided in Eco-LCA website [17]. This table is based on the 1997 491-sector model of the North American Industry Classification System (NAICS) standard. For instance, palm oil cultivation is represented by oilseed farming (NAICS sector 11112) and palm oil extraction by oilseed processing (NAICS sector 311223).

The current Eco-LCA software uses the functional unit of each resource in terms of U.S. economy (i.e., USD) for normalization. Therefore processes that are in the "economy level" need to be converted from their quantities (i.e., kg) in the process LCA-linked-flow to their corresponding prices.

3. Results and Discussions

The accounting of life cycle inventory for ISO-LCA yields a linked-flow described as Eq. 1.

$$0.206 \text{ ha·y} \rightarrow 5{,}184 \text{ kg}_{FFB} \rightarrow 1{,}089 \text{ kg}_{CPO} \rightarrow 1{,}000 \text{ kg}_{BDF} \quad (1)$$

Using the physical flow, the impact analysis based on the baseline impact categories given in the operational guide the ISO-LCA standard has been obtained and the results are presented in Table 1.

From impact assessment, it is inferred that global warming and eco-toxicity potentials are the main hotspots of palm oil biodiesel value chain. The climate change-related impact is associated with the land clearing process, the combustion of fossil fuels during electricity generation, fertilizer manufacturing and material transportation as well as methane release from anaerobic digestion of palm oil mill effluent (POME).
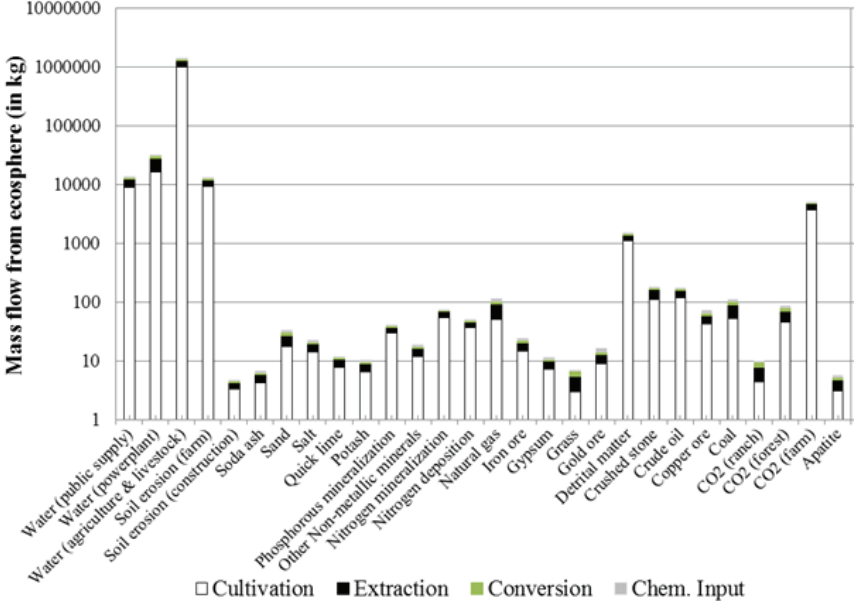
Figure 2: Resource Consumption per ton of POB.

Eutrophication and acidification are other significant impacts of the palm oil biodiesel value chain. These are associated with pesticides and insecticides use in the cultivation stage which are released to the air and waterways and result in potential eutrophication and acidification hazards.

From the Eco-LCA calculation, results show, as expected, the reliance of palm oil biodiesel on the natural capital provided by the ecosystem, including sunlight, carbon dioxide from atmosphere, detrital matter from biosphere, water from hydrosphere, as well as fossil fuels and various form of mineral from lithosphere such as coal, crude oil, natural gas, salt, sand, phosphorous and nitrogenous mineralization (Fig. 2). Although large quantities of ecosystem goods are consumed along the life cycle of palm oil biodiesel, in terms of mass, only a few of them are significant in quantity. Results show that carbon dioxide, detrital matter, fossil fuels, and soil erosion are the ecosystem goods and services that are consumed in the order of more than 100 kg per ton of POB.

Cumulative water inputs account for 1.4×10^3 ton, and CO_2 accounts for 5 tons per ton of POB as a result of water uptake and the process of CO_2 fixation during the photosynthesis associated with the cultivation of oil palm. Detrital matter, which accounts for 1.5 tons per ton of POB, is another significant input from ecosystem goods. It is important to note that compared to the other three unit processes, cultivation is the most crucial unit process during the whole biodiesel life cycle, embodying 74% of the mass input. This implies that the downstream process is very critical in the whole palm oil biodiesel life cycle, and therefore sustainable management of the downstream process contributes a lot to the sustainability of palm oil biodiesel supply chain. Result from energy analysis (graph not shown here) indicates that fossil fuels from the lithosphere and solar energy in ecological services are the major energy contributors providing more than 10^4 MJ of energy per ton of POB. Unlike results from the conventional LCA

where the role of solar energy is not counted, Eco-LCA result indicates that solar energy is the biggest contributor in terms of energy input. This indicates the large quantity of solar energy enters the economy via photosynthesis in the agricultural and forestry sectors.

4. Conclusions

This study has been able to demonstrate the static life cycle analysis part of the LCSA methodology through a novel approach that couples the ISO LCA and the Eco-LCA. This study has also provided insights on how ecosystem goods and services are associated with the value chain of palm oil biodiesel. Despite the fact that almost 100% of the energy inputs are renewable, it cannot be interpreted that the palm oil biodiesel is completely sustainable. The rates of consumption and regeneration are two key-factors which need to be considered in judging system sustainability; consumption rate that exceeds the ecosystem's ability for the regeneration will result in the deficit of ecological supply. This big picture is essential to understand the critical ecological issues in producing palm oil biodiesel, which is an important consideration in an integrated, system-perspective decision making process for formulating policies that favor sustainable development.

References

[1] S. J. Santosa, Palm oil boom in Indonesia: from plantation to downstream products and biodiesel, *Clean*, **36**, 453–465, (2008).

[2] S. Sumathi, S. P. Chai, and A. R. Mohamed, Utilization of oil palm as a source of renewable energy in Malaysia, *Renew Sustain Energy Rev*, **12**, 2404–2421, (2008).

[3] L. Reijnders, Conditions for the sustainability of biomass based fuel use, *Energy Policy*, **34**, 863–876, (2006).

[4] B. Wicke, R. Sikkema, V. Dornburg, M. Junginger, and A. Faiij, in *Drivers of land use change and the role of palm oil in Indonesia and Malaysia*, University of Utrecht, the Netherlands, 2008.

[5] M. Finkbeiner, E. M. Scau, A. Lehmann, and M. Traverso, Towards Life Cycle Sustainability Assessment, *Sustainability*, **2**, 3309–3322, (2010).

[6] A. Halog and Y. Manik, Advancing integrated systems modeling framework for life cycle sustainability assessment, *Sustainability*, **3**, 469–499, (2011).

[7] in *International Organization for Standardization, ISO 14040: Environmental Management – Life Cycle Assessment, Principles and Framework*, ISO, Geneva, 2006.

[8] Y. Zhang, A. Baral, and B. R. Bakshi, Accounting for ecosystem services in Life Cycle Assessment, Part II: toward an ecologically based LCA, *Environ Sci Technol*, **44**, 2624–2631, (2010).

[9] in *Handbook on Life Cycle Assessment: Operational Guide to the ISO Standards*, J. B. Guineé, Ed., Kluwer Academic, Dordrecht, 2002.

[10] J. H. Schmidt, Life Cycle Assessment of Rapeseed Oil and Palm Oil., 2007.

[11] S. Yusoff and S. B. Hansen, Feasibility study of performing an LCA on crude palm oil production in Malaysia, *Int J Life Cycle Assess*, **12**, 50–56, (2007).

[12] R. E. Da Costa and E. E. Lora, in *The energy balance in the production of palm oil biodiesel – two case studies*, Federal University of Itajuba, Brazil and Colombia, 2010.

[13] B. Wicke, V. Dornburg, M. Junginger, and A. Faaij, Different palm oil production system for energy purposes and their greenhouse gas implications, *Biomass Bioenergy*, **28**, 1322–1337, (2008).

[14] E. C. F. Japan, 2009, Palm Oil Mill Wastes-fired Power Generation Systems and CDM Project for Rural Electrification in Sumatra, Indonesia. Study Report. 59pp.

[15] A. Kumar and V. Nerella, Experimental Analysis of Exhaust Emissions from Transit Buses Fuelled with Biodiesel, *Open Environ. Eng. J.*, **2**, 81–96, (2009).

[16] Y. Manik and A. Halog, A meta-analytic review of life cycle assessment and flow analyses studies of palm oil biodiesel, *Integr Environ Assess Manag*, **9**, 134–141, (2013).

[17] Ohio State University, Ecologically-Based Life Cycle Assessment: Accounting for the role of nature in the life cycle of economic goods and services `http://resilience.eng.ohio-state.edu/ecolca-cv/`, Aug 24, 2015.

KnE Engineering

Knowledge E
Engaging minds

Conference Paper

Numerical Studies on Pinching Radius Effects to Current Densities of NX2 Plasma Focus

Nina Diana Nawi[1], Rakhmawati Farma[2], ST.Ong[1], Kashif Tufail Chaudhary[1], Jalil Ali[1], and Saktioto[1]

[1]Laser Centre, Ibnu Sina ISIR, Universiti Teknologi Malaysia 81300, Johor Bahru, Malaysia
[2]Kampus Bina Widya, Indonesia University of Riau, Pekan baru, 28293, Indonesia

Abstract

The pinching radius of ion beams effects are observed throughout the current densities obtained in the truncated end of NX2 plasma focus anode. The numerical experiments were carried out using RADPF code operating from 11 to 14kV of applied voltage using Neon as the filling gas with range of pressure 1.0–5.0 Torr. Energy beam acquired is studied with reference of the pinch radius and current densities. The theoretical calculations are studied. The radial speed will describe the energy transferred and will contribute to the drive parameter. The pinching radius of ion beam generated from the system plays an essential role in the determination of current densities that affects the energy beam produced. The highest energy beam, 156 J obtained at 4.0 Torr, where the current densities $7.3 \times 10^9 Am^{-2}$ and pinch radius 1.68mm.

Keywords: Plasma Focus, pinching radius, current density, energy beam

🔓 OPEN ACCESS

1. Introduction

The studies on Plasma Focus, PF device have manoeuver many findings on the future insights of energy sources [1, 2] due to its competency to produce multi-radiations such as soft X-rays, neutron, electrons and ions. The radiations are obtained through compression of plasma column. The dynamics enclosed in the system started when the current sheath is accelerated towards the open end of the inner electrodes by the Lorentz force J_r x **B**. The dynamics of the plasma and current sheath are important as it will highly affect the detail profiles of radiation output [3]. Gribkov [4] highlighted the fast ion beam generated within PF after current abruption and pinch phenomenon at the truncated end of anode (Fig. 1). Akel [5] described the decrease in induced voltage of the pre-pinch radial phase will affect the acceleration of the ions and will reduces the ion energy with higher pressures. Bhuyan [6, 7] mentioned the studies of energy flux of ion beam in PF and its characterization endeavor to possess broad understanding on fundamental physics, understand the mechanism of the production and the generation of high-energy ion.

Ion beam production is an important phenomenon to distinguish the properties of ions beams emitted from PF. In Fig. 1, beam of fast deuteron generated at plasma diode will interact with the hot and dense plasma at focus pinch column. Lee [8, 9], Gribkov [12] and Pimenov [10] have done substantial studies on ion beam based on the
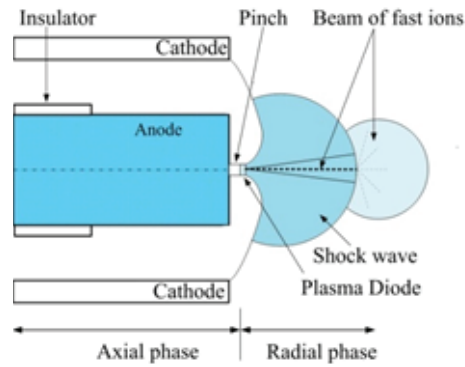
Figure 1: Schematic of the plasma dynamics in plasma focus device.

beam target mechanism. Lee defined beam that passing through a plasma target as cross-section = reaction rate (beam ion number flux x number of target particles). The beam kinetic energy and pinch inductive energy were associate to attain the numbers of beams ions per unit plasma volume traversed, n_b and beam ion speed, v_b according to the gas properties of neon [8]. This interrelation is governed by f_e parameter. f_e, defined as the fraction of energy converted from pinch inductive energy to beam kinetic energy. The equations consists of the effective charge Z_{eff}, mass number M, mass of the proton, electron and the diode voltage, U, Mass number of neon ion, M is 20 whilst m_p is 1.673×10^{27} kg. After computing extensive data fitting, Lee [8], described $U = V_{max} \cdot V_{max}$ is the maximum induced voltage of the pre-pinch radial phase. The derivation principle of flux J_b ,(Eq. 1) is significant for the studies of ion beam properties. The narrow beam will exit along the pinching axis after the post-pinch of shock wave. Flux, J_b (ions $m^{-2} s^{-1}$) is determined at the truncated of plasma anode based on the ion number per unit cross-section. By having estimation on plasma exit, the ion number per unit cross-section fluence, $J_b \tau$, energy beam and current densities properties are given in Eq. 2,3 and 4 [8, 9].

$$J_b = 2.75 \times 10^{15} \left(\frac{f_e}{M \ Z_{eff}} \right)^{1/2} \left\{ \frac{ln\left[\frac{b}{r_p}\right]}{r_p^2} \right\} \left(\frac{I_{pinch}^2}{U^{1/2}} \right) \tag{1}$$

$$\text{Fluence (ions m}^{-2}), \ J_b \tau \ = \ 2.75 \times 10^{15} \tau \left(\frac{f_e}{M \ Z_{eff}} \right)^{1/2} \left\{ \frac{ln\left[\frac{b}{r_p}\right]}{r_p^2} \right\} \left(\frac{I_{pinch}^2}{U^{1/2}} \right) \tag{2}$$

$$\text{Current density, Am}^{-2} \ = \ J_b \times e \cdot Z_{eff} \ \text{(ion charge)} \tag{3}$$

$$\text{Energy in beam, } (J) \ = \ n_b \times Z_{eff} \cdot U \tag{4}$$

These equations were incorporated in the Radiative Dense Plasma Focus, RADPF to study ion beam generation. Study are conducted by using different applied voltage to analyse the effects of pinching radius, current densities and energy beam obtained from the system.

2. Methodology

The current densities were studied at variation voltage to see its correlation with pinch radius. 11, 12, 13 and 14 kV voltages applied to the NX2 plasma machine where the static inductance, 20 nH, capacitance, 28 μF, stray resistance, 2.3 mΩ, cathode radius, 4.1 cm anode radius and length is 1.9 and 5 cm. Experiment conducted using 1.0- 5.0 Torr range of operating pressures with Neon as the working gas. The thermodynamics of neon gas and NX2 PF device configuration were incorporated in the RADPF code to ensure the system is reliable and consistent with the actual NX2 plasma focus machine. RADPF was used due to its capacity in comprehend the operation system of PF devices by incorporating the snow plough (axial phase) and slug model (radial phase). After amassed the NX2 machine configuration into the working platform of RADPF, the actual and computed experimental data were validate to ensure data are coordinate. The discharge current signal comprises the system dynamics and the information on prop-erties of multi-radiation, so, it was identified as the points of reference. The profiles of the discharged currents start from the breakdown phase until the end of pinch phase; and along the phases, it will signify the Joule heating, radiative emissions, and the expended column current flow that abruptly transited from the narrow pinch. The val-idation of computed PF system with the actual experiments were determined by cur-rent fitting techniques[11] that comprises model parameter of mass shedding effects and current shedding factor f_m, $f_{c,(axial)}$/ f_{mr}, $f_{cr\ (radial)}$. These parameters were scrutinized by parts to ensure interrelation with the dynamics, thermodynamics, electrodynamics, and radiation events of the PF. In the first stage to fit the measure current, the axial model parameter, f_m, f_c, were tuned to fit the actual the current inclination. This process was continues at the peak current zone until the peak current are prudently agree with the measured current profile. Then the second stage fitting process on the radial phase where, f_{mr} and f_{cr} were tuned until the slope of current dip and the end of dip in typically good agreement with the measured current profile. Nevertheless, the significant discrepancy of the computed and measured current profile after the current dip can be negligible, as our scope of study centered upon the radial phase; as in radial phase encompass appealing physic phenomenon to be in focus at. In instance, when the computed current profile was fitted with the measured current profile, the system ready to be run for detailed experimental calibration. The experiments conducted gives significant pattern on the results in RADPF. The data obtained were then accumulated by using Microsoft visual basic.

3. Results and Discussion

Fig. 2a shows the well fitted current profiles of the computed and actual PF machine with an average fitting deviation of ~5.87%. Good current discharge obtained when current dip is position at the region close to the peak current. The scrutiny deviation are due to the time delay in the spark gap switching during actual experimental. The axial phase duration is about 1.18 μs, then it's continuing with radial phase that last only at 0.214 μs where the radial phase ends at 1.399 μs. It can be observed in the Fig.
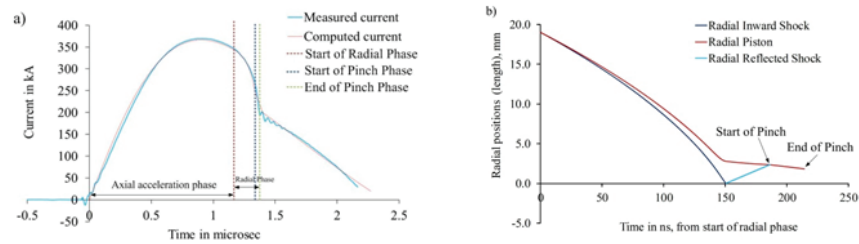
Figure 2: (a) Computed and measured current profile fitting, (b) Positions of shock front and magnetic piston for 1.7kJ NX2 PF operated at 2.6 Torr (Neon).

2b, within very short duration time of 214 ns, the radial inward shock phase started several tens of nanoseconds before entering the slope of current dip. The shock front was then reflected after 151 ns from the start of radial phase and the plasma column started to pinch at 186 ns that last for only 27.9 ns before it rapidly collapsed. The experiment were continue to study the current densities trend by integrating with the Eq. 3 and 4.

Fig. 3 shows the increasing of the current densities with the increase in gas pressure at the applied voltage, where the pinch radius is started to decreased. The results start to give a different pattern upon reaching certain value of pressure. From Fig. 3, maximum current densities $7.3 \times 10^9 Am^{-2}$ are achieved from 14 kV applied voltage with optimum pressure 4.0 Torr, results in smallest pinch radius 1.68 mm. The biggest pinch radius, 4.22 mm attained from the system will results in $4.3 \times 10^8 Am^{-2}$ from 11 kV applied voltage at pressure 5.0 Torr. From the result, it is evident the current densities phenomenon is affected by the pressure. This is due to the number of the ions and density of the plasma medium contributing to diffusion and transfer of energy. Thus, at optimum pressure, the electrons and ions are efficiently accelerated by the field. This will increase the number of ions collides where energy is transfer; so, more gas is ionized and will cause more generation of ions and electrons with higher energies which accelerate toward the cathode and the anode. Inadequate or over pressure might deliberate the effectiveness of the PF system. In achieving optimal pinch radius and current densities, it is important to stimulate the system using optimum pressure. The electrons and ions from the optimum pressure would stimulate driving force to pinch the pinching radius area. From the results, a consistency number of pinch radius at its minimum gives out maximum number of current density.

In Fig. 4a; the selected applied voltage would give same pattern, where increasing of pinching radius will lead to the decreasing in current density. At its radius locality, it will give identical pattern and values of current density. The increase of pinch radius from 1.68 mm to 5.58 mm would consent the current densities decreases from $7.3 \times 10^9 Am^{-2}$ to $2.2 \times 10^8 Am^{-2}$. This assures that pinching radius affect the current densities. These were further studied with respect of the pinch radius where 1.8mm and 2.6mm were plotted by its current densities (Fig. 4b). The current densities are increase with the increase in applied voltage where the pinch radius getting smaller.

The highest current densities obtain for 2.6mm of pinch radius is $2.7 \times 10^9 Am^{-2}$ at 14kV, whilst the minimum is $2.1 \times 10^9 Am^{-2}$ at 11kV. Significant different of current densities observed at 1.8mm pinch radius; where the maximum current densities
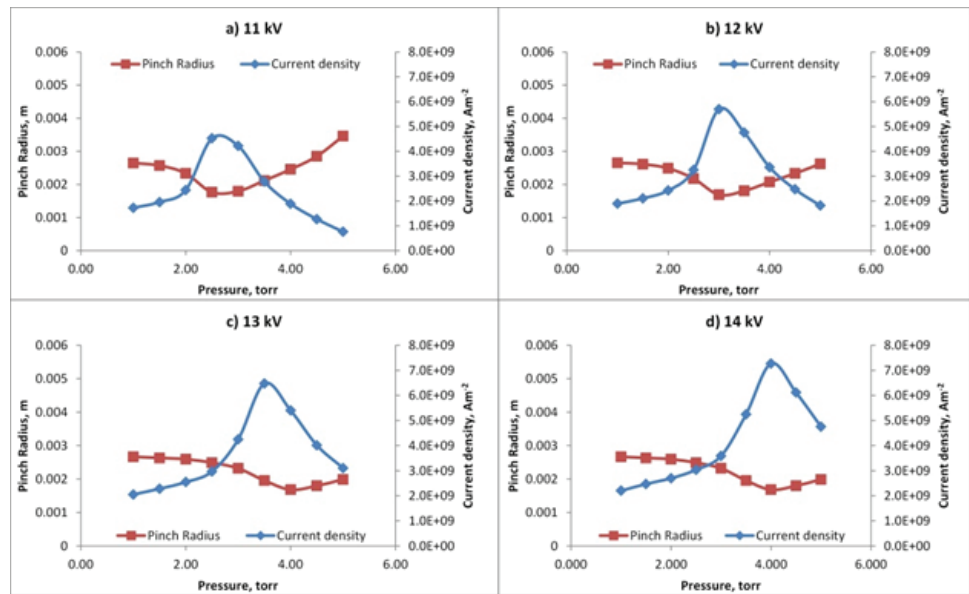
Figure 3: Current densities and pinch radius correlation with pressure with 11,12,13 and 14 applied voltages.
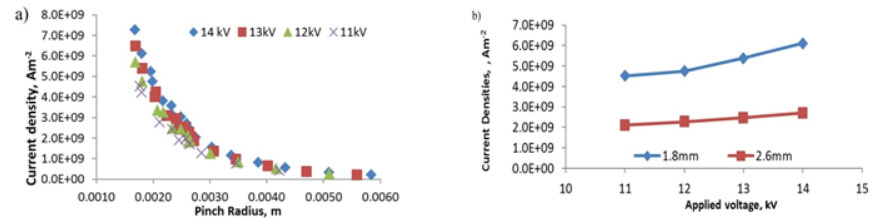
Figure 4: Correlation between current densities and pinch radius at different applied voltage.

obtained is 6.1×10^9 Am^{-2} at 14kV whilst the minimum is 4.5×10^9 Am^{-2} at 11kV. The poles apart between 1.8mm and 2.6mm pinch radius relative to the current densities, practically shows the current densities is dominated by the pinch radius. The phenomenon explained as follows. At optimum pressure with apt voltage applied, the Lorentz force will works efficiently and results in the optimum inward radial force. This allows significant constrain in the pinch area that compress the current flow per unit area.

4. Conclussion

The maximum energy beam 156 J is achieved at constrain pinch radius, the minimum energy beam obtained at the largest pinch radius with 38.4 J. The compression in the radius of ion beam gives higher current densities. Adding up from the applied voltage and optimum pressure applies, this study shows that the pinching radius of ion beams will affects the current densities generated at truncated end of NX2 plasma focus anode. From the current densities and pinch radius result, thus, we can estimate and control the energy beam requisite. This approach is significant to be used for applications in material deposition, modification and other relative industrial studies.
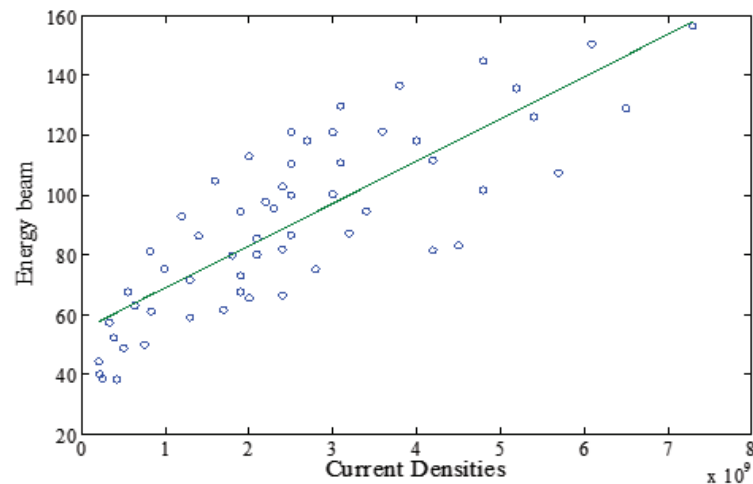
Figure 5: The energy beam correlation with the current densities.

Acknowledgement

References

[1] S. H. Saw and S. L., The plasma focus—trending into the future, *Int J Energy Res*, **36**, 1366–1374, (2012).

[2] L. Soto, New trends and future perspectives on plasma focus research, *Plasma Phys. Control. Fusion*, **47**, A361–A381, (2005).

[3] S. Lee, *Proceedings of IPFS Conference*, 2012, (29 March to 1 April), Bangkok .

[4] V. A. Gribkov, et al., *Applied Physics*, **40**, 3592–3607, (2007).

[5] M. Akel, S. A. Salo, S. H. Saw, and S. Lee, Properties of Ion Beams Generated by Nitrogen Plasma Focus, *J Fusion Energy*, **3**, 189–197, (2014).

[6] M. B., p. 208, (2010), Journal of Physics: Conference Series.

[7] A. Henriquez, et al., (2014), Journal of Physics: Conference Series.

[8] S. L. Saw, Physics of Plasma (2013), 20(062702).

[9] S. L. Saw, Physics of Plasma (2012), 19(112703).

[10] V. N. Pimenov, *3rd Research Coordination Meeting on Dense Magnetized Plasmas, 9-13 April 2007*, (2007).

[11] S. T. Ong, et al., *N Plasma Phys Control Fusion*, **56**, p. 075001, (2014).

Knowledge E
Engaging minds

Conference Paper

Effect of Input Amplitude to Power Amplification in Various Orientation of Ring Resonator

Haryana Mohd Hairi[1,2], **Toto Saktioto**[2,3], **Jalil Ali**[2], and **Siti Nor Hafiza Mohd Yusoff**[1]

[1]Faculty of Applied Sciences, Universiti Teknologi MARA,
Pasir Gudang Campus, 81750, Johor, Malaysia
[2]Laser Centre, Ibnu Sina ISIR, Universiti Teknologi Malaysia 81300, Johor Bahru, Malaysia
[3]University of Riau, Pekanbaru, 28293, Riau, Indonesia

Abstract

Photonic ring waveguide resonators have great potential applications in wavelength filtering, switching, modulation and multiplexing. The response of coupled ring resonators can be designed by using various coupling configurations. Particularly, ring resonators can be used as wavelength filter when the wavelength fits a whole multiple times in the circumference of the ring. In this paper, we investigate the effect of input amplitude to power amplification in four ring resonator configurations and vary the input amplitude on five different wavelengths. With OptiFDTD Photonics Simulation Software V8.0, the results show the intensity phenomenon of filtering in optical circuit.

 OPEN ACCESS

1. Introduction

Recently, optical ring resonator has become one of the most promising photonic integration platforms. The basic resonator consists of a straight waveguide coupled to a fiber ring with radius, r [1–5, 8]. A generic ring resonator consists of optical waveguide which is looped back on it, such that a resonance occurs when the optical path length of the resonator is exactly a whole number of wavelength [5]. The solution of Maxwell equations by Finite Difference Time Domain (FDTD) method was proved to be one of the important tools due to its simple implementation in software simulations. This mathematical method was used in a variety of photonics' studies. By using FDTD method, Hagness et. al described the design and experimental realization of a simple ring resonator. Modeling micro ring resonator is important due to the optical device offer a large free spectral range but also a narrow band [6-7]. In this study we simulated four different ring resonator configurations and vary the input amplitude on five different wavelengths. This paper studying the effect of input amplitude to power amplification for all configurations and also varies the input amplitude on five different resonant wavelengths. It is necessity to study the effect of structures on ring resonator since we discovered that power can be distributed while propagating through the structure for various performances. The output pattern of filter will varies

How to cite this article: Haryana Mohd Hairi, Toto Saktioto, Jalil Ali, and Siti Nor Hafiza Mohd Yusoff, "Effect of Input Amplitude to Power Amplification in Various Orientation of Ring Resonator," *KnE Engineering*, vol. 2016, 7 pages. DOI 10.18502/keg.v1i1.516

Page 1

due to particular orientation. Furthermore, we can optimize the profile of the output waves.

2. Design and Simulations of Resonators

The model is started by setting up the wafer dimensions to 60 μm in length and 20 μm in width. The 2D wafer's refractive index set to air's refractive index which is 1.00. The waveguide being used to model this simulation is to set the isotropic constant refractive index which is its real value of 1.54 and no imaginary part. The device configuration is composed by coupled up 4 double ring waveguide and a plane waveguide as shown in Fig. 1. The details of the configuration are as follows; the length of the linear waveguide has been set to 60.0 μm and the width of fiber is 1.0 μm. The waveguide is coupled to double ring waveguide with radius of 3.25 μm, both minor and major radius. The centers of the horizontal position for the upper and lower rings are located at approximately at 8 until 50 μm by difference of 22 μm between each other. While the vertical position of the upper ring is approximately 4.1 μm and the vertical position are about - 4.1 μm. The orientation angle of each ring waveguide is set to 0°. In this model, the default setting is used for the configuration of channel thickness tapering. The width of the ring is set to 1.0 μm and the depth is set similar to profile of plane waveguide. The vertical input plane is interfaced to the device as a power source. A continuous wave with wavelength of 1.55 μm has been used as the initial properties of the input plane for the Gaussian input field transverse. The plane geometry is set and wave configuration is 0.4 μm for its Z position being transverse in positive direction with 0° initial phase. The input power we used is 1.0 V/m.

3. Theory

The basic relations amongst the incident field, E_1, transmitted field, E_2, and circulating fields E_3, E_4 of a single resonator are inferred by combining the relations for the coupler with that of the feedback path.

In the spectral domain the field leaving the coupling region are related to the input fields via the subsequent unitary matrix;

$$\begin{pmatrix} E_4(\omega) \\ E_2(\omega) \end{pmatrix} = \begin{pmatrix} r & it \\ it & r \end{pmatrix} \begin{pmatrix} E_3(\omega) \\ E_1(\omega) \end{pmatrix} \tag{1}$$

where the lumped self- and cross-coupling coefficient, r and t are assumed to be autonomous of frequency and fulfill the relations of $r^2 + t^2 = 1$ [8]. The feedback path (of length $2\pi R$) connects the output from port 4 backward into input port 3 where the field is conveyed as:

$$E_3 = e^{-\frac{\alpha_{ring}}{2} 2\pi R} e^{ik2\pi R} E_4 \equiv a e^{i\varnothing} E_4 \tag{2}$$
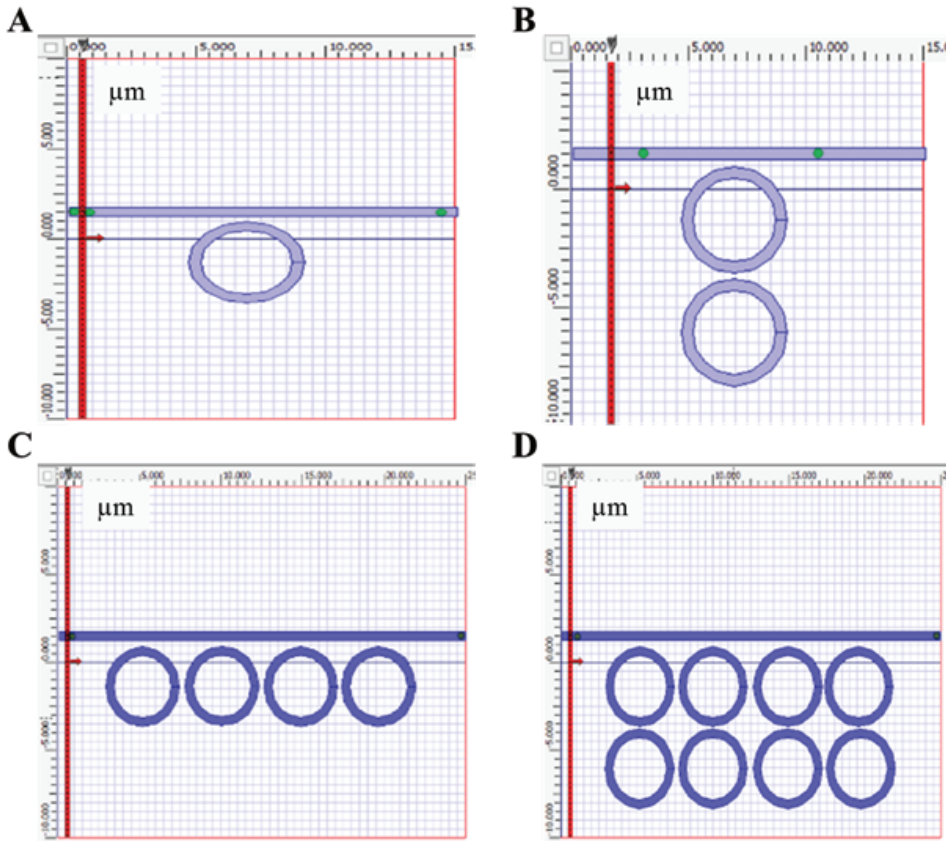
Figure 1: The schematics diagram of various configurations of ring resonators (a) single ring resonators (b) four serial-coupled single ring resonators (c) double ring resonators (d) four serial-coupled double ring resonators.

incident ray   transmitted ray
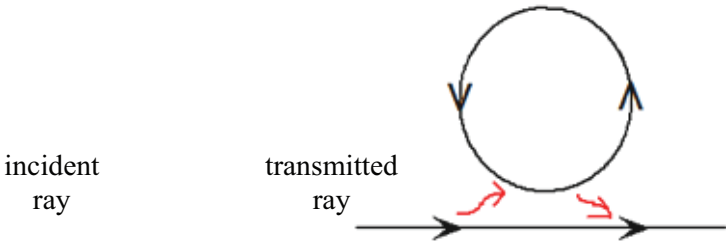
Figure 2: Electric field correlates with an all-pass ring resonator.

Here, α represents the single-pass amplitude transmission and $\varnothing$ represents the single-pass phase shift. Eq. 1 and 2 are solved to acquire an interpretation for the ratio of the circulating field to the incident field;

$$\frac{E_3}{E_1} = \frac{it\alpha e^{i\varnothing}}{1 - r\alpha e^{i\varnothing}} \tag{3}$$

The ratio of the circulating intensity to incident intensity, or the buildup factor B, is given by the squared modulus of this outcome,

$$B = \frac{I_3}{I_1} = \left| \frac{E_3}{E_1} \right|^2 \tag{4}$$

$$= \frac{\left(1 - r^2\right) a^2}{1 - 2ra \cos \phi + r^2 a^2} \tag{5}$$

The last outcomes may allude to the circumstance in which the incident light is resonant with the ring ($\varnothing = m2\pi$) and the attenuation is not considered ($a = 1$). A passive ring resonator under these conditions achieves the maximum ratio of circulating power to incident power. For cross-coupling values of 10% ($t^2 = 0.1$), the intensity in the ring can be 40 times higher than the intensity incident on the resonator in the input waveguide. Based on the intensity in the ring that can be higher than in the bus, ring resonator can be utilized for nonlinear optics applications with moderate input intensities [8].

4. Results and Discussions

4.1. Single Ring Resonator and a Linear Waveguide

Fig. 2 describes results of light intensity before and after propagating the ring structure of single ring resonator. This study is conducted based on five different wavelength; λ = 1.0 μm, λ = 1.25 μm, λ = 1.55 μm, λ = 2.9 μm, λ = 4.25 μm and the input power is set at 1 V/m. Based on the results, from Fig. 2 (a) it is found that the trend line is nearly symmetric at wavelength 0.9 μm to 1.1 μm and a peak is found to rise at λ = 1.0 μm. There seems that the filter rise gradually and the gain is high at this range. Fig. 2 (b) depicts that the trend line is not symmetric compared in (a). The filter is slightly exponential and the gain is high but the wavelength filter is short to be used in practical application as an optical filter. Fig. 2(c) shows that the peak at wavelength 1.55 μm is sharp and this makes it as a good filter in application. Besides, it depicts a comb wave rapidly and the gain is relatively high at this range compared in (a) and (b). As we increased the value of λ to 2.9 μm and 4.25 μm, it was found that the value of output power is less compared to input power being supplied to the system. Contrary to expectation, it is assumed that the power is being reticulate as it propagates through the ring structure.

4.2. Input Amplitude of 1 V/m, 5 V/m and 10 V/m

Fig. 3 depicts that the higher input amplitude produces the narrower band wave as this one of the ideal characteristic for an optical filter for λ = 1.55 μm. However at higher input amplitude, we cannot clearly observe the gap between the input source and output source compared to lower input amplitude. It is evident from the results; the trend line for various setting of input amplitude is similar to 1 V/m, 5 V/m and 10 V/m. These findings suggest that the power gain is generally good until it reaches λ = 1.55 μm. At 2.9 μm, the output power is 90◦ to 180 ◦ phase difference due to power delays although power amplification is high. As we increased theλ, they cannot acts as a good optical filter since it has wide broadband. For lower value ofλ, it can
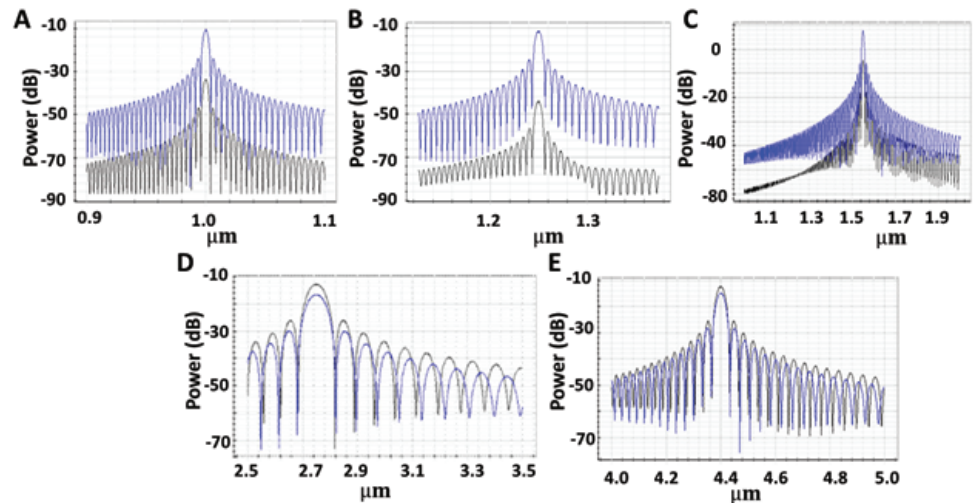
Figure 3: The transmission spectrum for single ring resonator with input amplitude of 1 V/m. (a) at λ = 1.0 μm, (b) at λ = 1.25 μm, (c) at λ = 1.55 μm, (d) at λ = 2.9 μm and (e) at λ = 4.25 μm.
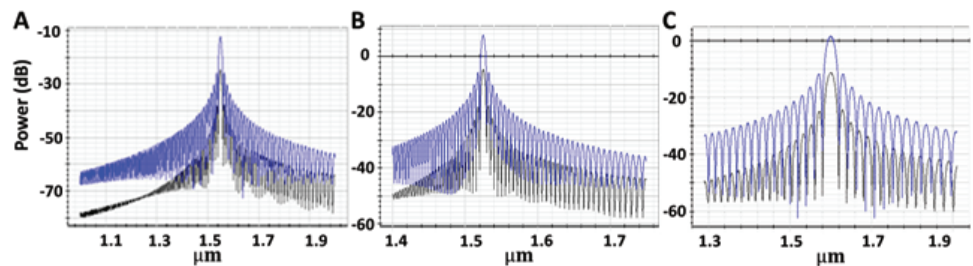
Figure 4: The transmission spectrum for single ring resonator for λ = 1.55 μm with (a) input amplitude of 1 V/m, (b) input amplitude of 5 V/m and (c) input amplitude of 10 V/m.

filter certain required wavelength since the peak is steep at certain range compared to bigger λ. These are due to the factor of higher wavelength carries high power energy. Four serial-single ring resonators is a good filter compared to single ring resonator. However the double ring resonator showing the sharp peak results. For increasing input amplitude 1 - 10 V/m, the effect of phase difference and group velocity affect the filter wave mainly at high wavelength source. The gain is sharp but for high input voltage the wave seems not sinusoidal, it suspects due to the effects of ring do not completely acts as resonator since some geometrical parameter is changed. It is the effect of nonlinear phenomenon occurs in the light wave as it propagates through the bus and ring structure.

4.3. Power Amplification of Light Intensity for Four-Coupled Double Ring Resonator

Fig. 4 shows the power amplification for optical light intensity in double ring resonator if varies the input amplitude from 1 – 10 V/m for wavelength range from 1 – 4.25 μm. This phenomenon occurs is expected due to time delay when the light is propogate in the ring. It is expected due to energy loss as it circulates in the ring. Furthermore, during the circulating, there are phase difference due to time delay between the first
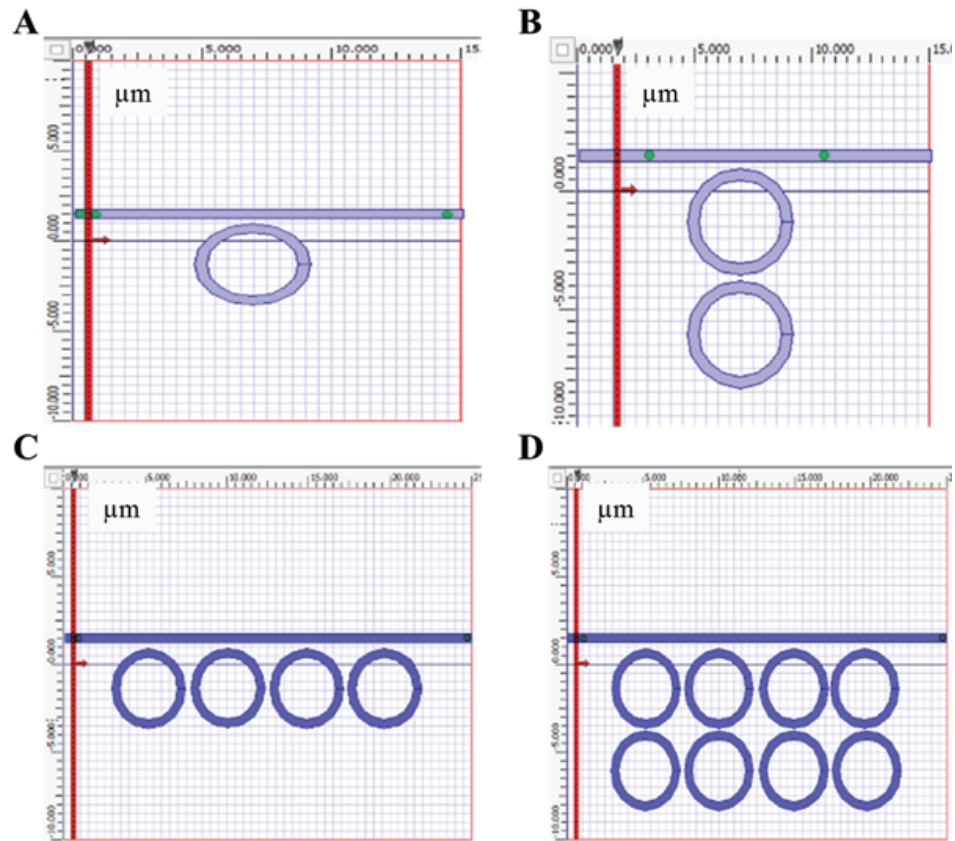
Figure 5: The power amplification of light intensity for double ring resonator. (a) at λ = 1.0 μm, (b) at λ = 1.25 μm, (c) at λ = 1.55 μm, (d) at λ = 2.9 μm and (e) at λ = 4.25 μm.

and the next wave. For larger wavelength, it carries low energy and it requires longer period to circulate in the ring.

5. Conclusion

In summary, we successfully designed and studied the effect of input amplitude to power amplification in four various ring resonator configuration. We began our analysis with a single bus waveguide coupled with single ring resonators. It shows that the peak at wavelength of 1.55 μm, the transmission spectrum from the output port at this specific wavelength is sharp and this makes it a good filter in optical application. In next section, we analyse the effect if we varies value of input amplitude of 1 V/m, 5 V/m and 10 V/m. It reveals for λ = 1.55 μm, the higher input amplitude produces the narrower band wave, as this one of the important characteristics for an optical filter. However, if we increase the input energy, it is uneasy see the gap between input and output optical spectrum. These also compared the transmission spectrum between four configurations to identify the optimum that match to fulfill the ideal optical filter.

Acknowledgements

References

[1] R. Orta, P. Savi, R. Tascone, and D. Trinchero, Synthesis of multiple-ring-resonator filters for optical sytem, *IEEE Photon Tech. Lett.*, **7**, 1447–1449, (1995).

[2] D. G. Rabus, in *Integrated Ring Resonator: The Compendium*, **127**, Springer Series in Optical Sciences, 2007.

[3] W. Bogaerts, P. Dumon, D. Van Thourhout, D. Taillaert, P. Jaenen, J. Wouters, S. Beckx, V. Wiaux, and R. Baets, Compact wavelength-selective functions in silicon-on-insulator photonics wires, *IEEE J Sel Top Quantum Electron*, **12**, 1394–1401, (2006).

[4] P. Dumon, W. Bogaerts, V. Wiaux, J. Wouters, S. Becks, J. Van Campenhout, D. Taillaert, B. Luyssaeert, P. Bientsman, D. Van Thourhout, and R. Beats, Low-loss SOI photonics wires and ring resonators fabricated with deep UV lithography, *IEEE Photonics Technol Lett*, **16**, 1328–1330, (2004).

[5] W. Bogaerts, P. D. Heyn, T. V. Vaerenbergh, K. D. Vos, S. K. Selvaraja, T. Claes, P. Dumon, P. Bientsman, D. V. Thourhout, and R. Baets, Silicon microring resonator, *Laser Photonics Rev*, **6**, 47–73, (2012).

[6] S. C. Hagness, D. Rafizadeh, S. T. Ho, and A. Taflove, FDTD Microcavity Simulations: Design and Experimental Realization of Waveguide-Coupled Single Mode Ring and Whispering-Gallery-Mode Disk Resonators, *J Lightwave Technol*, **15**, 2154–2165, (2007).

[7] H. M. Hairi, T. Saktioto, Dedi Irawan and J. Ali, "A Design of Twisted Double Channel SCISSORs for Optical Filter," Komunikasi Fisika Indonesia, 10(6), 2013.

[8] J. Heebner, R. Grover, and T. Ibrahim, Optical Microresonator: Theory, Fabrication and Application Springer Series in Optical Sciences 138, 2008.

Knowledge E

Engaging minds

Conference Paper

Comparison of Fabry – Perot Filter of Fiber Bragg Grating for Visible and Ultraviolet Spectra

Didik Puji Sutriyono[1], Saktioto[1], and Dedi Irawan[2]

[1]Magister Physics Program, Mathematics and Natural Sciences Faculty University of Riau, Pekanbaru, Indonesia
[2]Faculties of Sciences and Technology, University of Islam Negeri (Suska), Pekanbaru, Indonesia

Abstract

The use of Fiber Bragg Grating (FBG) as Fabry – Perot filter has been successfully developed for visible light and ultraviolet spectra. The characteristic of FBG is analyzed by using computational model with Transfer Matrix Method by order 2 with the coupled mode theory. The reflectivity, length of grating and bandwidth are parameters to determine the performance of FGB with laser source of 1 mW for 250 – 350 nm, ultraviolet and 380 – 780 nm, visible light. The simulation is also carried out by various grating from 0.5 cm – 9.5 cm with increment step of 1 cm. The simulation result showed that there is the filter discrepancy for maximum peak. This design of FGB can be used as a filter. Only selected wavelength is allowed to transmit the signal until the end of the optical fiber.

Keywords: Fiber Bragg Grating, visible light, ultraviolet spectrum, filter Fabry-Perot

🔓 **OPEN ACCESS**

1. Introduction

Configurations Fabry-Perot interferometers recently have been applied in telecommunications system scheme based on optical fiber. One of the application as optic resonator is by inserting Fiber Bragg Grating, (FBG) functioning as mirror. The grille placed separates at distance which have been determined, creating grille ante-room. Characteristic transmission wave propagation can be determined by passing Grille Bragg structure. Experiments which have been developed in general require costly expense and time relative longer. One of the solutions is by using method analyzed simulation with computer simulation. A method which is often used for the specifications of Grille Bragg is mode theory hold mutually (Coupled Mode Theory) and method of is transfer of matrix (Transfer of Matrix Method) capable to analyze periodic structure from grille found on single mode optical fiber [5].

FBG component has good benefit since it can be used as a sensor for nano and micro scale. It is computable to the solution of length scale by measuring the transmitted and reflected patterns, and then it can indirectly calculate the mechanical magnitudes. Although FBG can measure the mechanical magnitudes, it is also necessary to compare and characterize the effect of the visible and ultra violet wavelength source to FBG. This comparison will show the influence of the coupling amongst the source, fiber and

How to cite this article: Didik Puji Sutriyono, Saktioto, and Dedi Irawan, "Comparison of Fabry – Perot Filter of Fiber
Bragg Grating for Visible and Ultraviolet Spectra," *KnE Engineering*, vol. 2016, 6 pages. DOI 10.18502/keg.v1i1.517

Page 1

grating to FBG as the result of interference and disturbance between the photon source and the FBG refractive indices parameters. In this report, we present the application of FBG for range visible and ultra violet spectra as a source by using FBG and a detector to investigate the transmission and reflection pattern of wave output. This will allow describing the effect of the various spectra in FBG characteristics.

2. Methodology

FBG basically has to fulfill the change of momentum and energy. The first order is simple condition of Bragg:

$$\lambda_b = 2n_{eff}\Lambda \tag{1}$$

where λ_b is the Bragg Grating wavelength. At an empty space between wavelength grille centers from incident ray will be re-bounced from Bragg grille, and n_{eff} is effective refractive index from core of fiber. FBG performance is influenced by reflected peak, wide R of ribbon $\Delta\lambda$ and Bragg grille length L, the third parameter can be written as:

$$R = tanh^2\kappa. \tag{2}$$

and

$$\Delta\lambda \approx \frac{\lambda_b^2}{n_{eff}L}\left(1 + \frac{\kappa^2 L^2}{\pi^2}\right)^{1/2} \tag{3}$$

where

$$\kappa \approx \frac{\pi\Delta n I}{\lambda_b} \tag{4}$$

Δn the change of refractive index in I given by

$$I = 1 - exp\left(-\frac{2a^2}{w^2}\right) \tag{5}$$

where a is the radius core and the fiber depicts Gaussian dot size measure from fundamental mode. The difference of refractive index is immeasurable in fiber type, as in general it is defined as follows:

$$n_{eff} = \frac{\lambda_b}{2\Lambda} \tag{6}$$

where λ_b Bragg is wavelength and Λ is grille period.

The length of grille is a wide ribbon at reflected spectrum. The wide ribbon can go up or alight from long degradation and increase of grille during time constant nL. The Equation of grille is formulated.

$$L = \frac{\lambda_B^2}{\pi n_{eff} \Delta \lambda} \sqrt{\left(tanh^{-1} \left(\sqrt{R} \right) \right)^2 + \pi^2} \tag{7}$$

According to [3] the ideal modes at Equation of mode are hold mutually. Consider it is imposed by electrical field transverse component written down as ideal mode superposes which is symbolized with j (mode at an ideal wave guide without a hitch grille).

$$\vec{E}_t (x.y.z.t) = \sum_j \left[A_j (z) \, exp \left(j\beta_j z \right) + B_j (z) \, exp \left(-j\beta_j z \right) \right] \cdot \vec{e}_{jt} (x.y) \, exp \left(-i\omega t \right) \tag{8}$$

where A$_j$ (z) and B$_j$ (z) represent amplitude which creep slow at mode allowed of j at tinder direction + and z - z. A mode of electric field $\vec{e}_{jt}(x.y)$ describes as a boundary.

When orthogonal mode is at ideal wave guide [2], the attendance of dielectric trouble cause couple mode at A$_j$ (z) and B$_j$ (z) (j mode z) mount as long as z tinder, expressed with:

$$\frac{dA_j}{dz} = i \sum_k A_k \left(K_{kj}^t + K_{kj}^z \right) exp \left[i \left(\beta_k - \beta_j \right) z \right] + i \sum_k B_k \left(K_{kj}^t - K_{kj}^z \right) exp \left[-i \left(\beta_k + \beta_j \right) z \right] \tag{9}$$

$$\frac{dB_j}{dz} = -i \sum_k A_k \left(K_{kj}^t - K_{kj}^z \right) exp \left[i \left(\beta_k + \beta_j \right) z \right] - i \sum_k B_k \left(K_{kj}^t + K_{kj}^z \right) exp \left[-i \left(\beta_k - \beta_j \right) z \right] \tag{10}$$

Where $K_{kj}^t(z)$ is athwart coupling coefficient between j modus and passed to *k* equation:

$$K_{kj}^t (z) = \frac{\pi}{4} \iint_\infty dxdy \Delta \varepsilon (x.y.z) \, \vec{e}_{kt} (x.y) \cdot \vec{e}_{kt}^* (x.y) \tag{11}$$

Where $\Delta \varepsilon$ is the trouble, but in general $K_{kj}^z (z) \ll K_{kj}^t (z)$ for the modes of fiber, and that way this coefficient is generally disregarded, hence it is specified by two new coefficients:

$$\sigma_{kj} (z) = \frac{\omega n_{co}}{2} \delta n_{dc} (z) \iint_{core} dxdy \vec{e}_{kt} (x.y) \cdot \vec{e}_{kt}^* (x.y) \tag{12}$$

$$\kappa_{kj} (z) = \frac{\omega n_{co}}{4} \delta n_{ac} (z) \iint_{core} dxdy \vec{e}_{kt} (x.y) \cdot \vec{e}_{kt}^* (x.y) \tag{13}$$

Where σ is the coupling coefficient "dc" (period mean) and κ is coupling coefficient "ac". The coupling coefficient can be written down as:

$$K_{kj}^t (z) = \sigma_{kj} (z) + 2\kappa_{kj} (z) \cos \left[\frac{2\pi}{\Lambda} z + \phi(z) \right] \tag{14}$$
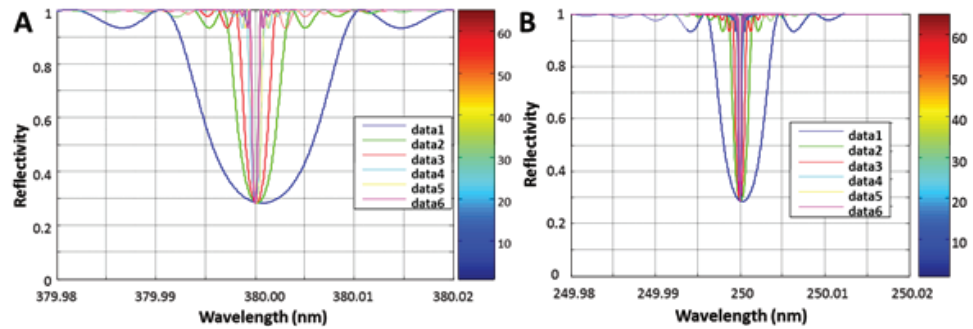
Figure 1: Characteristics for (A) 380 and (B) 250 nm each distance Fiber Brag Grating is from 0.458 cm until 9.458 cm for reflectivity of 0.715.

For the characteristics of light spectrum which creep at uniform grille, each grille deputizes order matrix two (matrix 2 X 2). With multiplying part of this matrix, it is obtained by matrix in general. The refractive index at one grille from Grille Bragg is assumed with:

$$n\left(z\right) = n_{eff} + \Delta n_i cos\left(\frac{2\pi}{\Lambda_i}\right) \tag{15}$$

$n_{eff\_}$index deflects the amplitude modulation. and Δn_ii part of grille period.
The uniform grille to each part of grille is described with matrix, given by Ti:

$$\begin{bmatrix} R_i \\ S_i \end{bmatrix} = T_i \begin{bmatrix} R_i \\ S_i \end{bmatrix} \tag{16}$$

with Ti to one part of Bragg grille, given by Equation:

$$T_i = \begin{bmatrix} cosh\left(\Omega_i dz_i\right) - j\frac{\sigma_i}{\Omega_i} sinh(\Omega_i dz_i) & -j\frac{\kappa_i}{\Omega_i} sinh\left(\Omega_i dz_i\right) \\ j\frac{\kappa_i}{\Omega_i} sinh\left(\Omega_i dz_i\right) & cosh\left(\Omega_i dz_i\right) + j\frac{\sigma_i}{\Omega_i} sinh(\Omega_i dz_i) \end{bmatrix} \tag{17}$$

In this case. $j = \sqrt{-1}$, where the amplitude variation of the round of waving at + and z – z, dz is length part of uniform grille i, σ and κ are coupling parameters to part of i.

3. Result and Discussion

The wavelength characteristics of 780 nm and 580 nm at grating distance 0.458 with reflectivity of 0.718 described two similar maximum peaks but it happen a long friction of wave that is in 780.025 nm and in 780.040 nm, and also in 580.0125 nm and 580.025 nm. In addition to the characteristics of the other wavelength there is only one maximum peak in good reflectivity upon the other grille distance.

Wavelength characteristics of 300 nm and 250 nm at Bragg grille distance of 6.458 cm and 9.456 cm with reflectivity of 0.518 shows the changes the maximum culminate which do not meet from low to high level. The other wavelength depicts regularly to maximum culminate from high level to the low one. The data implicitly describe that
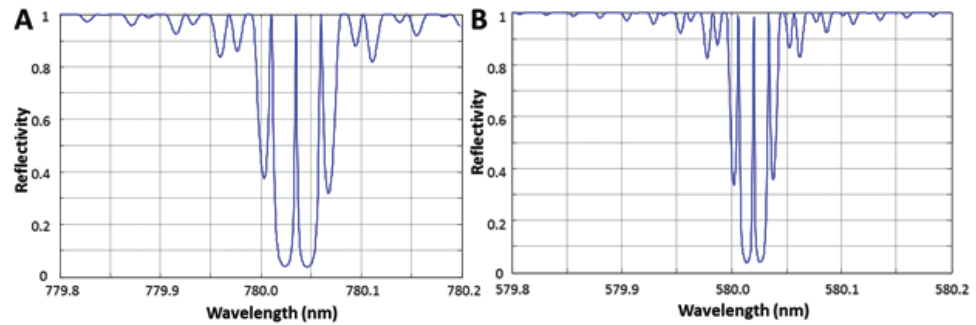
Figure 2: Characteristics for (A) 780 nm and (B) 580 nm with grating of 0.458 cm and reflectivity of 0.718.
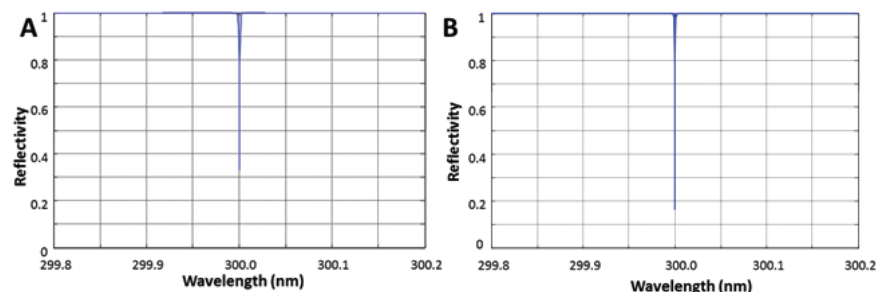
Figure 3: Characteristic for 300 nm with grating (A) 6.458 cm and (B) 9.458 cm and reflectivity of 0.518.
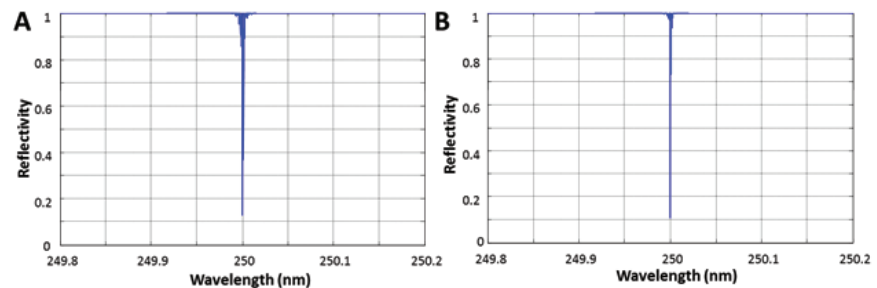
Figure 4: Characteristic for 250 nm with grating (A) 6.458 cm and (B) 9.458 cm and reflectivity of 0.518.

the wave pattern is relatively sharp and stable at peak beginning from the near grating to far one (9.5-0.5cm) either 380 nm or 780 nm wavelength source. The pattern change is due to the FBG adaptation of power source parameters.

4. Conclusion

The characteristics of FBG have been obtained at ultraviolet wavelength of 250 nm until 350 nm. and the visible light of 380 nm until 780 nm. When the wave propagates along the FBG several wavelengths is reflected and the others are transmitted by ignoring the losses. Several peaks are shown due to high transmission for the lower wavelength compared to the higher wavelength. This implicitly depicts that the higher energy corresponding to the lower wavelength can filter the wavelength well and vice versa.

References

[1] S. Pramuliawati and S. Defrianto, Pemodelan Tapis Fabry-Perot pada Serat optic dengan menggunakan Fiber Bragg Grating, *JOM FMIPA*, **2**, 186–190, (2015).

[2] P. Govind, Fiber – Optic Communication Systems third ed., A John Willey and Sons Publication 2002.

[3] E. Turan, Hiber Greating Spektra, *Jurnal Of Lightwafe Tecnology*, **15**, no. 8, p. 1277, (1997).

[4] Lozd. et al., Fundamentals of Optical Fiber Transmission, Max Born Institute, 2011.

[5] C. M. de Sterke, K. R. Jackson, and B. D. Robert, Nonlinear coupled-mode equations on a finite interval: a numerical procedure, *J Opt Soc Am B*, **8**, p. 403, (1991).

Left-Handed Metamaterial Structure for Side Lobe Suppression of Microstrip Array Antenna

Fitri Yuli Zulkifli, Pamela Kareen, Basari, and Eko Tjipto Rahardjo

Antenna Propagation and Microwave Research Group, Department of Electrical Engineering, Universitas Indonesia, Depok 16424, Indonesia

Abstract

In this paper, a Left-handed Metamaterial (LHM) structure is designed for side lobe suppression of a microstrip array antenna at frequency 2.8-3.1 GHz. The LHM structure is placed at the top of the microstrip array antenna with a space or gap between them. Side lobe suppression is very important for Radar system which needs antenna with high performance of its radiation properties. The linier array microstrip antenna consists of 4x1 elements. The simulation result using CST microwave studio shows that the Side Lobe Level (SLL) has been suppressed from -8.93 dB to -15.86 dB at phi = 0 while the measurement result shows suppression from -6.6 dB to -10.75 dB. Both simulation and measurement result shows a side lobe suppression using LHM structure.

Keywords: Left handed metamaterial, side lobe suppression, microstrip array antenna

1. Introduction

Radar (Radio Detection and Ranging) is a system that can detect an object and therefore needs high accuracy. Antenna as one important part of the Radar system plays an important role for the accuracy of the Radar to detect an object. The antenna exhibits radiation properties such as radiation pattern. The radiation pattern consists of major lobe and side lobes. The main lobe is used to detect an object precisely at a certain coordinate. If the side lobe is too high and has the magnitude almost the same as the main lobe, the radar can false detect the object with wrong coordinate. One method that can increase the accuracy is reducing the Side Lobe Level (SLL) from antenna performance of the radar. High SLL can cause false signal or false detection. There are several techniques that can reduce the SLL, which are Chebyshev [1], Electromagnetic Band Gap (EBG) [2] and Metamaterial (MTM). Electromagnetic Band Gap in [2] has reduced the antenna SLL around 2.5 dB from -12.69 dB to -15.24 dB.

Metamaterial is defined by the permittivity and the permeability of the material. A Material found in nature usually has positive permittivity and permeability, however, metamaterial is defined as engineered material or engineered structure that has negative permittivity with positive permeability or negative permeability with positive permittivity or has both negative permittivity ($\varepsilon < 0$) and negative permeability($\mu < 0$) and called as Left-Handed Metamaterial (LHM). LHM can cause backward wave propagation [3].

How to cite this article: Fitri Yuli Zulkifli, Pamela Kareen, Basari, and Eko Tjipto Rahardjo, "Left-Handed Metamaterial Structure for Side Lobe Suppression of Microstrip Array Antenna," *KnE Engineering*, vol. 2016, 6 pages. DOI 10.18502/keg.v1i1.518
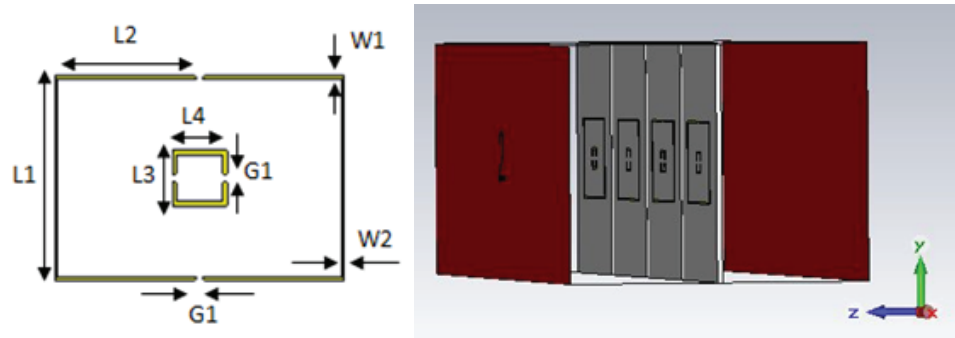
Page 1

Figure 1: (a) Dimension of the LHM structure, (b) Boundary condition of the LHM structure simulation setup.

Metamaterial has many different structure types like a rectangular, omega or S structure. The omega and the S type are not easy to construct and has a narrow bandwidth [4], while the rectangular structure has broader bandwidth and more easy to construct. Split Ring Resonator (SRR) is also a LHM structure. LHM contains a Split Ring Resonator (SRR) that produce a strong magnetic field [5] causing the permeability negative and a thin wire that cause a negative permittivity, but beside using a thin wire which is hard to apply in this application, the LHM structure can make a CLS (Capacitive Loaded Strip) at the LHM structure that can cause the permittivity to be negative too. LHM structure can also be placed at the top of the array antenna [6] because the negative characteristic can act as lens that can focus the radiation beam. A focus beam can make the main lobe much larger and reduce the size of the side lobe level. In this paper, a microstrip array antenna with LHM structure placed at the top of the antenna is proposed to suppress the side lobe level.

2. Design of Left Handed Metamaterial

The LHM structure is designed using FR-4 substrate with thickness h = 1.6 mm, relative permittivity ε_r = 4.6 and loss tangent 0.025, which is depicted in Fig. 1(a). Variable L, W, and G shows the length, width and gap of the LHM structure dimension. Where, L1 = 26 mm, W1 = 0.5 mm, G1 = 1 mm, L2 = 18 mm, W2 = 0.25 mm, G2 = 1 mm, L3 = 7 mm and L4 = 7 mm.

Simulation of the LHM structure is conducted using CST Microwave studio software. Before starting the simulation, the boundary condition has to be set. The top and bottom of the LHM structure (y-axis) is given Perfect Electric Conductor (PEC), the front and back (z-axis) of the LHM structure is given open add space, the left and right of the LHM (x-axis) is given Perfect Magnetic Condition (PMC). After the boundary condition has been set, the port is given at the z-axis as shown in Fig. 1(b).

Figure 2 shows the result S_{11} of the LHM structure which operates at frequency 2.8–3.1 GHz. The S_{11} is used for calculation to prove the new permeability and the permittivity of the LHM structure.

Formula Nicholson, Ross and Weir (NRW) [7] is used to find the permittivity and the permeability of the LHM structure used in Eq. 1 to Eq. 4:
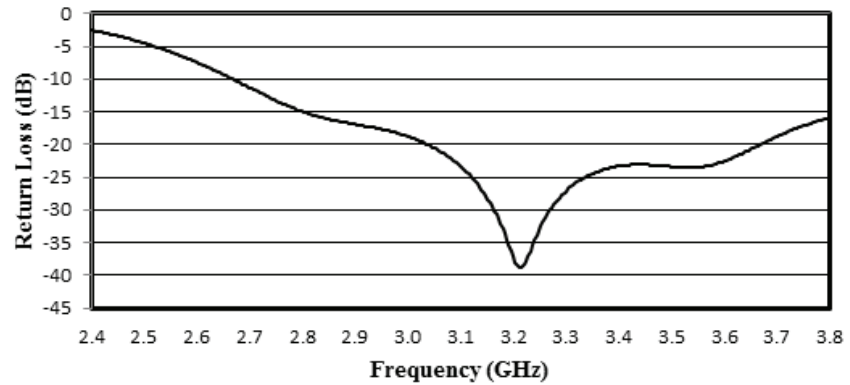
Figure 2: Return loss of the LHM structure.

$$\mu_r = \frac{2 \cdot c \left(1 - v_2\right)}{\omega \cdot d \cdot i \left(1 + v_2\right)} \tag{1}$$

$$v_1 = S_{11} + S_{21} \tag{2}$$

$$\varepsilon_r = \frac{2 \cdot c \left(1 - v_1\right)}{\omega \cdot d \cdot i \left(1 + v_1\right)} \tag{3}$$

$$v_2 = S_{21} - S_{11} \tag{4}$$

Where μ_r is the permeability, ε_r is the permittivity, ω is the frequency in radian, c is the speed of light, and d is the thickness of the substrate. The permittivity and the permeability that has been calculated is plot and shown in Fig. 3. Figure 3(a) shows the negative permittivity of the LHM structure while Fig. 3(b) shows the negative permeability. This means that the structure designed has both negative permittivity and negative permeability and called the LHM structure.

This LHM structure is then applied to microstrip antenna for radar application. Figure 4 shows the exploded view of the microstrip antenna array 4 elements for radar application [5] with the LHM structure. Between the microstrip and the LHM structure is given a space or a gap about 0.05λ.

The simulation result shows that the antenna design with LHM structure can suppress the side lobe level from -8.93 dB to -15.86 dB. This design with simulation result aforementioned is then fabricated to be a prototype.

3. Measurement Result

The LHM structure is fabricated and photo as depicted in Fig.5, the top view and the back view of the LHM structure is the same. The array antenna 4 element with the
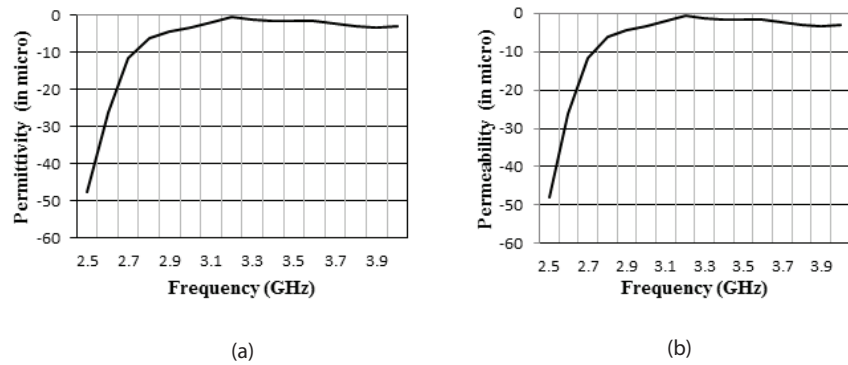
Figure 3: (a) Permittivity, (b) Permeability.
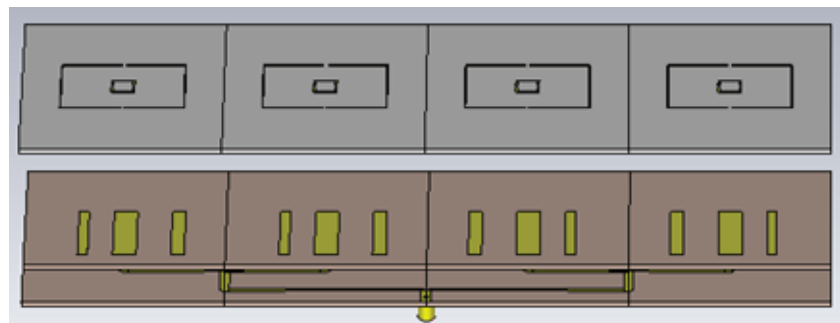
Figure 4: Exploded view of LHM Structure for antenna array 4x1 element.

Figure 5: Exploded view of the array antenna 4 element with the LHM structure.

LHM structure has a gap distance of 5 cm. Stereo foam is used to make the gap and support the substrate with the LHM structure on top of the antenna to avoid significant change of the radiation properties if using conductive materials.

The LHM structure with the array antenna 4 elements is measured in anechoic chamber at Electrical Engineering Department, Faculty of Engineering, Universitas Indonesia. Both the simulation and measurement result is plotted in Fig. 6. Although there is a slight difference of peaks and valleys of the S_{11} parameter, the simulation and measured frequency show the same bandwidth of the antenna which is about 320 MHz at $S_{11} \leq$ -10dB.

Figure 7 shows the linear plot of the radiation pattern at phi = 0. The simulated side lobe level from antenna with LHM structure is about -15.86 dB, the measured is about
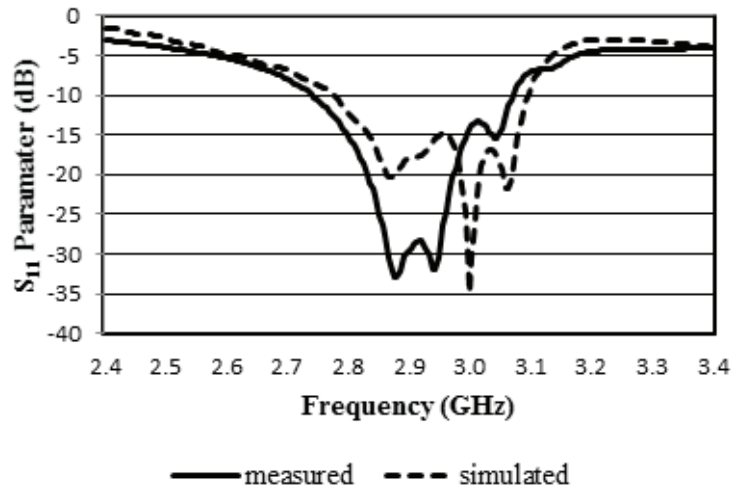
Figure 6: Simulation Result of S_{11} Parameter.
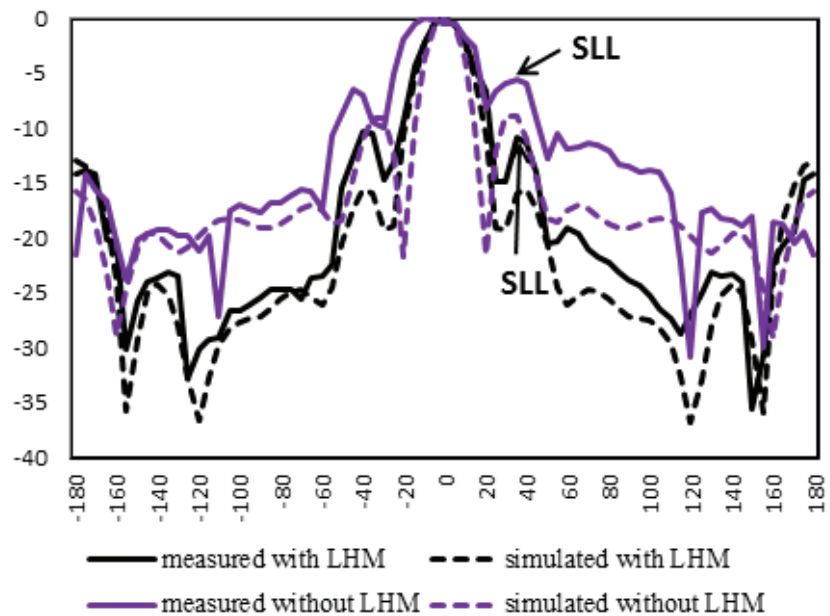
Figure 7: Linear plot at phi = 0.

-10.75 dB. Meanwhile, the simulated SLL without LHM structure is -8.93 dB and the measured is -6.6 dB. So simulation result shows a SLL suppression of 6.93 dB while measurement result shows suppression of 4.15 dB.

The slight difference between the simulation and measurement result is due to the imperfect condition of the antenna fabrication. In microwave, a slight difference of antenna dimensions between design and fabrication can cause shift of results because the impedance of the antenna can be easily influenced and therefore changed.

4. Conclusion

The LHM structure discussed in this paper has both negative permittivity and permeability. The microstrip antenna array 4 elements with a LHM structure can suppress the side lobe level of the antenna with simulation result shows a suppression of 6.93 dB while measurement result shows suppression of 4.15 dB.

Acknowledgement

References

[1] F. Y. Zulkifli, T. Hidayat, Basari, and E. T. Rahardjo, Sidelobe Level Suppression Using Unequal Four-Way Power Divider for Proximity Coupled Microstrip Antenna, *Asia Pacific Microwave Conference (APMC 2013)*, 1166–1168

[2] M. J. Asghari, F. H. Kashari, A. Malekijavan, and B. Bahirei, Using Mushroom EBG In Microstrip Array Antenna to Reduce Side Lobe Level, *Life Sci J*, **10**, 3s, (2013).

[3] T. J. Cui, D. R. Smith, and R. Liu, in *Metamaterials Theory, Design, and Applications*, Springer, 2010.

[4] W. Wang, Directive Antenna Using Metamaterial Substrates (2004).

[5] C. D. Moss, T. M. Grzegorczyk, Y. Zhang, and J. A. Kong, Numerical Studies of Left Handed Metamaterials, *Prog In Electromagn Res PIER*, **35**, 315–334, (2002).

[6] H. A. Majid, M. KA. Rahim, and T. Masri, Microstrip Antenna's Gain Enchancement Using Left-Handed Metamaterial Structure, *Prog In Electromagn Res M*, **8**, 235–247, (2009).

[7] R. W. Ziolkowski, Design, Fabrication and Testing of Double Negative Metamaterials, *IEEE Trans Antenn Propag*, **51**, p. 662, (2003).

KnE Engineering

Knowledge E
Engaging minds

Conference Paper

Binary Composite Fiber Elasticity Using Spring-Mass and Non-Interacting Parallel Sub-Fiber Model

Widayani, Sparisoma Viridi, and Siti Nurul Khotimah

Nuclear Physics and Biophysics Research Division, Faculty of Mathematics and Natural Sciences, Institut Teknologi Bandung, Jalan Ganeca 10 Bandung 40132, Indonesia

Abstract

Composite materials have been investigated elsewhere. Most of the studies are based on experimental results. This paper reports a numerical study of elasticity modulus of binary fiber composite materials. In this study, we use binary fiber composite materials model which consists of materials of types A and B. The composite is simplified into compound of non-interacting parallel sub-fibers. Each sub-fiber is modeled as N_s point of masses in series configuration. Two adjacent point of mass is connected with spring constant k (related and proportional to Young Modulus E), where it could be k_{AA}, k_{AB}, or k_{BB} depend on material type of the two point of masses. Three possible combinations of spring constant are investigated: (a) $[k_{AB} < \min(k_{AA}, k_{BB})]$, (b) $[\min(k_{AA}, k_{BB}) < k_{AB} < \max(k_{AA}, k_{BB})]$, and (c) $[\max(k_{AA}, kBB) < k_{AB}]$. The combinations are labeled as composite type I, II, and III, respectively. It is observed that only type II fits most the region limited by Voight and Reuss formulas.

Keywords: composite materials, one-dimension, spring, combination, sequence

OPEN ACCESS

1. Introduction

One of the important things in studies of composite materials is the relationship between mechanical properties of the composites with that of its components. Although many studies on composite materials are based on experimental results, but theoretical or numerical studies on mechanical properties of composites are also important.

This study is a numerical study of elasticity modulus of binary fiber composite materials, i.e. binary composite materials. In the binary composite model used, two adjacent point of mass is connected with spring constant k (related and proportional to Young Modulus E). This study focuses on the relationship between mechanical properties of the composites with that of its components through analysis on spring constant k.

Previously, binary composite materials have been discussed in 3-d experiment [1] and 2-d simulated based on granular particles [2], where the mixture could be homogenously dispersed [1] or the components can still be differed [3]. A model of binary composite materials are proposed in this work and compared to the Voight and Reuss formulas, which has been common as benchmark in studying composite models [4].
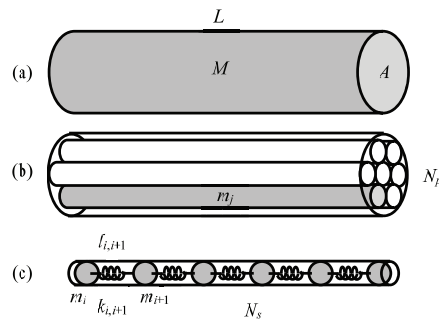
Figure 1: (a) A composite fiber with cross section A, mass M, and length L. (b) A bundle of N_p paralel non-interacting sub fibers. (c) Each sub-fiber consists of N_s point masses and N_s–1 springs.

2. Theory

A composite fiber can be modeled as a bundle of N_p parallel non-interacting sub-fibers as shown in Figure 1, where each sub-fiber consists of serial arrangements of point masse and spring systems.

In sub-fiber j with mass m_j there are N_s point masses and N_s–1 springs. Spring with spring constant $k_{i,i+1}$ and length $l_{i,i+1}$ connects point masses m_i and m_{i+1}.

Mass of the whole composite fiber is

$$M = \sum_{j=1}^{N_p} m_j = \sum_{j=1}^{N_p} \sum_{i=1}^{N_s} m_{ji} \tag{1}$$

with m_{ij} is point mass i in sub-fiber j.

Supposed that the composite fiber of material X has elastic modulus E_X with relation between stress F, strain ΔL, initial length L, and cross section A.

$$\frac{F}{A} = E_X \frac{\Delta L}{L} \tag{2}$$

and Hooke's law for elastic system

$$F = k_X \Delta L, \tag{3}$$

then a relation can be derived

$$k_X = E_X \frac{A}{L}. \tag{4}$$

Spring constant of fiber of material X is constructed from parallel arrangement of sub-fibers with spring constant k_j

$$k_X = \sum_{j=1}^{N_p} k_j = N_p k_j \tag{5}$$

Material	Elastic modulus	Spring constant	Type of connected point masses		Lennard-Jones (12,6) constants
			m_i	m_{i+1}	
A	E_A	k_{AA}	A	A	ε_{A-A}, σ_{A-A}
B	E_B	k_{BB}	B	B	ε_{B-B}, σ_{B-B}
Composite	E_{comp}	$k_{AB} = k_{BA}$	A	B	ε_{A-B}, σ_{A-B}
			B	A	

TABLE 1: Spring constants connecting two adjacent point masses, the elastic modulus, and Lennard-Jones (12,6) constants.

or

$$k_j = \frac{k_X}{N_p}.$$ (6)

This k_j in a sub-fiber j is built of serial arrangement of spring constants $k_{i,i+1}$ which connects point masses i and i+1

$$\frac{1}{k_j} = \sum_{i=1}^{N_s-1} \frac{1}{k_{i,i+1}} = \frac{N_s - 1}{k_{i,i+1}}$$ (7)

or

$$k_{i,i+1} = \left(N_s - 1 \right) k_j.$$ (8)

Substituting Equation 7 into Equation 9 will give

$$k_{i,i+1} = \frac{\left(N_s - 1 \right)}{N_p} k_X.$$ (9)

In this work only binary composite is considered, e.g. materials A and B. Three types of spring constants would be sufficient for the binary composite system k_{AA}, k_{AB}, and k_{BB}, where each spring constant connects point masses of types A-A, A-B (or B-A), and B-B, respectively. Table 1 give clearer picture of relation between spring constants $k_{i,i+1}$ and materials composing the composite fiber.

The spring constant $k_{i,i+1}$ can be considered as approximation of Lennard-Jones (12,6) potential [Jones, 1924] about its separation distance r_m which produces minimum potential. The potential is commonly expressed as

$$V_{\mathrm{LJ}} = 4\varepsilon \left[\left(\frac{\sigma}{r} \right)^{12} - \left(\frac{\sigma}{r} \right)^6 \right] = \varepsilon \left[\left(\frac{r_m}{r} \right)^{12} - 2 \left(\frac{r_m}{r} \right)^6 \right],$$ (10)

where ε is the depth of potential well, σ is the finite distance at which the inter-particle potential is zero, and r is distance between a pair of atoms or molecules. Equation 10 can be approximated using

$$V_{\text{LJ}} \approx V_{\text{LJ}}\Big|_{r=r_m} + \frac{dV_{\text{LJ}}}{dr}\Big|_{r=r_m}\left(r - r_m\right) + \frac{d^2V_{\text{LJ}}}{dr^2}\Big|_{r=r_m}\frac{\left(r - r_m\right)^2}{2!}, \tag{11}$$

which produces

$$V_{\text{LJ}} \approx -\varepsilon + \frac{36\varepsilon}{r_m^2}\left(r - r_m\right)^2. \tag{12}$$

Position $r = r_m$ can be chosen as local coordinate for equilibrium position and by shifting potential reference, so that Equation 12 can be adjusted to

$$V = \frac{36\varepsilon}{r_m^2}r^2 = \frac{1}{2}k_{i,i+1}r^2 \tag{13}$$

with $r_m = 2^{1/6}\sigma$. Then, it can be obtained that

$$k_{i,i+1} = \frac{72\varepsilon}{r_m^2} = \frac{72\varepsilon}{2^{1/3}\sigma^2}. \tag{14}$$

Value of ε and σ for pair of atoms, molecules, or cluster of molecules are already common [5-7]. Equations 10-14 are shown only for showing that it is possible to obtain k_{AA}, k_{AB}, and k_{BB} based on materials molecular interactions. In this work values of k_{AA} and k_{BB} will be proportional to E_A and E_B according to Equation 4 and k_{AB} will be a adjustable parameter.

Concentration of composite materials is defined as

$$c = \frac{N_{\text{B}}}{N_{\text{A}} + N_{\text{B}}}, \tag{15}$$

which means that $c = 0$ is for pure material of type A, while $c = 1$ is for pure material of type B.

3. Results and Discussion

Configurations of composite materials with $N_p = 1$ and $N_s = 2$–4 are given in Table 2, which shows that higher value of N_s will give smoother values of various concentration c. Probable occurring sequences S for each value of N_s are given. For $N_p > 1$ value of $k_{i,i+1}$ for certain concentration c will be fallen between minimum and maximum values of the k's of the all sequences at the concentration c.

Prediction of the well-known rules of mixture from Voight and Reuss [4] is shown in Figure 2 as solid (red) and dashed (blue) lines for isostrain and isostress conditions, respectively. The rules give upper and lower bounds for composite materials elasticity. The proposed model in this work, which is calculated using a spreadsheet-software, can go beyond these bounds by adjusting the parameter k_{AB}. Some sequences S are still between those two bounds, especially most in the type II. Materials of type I represents adhesive force is less than cohesive force, while type III represent adhesive force is more than cohesive force.

In the future, a rule how to select possible occurring sequence S should be defined, i.e. why some composite materials could be type I, II, or III.

N_s	c	S	$k_{i,i+1}$		N_s	c	S	$k_{i,i+1}$
2	0	AA	k_{AA}		4	0	AAAA	k_{AA} k_{AA} k_{AA}
	0.5	AB	k_{AB}			0.25	AAAB	k_{AA} k_{AA} k_{AB}
	0.5	BA	k_{AB}				AABA	k_{AA} k_{AB} k_{AB}
	1	BB	k_{BB}				ABAA	k_{AB} k_{AB} k_{AA}
							BAAA	k_{AB} k_{AA} k_{AA}
						0.5	AABB	k_{AA} k_{AB} k_{AA}
N_s	c	S	$k_{i,i+1}$				ABAB	k_{AB} k_{AB} k_{AB}
3	0	AAA	k_{AA} k_{AA}				ABBA	k_{AB} k_{BB} k_{AB}
	0.33	AAB	k_{AA} k_{AB}				BAAB	k_{AB} k_{AA} k_{AB}
		ABA	k_{AB} k_{AB}				BABA	k_{AB} k_{AB} k_{AB}
		BAA	k_{AB} k_{AA}				BBAA	k_{BB} k_{AB} k_{AA}
	0.67	ABB	k_{AB} k_{BB}			0.75	ABBB	k_{AB} k_{BB} k_{BB}
		BAB	k_{AB} k_{AB}				BABB	k_{AB} k_{AB} k_{BB}
		BAA	k_{AB} k_{AA}				BBAB	k_{BB} k_{AB} k_{AB}
	1	BBB	k_{BB} k_{BB}				BBBA	k_{BB} k_{BB} k_{AB}
						1	BBBB	k_{BB} k_{BB} k_{BB}

TABLE 2: Possible sequences S of a sub-fiber for N_s = 2–4 and its spring constant $k_{i,i+1}$ types.
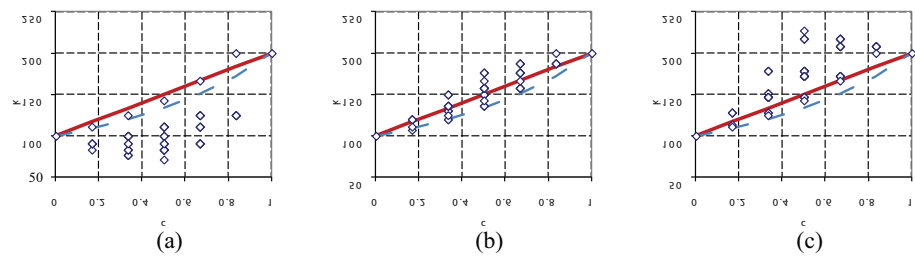

Figure 2: Composite spring constant k (N_p = 1, N_s = 4) as function of concentration c for: (a) type I with k_{AA} = 100, k_{AB} = 50, k_{BB} = 200, (b) type II with k_{AA} = 100, k_{AB} = 150, k_{BB} = 200, and (c) type III with k_{AA} = 100, k_{AB} = 250, k_{BB} = 200, with lower (dashed line) and upper (solid line) bounds.

4. Conclusions

A model to predict elasticity of composite materials based on spring-mass system has been conducted in this work. It can give bounds beyond upper and lower bounds predicted from Voight and Reuss formulas. Composite material of type II [$\min(k_{AA}, k_{BB})$ $< k_{AB} < \max(k_{AA}, k_{BB})$] is the most fitted to the formulas.

Acknowledgements

References

[1] Y. Widayani, et al., Compressive Elastic Modulus of Natural Fiber Based Binary Composites, in *AIP Conf. Proc.*, **1454**, 286–289, 2012.

[2] S. Viridi, S. N. Widayani, and Khotimah, 2-D Granular Model of Composite Elasticity using Molecular Dynamics Simulation, *AIP Conf. Proc*, 219–222, (2012).

[3] I. D. Aditya and S. Widayani, Viridi, S. N. Khotimah, Study of Internal Response of Epoxy Due to Compressive Load via Experiment and Simulation using Abaqus FEA Software, *Adv Mat Res*, **896**, 549–552, (2014).

[4] S. Widayani, Viridi, S. N. Khotimah, Theoretical Study on Mechanical Properties of 2-D Composite Models Containing Circular Fillers under Compression Load, Int, *J Compos Mater*, **5**, 47–51, (2015).

[5] J. E. Jones, On the Determination of Molecular Fields. II. From the Equation of State of a Gas, *Philos. T. R Soc.*, **A106**, 463–477, (1924).

[6] N. M. Putintsev and D. N. Putintsev, Method for Determining the Parameters of the Lennard-Jones Potential, *Dokl Phys Chem*, **399**, 278–282, (2004).

[7] M. Monajjemi, S. Ketabi, M. H. Zadeh, and A. Amiri, Simulation of DNA bases in water: comparison of the Monte Carlo algorithm with molecular mechanics force fields, *Biochemistry (Mosc)*, **71**, Suppl 1, S1–S8, (2006).

KnE Engineering

Knowledge E
Engaging minds

Conference Paper

Mechanical Properties of Metal Al/SiC and AlCu/SiC Metal Matrix Composites (MMCs)

Anggara B. S.[1,2] **and Bambang Soegijono**[2]

[1]Jurusan Fisika, FMIPA Universitas Negeri Jakarta, Indonesia 13220
[2]PPS Ilmu Material, Departemen Fisika, FMIPA, Universitas Indonesia, Indonesia

Abstract

The Metal Matrix Composite (MMCs) Al/SiC and AlCu/SiC through steering hot method have been done. The SEM images show that there are microstructure differences between the Al/SiC and AlCu/SiC. Tensile test results show the value of the yield stress of AlCu /SiC higher than Al/SiC. Meanwhile, the testing of wear resistance during 50 minutes earned the mass lost on Al/SiC 4.7% while AlCu/SiC 7.32%. We believed that the addition SiC particle can improve the mechanical properties and reduces the frictional resistance.

Keywords: Hot steering Al/SiC, AlCu/SiC, tensile test, wear resistance

🔓 **OPEN ACCESS**

1. Introduction

To date composite materials is potential to be developed due to their superiority in mechanical properties[1]. There are four typical engineered composite materials such as composite building, reinforce plastics, metal composite, ceramic composite. Metal matrix composites has excellent mechanical properties, such as strength, modulus of elasticity, toughness, impact resistance, electrical conductivity and high heat [2]. Metal matrix composites (MMCs) reinforced with ceramic particles are promising materials for structural applications due to excellent combination properties. The matrix ussualy light metal such as copper (Cu), magnesium (Mg) and aluminum (Al) which the reinforcement embedded [3]. Among these matrix, Al matrix composites posses low density, high stiffness and strength, superior wear resistance, controlled coefficient of thermal expansion, higher fatigue resistance and better stability at elevated temperature [4]. Therefore, these composites are used for the design of a wide range of components for advanced applications [5].

Preparation methods of metal-based composite materials have been demonstrated such as powder metallurgy, ppressure infiltration mmethod, single compaction, and laser powder deposition have been developed [5]. In this paper, we report Al matrix and AlCu composites reinforced with silicon carbide (SiC) particle. It's believed that the hardness and meling point will improve significantly [6-10]. Microstructure and mechanical properties of Al/SiC and AlCu/SiC were characterized systematical.
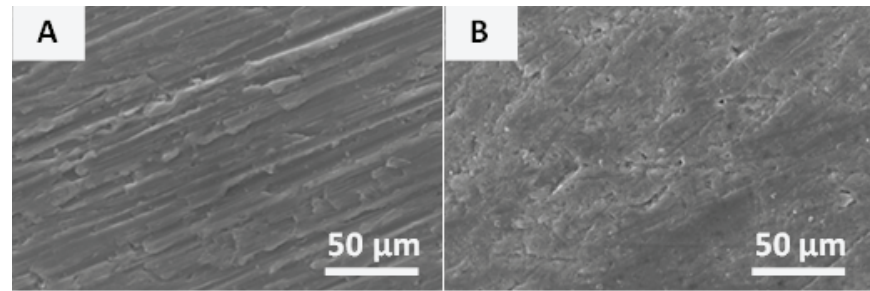
Figure 1: SEM images of (A) surfaces of Al/SiC and, (B) AlCu/SiC composites.

2. Experiment Method

The Al and Al+Cu (3.8 wt.%) were prepared through melting processes. The SiC (2 wt.%) as a ceramic particleshaving a size range of 0.4 to 1 mm. Then, Al and Al+Cu mixed with SiC particles. The stirring process (200 rpm) was performed during heating at temperature 900°C. After the stirring process, the crucible was taken from the furnace and the composites were poured into a metallic mold. After the cast composites were prepared, the heating process under melting temperature (annealing) at 400°C for 6 hours was performed in order to optimize the microstructure.

3. Results and Discussion

3.1. Morphology

Figure 1 show the SEM images of the surface of Al/SiC andd AlCu/SiC. The images indicate that the grain matrix composite of Al/SiC and AlCu/SiC not clearly formed. Nevertheless, The Al/SiC look more solid than the AlCu/SiC. The presence of each phase SiC as much as 2% can be identified by the existence of grain boundaries.

3.2. Tensile Test

The process of measuring the tensile test carried out on material Al, Al/SiC, AlCu and AlCu/SiC. All compositions stress-strain of the samples can be seen in Figure 2.

The value of tensile test results in the form of maximum stress, yield stress and maximum force can be seen in the Table 1. The amount of stress before plastic deformation (yield stress) relates to the value of maximum stress possessed by each composition. For AlCu, the value of the yield stress was not detected. It is due to the small area of the plastic material and AlCu is a brittle material.

3.3. Wear Resistance Test

The wear resistance testing was performed to the material Al, Al/SiC, AlCu and AlCu /SiC with the size dimensions of the rectangle (Table 1) and the broad surface average
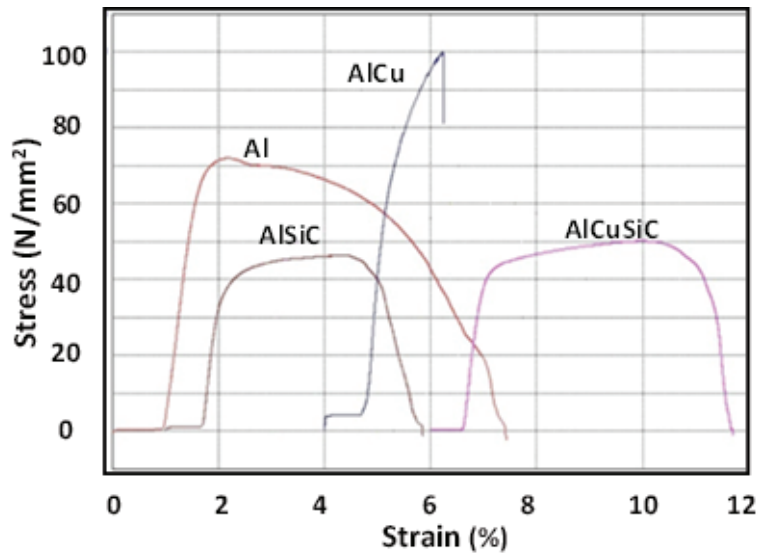
Figure 2: Stress-strain relationship of Al, Al/SiC, AlCu, and AlCu/SiC obtained from tensile test results.

Materials	Stress Max (N/mm^2)	Yield stress (N/mm^2)	Force max (N)
Al	71.894	67.335	509.426
Al-SiC	46.236	43.688	397.228
Al-Cu	100.247	-	778.551
Al-Cu-SiC	50.048	49.417	415.715

TABLE 1: The maximum stress, yield stress, and maximum force of Al, Al/SiC, AlCu, and AlCu/SiC.

of each sample was 48.07 mm^2. The results show that all samples have mass reduction after friction on sample surface (after the process for 50 minutes).

In Figure 3 graphics percentage mass loss against time for material Al, Al/SiC, AlCu, and AlCu /SiC. The overall mass of the sample decreased linearly due to the friction. Linear mass loss for all samples showed that the synthesized samples have homo-geneity.

The results of wear resistance test confirmed that the sample Al and Al/SiC have mass loss linearly and the mechanical properties improvement by addition of SiC (2 wt. %) (table 3). Furthermore, the mechanical properties of Al improved after combined with Cu as much as 3.8%. Meanwhile, the mechanical properties were decreased after SiC added.

Materials (Composition)	Length (mm)	Width (mm)	Thickness (mm)
Al	9.60	5.30	1.55
Al-SiC	9.00	5.60	1.63
Al-Cu	9.40	5.30	1.60
Al-Cu-SiC	8.60	5.30	1.60

TABLE 2: Samples size of Al, Al/SiC, AlCu, dan AlCu/SiC.
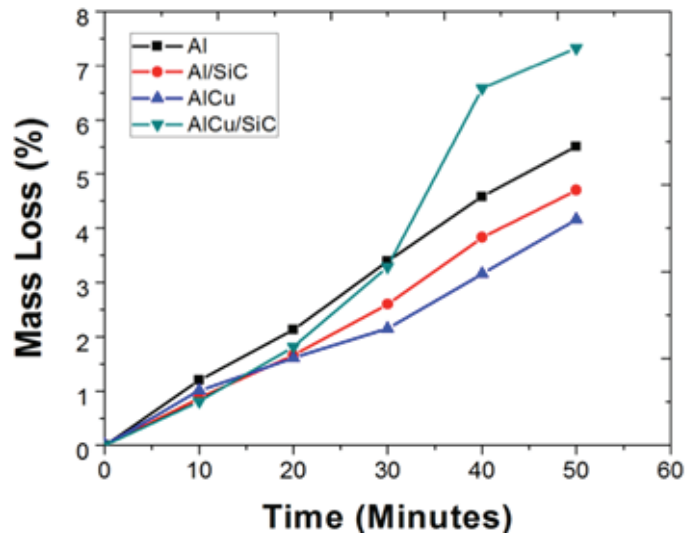
Figure 3: Percentage of mass loss of Al, Al/SiCp, AlCu, dan AlCu/SiCp.

No	Time (minutes)	Al		AlCu		Al/SiC		Al-Cu/SiC	
		Mass (gr)	Mass Lost (% wt)	Mass (gr)	Mass Lost (% wt)	Mass (gr)	Mass Lost (% wt)	Mass (gr)	Mass Lost (% wt)
1	0	0.1505	0	0.1489	0	0.1384	0	0.1489	0
2	10	0.1486	1.20	0.1474	1.01	0.1372	0.87	0.1477	0.81
3	20	0.1472	2.13	0.1465	1.61	0.1361	1.66	0.1462	1.81
4	30	0.1453	3.39	0.1457	2.15	0.1348	2.60	0.1440	3.29
5	40	0.1435	4.58	0.1442	3.16	0.1331	3.83	0.1391	6.58
6	50	0.1421	5.51	0.1427	4.16	0.1319	4.70	0.1380	7.32

TABLE 3: The mass values of composite material Al, Al/SiC, AlCu, dan AlCu/SiC.

4. Conclusions

In conclusions, the Al matrix and AlCu composites reinforced with silicon carbide (SiC) particle have been demonstratedd by steering at 900°C. Tensile test shows the value of the yield stress of AlCu/SiC higher than Al/SiC. Testing of wear resistance during 50 minutes earned the mass lost on Al/SiC 4.7% while AlCu/SiC 7.32%.

Acknowledgments

References

[1] R. Earl, Material for Missiles and Spacecraft, Mc Graw-Hill Book Company, Inc, New York, 25-41 and 46-51, 1963.

[2] S. L. Kampe, In situ Metal Matrix Composite Processing, *An Overview, ASM/TMS Spring Symposium Multiphase and Composite Materials*, (2006).

[3] O. Ozdemir, M. Usta, C. Bindal, and A. H. Ucisik, Hard iron boride (Fe2B) on 99.97wt% pure iron, *Vacuum*, **80**, 1391–1395, (2006).

[4] Jaswinder Singh and Amit Chauhan, (2015) Characterization of hybrid aluminum matrix composites for advanced applications-review, J. Materials research and technology, in press.

[5] X.-Y. Xu, et al., SiC particulate reinforced aluminum matrix composite coatings prepared by laser powder deposition, *J Ceram Process Res*, **7**, 167–171, (2006).

[6] J. Kissel, Aluminum Structures (A Guide to Their Spesification and Design), John Wiley & Sons, Inc, New York, 546.

[7] M. Gupta and S. Qin, Effect of interfacial characteristics on the failure-mechanism mode of a SiC rain forced Al based metal-matrix composite, *J Mater Process Technol*, **67**, 94–99, (1997).

[8] Z. Gnjidic, D. Bozic, and M. Mitkov, The influence of SiC particles on the compressive properties of metal matrix composites, *Mater Charact*, **47**, 129–138, (2001).

[9] C. Kaynak and S. Boylu, Effects of SiC particulates on the fatigue behavior of an Al-alloy matrix composite, *J Mater Des*, corrected proof.

[10] M. Singla, D. D. Dwivedi, L. Singh, and V. Chawla, Development of aluminum based silicon carbide particulate metal matrix composite, *J Miner Mater Charact Eng*, **8**, 455–467, (2009).

Knowledge E
Engaging minds

Conference Paper

The Critical Load Measurements of Pineapple Leaf Fibre Reinforced Polyester Composite Using Single Edge Notched Beam (SENB) Testing

Hendery Dahlan, Mulyadi Bur, Isratul Rahmad and Meifal Rusli

Mechanical Engineering Department, Engineering Faculty, Andalas University, Padang, West Sumatera, Indonesia

Abstract

Pineapple leaf fibre has potential as reinforcement in composite material due to their advantages such as renewable fibre and abundantly available. Some studies have been conducted relating to their mechanical properties using tensile, impact and bending testing. However the analysis of crack propagation in pineapple leaf fibre reinforced polyester composite is still limited. In this paper, the main attention is therefore the critical load leading to crack propagation in the composite material for two different fibre orientations. The crack propagation is investigated using single edge notched beam (SENB) testing. The composite material was manufactured by hand lay-up with two different nonwoven fibre orientations i.e. 0°/90° and +45°/-45°. Then, five different initial crack lengths are given in experimental specimen. The result reveals that increasing initial crack length will decrease the value of critical load for both fibre orientations. Furthermore, the fibre orientation influences the critical loading. In general the critical load leading to crack propagation for composite with +45°/-45° orientation has higher value than composite with 0°/90° orientation. It can be concluded that the composite material with +45°/-45° orientation has good resistance to the crack growth.

Keywords: Natural fibre composites, pineapple leaf fibre, crack propagation

🔓 **OPEN ACCESS**

1. Introduction

The using of natural fibre reinforced polymer composite materials is significantly increasing in industrial applications and fundamental research. The natural fibres are emerging as realistic alternative solution to replace the glass reinforced composite in many applications due to their advantages such as renewable, low cost, low density [1] and low environmental impact [2].

The one of natural fibres is pineapple leaf fibre which has potential as reinforcement in composite material due to their advantages such as renewable fibre and abundantly available [1]. Some studies have been conducted relating to mechanical properties of pineapple leaf fibre reinforced composite materials using tensile and bending testing [3]. However the studies of crack propagation in pineapple leaf fibre reinforced polyester composite is still lack of data. Some studies regarding to fracture criteria

How to cite this article: Hendery Dahlan, Mulyadi Bur, Isratul Rahmad and Meifal Rusli, "The Critical Load Measurements of Pineapple Leaf Fibre Reinforced Polyester Composite Using Single Edge Notched Beam (SENB) Testing," *KnE Engineering*, vol. 2016, 5 pages. DOI 10.18502/keg.v1i1.521

Page 1

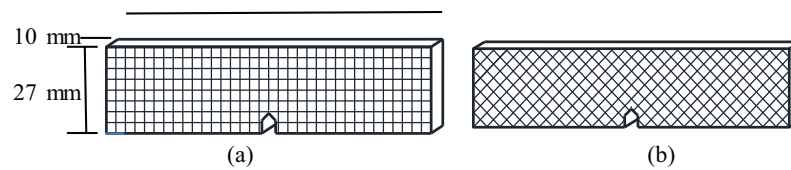**Figure** 1: Fibre orientation (a) 0°/90°, (b) +45°/-45°.

have been conducted to other natural fibres such as bamboo[4], coconut fibre [5], sisal [5,6] and etc.

The studies of crack propagation relate to how relationship between the critical load and initial crack length. The critical load is required to be observed to prevent the catastrophic crack propagation occur in structure. The main attention in this paper is therefore the critical load leading to crack propagation for the pineapple leaf fibre reinforced polyester composite. Thus the effect of fibre orientation in composite in crack propagation also investigated regarding to critical load and initial crack length.

2. Experimental

The dimension of test specimen in this research are illustrated in Fig. 1. The composite material was manufactured by hand lay-up with two different nonwoven fibre orientations i.e., 0°/90° and +45°/-45° as shown in Fig. 1. The composite materials was fabricated using polyester as matrix and layer of pineapple leaf fibre as reinforcement. The fibre layer and polyester was put in mould and then wait until 4-6 h for dismolding. The mass fraction of fibre layer is 3.2%. The whole process was performed at room temperature. In sequence the composite materials was cut and polished based on size of test specimen. Thus five different initial crack lengths (a) are given using blade cutter manually in test specimen namely 7 mm, 9 mm, 11 mm, 13 mm and 15 mm for each type of fibre orientation as shown in Fig. 2.

The experiment are conducted using Com-ten testing. The test uses the single edge notches beam (SENB) testing with three point flexure. The tests are performed at room temperature. Five test specimens are performed for each type of test specimen. Load–displacement curves are recorded for all tests and then the average values are determined for each type of test specimen.

3. Results and Discussion

Fig. 3 shows the critical load on average occuring at five different initial crack length for two variations in fibre orientation. In this figure can be seen that the loading experienced by the test specimen is inversely proportional to the given initial cracks value. The larger initial crack length is given, then the smaller the load needed to crack growth. In general, specimens with 0°/90° orientation has critical loading lower than specimens with +45°/-45° orientation except at the given first crack length (7 mm) has a larger critical loads than +45°/-45° orientation. This deviation occurs because of the
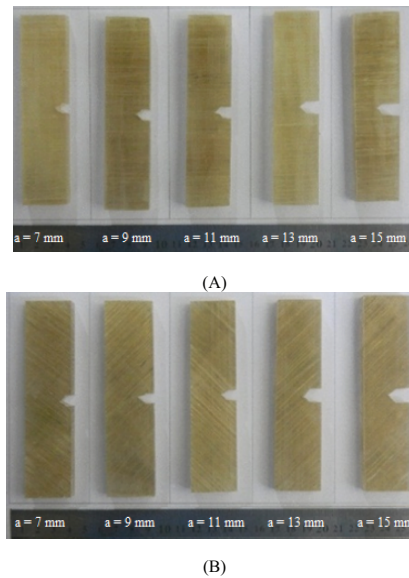
Figure 2: Test specimens (a) 0°/90° orientation and (b) +45°/-45° orientation.
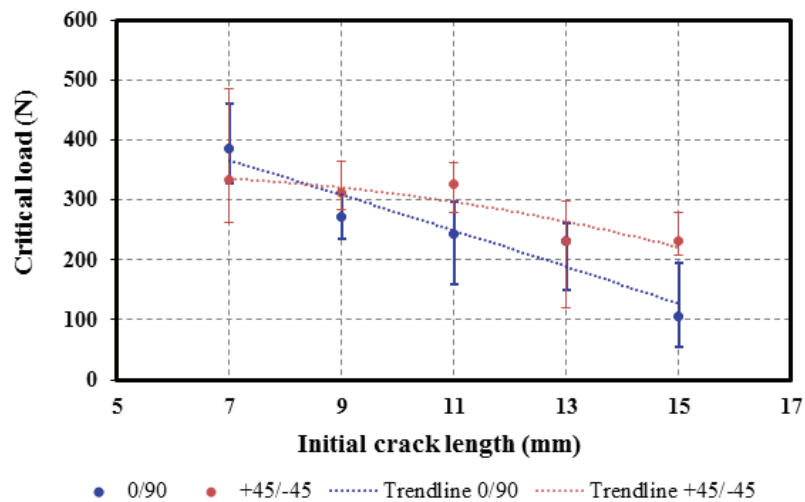
Figure 3: The critical load (N) versus initial crack length (mm) for 0°/90° and +45°/-45° orientation.

given initial crack length using blade cutter manually so that the initial crack length is not exactly same size for both fibre orientation.

The fibre orientation affect significantly to propagate the crack. For the composite material with 0°/90° orientation, the critical load will sharply decrease along with increasing initial crack length. In contrast, for composite material with +45°/-45° orientation, the critical load will gradually decrease along with increasing initial crack length. This shows that composite material with +45°/-45° orientation has good resistance to the crack growth.

The crack propagation path after testing is shown in Fig. 4. It can be seen from figure that the crack propagation follow opening mode in which the direction of crack growth is perpendicular to normal stress direction for both fibre orientation.
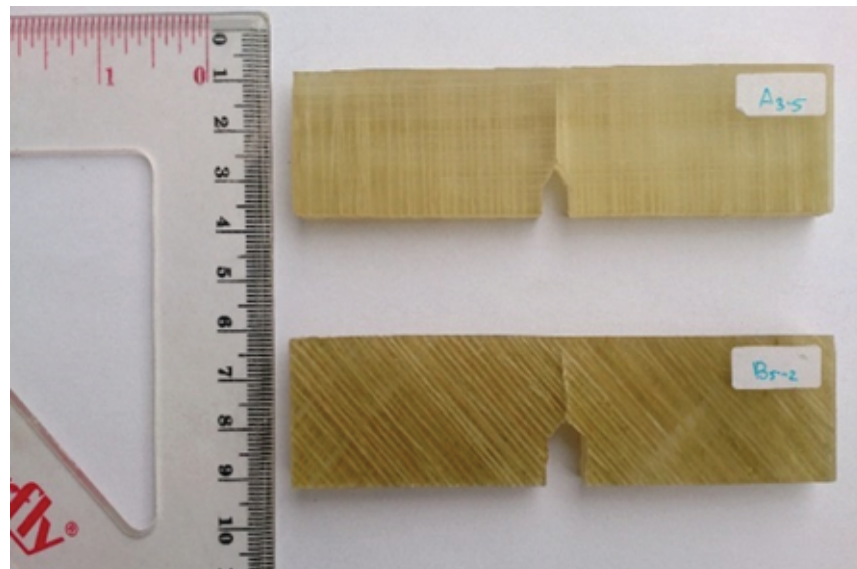
Figure 4: SENB test specimen after testing.

4. Summary

The result reveals that increasing initial crack length will decrease the value of critical load for both fibre orientations. Furthermore, the fibre orientation influences the critical loading. In general the critical load leading to crack propagation for composite with +45°/-45° orientation has higher value than composite with 0°/90° orientation. It can be concluded that the composite material with +45°/-45° orientation has good resistance to the crack growth.

Acknowledgement

References

[1] O. Faruk, A. K. Bledzki, H. P. Fink, and M. Sain, Biocomposites reinforced with natural fibers: 2000–2010, *Prog Polym Sci*, **37**, 1552–1596, (2012).

[2] A. K. Mohanty, M. Misra, and L. T. Drzal, in *Natural fibres, Biopolymers, and Biocomposites*, Taylor & Francis, Boca Raton, Florida, 2005.

[3] R. M. N. Arib, S. M. Sapuan, M. M. H. Ahmad, M. T. Paridah, and H. M. D. Khairul Zaman, Mechanical properties of pineapple leaf fibre reinforced polypropylene composites, *Mater Des*, **27**, 391–396, (2006).

[4] K. J. Wong, S. Zahi, K. O. Low, and C. C. Lim, Fracture characterisation of short bamboo fibre reinforced polyester composites, *Mater Des*, **31**, 4147–4154, (2010).

[5] R. V. Silva, D. Spinelli, W. W. Bose Filho, S. Claro Neto, G. O. Chierice, and J. R. Tarpani, Fracture toughness of natural fibres/castor oil polyurethane composites, *Compos Sci Technol*, **66**, 1328–1335, (2006).

[6] J. M. L. Reis, Sisal fibre polymer mortar composites: introductory fracture mechanics approach, *Construct Build Mater*, **37**, 177–180, (2012).

KnE Engineering

Knowledge E
Engaging minds

Conference Paper

Renewable Silica-Carbon Nanocomposite and Its Use for Reinforcing Synthetic Wood Made of Rice Straw Powders

I Wayan Karyasa[1], I Wayan Muderawan[1], and I Made Gunamantha[2]

[1]Chemistry Education Department, Ganesha University of Education, Singaraja, Bali, Indonesia
[2]Chemical Analyst Department, Ganesha University of Education, Singaraja, Bali, Indonesia

OPEN ACCESS

Abstract

The current study was aimed to prepare and to characterize a renewable silica-carbon nanocomposite from rice straw ashes. It was purposed also to study the use of the produced nanocomposite as reinforcing material in producing a synthetic wood made of three axial blend of treated rice straw powder, phenolfrmaldehyde resin, and the nanocomposite. A simple preparation route of nanocomposite silica-carbon from rice straw was formulated containing three steps, namely pretreating of rice straw, preparing of ultra fine amorphous black silica, and composing silica-carbon nanocomposite. The nanocomposite product was characterized using XRD, XRF, FTIR and SEM methods. The characterization results comfirmed that the silica-carbon nanocomposite was succesfully prepared. The utilizing of the nanocomposite as reinforce material in producing synthetic woods was conducted through hot-pressing some three axial blend compositions of the pretreated rice straw powder, phenolformaldehyde resin, and the nanocomposite. The synthetic wood products were characterized their physical and mechanical properties. As a result, the addition of the nanocomposite could improve the properties of the synthetic wood products.

Keywords: Rice straw, silica-carbon nanocomposite, synthetic wood

1. Introduction

Some high siliconeous tropical plants were prepeviously investigated in order to find prospective raw material candidates for producing renewable silica based materials [1]. Both rice husk and rice straw are the best candidate as raw materials for producing renewable silica powder because of their high content of silicon, natural abundance as tropical agricultural waste as well as low cost production. Thus the renewable silica from high siliconeous tropical agricultural wastes especially from paddies wastes has some advantages comparing to silica from earth deposits. The renewable silica powder is mailny amorphous and more reactive than silica powder of crystalline quarts minerals. Instead of amorphous silica powder, the rice husk and straw wastes can produce active carbon powders having high surface area [2]. The ratio contents of silica and carbon of the burned high siliconeous biomasses depend on pre-teatments, burning temperatures and length of burning as reported previously by some researchers [3,4]. The ash fine powders with certain silica-carbon ratios are potentially resembled into a renewable silica-carbon nanocomposite.

Silica-carbon nanocomposites, nowdays, have been taken into attractive attention because of their superior properties, namely mechanical, thermal, and dispersion properties [5] and their ability as reinforcement materials [6]. Some synthesis methods of silica-carbon nanocomposites had already reported previously [5,7], but the methods used non renewable starting materials causing high cost of production. Considering the reactive properties of amorphous silica and carbon contents of the black ashes produced from the controlled burning of high siliconeous agricultural wastes, such as rice straw and rice husk, a renewable nanocomposite silica-carbon could be synthesized cheaply and environmental friendly. The term renewable silica-carbon nanocomposite here means that the composite is produced from renewable raw materials from plants or animals, in this case, the raw material is rice straw.

Nowadays, the reduce of tropical rain forests because of the massive uses of tropical woods becomes sensitive global issues. It leads to the campaigne of substituting natural woods by synthetic woods. Since it was firstly patented by Himmelhelber et al. [8] as particle board, the synthetic woods were improved their technologies by some further inventions, such as a borate treated consolidated wood particle board [9], compression moulding of cellulosic fibers with thermoplastic additives [10], multilayer particle board with varying densities [11], and reinforcement of particle board during manufacture by using glass fiber [12]. However, the synthetic wood production technologies mostly used the natural wood particles as raw material or as cellulosic fiber resources. Non-wood cellulosic fibers such as wheat straws [13,14] were rarely used as raw materials because of some structural and mechanical limitation instead of their environmental and production cost advantages. Nanocomposite silica-carbon made from high siliconeous tropical biomasses may overcome those limitation by reinforcing the wood synthetic during manufacture. This current study was aimed to prepare nanocomposite silica-carbon from rice straw ash and to use it for reinforcing synthetic wood from rice straw lignocellulosic powder and phenolformaldehyde resin as binder.

2. Experimental Part

The experiments consisted of three parts, namely the preparation of ultrafine amorphous silica-carbon powder (UFASCP) from rice straw and silica-carbon nanocomposite (SCNC) from the UFASCP, the characterization of UFASCP and SCNC, and the utilizing of SCNC as reinforce material in the production of synthetic wood.

Firstly, the preparation processes of UFASCP and SCNC were conducted as follows. The rice straws of IR-64 paddy variety were taken from rice field of Tabanan Regency of Bali Province. The straws were chopped, leached using HCl 1 M, cleaned using water and then dried. The dried chopped straws were burnt in a furnace at the controlled temperature of 400°C and less oxygen atmosphere for about four hours to produce black ash powder. The rice straw black ash powder (RSBAP) was measured its silicon content and its impurities using XRF spectroscopy. RSBAP was rinsed using HCl 1 M, 2 M, and 3 M respectively, and finally it was rinsed using distilled water, hence metal oxides containing in the RSBAP could be removed. The rinsed RSBAP was acidified

using H_2SO_4 solution 1 M. Furthermore it was heated in hydrothermal condition at 100°C (1 atm, 24 hours) in a sealed autoclap. The resulted powder was wetted by adding some drops of distilled water. The wet powder was finally milled using ball-mill a long 24 hours. The fine milled black powder was neutralized using NaOH solution 1M and then rinsed using distillated water. The rinsed black powder was dried. The dried fine powder was further calcined at 110°C for 4 hours. The resulted dried fine powder was then called as UFASCP. The transformation of UFASCP into SCNC was conducted in several steps. UFASCP was mixed with organic solvent of etanol 10% v/v and NaOH solution 0.2 M. The mixture was blended and milled using ball-mill in room temperature for 24 hours. The milled mixture was autoclapped over night (at least 24 hours) at 100°C (1 atm.) hidrotermally. The autoclapped powder was rinsed using solutions of HCl 3 M, 2M, 1 M, and distillated water respectively until the residual water was neutral. After drying, the powder was calcined at 100°C for one hour. The final powder was called silica-carbon nanocomposite (SCNC) from rice straw.

Secondly, the resulted UFASCP and SCNC powders were characterized by using several instruments, namely XRF, XRD, SEM, and FTIR spectroscopy. XRF PANalytical Minipal 4 Sulfur was used for elemental analysis with parameters of measurement of 28.00 kV, 53 uA (air, 60 sec., 41695.4 cps, standardless). Philip X'Pert Powder Diffractometer was performed for XRD measurements at tension of 20 kV, current of 5 mA and using Cu-Kα anode, 2 theta of 5 – 85 degree for 0.02 step/sec.. SEM measurements were conducted by using JEOL-JSM-6510LV in high vacuum mode 3.0 nm (25 kV) with magnifician of 30.000x. FTIR-8000 PC Shimadzu was performed for infra red spectroscopy measurements of samples with wave length number of 400 – 4000 cm^{-1}.

Finally, the experiment of using the SCNC as reinforcing materials in the synthetic wood from rice straw was conducted in four steps, ie. preparation of lignocellulosic fiber powder from rice straw, preparation of phenolformaldehyde (PF) resin using procedure elsewhere [15], preparation of three axial blends containing lignocellulosic fiber powder, PF resin, and SCNC powder in five compositions, namely: 80: 20: 0; 75: 20: 5; 70: 20: 10; 65: 20: 15; and 60: 20: 20 respectively, and preparation of the wood products by hot pressing the blends using hidraulic hot press at pressure comparable to stress of 200 Kg/cm^2, and at temperature of 80°C. The resulted synthetic woods were characterized their water absorptions measured using the standard test method of ASTM D7433 and compressive strenghts using Universal Testing Machine with standard of measurement ASTM D143 to see the reinforcing effects of the silica-carbon nanocomposite towards those properties of the resulted synthetic woods.

3. Result and Discussion

XRF analysis results on the samples of SBAP, UFASCP, and SCNC were depicted on the Table 1. Along processes of making UFASCP from RSBAP there was removal of metal oxide impurities, thus the percentage of silicon content was increased significantly, although not all elements could be detected by XRF, for instances sodium, carbon, oxygen, and other elements. The comparison reported here was only the observed elements by XRF spectroscopy.

Sample	XRF Elemental Analysis in procentage												
RSBAP	Si	S	K	Ca	Cr	Mn	Fe	Ni	Cu	Zn	Mo	Yb	Re
	24.5	29.2	3.15	7.11	0.38	0.19 ± 0.01	3.11 ± 0.01	0.29 ± 0.02	0.20 ± 0.01	0.42 ± 0.01	31.00 ± 0.50	0.10 ± 0.05	0.30 ± 0.04
UFASCP	Si	K	Ca	Ti	Fe	Ni	Cu	Zn	Ba	Yb	Re		
	83.0 ± 0.6	0.94 ± 0.01	10.70 ± 0.10	0.20 ± 0.03	1.30 ± 0.03	0.20 ± 0.09	0.63 ± 0.02	0.10 ± 0.03	1.40 ± 0.01	0.60 ± 0.03	1.00 ± 0.01		
NCSC	Si	K	Ca	Cr	Mn	Fe	Ni	Cu	Zn	Yb	Re		
	89.9 ± 0.06	1.60 ± 0.03	4.47 ± 0.04	0.36	0.18	2.21 ± 0.02	0.22 ± 0.03	0.35 ± 0.01	0.07 ± 0.01	0.10 ± 0.02	0.60 ± 0.01		

TABLE 1: Results of XRF Analysis on SBAP, UFASCP, and NCSC Samples.
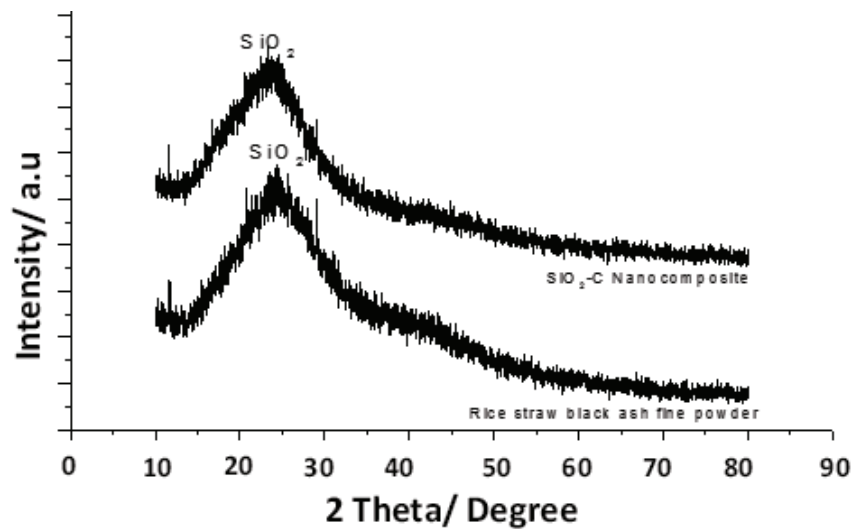
Figure 1: Diffractograms of UFASCP and SCNC.

Diffractograms resulted by XRD measurement of UFASCP and SCNC can be seen in Fig. 1. Both diffractograms have broadening peaks that indicate amorphous phase with small particle sizes. SCNC diffractogram has more boadening peak and the peak shifts to smaller 2 theta. The facts mean that SCNC is more amorphous and bigger grain size that those of UFASCP.

Comparing with the micrograph of UFASCP, the grains on micrograph of SCNC are more bigger size and more homogen than those of UFASCP as shown by Fig. 2. It can be confirmed by the results of EDX measurement showing the grains composed from only three elements Si, O, and C. The data shown on Fig. 1 and Fig. 2 may comfirm that a silica-carbon nanocomposite could be formed.

The characterization on synthetic wood produced by hot-pressing the three axial blends with variation of composition showed that the addition of SCNC can inprove the quality of the resulted synthetic woods, namely smaller water absorption and higher compressive strength values, as depicted on Fig. 3. The composition of the lignosellulosic agrifiber, PF resin, and SCNC of 70: 20: 10 can be chosen as the most
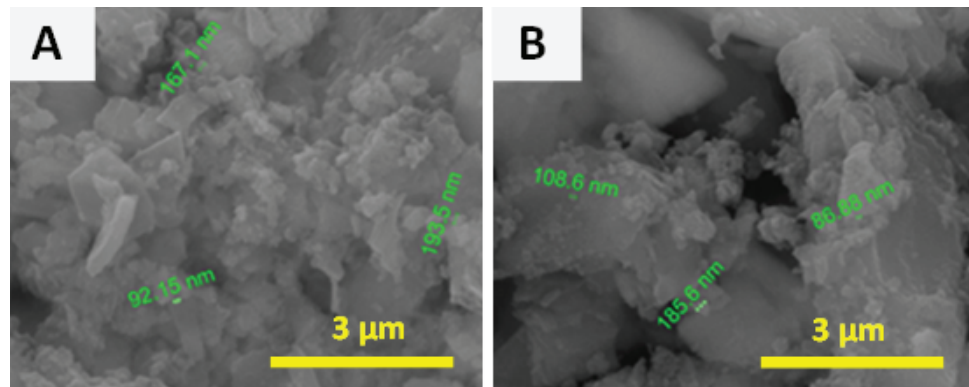
Figure 2: SEM Micrographs of UFASCP and SCNC.
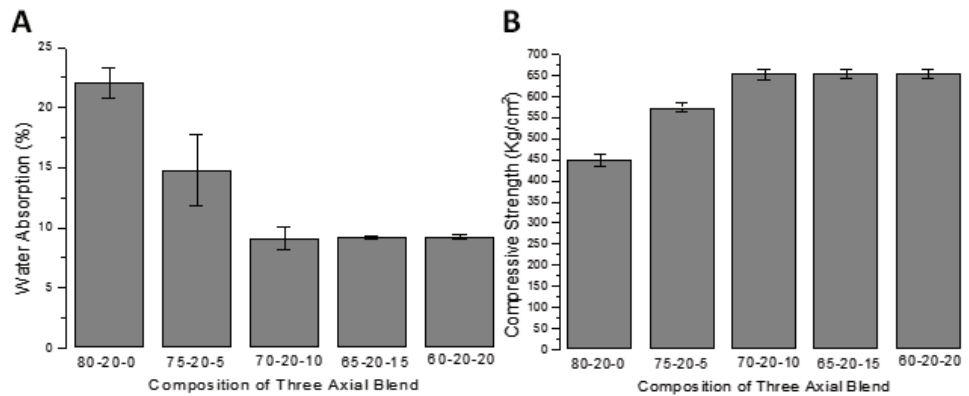
Figure 3: (A) Water Absorption and (B) Compressive Strength of Synthetic Woods.

effective composition of the three axial blend in producing synthetic wood using this procedure.

4. Conclusion

Silica-carbon nanocomposite was successfully prepared through transforming the ultrafine amorphous silica-carbon powder. The ultrafine powder was prepared from rice straw powder through pre-treating, controlled burning to produce black ash, and treating the ash. The use of the resulted nanocomposite can reinforce the properties of synthetic wood from rice straw lignocellulosic fiber.

Acknowledgement

References

[1] I. W. Karyasa, Meta-analisis on renewable silica based materials from rice husk and mapping on high siliconeous tropical biomasses, *Proceeding of National Seminar on Mathematics and Natural Sciences*, (2012).

[2] K. S. Kim and H. C. Choi, Characteristics of adsorption of rice-hull activated carbon, *Water Sci Technol*, **38**, 4–5, (1998).

[3] C. Real, M. D. Alcala, and J. M. Criado, Preparation of silica from rice husks, *J Am Ceram Soc*, **79**, 2012–2016, (1996).

[4] N. Thundaij and A. Nuntiya, Preparation of nanosilica powder from rice husk ash by precipating method, *Warasan Khana Witthayasat Maha Witthayalai Chiang Mai*, **35**, 206–2011, (2008).

[5] S. Jankong and K. Srikulkit, Preparation of polypropylene/hydrophobic silica nanocomposite, *Journal of Metals, materials and Minerals*, **18**, no. 2, 143–146, (2008).

[6] K. Jindal, L. F. Francis, and A. V. McCormick, Stress development in nanocomposite silica coating, *The 14th International Coating Science and Technology Symposium*, (2008).

[7] Q. Hu, R. Kou, J. Pang, T. L. Ward, M. Cai, Z. Yang, Y. Lu, and J. Tang, Mesoporous carbon/silica nanocomposite through multi-component assembly, *Chem Commun (Camb)*, 601–603, (2007).

[8] M. Himmelhelber, K. Steiner, and W. Kull, U. S. Patent 2,923,030 (1960).

[9] R. M. Knudson and M. J. Gnatowski, U. S. Patent 4,879,083 (1989).

[10] S. Nishibori, U. S. Patent 2,725,939 (1998).

[11] B. Nilsson, U. S. Patent US2012/0217671 A1 (2012).

[12] L. Hammarberg, U. S. Patent 4,514,258 (1985).

[13] B. J. Sullivan and L. J. Du Mouchel, U. S. Patent 6,143,220 (2000).

[14] D. Ward, U. S. Patent US7,699,951 B2 (2010).

[15] R. W. Martin, in *The Chemistry of Phenolic Resins*, John Willey, 1999.

KnE Engineering

Knowledge E
Engaging minds

Conference Paper

Compressive Load Effect on Electrical Properties of Carbon Composite

Nuning Anugrah Putri Namari, Irfan Dwi Aditya, and Suprijadi

Department of Physics, Faculty of Mathematics and Natural Sciences, Institut Teknologi
Bandung Jalan Ganesha no 10 Bandung, Indonesia 40132

Abstract

Contrary to its name, the "lead" in pencil is predominately made up of combination of
graphite and clay or polymer, hence it can be considered as carbon composite. It has
been proven that the more amount of carbon, the greater Young Modulus will increase
and vice versa. Some researches on electric property of carbon composite also have
shown that pencil drawn can be treated as a strain gauges and chemiresistors on
paper. It means that in pencil's lead, the mechanical and electrical properties are
related to one another. In this study, we applied a compressive load on pencil's lead
and measured the effect on its resistivity. The results show that the resistivity will
decrease while the strain will increase.

Keywords: Carbon composite, Experiment, Resistance, Stress, Strain

Corresponding Author:
Nuning Anugrah Putri
Namari; email: nun-
ing_apn@cphys.fi.itb.ac.id

🔓 **OPEN ACCESS**

1. Introduction

Carbon is the fifth most abundant element in this world. It has several Allotropes,
and one of them is graphene. Over the recent years, graphene has been investigated
for applications in microelectronic. And due to their low specific resistivity, graphene
is used for applications in interconnects as well [1]. Several graphene layers which
stacked with each other are called Graphite and used in many Carbon Composites.
Composite is a material that consists of two different materials, and it is made to create
a material with unique properties that are lighter and stronger. In this paper, we used
mechanical pencil lead as a carbon-composite which consists of graphite, polymer, and
clays as matrix.

Pencil is chosen because many paper-based electronics devices, such as ultraviolet
sensors, solar cells, and energy storage devices also use this item. Their potential to
produce a flexible, thin, low-cost, portable, and environmental-friendly product makes
paper-based electronics are more advantageous. Furthermore, the research on Pencil
drawn shows that Pencil traces can be regarded as conductive thin films and mainly
used as passive conductive in many devices, such as resistors, transistors, UV sensors,
and many more. Pencil traces are also relatively stable against moisture, chemicals,
and UV irradiation [2]. Seeing that pencil has so many utilities, we are interested to do
some research related to the relation between mechanical and electronics properties
for each type of carbon composite used in pencil.
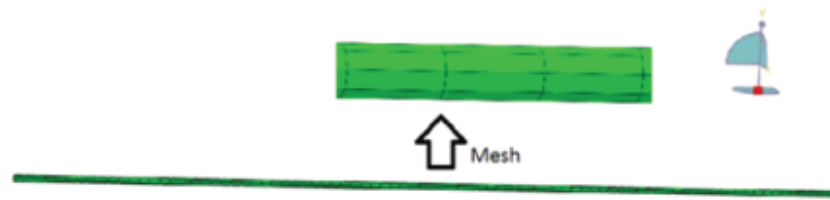
How to cite this article: Nuning Anugrah Putri Namari, Irfan Dwi Aditya, and Suprijadi, "Compressive Load Effect on
Electrical Properties of Carbon Composite," *KnE Engineering*, vol. 2016, 5 pages. DOI 10.18502/keg.v1i1.523

Page 1

Figure 1: Dimensional geometry of simulation model.

2. Computation

Computational method that we use in this research is Finite Element Method (FEM) using Abaqus. The dimensional geometry of the simulation model is similiar to the geometry of thespecimens tested in the experiment, it is 0.5 mm for the diameter and 60 mm for the length. Tomeshing the model, we use rectangular shape with the same size all over the model. Thecomputation are performed by compressed the model along z-axis. The result will give use xplanation about strain distribution of the composite.

3. Experiment

Compress test was conducted by using 10KN Universal Testing Machine type SM-10. This evaluation gave us force value with ±0.01 accuracy and displacement with ±0.00001 accuracy. In this case, we used the B, 3B, H, and 2H pencil lead with dimension of 0.5 x 60 mm as carbon composite. Resistance of carbon composite was measured using multimeter with ±0.1 accuracy which are connected to graphite. Graphite was being used as a pad for carbon composite as long as the pencil underwent compress test (since pure graphite is harder than carbon composite, so the compression on the pad will not effect the measurement process significantly).

   This experiment was carried out at room temperature and it will last until the pencil lead breaks. From this experiment, we get the Strain-Stress Curve which will make us to be able to obtain the Young Modulus of carbon composite as well. Then, to analyze the relation between mechanical and electric properties, we used Stress-Strain curve and Resistance-Strain curve. We will compare carbon composite type B with 3B, and type H with 2H; the comparison among all of them in the same curve will not be done, because we used different pencil lead product for type B and H.

4. Results and Discussions

The computational result of system on Fig 3(a) and (b) shows that the Force act on the composite is uneven. Greatest displacement happen in the upper part (part which force was given) and the smallest displacement happen in the down part. This caused the speciment to bent. The type of pencil H and B represent the "Hardness" and "Blackness". The hardness of pencil is obtained from the clay. So, the higher number
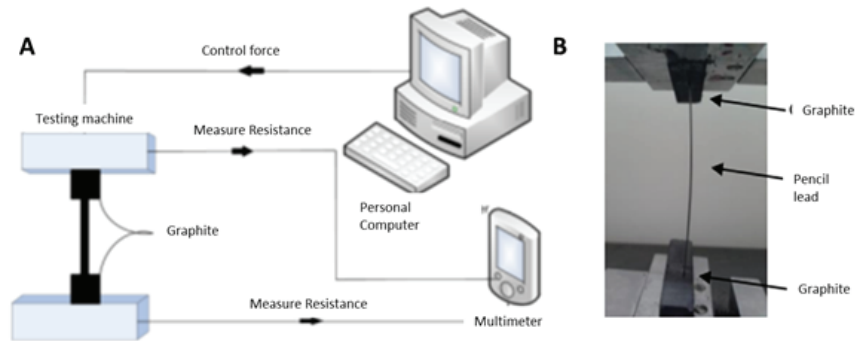
Figure 2: (a) Diagram of experiment and (b) Pencil lead under compression.
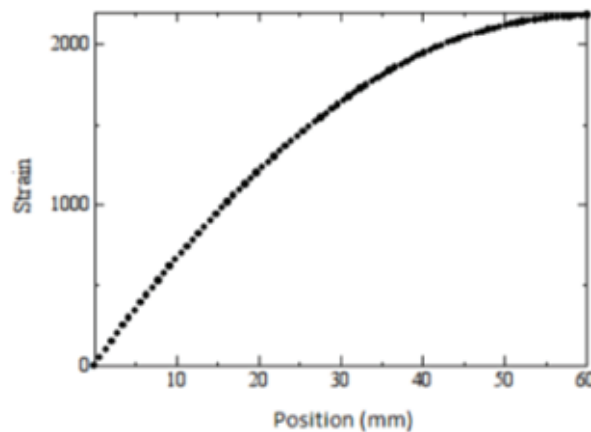

Figure 3: Strain distribution on compressed carbon obtained from computational result.

of H type contains more clay. Meanwhile the Blackness of pencil are obtained from the graphite. Graphite will give soft texture to the pencil traces. The higher number of B type contains more graphite [3]. In the Fig 4(a) we can see that pencil with type H is stronger than B and also have higher value of resistance because it contain less graphite. Pencil lead with H type also have more ductile properties than B, because it contains morepolymer as a binder.

Fig 4(A) and Fig 4(B) show the that Stress-Strain curve has both linear and non-linear graph. This linear graph is called elastic region while the non-linear graph is called plastic region. Elastic deformation occurs in the elastic region; it happens when the interatomic bonds are stretched, but they have the capability to go back to their original nearest neighbors (each carbon in Graphite is covalently bonded to three other carbon atoms). On the other hand, permanent deformation occurs in plastic region. Permanent deformation takes place when some atoms move away from their original nearest neighbors, and it cause some of the interatomic bonds to break up. This permanenet deformation can cause a fracture or even damage on the material.

In addition, Fig 4(A) and Fig 4(B) also show that the composite materials consists of ductile and britlle mixture. It can be seen from the elastic region, that the composite is not broken immediately after the ultimate point, but it breaks after encounter some elongation in plastic region and then break at ultimate rupture strain. The key of this
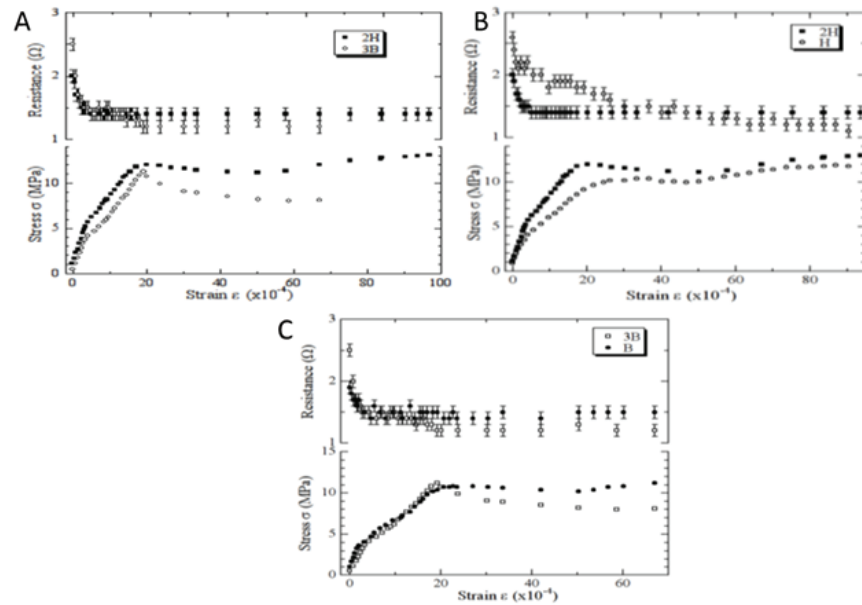
Figure 4: Mechanical Properties of (a) type 2H &3B, (b)H &2H and (c) B & 3B.

phenomenon is the composition of pencil lead. Graphite and clay are indeed considered as brittle materials, but the pencil lead we used has polymer as a binder (polymer is included in ductile material). So, the ductile found in the properties are caused by the polymer.

Other than that, Fig 4(A) shows that 2H has higher stress and resistance than H. It is found in the reference [3], that 2H has more clay and less graphite. Composite that have less graphite will have bigger resistance because graphite is conductive material. In this results, we got the resistance value of 1.4Ω for the 2H and 1.1Ω for H. On the contrary, Clay give hardness to pencil lead; in this experiment, we use pencil lead which contains polymer. Polymer is known as the elastic material. In this investigation, 2H that contains more mixture of clay and polymer has higher stress (around 13.1 MPa) than H (around 11.77 MPa). Meanwhile, B type which has higher number contains of more graphite. It can be seen from Fig 4(B) that 3B has lower resistance and stress than B (resistance of B is 1.5Ω and 3B is 1.2Ω). The Stress-Strain curve for the B type shows that B has higher Stress (around 11.52 MPa) than 3B (aroung 8.1 MPa) in Ultimate rupture strain. The result of this study represents that harder composite has more ultimate rupture strain. If we arranged it in descending order, it would be 2H, H, B, then 3B.

Now, we are going to compare the Ultimate point of each type. H type has Ultimate point in 9.17 MPa while 2H is in 11.77 MPa. We can see that hardest composite will have higher ultimate point for the H type. As explained before, 2H has less graphite, so it must be stronger than H. And about the B type, B has ultimate point in 10.70 MPa while 3B is in 11.21 MPa.

Fig 4(A) and Fig 4(B) illustrate that the electrical properties run into three phases. First is the sharp fall of resistance, second is slowly down of resistance, and the last is stable resistance. Similar to them, the mechanical properties also experience three stages. First is sharp linear graph, second is also linear graph with lower slope, and the

last is graph that tends to be more stable. We can see that elastic region obeys the resistance equation, where resistance is proportional to the length and density while inverse with the area of material. When the composite encounter the compress test, the length of material is shorter, therefore the resistance will also down. Meanwhile, in plastic region, the resistance equation is not applicable because some atom has encounter permanent deformation that makes small change in the density and length of material.

Through Fig 4(A) and Fig 4(B), we can investigate the strain between ultimate point in Stress-Strain curve and Resistance-Strain Curve of each type. The results shows that all the type reach their ultimate point of resistivity first and then ltimate point of stress. For the H type, the strain differences between that two ultimate point is 18.29 for H and 14.95 for 2H. Meanwhile, for the B type, the strain differences is 19.95 for B and 17.73 for 3B. We can see that there is an inverse result between H and B type. In H type, the Harderst pencil has a closest differences between two ultimate point. It may happen because 2H have biggest resistance, so it would reach the ultimate point of resistance in longer strain than H. So, that's why, for the same strain of ultimate point of stress, 2H will have little strain differences. Meanwhile, for the B that has more resistivity than 3B, it ecounter more strain differences but not too specific. Further investigation of the lead composition needed to explain this phenomenon.

5. Conclusion

The force distribution on carbon composite is uneven, therefore the displacement are different in every point and the result shows that composite will be bent. Computational result shows that the highest displacement is happen in the upper part (part which force was given directly) .Carbon composite with the mixture of polymer and clay as a binder has ductile and brittle properties. Composite with more graphite has lower resistance and lower stress. The resistance equation just applied in elastic region. In plastic region, the resistance equation is not applied and the resistance tends to be more stable. In H type, the strain differences between two ultimate point is more specific than B type.

References

[1] F. Kreupl, Carbon-based Materials as Key-enabler for "More Than Moore", Milpitas, CA95035, USA.

[2] C. Lin, et al., Pencil Drawn Strain Gauges and Chemiresistors on Paper,Northwestern University, USA.

[3] Queensland Studies Authority, Extended experimental investigation : Electrical conductivity of graphite, Queensland, Australia.

[4] N. Kuganathan, Electronic Properties of Graphite and Single Walled Carbon Nanotubes- A DFT Stuy, *The Internet Journal of Nanotechnology*, **3**, no. 2, (2010).

[5] J.-M. Ducere, C. Lepetit, and R. Chauvin, Carbo-graphite: Structural,Mechanical, and Electronic Properties, *J Phys Chem C*, **117**, 21671–21681, (2013).

KnE Engineering

Knowledge E
Engaging minds

Conference Paper

Synthesis of Electrospun Nanofibers Membrane and Its Optimization for Aerosol Filter Application

Abdul Rajak[1], Asti Sawitri[1], Muhammad Miftahul Munir[2,3], Ferry Iskandar[1], and Khairurrijal[1,3]

[1]Physics of Electronic Materials Research Division, Institut Teknologi Bandung, Jalan Ganesa 10, Bandung 40132, Indonesia
[2]Theoretical High Energy Physics and Instrumentation Research Division, Institut Teknologi Bandung, Jalan Ganesa 10, Bandung 40132, Indonesia
[3]Research Center for Bioscience and Biotechnology, Institut Teknologi Bandung, Jalan Ganesa 10, Bandung 40132, Indonesia

Abstract

Nanofibers membranes were synthesized using electrospinning method for air filtration application. Polyacrylonitrile (PAN) with three different concentrations as the polymeric matrix of the nanofibers membrane is used. In the aerosol filtration, the pressure drop is one of the most important parameters, which is determined by the membrane characteristics. One of the parameters that influence the characteristics of membrane is concentration of polymer solution, in which it will determine the diameter of fiber. In this study, the relation between the PAN concentration and the pressure drop in air filtration test was examined. Three different concentrations of PAN solution (6, 9, and 12 wt.%) were employed under the same process parameters of electrospinning. The fiber diameter distribution of each membrane was measured from its scanning electron microscope (SEM) image. The three concentrations resulted in significant different effect to the pressure drop that proved the existing correlation between the polymer concentration and the air pressure drop.

Keywords: nanofiber membrane, electrospinning, concentration, pressure drop

OPEN ACCESS

1. Introduction

Air pollution is caused by the presence of other material substances in air such as dust, smoke, and others, which are harmful and contaminated in large quantities. Nowadays, air pollution happens more frequently along with the rapid population growth. Polluted air contains toxic substances which are fine particles with diameters ranging from 0.1 to 2.5 μm (PM2.5) [1]. Fine particles in air, which is called as aerosol, are the major cause of respiratory disorders. Separation between air and its pollutant is one way to solve the pollution problem. Researches regarding the air pollution problem are thus related to the finding of media that can separate the air and its pollutant. A filtration method by means of nanofibers materials is believed to answer the air pollution problem. Nanofibers membrane can capture fine particles from the aerosol flow through pile of fibers and pass the clean air through the pores [2-4]. Good distribution of membrane porosity can then increase the filtration efficiency [5,6].

How to cite this article: Abdul Rajak, Asti Sawitri, Muhammad Miftahul Munir, Ferry Iskandar, and Khairurrijal, "Synthesis of Electrospun Nanofibers Membrane and Its Optimization for Aerosol Filter Application," *KnE Engineering*, vol. 2016, 7 pages. DOI 10.18502/keg.v1i1.524

Page 1

There are diversely wide range of techniques to produce nanofibers and electro-spinning is one of the simplest techniques [7,8]. The nanofibers obtained via electro-spinning technique can be applied to various fields such as filters, biomedical tools, energy and sensor [9-10]. The morphology of nanofibers depends on various factors such as viscosity, conductivity, surface tension, flow rate, rate of solvent evaporation, voltage, and electric current [11]. In filter application, the efficiency of membrane can be optimized by adjusting the morphology and structure.

Recently, we have successfully synthesized nanofibers membrane from polyacry-lonitrile (PAN) material for antibacterial activity in water filtration application [12]. Some researchers have tried to use PAN in air filtration application [4,5,13]. However, they did not discuss in detail about pressure drop and its relation to the concentration of polymer solution. Excellent air filters have special characteristics such as high particle collection efficiency, low pressure drop, and long lifetime [14]. Pressure drop is a very important parameter in air filter testing, because it is related to pressure or energy being applied in filtration process. Moreover, pressure drop is greatly affected by the shape and morphology of the membrane such as thickness and porosity [5]. The membrane porosity is also influenced by fibers diameter that can be controlled by adjusting the concentration of polymer solution [11]. In this study, PAN membranes were produced by employing different concentrations for air filtration application. The effect of each concentration to the pressure drop was then analyzed.

2. Experimental

2.1. Materials

The materials used in this experiment included polyacrylonitrile (PAN) with molecu-lar weight of 150,000 g/mol and N,N-dimethylformamide (DMF) solvent; both were obtained from Sigma Aldrich. The PAN was dissolved in DMF to produce a suitable concentration of the polymer solution. The calculation of polymer (solute) weight con-centration and solvent is calculated by weight percentage (wt.%) using Eq. 1.

$$C = \left(\frac{X}{X+Y} \times 100 \right) wt.\% \tag{1}$$

where X is the weight of solute and Y is the weight of solvent. In this experiment, three concentrations of PAN solution were made, i.e., 6, 9, and 12 wt.%.

2.2. Electrospinning

Figure 1 shows the schematic of a Nachriebe 600 electrospinning system that we have developed. The system uses a high-voltage power supply with a high voltage flyback transformer (HVFBT). A syringe, where the polymer solution is contained, is placed on a syringe pump with controllable flow rate. A metal drum collector that can be rotated with controllable speed is used. The system is also equipped with a camera with a high magnification to observe the shape of jet at the tip of the syringe in real time. To
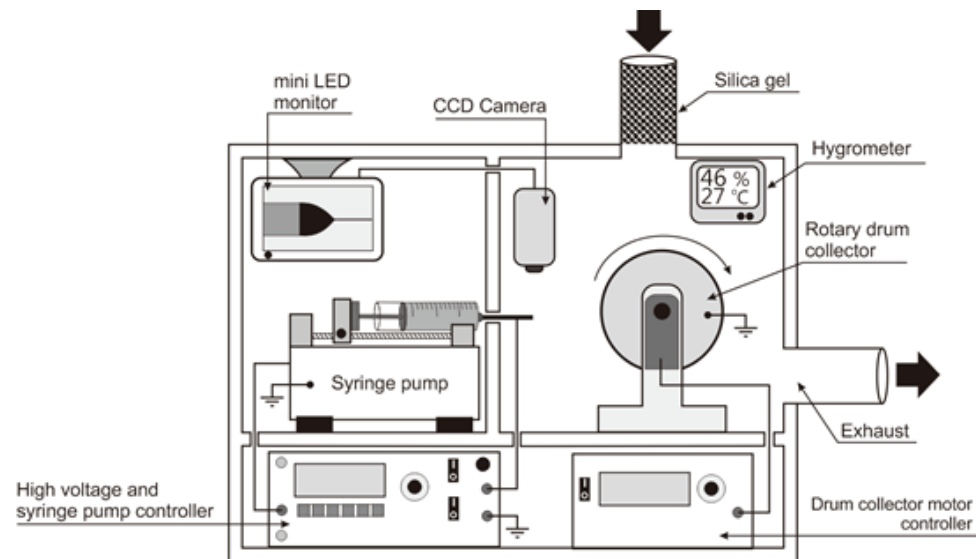
Figure 1: A schematic diagram of Nachriebe 600 electrospinning system.

control the relative humidity, silica gel and the exhaust is used to circulate the dry air into chamber.

2.3. Membrane Filter Test

Figure 2 shows the schematic of developed air filter test system. Air is pumped to undergo an initial filtration in the foam filter and then flowed through a buffer to collect the air. The collected air is subsequently dried in the diffusion dryer using silica gel. After dehumidification, the air is filtered again using a HEPA filter. The dehumidified air is then flowed with controllable flow rate through the membrane filter under test. The pressure drop, which is the pressure difference of two sides of the membrane filter, is measured using Sensirion SDP600. The pressure drop in this condition was controlled by changing the air flow in the flowmeter 2 while keeping the air flow in the flowmeter 1 constant. As the pressure drop sensor Sensirion SDP600 output is digital, a microcontroller system was employed to process the data.

3. Results and Discussion

3.1. Electrospun fibers

A sheet of cloth was used as a wrapper to the metal drum collector to ensure easy removal of the obtained fibers membrane. In order to produce a desired thick membrane, the electrospinning process lasted for 4 hours. Figure 3 shows a photograph of the obtained membrane on the cloth collector. SEM images of the obtained membranes for different concentrations are presented in Fig. 4. It is shown that the PAN membranes obtained from the concentrations of 6, 9, and 12 wt.% have different fibers diameter distributions with average diameters of 0.6, 0.8, and 1.2 μm, respectively. In
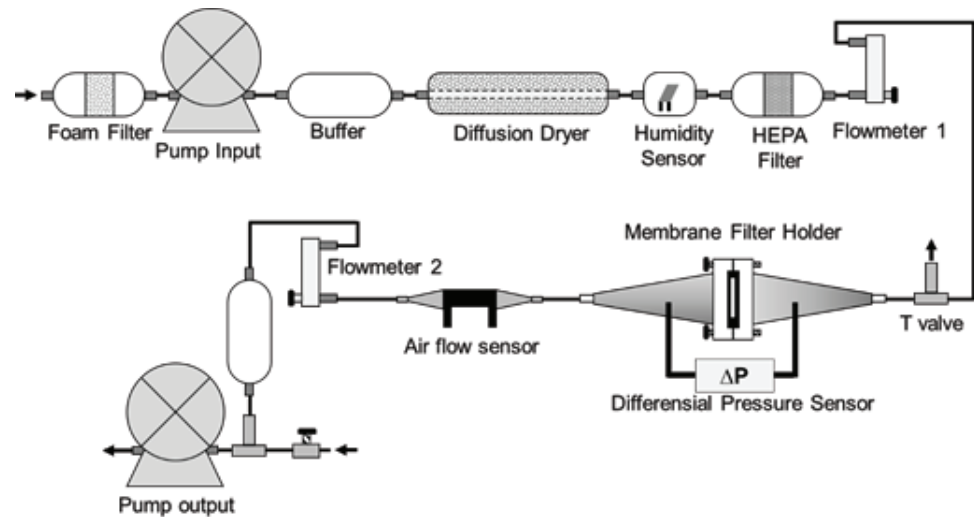
Figure 2: A schematic diagram of the aerosol filter test for pressure drop measurement.

Figure 3: A photograph of PAN nanofibers membrane exfoliated from the cloth collector.

addition, as given in Fig. 4(c), the fibers membrane obtained from 12 wt.% in concentration is more uniformity fiber than the others. This result is similar to those have been reported by Munir, et al. and Zhang, et al. [11,15]. Note that uniform fibers has good characteristic in porosity, and it thus increases the efficiency of filtration.

3.2. Aerosol Filtration Test

Figure 5 shows the pressure drop measurement as a function of air flow. The pressure drop rises with the increase of air flow as described by the Darcy's law stating that the air flow or debit Q is given by Eq. 2.

$$Q = \frac{KA}{L}\Delta p \qquad (2)$$

where Q is the air flow or debit, K is the Darcy constant, A is the area of membrane, L is the thickness of membrane, and Δp is the pressure drop.

Moreover, it has been found that the pressure drop increases with increasing the concentration of polymer solution. It can be explained by looking at Fig. 4 in which the
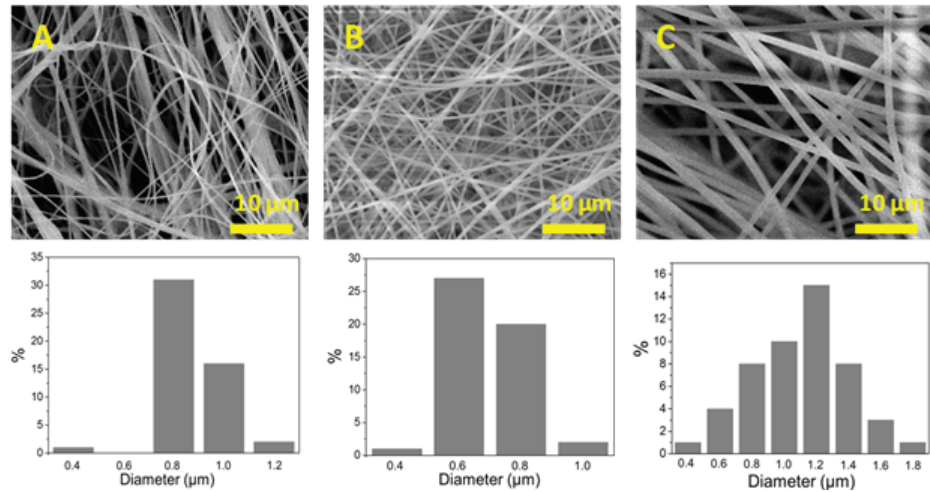
Figure 4: SEM images of PAN membranes obtained from the polymer solution concentrations of (a) 6, (b) 9, and (c) 12 wt.%.
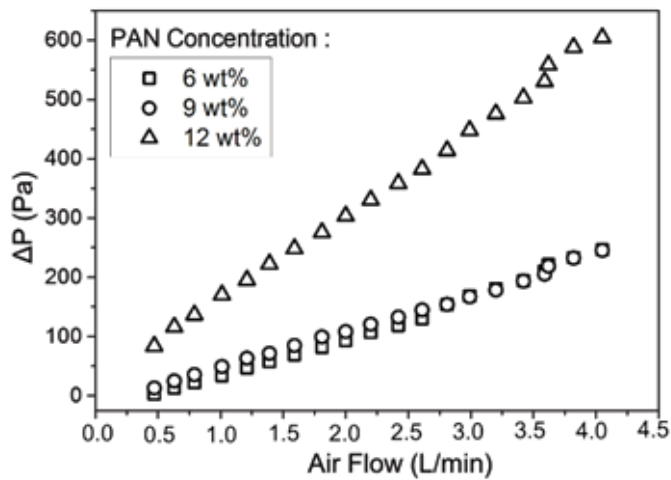
Figure 5: Pressure drop characteristics from each membrane.

average fiber diameter increases with the increase of polymer solution concentration. Larger fiber diameter will make the pores of membrane become smaller and it causes air difficult to flow through the membrane so that the pressure drop increases.

4. Conclusion

Nanofibers membranes of polyacrilonitrille (PAN) has been prepared by using electrospinning with three concentrations (6, 9, and 12 wt.%) of PAN solution. It has been found that the increase of polymer concentration caused the fibers diameter increases and its fibers diameter distribution became more uniform. The membrane obtained from the PAN solution concentration of 12 wt.% had the best morphology because of its homogeneity in fiber diameter, but the highest pressure drop as compared to the concentrations of 6 and 9 wt.%.

Acknowledgement

References

[1] P. I. Jalava, M. S. Happo, K. Huttunen, M. Sillanpää, R. Hillamo, R. O. Salonen, and M. R. Hirvonen, Chemical and microbial components of urban air PM cause seasonal variation of toxicological activity, *Environ Toxicol Pharmacol*, **40**, 375–387, (2015).

[2] R. S. Barhate, C. K. Loong, and S. Ramakrishna, Preparation and characterization of nanofibrous filtering media, *J Membr Sci*, **283**, 209–218, (2006).

[3] K. M. Yun, C. J. Hogan Jr, Y. Matsubayashi, M. Kawabe, F. Iskandar, and K. Okuyama, Nanoparticle filtration by eletrospun polymer fibers, *Chem Eng Sci*, **62**, 4751–4759, (2007).

[4] K. M. Yun, A. B. Suryamas, F. Iskandar, L. Bao, H. Niinuma, and K. Okuyama, Morphology optimization of polymer nanofiber for applications in aerosol particle filtration, *Separ Purif Tech*, **75**, 340–345, (2010).

[5] Z. Wang, C. Zhao, and Z. Pan, Porous bead-on-string poly(lactic acid) fibrous membranes for air filtration, *J Colloid Interface Sci*, **441**, 121–129, (2015).

[6] S. Sundarrajan, K. L. Tan, S. H. Lim, and S. Ramakrishna, Electrospun nanofibers for air filtration applications, *Procedia Eng*, **75**, 159–163, (2014).

[7] M. M. Munir, F. Iskandar, , and K. Okuyama, High performance electrospinning system for fabricating highly uniform polymer nanofibers, *Rev Sci Instrum*, **80**, p. 026106, (2009).

[8] M. M. Munir, F. Iskandar, , and K. Okuyama, A constant-current electrospinning system for production of high quality nanofibers, *Rev Sci Instrum*, **79**, p. 093904, (2008).

[9] H. Widiyandari, M. M. Munir, F. Iskandar, and K. Okuyama, Morphology-controlled synthesis of chromia-titania nanofibers via electrospinning followed by annealing, *Mater Chem Phys*, **116**, 169–174, (2009).

[10] A. B. Suryamas, M. M. Munir, F. Iskandar, and K. Okuyama, Photoluminescent and crystalline properties of $Y_{3-x}Al_5O_{12}:Ce-x(3)$ phosphor nanofibers prepared by electrospinning, *J Appl Phys*, **105**, p. 064311, (2009).

[11] M. M. Munir, A. B. Suryamas, F. Iskandar, and K. Okuyama, Scaling law on particle-to-fiber formation during electrospinning, *Polymer (Guildf)*, **50**, 4935–4943, (2009).

[12] M. M. Munir, M. P. Ekaputra, A. Rajak, et al., Synthesis of antibacterial nanofibrous membrane based on polyacrylonitrile (PAN)/chitosan by electrospinning technique for water purification application, *Adv. Mater. Res.*, **1112**, 76–79, (2015).

[13] M. Abedi, M. Sadeghi, and M. P. Chenar, Improving antifouling performance of PAN hollow fiber membrane using surface modification method, *J. Taiwan Ins. Chem. Eng.*, **55**, 42–48, (2015).

[14] A. Podgorski, A. Balazy, and L. Gradon, Application of nanofibers to improve the filtration efficiency of the most penetrating aerosol particles in fibrous filters, *Chem Eng Sci*, **61**, 6804–6815, (2006).

[15] H. Zhang, H. Nie, D. Yu, C. Wu, Y. Zhang, C. J. B. White, and L. Zhu, Surface modification of electrospun polyacrylonitrile nanofiber towards developing an affinity membrane for bromelain adsorption, *Desalin*, **256**, 141–147, (2010).

KnE Engineering

Knowledge E
Engaging minds

Conference Paper

Predicting the Motion of an Intruder in a Vertically Vibrated 2D-Granular-Bed using Contact Points Approximation

Siti Nurul Khotimah[1], Sparisoma Viridi[1], Widayani[1], Trise Nurul Ain[2], and Hari Anggit Cahyo Wibowo[2]

[1]Nuclear Physics and Biophysics Research Division, Faculty of Mathematics and Natural Sciences, Institut Teknologi, Bandung, Indonesia
[2]Master Program in Physics Teaching, Faculty of Mathematics and Natural Sciences, Institut Teknologi Bandung, Indonesia

Abstract

In this study, 2-dimensional Brazil nut effect experiments were setup. An intruder moves from its initial position at the middle-bottom of a container to its final position at the top of the granular bed. To predict the motion of the intruder, the number of contact points for each grain around the intruder was counted manually for grains in the first layer until the third layer. The average numbers of contact points from grains in each of 8 directions respected to the center of the intruder were calculated to determine the direction of total force acting on the intruder by grains in the first layer, in the first two-layers, and in the first three-layers. The result will be more acceptable using the data of two or three layers of grains in predicting intruder movement.

Keywords: granular materials, vibration, Brazil-nut effect, contact points

🔓 OPEN ACCESS

1. Introduction

Brazil-nut effect (BNE) is a phenomenon when larger grains rise to the top of smaller grains subjected to vibration [1]. The opposite phenomenon when an intruder (larger grain) sinks in a vibrated granular bed (smaller grains) is called reverse Brazil-nut effect [2]. However, it also was found that the position of an intruder in a vibrated granular bed remains unchanged when compaction occurred [3]. There are many points of view to explain this BNE, such as through its phenomenon of void filling [4] and a condensation mechanism [2,5], through its intrinsic properties of grains such as the comparison of mass ratio and diameter ratio of the two grain types [5], the surface roughness of intruder [6], the base roughness of the container [6] and also through the reduction in potential energy of the system [7,8].

BNE occurred in 2-D and pseudo 2-D granular system [9,10,11] where grain configurations can be recorded and the intruder can also be traced automatically, e.g., using OpenCV application [10]. The positions of all grains were determined using a screen snapshot or an image of the system to be digitized using web browser running an HTML equipped with a JavaScript code and represented in pixels [12] and in SI-units [13]. The zigzag trajectory of an intruder in pseudo 2-D granular bed had been observed
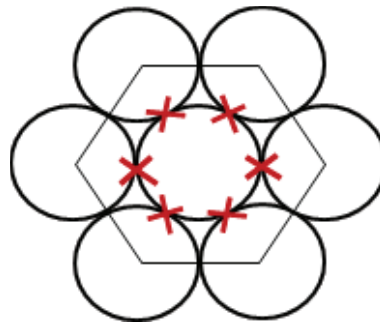
Figure 1: A grain has maximum 6 contact points in hexagonal closed packed arrangement.
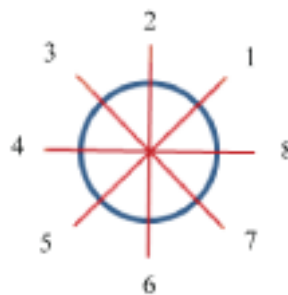

Figure 2: Eight directions with its origin at the center of intruder.

in the previous work [10]. However, when hexagonal closed packed configuration in the granular bed has been attained then the intruder is difficult to move [8,14,15].

This paper discusses about motion of an intruder in a vertically vibrated 2D-granular-bed in which BNE phenomenon occurred. The intruder motion is influenced by the arrangement of grains around the intruder resulted from the vibration. The number of contact points among grains around the intruder is counted to determine the total force acting on the intruder in order to predict the direction of the intruder motion.

2. Theory

In this study, all possible states of a 2-D granular material are visualized by the configurations of the grains and are expressed by the number of contact points among grains. Indeed, contact point is actually a projection of contact line between two grains on a plane which is perpendicular to the line; the plane is the front surface of the 2-D container. The number of contact points on a grain with all its nearest neighbors is counted. Hence, number of contact points is greater for denser grain arrangement. Using thin cylindrical grains, the maximum number of contact points on a grain is 6 that occurred when hexagonal closed packed arrangement established.

It is proposed for simplicity that there are 8 directions which may sufficient to encounter the influences from the nearest grains to predict the direction of the intruder movement as illustrated in Fig 2. Grains nearby an intruder are grouped to be the first layer, second layer, and third layer as shown in Fig 3.
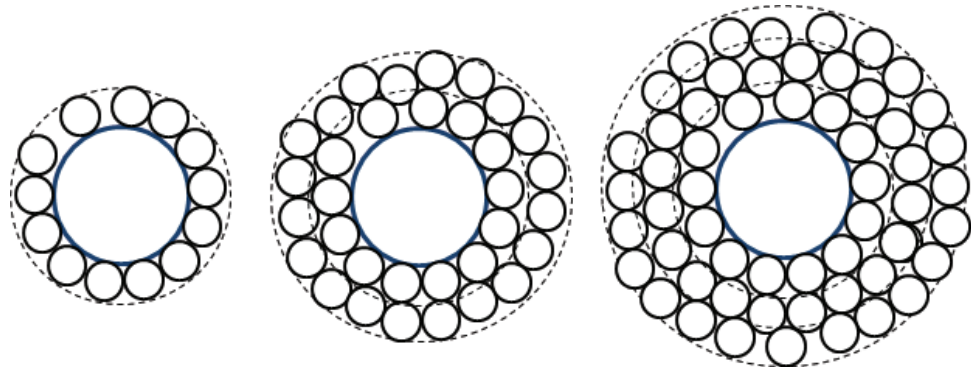
Figure 3: Grains around an intruder: (a) one layer, (b) two layers, and (c) three layers.

The number of contact point for each grain in the first layer, second layer, and third layer around an intruder is counted manually. Pressure is proportional to the number of contact points. It can be seen from Fig. 3 that intruder is subjected to pressure by grains from all direction. If the pressure to the intruder is not the same in all directions then intruder moves toward the region of lower pressure. The total force $\vec{F}_k$ acting on the intruder by N_k grains in k layers (k = 1, 2 or 3) is proportional with the number of contact points as follows:

$$\vec{F}_k \approx -\frac{1}{8} \sum_{i=1}^{8} \bar{c}_{ik} \vec{r}_i \tag{1}$$

$$\bar{c}_{ik} = \frac{\sum_{j=1}^{N_{ik}} c_{ijk}}{N_{ik}}. \tag{2}$$

$\bar{c}_{ik}$ is the average number of contact points of N_{ik} grains inside k layers in direction i with respect to intruder and $\vec{r}_i$ is the position of grains in direction i with respect to intruder

$$\vec{r}_i = \left[\cos\left(\frac{2\pi i}{8}\right), \sin\left(\frac{2\pi i}{8}\right)\right]; \quad i = 1, 2, 3, ..., 8. \tag{3}$$

Since the grain arrangement changes from time to time due to vertical vibrations to the granular bed thus the number of contact points of each grain is a function of time. Therefore, the total force $\vec{F}_k$ acting on the intruder is also a function of time. This total force is used to predict the direction of intruder movement and this prediction is compared to the experimental results of intruder position in the next time step.

3. Experimental Setup

A 2-dimensional Brazil-nut effect experiment was setup with the diameter of intruder and bed granular are 2.4 cm and 0.68 cm respectively in a slab container with sizes 20 cm ×10 cm × 0.2 cm for internal heigh, width, and thickness respectively. The
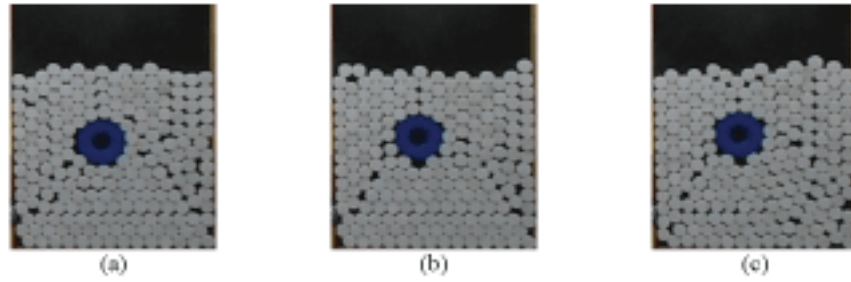
Figure 4: Pictures are taken at different time: (a) t = 84, (b) t = 85 and (c) t = 86.
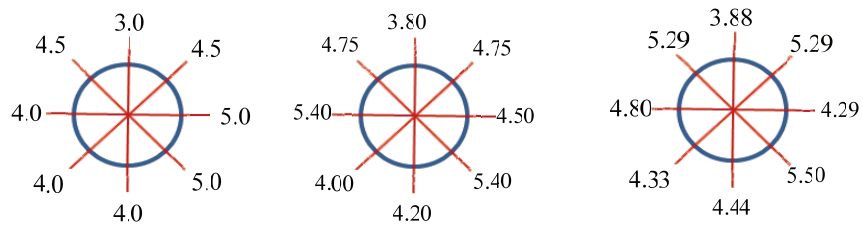

Figure 5: Average numbers of contact points around an intruder for grains at t =84 within: (a) the first layer, (b) the first two- layers, and (c) the first three-layers.

density (g/cm^3) is 0.4375 for intruder and 0.118 for bed granular. The granular system was vertically vibrated with frequency of 14 Hz and constant dimensionless vibration acceleration Γ of 3. In order to give time in taking picture of the granular system, the system was discontinued each time after one-second vibration. Pictures were taken each second from initial observation (t = 1) when intruder at the bottom until at the top of the granular bed (t = 100) [3]. Position of intruder was determined [13] and the number of contact points of each grain around intruder were then obtained manually from the pictures.

4. Results and Discussion

Figure 4 shows three pictures taken sequential at time t = 84, 85 and 86. Position $\vec{R}_t(x, y)$ of intruder at time t = 84, 85 and 86 are $\vec{R}_{84}$ (4.45, 5.26), $\vec{R}_{85}$ (4.26, 5.49), and $\vec{R}_{86}$ (4.24, 5.62) in centimeters with origin of the coordinate is at the bottom of the slab container in the left. Intruder moved to about direction 3 or upper-left from t = 84 to t = 85 and a little bit upward from t = 85 to t = 86.

The average numbers of contact points of grains around the intruder using only the first layer, the first two- layers, and the first three-layers for picture at t =84 are shown in Fig. 5.

In this paper, it is only the direction of total force acting on the intruder was obtained. The direction of the total force $\vec{F}_k \left(F_{kx}, F_{ky} \right)$ at time t = 84 using grains the first layer, the first two-layers, and the first three-layers are $\vec{F}_1$ (−0.21, 0.13), $\vec{F}_2$ (−0.01, 0.04), and $\vec{F}_3$ (−0.04, 0.01). Using the same method for t = 85, it is obtained $\vec{F}_1$ (−0.02, −0.52), $\vec{F}_2$ (0.14, 0.24), and $\vec{F}_3$ (0.11, 0.02). These results show that using grains more than one layer give similar tendency for the total force, i.e. $\vec{F}_2$ and $\vec{F}_3$ have similar directions. The

use of number of contact points of grains in the first layer could give correct direction of total force if there is no empty space (vacancy) in the layer in size of about one grain. Figure 4b shows that there is free space below intruder in size almost one bed particle so that the prediction using one layer is not sufficient. The direction of total force at t = 84 predicted that intruder would move to the upper-left and this is accepted for the intruder movement from t = 84 to t = 85. However, for t = 85, the result predicted that intruder would move upper-right but the experiment showed intruder move upward.

5. Conclusions

Intruder movement in a 2-D vibrated granular bed has been predicted using contact points approximation. The direction of total force acting on intruder can be obtained from the number of contact point of grains around the intruder. The result will be more acceptable using the data of two or three layers of grains since the use of only one layer could not overcome vacancy of a grain.

Acknowledgements

References

[1] R. M. Nedderman, in *Statics and Kinematics of Granular Materials*, Cambridge University Press, 1992.

[2] A. P. J. Breu, H.-M. Ensner, C. A. Kruelle, and I. Rehberg, Reversing the Brazil-nut effect: competition between percolation and condensation, *Phys Rev Lett*, **90**, p. 014302, (2003).

[3] T. N. Ain, in *Evolusi Energi Potensial dan Kontaktopi Material Butiran Dua Dimensi dalam Kasus Kompaksi Penghambat Efek Kacang Brazil, Tesis MPFis*, Institut Teknologi Bandung, Indonesia, 2015.

[4] A. Rosato, K. J. Strandburg, F. Prinz, and R. H. Swendsen, Why the Brazil nuts are on top: size segregation of particulate matter by shaking, *Phys Rev Lett*, **58**, 1038–1040, (1987).

[5] D. C. Hong, P. V. Quinn, and S. Luding, Reverse Brazil nut problem: competition between percolation and condensation, *Phys Rev Lett*, **86**, 3423–3426, (2001).

[6] C.-C. Liao, S.-S. Hsiau, and C.-S. Wu, Combined Effects of Internal Friction and Bed Height on the Brazil-Nut Problem in a Shaker, *Powder Technol*, **253**, 561–567, (2014).

[7] S. Viridi and S. N. Khotimah, Competition between Potential Energy Minimization and Number of Contact Points in Two-Dimension Granular Materials Exhibiting

Brazil-Nut Effect, *Proceeding of International Conference on Mathematics and Natural Sciences (ICMNS 2014)*, (2015).

[8] in *S. Viridi, Novitrian, S. N. Khotimah, dan Widayani, Evolusi Energi Potensial dan Jumlah Titik Kontak Material Butiran Dua Dimensi dalam Kasus Efek Kacang Brazil, Prosiding Seminar Nasional Fisika (SNF 2014)*, , et al., Ed., 149–153, Serpong, Indonesia, 2014.

[9] J. Ellenberger, C. O. Vandu, and R. Krishna, Vibration-induced granular segregation in a pseudo-2D column: The (Reverse) Brazil Nut Effect, *Powder Technol*, **164**, 168–173, (2006).

[10] C. N. Utama, D. N. Persia, R. R. Septiawan, S. N. Khotimah, and S. Viridi, Pemodelan empiris gerak apung intruder pada efek kacang Brasil 2-D dan pengamatannya dengan OpenCV (2013)., Prosiding the 1st Indonesian Student Conference on Science and Mathematics (ISCSM-1), edited by M. A. Martoprawiro et al., Bandung, Indonesia, 24-25 June 2013, in press.

[11] H. A. C. Wibowo, in *Studi Eksperimen Konveksi Granular Pada Efek Kacang Brazil Pseudo Dua-Dimensi dan Dua-Dimensi, Tesis MPFis*, Institut Teknologi Bandung, Indonesia, 2015.

[12] S. Viridi and S. N. Khotimah, Novitrian, Widayani, L. Haris and D.P.P. Aji, Studying Brazil-Nut Effect History Line using Disk-Formed Objects, Scanner, and Web Browser, *International Conference on Advances in Education Technology (ICAET 2014)*, 162–165, (2014)., Eds. Khairurrijal et al.

[13] D. Praja, T. N. Ain, H. A. Cahyo, S. N. Khotimah, and S. Viridi, 2015, Pengembangan Piranti Lunak Digitasi Berbasiskan Web untuk Mengamati Posisi Partikel Bed dan Intruder dalam Efek Kacang Brazil Dua-Dimensi, Prosiding Simposium Nasional Inovasi dan Pembelajaran Sains 2015 (SNIPS 2015), Eds. D. Irwanto et al., Bandung, Indonesia, 8 dan 9 Juni 2015, pp. 5-8.

[14] H.-C. Chang and L.-C. Wang, A Simple Proof of Thue's Theorem on Circle Packing, arXiv:1009.432.v1.

[15] P. J. Skrdla, Atomistic Description of Two-Dimensional Hexagonal Close-Packed Critical Nuclei Exhibiting Quantization of the Activation Energy Barrier, Cryst, *Growth*, **13**, 1970–1977, (2013).

KnE Engineering

Knowledge E
Engaging minds

Conference Paper

The Application of Artificial Neural Networks in Predicting Structural Response of Multistory Building in The Region of Sumatra Island

Reni Suryanita, Hendra Jingga, and Enno Yuniarto

Civil Engineering Department, Faculty of Engineering University of Riau Kampus Bina Widya Jl. HR. Soebrantas KM.12.5 Pekanbaru, Indonesia

Abstract

Artificial Neural Network (ANN) method is a prediction tool which is widely used in various fields of application. This study utilizes ANN to predict structural response (story drift) of multi-story reinforced concrete building under earthquake load in the region of Sumatera Island. Modal response spectrum analysis is performed to simulate earthquake loading and produce structural response data for further use in the ANN. The ANN architecture comprises of 3 layers: an input layer, a hidden layer, and an output layer. Earthquake load parameters from 11 locations in Sumatra Island, soil condition, and building geometry are selected as input parameters, whereas story drift is selected as output parameter for the ANN. As many as 1080 data sets are used to train the ANN and 405 data sets for testing. The trained ANN is capable of predicting story drift under earthquake loading at 95% rate of prediction and the calculated Mean-Squared Errors (MSE) as low as $1.6.10^{-4}$. The high accuracy of story drift prediction is more than 90% can greatly assist the engineer to identify the building condition rapidly due to earthquake loads and plan the building maintenance routinely.

Keywords: Artificial Neural Networks, earthquake load, Mean-Squared Error, response spectrum, story drift

🔓 **OPEN ACCESS**

1. Introduction

Story drift is one of the most important limit states in multi-story building structure design. Building shall not drift excessively to provide better performance and prevent damage to non-structural elements such as walls and doors. Provisions that limit story drift vary depending on which code is used [1-3]. Frequently, story drift governs the design of structural elements rather than strength.

Finite Element Mehod (FEM) is currently the best available method to analyticaly calculate the story drift of multi-story buildings. Performing FEM for such complex buildings could be very tedious to be hand-calculated if not practically impossible. To help in faster and more accurate calculations, many FEM softwares specialized for Civil Engineering application are developed and widely available in the market. However, precisely modeling and running analysis for building structures in FEM softwares is indeed very time-consuming especially for nonlinear and dynamic analysis.Though

How to cite this article: Reni Suryanita, Hendra Jingga, and Enno Yuniarto, "The Application of Artificial Neural Networks in Predicting Structural Response of Multistory Building in The Region of Sumatra Island," *KnE Engineering*, vol. 2016, 6 pages. DOI 10.18502/keg.v1i1.526

Page 1

Finite Element Method for structural analysis is accurate, it is relatively slow. To provide an adequate early prediction on story drift at faster rate, Artificial Neural Network (ANN) method may be used. ANN method is a general prediction tool which is widely used in various fields of application, including Civil Engineering. Many researchers have studied the application of ANN in multystorey shear structure to predict the health of building, such as [4] and [5]. In this study, the ANN is used to predict story drift of reinforced concrete multi-story building under earthquake loading in the region of Sumatra Island. The Sumatra Island is located between the Indo-Australian and Southeastern Eurasian plates. This region has fault slip up to 15 meters occurred near Banda Aceh, Sumatra [6].

Artificial Neural Networks are simplified models of the biological nervous system and have drawn their motivation from the kind of computing performed by a human brain [7]. An Artificial Neural Network is organized into a sequence of layer with full or random connections between the layers. A typical Neural Networks is fully connected, which means there is a connection between each neuron in any given layer to each neuron in the next layer. Artificial Neural Network (ANN) is capable of modeling nonlinear relationship between input and output parameters. ANN works by processing weighted input data using certain algorithm to produce a desired output [8]. The relationship between neurons in ANN is represented by weight factors that will be modified through a training process. If sufficient data sets are available and learning algorithm is correctly chosen, the training process will modify the weight factors by each iteration performed and eventually the desired output will be achieved. The high accuracy of story drift prediction can greatly assist the engineer to identify the building condition rapidly due to earthquake loading in the region of Sumatra Island and plan the building maintenance routinely.

2. Methodology

2.1. Modal Response Spectrum Analysis

The data sets to be fed into the ANN are collected through a Modal Response Spectrum (MRS) analysis. The MRS analysis is performed using Finite Element Method software. The selected reinforced concrete (RC) building models are: Model 1 (10 stories or 40.5 m in total height), Model 2 (15 stories or 60.5 m in total height), and Model 3 (20 stories or 80.5 m in total height) as shown in Fig. 1. For all models, the floor plan is identical (Fig. 2).

The reinforced concrete building models are already proportioned to satisfy the dynamic requirements provided in SNI 1726-2012 [3]. The RC building models are subject to earthquake loading. The design response spectrum functions are obtained from the lastest Seismic Hazard Map for Indonesia. Eight capital cities and three other cities in Sumatera Island are selected as seismic location (eleven in total). By taking three ground conditions (hard, medium, and soft) into account, 33 response spectrum functions are obtained. Then for 3 building models, a total of 1485 story drift data sets are generated from all stories in MRS analysis.
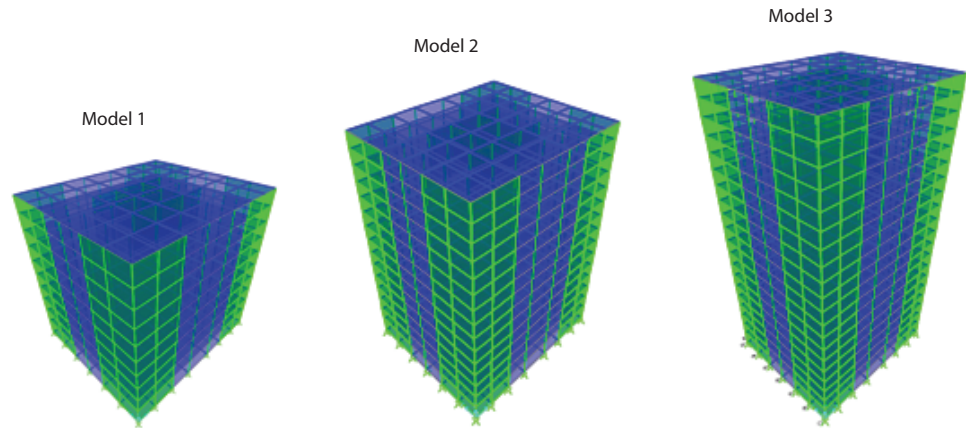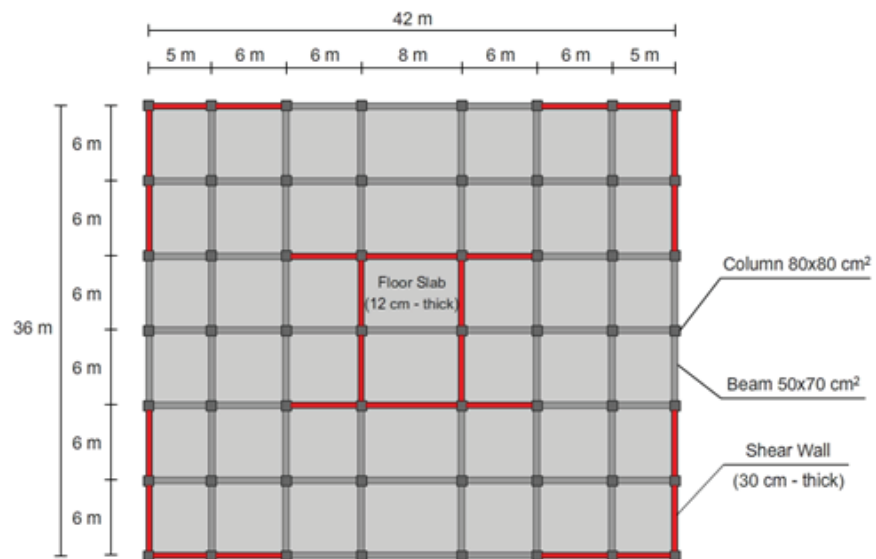
Figure 1: Reinforced Concrete Building Models.

Figure 2: Floor Plan of Reinforced Concrete Building Model.

2.1.1. ANN Architecture

The Neural Network used in this study is Backpropagation ANN (algorithm details can be found at [9]). The ANN architecture consists of 3 layers: input layer, hidden layer, and output layer (Fig. 3). Input layer contains 8 neurons which represent 8 input parameters: 5 earthquake response spectrum function parameters (PGA, S_{DS}, S_{D1}, T_0, Ts), ground or soil condition, and 2 geometric characteristics (total building height and i-th story elevation). Whereas output layer has 2 neurons, that is, to represent story drift in both X and Y horizontal direction. The target story drift data obtained from modal response spectrum analysis is fed into the ANN, and then errors and rate of predictions are calculated. The number of neurons in hidden layer and training parameters such as learning rate, momentum coefficient, and variable normalization range are selected by trial and error to achieve highest rate of prediction. With this architecture, the neural network is intended to learn the capability to predict story drift for any given elevation of the RC building models.
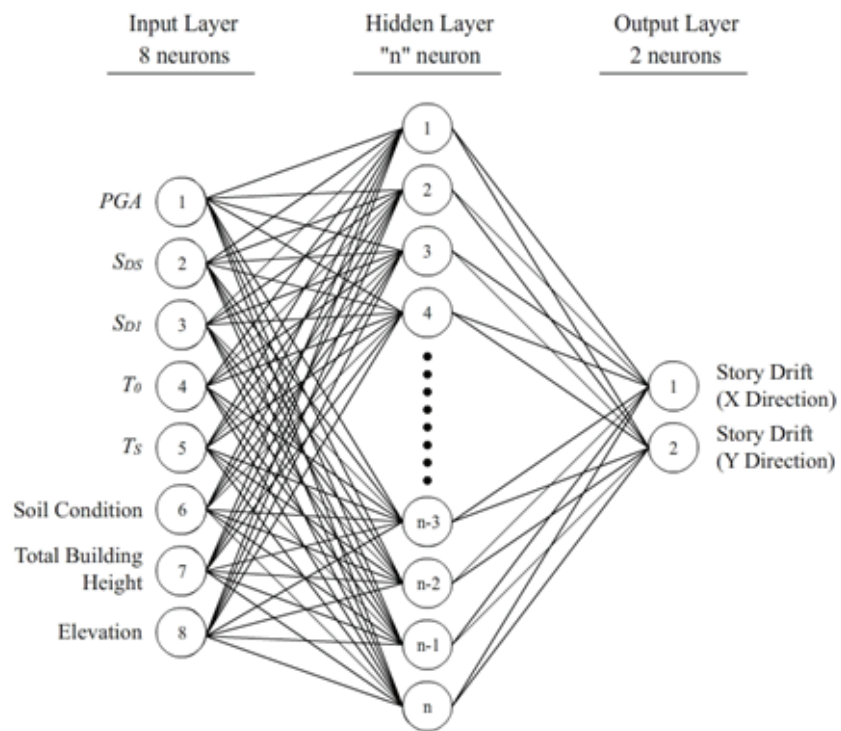
Figure 3: ANN Architecture to Predict Story Drift.

Num.	Seismic Location	Input Parameters								Output Parameters	
		PGA (g)	S_{DS} (g)	S_{D1} (g)	T_0 (sec)	T_s (sec)	Soil Con-dition	Building Height (m)	Eleva-tion (m)	Target Story Drift (X Direction)	Target Story Drift (Y Direction)
1.	B. Aceh	0.621	0.899	0.557	0.124	0.619	0	40.5	4.5	0.0067	0.0075
2.	B. Aceh	0.621	0.899	0.557	0.124	0.619	0	40.5	8.5	0.0146	0.0161
3.	B. Aceh	0.621	0.899	0.557	0.124	0.619	0	40.5	12.5	0.0237	0.0260
4.	B. Aceh	0.621	0.899	0.557	0.124	0.619	0	40.5	16.5	0.0338	0.0368
5.	B. Aceh	0.621	0.899	0.557	0.124	0.619	0	40.5	20.5	0.0442	0.0480
6.	B. Aceh	0.621	0.899	0.557	0.124	0.619	0	40.5	24.5	0.0548	0.0594
...	...	...	...	...	...	...	...	...	...	...	...
1077.	B. Lampung	0.369	0.604	0.587	0.195	0.973	2	80.5	68.5	0.2385	0.2526
1078.	B. Lampung	0.369	0.604	0.587	0.195	0.973	2	80.5	72.5	0.2542	0.2691
1079.	B. Lampung	0.369	0.604	0.587	0.195	0.973	2	80.5	76.5	0.2695	0.2852
1080.	B. Lampung	0.369	0.604	0.587	0.195	0.973	2	80.5	80.5	0.2846	0.3009

TABLE 1: Story Drift Data Sets for ANN Training Process.

3. Discussion

The story drift data sets obtained from MRS analysis is tabulated in Table 1 and Table 2. The 1080 data sets in Table 1 is related to 8 capital cities in Sumatera Island as seismic location, whereas another 405 data sets in Table 2 is related to 3 other cities in Sumatera Island as seismic location. Table 1 and Table 2 is used for ANN training and testing process respectively.

Based on trial and error process, the ANN achieve the lowest error with 24 neuron at hidden layer and the following training parameters; learning rate 0.1, momentum coefficient 0.1, variable normalization range 0 ~ 0.5.

Num.	Seismic Location	Input Parameters								Output Parameters	
		PGA (g)	S_{DS} (g)	S_{D1} (g)	T_0 (sec)	T_s (sec)	Soil Condition	Building Height (m)	Elevation (m)	Target Story Drift (X Direction)	Target Story Drift (Y Direction)
1.	Dumai	0.143	0.221	0.22	0.2	0.998	0	40.5	4.5	0.0017	0.0019
2.	Dumai	0.143	0.221	0.22	0.2	0.998	0	40.5	8.5	0.0036	0.0042
3.	Dumai	0.143	0.221	0.22	0.2	0.998	0	40.5	12.5	0.0058	0.0067
4.	Dumai	0.143	0.221	0.22	0.2	0.998	0	40.5	16.5	0.0083	0.0095
5.	Dumai	0.143	0.221	0.22	0.2	0.998	0	40.5	20.5	0.0109	0.0124
6.	Dumai	0.143	0.221	0.22	0.2	0.998	0	40.5	24.5	0.0135	0.0153
...	...	...	...	...	...	...	...	...	...	...	...
402.	Bukittinggi	0.611	0.915	0.969	0.212	1.059	2	80.5	68.5	0.3936	0.4172
403.	Bukittinggi	0.611	0.915	0.969	0.212	1.059	2	80.5	72.5	0.4195	0.4444
404.	Bukittinggi	0.611	0.915	0.969	0.212	1.059	2	80.5	76.5	0.4448	0.4710
405.	Bukittinggi	0.611	0.915	0.969	0.212	1.059	2	80.5	80.5	0.4697	0.4970

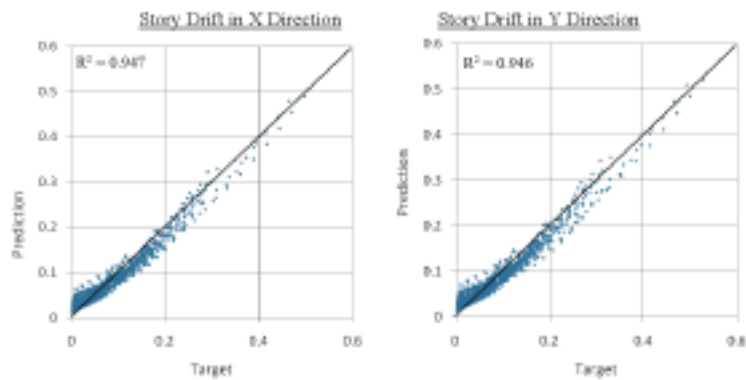TABLE 2: Story Drift Data Sets for ANN Testing Process.

Figure 4: Target vs. Prediction Plot for Story Drift at Training Process.
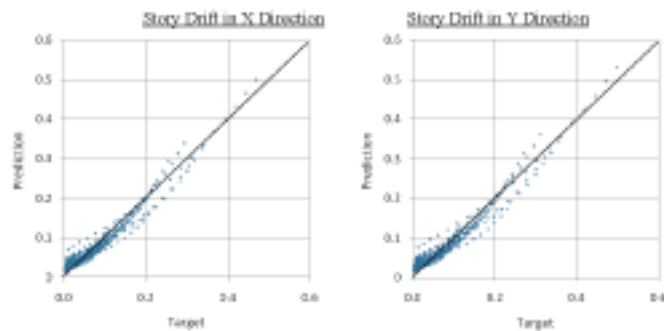

Figure 5: Target vs. Prediction Plot for Story Drift at Testing Process.

After 5000 iterations with the configurations stated above, the calculated MSE at training and testing process is 1.7×10^{-4} and 1.9×10^{-4}, respectively. Fig. 4 and Fig. 5 shows the target vs. prediction plot for story drift at training and testing process. From the plots, it can also be seen that the trained ANN has 95% of prediction rate, which indicates that the trained ANN is capable of predicting story drift at adequate accuracy especially at higher elevation on the building.

4. Summary

After 5000 iterations during ANN training with 1080 data sets, the rate of prediction is calculated as high as 95 percent and MSE is 1.6×10^{-4}. From this study, it can be concluded that ANN is a very promising tool to provide early prediction on structural response such as story drift at multi-story building in the region of Sumatra Island to assist further FEM analysis.

References

[1] in *FEMA 273 NEHRP guidelines for the seismic rehabilitation of buildings*, **1**, Federal Emergency Management Agency, Council, B.S.S., U.S.F.E.M. Agency, and A.T. Council, 1997.

[2] C. Yang, Study on Indonesian Seismic Code SNI 03-1726-2002 and Seismic Impact to High-rise Buildings in Jakarta, Indonesia, *Proceedings of World Academy of Science: Engineering and Technology*, p. 50, (2009).

[3] SNI-1726-2012, Standar Perencanaan Ketahanan Gempa Untuk Struktur Bangunan Gedung, 2012, Badan Standarisasi Nasional.

[4] D. M. Sahoo, A. Das, and S. Chakraverty, Interval data-based system identification of multistorey shear buildings by artificial neural network modelling, *Archit Sci Rev*, 1–11, (2014).

[5] M. Vafaei, A. Adnan, and A. B. Abd Rahman, Real-time Seismic Damage Detection of Concrete Shear Walls Using Artificial Neural Networks, *J Earthquake Eng*, **17**, 137–154, (2012).

[6] T. Lay, H. Kanamori, C. J. Ammon, M. Nettles, S. N. Ward, R. C. Aster, S. L. Beck, S. L. Bilek, M. R. Brudzinski, R. Butler, H. R. DeShon, G. Ekström, K. Satake, and S. Sipkin, The great Sumatra-Andaman earthquake of 26 December 2004, *Science*, **308**, 1127–1133, (2005).

[7] S. Rajasekaran and G. AV. Pai, in *Neural Network, Fuzzy logic, and Genetic Algorithms Syntesis and Applications*, Prentice Hall of India, New Delhi, 2007.

[8] V. S. Kanwar, et al., Monitoring of RCC structures affected by earthquakes, *Geomatics Nat Hazards Risk*, 1–29, (2014).

[9] I. A. Basheer and M. Hajmeer, Artificial neural networks: fundamentals, computing, design, and application, *J Microbiol Methods*, **43**, 3–31, (2000).

Conference Paper

Development of a FAHP Algorithm Based Performance Measurement System for Lean Manufacturing Company

Anita Susilawati[1] and John Tan[2]

[1]Mechanical Engineering Department, University of Riau, Pekanbaru 28293, Indonesia
[2]Mechanical and Construction Engineering Department, Northumbria University, Newcastle, NE1 8ST, United Kingdom

Abstract

For companies that implement Lean Manufacturing, it is essential to measure the extent of success in terms of the achievements of optimum performances. This paper describes the development of a Fuzzy Analytical Hierarchy Process (FAHP) algorithm based Performance Measurement System (PMS) application software for lean companies. The PMS software, which was developed using the C++ language, was designed as a decision making system to aid lean manufacturing companies. The software allows decision making analysis based FAHP facilitating data input, pairwise comparisons, weight calculation and lean company scores. A case study of a lean manufacturing is presented to illustrate the theoretical and practical aspects of the PMS software. The case study demonstrated the software tool can assent to a lean company to implement PMS in a much easier manner yielding more accurate and consistent results that include a list of recommended actions to address issues identified. Therefore, it can improve the company performance.

Keywords: Fuzzy AHP based Algorithm, Lean Manufacturing, Performance Measurement

1. Introduction

Developing a Performance Measurement System (PMS) which fosters continuous improvement and is based on a company's strategy and characteristics of its processes can be challenging due to, amongst other factors, the diversity of criteria, activities and companies' strategic preferences. The traditional approaches to PMS, which is based purely on financial measures, may not be adequate to measure the performance of lean companies due to the relatively wide range of financial and non-financial characteristics and specific lean related tools and techniques which they employ in their activities.

Ohno [1] from Toyota Production System (TPS) defined lean manufacturing as activities that involve value-added work, continuously removing waste and non-value added work. The characteristics of lean manufacturing were identified by Shah and Ward [2] as continuous improvement, waste elimination, quality improvement, low inventories, short cycle times, process control, supplier development, pull system,

How to cite this article: Anita Susilawati and John Tan, "Development of a FAHP Algorithm Based Performance Measurement System for Lean Manufacturing Company," *KnE Engineering*, vol. 2016, 7 pages. DOI 10.18502/keg.v1i1.527

Page 1

continuous flow, quick changeover, preventive maintenance, statistical process control, employee and customer involvement. Womack *et al* [3]; Ferdousi & Ahmed [4] identified lean characteristics such as value stream mapping, just-in-time production, 5S, error proofing, work standardized, kanban and automation.

By clearly identifying the lean characteristics, it is then possible to design a PMS that effectively measures performances in companies that implement lean systems. The extent to which a company implements lean systems and the success factors depend on a set of consistent lean characteristics that are linked with the PMS. Therefore, a clear definition of lean characteristics is an important pre-requisite in the measurement and monitoring of a company's performance with respect to lean manufacturing activities.

This paper makes use of accepted lean manufacturing characteristics as the basis for the development of a PMS. In terms of its underpinning theory, the widely accepted Fuzzy Analytical Hierarchy Process (FAHP) is adopted so as to handle the inherent vagueness and Multiple Criteria Decision Making (MCDM) nature of lean performance measurement. The FAHP method, which is a result of combining AHP (Analytical Hierarchy Process) with the fuzzy concept, has been applied to many areas since being introduced by Laarhoven & Pedrycz [5] followed by several other authors [6-10]. Noci & Toletti [6] applied FAHP to identify quality based priorities. The FAHP was also applied in the selection of suppliers based on the most satisfaction criteria for the decision maker [7]. Kabir & Hasin [8] stated that the FAHP was more balance scale of judgment and it was not containing subjective judgment in terms of selection and preference of decision-makers. Regarding Lee *et al*. [9], the FAHP can obtain the relative importance in real practice where an uncertain pairwise comparison environment exists. Furthermore, according Tan *et al.* [10], it can be used to account for variations in degrees of confidence, such as nuances/traces.

In terms of the AHP method, algorithm program applications are available, such as the "Expert Choice" to solve the AHP implementation problems (Expert Choice, 2012) [11]. However, to the author's knowledge, the FAHP commercial algorithm program is not available. Therefore, this paper developed the algorithm program for lean manufacturing PMS. The PMS is implemented as a software tool developed using the C++ language so that practitioners can apply this PMS without having to perform the tedious and complicated computations associated with FAHP.

2. Methodology

The PMS for lean company can be developed based on the characteristics of lean such as discussed in Introduction. This paper employed a set of lean company characteristics based on lean manufacturing performance in Susilawati *et al* [12] and [13]. The PMS for lean manufacturing companies is based on a MCDM method, the FAHP. The FAHP method is a systematic approach using the concepts of fuzzy set theory and hierarchical structure analysis, which makes it more effective than conventional Analytical Hierarchy Process (AHP) in real implementation when choice, ranking and decision problems are encountered. An algorithm in the form of a FAHP program is

developed using the C++ language. The flowchart of the design steps of algorithm PMS using FAHP is shown in Fig. 1. The steps for FAHP used in this paper: establish a decision group, members of the decision groups make a judgment on the importance of the lean manufacturing activities, aggregate judgments of the decision maker, check consistence, and calculate the weight.

The members of the decision group make a judgment of relative preference and importance of one lean practice parameter over another with a pairwise comparison. Due to the vagueness of the judgment, the score awarded to the pairwise lean practice does not exactly represent the real condition. The crisp score awarded by a member of the decision group is then transformed into a fuzzy number, in order to capture the vagueness. Because the decision maker cannot reach 100% confidence in their judgment, this degree of confidence should be captured in the FAHP method. Next, the fuzzy pairwise comparison from several decision makers is combined to form an overall group decision then aggregated. The decision makers can revise and make right the decision-maker/assessor inconsistency when making pairwise comparisons, which are checked by the Consistency Ratio (CR). The CR is a comparison between Consistency Index (CI) and Random Index (RI) [14]. The CR can reflect the decision maker/assessor understanding on his/her own preferences. If the CR is >0.10, the decision-maker should re-evaluate his/her pairwise comparisons [14]. Finally, the weight of lean practices is calculated. By inputting the information and data of current state of lean activities and establishing the base line and target improvement lean activities are then revealed as the final score of lean company. These performance scores will give the managers and decision makers some real insights into the lean company's activities and their company's performance.

3. Tool Evaluation

The lean manufacturing PMS's algorithm program has been applied as a case study for an automotive company in the Indonesian manufacturing industry. The company needed to measure and to improve the company's overall performance by achieving the company's strategic goals, which use six specific perspectives: financial perspectives, supplier issues customer issues, process, people and future (Fig. 2). Fig. 3 presents the pairwise comparisons and degree of confidence for the assessors. The scores of performance of the company are presented in Fig. 4.

Fig. 4 demonstrates the competitive business priority on a company performance and in this instance is defined based on the financial perspectives and customer issues (the computer software has been designed with complete flexibility to allow companies to tailor the performance based on their needs). The current lean score is 0.208 for the financial perspectives and 0.023 for supplier issues. The optimum lean score target, which can be achieved for next year is 0.297 for the financial perspectives and 0.262 for customer issues. The current overall score for the lean activities in the perspectives performance impact with regards to overall performance scores is 0.574.

It can be seen that last year's achievements are used as a baseline score for every lean activity. In this case, due to the lean manufacturing PMS started in this current
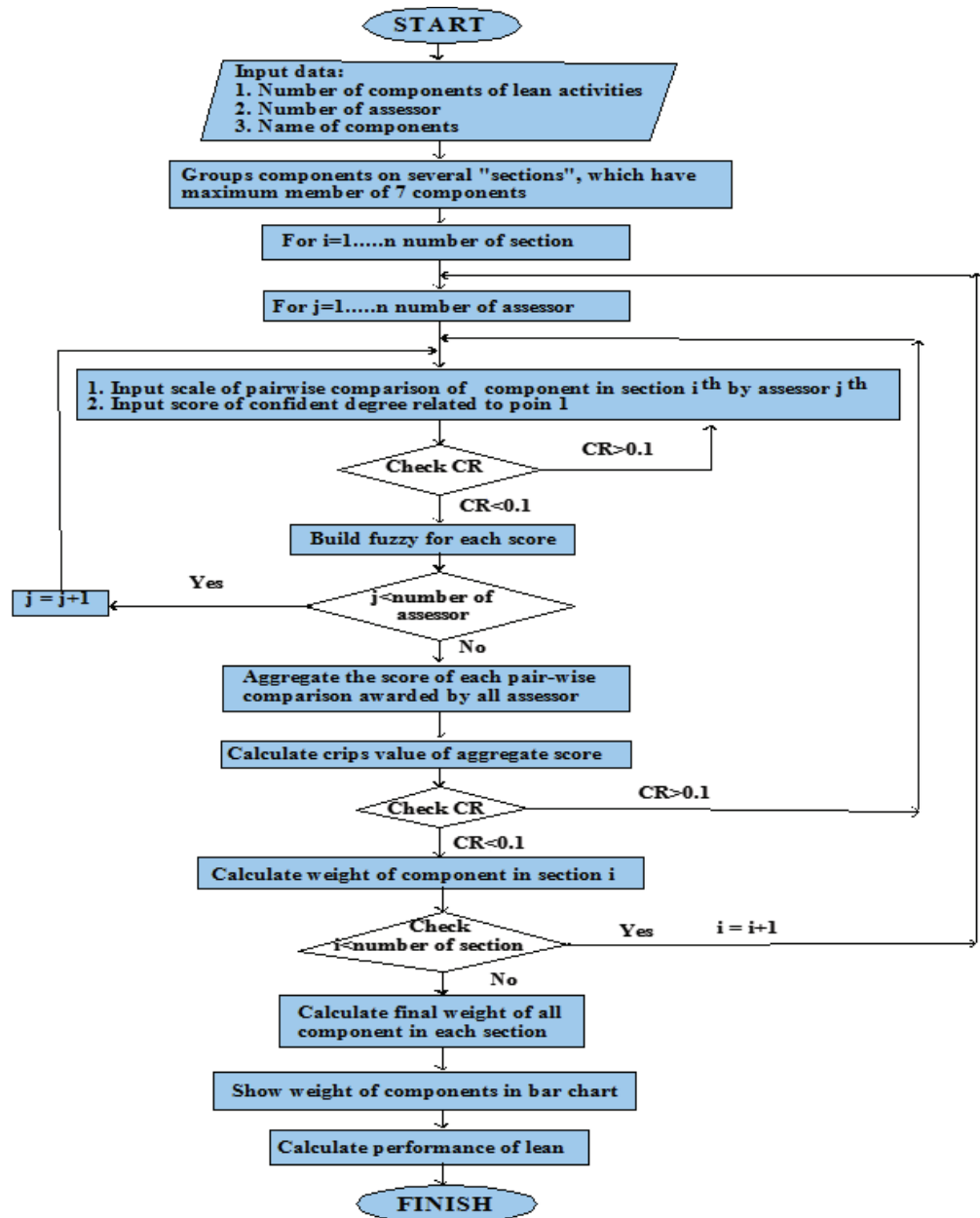
Figure 1: Flowchart to develop the FAHP algorithm program for lean manufacturing PMS.

year, the baselines were set to zero. The target improvement is the change needed to achieve the company's future state. This was obtained from the differences between the current results and the base lines. The current results were collected from the company's data, which is the difference in the current year's state and last year's state. The lean score for the current condition was calculated as a real achievement (current results) divided by target improvement and multiplied by the weight of the lean activities for a given time period. In this case, the period of time is 1 year. Future-state is at 100%, due to the fact that it was established as an optimum, in order to achieve improvement.
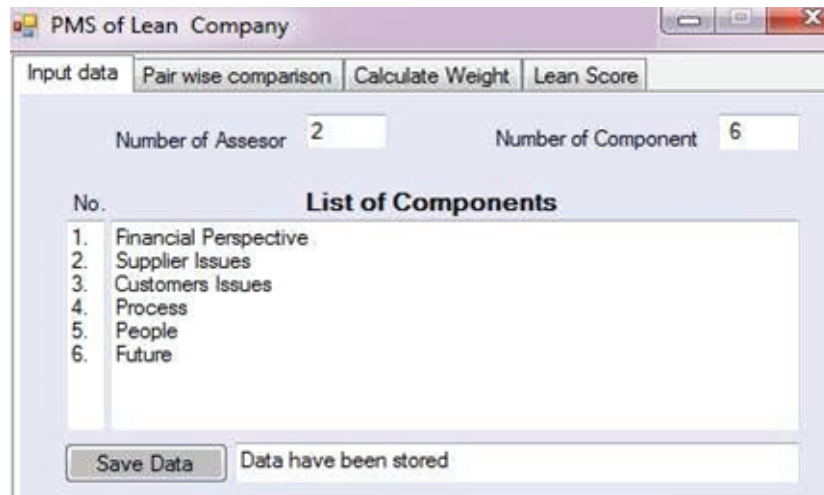
Figure 2: Input data by assessors for components of the lean performance perspectives.
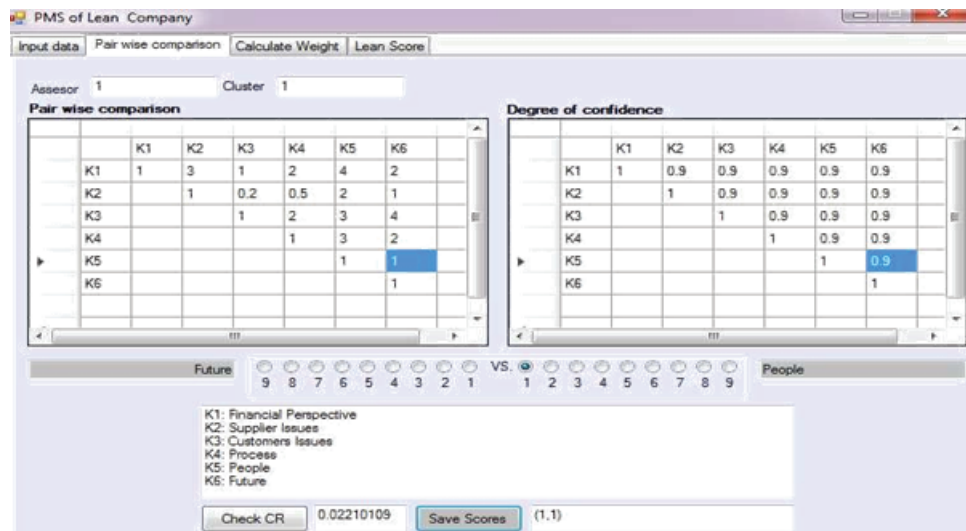

Figure 3: Pairwise comparisons by a member of group decision maker for the lean performance perspectives and its degree of confidence.

4. Summary

This paper describes a PMS model for lean company in the form of computer software tool. The software tool is flexible and practical, allowing practitioners to apply PMS in companies that vary in size and system, within a range of industries and can help a company to measure its progress toward its goals and enable decisions to be made on its strategies and activities for continuous improvement. The case study revealed that the software tool easily implemented and work well with a number of advantages: data obtained from the assessment have better accuracy considering the vagueness and degree of confidence of assessors in the scores that they provided; data analysis can be done more easily and accurately so that the companies could facilitate the process of planning activities of lean manufacturing in the future.
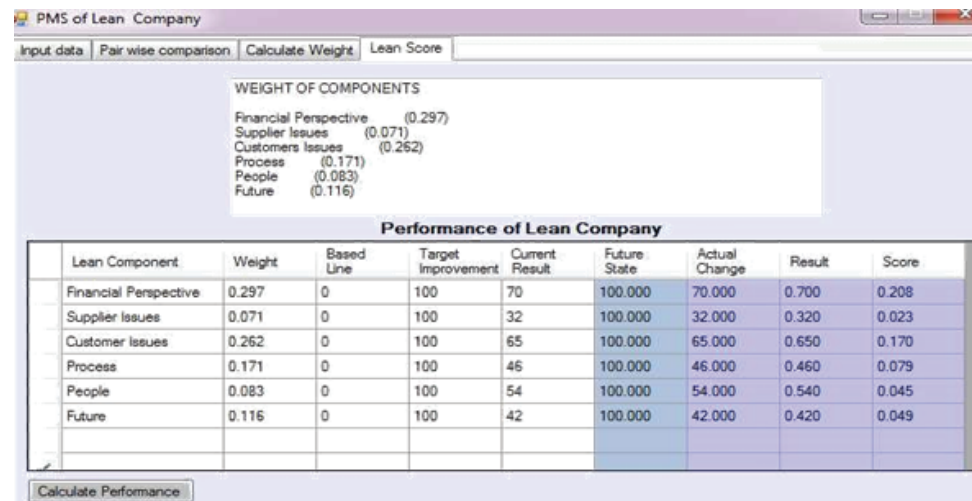
Figure 4: The performance scores of the lean company.

References

[1] R. Shah and P. T. Ward, Defining and developing measure of lean production, *J Oper Manage*, **25**, 155–166, (2007).

[2] T. Ohno, in *The Toyota Production System: Beyond Large-scale Production*, Productivity Press, Portland, OR, 1988.

[3] J. P. Womack, D. T. Jones, and D. Ross, in *The Machine That Changed the World*, Macmillan, New York, 1990.

[4] F. Ferdousi and A. Ahmed, A manufacturing strategy: an overview of related concepts, principles and techniques, *Asian J. Bus. Manage*, **2**, 35–40, (2010).

[5] P. J. M. Van Laarhoven and W. Pedrycz, A fuzzy extension of Saaty's priority theory, *Fuzzy Sets Syst*, **11**, 229–241, (1983).

[6] G. Noci and G. Toletti, Selecting quality based programmes in small firms: a comparison between fuzzy linguistic approach and analytic hierarchy process, *Int J Prod Econ*, **67**, 113–133, (2000).

[7] F. T. S. Chan and N. Kumar, Global supplier development considering risk factors using fuzzy extended AHP-based approach, *Omega Int. J. Manage Sci*, **35**, 417–431, (2007).

[8] G. Kabir and M. AA. Hasin, Evaluation of customer oriented success factors in mobile commerce using fuzzy AHP, *J. Ind Eng. Manage*, **4**, 361–386, (2011).

[9] A. H. I. Lee, W. C. Chen, and C. J. Chang, A fuzzy AHP and BSC approach for evaluating performance of IT department in the manufacturing industry in Taiwan, *Expert Syst Appl*, **34**, 96–107, (2008).

[10] R. R. Tan, L. MA. Briones, and A. B. Culaba, Fuzzy data reconciliation in reacting and non-reacting process data for life cycle inventory analysis, *J Clean Prod*, **15**, 944–949, (2007).

[11] Expert Choice (2012), Expert Choice Desktop, Information on: `http://www.expertchoice.com/productsservices/expertchoicedesktop/,` (Accessed 19/10/2012).

[12] A. Susilawati, J. Tan, D. Bell, and M. Sarwar, Develop a framework of performance measurement and improvement system for lean manufacturing activity, *Int. J. Lean Think*, **4**, 51–64, (2013).

[13] A. Susilawati, J. Tan, D. Bell, and M. Sarwar, Fuzzy logic based method to measure degree of lean activity in manufacturing industry, *J Manuf Syst*, **34**, 1–11, (2015).

[14] T. L. Saaty and L. G. Vargas, in *Models, Methods, Concepts and Applications of the Analytic Hierarchy Process*, Kluwer Academic Publishers, Norwell, 2001.